FEB 2 4 1950

THE PHYSICAL REVIEW

Vol. 77 Second Series NUMBER 4

FEBRUARY 15, 1950

Published for the

AMERICAN PHYSICAL SOCIETY

by the

AMERICAN INSTITUTE OF PHYSICS

Lancaster, Pa. and New York, N. Y.

THE PHYSICAL REVIEW

A journal of experimental and theoretical physics established by E. L. Nichols in 1893

Published by the American Institute of Physics for the

AMERICAN PHYSICAL SOCIETY

Officers

President

L. I. RABI
Columbia University
New York, New York

Vice-President

C. C. LAURITSEN
California Institute of Technology
Pasadena, California

Secretary

K. K. DARROW
Bell Telephone Laboratories
Office:
Columbia University
New York 27, New York

Treasurer

G. B. PEGRAM
Columbia University
New York 27, New York

Local Secretary for the Pacific Coast

J. KAPLAN
University of California at Los Angeles
Los Angeles, California

Managing Editor

JOHN T. TATE
University of Minnesota
Minneapolis, Minnesota

BOARD OF EDITORS

Editor

JOHN T. TATE

Assistant Editor

J. W. BUTLER

Associate Editors

S. A. GOUDSMIT — W. E. LAMB, JR. — HARVEY BROOKS
L. M. PURCELL — R. G. HERB — R. F. CHRISTY
K. T. WHITMOW — J. BARDEEN — ERWIN HAHN

Manuscripts for publication should be submitted to John T. Tate, University of Minnesota, Minneapolis, Minnesota. The authors' institutions are requested to pay a publication charge of $8 per page which, if honored, entitles them to 100 free reprints. Instructions will be sent with galley proofs.

Send all correspondence concerning papers in the process of publication should be addressed to the Publication Manager, American Institute of Physics, 57 East 55 Street, New York 22, New York.

Subscription Price

United States and Canada $25.00
Elsewhere $27.00

Back Numbers[1]

Yearly back number rate when complete year is available:
Prior to 1949: $20.00
Thereafter: $27.00
Single copies: $2.00 each, prior to July, 1929;
$1.00 each, July, 1929–December, 1941;
$2.00 each, January, 1942–December, 1946;
$1.00 each, January, 1947–December, 1948;
$1.25 each, thereafter.
General index, 1893–1920: $4.00.

Subscriptions and orders for back numbers should be addressed to Prince and Lemon Streets, Lancaster, Pennsylvania, or to the American Institute of Physics, 57 East 55 Street, New York 22, New York.

Changes of address in the case of members of the American Physical Society should be addressed to the Treasurer; in the case of other subscribers to the Circulation Manager, American Institute of Physics.

[1] For Series I issues of Physical Review, Cornell University, Ithaca, New York.

The Physical Review is published semi-monthly at Prince and Lemon Streets, Lancaster, Pennsylvania.

Entered as second-class matter March [illegible], at the Post Office at Lancaster, Pennsylvania, under the Act of March 3, [illegible].

Acceptance for mailing at special rate of postage provided for in paragraph (d-2), section 34.40, P. L. & R. of 1948, authorized January 27, [illegible].

THE
PHYSICAL REVIEW

A journal of experimental and theoretical physics established by E. L. Nichols in 1893

SECOND SERIES, VOL. 77, NO. 4 FEBRUARY 15, 1950

Penetration and Diffusion of X-Rays. V. Effect of Small Deflections upon the Asymptotic Behavior

U. FANO, H. HURWITZ, JR.* AND L. V. SPENCER
Knolls Atomic Power Laboratory, Schenectady, New York, and *National Bureau of Standards, Washington, D. C.*†
(Received October 17, 1949)

The effect of small angular deflections upon the asymptotic trend of the x-ray intensity requires that the constant K_0 in the earlier formula $x^{K_0}\exp(-\mu_0 x)$ be replaced with the eigenvalue of an equation due to Wick.

AN expression for the asymptotic variation of x-ray intensity at great depths within a barrier was presented in the first[1] of a series of recent papers.[2-4] The treatment disregarded the effect of the small angular deflections which accompany small energy degradations by Compton scattering. In this note we wish to correct for this effect. However, we still limit our treatment, as in I, to the case where the absorption coefficient increases monotonically as the photon energy decreases. Progress has been facilitated by the application of the methods developed by Wick[5] for the analogous problem of neutron diffusion.

We consider the spectral energy density[2] $Y(x, \lambda, \omega)$ for photons of wave-length λ (in Compton units) at a depth x and traveling in a direction ω. The Laplace transform of Y with respect to the variable x obeys an equation analogous to (3, II):

$$(\mu - p\cos\theta)y(p,\lambda,\omega) = \int_{\lambda_0}^{\lambda} k(\lambda',\lambda)d\lambda' \times \int_{4\pi} d\omega' \delta(1-\omega\cdot\omega'-\lambda+\lambda')y(p,\lambda',\omega')/2\pi + \lambda_0 k(\lambda_0,\lambda)\delta(1-\cos\theta-\lambda+\lambda_0)/2\pi(\mu_0-p), \quad (1)$$

where θ is the angle between ω and the x axis.

It has been shown[1] that the asymptotic behavior of Y for large x depends entirely on the behavior of Y or y for λ very near λ_0. Therefore the following simplifying assumptions appear fully justified for a strictly asymptotic treatment:[2]

(a) $\mu \sim \mu_0 + \dot{\mu}_0(\lambda-\lambda_0)$
(b) $k(\lambda',\lambda)\sim C$
(c) $\omega\cdot\omega' \sim 1 - |\omega-\omega'|^2/2$
(d) $\cos\theta \sim 1-\theta^2/2$.

Wick's method proceeds by applying a Laplace transformation in λ and a Fourier transformation in ω. To this end one multiplies (1) by $\exp[-\eta(\lambda-\lambda_0) + i\eta^{\frac{1}{2}}\sigma\cdot\omega]/2\pi$ and integrates over λ and ω. The resulting equation is:

$$\{\mu_0 - p - \dot{\mu}_0[\partial/\partial\eta - 1/\eta - (\sigma/2\eta)\partial/\partial\sigma] - (p/2\eta)\Delta_\sigma\}W(p,\eta,\sigma) = (C/\eta)\exp(-\sigma^2/2)W + \lambda_0 C\exp(-\sigma^2/2)/2\pi(\mu_0-p). \quad (2)$$

Still following Wick, we write:

$$W(p,\eta,\sigma) = \sum_{n=0}^{\infty} a_n(p,\eta)U_n(\sigma)\exp(\dot{\mu}_0\sigma^2/4p),$$

where U_n is the n-th eigenfunction with cylindrical symmetry of the equation:

$$[(p/\dot{\mu}_0)\Delta_\sigma/2 - (\dot{\mu}_0/p)\sigma^2/8 + 1/2 + (C/\dot{\mu}_0)\exp(-\sigma^2/2)]U + QU = 0. \quad (4)$$

The functions a_n can be calculated by solving first order linear differential equations. The asymptotic behavior of $Y(x, \lambda, \omega)$ can then be determined by

* Knolls Atomic Power Laboratory.
† Work supported by an ONR contract.
[1] Bethe, Fano, and Karr, Phys. Rev. **76**, 538 (1949).
[2] U. Fano, Phys. Rev. **76**, 739 (1949).
[3] P. R. Karr and J. C. Lamkin, Phys. Rev. **76**, 1843 (1949).
[4] L. V. Spencer and F. Jenkins, Phys. Rev. **76**, 1885 (1949).
[5] G. C. Wick, Phys. Rev. **75**, 738 (1949), especially p. 753 ff.

TABLE I. Set of values of $-Q_0$ obtained by the various methods

Material	Energy	$\mu_0/\dot{\mu}_0$	$K_0=C/\dot{\mu}_0$	$-Q_0$ Perturbation	Variation	(Moment methods) Expansion	Iteration
C	5.10 Mev	0.19	1.07	0.92	0.92	0.92	0.92
	2.55	0.36	1.39	1.08	1.08	1.09	1.07
	1.70	0.57	1.77	1.25	1.26	1.29	1.23
Al	5.10	0.25	1.30	1.07	1.07	1.07	1.07
	2.55	0.40	1.53	1.17	1.17	1.19	1.16
	1.70	0.59	1.83	1.28	1.29	1.33	1.26
Cu	5.10	0.64	2.8	2.00	2.00	2.14	1.93
	2.55	0.94	1.95	1.41	1.42	1.47	1.39
	1.70	0.63	1.92	1.33	1.34	1.39	1.31
Sn	2.55	0.78	2.6	1.75	1.76	1.87	1.72
	1.70	0.65	1.90	1.30	1.31	1.36	1.28
	1.28	0.74	1.87	1.23	1.24	1.28	1.21
Pb	1.70	0.57	1.40	0.97	0.98	1.00	0.98
	1.28	0.56	1.15	0.79	0.80	0.81	0.79
	1.02	0.60	1.04	0.70	0.70	0.71	0.70

examining the properties of the successive inverse transformations. One finds the asymptotic formula:

$$Y(x, \lambda, \omega) \sim x^{-Q_0} \exp(-\mu_0 x) f(\lambda, \omega) \qquad (5)$$

which is analogous to (11), (12a), and (13a) of II.** Here Q_0 is the lowest eigenvalue of (4) when $p=\mu_0$; and $f(\lambda, \omega)$ is a function whose behavior is immaterial for our present purpose.

Our main problem lies in the determination of $-Q_0$, which takes the place that $K_0=C/\dot{\mu}_0$ held in I and II. The effects of angular deflections are small when $\mu_0/\dot{\mu}_0$ is small; and $Q_0 \to -C/\dot{\mu}_0$ in the limit when $\mu_0/\dot{\mu}_0 \to 0$.

In many interesting cases, $\mu_0/\dot{\mu}_0$ lies between 0.2 and 0.8 and one can attack the eigenvalue problem (4) by a perturbation method starting from the limit $\mu_0/\dot{\mu}_0 \to 0$. (In this limit (4) reduces to the Schrödinger equation for a two-dimensional oscillator.) The perturbation method yields:

$$-Q_0 = K_0 + 1/2 - \alpha/2 + K_0\epsilon^2/\alpha(\alpha+\epsilon) + K_0^2\epsilon^4(2\alpha+\epsilon)^2/\alpha^3(\alpha+\epsilon)^4 \qquad (6)$$

$$K_0 = C/\dot{\mu}_0; \quad \epsilon = \mu_0/\dot{\mu}_0; \quad \alpha = (1+4K_0\epsilon)^{\frac{1}{2}}.$$

Alternately one may use a variational method, as was done by Wick.

** The exponent $-Q_0$ differs by unity from Wick's because we deal here with a monodirectional source.

An entirely different procedure consists of studying the angular moments

$$y_r(p, \lambda) = \int_{4\pi} (1-\cos\theta)^r y(p, \lambda, \omega) d\omega.$$

These moments obey an inhomogeneous system of equations which one obtains by multiplying (1) by powers of $1-\cos\theta$ and integrating over ω. The important properties of the moments depend upon the behavior of the associated homogeneous system, which, in turn, leads to an eigenvalue problem equivalent to (4). This problem can be attacked either by expansion into powers of $\mu_0/\dot{\mu}_0$ or by a somewhat more effective iteration procedure.***

Table I shows a set of numerical values of $-Q_0$ obtained by the various methods. These results appear to converge rather satisfactorily toward a common limit. Nevertheless, none of the methods seems to lend itself well to the accurate determination of eigenfunctions. Therefore, we may not expect that successive approximations to the eigenvalue will converge any better than asymptotically. Moreover, the eigenfunctions are needed to determine the dependence of Y on λ and ω.

In conclusion, we are now able to determine values of the exponent of x in the asymptotic expression for Y, which seem to be unaffected by any approximation made. However, (5) above, like (5) of I and (13a) of II, holds only where μ increases monotonically with λ. This extreme asymptotic expression represents the leading term of a complicated expansion which converges rather slowly. In order to solve problems of practical importance one must take into account the various terms of the expansion (3) and employ a more refined treatment of the inverse transforms. Finally, one must evaluate the effect of the simplifying assumptions made here, among which (b) is particularly restrictive. Calculations to this end are in progress and will be the object of a more detailed report.

*** The expansion into powers seems to be equivalent to solving (4) by means of the ansatz $U=\exp(-\mu_0\sigma^2/4p)[\sum_{n=0}^{\infty} b_n\sigma^{2n}]$, successively higher powers in the summation being retained to give higher approximations to $-Q_0$.

The Hyperfine Structure of the Stable Isotopes of Indium*

A. K. MANN† AND P. KUSCH
Columbia University, New York, New York
(Received October 26, 1949)

The atomic beams magnetic resonance method has been applied to the study of the h.f.s. of the metastable $^2P_{3/2}$ state of both In^{113} and In^{115}. It has been found that the separations of the energy levels at zero external magnetic field are completely described by the equation $W=haC/2+hbC(C+1)$, where $C=F(F+1)-I(I+1)-J(J+1)$, and a and b are the magnetic dipole and electric quadrupole interaction constants, respectively. No evidence has been found to indicate the existence of a nuclear moment of higher order than the quadrupole moment. These are the heaviest atoms in which a critical search for such moments has been made.

The numerical values of the constants for In^{115} are:

$$a^{115}=242.165\pm0.002 \text{ mc/sec.}$$
$$b^{115}=1.56098\pm0.00006 \text{ mc/sec.}$$

The ratio a^{115}/a^{113} has been determined by Hardy and Millman to be 1.00224 ± 0.00010. From this value, and the results of our measurements, the numerical values of the constants for In^{113} are:

$$a^{113}=241.624\pm0.024 \text{ mc/sec.}$$
$$b^{113}=1.53855\pm0.00015 \text{ mc/sec.}$$

where the uncertainties in a^{113} and b^{113} follow from the uncertainty in the ratio of the a's. The numerical values of the electric quadrupole moments are:

$$Q^{115}=1.161\times10^{-24} \text{ cm}^2$$
$$Q^{113}=1.144\times10^{-24} \text{ cm}^2.$$

It is seen from the ratios $I^{115}/I^{113}=1$, $a^{115}/a^{113}=1.00224$, $b^{115}/b^{113}=1.0146$, that in these measurable nuclear properties In^{113} and In^{115} exhibit the greatest degree of similarity observed for any pair of isotopes of odd mass differing in mass by two units.

INTRODUCTION

THE methods of atomic beams have been applied to the study of the h.f.s. of indium in several previous experiments. The first of these experiments was that of Millman, Rabi, and Zacharias,[1] in which the atomic beam zero moment method was applied to the measurement of the h.f.s. separation of the $^2P_{\frac{1}{2}}$ state, the nuclear spin, and the magnetic moment of In^{115}. This was followed by the work of Hamilton,[2] who used the zero moment method to study the h.f.s. of the $^2P_{3/2}$ state of In^{115}. Hamilton verified the previously determined value of the nuclear spin, and measured the constants, ha^{115}, the energy of interaction of the magnetic dipole moment of the nucleus with the magnetic field of the orbital electrons, and, hb^{115}, the energy of interaction of the nuclear electric quadrupole moment with the gradient of the electric field at the nucleus. The uncertainty in these measurements was about 1 percent. Hamilton further set an upper limit on the value of c^{115}, the octupole moment interaction constant. It is of interest to note that in neither of these experiments was any structure found which could be attributed to the rarer of the two stable indium isotopes, In^{113}, even though the abundance of the isotope is sufficiently great so that structure arising from it could have been observed. Somewhat later, the atomic beam magnetic resonance method was utilized by Hardy and Millman[3] to measure the nuclear spin and h.f.s. separation ($\Delta\nu$) of the $^2P_{\frac{1}{2}}$ state of In^{113}. Hardy and Millman also remeasured the same quantities for the $^2P_{\frac{1}{2}}$ state of In^{115} with greater precision than that of the previous experiment.[1] Finally, Kusch and Foley[4] and Taub and Kusch,[5] in their work on the magnetic moments of the electron and proton, respectively, have measured the ratio of the g_J of indium in the $^2P_{\frac{1}{2}}$ state to that of sodium in the $^2S_{\frac{1}{2}}$ state, the h.f.s. separation of the $^2P_{\frac{1}{2}}$ state of In^{115}, and the ratio $g_I(In^{115})/g_J(^2P_{\frac{1}{2}})$ with high precision.

The results of these experiments that are of primary interest here are as follows: (1) The nuclear spin of In^{115} and that of In^{113} are both equal to 9/2, and (2) the h.f.s. separation of the ground state of In^{115} is equal to that of In^{113} within about 1 part in 500 ($\Delta\nu_{115}/\Delta\nu_{113}=1.00224\pm0.00010$). The very small difference between these $\Delta\nu$'s requires for its observation the high resolution characteristic of the magnetic resonance method. The ratio $\Delta\nu_{115}/\Delta\nu_{113}$ is equal to the ratio a^{115}/a^{113}, except for possible perturbations, e.g., that which might arise from the existence of matrix elements between the two states $J=1/2$ and $J=3/2$. This perturbation, if it exists, will affect the levels of the two isotopes in exactly the same way, except for the difference in their $\Delta\nu$'s, and, consequently, since the $\Delta\nu$'s are so nearly the same, it may be neglected. With these facts available, it is of interest to know the ratio of the electric quadrupole interaction constants of the two indium isotopes with at least as great a precision as that with which the ratio of the magnetic dipole interaction constants is known. The remainder of this paper will describe experiments, utilizing atomic beams magnetic resonance methods, on the h.f.s. of the $^2P_{3/2}$ state of both In^{115} and In^{113}, from which this information is obtained.

DESCRIPTION OF THE ENERGY LEVELS

The Hamiltonian expression for the interactions of an atom with nuclear spin **I**, total electronic angular momentum **J**, with a magnetic field may be written

* This research has been supported in part by the ONR.
† Now at the University of Pennsylvania, Philadelphia, Pennsylvania.
[1] Millman, Rabi, and Zacharias, Phys. Rev. **53**, 384 (1938).
[2] D. R. Hamilton, Phys. Rev. **56**, 30 (1939).
[3] T. C. Hardy and S. Millman, Phys. Rev. **61**, 459 (1942).
[4] P. Kusch and H. M. Foley, Phys. Rev. **74**, 250 (1948).
[5] H. Taub and P. Kusch, Phys. Rev. **75**, 1481 (1949).

as:[6]

$$\mathcal{H}=a\mathbf{I}\cdot\mathbf{J}+b2\mathbf{I}\cdot\mathbf{J}(2\mathbf{I}\cdot\mathbf{J}+1)+\mu_0 H(g_J J_z+g_I I_z) \quad (1)$$

where the first two terms arise from the interaction of the nuclear magnetic dipole and nuclear electric quadrupole, respectively, with the orbital electrons. For a spherically symmetric charge distribution of the orbital electrons, i.e., for $J=0$ or $1/2$, the quadrupole term vanishes. The last two terms in (1) are the interaction of the external field, taken in the z direction, with the electrons and nucleus, respectively. Terms due to moments of a higher order than the quadrupole moment are omitted in (1) for simplicity. For the case of the $^2P_{3/2}$ state of indium ($I=9/2$), the resulting secular determinant of forty rows and columns factors according to the total magnetic quantum number, giving rise to two secular equations of the first, second, and third degrees, and seven quartic equations. These equations may be solved for the energies of the levels in terms of the constants a, b, g_J, g_I and H. The higher degree equations may be simplified by use of the substitution

$$W/a=W_0/a+\delta W/a, \quad (2)$$

where W_0/ha is the weak field, first-order approximation to the energy of the level. Using Hamilton's[2] values of a and b, and the value of g_I obtained by Hardy and Millman,[3] several selected energy levels are plotted as a function of $x=\mu_0 g_J H/ha$ in Fig. 1. The levels are labelled in both the weak field (F, m_F) and strong field (m_I, m_J) notations. The energies of these particular levels (which comprise less than one-fourth of the total number) were calculated in detail primarily because the information was necessary to the measurement of the ratio $g_J(^2P_{3/2}\mathrm{In}^{115})/g_J(^2P_{\frac{1}{2}}\mathrm{In}^{115})$, which is described in the following paper. In the apparatus used in the present series of experiments, it is possible to observe only those lines which are designated in the high field notation by $\Delta m_J=\pm 1$, $\Delta m_I=0$. It is possible to observe the lines at a field strength at which m_J and m_I are not appropriate quantum numbers; however, the transitions observable at low and intermediate fields must be capable of an "adiabatic" transformation to the high field case. The states shown in Fig. 1 are, therefore, the particular states which give rise to the observable transitions $\Delta F=0$, $\Delta m_F=\pm 1$ at low and intermediate magnetic fields. No need has arisen in any part of this work to calculate at intermediate fields the energies of any other levels.

For zero external magnetic field, the first two terms in (1) are diagonal in the F, m_F representation ($F=I+J$, $\cdots$, $I-J$), with matrix elements given by $aC/2$

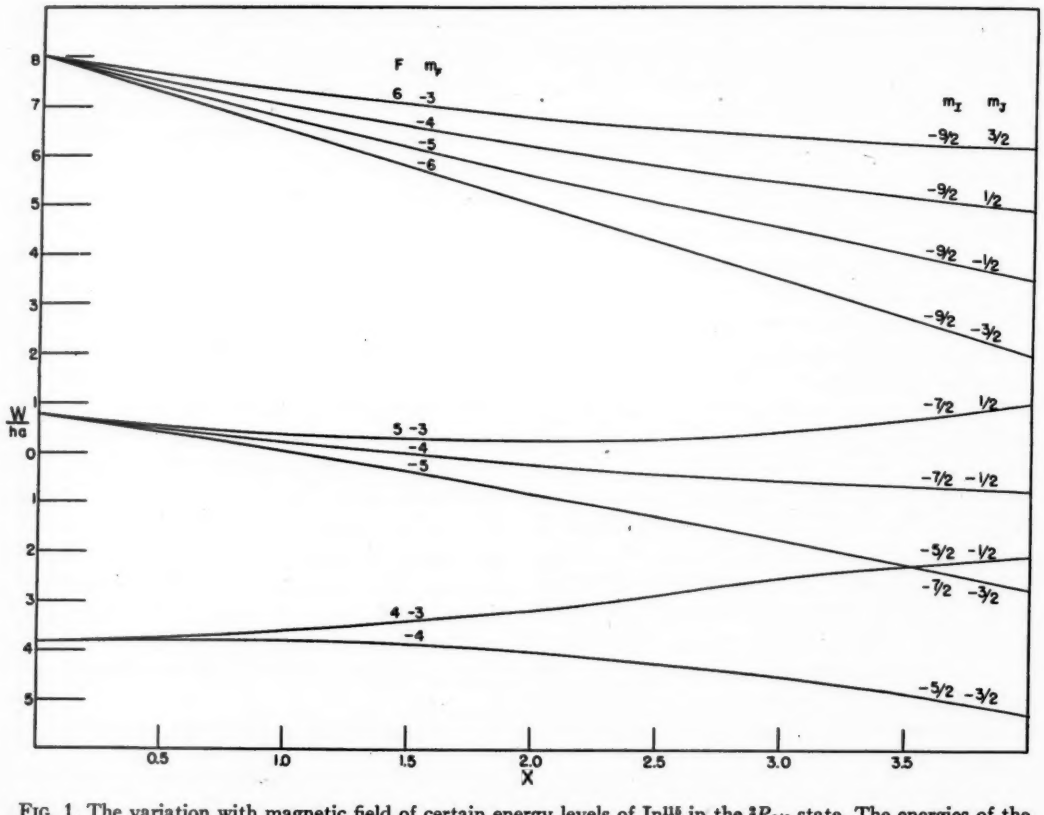

FIG. 1. The variation with magnetic field of certain energy levels of In^{115} in the $^2P_{3/2}$ state. The energies of the levels have been calculated exactly for the values of x shown in the figure. A magnetic field strength of approximately 130 gauss corresponds to $x=1$.

[6] H. B. G. Casimir, *On the Interaction between Atomic Nuclei and Electrons* (Teyler's Tweede Genootschap, Netherlands, 1936).

$+bC(C+1)$ where $C=F(F+1)-I(I+1)-J(J+1)$. There are, then, four levels corresponding to the four possible values of F. If C is evaluated for each F, one obtains expressions for the energy of each level in terms of a and b. The allowed frequencies ($\Delta F=\pm 1$) corresponding to the energy differences between these levels are:

$$\begin{aligned}(W_6-W_5)/h&=f_6=6a+192b\\(W_5-W_4)/h&=f_5=5a-60b\\(W_4-W_3)/h&=f_4=4a-192b,\end{aligned}\tag{3}$$

where a and b are expressed in frequency units. These frequencies are, for the $^2P_{3/2}$ state of indium, in the range 650–1750 mc/sec.

In general, atomic beam transitions cannot be observed in zero magnetic field. The necessity for a field arises from the fact that transitions are detected by observing changes in magnetic moment which accompany them. In order to detect changes in magnetic moment, the atoms must pass through inhomogeneous magnetic fields before and after undergoing a transition. If the field strength in the region in which the transition takes place is zero, there will be induced "non-adiabatic transitions." A field of sufficient magnitude to avoid this must therefore be present in the transition region.

At very low magnetic fields, the splitting of each F-level into $(2F+1)$ levels is adequately described, without recourse to the exact solutions of the secular equations, by the first-order (Zeeman) approximation,

$$W_{F,m_F}=W_F+\mu_0 m_F g_F H \tag{4}$$

where

$$g_F=g_J\frac{F(F+1)+J(J+1)-I(I+1)}{2F(F+1)}+g_I\frac{F(F+1)-J(J+1)+I(I+1)}{2F(F+1)}.$$

Since $|g_I/g_J|\simeq 0.0005$ for the $^2P_{3/2}$ state of both indium isotopes, the second term in the expression for g_F may be neglected within the precision of the present experiment. The pattern of the line frequencies arising from transitions between the levels described by Eq. (4) is obtained by applying the selection rules for magnetic dipole radiation, namely: $\Delta F=0,\ \pm 1$; $\Delta m_F=0,\ \pm 1$.‡ At very weak magnetic fields the transitions for which $\Delta F=0$, $\Delta m=\pm 1$, give rise to four lines, since each F-level is characterized by a particular value of g_F. Observation of these lines contributes no information about the nuclear interaction constants, but does aid in determining the nuclear spin, and if the spin is known, can serve to determine the magnetic field at which observations have been made. The transitions for which $\Delta F=\pm 1$, $\Delta m=\pm 1$ (π-lines) are those caused by the component of the oscillating magnetic field perpendicular to the constant field, H, while transitions for which $\Delta F=\pm 1$, $\Delta m=0$ (σ-lines) result from the component parallel to H. Figure 2 shows the field dependence of the frequencies of the π-lines in the Zeeman region. The figure is, of course, applicable only to the case for which $I=9/2$. For convenience, the diagram has been cut off at $H=1$ gauss. The lines are labelled in accord with the convention $(F,m)\leftrightarrow(F',m')$. The observable lines are indicated by solid lines. Certain of the π-lines cannot be observed because the corresponding high field lines are those for which $\Delta m_J=0$, $\Delta m_I=\pm 1$. These are the dashed lines in Fig. 2.

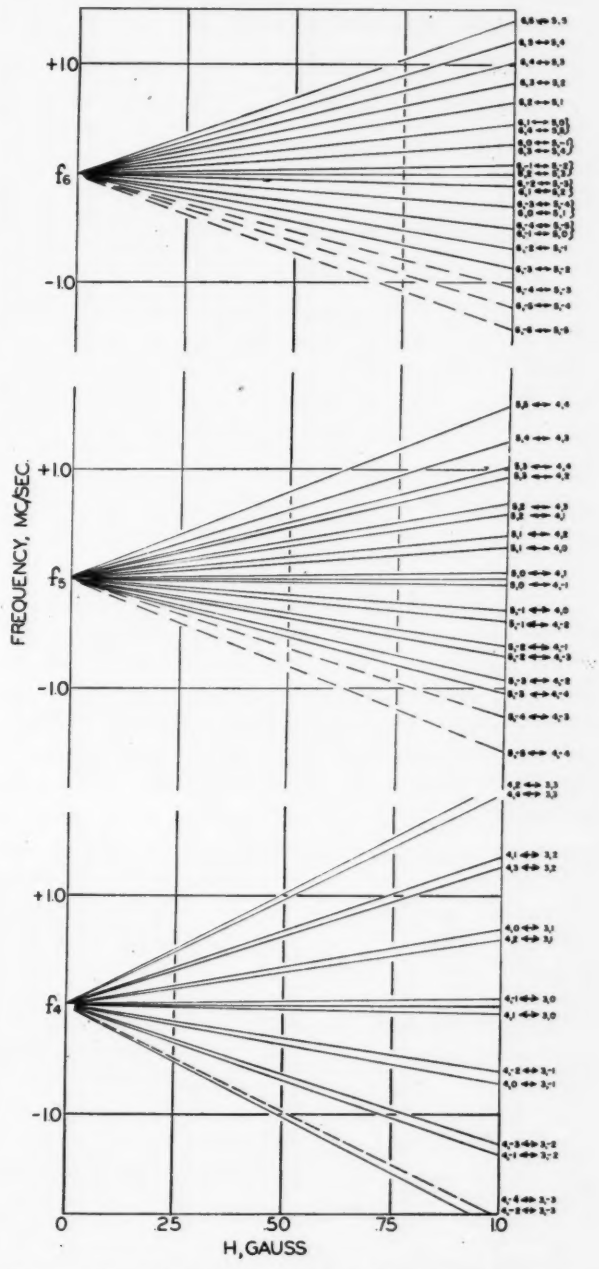

FIG. 2. The field dependence in the Zeeman region of the frequencies of the π-lines ($\Delta F=\pm 1$, $\Delta m_F=\pm 1$) in the spectrum of the $^2P_{3/2}$ state of In^{115}.

‡ Henceforth m_F will be referred to as m.

TABLE I. Results of the measurements of f_4^{115}.

Transition	Observed frequency, mc	Approx. H, gauss	f_4^{115} mc
4,−1↔3,0	669.102	2.10	
			668.969
4,1↔3,0	668.890		
4,2↔3,1	670.275		
			668.974
4,−2↔3,−1	667.721		
4,0↔3,1	670.469		
			668.976
4,0↔3,−1	667.538		
4,3↔3,2*	671.625		
			668.963
4,1↔3,2*	671.825		
4,−1↔3,0	669.187	3.30	
			668.952
4,1↔3,0	668.854		
4,2↔3,1	670.996		
			668.945
4,−2↔3,−1	667.014		
4,0↔3,1	671.332		
			668.946
4,0↔3,−1	666.695		
4,−1↔3,0	669.527	6.60	
			668.954
4,1↔3,0	668.911		
			Mean 668.960

* These lines do not constitute a symmetrical pair. A value of f_4 was computed from each of these lines using the field strength, H, obtained from the other lines observed in the same run. The mean of the two values of f_4 is entered in the last column.

The validity of Eq. (4) at any given field strength can be tested simply by determining whether or not, within experimental error, the line frequency pattern does have the predicted symmetry. For fields at which the departures from this symmetry become evident, but are small, the second-order approximation can be used to introduce a term in H^2 to Eq. (4), which then becomes

$$W_{F,m}=W_F+\mu_0 m g_F H + \left(\frac{\alpha^2}{W_F-W_{F+1}}+\frac{\beta^2}{W_F-W_{F-1}}\right)(\mu_0 g_J H)^2, \quad (5)$$

where

$$\alpha^2=\frac{(F+1-I+J)(F+1+I-J)(I+J+2+F)\times(I+J-F)[(F+1)^2-m^2]}{4(F+1)^2(2F+1)(2F+3)}$$

$$\beta^2=\frac{(F-I+J)(F+I-J)(I+J+1+F)\times(I+J+1-F)(F^2-m^2)}{4F^2(2F-1)(2F+1)}.$$

In this experiment, all line frequencies were observed at magnetic fields at which the second-order terms were small corrections to the total frequency (approximately 1 part in 10^4 or less). The lines occur as pairs, $F, m\leftrightarrow F'$, $(m\pm1)$ and $F, -m\leftrightarrow F', -(m\pm1)$. To the first order, the mean frequency of a pair is equal to the zero field frequency, $(W_F-W_{F'})/h$. The magnetic field can readily be determined by noting that the difference in the frequencies of any symmetrical pair of lines is $2[mg_F-(m\pm1)g_{F'}]\mu_0 H/h$. The magnetic field can be calculated from these differences with sufficient accuracy to enable the second-order correction to be made within the error of the observations.

APPARATUS AND PROCEDURE

General Discussion

The principal difficulty encountered in this experiment may be seen from elementary considerations of the properties of the atoms involved. The relative abundances of the indium isotopes are 95.5 percent for In^{115}, and 4.5 percent for In^{113}. The metastable $^2P_{3/2}$ state of the atoms lies 2212.6 cm^{-1} $(=\Delta\nu')$ above the ground state. The ratio of the number of atoms in the higher state to the number in the lower state is given by the Boltzmann factor multiplied by the ratio of the statistical weights, that is, by $2e^{-hc\Delta\nu'/kT}$. At an oven temperature of about 1500°K, required to give a beam of indium by use of conventional techniques, the expected abundance of the metastable state is about 20 percent. Since there are $(2J+1)(2I+1)$, or 40, magnetic levels in the $^2P_{3/2}$ state, and a radiofrequency transition involves only two levels, with a maximum of about 75 percent[7] of the atoms in these levels reorienting, the maximum intensity change due to a transition in In^{115} is approximately $95.5\times0.2\times0.05\times0.75$, or 0.72 percent of the total beam intensity. The maximum change resulting from a transition in In^{113} is $4.5\times0.72/95.5$, or 0.034 percent of the total intensity. Changes in intensity of the order of those expected in In^{115} can, in general, be observed under the conditions of beam steadiness usually obtained in an atomic beam apparatus. However, intensity changes of the magnitude expected in In^{113} require the use of some method which removes from the beam a large fraction of the atoms in states not involved in the transitions to be studied, and thus increases the signal to noise ratio at the detector to a value at which measurements are possible. There have been employed in the past several different methods for this purpose. The primary considerations in the selection of one of these methods in a particular application are the properties of the atoms to be studied, and the information to be derived from the experiment. As stated previously, the constants, a^{115} and b^{115}, were measured by Hamilton[2] with a precision of about 1 percent, and a correspondingly high upper limit placed on c^{115}. In order to accomplish the purpose of the present experiment, it was necessary to remeasure all of these same quantities with considerably greater precision. In the event that the more precisely meas-

[7] H. C. Torrey, Phys. Rev. 59, 293 (1941).

ured a^{115} and b^{115} are sufficient to describe the h.f.s., then a^{113} may be calculated directly from the known[3] ratio a^{115}/a^{113}, and there remains only b^{113} to be measured. For this reason, in addition to intensity considerations, different procedures were employed in the study of the two isotopes.

Method—Indium^{115}

The main features of the apparatus and techniques used in this experiment on In^{115} have been described in detail in previous papers.[3,8,9] Essentially, a beam of atoms issues from a narrow source slit, and is first deflected in an inhomogeneous magnetic field, H_A. Some of these atoms then pass through a collimating slit and an homogeneous magnetic field, H_C, on which is superimposed a weak radiofrequency oscillating field. Finally, the atoms are deflected in the opposite direction to that in magnet A by a second inhomogeneous field, H_B, and, if the deflection produced at the detector by B is just equal to that produced by A, strike a detector filament. The condition for an atom to have zero net deflection at the detector in the present apparatus requires that its effective dipole moment be the same in both the A and B magnets. If an atom is caused to undergo a transition in the C magnet from one energy level to another, the condition for zero net deflection usually no longer holds, and the result is a diminution of beam intensity at the detector. It will be seen from the expressions for the energy levels in the previous section that the frequency required to produce a transition depends only on¶ H_C, and the properties of the atoms in the beam. Consequently, for a given value of H, the line frequencies are completely determined, and are the only data of the experiment.|| The particular magnitude of H at which observations are made depends on the information desired from the experiment. The magnitudes of H_A and H_B are chosen to satisfy the deflection conditions imposed by the properties of the atoms and the dimensions of the apparatus, and are, in general, not critical. The lengths of the A and B magnets used in this experiment were 10.4 and 16.5 cm, respectively, with a ratio of gradient to field equal to 3.2 cm^{-1}. The widths of the oven and collimating slits and of the detector were about 0.02 mm. The actual length of the C magnet in which transitions took place was about 2 cm, and therefore the theoretical half-width of the lines was about 50 kc/sec. This width was observed in the experiments.

With this arrangement, and the oscillating magnetic field designed to be perpendicular to the homogeneous field, almost all transitions, $\Delta F=\pm1$; $\Delta m=\pm1$, were observable.** Hence all frequencies occurring in Eqs. (3) could be measured, and, in consequence, the constants a, b and c for In^{115} could be evaluated.

TABLE II. Results of the measurements of f_6^{115}.

Transition	Observed frequency, mc	Approx. H, gauss	f_6^{115} mc
5,0↔4,1	1117.501	7.27	1117.150
5,0↔4,−1	1116.823		
5,0↔4,1	1117.416	5.44	1117.155
5,0↔4,−1	1116.908		
			Mean 1117.153

TABLE III. Results of the measurements of f_6^{115}.

Transition	Observed frequency, mc	Approx. H, gauss	f_6^{115} mc
(6,−1↔5,−2)(6,2↔5,3)	1753.088	4.10	1752.714
(6,1↔5,2)(6,−2↔5,−3)	1752.331		
(6,1↔5,0)(6,4↔5,5)	1754.613		1752.695
(6,−1↔5,0)(6,−4↔5,−5)	1750.795		
(6,0↔5,−1)(6,3↔5,4)	1753.854		1752.702
(6,0↔5,1)(6,−3↔5,−4)	1751.558		
(6,−1↔5,−2)(6,2↔5,3)	1753.288	6.26	1752.712
(6,1↔5,2)(6,−2↔5,−3)	1752.120		
(6,−1↔5,−2)(6,2↔5,3)	1753.460	8.44	1752.688
(6,1↔5,2)(6,−2↔5,−3)	1751.885		
			Mean 1752.702

The radiofrequency current was supplied by a grounded grid coaxial line oscillator (Radar Jammer T-85/APT-5) using a 3C22 lighthouse tube. This oscillator was used for all measurements in the frequency range 650–1750 mc. Frequency measurements were made with a General Radio heterodyne frequency meter, Type 620A. No attempt was made to determine the shapes of the resonance lines, but the continuously variable oscillator was set at the frequency producing maximum change in beam intensity, and the frequency meter was simultaneously tuned to zero beat. The frequency of the quartz crystal against which the frequency meter was calibrated was in turn calibrated against a signal from WWV, and proper corrections made in the measured values of the transition frequencies.

[8] Kusch, Millman, and Rabi, Phys. Rev. **57**, 765 (1940).
[9] G. Becker and P. Kusch, Phys. Rev. **73**, 584 (1948).
¶ H_C will henceforth be denoted by H.
|| In order to apply the second-order corrections (discussed above) to the measured frequencies, it is necessary to know only the approximate value of H, which may be calculated from the measured frequencies of certain lines.

** In general, the A and B magnets are designed to operate at a fairly high magnetic field. This serves to keep the beam trajectory short, and thus to give a high level of beam intensity and improved stability. In the high fields, however, the m_J and m_I quantization is appropriate, and a significant moment change occurs only when $\Delta m_J=\pm1$. No loss of information results from this circumstance since in the low magnetic field of the transition region many more lines can be observed than are required to determine the desired constants.

TABLE IV. Results of the measurements of f_b^{113} and f_b^{115}.

I	II	III	IV	V	VI
Transition	Observed frequency 115, mc	f_b^{115}, mc	Observed frequency 113, mc	f_b^{113}, mc	(II–IV) mc
5,2↔4,3	1123.834	1117.165	1122.494	1115.825	1.340
5,−2↔4,−3	1110.724		1109.384		1.340
5,2↔4,1	1122.779	1117.126	1121.480	1115.821	1.299
5,−2↔4,−1	1111.453		1110.142		1.311
5,1↔4,2	1120.727	1117.154	1119.365	1115.796	1.362
5,−1↔4,−2	1113.699		1112.343		1.356
5,1↔4,1	1120.174	1117.152	1118.892	1115.844	1.282
5,−1↔4,−1	1114.155		1112.821		1.334
5,1↔4,0	1119.753	1117.143	1118.413	1115.780	1.340
5,−1↔4,0	1114.526		1113.186		1.340
5,0↔4,1	1117.615	1117.132	1116.253	1115.803	1.362
5,0↔4,−1	1116.720		1115.346		1.374
5,0↔4,0*	1117.154	1117.149	1115.786	1115.781	1.368
	Mean	1117.148		1115.807	

* This is the center line of the pattern, and, consequently, gives the zero field frequency directly after the application of a quadratic field correction.

Method—Indium^{113}

An attempt was made to observe the spectrum of In^{113} by utilizing a mass spectrometer as the detecting element of the atomic beam apparatus. If the use of the mass spectrometer does not result in an appreciable loss of intensity, then the problem of observing the spectrum of In^{113} with the mass spectrometer is identical to the problem of observing the spectrum of In^{115} in the total beam. However, a substantial loss of intensity does occur in the mass spectrometer, and the spectrometer itself introduces new instabilities to the detected beam, so that this method was found to be less adequate than the method subsequently described for a careful analysis of the spectrum of In^{113}. Nevertheless, it should be mentioned that observation, by use of the mass spectrometer, of certain lines at intermediate magnetic fields did serve to determine a value of b^{113} which is in agreement with that determined by other means, but of somewhat lower precision.

The experimental arrangement finally used for the study of In^{113} was almost identical with that first used by Zacharias[10] in the measurement of the spin and h.f.s. separation of K^{40}. In this method the deflections produced by the two inhomogeneous magnetic fields are not equal and opposite for an atom in a fixed state. Thus the beam intensity observed at the detector is effectively zero. Atoms are refocused at the detector only when a transition occurs in the transition region which results in some particular moment change. In general, relatively few transitions are observable for any given instrumental arrangement, and the amount of information which may be obtained from an experiment is considerably more limited than in the case of the experiment described for In^{115}. The arrangement employed in the present instance could detect transitions which resulted in a change in the sign of the moment but no change in the magnitude. Since the atoms are substantially in the Paschen-Back region in the deflecting fields, only transitions whose high field equivalent is $(m_J=\frac{1}{2},\ m_I)\leftrightarrow(m_J=-\frac{1}{2},\ m_I)$ could be detected. Of the transitions $\Delta F=\pm1$, $\Delta m=0,\ \pm1$, only those arising between the levels $F=4,\ 5$ were observable. Other lines of the type $\Delta F=0$, $\Delta m=\pm1$ were also observable; in the present case these lines were not investigated principally because of the difficulty in locating a line of small absolute intensity by exploration. It should be emphasized that a rearrangement of components of the apparatus would make it possible to observe other transitions as well.

The actual experimental arrangement differed from that used for In^{115} in only two essentials. First, the direction of the gradient of the B magnet was changed to be the same as that in the A magnet. This caused most of the atoms in the $^2P_{3/2}$ state and some in the $^2P_{\frac{1}{2}}$ state to be so strongly deflected that they did not strike the detector. Second, a stop-wire was placed in the direct line of the beam to eliminate the remainder of the atoms which, because of their very small moments or very high velocities, were not deflected sufficiently to miss the detector. Under these conditions, the background beam intensity was about 0.1 percent of the total beam striking the detector with the magnets off and the wire not in the beam path. If a transition took place in the C magnet which was accompanied only by a change of sign of the effective magnetic moment, then the atoms undergoing that transition were deflected by the B magnet in the proper direction to enable them to strike the detector, providing their deflection was great enough to cause them to miss the stop-wire. The diameter of the stop-wire, and its position in the B magnet, which would allow passage of the reoriented atoms were calculated from the deflection properties of the apparatus.

RESULTS

Indium^{115}

The results of the experiments on In^{115} are presented in Tables I–III. The first column in each table gives the observed transition, labelled by the weak field quantum numbers F and m. It is to be noted that coincidences occur for the lines $(6,m)\leftrightarrow(5,m')$. The line frequencies actually differ by terms of the magnitude of $g_I\mu_0H/h$, but at the magnetic fields at which measurements were made these terms are of the order of a few kc/sec., and the lines cannot be resolved. In the

[10] J. R. Zacharias, Phys. Rev. 61, 270 (1942).

second column are shown the observed frequencies of line pairs which are symmetrically situated (except for second-order corrections) about the zero field frequency. The third column shows the approximate field strength at which the observations were made. Each pair of lines determines a value of the field, as discussed previously. The mean of these values, with due weight given to the fact that the accuracy of a value depends directly on the frequency difference between symmetrical lines, is given in the third column. It should be emphasized that these values of H are used only to apply second-order corrections to the observed frequencies. Finally, the last column in each table lists the zero field frequency obtained from each line pair after all corrections are made. From general experimental considerations, we estimate the uncertainty in the absolute values of the zero field frequencies to be 1 part in 5×10^4. The relative values are, however, to a first approximation independent of any error in the calibrating crystal of the frequency meter, and consequently we assign an uncertainty of 1 part in 7.5×10^4 to the relative values of the zero field frequencies.

Using the mean values of the zero field frequencies, and Eqs. (3), the constants a and b may be calculated. The results of a least squares solution are $a^{115}=242.165\pm0.002$ mc/sec., and $b^{115}=1.56098\pm0.00006$ mc/sec. If these values are substituted in Eqs. (3), the calculated frequencies agree with those observed within the precision of the measurements, i.e., within 1 part in 7.5×10^4.

It is also possible to place an upper limit on the magnitude of interactions due to nuclear moments of a higher order than the quadrupole moment. The inclusion of the interaction of a magnetic octupole moment with the orbital electrons requires the addition of the term[11] $c(C^3+4C^2+4C/5)$ to the equation for the energy of the h.f.s. levels at zero external field. The terms $3084.4c$, $345.5c$, and $3186.6c$ must then be added to the expressions for f_4, f_5, and f_6, respectively. The three equations then determine a, b, and c to be $a=242.163$, $b=1.56098$, and $c=6.8\times10^{-6}$, all in mc/sec. This value of c^{115} is too small to be meaningful, and thus it may be concluded that no observable octupole interaction occurs to within the precision of the measurements.

Indium[113]

The results of the run on In^{113} are shown in Table IV. Since lines in the spectrum of the abundant isotope were observed as a check on the procedure, these observations are included in the table. As before, the first column lists the transitions. The second and fourth columns give the observed frequencies of line pairs in In^{115} and In^{113}, respectively. The mean field strength calculated from the observed frequencies is 9.36 gauss. In the third and fifth columns are shown the values of the zero field frequencies of the two isotopes obtained from the observed line pairs. Finally, the sixth column gives the frequency separation $f^{115}-f^{113}$ for each of the observed lines. This separation is practically independent of the quadratic field correction. It serves to indicate the consistency of the interpretation of the spectra, and the precision of measurement. It will be noted that the mean value of f_5^{115} in Table IV is in good agreement with that of Table II.

Using $a^{115}/a^{113}=1.00224\pm0.00010$, and $a^{115}=242.165$ mc/sec., we have, $a^{113}=241.624\pm0.024$ mc/sec. From the equation for f_5, we then obtain, $b^{113}=1.53855\pm0.00015$ mc/sec., and therefore, $b^{115}/b^{113}=1.0146\pm0.0001$, where the uncertainty in a^{113} and b^{113} is that of the ratio of the a's.

It is of interest to note that σ-lines were observed, and are listed in the data of Table IV, although the oscillating magnetic field at the position at which a perfectly aligned beam traverses the r-f region is perpendicular to the homogeneous field, and only π-lines had been observed previously. Since the σ-lines also exhibited a complex structure, a careful investigation was made to account for their presence. Figure 3 shows a detailed plot of a portion of the In^{115} spectrum, taken under the same conditions as the data in Table IV. The two outside lines are π-lines whose width is determined by the transit time of the atoms in the r-f region. The mean frequency of the symmetrical struc-

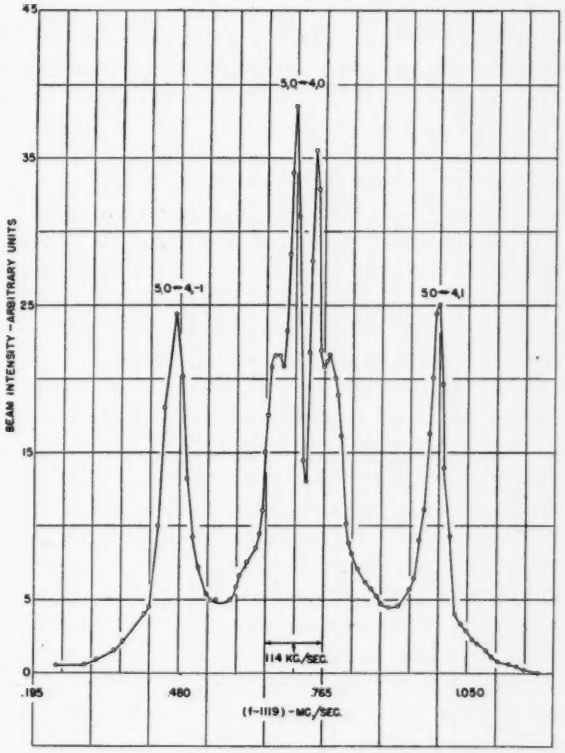

FIG. 3. A detailed plot of a portion of the spectrum of In^{115}. This curve was obtained under the special conditions described in the text.

[11] H. B. G. Casimir and H. Korsching, Zeits. f. Physik **103**, 434 (1936).

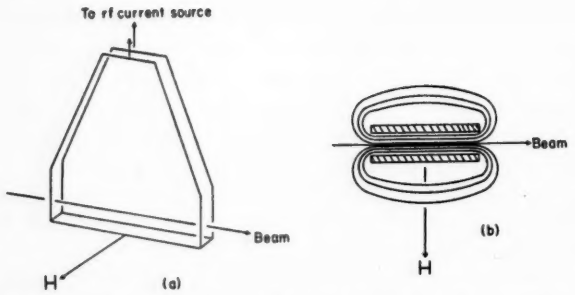

FIG. 4. The arrangement for superimposing the oscillating magnetic field, H_{r-f}, on the constant field, H. (a) The general arrangement of the r-f circuit and the beam. (b) A cross section of the circuit in a plane traversed by the beam.

ture in the center is that of a σ-line. It was found that the relative intensities of the π- and σ-lines were critically dependent on the strength of the oscillating magnetic field. At an r-f current of approximately one-quarter that at which the data in Fig. 3 were taken, the center structure had almost entirely disappeared, and the π-lines increased in intensity by a factor of about two. The positions of the π-lines remained undisturbed. The relative intensities were also found to be dependent on the position and direction of the beam path in the oscillating magnetic field. Changes in the position and direction of the beam path produced effects similar to those resulting from changes in the r-f current.

The presence of the σ-lines, and the details of their structure can be explained by considerations due to Ramsey,[12] who has calculated the resonance spectrum to be expected when the oscillating magnetic field is concentrated in two regions at the beginning and end of the homogeneous field, and of a length small compared to the distance between the two regions. The general arrangement of the r-f circuit in space is shown in Fig. 4a. A cross section of the circuit in a plane traversed by the beam is shown in Fig. 4b. It is evident from the latter of these figures that a beam which traverses the circuit symmetrically does not pass through a region in which the r-f magnetic field is parallel to the constant field, H. However, if either the circuit or the beam is misaligned such as to cause an assymmetrical traversal, the beam will pass through regions in which the r-f field has a component parallel to H. In general, both the length of and the r-f amplitude in such regions will be so small that the probability of transition is also small. If, however, the r-f amplitude is much larger than the optimum required to produce π-transitions in the center region of the r-f circuit, it is possible to induce σ-transitions in the two end regions. The complex structure observed in the σ-line is then essentially the result of interference between the probabilities of transition in each of the two short, end regions. The exact details of the pattern depend on the relative amplitudes of the r-f in the two regions which contain the appropriate r-f field, and on the relative phases. If the amplitudes are equal, and the fields are out of phase by 180°, a structure such as that shown in Fig. 3 is observed. The normal frequency of the center of the σ-line corresponds to the central minimum of the pattern in Fig. 3, and a number of equally spaced maxima appear on either side of the center. The separation of the two central peaks is calculated to be approximately $1.2\alpha/l$, where α is the most probable velocity of atoms in the oven, and l is the distance between the oscillating fields. In the present case, this quantity is estimated to be about 30 kc/sec., which compares favorably with the observed value of 40 kc/sec.

With the arrangement as shown in Fig. 4, the details of the structure of the σ-line depend critically on accidental factors in the geometry of the apparatus. In the most general case, effects of the indicated type arising from instrumental errors would result in a distortion of the line shape not subject to easy interpretation. It is evident that with the present arrangement it is not possible to observe similar effects for the π-lines.

THE QUADRUPOLE MOMENTS

The relations between the interaction constants and the nuclear moments have been given by Casimir.[6] The main difficulty in the application of these relations arises from the necessity of evaluating the terms $\langle(r^{-3})\rangle_{Av}$, and $\langle[(3\cos^2\theta-1)/r^3]_{J,J}\rangle_{Av}$, which occur in the expressions for a and b, respectively. It has been pointed out by Davis, Feld, Zabel, and Zacharias,[13] that, in the approximation in which the electron wave function is separable, the dependence of both a and b on r is through the same factor $\langle(r^{-3})\rangle_{Av}$, and the ratio b/a is therefore independent of the radial factor. One can then write

$$Q=-\frac{8}{3}\frac{\mu_0^2}{e^2}g_I\frac{F}{R}\frac{b}{a}\frac{I(2I-1)(2J-1)(L+1)(2L+3)}{(J+1)}, \quad \text{for } J=L+\tfrac{1}{2} \quad (6)$$

where R and F are small relativistic corrections given by Casimir. This result is the same as that given by Davis *et al.* for chlorine, except that b is defined differently here,†† and that the change in the sign of b required for chlorine is not required in this case. The sign changes occur because in the case of chlorine an electron shell which lacks a single electron of being closed is considered, while for indium there is a single valence electron ($5p$) beyond the ($5s$) closed shell.

Observation[5] of the spectrum of the $^2P_{\frac{1}{2}}$ state of In^{115} has yielded directly the ratio $g_I(In^{115})/g_J(^2P_{\frac{1}{2}})=-9.95$

[12] N. F. Ramsey, Phys. Rev. **75**, 1326A (1949); **76**, 996 (1949). We are also indebted to Professor Ramsey for a private communication.

[13] Davis, Feld, Zabel, and Zacharias, Phys. Rev. **76**, 1076 (1949). We are also indebted to the group at M.I.T. for sending us a prepublication copy of their paper.

†† If b' denotes the constant used by the M.I.T. group, and b the constant used here, then $b'=8/3IJ(2I-1)(2J-1)b$.

$\times 10^{-4}$, where $g_J(^2P_{\frac{1}{2}})=0.66599$. For indium F/R is 0.94930. Insertion of the numerical quantities in Eq. (6) gives $Q^{115}=1.161\times 10^{-24}$ cm^2.

It is to be noted that the diamagnetic correction customarily applied to observed nuclear g values has not been applied here. It is not at all clear from the present state of the theory that this correction should be made. It seems doubtful that the theory is sufficiently good to enable one to calculate quadrupole moments with a precision limited only by uncertainties in observed quantities. It should also be noted that in several instances the measured ratio of the h.f.s. separations of the same states of two isotopes is not simply derived from the measured ratio of the nuclear magnetic dipole moments.[14] The presence of such an effect in indium would cause the calculated quadrupole moment to be in error. For atoms with the same spin, the magnitude of the effect presumably is small compared to the error arising from uncertainties in the application of the diamagnetic correction.

[14] J. E. Nafe and E. B. Nelson, Phys. Rev. **73**, 718 (1948); F. Bitter, Phys. Rev. **76**, 150 (1949); P. Kusch and A. K. Mann, Phys. Rev. **76**, 707 (1949).

To a very high order of approximation

$$Q^{115}/Q^{113}=b^{115}/b^{113}=1.0146$$

which leads to the value $Q^{113}=1.144\times 10^{-24}$ cm^2, where the diamagnetic correction has not been made.

CONCLUSIONS

The h.f.s. of the $^2P_{3/2}$ state of indium can be described exactly in terms of two interaction constants. No experimental evidence has been found to indicate the existence of a nuclear moment of higher order than the quadrupole moment. This is the heaviest atom in which a critical search has been made for higher order nuclear moments.

The addition of two neutrons to In^{113} produces an isotope which differs only very slightly from In^{113} in certain measurable nuclear properties. The spins are identical, the magnetic dipole moments differ by 0.22 percent, and the electric quadrupole moments differ by 1.46 percent. This is the greatest degree of similarity observed for any pair of isotopes of odd mass differing in mass by two units.

PHYSICAL REVIEW VOLUME 77, NUMBER 4 FEBRUARY 15, 1950

Further Data on the Spin Gyromagnetic Ratio of the Electron*,†

A. K. MANN‡ AND P. KUSCH
Columbia University, New York, New York

(Received October 26, 1949)

The atomic beam magnetic resonance method has been used to compare the g_J values of In in the $^2P_{3/2}$ and $^2P_{\frac{1}{2}}$ states in order to obtain a value of the spin gyromagnetic ratio of the electron. The determination of the g_J ratio involved only the measurement of frequencies of lines in the h.f.s. spectra of both states at constant magnetic field. Lines with widely different frequency dependence on field were selected to avoid possible systematic errors arising from inhomogeneities in the field. The result of these measurements is $g_J(^2P_{3/2})/g_J(^2P_{\frac{1}{2}})=2(1.00200\pm 0.00006)$. Assuming Russell-Saunders coupling, and $g_L=1$, the spin gyromagnetic ratio of the electron may be calculated. The result is $g_S=2(1.00133\pm 0.00004)$, which is to be compared with the value $g_S=2(1.00119\pm 0.00005)$ obtained by Kusch and Foley. The discrepancy is greater than the sum of the experimental errors. The $^2P_{\frac{1}{2}}$ state of In is believed to be free of significant perturbations which might affect the total electronic g value. However, in view of possible perturbations of the $^2P_{3/2}$ state, the agreement must be considered as very good. The present result confirms the conclusions of the previous experiment, both as to the existence of the intrinsic magnetic moment of the electron, and as to its approximate magnitude.

INTRODUCTION

In a recent experiment, Kusch and Foley[1] have measured the ratio of the electron spin g value (g_S) to the orbital g value (g_L) by comparing the total electronic g values of gallium in the $^2P_{\frac{1}{2}}$ and $^2P_{3/2}$ states, indium in the $^2P_{\frac{1}{2}}$ state, and sodium in the $^2S_{\frac{1}{2}}$ state. Three independent intercomparisons gave three values for the ratio g_S/g_L which are in agreement to within 7 parts in 10^5. In addition, the experimental result is in good agreement with the result obtained by Schwinger[2] from a first-order theoretical investigation.

The method employed by Kusch and Foley avoids the difficulty of producing a magnetic field which is known to a high order of precision in terms of absolute standards, and which is required for a precision measurement of the absolute value of a gyromagnetic ratio. However, the validity of any individual determination of the ratio g_S/g_L by the method of Kusch and Foley may be limited by deviations of the properties of the atomic systems from the simple description implicit in

* A brief account of the material in this paper was given at the April, 1949 meeting of the American Physical Society.

† This research has been supported in part by the ONR.

‡ Now at the University of Pennsylvania, Philadelphia, Pennsylvania.

[1] P. Kusch and H. M. Foley, Phys. Rev. **74**, 250 (1948).

[2] J. Schwinger, Phys. Rev. **73**, 416 (1948).

TABLE I. Observations of lines in the spectra of the $^2P_{\frac{1}{2}}$ and $^2P_{3/2}$ states of indium, and a comparison of the apparent values of H'.

State	Line	Frequency mc/sec.	H'	Deviation
$^2P_{\frac{1}{2}}$	5,5↔5,4	23.056	355.582	−0.018
	5,4↔5,3	23.152	355.596	−0.004
	5,3↔5,2	23.247	355.617	+0.016
	5,−1↔5,−2	23.639	355.606	+0.006
		$H'(^2P_{\frac{1}{2}})$ =	355.600 ±	0.011
$^2P_{3/2}$	6,−4↔6,−3	134.043	356.308	−0.001
	6,−5↔6,−4	139.916	356.287	−0.022
	5,−5↔5,−4	142.941	356.297	−0.012
	6,−6↔6,−5	146.075	356.345	+0.036
		$H'(^2P_{3/2})$ =	356.309 ±	0.018
		$\Delta H'/H' = 0.00199$		

the theory underlying the experiment. In general, such deviations cannot be calculated with precision, and the validity of an individual measurement of g_S/g_L is determined by its consistency with values of the ratio obtained from other atomic systems. The fact that three independent sets of experimental data yield substantially identical values indicates that perturbations which affect the total electronic g values of the atomic energy states are small. It is, however, desirable to investigate various atomic systems in an effort to improve the precision of the experimental value of g_S/g_L. In the experiment to be described in this paper, a value of g_S/g_L is obtained from a comparison of the g_J values of indium in the $^2P_{\frac{1}{2}}$ and $^2P_{3/2}$ states. This measurement is possible because the interaction constants of indium in the $^2P_{3/2}$ state have recently been measured[3] with sufficient precision to allow the use of that state in the present experiment.

THEORY OF THE EXPERIMENT

The g_J value of any atomic energy state may be expressed as a linear combination of g_S and g_L. In particular, if Russell-Saunders coupling is assumed,

$$g_J(^2P_{3/2}) = g_S/3 + 2g_L/3$$
$$g_J(^2P_{\frac{1}{2}}) = -g_S/3 + 4g_L/3. \quad (1)$$

It is evident that a measurement of the ratio $g_J(^2P_{3/2})/g_J(^2P_{\frac{1}{2}})$ will yield a value of the ratio g_S/g_L. For reasons discussed previously,[1] it is convenient to take $g_L=1$, and, on the basis of this assumption, to calculate g_S directly.

If the interaction constants which determine the h.f.s. levels of the electronic states in question are known, it is possible to find the ratio of the g_J values of those states by observing chosen lines in the h.f.s. spectrum of each state in a fixed magnetic field. The expressions for the frequencies of the h.f.s. lines always contain the quantity $H' = (\mu_0 H/h) \times 10^{-6}$, in mc/sec., which occurs in the products $g_J H'$ and $g_I H'$. Accordingly, if lines are observed, at the same value of the magnetic field, in both the $^2P_{\frac{1}{2}}$ and $^2P_{3/2}$ states, the product $g_J H'$ can be found for each of the states, and the ratio of the g_J values can be determined. For convenience in the actual calculation, we have assumed that $g_J^0(^2P_{\frac{1}{2}}) = 2/3$ and that $g_J^0(^2P_{3/2}) = 4/3$. Unless the ratio of the g_J values is exactly as assumed, the calculated values of H' will not be identical and the true ratio of the g_J values may be found from the calculated values of H'. If $\Delta H' = H'(^2P_{3/2}) - H'(^2P_{\frac{1}{2}})$, then

$$R = g_J(^2P_{3/2})/g_J(^2P_{\frac{1}{2}}) = [g_J^0(^2P_{3/2})/g_J^0(^2P_{\frac{1}{2}})][1 + \Delta H'/H'(^2P_{\frac{1}{2}})]. \quad (2)$$

From Eqs. (1), it follows at once that

$$g_S/g_L = 2(2R-1)/(R+1). \quad (3)$$

If g_S differs from the value predicted by the Dirac theory by a small quantity, δ_S, and if g_L is assumed equal to one, we may write

$$g_S = 2(1+\delta_S)$$

where

$$\delta_S = (R-2)/(R+1).$$

For small $\Delta H'$, $\delta_S = 2\Delta H'/3H'$, where it is not necessary within the present precision to distinguish between $H'(^2P_{3/2})$ and $H'(^2P_{\frac{1}{2}})$.

To find the value of H' which corresponds to any observed line frequency in the h.f.s. spectrum of the $^2P_{\frac{1}{2}}$ state, it is necessary to know, in addition to the spin, the h.f.s. separation at zero field ($\Delta\nu$) and the ratio $g_I/g_J(^2P_{\frac{1}{2}})$. These quantities have been measured with high precision,[4] and application of the well-known equations[1] which describe the energies of the h.f.s. levels of an atom for which $J=\frac{1}{2}$, readily yields H'. To find the value of H' which corresponds to any observed line frequency in the spectrum of the $^2P_{3/2}$ state, it is necessary to know the interaction constants a and b, and the ratio $g_I/g_J(^2P_{3/2})$. The values of a and b have been reported in the preceding paper.[3] The ratio $g_I/g_J(^2P_{3/2})$ can be found to sufficient accuracy, since g_I is very much smaller than g_J, by using the value of $g_I/g_J(^2P_{\frac{1}{2}})$ and assuming that $g_J(^2P_{3/2})/g_J(^2P_{\frac{1}{2}})$ is the same for indium as for gallium.[1] In the most general case, it is then necessary to find a value of H' such that the difference between roots of the appropriate secular equations has a value corresponding to the observed line frequency. The secular equations are of considerable complexity and will not be reproduced here.

PROCEDURE

The general experimental procedures employed in this experiment are identical to those previously described[1] for the determination of the ratio g_S/g_L from a comparison of the g_J values of gallium in the $^2P_{\frac{1}{2}}$ and $^2P_{3/2}$ states. The experimental difficulties are, however,

[3] A. K. Mann and P. Kusch, Phys. Rev. **77**, 427 (1950).

[4] H. Taub and P. Kusch, Phys. Rev. **75**, 1481 (1949).

considerably greater in the present case. This arises from the fact that the spin of indium is 9/2 as compared to a spin of 3/2 for gallium, and that the population of indium in the $^2P_{3/2}$ state is very much smaller than that of gallium in the same state. The high multiplicity of states corresponding to the high spin value and the low population of the upper state result in lines of small intensity which are difficult to observe.

Of the lines in the $^2P_{3/2}$ state which are designated in the weak field notation by F, $m\leftrightarrow F$, $m\pm1$ those lines which become m_J, $m_I\leftrightarrow m_J\pm1$, m_I at high fields are the most satisfactory for determining the value of g_J, because at weak fields the frequencies of those lines are $\mu_0 g_F H/h$, and at high fields the frequencies are, except for constant terms, $\mu_0 g_J H/h$. At all magnetic fields the line frequencies have a first-order dependence on both g_J and H. This is not true of the lines F, $m\leftrightarrow F$, $m\pm1$ which become the lines m_J, $m_I\leftrightarrow m_J$, $m_I\pm1$ at high fields because these lines are dependent on the field at high field only through the term $\mu_0 g_I H/h$. The use of the lines F, $m\leftrightarrow F\pm1$, $m\pm1$ would increase the difficulty of the experiment and its interpretation since the expressions for these lines contain, in addition to the field dependent terms $\mu_0 g_F H/h$, large constant terms. In the apparatus employed in the present experiment, it was possible to observe a number of the most favorable set of lines, namely, those lines F, $m\leftrightarrow F$, $m\pm1$ for which the energy levels are shown in Fig. 1 of the preceding paper. The remainder of the lines F, $m\leftrightarrow F$, $m\pm1$ were not observable because at high fields they become the lines m_J, $m_I\leftrightarrow m_J$, $m_I\pm1$, and the deflection properties of the apparatus prevent such lines from being observed. The fact that a large number of lines are unobservable in this apparatus simplifies the interpretation of the data since identification of the observed lines can be made without extensive calculation, and inappropriate lines will not be observed.

In the $^2P_{\frac{1}{2}}$ state, transitions of the type F, $m\leftrightarrow F$, $m\pm1$ were observed. These are again, for the reasons given above, the most satisfactory transitions for determining g_J. It should be noted that a high field condition for indium in the $^2P_{3/2}$ state occurs at a very much lower absolute value of the field than the high field condition for the $^2P_{\frac{1}{2}}$ state of indium. Accordingly, a field strength at which high field conditions prevail in the deflecting fields for the $^2P_{3/2}$ state represents low intermediate field conditions for the $^2P_{\frac{1}{2}}$ state. This circumstance permits the observation of all transitions F, $m\leftrightarrow F$, $m\pm1$ in the $^2P_{\frac{1}{2}}$ state, even though these would become m_J, $m_I\leftrightarrow m_J$, $m_I\pm1$ transitions at high field. The intensity of these lines is low because the moment change involved in the transitions is small. However, under experimental conditions for which it is possible to observe the low intensity lines in the $^2P_{3/2}$ state, it is also possible to observe these lines in the $^2P_{\frac{1}{2}}$ state.

The value of the magnetic field employed in this experiment was about 250 gauss. At this field the width of the observed lines was substantially determined by the transit time width and did not appear to be affected by inhomogeneities in the magnetic field. At larger values of the magnetic field, the increase in field inhomogeneity in our magnet resulted in increased width of the more field dependent lines in the spectrum of the $^2P_{3/2}$ state. The lower limit of the magnetic field is, of course, determined by the requirement that the lines F, $m\leftrightarrow F$, $m\pm1$ in the $^2P_{\frac{1}{2}}$ state, which are all coincident at weak magnetic field, should be completely resolved. At the field strengths at which observations were actually made, the frequencies of the lines arising in the $^2P_{3/2}$ state are markedly different in their field dependence. The fact that the results are identical, within experimental error, for all lines in the $^2P_{3/2}$ state, indicates that effects due to field inhomogeneity were negligible.

TABLE II. A summary of all data taken in the present experiment.

Run	$\Delta H'/H'$	Deviation
1	0.00207	+0.00007
2	0.00186	−0.00014
3	0.00209	+0.00009
4	0.00199	−0.00001
5	0.00200	0.0
	Mean 0.00200±0.00006	

The particular apparatus used in this experiment was the same as that used in the measurement of the interaction constants of indium 115, and was described in detail in the preceding paper. However, at the field strengths employed in this experiment, the field was not entirely constant. In order that a measurement of the ratio of the g_J values may be made, transitions resulting in lines whose frequencies are to be compared must occur in the same magnetic field, although no further knowledge of the field is required. It was therefore necessary to correct for variations in the magnetic field. The procedure for making this correction has been discussed at length in previous references.[1,4] In this experiment, the principle limitation on the precision of measurement was imposed by the line widths and not by the stability of the field.

The rarer of the two isotopes of indium (In^{113}), with a relative abundance of about 5 percent, has no effect on the present observations. The lines in the $^2P_{\frac{1}{2}}$ state are observed under very weak field conditions. The frequencies are given almost entirely by $\mu_0 g_F H/h$; the lines are resolved because of a small differential quadratic term containing the factor $1/\Delta\nu$. Since the $\Delta\nu$'s of the two isotopes are equal to within 1 part in 500, the lines of both isotopes are substantially coincident at the magnetic fields in question. The actual shift of the lines due to the isotope effect is very much less than that calculated from the $\Delta\nu$'s because of the low abundance of In^{113}. In the $^2P_{3/2}$ state, the lines of the two isotopes are entirely resolved, and only a fortuitous coincidence of two lines at a given field strength is

TABLE III. Observed ratios of atomic g values and the corresponding values of δ_S obtained in this experiment, and the experiment of Kusch and Foley.

	Experimental ratio	δ_S
I	$\frac{g_J(\mathrm{Ga}\ ^2P_{3/2})}{g_J(\mathrm{Ga}\ ^2P_{\frac{1}{2}})}=2(1.00172\pm0.00006)$	0.00114 ± 0.00004
II	$\frac{g_J(\mathrm{Na}\ ^2S_{\frac{1}{2}})}{g_J(\mathrm{Ga}\ ^2P_{\frac{1}{2}})}=3(1.00242\pm0.00006)$	0.00121 ± 0.00003
III	$\frac{g_J(\mathrm{Na}\ ^2S_{\frac{1}{2}})}{g_J(\mathrm{In}\ ^2P_{\frac{1}{2}})}=3(1.00243\pm0.00010)$	0.00121 ± 0.00005
IV	$\frac{g_J(\mathrm{In}\ ^2P_{3/2})}{g_J(\mathrm{In}\ ^2P_{\frac{1}{2}})}=2(1.00200\pm0.00006)$	0.00133 ± 0.00004

possible. Such a coincidence would still introduce an error of magnitude appreciably less than our experimental error.

EXPERIMENTAL RESULTS

The results of one series of observations are shown in Table I in order to indicate the degree of consistency of individual measurements. In the first column of the table the atomic state is given. The second column lists the transitions denoted by the weak field quantum numbers. The third column shows the observed line frequencies. Each of the values in this column is the mean of several observations all reduced to a common value of the magnetic field. In the fourth column are given the values of H' computed from the equations for the line frequencies. The fifth column in Table I lists the deviations of the individual values of H' from the mean. It should be noted that the difference between the values of $H'(^2P_{3/2})$ and $H'(^2P_{\frac{1}{2}})$ is approximately thirty-nine times as great as the largest of the mean deviations.

A summary of the results of all the data taken in the present experiment is shown in Table II. Each of the values listed in this table represents a series of observations similar to that given in Table I. The experimental conditions under which these observations were made were purposely varied between successive series. A very large number of lines in the spectrum of the $^2P_{\frac{1}{2}}$ state were observable, and the particular lines which were observed were chosen at random. In all cases, however, enough lines were observed, with reduced precision, to make the identification of the lines positive. Six lines were observable in the spectrum of the $^2P_{3/2}$ state, and the particular lines chosen for observation were varied between series. In addition, the magnitude of the magnetic field strength was varied between series, and the direction of the magnetic field was changed from time to time. It is therefore to be expected that the errors in the determination of $\Delta H'/H'$ are primarily statistical in character.

DISCUSSION

The values of the ratio $g_J(\mathrm{In}\ ^2P_{3/2})/g_J(\mathrm{In}\ ^2P_{\frac{1}{2}})$, and of δ_S, obtained in the present experiment are presented in Table III, which also gives the results of the experiment of Kusch and Foley. It is seen that the last value of δ_S differs from the average of the first three values by more than the sum of the experimental errors.

It appears likely that this discrepancy is the result of effects similar to those mentioned in an earlier section of this paper. It is evident that perturbations of the atomic states in question could in principle bring about deviations from the g_J values computed on the basis of the Russell-Saunders coupling scheme. Such deviations have been found, for example, by Kusch and Taub[5] in the g_J values of rubidium and caesium, which are greater than the g_J of the other alkalis by 5 and 13 parts in 10^5, respectively. It will be noted that these effects are of the magnitude of the discrepancy between the values in Table III. The possible origin of such perturbations has been discussed previously.[1] At the present time, no quantitative theory of the effect is available.

From the agreement of the data in rows II and III of Table III, it may be inferred that perturbations which affect the g_J values of the $^2P_{\frac{1}{2}}$ states of indium and gallium are small, and that therefore the g_J values are nearly those characteristic of a pure $^2P_{\frac{1}{2}}$ state. It is, consequently, reasonable to assume that it is the $^2P_{3/2}$ state of indium which is perturbed sufficiently to account for the discrepancy in Table III. In spite of this discrepancy, however, the present result must be considered as confirming the conclusions of the previous experiment,[1] both as to the existence of the intrinsic magnetic moment of the electron, and as to its approximate magnitude.

[5] P. Kusch and H. Taub, Phys. Rev. **75**, 1477 (1949).

An Investigation of the Disintegration Schemes of Ru^{103} and Rb^{86}*

C. E. MANDEVILLE AND E. SHAPIRO
Bartol Research Foundation of The Franklin Institute, Swarthmore, Pennsylvania

(Received October 20, 1949)

The disintegration schemes of the 42-day Ru^{103} and the 19-day Rb^{86} have been studied with the use of absorption and coincidence methods. Ninety-two percent of the disintegrations of Ru^{103} proceed by way of an inner beta-ray group at 0.15-Mev coincident in time with a gamma-ray of energy 0.52 Mev, which is (4±1) percent converted. A harder beta-spectrum having a maximum energy of 0.68 Mev leads to the ground state of Rh^{103}.

It is estimated that (12±2) percent of the beta-rays of Rb^{86} are contained in the inner spectrum. Absorption measurements confirm the energy values given by the Indiana group.

INTRODUCTION

THE activities described in the present manuscript were induced in oxides of ruthenium and rubidium which were irradiated by slow neutrons in the Oak Ridge pile. Chemical purification of the irradiated material was carried out in regard to both activities.

The pile irradiated RuO_2 was aged for about two months to allow for decay of the 2.8-day ruthenium (97), after which time RuO_4 was distilled from a suspension of 100 mg of RuO_2 in 5 ml of concentrated H_2SO_4 and 5 ml of sixty percent $HClO_4$. The distillate was collected in 25 ml of 6N NaOH. This solution was boiled with alcohol to precipitate ruthenium metal which was then removed by centrifugation, dissolved in 1N HCl, and reprecipitated with magnesium powder. The excess magnesium was dissolved in HCl, and the ruthenium was removed by filtration, washed with alcohol and ether and dried for use.

Neutron irradiated rubidium carbonate was freed of its principal impurity, cesium, by three precipitations of cesium silicotungstate from a 6N HCl solution, using weights of carrier cesium in each precipitation comparable to the initial weight of rubidium. The third filtrate was treated with 5 ml of $HClO_4$, evaporated to $HClO_4$ fumes, and centrifuged. Five ml of absolute alcohol was added to the supernatant, precipitating $RbClO_4$ which was removed by filtration, washed with alcohol and ether and dried for measurement. The yield of $RbClO_4$ was about 20 percent.

The beta-rays of Ru^{103} have been said to have energies of 0.25 Mev,[1] 0.3 Mev (95 percent), 0.8 Mev (5 percent),[2] and 0.75 Mev.[3] The gamma-radiation is reported as having a quantum energy of 0.56 Mev[2,4] and of 0.4 Mev.[3] All of the above quoted data were obtained by absorption methods.

Spectrometric and coincidence data have been combined by the Indiana group[5] to show that the 19-day Rb^{86} decays with the emission of beta-ray spectra having end points at 1.822 Mev and 0.716 Mev. The gamma-ray energy was measured as 1.081 Mev. It is estimated by the Indiana group that twenty percent of the disintegration proceeds by way of the inner beta-ray group.

The energies of the radiations of Ru^{103} and Rb^{86} reported in the present paper were measured by absorption methods. Beta-gamma, beta-beta, and gamma-gamma-coincidences were observed with the aid of a coincidence circuit having a resolving time of 0.10 microsecond. No attempt was made to study the soft radiations of the well-known metastable state of Rh^{103} having a half-period of about one hour.

Ru^{103}

The beta-rays of Ru^{103} were absorbed as shown in the logarithmic plot of Fig. 1. The end point of the inner

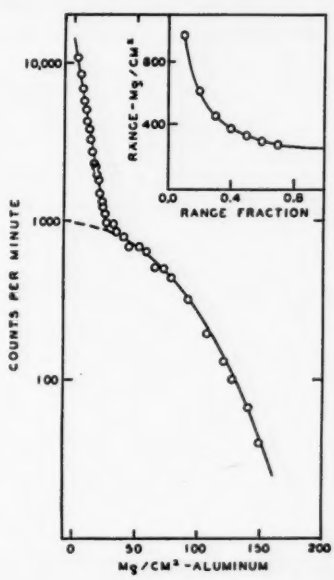

FIG. 1. Absorption in aluminum of the beta-rays of the 42-day Ru^{103}. The end points occur at 0.15 Mev and 0.68 Mev. The softer component constitutes 92 percent of the total beta-radiation.

* Assisted by the Joint Program of the ONR and the AEC.

[1] W. E. Grummitt and G. Wilkinson, Nature **158**, 163 (1946).

[2] Sullivan, Slight, and Gladrow, Plutonium Project Report CC-1493 (March 1944), quoted by Seaborg and Perlman, Rev. Mod. Phys. **20**, 585 (1948).

[3] E. Bohr and N. Hole, Arkiv. f. Mat. Astr. O. Fys. **32A**, No. 15 (1948).

[4] L. E. Glendenin, Plutonium Project Report CC-920, 43 (September 1943), quoted by Seaborg and Perlman.

[5] Zaffarano, Kern, and Mitchell, Phys. Rev. **74**, 682 (1948). E. T. Jurney, Phys. Rev. **74**, 1049 (1948).

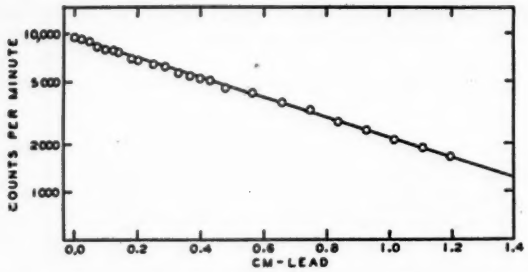

FIG. 2. Absorption in lead of the quantum radiations of Ru^{103}. The energy taken from the slope of the curve is 0.52 Mev.

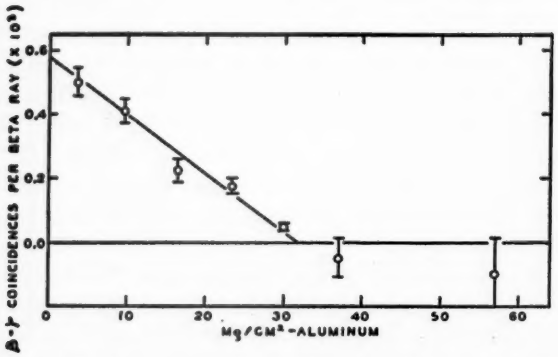

FIG. 3. The beta-gamma-coincidence rate of Ru^{103} as a function of the surface density of aluminum placed before the beta-ray counter. These data show that the softer spectrum is coincident in time with the gamma-ray of energy 0.52 Mev.

group occurs at 28 mg/cm², corresponding to an energy of 150 kev. From the Feather plot also shown in Fig. 1, the harder spectrum appears to have a maximum range of 250 mg/cm², corresponding to an energy of 0.68 Mev. Extrapolation of the two spectra to zero absorber thickness shows that only eight percent of the beta-particles fall in the harder spectrum.

The gamma-rays of Ru^{103} were absorbed in lead as shown in Fig. 2. The slope of the curve corresponds to a quantum energy of 0.52 Mev.

The beta-gamma-coincidence rate of Ru^{103} was measured as a function of the surface density of aluminum placed before the beta-ray counter. These data are

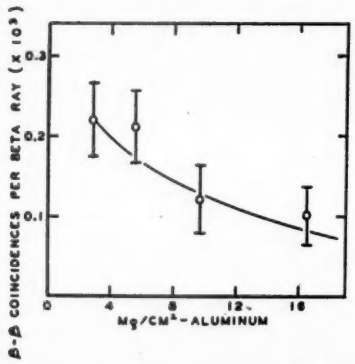

FIG. 4. The beta-beta-coincidence rate of Ru^{103} as a function of the surface density of aluminum placed before both counters. It is estimated that the total conversion coefficient of the gamma-ray at 0.52 Mev is (4±1) percent.

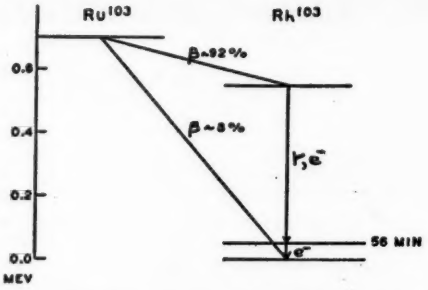

FIG. 5. Proposed disintegration scheme of the 46-day Ru^{103}.

shown in Fig. 3 where the beta-gamma-coincidence rate is seen to decrease from an extrapolated value of 0.58×10^{-3} coincidence per beta-ray at zero absorber thickness to zero at ~30 mg/cm², showing that the intense soft spectrum of Fig. 1 is coincident in time with gamma-radiation and that the weak spectrum at 0.68 Mev goes to the ground state of the residual nucleus. Calibration of the gamma-ray counter showed that the beta-gamma-coincidence rate at zero absorber thickness is consistent with the view that 92 percent of the nuclear beta-rays are followed by a gamma-ray of energy 0.52 Mev.

No gamma-gamma-coincidences were found in the disintegration of Ru^{103}.

Beta-beta-coincidences were measured as a function of the surface density of aluminum absorbers placed before both beta-ray counters. The curve of these data is shown in Fig. 4. From the coincidence rates of the beta-beta-coincidence counting arrangement, it is estimated that the 0.52-Mev gamma-ray is converted to the extent of (4±1) percent.

The absorption and coincidence data are combined in Fig. 5 to give a disintegration scheme.

Rb^{86}

The beta-gamma-coincidence rate of Rb^{86} is shown in Fig. 6 where the coincidence rate is seen to decrease to zero in the vicinity of a kinetic energy of 0.5 Mev.

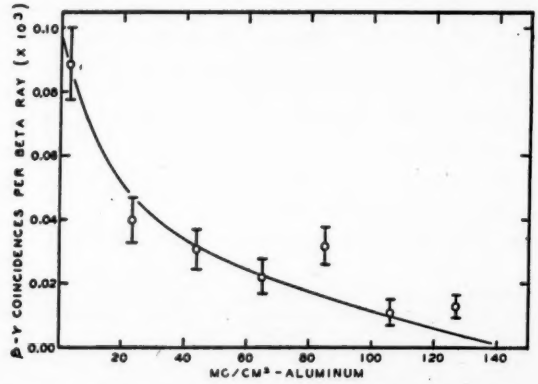

FIG. 6. The beta-gamma-coincidence rate of Rb^{86} as a function of the aluminum absorber thickness placed before the beta-ray counter. It is estimated that (12±2) percent of the total beta-radiation lies in the soft spectrum.

From the calibration of the gamma-ray counter and the coincidence rate at zero absorber thickness it is estimated that (12±2) percent of the total beta-radiation lies in the inner beta-ray group which is coupled with the 1.08-Mev gamma-ray. This is to be compared with previous estimates of 20 percent obtained from spectrometric data and 33 percent as indicated by an absorption method.[5] Absorption of the radiations of Rb^{86} in aluminum and lead confirmed the conclusions of the Indiana group as to the energies.

ACKNOWLEDGMENT

The writers wish to acknowledge the continued interest of Dr. W. F. G. Swann, Director of Bartol.

PHYSICAL REVIEW VOLUME 77, NUMBER 4 FEBRUARY 15, 1950

The Neutron-Proton Interaction

RICHARD S. CHRISTIAN AND EDWARD W. HART
Radiation Laboratory, Department of Physics, University of California, Berkeley, California
(Received October 14, 1949)

An analysis of the high energy (40 and 90 Mev) experimental neutron-proton scattering results is presented. It is shown that there is good agreement with the theoretical predictions based on a potential model having a $\frac{1}{2}(1+P_x)$ exchange dependence and a "long-tailed" radial dependence. There is evidence, furthermore, from the scattering for the inclusion of a tensor force. A comparison of the predictions of square well, exponential, and Yukawa radial dependences is included to illustrate the effect of different shape characteristics.

INTRODUCTION

THE purpose of the present paper is to ascertain if it is possible to determine a phenomenological description of the neutron-proton interaction in terms of a potential. A further aim is to determine with what uniqueness this potential can be determined from the present experiments, particularly those at high energies. The program will be to assume a number of potential models so adjusted that they fit the low energy region and attempt to correlate the high energy scattering with the various features of each model.

It is well known that the experimental results in the low energy region can be described by an interaction potential; however, for sufficiently high energies relativistic corrections may be expected to be of major importance. Detailed scattering calculations, using a field theory, show that the use of relativistic momenta corresponds to calculating the kinematical aspects relativistically, but that the dynamical corrections depend on the specific theory employed. Scattering deduced from a field theory[1] has, in general, relativistic corrections proportional to $(v/c)^2$; for example, at 90 Mev $(v/c)^2$ is 0.05 while approximately 10 percent corrections are found by application of the Møller method to the scalar and vector meson theories.[2] Thus a choice cannot be made between two models both of which agree within 10 percent with the experimental results at 90 Mev.

The experimental results of the low energy region (including some derived quantities) are summarized in Table I. None of these experiments give information concerning the explicit radial dependence of the forces or of the forces in other than S states, and, in fact even the ranges are determined only approximately. In the triplet state there is a further uncertainty in the relative central and tensor ranges. This latter uncertainty would be removed considerably if it were assumed that the magnetic moment gave a measure of the D state admixture due to tensor forces. Unfortunately, because of uncertain relativistic corrections[3] this forms an unreliable restriction. The depths of the various potentials, i.e., singlet and triplet central and triplet tensor, are, however, accurately determined for any specified combination of ranges.

The high energy experimental angular distributions are shown in graphical form in Fig. 1. The expansion (in Legendre polynomials, $P_n(\theta)$) for the 90-Mev distribution is

$$4\pi\cdot\sigma(\theta)=\sigma[1-0.14P_1(\theta)+0.73P_2(\theta)+0.08P_3(\theta)+0.17P_4(\theta)],$$

with an estimated error of ±0.1 for the coefficients of $P_1(\theta)$ through $P_4(\theta)$. The most noteworthy result is the near symmetry about 90°. We have therefore assumed that the 40-Mev angular distribution, which has been determined only in the range 60°–180°, is symmetrical

[1] L. Rosenfeld, *Nuclear Forces* (Interscience Publishers, Inc., New York), Vol. 2, p. 311 ff. It might appear at first sight that corrections due to spin orbit coupling are of order v/c. Actually, in a field theory calculation corrections which introduce this coupling include also a gradient of the potential (e.g., the Thomas term for the hydrogen atom) which in scattering produces an additional factor of v/c.

[2] H. Snyder and R. E. Marshak, Phys. Rev. **72**, 1253 (1947).

[3] R. G. Sachs, Phys. Rev. **72**, 91 (1947); H. Primakoff, Phys. Rev. **72**, 118 (1947); G. Breit and I. Bloch, Phys. Rev. **72**, 135 (1947).

TABLE I. Derived quantities

Quantity	Notation	Magnitude	Source (with error)
Singlet scattering length	^1a	$-23.70\pm0.10\times10^{-13}$ cm	Ortho-parascattering[a] ($\pm0.03\times10^{-13}$ cm) Crystal scattering[b] ($\pm0.05\times10^{-13}$ cm) Zero energy cross section[c] ($\pm0.06\times10^{-13}$ cm)
Radius of deuteron	r_d	$4.332\pm0.025\times10^{-13}$ cm	Binding energy[d]
Triplet scattering length	^3a	$5.26\pm0.12\times10^{-13}$ cm	Ortho-parascattering ($\pm0.09\times10^{-13}$ cm) Crystal scattering ($\pm0.15\times10^{-13}$ cm) Zero energy cross section ($\pm0.03\times10^{-13}$ cm)
Triplet effective range (shape-independent approx.)	^3r	$1.53\pm0.20\times10^{-13}$ cm	From ^3a ($\pm0.17\times10^{-13}$ cm) From r_d ($\pm0.03\times10^{-13}$ cm)
Singlet effective range	^1r	$<3\times10^{-13}$ cm	Scattering between 0 and 6 Mev
Electric quadrupole moment	Q	$2.73\pm0.05\times10^{-27}$ cm^2	Directly determined[e]
Percent D state	W_D	3.9 percent	Magnetic dipole moment, neglecting relativistic effects

[a] Sutton, Hall, Anderson, Bridge, DeWire, Lavatelli, Long, Snyder, and Williams, Phys. Rev. **72**, 1147 (1947).
[b] Shull, Wollan, Morton, and Davidson, Phys. Rev. **73**, 842 (1948).
[c] W. B. Jones, Jr., Phys. Rev. **74**, 364 (1948); Melkonian, Rainwater, and Havens, Phys. Rev. **75**, 1295 (1949).
[d] R. E. Bell and L. G. Elliot, Phys. Rev. **74**, 1552 (1948); W. E. Stephens, Rev. Mod. Phys. **19**, 19 (1947); W. E. Stephens, Phys. Rev. **76**, 181 (1949); Tollestrup, Jenkins, Fowler, and Lauritsen, Phys. Rev. **75**, 1947 (1949).
[e] A. Nordsieck, Phys. Rev. **58**, 310 (1940).

about 90° with the consequent expansion

$$4\pi\sigma(\theta)=\sigma(1+0.26P_2(\theta)+0.02P_4(\theta)),$$

with an estimated error of ±0.1 for the $P_2(\theta)$ and $P_4(\theta)$ coefficients. The experimental total cross sections are tabulated in Table II. The low values for the total cross sections appear to be further corroboration of the lack of odd harmonics in scattering.

A unique analysis into phase shifts of the experimental angular distribution is impossible due to the presence of the mixture of singlet and triplet states as well as the complication of the tensor force. Nevertheless, on the simplifying assumption of scattering with no spin dependence, the 90-Mev angular distribution may be analyzed to give the order of magnitude of the phase shifts. The results of this are: S wave, $53°\pm5°$; P wave, $-1°\pm1°$; D wave, $5°\pm1°$. Since the P and D phase shifts are so small, we may conclude that at 90 Mev the S scattering accounts for about 90 percent of the total scattering cross section. The high energy cross sections, therefore, determine the S scattering fairly unambiguously. The potentials usually considered show significant differences in S scattering above 30–40 Mev when adjusted to have the same low energy properties. The comparison then of the S wave cross sections provides one method of detemining the potential shape.

The angular distribution at a particular energy yields information primarily concerning the exchange character of the forces. For example, theories such as the "charged" or "neutral" which predict large scattering in odd states may be immediately discarded as unacceptable. The low values of the high energy cross sections also favor theories without large scattering in odd states.

Finally, comparison of angular distributions at two or more high energies enables one to distinguish shape features of the various potentials. This final comparison is a critical test of the potential shape since, while it is possible with any shape, by a proper choice of range, to fit the angular distribution at 90 Mev and the low energy data simultaneously, it will not, in general, be possible to also fit the 40-Mev angular distribution.

COMPUTATIONAL METHODS

Various approximate methods were employed to avoid the many tedious numerical integrations required for a comprehensive investigation of the effect of the many parameters. These are principally concerned with the integration of the radial equations to yield phase shifts or eigenvalues.

Most of the calculations were done by iteration of trial functions in the integral form of the equations. In order that this procedure might converge rapidly, it was necessary to have good initial trial functions, especially in the case of potentials with a deep hole at the origin. Suitable trial functions were provided by the WKB approximation (explicitly using one-third order Bessel functions as the asymptotic representations).[4] This approximation has been further extended to the case of coupled equations as follows.

Let the differential equations to be solved be:

$$u''+A(x)u+B(x)w=0$$
$$w''+C(x)w+B(x)u=0.$$

The desired representation of the solution is then

$$u=\cos\eta\cdot(S/S')^{\frac{1}{2}}Z_{1/3}(S)$$
$$w=\sin\eta\cdot(S/S')^{\frac{1}{2}}Z_{1/3}(S).$$

[4] R. E. Langer, Phys. Rev. **51**, 669 (1937).

Where

$$S_{\pm}=\frac{1}{2^{\frac{1}{2}}}\int_{x_1}^{x}\{A+C\pm[(A-C)^2+4B^2]^{\frac{1}{2}}\}^{\frac{1}{2}},$$

$$\tan\eta=[(S_{\pm}')^2-A]/B,$$

with x_1 being a turning point of $(S_{\pm}')^2$. The + and − signs correspond to two independent representations. The Z's are Bessel functions of order one-third. The usual phase integral condition for the bound state is replaced by the similar condition,

$$\int_{x1}^{x2}S'dx=S_n,$$

where x_1 and x_2 are the turning points and S_n is a root of

$$(d/dS)(S)^{\frac{1}{2}}[J_{1/3}(S)+J_{-1/3}(S)]=0.$$

These representations have been found to yield close approximations to the wave functions at all energies, the S wave phase shifts being, in general, in error by less than five degrees, and the wave functions exhibiting the correct general behavior. When applied to the bound state, the phase integral condition yields potential depths that are within 10 percent of the correct value.

The bound deuteron state was numerically iterated using the variation-iteration[5] method, using as a trial function the approximate WKB functions above. Three iterations yielded an eigenvalue and wave functions with an accuracy of about one percent. The accuracy was essentially limited by the numerical methods used (intervals corresponding to one- to two-tenths of the effective range were used).

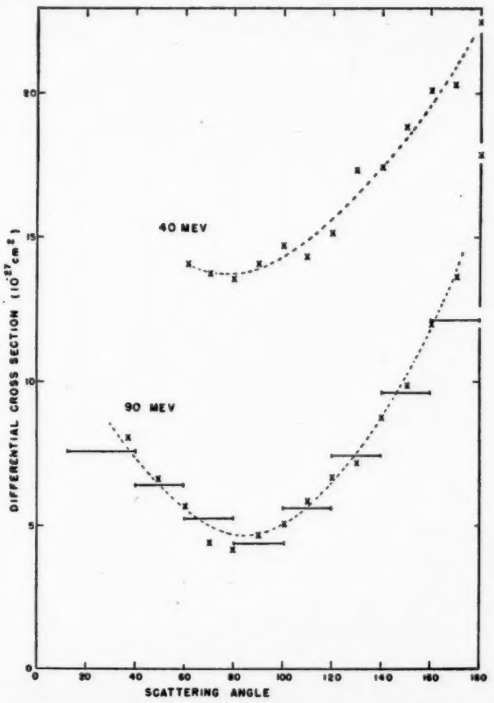

FIG. 1. Experimental angular distribution. The crosses are the counter data (see Table II, reference a); the horizontal lines at 90 Mev are the coud-chamber data. [See Brueckner, Hartsough, Hayward, and Powell, Phys. Rev. 75, 555 (1949).] The normalization chosen agrees with the total cross section as given in Table II.

[5] N. Svartholm, The binding energies of the lightest atomic nuclei, University of Lund (thesis Phys. Inst. 86 pp. (1945)). J. Schwinger, Phys. Rev. 72, 742(A) (1947), and hectographed "Notes on nuclear theory," Harvard (1947).

TABLE II. High energy total cross sections. The error in the mean energy arises from uncertainties in detector efficiency, neutron beam distribution, and variation of cross section with energy. The "average" $\sin^2\delta_s$ is determined by subtracting the contributions of the higher partial waves as derived from the angular distribution on the basis of no spin dependence in scattering.

Mean energy Mev	Total cross section with statistical error 10^{-24} cm	Detection method	Average $\sin^2\delta_s$
41±4	0.174±0.010	Proton recoils	0.67±0.11[a]
40±4	0.202±0.007	$C^{12}(n, 2n)C^{11}$	0.76±0.11[b]
83±7	0.083±0.004	$C^{12}(n, 2n)C^{11}$	0.66±0.08[c]
90±3	0.079±0.007	Proton recoils	0.68±0.08[a]
95±5	0.073±0.002	Bi fission	0.66±0.06[d]

[a] Hadley, Kelly, Leith, Segrè, Wiegand, and York, Phys. Rev. 75, 351 (1949).
[b] R. H. Hildebrand and C. E. Leith, Phys. Rev. 76, 587 (1949); also private communication.
[c] Cook, McMillan, Peterson, and Sewell, Phys. Rev. 72, 1264 (1947).
[d] DeJuren, Knable, and Moyer, Phys. Rev. 76, 589 (1949).

For the $^3S_1+^3D_1$ scattering state, the appropriate WKB functions furnished trial functions for the coupled integral system

$$u=A\sin kx+M/\hbar^2\int_0^{\infty}G_0(kx, kx')\times[V_c(x')u(x')+2^{\frac{1}{2}}\gamma V_t(x')w(x')]dx'$$

$$w=Bg_2(kx)+M/\hbar^2\int_0^{\infty}G_2(kx, kx')\times\{[V_c(x')-2\gamma V_t(x')]w(x')+2^{\frac{1}{2}}\gamma V_t(x')u(x')\}dx',$$

where $A=1$, $B=0$ corresponds to the choice of the positive sign in $(S_{\pm}')^2$ and

$$A=\frac{M}{\hbar^2k}\int_0^{\infty}\cos kx'[V_c(x')u(x')+2^{\frac{1}{2}}\gamma V_t(x')w(x')]dx',$$

$B=1$ corresponds to the negative sign. Further,

$$G_0(kx, kx')=(1/k)\sin kx_<\cos kx_>$$
$$G_2(kx, kx')=(1/k)^3g_2(kx)_<k^2g_{-2}(kx)_>.,$$

where $x_<$ means the lesser of x and x', and $g_2(kx)$ and $g_{-2}(kx)$ are the regular and irregular spherical Bessel functions of order 5/2.

The potential has been written in the form

$$V(r, \sigma)=V_c(r)+\gamma S_{12}V_t(r).$$

The iteration of the integral equations above was carried out numerically with the normalization of the trial functions so chosen that the iterated functions matched the trial functions in the region where the kernel of the integral system is largest. Three iterations for the

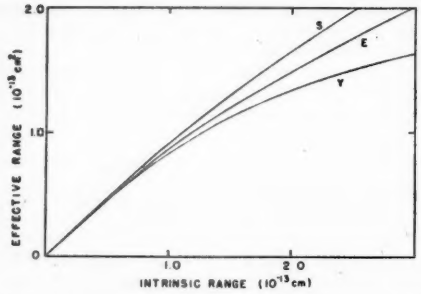

FIG. 2. The triplet effective range for the Yukawa (Y), exponential (E), and the square well (S) potentials. The intrinsic range is 2.12 R, 3.54 R, and R for the three potentials in the order named above. R is the usual parametric range that occurs in the radial dependence, i.e., $\exp(-r/R)/(r/R)$, $\exp(-r/R)$ for the Yukawa and exponential potentials and a constant potential extending a distance R for the square well potential.

S dominant mode (i.e., with $A=1$, $B=0$) and one for the D dominant mode yielded phase shifts with an accuracy of about two percent.

The phase shift in the $^3D_2$ state was calculated using the variational procedure with the $^3D_2$ component of the plane wave as a trial function. The phase shift in the $^3D_3+^3F_3$ state was computed using the same procedure as for the $^3S_1+^3D_1$ state. One iteration yielded an accuracy of two percent.

The Born approximation was used to effect the inclusion of the angular momentum states for $l\geq 4$ in the scattering sum. The sum was, in general, done by actually summing the individual terms for $l\leq 3$, using calculated phase shifts, and adding the Born cross section from which these states had been suitably subtracted. The angular distributions so derived are accurate within two to five percent.

CENTRAL FORCES

We shall consider in this section the results of scattering from a model which consists only of central forces since, as will be seen later, it is possible to make a state-by-state comparison of the scattering from a central force model and from one which includes tensor forces.

The details of low energy scattering will not be treated here, but, rather, the reader is referred to the

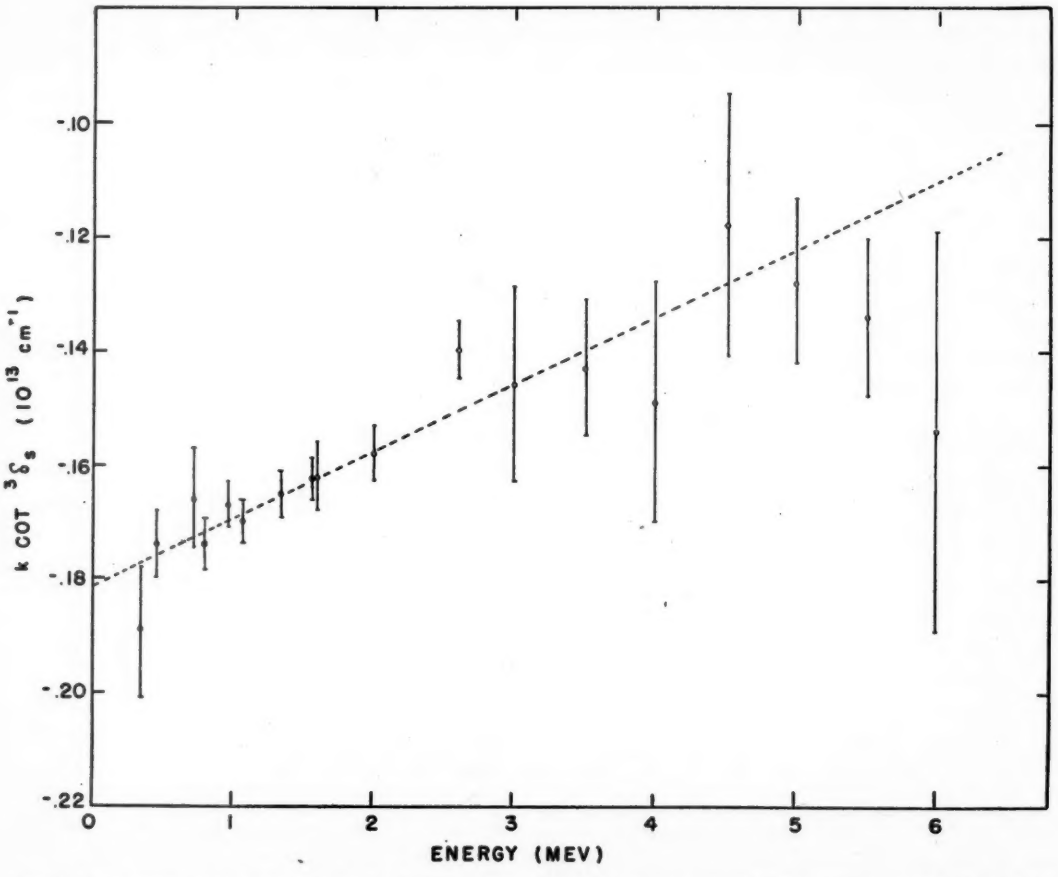

FIG. 3. Low energy triplet scattering on the assumption of a 3.0×10^{-13}-cm singlet effective range. This plot yields $5.51\pm0.16\times10^{-13}$ cm and $1.98\pm0.26\times10^{-13}$ cm for the triplet scattering length and effective range, respectively. The experimental points [open circles, (Bailey, Bennett, Bergstralh, Nuckolls, Richards, and Williams, Phys. Rev. **70**, 583 (1946)), solid circles (Professor J. H. Williams has kindly communicated to us more recent values of the experiments of Lampi, Freier, and Williams, Phys. Rev. **76**, 188 (1949). Further experiments are still in progress.)] are from the data of the Minnesota group.

review of Blatt and Jackson.[6] One result of their work is that in the expansion (the notation is explained in Table I)

$$k \cot {}^3\delta_S = -(1/{}^3a) + \tfrac{1}{2}({}^3r)k^2 - {}^3Tk^4 + \cdots$$

the shape dependent coefficient, T, is sufficiently small that below 6 Mev it can be neglected, and, in interpreting the experiments, the shape independent approximation may be used. The effective range in the triplet state is determined, therefore, by the approximate relation

$$(1/{}^3a) = (1/r_d)[1 - \tfrac{1}{2}({}^3r/r_d)].$$

Substituting the experimental values from Table I, we obtain

$${}^3r = 1.53 \pm 0.20 \times 10^{-13} \text{ cm}.$$

Figure 2 is a plot of effective range *versus* intrinsic range for the triplet state of the various potentials. The singlet effective range is not well determined by the present experiments, as can be seen by reference to Figs. 3 and 4.

To simplify the analysis of the high energy data, it is convenient (and reasonable) to assume exact symmetry of scattering about 90°. This means that the potential is assumed to be zero in odd parity states. The experimental results are actually compatible with a small repulsive potential in odd states, but this shall be considered as a small perturbation which will not essentially alter any of the following conclusions. The factor $\frac{1}{2}(1+P_x)$ will, therefore, be included as a factor in the potential and will have as one consequence that the total cross section computed for any radial dependence will be the minimum possible over any other choice of exchange dependence. The main effect of any admissible odd wave phase shifts is the interference with the large S wave phase shift, which is in evidence only in the angular distribution, and its actual effect on the total cross section is negligible.

In order to compare different potential shapes, the effective range has been taken as a common parameter. For example, we have plotted (Fig. 5) the S wave phase shift at 90 Mev for the various potentials *versus* the effective range. This device insures similar low energy behavior for the same abscissa.

In Fig. 6 are plots at 90 Mev, for the various potentials, of the total cross section and of 4π times the

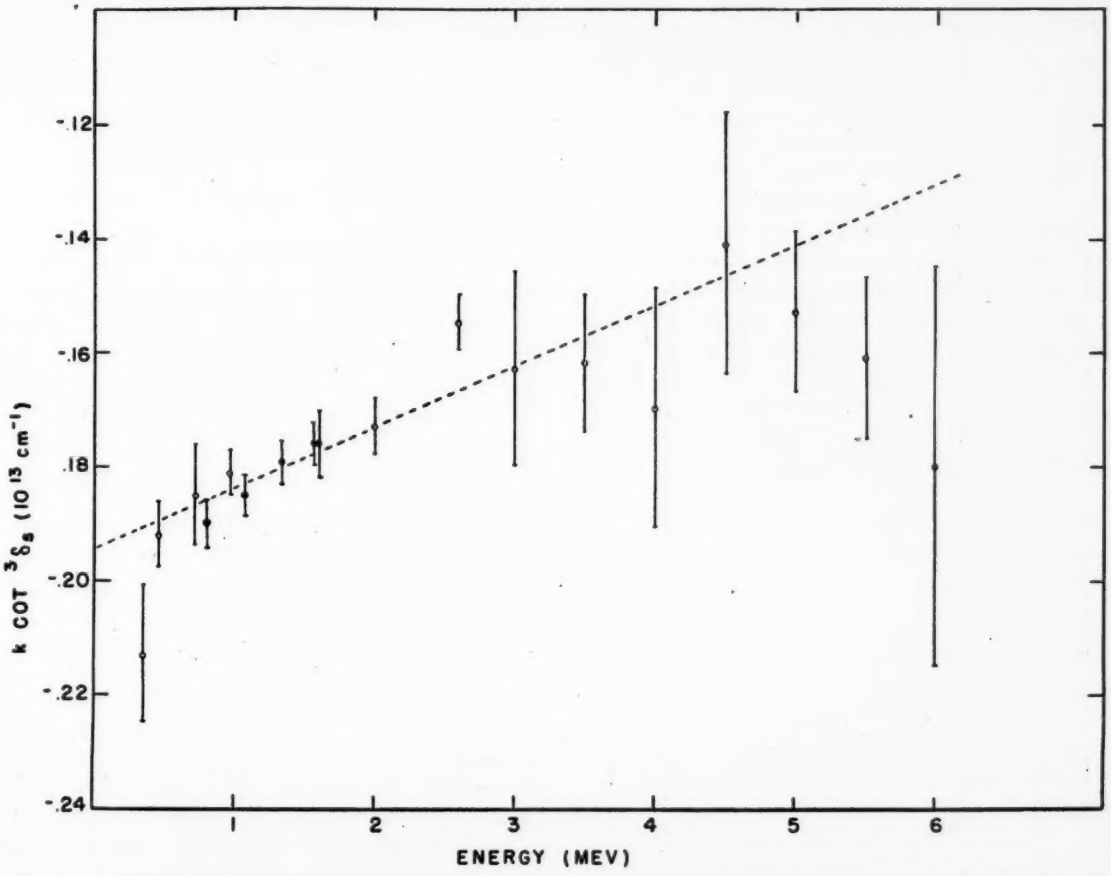

FIG. 4. Low energy triplet scattering on the assumption of a zero singlet range. This plot yields $5.14 \pm 0.16 \times 10^{-13}$ cm and $1.77 \pm 0.26 \times 10^{-13}$ cm for the triplet scattering length and effective range, respectively.

[6] J. M. Blatt, Phys. Rev. **74**, 92 (1948); J. M. Blatt and J. D. Jackson, Phys. Rev. **76**, 18 (1949).

differential cross section for scattering at 90° and 180° as functions of the effective range on the assumption of no odd parity interaction. For the plots of complete total cross section, i.e., the sum of triplet and singlet scattering, it is necessary to make some choice of a singlet range corresponding to a particular triplet range. The low energy region implies only loose restrictions on the singlet range; we may, therefore, choose the singlet range so that the singlet and triplet intrinsic ranges are equal. The results for the complete cross sections are also shown in Fig. 6. From these plots it is possible to make further limitations on the allowable triplet ranges by a comparison with the experimental values of $\sigma(180°)/\sigma(90°)$.

With the Yukawa or exponential potential, a range adjusted for the 90-Mev ratio predicts a 40-Mev ratio within the experimental limits. However, with the square well potential, the range required at 40 Mev is considerably larger than that required at 90 Mev. This difference in behavior results primarily from the more rapid decrease in σ (90°) with energy increase for the "cut-off" potential than for the "long-tailed" potentials. This, in turn, can be interpreted in terms of the destructive interference between the S and D waves at 90°. In detail, the S wave phase shift decreases more rapidly (as a function of energy) for the cut-off potentials (Fig. 7). Further the D wave phase shift is nearly a linearly increasing function of energy for the long-tailed potentials, while the increase with energy is much more rapid for the cut-off potentials (Fig. 8).

For potentials which have a "deep hole" at the origin (e.g., the Yukawa and exponential), the long-tail is necessary to give a sufficiently long effective range. However, as the energy increases the contributions to the S wave phase shift come from regions closer to the origin, and, consequently, at high energies the deep hole (and, therefore, long-tailed) potentials yield larger phase shifts than the cut-off potentials (e.g., the square well or Gauss potentials). These remarks are further illustrated by reference to Figs. 5 and 7.

While it is impossible to define the limits of the singlet effective range with any accuracy, for ${}^3\gamma < 1.7 \times 10^{-13}$ cm, the best fits for the angular distribution are obtained with the singlet effective range between $2.5-3.0\times10^{-13}$ cm.

The complete angular distribution is shown in Figs. 9 and 10, for the Yukawa and exponential potentials with ranges chosen such that they are both good fits of the angular distribution at 90 Mev. From this the superiority of the Yukawa angular distribution at 40 Mev is apparent. The total cross sections, however, are in much better agreement with the exponential potential.

The only partial waves contributing appreciably to the cross sections are the S and D waves, consequently, the angular distribution can be expanded in terms of Legendre polynomials P_0, P_2, and P_4. The coefficient of P_0 is identical with the total cross section, that of P_2 arises primarily from the interference between the S and D states, and that of P_4 arises primarily from the combinations of the various D states. These coefficients allow a rapid comparison of theory and experiment and are therefore tabulated in Table III for all models mentioned explicitly.

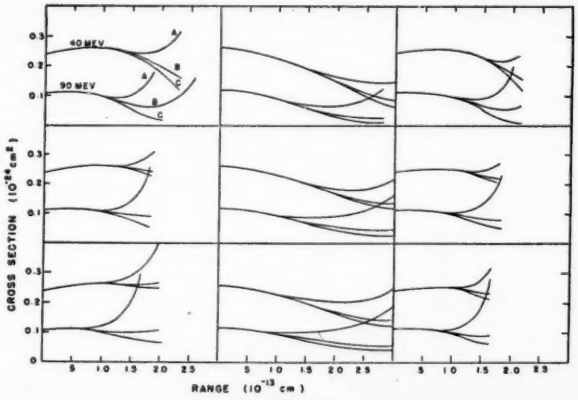

FIG. 6. Central force scattering at 40 and 90 Mev. The first column gives the triplet scattering; the second, the singlet scattering; and the third, the complete scattering (assuming equal intrinsic ranges). The first row is for the square well; the second, for the exponential; and the third, for the Yukawa potential. In each figure the upper set of three curves is for 40 Mev; the lower, for 90 Mev. For each set of three curves the uppermost is $4\pi\cdot\sigma(180°)$; the middle curve is the total cross section; and the lower is $4\pi\cdot\sigma(90°)$. (Illustrated in the first figure by A, B, and C, respectively.) In all cases the exchange dependence is assumed to be $\frac{1}{2}(1+P_x)$ [therefore, $\sigma(180°)=\sigma(0°)$], and the depths are chosen to fit the deuteron and the zero energy scattering.

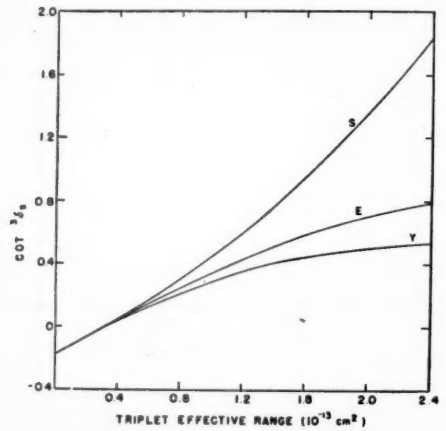

FIG. 5. Triplet S wave scattering at 90 Mev.

If we consider the Yukawa and exponential potentials of Figs. 9 and 10, we see that the only discrepancy with the experimental values of the coefficients occurs in the magnitude of the P_4 coefficient which is perhaps a factor of two to three too large. This is manifested in the angular distribution by a theoretical prediction that is somewhat too flat in the region about 90°.

Figure 9 and Table III show the effect of adding a small repulsive potential in the odd parity states. This modification may be expressed by a potential factor, $(1-a+aP_x)$. The best fit for this type of exchange interaction is $a=0.55\pm0.05$.

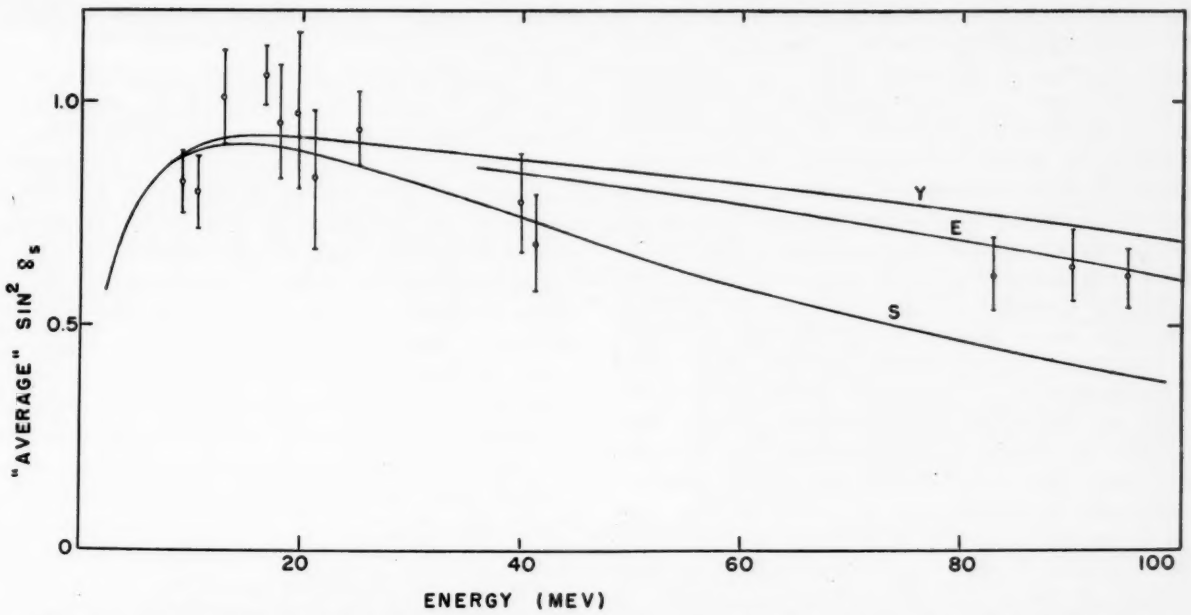

FIG. 7. S wave scattering phase shift, illustrated for a triplet effective range of 1.65×10^{-13} cm and a singlet effective range of 3.0×10^{-13} cm. Y, E, and S refer to the Yukawa, exponential, and square well central potentials, respectively. The experimental points below 25 Mev are from the data of W. Sleator, Jr., Phys. Rev. **72**, 207 (1947), and R. Sherr Phys. Rev. **68**, 240 (1945) (above 40 Mev, see Table II).

The large odd state potentials in the singlet state required by the symmetrical theory produces far too much exchange scattering for any potentials with a tail and a range compatible with low energy scattering. For cut-off potentials such as the square well, the observed ratio $\sigma(180°)/\sigma(90°)$ may be fitted at 90 Mev with a range of $1.7-1.8\times10^{-13}$ cm; however, at 40 Mev, a fit to $\sigma(180°)/\sigma(90°)$ would require a range longer than 2.0×10^{-13} cm. Furthermore, in these latter cases the shape of the predicted angular distribution is not similar to the experimental results for small angle scattering. The symmetrical theory can, therefore, be ruled out for central forces.

TENSOR FORCES

A. The Bound State and Low Energy Scattering

The existence of the deuteron quadrupole moment requires the inclusion of a tensor potential in the neutron-proton interaction. We consider first the case where the radial dependence is chosen the same for both the central and tensor potentials. The extreme cases of long-tailed and cut-off potentials are exemplified by the Yukawa and square well, respectively. Calculations of the quadrupole moment have been made for these potentials as a function of range and tensor depth with the central depth adjusted to give the correct binding energy. The results are presented graphically in Figs. 11–13.

The calculations of Rarita and Schwinger[7] have shown that at least for the choice of a square potential, there is only slight modification of the low energy scattering properties upon the introduction of tensor forces. Such behavior can be expected for more general potential shapes with ranges shorter than the deuteron radius since the S wave component is determined primarily from the boundary conditions at the origin and asymptotically.[8]

We can put these arguments on a quantitative basis by the consideration of an "equivalent central potential," "$V(r)$." For the potential $V(r)=V_c(r)+\gamma S_{12}V_t(r)$, the equivalent central potential for the S wave is

$$"V(r)"=V_c(r)+2^{\frac{1}{2}}\gamma V_t(r)\cdot R(r),$$

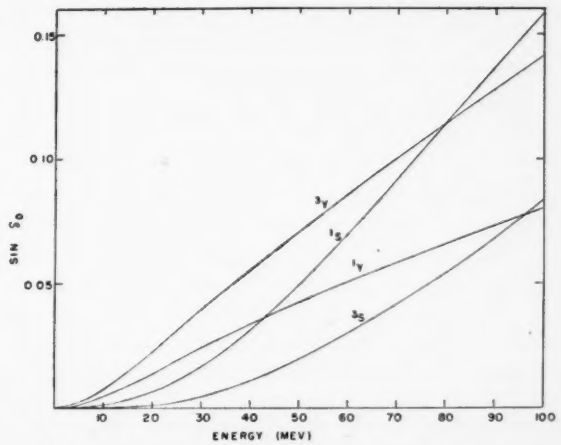

FIG. 8. D wave scattering. The quantity plotted is the sine of the D wave phase shift for the singlet and triplet Yukawa (labeled ^1Y and ^3Y) and for the singlet and triplet square well potentials (labeled ^1S and ^3S).

[7] W. Rarita and J. Schwinger, Phys. Rev. **59**, 436 (1941).

[8] W. Hefner and R. Peierls, Proc. Roy. Soc. **181**, 43 (1942).

where $R(r)$ is the ratio of the D wave to the S wave. $R(r)$ will be, in general, a slowly varying function of the energy (at least in the region where the potential is large). Its form may then be estimated from considerations of the bound state solutions. It is found then that $R(r)$ is zero at the origin, increases to a maximum value (about 0.2 or 0.3) somewhere between the maximum of the S wave radial function and the tensor force range, and decreases a symptotically to a small value (somewhere under 0.1). Then if we consider the ratio of the equivalent potential "$V(r)$" to the central potential $V_c(r)$ (the latter adjusted to give binding by itself), we would find the ratio to be less than unity at the origin, greater than unity in the neighborhood of the range, and again less than unity asymptotically. Thus the equivalent potential will be shallower at the origin and asymptotically, and will be deeper in the neighborhood of the tensor range.

This can be further illustrated in terms of the WKB approximation. In this approximation, $R(r)$ is independent of energy and decreases asymptotically to zero. The equivalent potential in this approximation is

$$"V"=V_c-\gamma V_t-\frac{3}{r^2}+\left[\left(\gamma V_t+\frac{3}{r^2}\right)^2+8(\gamma V_t)^2\right]^{\frac{1}{2}}.$$

Since the centrifugal potential is usually large compared to the tensor potential, this may be simplified to

$$"V"=V_c+\tfrac{4}{3}(\gamma r V_t)^2,$$

which is clearly in agreement with the preceding remarks.

The analysis of the low energy scattering is again conveniently carried out in terms of the expansion of the phase shift in powers of the energy.[9] Since the shape-independent approximation is valid for Yukawa ranges less than 1.4×10^{-13} cm and for all square well ranges considered, the effective range is essentially determined from the triplet scattering length. (The explicit value of the shape-dependent coefficient as well as the effective ranges are shown in Table IV for a number of cases.) We have chosen, therefore, in order to relate the scattering characteristics of a potential with its ability to produce a quadrupole moment, to plot $1/\gamma$ *versus* the scattering length (Fig. 14) with the range indicated parametrically along the curves. From this plot we can conclude that with the accepted value of the scattering length, the proportion of tensor potential must be quite large, the actual amount being lower for the long-tailed potential.

The low energy constants for the case in which the tensor force range is increased relative to the central force range are given in Table IV and Fig. 15. From the equivalent potential we see that the main effect is to increase the long-tailed character of the potential. This is evident by the decrease in the percentage D state and by the increase in the shape-dependent coefficient.

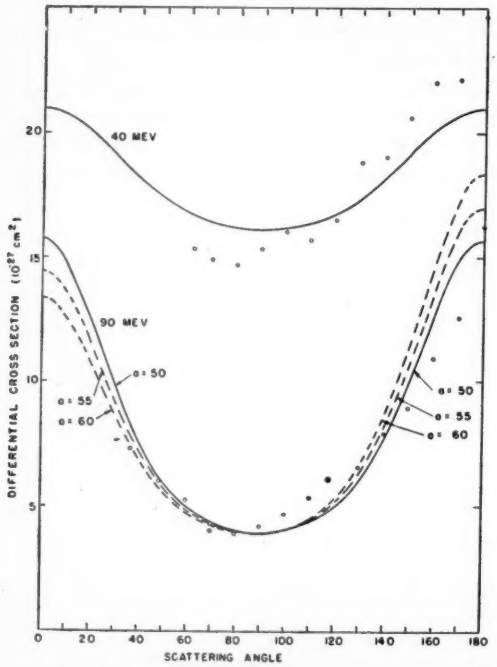

FIG. 9. Scattering at 40 and 90 Mev from an exponential potential, $\exp(-r/R)$, ($R=0.7\times10^{-13}$ cm for both singlet and triplet states) without tensor force. The solid lines are for a $(1+P_x)/2$ exchange dependence; the dotted curves illustrate the effect of increasing the amount of exchange forces. The total cross sections for this potential are 21.7×10^{-26} cm^2 and 7.9×10^{-26} cm^2 at 40 and 90 Mev, respectively. The experimental points (see Fig. 1) have been normalized to fit the theoretical angular distribution.

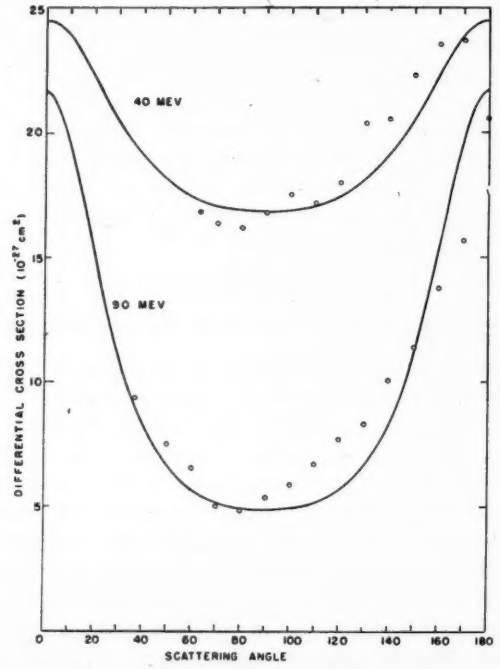

FIG. 10. Scattering from the Yukawa potential $\exp(-r/R)/(r/R)$ at 40 and 90 Mev for a range $R=1.35\times10^{-13}$ cm for both singlet and triplet states without tensor force. The total cross sections are 22.9 and 9.3×10^{-26} cm^2 at 40 and 90 Mev respectively.

[9] R. Christian, Phys. Rev. 75, 1675 (1949).

TABLE III. High energy scattering behavior of various models. The range (R) is the same in singlet and triplet states. For all cases where $\gamma \neq 0$, γ is adjusted to $Q=2.73\times10^{-27}$ cm². σ is the total cross section, the differential cross section being $4\pi\sigma(\theta)=\sigma\cdot\Sigma a_n P_n(\theta)$, where $a_0=1$.

Model				90 Mev							40 Mev		
Exchange dependence	Range (10^{-13} cm)	Radial dependence	γ	σ (10^{-26} cm²)	a_1	a_2	a_3	a_4	$\frac{\sigma(180)}{\sigma(90)}$	$\frac{\sigma(0)}{\sigma(90)}$	σ (10^{-26} cm²)	a_2	$\frac{\sigma(180)}{\sigma(90)}$
$\frac{1}{2}(1+Px)$	1.18	Y	0	9.0	0	0.77	0	0.39	3.25	3.25	23.1	0.15	1.26
$\frac{1}{2}(1+Px)$	1.18	Y	5.6	9.9	0	0.75	0	0.04	2.91	2.91	—	—	—
$\frac{1}{2}(1+Px)$	1.35	Y	0	9.3	0	0.98	0	0.57	4.6	4.6	22.9	0.21	1.45
$\frac{1}{2}(1+Px)$	1.35	Y	1.9	10.2	0	0.78	0	0.14	3.20	3.20	23.1	0.24	1.46
$(0.37+0.63Px)S_{12}$*	1.35	Y	1.9	10.7	−0.20	0.70	0.12	0.12	3.04	2.95	—	—	—
$(0.24+0.76Px)S_{12}$*	1.35	Y	1.9	12.0	−0.35	0.66	0.24	0.06	2.61	2.46	—	—	—
$0.45+0.55Px$	1.35	Y	1.9	10.3	−0.16	0.78	−0.02	0.15	3.52	2.84	—	—	—
$0.4+0.6Px$	1.35	Y	1.9	10.4	−0.32	0.77	−0.05	0.16	3.78	2.48	—	—	—
$\frac{1}{2}(1+Px)$	0.7	E	0	7.9	0	0.99	0	0.39	4.00	4.00	21.5	0.17	1.30
$0.45+0.55Px$	0.7	E	0	7.9	−0.10	0.99	−0.07	0.39	4.33	3.69	—	—	—
$0.4+0.6Px$	0.7	E	0	8.0	−0.20	1.00	−0.16	0.41	4.68	3.39	—	—	—
$\frac{1}{2}(1+Px)$	0.75	E	1.8	8.7	0	0.92	0	0.03	3.8	3.8	21.7	0.18	1.33
$-\frac{1}{2}(\sigma_1\cdot\sigma_2)(\tau_1\cdot\tau_2)$	2.0	S	0	7.1	−0.86	1.13	−0.34	0.12	9.57	1.59	21.3	0.11	1.42
$-\frac{1}{2}(\sigma_1\cdot\sigma_2)(\tau_1\cdot\tau_2)$	1.8	S	0	7.4	−0.61	0.63	−0.19	0.05	3.50	1.30	22.2	0.04	1.14
Experimental value				7.9±1.0	−0.14±0.10	0.73±0.10	0.08±0.10	0.17±0.10	3.6±0.6	3.0±1.0	19.4±2.0	0.26±0.10	1.55±0.20

* The exchange dependence for the central force is $\frac{1}{2}(1+Px)$.

B. High Energy Scattering

We will attempt in the next paragraphs to gain a qualitative understanding of the relation between central and tensor scattering. Then we will consider the result of various models, the calculations being carried out by the methods previously described.

As in the case of central forces we must adjust the ranges so that only the S and D partial waves contribute to the cross section. We would then expect that if the tensor force were a weak effect we could add the tensor scattering which would be present in Born approximation. Actually, as we have seen, the tensor force is far from weak and the approximation can only be expected to give the general trend. The characteristic peaking of the Born approximation cross section around 45 and 135° (the exact angle depending upon the model, range, and energy with a maximum occurring roughly where $2kR\sin\theta/2\sim1$) is, in fact, the type of correction needed to explain the discrepancy between the shapes of the experimental curves and the central force curves shown in Figs. 9 and 10, i.e., such a correction could convert the U-shaped central force curves into the more V-shaped experimental curves.

For a somewhat more detailed comparison we will again use the WKB approximation to approximate the equivalent central potentials, "$V_L{}^J$," for each of the states L and J, with the result

$$"V_0{}^1" = V_c-\gamma V_t-\frac{3}{r^2}+\left[\left(\frac{3}{r^2}+\gamma V_t\right)^2+8(\gamma V_t)^2\right]^{\frac{1}{2}} \approx V_c+\frac{4}{3}(\gamma r V_t)^2,$$

$$"V_2{}^1" = V_c-\gamma V_t-\frac{3}{r^2}-\left[\left(\frac{3}{r^2}+\gamma V_t\right)^2+8(\gamma V_t)^2\right]^{\frac{1}{2}} \approx V_c-2\gamma V_t+\frac{4}{3}(\gamma r V_t)^2-\frac{6}{r^2},$$

$$"V_2{}^2" = V_c+2\gamma V_t-\frac{6}{r^2},$$

$$"V_2{}^3" = V_c-\gamma V_t-\frac{13}{r^2}+\left[\left(\frac{7}{r^2}+\frac{3}{7}\gamma V_t\right)^2+3\left(\frac{12}{7}V_t\right)^2\right]^{\frac{1}{2}} \approx V_c-\frac{4}{7}\gamma V_t+\frac{3}{14}\left(\frac{12}{7}\right)^2(\gamma r V_t)^2-\frac{6}{r^2}.$$

In the approximation where we neglect the asymptotic amplitude of the coupled mode, as above, in the evaluation of the phase shifts there will be no difference between states of different magnetic quantum number, m_s; however, the WKB approximation yields angular distributions which agree with the results of a more accurate calculation within 10 to 20 percent.

As can be expected on the basis of the "equivalent potentials," there is only a small difference in the total scattering from the ${}^3S_1$ state. Further, we can summarize the behavior of the various D states in the following: (${}^3D_1$) Increasing the tensor depth (i.e., γ) decreases the equivalent potential and for strong tensor forces the resulting potential will be strongly repulsive. (${}^3D_2$) Increasing γ increases the potential depth to such an extent that for $\gamma\gtrsim1$, the depth is three to four times as deep as the depth on the central force model. (${}^3D_3$) The potential decreases for increasing γ such that for $\gamma\gtrsim1$ the potential will be just barely repulsive. (Approximately the same effects can be achieved by increasing the tensor range instead of the depth.)

To illustrate these remarks we will consider the high energy scattering from two extreme examples (calculated exactly): (1) The central and tensor depth are approximately equal with the square well radial dependence of range 2.7×10^{-13} cm; (2) the tensor depth accounts for practically all the binding with a Yukawa dependence and range of 1.2×10^{-13} cm. In Table V we have summarized the contribution of each state to the total cross section and indicated the sign of the phase

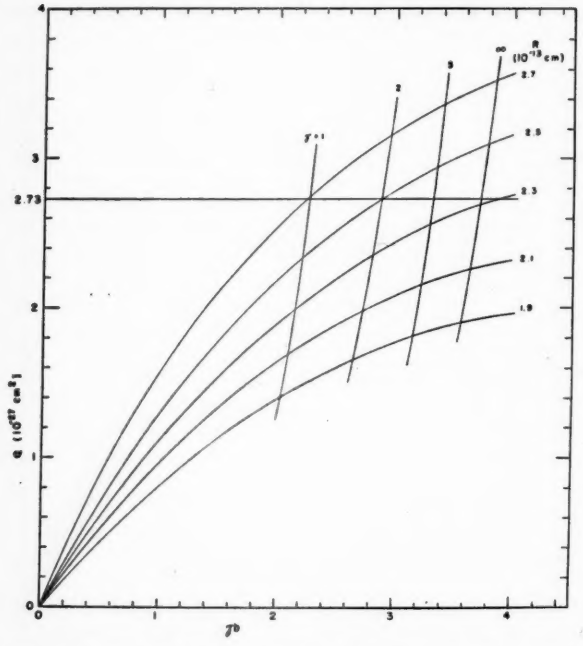

FIG. 11. Quadrupole moment for the square well. The binding energy used is 2.23 Mev, and the tensor and central ranges, R, are equal. b is the customary dimensionless well depth, equal to $MV_cR^2/\hbar$.

shift (i.e., the average over m_s). The results of the central force model with the same range and radial dependences are included for comparison.

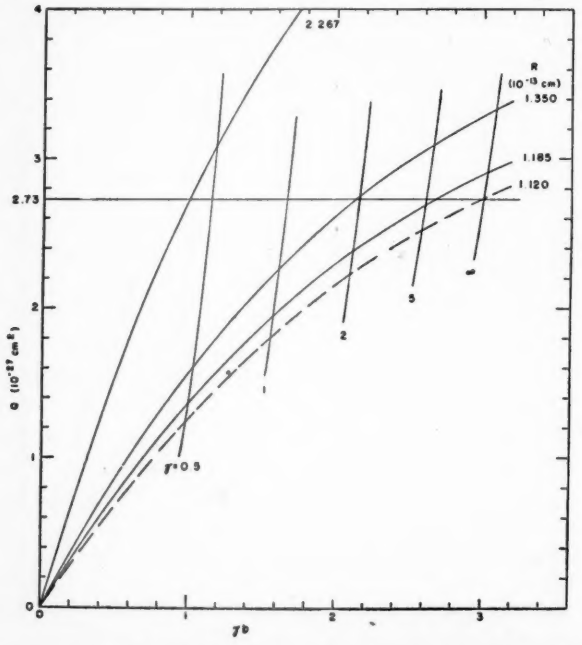

FIG. 12. Quadrupole moment for the Yukawa well. (The results for $R=1.185\times10^{-13}$ cm are in agreement with those from more precise calculations communicated to the authors by H. Feshbach.) The binding energy used is 2.183 Mev, and the tensor and central ranges, R, are equal. b is the customary dimensionless well depth, equal to $MV_cR^2/\hbar$. The curve for $R=1.120\times10^{-13}$ cm, shown as dashed, is extrapolated.

Utilizing this comparison between the tensor and central force models we can conclude that the potential must be long-tailed in order to maintain the relatively large scattering in the D state at 40 Mev without excessively large scattering in the D state at 90 Mev. Cut-off (e.g., square and Gauss) potentials where the tensor force has nearly the same range as the central forces are, therefore, unsuitable. An addition of a long shallow tail (5–6×10^{-13} cm) to the square well is required in the central force case to fit with the 40- and 90-Mev scattering and would, therefore, also be required for tensor forces. Potentials formed by the addition of such long-tails would seem to be indistinguishable from naturally long-tailed potentials such as the exponential or the Yukawa potential.

The results of using the Yukawa and exponential radial dependences (see Figs. 16–18) indicate that the addition of tensor forces causes only relatively small changes in the scattering. The best fits of the angular distribution require slightly longer ranges than for the purely tensor model. A detailed comparison, using the Legendre coefficients, shows that the $P_4(\theta)$ component is reduced in the tensor model. It is this decrease which allows considerably better fits of the angular distribution and is therefore evidence for the presence of tensor forces in scattering. The total cross section is increased, however, approximately 10 percent with the addition of tensor forces so that the agreement with the experimental value of the total cross section is poorer.

The same situation holds for the tensor model as for the central model regarding the intercomparison of the Yukawa and exponential potentials. That is, the Yukawa potential fits the angular distributions at both 40 and 90 Mev noticeably better, however the total cross section is 20 to 30 percent too high. The total cross section with the exponential potential is only 10 to 15 percent too high. Since the long-tail, which is necessary to fit the angular distribution, forces the potentials considered here to have a deep hole also and consequently high cross section, it would seem that an essentially more complicated radial dependence would be necessary to fit the experimental results more closely. It is believed, though, that the present experimental data (as well as uncertain relativistic effects) do not exclude either the Yukawa or exponential potentials.

The exchange character found necessary for the central force model is also valid, in the main, for the tensor force model (see Table III). As an example of spin dependent exchange dependence we have considered the case when the central force has a $\frac{1}{2}(1+Px)$ exchange dependence and the tensor force exchange dependence was of the form $(1+a-aPx)$. This does not produce as large asymmetries in the angular distribution as when $(1+a-aPx)$ is taken as a factor of both the central and tensor potential. The restriction on the magnitude of a now arises mainly from the

TABLE IV. Properties of selected Yukawa potentials. $^3\rho$ is the effective range as determined by using the deuteron wave function. ^3T, the shape dependent coefficient, has been determined from the approximate relation $^3T=\frac{1}{4}(^3\gamma)^2(^3\rho-^3\gamma)$, and checked by neglecting in the exact expression for ^3T all terms involving the coupled D state.[a] All the above potentials gave a value of 0.28 (within two percent) for the ratio of the cross sections for photo-magnetic to photoelectric disintegrations of the deuteron for the 2.76-Mev Na γ-ray using a value of 2.23 Mev as the binding energy of the deuteron. (For experimental values see Woodward and Halpern and Meiners.[b])

Central range (10^{-13} cm)	Tensor range (10^{-13} cm)	γ	W_D	$^3\rho$ (10^{-13} cm)	$^3\gamma$ (10^{-13} cm)	^3T (10^{-26} cm^3)	^3a (10^{-13} cm)
1.18	1.18	5.6	5.3	1.56	1.48	0.3	5.22
1.18	1.69	0.8	3.2	1.71	1.49	1.0	5.29
1.18	1.98	0.5	2.8	1.76	1.50	1.2	5.30
1.18	3.91	0.16	1.7	1.90	1.45	2.1	5.35
1.18	(No tensor force)	—	—	1.67	1.54	0.6	5.29
1.35	1.35	1.91	4.2	1.71	1.58	0.55	5.32
1.35	(No tensor force)	—	—	1.85	1.63	0.96	5.39

[a] See reference 9.
[b] W. M. Woodward and I. Halpern, Phys. Rev. **76**, 107 (1949); E. Meiners, Phys. Rev. **76**, 259 (1949).

increase in the total cross section. These limits are estimated to be $a=0.6\pm0.1$.

The principal change in the high energy scattering with increase in tensor range, is according to the WKB arguments, similar to an increase in the long-tailed character of the potential. The high energy scattering results are shown in Fig. 19 for the cases listed in Table IV. There is an increase in scattering from the higher states which may be interpreted as the increase in the long-tailed character or alternatively as showing that the characteristic Born approximation tensor peaking is displaced to smaller angles.

We wish to note here that all of the models seriously considered (because of the smallness of the odd state potentials) predict nearly isotropic distribution at 14 Mev in agreement with the recent experiments of Barschall and Taschek[10] who find isotropy within their statistical accuracy of six percent.

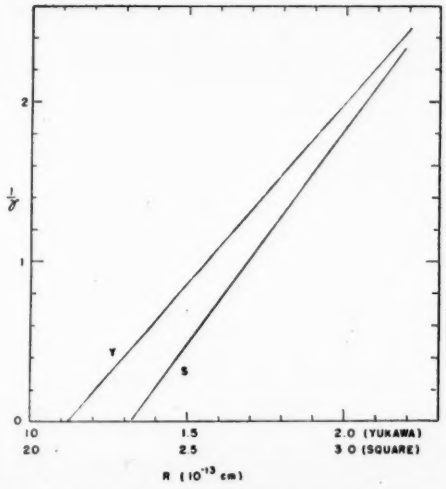

FIG. 13. Ratio of central well depth to tensor well depth for quadrupole moment equal to 2.73×10^{-27} cm^2. The binding energy fitted for the Yukawa (Y) case is 2.183 Mev and for the square well (S) case is 2.23 Mev.

[10] H. H. Barschall and R. F. Taschek, Phys. Rev. **75**, 1819 (1949).

CONCLUSIONS

1. Exchange character. If the potential has approximately the same radial dependence in all states (i.e., even and odd parity, singlet and triplet) and the range is chosen within acceptable limits, we may conclude that for a good fit, $a=0.55\pm0.05$, or, more generally, allowing for a different exchange character in single and triplet states, the depths of odd potentials, V_{odd}, must satisfy the approximate relation

$$0>\tfrac{1}{4}(^1V_{\text{odd}})+\tfrac{3}{4}(^3V_{\text{odd}})>-\tfrac{1}{5}(^3V_{\text{even}}).$$

2. Radial dependence. The $(1+P_x)/2$ potentials, when compared for equal effective ranges differ by at most a factor of two in the total cross section or in the ratio $\sigma(180°)/\sigma(90°)$. However, these differences may be correlated with general shape features. Further, the experiments are adequate to distinguish among the potential shapes.

(a) A long-tailed potential is necessary to explain the large scattering from the higher angular momentum states at 40 Mev without violently affecting the 90-Mev scattering. On this basis the square and gauss potentials are unacceptable while the exponential and Yukawa potentials are allowable.

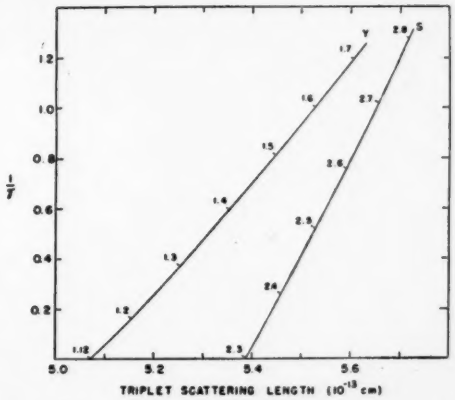

FIG. 14. Low energy scattering with tensor forces for the Yukawa (Y) and the square well (S) potentials. The range, R, is indicated (in units of 10^{-13} cm) parametrically along the curves. (Depths are adjusted to fit the binding energy and the quadrupole moment of the deuteron.)

TABLE V. Comparison of contributions of various states to total cross section.

State	Square well		Yukawa	
	Tensor forces (10^{-26} cm^2)	Central forces (10^{-26} cm^2)	Tensor forces (10^{-26} cm^2)	Central forces (10^{-26} cm^2)
$^3S_1$	2.95^+	3.25^+	8.82^+	9.58^+
$^3D_1$	0.35^-	0.95^+	0.55^-	0.14^+
$^3D_2$	5.87^+	1.58^+	1.82^+	0.24^+
$^3D_3$	0.72^+	2.21^+	0.14^-	0.33^+

(b). The Yukawa potential, because of its singular nature, predicts high total cross sections (approximately 20 to 30 percent higher than the best experimental value) for any combination of ranges. The exponential potential for approximately the same angular dependence predicts cross sections 10 percent to 20 percent lower, however, the detailed fit of the angular distribution is poorer. Both are acceptable, however, with the present experimental uncertainties.

The best fit for these potentials is (assuming the same range for all the forces)

$$R=0.75\times10^{-13} \text{ cm (exponential)}$$
$$R=1.35\times10^{-13} \text{ cm (Yukawa).}$$

(For calculations, where the tensor force is unimportant a central force model with a Yukawa range of 1.18×10^{-13} cm can be used.)

(c) The shape of the angular distribution about 90° is evidence of a tensor force in scattering. Here, with a $\frac{1}{2}(1+P_x)$ dependence, a purely central force yields a flatter distribution than an interaction including tensor forces. The latter distribution agrees significantly better with experiment.

3. Singlet range. The total cross-section measurements imply a singlet effective frange greater than 2×10^{-13} cm. A long singlet range is further favored by the angular distribution. Low energy scattering yields only the requirement that the singlet range be less than 3×10^{-13} cm.

4. Triplet range. The low energy limits on the effec-

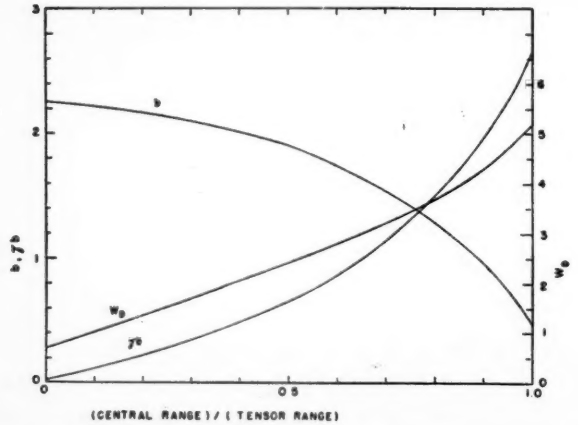

FIG. 15. Variation of deuteron fitting parameters for increase of tensor range. The interaction is that of the Yukawa well for which the central range is 1.185×10^{-13} cm. W_D is the percentage of D state; b is the dimensionless central well depth equal to $MV_cR^2/\hbar$; γb is the tensor well depth. The binding energy fitted is 2.183 Mev.

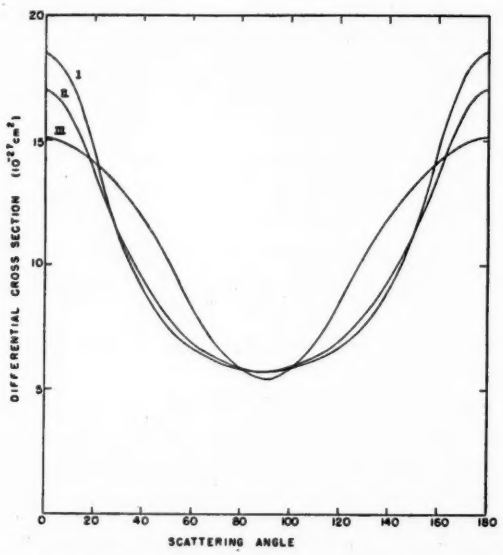

FIG. 16. Effect of increasing the tensor depth (at 90 Mev) with constant binding energy illustrated for a Yukawa potential ($R=1.18\times10^{-13}$ cm). Curve I: $\gamma=0$, triplet cross section $=9.9\times10^{-26}$ cm^2. Curve II: $\gamma=0.5$, triplet cross section $=9.6\times10^{-26}$ cm^2. Curve III: $\gamma=6$, triplet cross section, $=11.1\times10^{-26}$ cm^2.

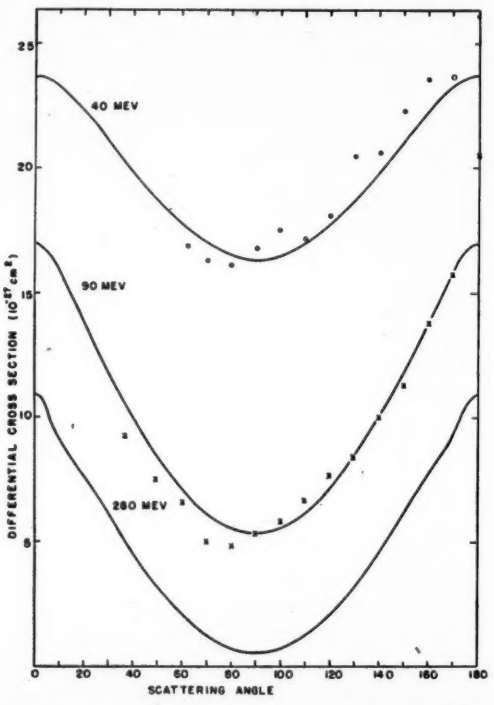

FIG. 17. Scattering from the Yukawa potential ($R=1.35\times10^{-13}$ cm) at 40, 90, and 280 Mev with inclusion of tensor force. The total cross sections are 23.1×10^{-26} cm^2, 9.8×10^{-26} cm^2 and 2.7×10^{-26} cm^2. (The 280-Mev angular distribution and total cross section are in agreement with the preliminary results recently reported.) (Kelly, Leith, and Wiegand, Phys. Rev. **76**, 589 (1949).)

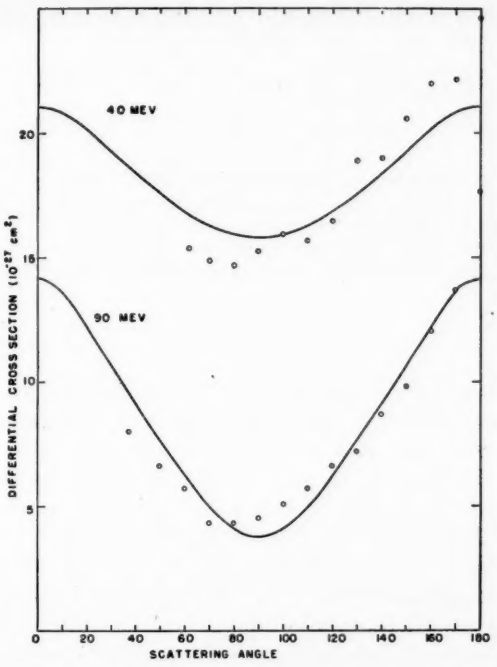

FIG. 18. Scattering from the exponential potential ($R=0.75\times10^{-13}$ cm) at 40 and 90 Mev with inclusion of tensor force. The total cross sections are 21.7×10^{-26} cm^2 at 40 Mev and 8.7×10^{-26} cm^2 at 90 Mev.

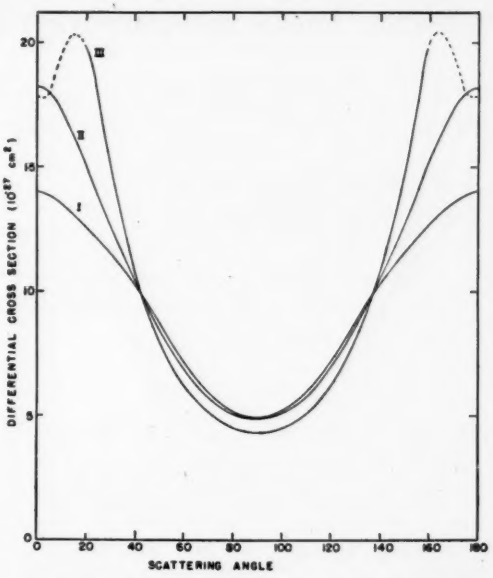

FIG. 19. Effect of increasing the tensor range (at 90 Mev) with constant binding energy and quadrupole moment illustrated for a Yukawa potential (central range$=1.18\times10^{-13}$ cm). Curve I: Tensor range$=1.18\times10^{-13}$ cm, complete cross section$=9.9\times10^{-26}$ cm^2. Curve II: Tensor range$=1.69\times10^{-13}$ cm, complete cross section$=10.5\times10^{-26}$ cm^2. Curve III: Tensor range$=3.91\times10^{-13}$ cm, complete cross section$=10.7\times10^{-26}$ cm^2.

tive range are $1.53\pm0.20\times10^{-13}$ cm. The determination of the limits on the range from high energy scattering depend upon the explicit model used but for all models considered it has been found to be within the above limits.

5. Tensor force range. The tensor range may be increased relative to the central range by as much as a factor of two without adversely affecting either the low or high energy results.

ACKNOWLEDGMENTS

The authors wish to express their thanks to Professor Robert Serber for continued guidance in the general theory and in interpretation of the experiments. We also wish to thank Messrs. Richard Huddelstone and Donald Swanson for aid and suggestions with the calculations. This work was carried out under the auspices of the AEC.

Stark-Zeeman Effects on Symmetric Top Molecules with Nuclear Quadrupole Coupling*

F. COESTER
Department of Physics, The State University of Iowa, Iowa City, Iowa
(Received October 7, 1949)

The effects of simultaneous electric and magnetic fields on symmetric top molecules with quadrupole coupling are investigated. In weak parallel fields the Stark components are merely moved by the magnetic field if the Stark effect is linear, and split into two lines if the Stark effect is quadratic. In strong parallel fields the Stark components are split into two or four lines respectively. The intensities are not affected by the relative strength of the fields. In crossed fields a more complex pattern results. The intensities depend on the relative strength of electric and magnetic fields.

I. INTRODUCTION

THE purpose of this paper is to investigate the effects of simultaneous electric and magnetic fields on the rotational spectrum of symmetric top molecules one nucleus of which has a quadrupole moment. The Hamiltonian of such a molecule consists of four parts.

$$H=H_0+H_q+H_e+H_m, \tag{1}$$

where H_0 is the energy of the free symmetric top; H_q is the interaction of the nuclear quadrupole with the electrostatic field of the molecule; and H_e is the interaction of the molecule with the external electric field $\mathcal{E}$.

$$H_e=-\mu\mathcal{E}\cdot\mathbf{X}, \tag{2}$$

where μ is the strength of the electric dipole; $\mathbf{X}$ is the unit vector in the direction of the figure axis; and H_m is the interaction of the molecule with the external magnetic field $\mathcal{H}$.

$$H_m=-\mu_0 g_{\mathrm{mol}}(\mathcal{H}\cdot\mathbf{J})+g_N(\mathcal{H}\cdot\mathbf{I}), \tag{3}$$

where μ_0 is the nuclear magneton; g_{mol} is the Landé factor of the molecule; g_N is the Landé factor of the nucleus with quadrupole moment; $\mathbf{I}$ is the spin vector of the nucleus with quadrupole moment; and $\mathbf{J}$ is the angular momentum of the top. We denote the total angular momentum $\mathbf{I}+\mathbf{J}$ by $\mathbf{F}$ and define the quantum numbers I, J, F, as usual, such that $I(I+1)$, $J(J+1)$, $F(F+1)$ are the eigenvalues of $\mathbf{I}\cdot\mathbf{I}$, $\mathbf{J}\cdot\mathbf{J}$ and $\mathbf{F}\cdot\mathbf{F}$ respectively.

The effect of H_q on the spectrum in the absence of external fields is well known.[1] The Stark effect and the Zeeman effect have been investigated separately.[2] It may, however, sometimes be advantageous to have both effects simultaneously. For the influence of the magnetic field on the Stark components is considerably simpler than the Zeeman effect on the unsplit lines. For parallel fields the Stark components will be either split into two or simply moved by the magnetic field. The selection rules are not altered by the magnetic field. A magnetic field perpendicular to the electric field changes the selection rules; the line pattern will change in a characteristic way. For parallel fields H_e and H_m commute. One can therefore obtain the energy levels simply by combining Jen's results with those of Low and Townes.[2] We shall discuss this case here in some detail even though the main results are known, since this will serve as a basis for the consideration of the more complicated case of crossed fields.

The eigenvalues of H_0 are

$$E_0(J,K)=BJ(J+1)+(A-B)K^2, \tag{4}$$

where $-J\leq K\leq J$ is an eigenvalue of the component of J in the direction of the figure axis. A and B are related to the principle moment of inertia I_A, I_B by

$$A=1/(2I_A), \quad B=1/(2I_B). \tag{5}$$

The eigenstates of H_0 may be characterized for instance by $IJKFM$ on $IJKM_JM_I$; where M_I, M_J, M are eigenvalues of I_3, J_3 and F_3 respectively. $H'=H_q+H_e+H_m$ is treated as a perturbation. To obtain the first-order energy correction one ought, in general, to diagonalize the submatrix of H' with respect to all states having the same zero-order energy:

$$(IJKM_JM_I|H'|I'JK'M_J'M_I') \quad (K'=\pm K),$$

where

$$(IJKM_JM_I|H_q|I'JK'M_J'M_I')$$
$$=\frac{eqQ\cdot\delta_{KK'}\delta_{II'}}{(2J-1)(2J+3)I(2I-1)}\left(\frac{3K^2}{J(J+1)}-1\right)$$
$$\times(IJKM_JM_I|3(\mathbf{J}\cdot\mathbf{I})^2+\tfrac{3}{2}\mathbf{J}\cdot\mathbf{I}-\mathbf{J}^2\mathbf{I}^2|IJKM_J'M_I') \quad (I\geq 1), \tag{6}$$

where Q=nuclear quadrupole moment and $q=(\partial^2V)/(\partial z^2)$ = second derivative of the electrostatic potential in the direction of the figure axis.[3]

* Supported in part by ONR.

[1] H. B. G. Casimir, *On the Interaction between Atomic Nuclei and Electrons* (Teylers Tweede Genootschap E. F. Bohn Haalem, 1936). Kellog, Rabi, Ramsey, and Zacharias, Phys. Rev. **57**, 677 (1940). D. K. Coles and W. E. Good, Phys. Rev. **70**, 979 (1946). J. M. Jauch, Phys. Rev. **72**, 715 (1947). J. Bardeen and C. H. Townes, Phys. Rev. **73**, 97 (1948); **73**, 627 (1948).

[2] C. K. Jen, Phys. Rev. **74**, 1936 (1948) (Zeeman effect). U. Fano, J. Research Nat. Bur. Stand. **40**, March, 1948 (Stark effect on linear molecules). W. Low and C. H. Townes, Phys. Rev. **76**, 1295 (1949) (Stark effect on symmetric top molecules).

[3] Some authors denote q/e by q.

Obviously H' has no off-diagonal elements with respect to I. From the eigenfunctions of the symmetric top one can see that there are no off-diagonal elements with respect to K either.[4] Since the constituents of H' do not commute one would, in general, have to solve numerically a secular equation of order $(2J+1)(2I+1)$. Solutions in closed form can be given however for weak fields $H_q \gg H_e+H_m$ and for strong fields $H_q \ll H_e+H_m$.[5] In these cases we may consider first the influence of the large perturbation alone and treat the small part as a perturbation on the perturbation.

II. PARALLEL FIELDS

(A) Weak Fields $H_e+H_m \ll H_q$

H_q given by (6) is diagonal in the $IJKFM$ representation. The diagonal elements are[1]

$$E_q(IJKF)=eqQ\left(\frac{3K^2}{J(J+1)}-1\right)G(I,J,F), \quad (7)$$

where[6]

$$G=\frac{\frac{3}{4}C(C+1)-I(I+1)J(J+1)}{2(2J+3)(2J+1)I(2I-1)},$$

$$C=F(F+1)-I(I+1)-J(J+1). \quad (8)$$

H_q has off-diagonal matrix elements with respect to J which give rise to a second-order correction to E_q. This second-order correction can easily be obtained from the matrix elements given by Bardeen and Townes.[7] It will, however, be disregarded here, even though it may be of the same order as the influence of H_e and H_m, since it affects only the position of a line and not the M-dependent Stark-Zeeman pattern.

The energy shift due to H_m is for $\mathcal{H}=\{0, 0, \mathcal{H}\}$ and $\mathcal{E}=\{0, 0, \mathcal{E}\}$ up to the second order.

$$E_m=(FM|H_m|FM)+\sum_{F'\neq F}\frac{|(FM|H_m|F'M)|^2}{E_q(F)-E_q(F')}, \quad (9)$$

since H_m has no off-diagonal elements with respect to M. With $\eta_N=\mu_0 g_N \mathcal{H}$, $\eta_{\mathrm{mol}}=\mu_0 g_{\mathrm{mol}}\mathcal{H}$ and (3)

$$E_m=-\eta_{\mathrm{mol}}(FM|J_3|FM)-\eta_N(FM|I_3|FM)+\frac{|(FM|\eta_{\mathrm{mol}}J_3+\eta_N I_3|F-1M)|^2}{E_q(F)-E_q(F-1)}+\frac{|(FM|\eta_{\mathrm{mol}}J_3+\eta_N I_3|F+1M)|^2}{E_q(F)-E_q(F+1)}. \quad (10)$$

The matrix elements of J_3 and I_3 can be obtained from the commutation properties of $\mathbf{J}$, $\mathbf{I}$ and $\mathbf{F}$.[8]

$$(FM|J_3|FM)=\alpha_J M$$
$$(FM|I_3|FM)=\alpha_I M, \quad (11)$$

where

$$\alpha_J=\frac{F(F+1)-I(I+1)+J(J+1)}{2F(F+1)},$$
$$\alpha_I=\frac{F(F+1)-J(J+1)+I(I+1)}{2F(F+1)}, \quad (12)$$

and

$$|(FM|\eta_{\mathrm{mol}}J_3+\eta_N I_3|F-1M)|^2=(\eta_N-\eta_{\mathrm{mol}})^2(F^2-M^2)R(F), \quad (13)$$

where

$$R(F)=\frac{(F^2-(I-J)^2)((I+J+1)^2-F^2)}{4F^2(2F-1)(2F+1)} \quad (F\geq 1).$$

Hence[9]

$$E_m=-M(\eta_{\mathrm{mol}}\alpha_J+\eta_N\alpha_I)+\frac{(\eta_N-\eta_{\mathrm{mol}})^2}{eqQ\left(\frac{3K^2}{J(J+1)}-1\right)}\times\left\{\frac{R(F)(F^2-M^2)}{G(F)-G(F-1)}+\frac{R(F+1)((F+1)^2-M^2)}{G(F)-G(F+1)}\right\}. \quad (14)$$

Similarly the shift due to H_e[10] is with $\epsilon=\mathcal{E}\mu$.

$$E_e=\epsilon(FM|X_3|FM)+\epsilon^2\sum_{F',J'\neq F,J}\frac{|(IJKFM|X_3|IJ'KF'M)|^2}{E^0(IJKFM)-E^0(IJ'KF'M)}, \quad (15)$$

where $E^0=E_0+E_q$. The sum in the second-order term may be split up into two parts.

$$\epsilon^2\sum_{F'\neq F}\frac{|(IJKFM|X_3|IJKF'M)|^2}{E_q(F)-E_q(F')}+\epsilon^2\sum_{F'}\sum_{J'\neq J}\frac{|(IJKFM|X_3|IJ'KF'M)|^2}{E_0(J)-E_0(J')}. \quad (16)$$

In the second term of (16) we neglect E_q in the denominator. The second term is negligible compared to the first order effect for $K\neq 0$. We shall therefore put $K=0$ in this term. The matrix elements $(JKM_J|X_3|J'K'M_{J'})$ have been calculated by F. Reiche and H. Rademacher[4] from the eigenfunctions

[4] See F. Reiche and H. Rademacher, Zeits. f. Physik **41**, 453 (1927).

[5] Inequalities of this form are meant symbolically: The off-diagonal elements of the "small operator" shall be small compared to the differences between corresponding eigenvalues of the "large operator." For extreme values of the field strength $H_e \ll H_q$ could of course be stated as $\mathcal{E}\mu \ll eqQ$. Near the limit of validity of the perturbation theory this latter inequality may, however, be misleading.

[6] A numerical table for G has been given by J. Bardeen and C. H. Townes, Phys. Rev. **73**, 97 (1948).

[7] J. Bardeen and C. H. Townes, Phys. Rev. **73**, 627 (1948).

[8] E. U. Condon and G. H. Shortley, *Theory of Atomic Spectra* (Cambridge University Press, London, 1935), p. 64 ff.

[9] The first term has been given by C. K. Jen, Phys. Rev. **74**, 1936 (1948).

[10] See W. Low and C. H. Townes, Phys. Rev. **76**, 1295 (1949).

of the symmetric top.

$$(JKM_J|X_3|J'K'M_J')=\delta_{KK'}\delta_{M_JM_J'}\Big\{\delta_{JJ'}\frac{M_JK}{J(J+1)}+\delta_{J'J-1}(J^2-M_J^2)^{\frac{1}{2}}\Big(\frac{J^2-K^2}{J^2(2J+1)(2J+1)}\Big)^{\frac{1}{2}}+\delta_{J'J+1}((J+1)^2-M_J^2)^{\frac{1}{2}}\times\Big(\frac{(J+1)^2-K^2}{(J+1)^2(2J+1)(2J+3)}\Big)^{\frac{1}{2}}\Big\}. \quad (17)$$

From (17) we get the desired matrix elements by applying the unitary transformation

$$(FM|S(I,J)|M_JM_I)=\delta_{M,M_I+M_J}C_{M_J}(J,F,M) \quad (18)$$

transforming from the M_J, M_I representation to the F, M representation.

$$(IJKFM|X_3|IJKF'M)=\sum_{M_J}C_{M_J}(J,F,M)C^*_{M_J}(J,F',M)\frac{M_JK}{J(J+1)}=\frac{K}{J(J+1)}(IJFM|J_3|IJF'M). \quad (19)$$

The matrix elements of J_3 needed here are given in (11) and (13). For the second term of (16) we need

$$\sum_{F'}|(IJ0FM|X_3|IJ-10F'M)|^2=\sum_{M_J}|C_{M_J}(J,F,M)|^2|(J0M_J|X_3|J-10M_J)|^2=\sum_{M_J}|C_{M_J}(J,F,M)|^2\frac{J^2-M_J^2}{(2J+1)(2J-1)}. \quad (20)$$

Hence

$$\epsilon^2\sum_{F'}\sum_{J'\neq J}\frac{|(IJKFM|X_3|IJ'KF'M)|^2}{E_0(J)-E_0(J')}=-\frac{\epsilon^2}{2B}\sum_{M_J}|C_{M_J}(J,F,M)|^2\times\frac{3M_J^2-J(J+1)}{J(J+1)(2J-1)(2J+3)}. \quad (21)$$

However

$$\sum_{M_J}|C_{M_J}|^2=(FM|SS^+|FM)=1, \quad (22)$$

and

$$\sum_{M_J}|C_{M_J}(J,F,M)|^2M_J^2=(IJFM|J_3^2|IJFM). \quad (23)$$

The matrix elements of $\mathbf{J}$ are given by Condon and Shortley.[8] With

$$J_3^2=\tfrac{1}{3}\mathbf{J}^2+\tfrac{2}{3}\{J_3^2-\tfrac{1}{2}(J_1^2+J_2^2)\},$$

we find

$$(IJFM|J_3^2|IJFM)=\frac{J(J+1)}{3}+\tfrac{1}{3}(3M^2-F(F+1))\times\{(F\vdots J\vdots F)^2-(F\vdots J\vdots F-1)^2-(F\vdots J\vdots F+1)^2\},$$

where

$$(F\vdots J\vdots F)^2=\frac{D}{2F(F+1)}$$

$$D=F(F+1)-I(I+1)+J(J+1)$$

$$(F\vdots J\vdots F-1)^2=\frac{F^2(2I(I+1)+2J(J+1)+1)-(J(J+1)-I(I+1))^2-F^2}{4F^2(2F-1)(2F+1)}.$$

Hence[11]

$$\sum_{M_J}|C_{M_J}(J,F,M)|^2M_J^2=\frac{J(J+1)}{3}+\frac{3M^2-F(F+1)}{3}\,\frac{3D(D-1)-4F(F+1)J(J+1)}{2F(F+1)(2F-1)(2F+3)}. \quad (24)$$

Inserting these results into (15) we get

$$E_e=-\epsilon\alpha_J\frac{KM}{J(J+1)}+\frac{\epsilon^2K^2}{eqQ\Big(\dfrac{3K^2}{J(J+1)}-1\Big)(J(J+1))^2}\Big\{\frac{R(F)(F^2-M^2)}{G(F)-G(F-1)}-\frac{R(F+1)((F+1)^2-M^2)}{G(F)-G(F+1)}\Big\}-\frac{\epsilon^2[3M^2-F(F+1)][3D(D-1)-4F(F+1)J(J+1)]}{B2J(J+1)(2J-1)(2J+3)2F(F+1)(2F-1)(2F+3)}. \quad (25)$$

These formulas are derived for $J\geq 1$; for $J=0$, $K=0$ we have $E_q=0$, $M=M_I$.

$$E_m=-M\eta_N \quad (26)$$

$$E_e=-(\epsilon^2/2B)|(000|X_3|100)|^2=-(\epsilon^2/6B). \quad (27)$$

For $K\neq 0$ the magnetic field does not split the Stark components but moves them by an amount determined by (14). For $K=0$, $J\geq 1$ each level is split into two according to $\pm|M|$. The level $J=0$ is split into $2I+1$ components. For a wave polarized in the direction of the fields this means that all lines are in general split in two by the magnetic field.

[11] This result has been given by Fano, reference 2.

(B) Strong Fields $H_e+H_m \gg H_q$

In this case the $IJKM_JM_I$ representation is appropriate. H_m is diagonal in this representation.

$$E_m=-(M_I\eta_N+M_J\eta_{\mathrm{mol}}). \tag{28}$$

The energy shift due to H_e is up to the second order

$$E_e=-\epsilon(JKM_J|X_3|JKM_J)+\epsilon^2\sum_{J'\neq J}\frac{|(JKM_J|X_3|J'KM_J)|^2}{E_0(J)-E_0(J')}, \tag{29}$$

or inserting the matrix elements from (17)

$$E_e=-\epsilon\frac{M_JK}{J(J+1)}-\frac{\epsilon^2}{2B}\frac{3(M_J^2+K^2)-J(J+1)}{J(J+1)(2J-1)(2J+3)}+\frac{\epsilon^2}{2B}M_J^2K^2\frac{5J(J+1)+3}{(J(J+1))^3(2J-1)(2J+3)}. \tag{30}$$

To obtain the quadrupole effect we need the M_JM_I representation of $3(\mathbf{I}\cdot\mathbf{J})^2+\frac{3}{2}\mathbf{J}\cdot\mathbf{I}-\mathbf{I}^2\mathbf{J}^2$. With

$$(JM_J|J_3|JM_J')=\delta_{M_J'M_J}M_J,\qquad (IM_I|I_3|IM_I)=\delta_{M_I'M_I}M_I, \tag{31}$$

and

$$(M_J|J_1\mp iJ_2|M_J^2)=\delta_{M_J'M_J\pm1}(J(J+1)-M_J(M_J\pm1))^{\frac{1}{2}},\qquad (M_I|I_1\mp iI_3|M_I')=\delta_{M_I'M_I\pm1}(I(I+1)-M_I(M_I\pm1))^{\frac{1}{2}}, \tag{32}$$

there follows

$$\begin{aligned}(IJKM_JM_I|H_q|IJKM_J'M_I')&=P(I,J,K)\{\delta_{M_J'M_J}\delta_{M_I'M_I}[3M_I^2-I(I+1)]\\&\times[3M_J^2-J(J+1)]+\delta_{M_J'M_J\pm1}\delta_{M_I'M_I\mp1}\\&\times[\tfrac{3}{2}+3M_IM_J+3(M_I\mp1)(M_J\pm1)]\\&\times([I(I+1)-M_I(M_I\mp1)]\\&\times[J(J+1)-M_J(M_J\pm1)])^{\frac{1}{2}}\\&+\delta_{M_J'M_J\pm2}\delta_{M_I'M_I\mp2}\tfrac{3}{2}([J(J+1)-M_J(M_J\pm1)]\\&\times[J(J+1)-(M_J\pm1)(M_J\pm2)]\\&\times[I(I+1)-M_I(M_I\mp1)]\\&\times[I(I+1)-(M_I\mp1)(M_I\mp2)])^{\frac{1}{2}}\},\end{aligned} \tag{33}$$

where

$$P=\frac{eqQ}{4(2J-1)(2J+3)I(2I-1)}\left(\frac{3K^2}{J(J+1)}-1\right).$$

The quadrupole energy is given by the diagonal element

$$E_q=P(3M_I^2-I(I+1))(3M_J^2-J(J+1)), \tag{34}$$

except if $K=0$, $M_J=\pm1$ and $|\eta_N|+|\eta_{\mathrm{mol}}|\lesssim eqQ$. In this case E_0+E_e is the same for the two states $I, J, 0, 1, M_I$ and $I, J, 0, -1, M_I+2$. In all other cases there is no degeneracy of states connected by off diagonal elements of H_q. For $K=0$, $M_J=\pm1$, $|\eta_N|+|\eta_{\mathrm{mol}}|\lesssim eqQ$ we must diagonalize H_q+H_m. The solution of the secular equation is easily obtained from (28) and (33).

$$\begin{aligned}E=E_0+E_e-\eta_NM&-P(3-J(J+1))(3(M^2+1)-I(I+1))\\&\pm((\eta_{\mathrm{mol}}-\eta_N-6PM[3-J(J+1)])^2\\&+9/4P^2(J(J+1))^2(I(I+1)-M(M+1))\\&\times(I(I+1)-M(M-1)))^{\frac{1}{2}}\ (M=M_I+M_J).\end{aligned} \tag{35}$$

For $K\neq0$, $H_e\gg H_q$, $H_m=0$ the levels are characterized by $IJKM_JM_I^2$ the magnetic field will split each of them into two levels distinguished by the sign of M_I.

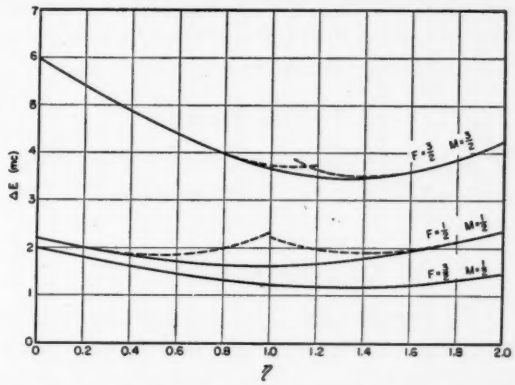

FIG. 1. Energy levels $M=\frac{1}{2}, \frac{3}{2}$ for $\epsilon=20(1-\frac{1}{2}\eta)$. The full lines give the solutions of the secular Eqs. (57) and (58). The broken lines are obtained from perturbation theory (55) and (56).

If $K=0$ and g_{mol} is appreciable each level will be split into four levels. If the wave is polarized in the direction of the fields the magnetic field will split the strong field Stark lines into two components for $K\neq0$ and into four components for $K=0$.

(C) Intermediate Field Strength. $H_e+H_m\sim H_q$

For intermediate field strength we have to diagonalize the submatrix $H'=H_e+H_m+H_q$. It is convenient to start with the $IJKM_JM_I$ representation and label the states by M_JM rather than by M_JM_I. Since F_3 commutes with H', H' is already diagonal with respect to M. There remain the submatrices

$$(IJKMM_J|H'|IJKMM_J')$$

to be diagonalized. The off-diagonal elements come from H_q only and are given by (33). The diagonal elements are $E_e+E_m+E_q$ taken from (28), (30) and (34).[12] The

[12] It is easy to see that one may evaluate the second-order perturbation for the Stark effect first and transform afterward to the correct representation. See Eq. (21).

TABLE I. Displace of the Stark-Zeeman line as a function of η for $\epsilon=10$.

η	$\frac{1}{2}\rightarrow\frac{1}{2}$	$-\frac{1}{2}\rightarrow-\frac{1}{2}$	$-\frac{1}{2}\rightarrow\frac{1}{2}$	$-\frac{1}{2}\rightarrow\frac{1}{2}$
0.0	0.111	1.89	2.11	4.11
0.5	0.196	1.92	2.26	4.43
1.0	0.39	2.05	2.83	5.27
1.5	0.62	2.28	3.52	6.42
2.0	0.86	2.58	4.30	7.75
3.0	1.35	3.31	6.00	10.65

order of the secular equation depends on M. For $-|I-J|\leq M\leq|I-J|$ we have $-J\leq M_J\leq J$. Hence their order is $2J+1$ if $J\leq I$, $M-I\leq M_J\leq M+I$ hence the order is $2I+1$ if $I\geq J$. For $|I-J|\leq M\leq I+J$ we have $M-I\leq M_J\leq J$. Hence the order is $J+I-M+1$. For $-(I+J)\leq M\leq-|I-J|$ we have $-J\leq M_J\leq M+I$ hence order is $J+I-M+1$.

III. CROSSED FIELDS

The Hamiltonian is again given by (1); but now we assume $\mathcal{E}=(0, 0, \mathcal{E})$ and $\mathfrak{M}=(\mathfrak{M}, 0, 0)$ in (2) and (3). That is

$$H_e=-\epsilon X_3 \tag{36}$$

$$H_m=-(\eta_{\mathrm{mol}}J_1+\eta_N I_1). \tag{37}$$

Let M, M_J, M_I be eigenvalues of F_3, J_3, I_3 respectively, as before, and let N, N_J, N_I be eigenvalues of F_1, J_1, I_1 respectively.

(A) Weak Fields $H_q\gg H_e+H_m$

The quadrupole splitting is the same as before (7). Neither M nor N, however, are now "good" quantum numbers. To determine the Stark-Zeeman effect we would in general have to solve a secular equation of order $(2F+1)$. Closed formulas can be obtained for $H_e\gg H_m$ and $H_m\gg H_e$. We shall see that the energy may be determined fairly accurately for all intermediate ratios of the fields strength by graphical interpolation, if the secular equation has been solved for one ratio.

(α) $H_e\gg H_m$

The Stark splitting is given by (25). H_m has no diagonal elements in the $IJKFM$ representation. The magnetic field affects the energy only in the second order.

$$E_m=\sum_{F'\neq F}\sum_{M'}\frac{|(FM|H_m|F'M')|^2}{E_q(F)-E_q(F')}+\sum_{M'}\frac{|(FM|H_m|FM')|^2}{E_e(M)-E_e(M')}. \tag{38}$$

In the first term E_e has been neglected in the denominator. Since $H_e\ll H_q$, the first term is small compared to the second and will be neglected entirely in the following.

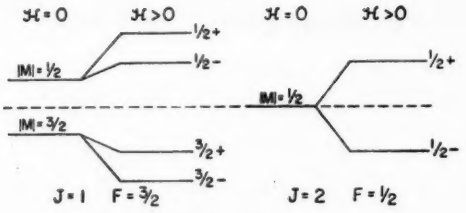

FIG. 2. Schematic picture of the levels.

For $K\neq0$ E_e is non-degenerate. We may insert the matrix elements

$$\begin{aligned}(IJKFM|I_1|IJKFM\pm1)&=\frac{\alpha_I}{2}(F(F+1)-M(M\pm1))^{\frac{1}{2}}\\(IJKFM|J_1|IJKFM\pm1)&=\frac{\alpha_J}{2}(F(F+1)-M(M\pm1))^{\frac{1}{2}},\end{aligned} \tag{39}$$

into (38) and obtain

$$E_m=-\frac{(\alpha_I\eta_N+\alpha_J\eta_{\mathrm{mol}})^2J(J+1)M}{2\epsilon\alpha_J K}. \tag{40}$$

For $K=0$ E_e is degenerate for $M=\pm\frac{1}{2}$. We must first transform away the off-diagonal elements between $+\frac{1}{2}$ and $-\frac{1}{2}$.

$$E_m=(\bar{M}|\bar{H}_m|\bar{M})+\sum_{M'\neq M}\frac{|(\bar{M}|\bar{H}_m|\bar{M}')|^2}{E_e(\bar{M})-E_e(\bar{M}')}, \tag{41}$$

where $\bar{H}_m=\mathbf{S}^+H_m\mathbf{S}$ with

$$\begin{aligned}&(M|\mathbf{S}|\bar{M})=\delta_{M\bar{M}}\text{ for }M\neq\pm\tfrac{1}{2}\\&(\tfrac{1}{2}|\mathbf{S}|\tfrac{1}{2})=(\tfrac{1}{2}|\mathbf{S}|-\tfrac{1}{2})=(-\tfrac{1}{2}|\mathbf{S}|\tfrac{1}{2})=1/\sqrt{2}\\&(-\tfrac{1}{2}|\mathbf{S}|-\tfrac{1}{2})=-1/\sqrt{2}\\&\bar{M}^2=M^2.\end{aligned} \tag{42}$$

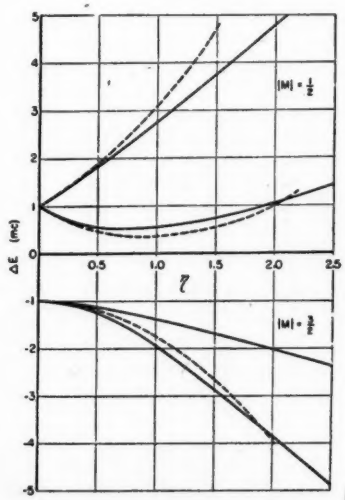

FIG. 3. Levels as functions of η for $\epsilon^2/100B$. The full lines give the solutions of the secular Eqs. (61). The broken lines are obtained from perturbation theory (59).

TABLE II. Splitting of a Stark line by a weak magnetic field.

1.4η	$\frac{1}{2}+\rightarrow\frac{1}{2}+$	$\frac{1}{2}+\rightarrow\frac{1}{2}-$	$\frac{1}{2}-\rightarrow\frac{1}{2}+$	$\frac{1}{2}-\rightarrow\frac{1}{2}-$
0.0	−1.00	−1.00	−1.00	−1.00
0.2	−1.05	−1.38	−0.65	−0.98
0.5	−1.16	−1.99	−0.24	−1.07
1.0	−1.40	−3.06	+0.33	−1.33
1.5	−1.68	−4.18	+0.68	−1.82
2.0	−1.98	−5.31	+0.94	−2.40
3.0	−2.61	−7.61	+1.35	−3.65

Hence for $M\neq\pm\frac{1}{2}$

$$E_m=-\frac{B}{6\epsilon^2}(\alpha_I\eta_N+\alpha_J\eta_{\mathrm{mol}})^2\frac{F(F+1)+M^2}{(4M^2-1)L(I,J,F)},\quad(43)$$

where

$$L(I,J,F)=\frac{3D(D-1)-4F(F+1)J(J+1)}{2J(J+1)(2J-1)(2J+3)\times 2F(F+1)(2F-1)(2F+3)}\quad(44)$$

and for $M=\pm\frac{1}{2}$

$$E_m=\pm(\tfrac{1}{2}|H_m|-\tfrac{1}{2})+\frac{|(\frac{1}{2}|H_m|\frac{3}{2})|^2}{E_e(\frac{1}{2})-E_e(\frac{3}{2})},\quad(45)$$

that is

$$E_m=\pm(\eta_N\alpha_I+\eta_{\mathrm{mol}}\alpha_J)\tfrac{1}{2}(F+\tfrac{1}{2})+\frac{B(\eta_N\alpha_I+\eta_{\mathrm{mol}}\alpha_J)^2(F(F+1)-\frac{3}{4})}{24\epsilon^2L(I,J,F)}.\quad(46)$$

(β) $H_e\ll H_m$

The Zeeman splitting is obtained from (14) replacing M by N

$$E_m=-N(\eta_{\mathrm{mol}}\alpha_J+\eta_N\alpha_I)+\frac{(\eta_N-\eta_{\mathrm{mol}})^2}{eqQ\left\{\frac{3K^2}{J(J+1)}-1\right\}}\times\left\{\frac{R(F)(F^2-N^2)}{G(F)-G(F-1)}+\frac{R(F+1)((F+1)^2-N^2)}{G(F)-G(F+1)}\right\}.\quad(47)$$

H_e has no diagonal elements in the $IJKFN$ representation. The electric field affects the energy only in the second order.

$$E_e=\epsilon^2\left\{\sum_{N'\neq N}\frac{|(IJKFN|X_3|IJKFN')|^2}{E_m(N)-E_m(N')}+\sum_{N'}\sum_{F'\neq F}\frac{|(IJKFN|X_3|IJKF'N')|^2}{E_q(F)-E_q(F')}+\sum_{N'}\sum_{F'}\sum_{J'\neq J}\frac{|(IJKFN|X_3|IJ'KF'N')|^2}{E_0(J)-E_0(J')}\right\}.\quad(48)$$

Higher order corrections in the energy denominators are always neglected. For $K\neq0$ the second and the third term are small compared to the first one and shall be neglected in the following. For $K=0$ the first and the second term vanish. The third term gives then the Stark effect. Similar to (19) we have

$$(IJKFN|X_3|IJKFN\pm1)=\frac{K}{J(J+1)}(IJFN|J_3|IJFN\pm1)=\pm i\frac{K}{J(J+1)}\frac{\alpha_J}{2}(F(F+1)-N(N\pm1))^{\frac{1}{2}}.\quad(49)$$

Hence for $K\neq0$

$$E_e=-\frac{\epsilon^2K^2\alpha_J^2N}{2(\alpha_J\eta_{\mathrm{mol}}+\alpha_I\eta_N)(J(J+1))^2}\quad(50)$$

and for $K=0$

$$E_e=\frac{\epsilon^2}{2B}\sum_{N_J}\sum_{N_{J'}}|C_{N_J}(J,F,N)|^2\times\left\{\frac{|(J0N_3|X_3|J-10N_3')|^2}{J}-\frac{|(J0N_J|X_3|J+10N_J')|^2}{J+1}\right\}.\quad(51)$$

From (17) and the transformation properties of X_3 under infinitesimal rotations[13] we find

$$|(J0N_J|X_3|J+10N_J\pm1)|^2=\frac{1}{4}\frac{(J+1\pm N_J)(J+2\pm N_J)}{(2J+1)(2J+3)}$$

$$|(J0N_J|X_3|J-10N_J\pm1)|^2=\frac{1}{4}\frac{(J\mp N_J)(J-1\mp N_J)}{(2J-1)(2J+1)}.\quad(52)$$

Inserting (52) into (51) yields

$$E_e=\frac{\epsilon^2}{2B}\sum_{N_J}|C_{N_J}|^2\frac{3N_J^2-J(J+1)}{2J(J+1)(2J-1)(2J+3)},\quad(53)$$

TABLE III. Additional lines appearing with a stronger magnetic field.

1.4η	$\frac{1}{2}-\rightarrow\frac{1}{2}+$	$\frac{1}{2}-\rightarrow\frac{1}{2}-$	$\frac{1}{2}+\rightarrow\frac{1}{2}+$	$\frac{1}{2}+\rightarrow\frac{1}{2}-$
0.0	1.00	1.00	1.00	1.00
0.2	1.18	0.85	1.18	0.85
0.5	1.53	0.70	1.49	0.66
1.0	2.33	0.67	2.07	0.40
1.5	3.32	6.82	2.68	0.18
2.0	4.40	1.06	3.81	−0.02
3.0	6.65	1.65	4.61	−0.39

[13] Condon and Shortley, see reference 8, p. 63.

or with (22) and (24)

$$E_e=\frac{\epsilon^2}{2B}(3N^2-F(F+1))L(I,J,F). \tag{54}$$

(γ) $H_e\sim H_m$

For a rigorous diagonalization of $(FM|H_e+H_m|FM')$ one starts best from the FM representation in which H_e is diagonal while the off-diagonal elements of H_m are readily obtained from (39).

To illustrate our results and to compare the perturbation formulas under (α) and (β) with the exact solution of the secular equation let us consider a simple line in the absorption spectrum of CH_3I where $B=7500$ mc, $eqQ=-1934$ mc,[14] $I=5/2$, $g_{\text{mol}}\approx 0$, $g_N=0.200$,[15] $\mu=2.8$ debye.[16] We choose the transition $J=1\to 2$, $F=\frac{3}{2}\to\frac{1}{2}$, $K=1$. The wave shall be polarized in the direction of the electric field. ϵ, η and all energies are measured in megacycles.

$\epsilon\gg\eta$

$$\begin{aligned} &J=1:\ \Delta E=[0.2\epsilon+4.9(\eta^2/\epsilon)]M,\\ &J=2:\ \Delta E=[0.2222\epsilon+12.25(\eta^2/\epsilon)]M, \end{aligned} \tag{55}$$

$\eta\gg\epsilon$

$$\begin{aligned} &J=1:\ \Delta E=-N[1.4\eta+0.01429(\epsilon^2/\eta)],\\ &J=2:\ \Delta E=-N[2.3333\eta+0.0106(\epsilon^2/\eta)]. \end{aligned} \tag{56}$$

The level labeled M for $\eta\ll\epsilon$ goes over into the level $N=-M$ for $\eta\gg\epsilon$.

The secular equation is of the second order for $F=\frac{1}{2}$, $J=2$, and can be solved in closed form:

$$J=2:\ \Delta E=\pm(4.938\cdot 10^{-2}\epsilon^2+1.361\eta^2)^{\frac{1}{2}}. \tag{57}$$

For $J=1$, $F=\frac{3}{2}$ the secular equation is of the fourth order. It can still be solved in closed form since it does not depend on the odd powers of ΔE.

$$\begin{aligned} (\Delta E)^2=&0.05\epsilon^2+2.45\eta^2\\ &\pm(0.0016\epsilon^4+0.1568\epsilon^2\eta^2+3.842\eta^4)^{\frac{1}{2}}. \end{aligned} \tag{58}$$

Figure 1 gives the energy levels $M=\frac{1}{2}$, $\frac{3}{2}$[17] for $\epsilon=20[1-(\eta/2)]$ $0\le\eta\le 2$. In general a fairly accurate graphical interpolation ought to be possible if one intermediate point is known. Table I gives the displacement of the Stark-Zeeman lines as a function of η for $\epsilon=10$. Only the transitions with positive frequency shift are listed; the pattern is symmetrical with respect to the undisplaced line.

$\frac{1}{2}\to\frac{1}{2}$ is the only allowed transition for $\eta=0$; for $\eta\gg\epsilon$ it is forbidden. The intensity of this line will decrease as the magnetic field increases.

$-\frac{3}{2}\to-\frac{1}{2}$ These transitions are forbidden for $\eta=0$. For $\eta\gg\epsilon$ they are the only allowed transitions. The intensity of these lines will increase with increasing magnetic field.

$-\frac{3}{2}\to\frac{1}{2}$ This transition is forbidden for both very large and very small η. For intermediate η this line may appear.

As an example for the quadratic Stark effect let us look at the same line for $K=0$. For $J=2$, $F=\frac{1}{2}$ the Stark effect vanishes. The level shift is according to (47) neglecting the quadratic correction

$$E=\mp 1.1665\eta \quad \text{for} \quad N=\pm\tfrac{1}{2}.$$

$J=1$, $F=\frac{3}{2}$:

(α) $\epsilon^2/B\gg\eta$

$$\begin{aligned} &|M|=\tfrac{3}{2}:\ \Delta E=-\frac{\epsilon^2}{100B}-\frac{100B\eta^2}{\epsilon^2}0.735\\ &|M|=\tfrac{1}{2}:\ \Delta E=\frac{\epsilon^2}{100B}\mp 1.4\eta+\frac{100B\eta^2}{\epsilon^2}0.735. \end{aligned} \tag{59}$$

(β) $\eta\gg\epsilon^2/B$

$$\begin{aligned} &N=\pm\tfrac{3}{2}:\ \Delta E=\mp 4.2\eta+\frac{\epsilon^2}{200B}\\ &N=\pm\tfrac{1}{2}:\ \Delta E=\mp 1.4\eta-\frac{\epsilon^2}{200B}. \end{aligned} \tag{60}$$

Figure 2 gives a schematic picture of the levels. For large $\mathcal{H}$,

$$\begin{aligned} &\tfrac{3}{2}+\to N=+\tfrac{1}{2},\quad \tfrac{3}{2}-\to N=+\tfrac{3}{2},\\ &\tfrac{1}{2}+\to N=-\tfrac{3}{2},\quad \tfrac{1}{2}-\to N=-\tfrac{1}{2}. \end{aligned}$$

The secular equation of the fourth order can be factored into two quadratic equations.

$|N|=\frac{1}{2}$:

$$\Delta E=\pm 0.7\eta+\left((1.4\eta)^2+\left(\frac{\epsilon^2}{100B}\right)^2\pm 1.4\frac{\epsilon^2\eta}{100B}\right)^{\frac{1}{2}} \tag{61}$$

$|M|=\frac{3}{2}$:

$$\Delta E=\pm 0.7\eta-\left((1.4\eta)^2+\left(\frac{\epsilon^2}{100B}\right)^2\pm 1.4\frac{\epsilon^2\eta}{100B}\right)^{\frac{1}{2}}.$$

Figure 3 gives the levels as functions of η for $\epsilon^2/100B=1$. For $\eta=0$ the selection rule $\Delta M=0$ holds we have only only one Stark line which is split into four lines by a weak magnetic field (Table II). In a stronger magnetic field four more lines appear (Table III).

(B) Strong Electric Field $H_e\gg H_q$

The Stark effect here is the same as in Section II(B).

$$\begin{aligned} E_e=&\epsilon\frac{M_J K}{J(J+1)}-\frac{\epsilon^2}{2B}\frac{3(M_J^2+K^2)-J(J+1)}{J(J+1)(2J-1)(2J+3)}\\ &+\frac{\epsilon^2}{2B}M_J^2K^2\frac{5J(J+1)+3}{(J(J+1))'(2J-1)(2J+3)}. \end{aligned} \tag{30}$$

[14] See W. Gordy, Rev. Mod. Phys. **20**, 711, 713 (1948).
[15] J. R. Zimmerman and D. Williams, Phys. Rev. **76**, 350 (1949).
[16] C. H. Townes, private communication.
[17] We label an energy level by the value M which characterizes it for $\eta=0$.

Since H_q and H_m do not commute we get closed formulas for the energy only if $H_q \gg H_m$ or $H_m \gg H_q$.

$$(\alpha)\quad H_m \ll H_q$$

$$E_m = -(N_I\eta_N + N_J\eta_{\mathrm{mol}}). \tag{62}$$

From (6), (31) and (32) we get

$$\begin{aligned} E_q &= (IJKM_JN_I|H_q|IJKM_JN_I) \\ &= -P(I,J,K)\{9/2N_I^2M_J^2 - \tfrac{3}{2}(N_I^2J(J+1) \\ &\quad + M_J^2I(I+1)) + \tfrac{1}{2}J(J+1)I(I+1)\}. \end{aligned} \tag{63}$$

$$(\beta)\quad H_q \gg H_m$$

For $K \neq 0$, E_q is given by (34). The magnetic levels shift E_m is now a sum of a term depending on g_{mol} and one depending on g_N only, $E_m = E_m^{(\mathrm{mol})} + E_m^{(N)}$. They are best treated separately. E_m is again of the second order in η. In $E_m^{(\mathrm{mol})}$ we have the Stark energies in the denominator while in $E_m^{(N)}$ we have the quadrupole energies in the denominator, higher order corrections being always neglected. For comparable g_{mol} and $g_N E_m^{(\mathrm{mol})}$ is therefore small compared to $E_m^{(N)}$.

$$\begin{aligned} E_m^{(\mathrm{mol})} &= \frac{\eta_{\mathrm{mol}}^2 J(J+1)}{\epsilon K} \\ &\quad \times (|(M_J|J_1|M_J+1)|^2 - |(M_J|J_1|M_J-1)|^2) \\ &= \eta_{\mathrm{mol}}^2 \frac{2J(J+1)M_J}{\epsilon K}. \end{aligned} \tag{64}$$

For $3M_J^2 = J(J+1)$ E_q vanishes for all M_J, hence

$$E_m^{(N)} = -\eta_N N_I. \tag{65}$$

For $3M^2 \neq J(J+1)$, $|M_I| \neq \frac{1}{2}$.

$$\begin{aligned} E_m^{(N)} &= \eta_N^2 \sum_{M_I'} \frac{|(M_I|I_1|M_I')|^2}{E_q(M_I) - E_q(M_I')} \\ &= \eta_N^2 \frac{2}{3} \frac{I(I+1) + M_I^2}{(4M_I^2-1)P(3M_J^2 - J(J+1))}. \end{aligned} \tag{66}$$

For $|M_I| = \frac{1}{2}$ we have in analogy to (45)

$$E_m^{(N)} = \pm\eta_N(\tfrac{1}{2}|I_1|-\tfrac{1}{2}) - \frac{\eta_N^2|(\frac{1}{2}|I_1|\frac{3}{2})|^2}{6P(3M_J^2 - J(J+1))}, \tag{67}$$

or

$$E_m^{(N)} = \pm\eta_N\tfrac{1}{2}(I+2) - \eta_N^2 \frac{(I+\frac{1}{2})^2 - 1}{6P(3M_J^2 - J(J+1))}. \tag{68}$$

For $K=0$ E_q is given by (34) if $M_J \neq 1$. For $M_J = \pm 1$ we must diagonalize H_q (see Eq. (35))

$$\begin{aligned} E_q(M, \bar{M}_J) &= P(3 - J(J+1))(3(M^2+1) - I(I+1)) \\ &\quad \pm (36P^2M^2(3 - J(J+1))^2 + 9/4P^2(J(J+1))^2 \\ &\quad \times [I(I+1) - M(M+1)][I(I+1) - M(M-1)])^{\frac{1}{2}} \\ &\quad \text{for } \bar{M}_J = \mp 1. \end{aligned} \tag{69}$$

The transformation matrix $(M_J|T|\bar{M}_J)$ which diagonalizes H_q for $|M_J| = 1$ is

$$T = \begin{pmatrix} \tau & \sigma \\ -\sigma & \tau \end{pmatrix}$$

$$\tau = \frac{b}{(2[a^2 + b^2 + a(a^2+b^2)^{\frac{1}{2}}])^{\frac{1}{2}}}, \qquad \sigma = \frac{a + (a^2+b^2)^{\frac{1}{2}}}{(2[a^2 + b^2 + a(a^2+b^2)^{\frac{1}{2}}])^{\frac{1}{2}}}, \tag{70}$$

$$\begin{aligned} a &= 6PM(3 - J(J+1)), \\ b &= \tfrac{3}{2}PJ(J+1)((I(I+1) - M(M+1)) \\ &\quad \times (I(I+1) - M(M-1)))^{\frac{1}{2}}. \end{aligned}$$

We must transform H_m with T before applying the usual perturbation formulas. Hence for $|M_J| \neq 1$

$$\begin{aligned} E_m^{(\mathrm{mol})} &= \eta_{\mathrm{mol}}^2 \sum_{M_J'} \frac{|(M_J|J_1|M_J')|^2}{E_e(M_J) - E_e(M_J')} \\ &= \frac{\eta_{\mathrm{mol}}^2 B}{\epsilon^2} \frac{4}{3} \frac{J(J+1)(2J-1)(2J+3) \times (J(J+1) + M_J^2)}{4M_J^2 - 1}, \end{aligned} \tag{71}$$

and

$$E_m^{(\mathrm{mol})} = (1 \pm 2\tau\sigma)\frac{\eta_{\mathrm{mol}}^2 B}{\epsilon^2} \frac{4}{9} J(J+1)(2J-1)(2J+3) \times (J(J+1)+1) \tag{72}$$

for $\bar{M}_J = \mp 1$. For $|M_J| \neq 1$ $E_m^{(N)}$ is given by (50), (66) or (68). For $|M_J| = 1$

$$E_m^{(N)} = \eta_N^2 \sum_{M'\bar{M}_J'} \frac{|(M\bar{M}_J|I_1|M'\bar{M}_J')|^2}{E_q(M, \bar{M}_J) - E_q(M_J', \bar{M}_J')} \tag{73}$$

if $M \neq \frac{1}{2}$, and

$$\begin{aligned} E_m^{(N)} &= \pm(-\tfrac{1}{2}, \bar{M}_J|\bar{I}_1|\tfrac{1}{2}, \bar{M}_J) \\ &\quad + \eta_N^2 \sum_{\bar{M}_J'} \frac{|(\frac{1}{2}, \bar{M}_J|\bar{I}_1|\frac{3}{2}, \bar{M}_J')|^2}{E_q(\frac{1}{2}, \bar{M}_J) - E_q(\frac{3}{2}, \bar{M}_J')} \end{aligned} \tag{74}$$

if $|M| = \frac{1}{2}$. The matrix elements are

$$\begin{aligned} &|(M, +1|\bar{I}_1|M+1, +1)|^2 \\ &\quad = \tfrac{1}{4}(\tau(M)\tau(M+1)(I(I+1) - M(M-1))^{\frac{1}{2}} \\ &\quad + \sigma(M)\sigma(M+1)(I+1) - (M+1)(M+2))^{\frac{1}{2}})^2, \\ &|(M, -1|\bar{I}_1|M+1, -1)|^2 \\ &\quad = \tfrac{1}{4}(\tau(M)\tau(M+1)(I(I+1) - (M+1)(M+2))^{\frac{1}{2}} \\ &\quad + \sigma(M)\sigma(M+1)(I(I+1) - M(M-1))^{\frac{1}{2}})^2, \\ &|(M, +1|\bar{I}_1|M+1, -1)|^2 \\ &\quad = \tfrac{1}{4}(\tau(M)\sigma(M+1)(I(I+1) - M(M-1))^{\frac{1}{2}} \\ &\quad - \sigma(M)\tau(M+1)(I(I+1) - (M+1)(M+2))^{\frac{1}{2}})^2, \\ &|(M, -1|\bar{I}_1|M+1, +1)|^2 \\ &\quad = \tfrac{1}{4}(\tau(M)\sigma(M+1)(I(I+1) - (M+1)(M+2))^{\frac{1}{2}} \\ &\quad - \sigma(M)\tau(M+1)(I(I+1) - M(M-1))^{\frac{1}{2}})^2. \end{aligned} \tag{75}$$

A simple example for the results of this section is the transition $J=1\rightarrow 2$, $K=1$, $M_J=0$ in CH_3I. The frequency of this Stark component is

$$\nu=30,132+\mathcal{E}^2 1.79\cdot 10^{-4}, \tag{76}$$

where $\mathcal{E}$ is measured in volt/cm. The Zeeman pattern is

$$\delta\nu=\begin{cases} 3\eta-0.313\eta^2 \\ 0\ -0.313\eta^2 \\ -3\eta-0.313\eta^2. \end{cases} \tag{77}$$

(γ) $H_m\sim H_q$

To solve the secular equation of order $2I+1$ in this case it is convenient to start with the $IJKM_JM_J$ representation for $K\neq 0$. H_q is then diagonal for fixed M_J the diagonal elements being (34) the off diagonal elements come from $(M_I|I_1|M_I\pm 1)$ only. $E_m^{(\mathrm{mol})}$ is given by (64). For $K=0$ we must take the $\bar{M}_JM_I$ representations. The diagonal elements are then (34) for $M_J\neq 1$, (69) for $M_J=1$; the off-diagonal elements for $M_J=1$ can be obtained from (75). $E_m^{(\mathrm{mol})}$ is given by (71) and (72).

(C) Intermediate Field Strength. $H_e\sim H_q\sim H_m$

Here we have three operators of equal order no two of which commute. In this case the secular quotation of order $(2J+1)(2I+1)$ must be solved numerically for each value of the parameters. The matrix elements in the $IJKM_JM_I$ representation have all been given in (30), (31), (37) and (33).

I wish to thank Dr. A. Roberts for drawing my attention to this problem.

PHYSICAL REVIEW VOLUME 77, NUMBER 4 FEBRUARY 15, 1950

Range-Energy Relation for Protons in Nuclear Emulsions

HUGH BRADNER, FRANCES M. SMITH, WALTER H. BARKAS,* AND A. S. BISHOP
Radiation Laboratory, University of California, Berkeley, California
(Received September 19, 1949)

An experimental range-energy relation in Ilford C-2 emulsion has been obtained for protons up to 39.5 Mev. In the region from 17 to 33 Mev the relation for dry emulsion is fitted by the empirical equation $E_{(\mathrm{Mev})}=0.251R_{(\mu)}{}^{0.581}$. Variations in water content due to changes in atmospheric humidity make several percent difference in range. The range in Ilford glass is found to be 18±4 percent longer than in dry C-2 emulsion.

INTRODUCTION

THE ranges of protons of energies up to 13.1 Mev in nuclear track emulsions were measured by Lattes, Fowler, and Cuer,[1] with 50μ thick Ilford B1 emulsion. Extrapolations[2] of these data were used by Bishop[3] to calculate masses of mesons whose range in emulsion and initial momentum are known. The region of interest corresponded to proton ranges of approximately 4000μ, or 31-Mev energy. For tracks of this length the extrapolation gave energy values accurate to only ±8 percent.

In the present study the ranges of protons up to 39.5 Mev were measured in Ilford nuclear emulsions. C2 plates used in this study are stated by Ilford Ltd. to have identical chemical composition to B1 plates.

METHOD

Monoenergetic protons were obtained from the circulating beam of the 184-in. Berkeley cyclotron in an arrangement shown in Fig. 1. Protons which struck a $\frac{1}{8}$ in.×$\frac{1}{16}$ in.×3 in. copper ribbon target at, say, 30 inches from the cyclotron center scattered in all directions with a variety of energies. A C2 plate placed behind a short channel at 80 inch radius recorded those protons which left the target in a backward direction with such an energy that their paths had approximately 25 inches radius of curvature in the cyclotron magnetic field. With an accurate knowledge of the field it was possible to calculate the energy of a proton entering normal to the edge of the plate. Plates were put at 80 inch radius for all exposures, and the target radius was varied to obtain different proton energies.

Plates were tilted approximately 3° from horizontal so that protons would enter the surface of the emulsion. Distortion of the emulsion upon processing prevents accurate determination of entrance angle if one uses particles coming through the edge of the emulsion. This tilt, plus scattering of the protons in the emulsion made it difficult to find tracks in 200μ plates which stayed in the emulsion for 7000μ. Hence, the study was not extended beyond ~39 Mev.

Plates were processed in 3:1 D-19 at 68°F for 20 to 25 minutes, followed by shortstop and commercial hardening fixer. Plates suffered 50±5 percent thickness shrinkage in processing, but negligible transverse

* ONR, San Francisco, California.
[1] Lattes, Fowler, and Cuer, Proc. Phys. Soc. London **59**, 883 (1947).
[2] V. Camerini and C. M. G. Lattes, Ilford technical data (revised March 27, 1948).
[3] A. S. Bishop, Phys. Rev. **75**, 1468 (1949).

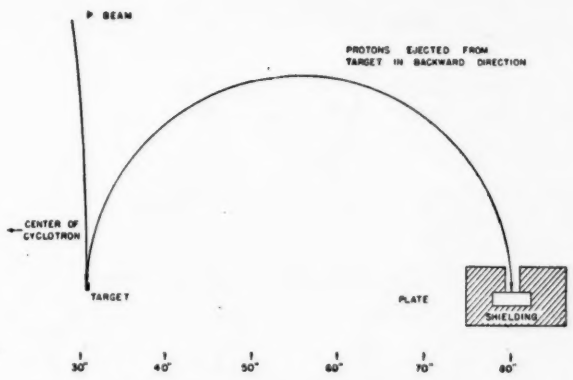

FIG. 1. Schematic diagram of arrangement for range-energy experiment.

shrinkage. Track lengths were measured both by eyepiece reticle and by dial indicator attached to the microscope stage. Corrections were made for angle of dip of protons in the emulsion.

RESULTS

Results of the measurements are presented in Figs. 2 and 3. It will be noted that the data fit a straight line on log-log plot between 17 and 35 Mev and fit the data of Lattes at 8 Mev. A least squares analysis gives for this portion the relation:

$$E_{(\mathrm{Mev})}=0.251R_{(\mu)}{}^{0.581}, \qquad (1)$$

where the energy E is expressed in Mev and the range R is measured in microns.

The original values predicted by Camerini and Lattes,[4] and a recent relativistically correct extrapolation made by Aron,[5] are indistinguishable from the present experimental results up to 35 Mev.

The effect of widely different humidity conditions on plates before exposure is indicated by the 3 points at 33.5 Mev, and the 2 points at 17.6 Mev. It was necessary to evacuate plates for at least 6 minutes before exposure so that moisture conditions were not accurately known. No difference was found between 6 minutes and 6 hours evacuation of 100μ emulsions which had previously come to equilibrium in a normal Berkeley atmosphere (75°F, 60 percent R.H.) and these plates are therefore called "dry" in the present study. However, the 17.6-Mev point shows difference between 6 minutes evacuation of such a plate and 6 minutes evacuation of a plate which had been exposed to several hours of rainy weather (95 percent R.H.). Large changes occurred as shown at the 33.5-Mev point, when 200μ plates were given 6 minutes evacuation after 24 hours exposure to 93 percent R.H. at 75°F in a $NH_4H_2PO_4$ constant humidity chamber. The 80 percent humidity point was obtained with a plate which had been maintained for 24 hours over wet NH_4CL.

An approximate value for the range of protons in the glass backing of C2 plates was found by measuring the length of tracks which had traveled most of their range in the glass. Protons from the monoenergetic (±100 kev) beam of the Berkeley linear accelerator were used in this experiment. The range of the protons of approximately 30-Mev energy was found to be 18±4 percent larger in glass than in dry C2 emulsion.

DISCUSSION

The numbers used above to illustrate the calculation of momentum from target and plate radius are only approximate because the protons did not follow a circular orbit in the radially decreasing cyclotron field. Protons leaving the target at a cyclotron radius r_1 at a small angle θ_1 from the backward direction, enter the plate (r_2) at a different small angle θ_2 to perpendicular, and have a momentum given by the expression

$$\langle Hr\rangle_{Av}=\frac{1}{r_1\cos\theta_1+r_2\cos\theta_2}\int_{r_1}^{r_2}Hrdr.$$

Stepwise integration is required to evaluate the integral. Figure 4 shows a group of values of θ_1 determined graphically by stepwise trajectory plotting starting

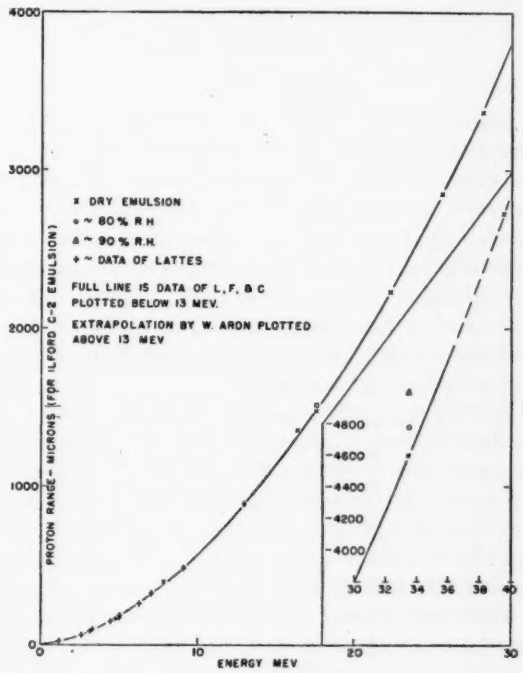

FIG. 2. Range of protons *vs.* energy.

E (Mev)	R (μ)	
7.8	389	±2.7
16.4	1358	8.1
17.6	1465	4.5
17.6	1497	6.0
22.3	2244	8.9
25.6	2849	7.1
28.2	3369	10.0
33.5	4597	13.8
33.5	4762	24.0
33.5	4996	10.0
39.5	6123	18.0

[4] V. Camerini and C. M. G. Lattes, Ilford technical data (1947).
[5] W. Aron (private communication).

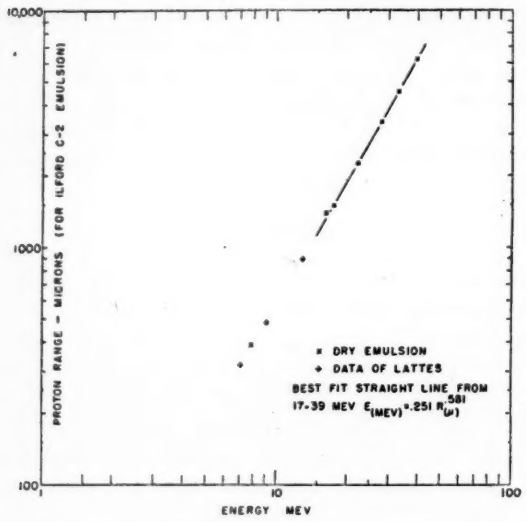

FIG. 3. Power law approximation for range-energy relation.

with various values of θ_2. In the range-energy study only tracks entering the emulsion at $0°\pm5°$ were measured, so that the difference between $\cos\theta_1$ and $\cos\theta_2$ was negligible, and the expression for $\langle Hr\rangle_{Av}$ could be written

$$\langle Hr\rangle_{Av}=\frac{\sec\theta_2}{r_1+r_2}\int_{r_1}^{r_2} Hr\,dr.$$

The value of the integral was obtained by numerical integration using absolute field calibration at 4 points by nuclear induction to 4-gauss accuracy in the 14,000-gauss field, and flip coil measurements[6] of relative fields at 1-inch intervals along a radius. The relative values at the different points in the flip coil measurements were estimated to be accurate to 0.1 percent. The field is shown as a function of cyclotron radius in Fig. 5. It was assumed, in the integration, that the cyclotron field had azimuthal symmetry.

The chief limit to the accuracy of the results was due to scatter in range of supposedly monoenergetic protons. The mean square scatter of 1 percent to 3 percent in ranges was partly caused by inaccuracies in measurement of entrance angle, partly by "skipping" of protons along the emulsion so that the actual beginning in the emulsion was missed, and sometimes caused by surface fog which prevented exact determination of the beginning of a track. Approximately half, however, could be accounted for theoretically by straggling. Probable error of the mean due to scatter in range was less than 0.7 percent for each energy value. However, it seems unwise to claim better than ±2 percent accuracy for the range-energy relation because of incomplete control of emulsion moisture, and ignorance of possible variations in emulsion composition.

The point at 16.4 Mev which lies 2 percent above the curve may be caused by "skipping" or perhaps an error in the radius to which the target was set. All other points lie within $\frac{1}{2}$ percent of the curve defined by the relation (1). The relation is probably accurate to better than 2 percent for any batch of dry B1, B2, C2, C3 or G5 plates.

The authors wish to express their appreciation of the stimulating interest of Professor E. O. Lawrence, and of the cooperation of the cyclotron crew.

The work described in this paper was done under the auspices of the AEC.

[6] D. Sewell (private communication).

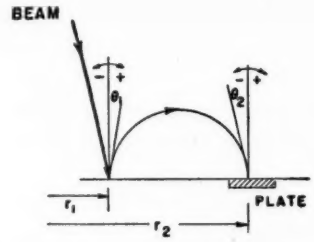

FIG. 4. Emission angle *vs.* entrance angle.

R_2	θ_2	R_1	θ_1
80″	0	27.3	−1° 45′
80″	−3°	27.4	+1° 15′
80″	+3°	27.6	−5° 0′
80″	0	33.0	−2° 35′
80″	−3°	33.1	+1° 25′
80″	+3°	33.2	−4° 45′
80″	0	37.7	−1° 45′
80″	−3°	37.7	+1° 25′
80″	+3°	37.8	−4° 40′

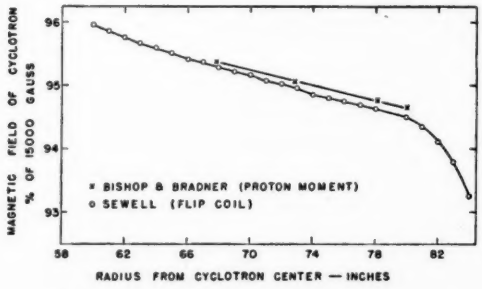

FIG. 5. Cyclotron magnetic field *vs.* radius.

PHYSICAL REVIEW VOLUME 77, NUMBER 4 FEBRUARY 15, 1950

The Lifetime of the Positive π-Meson

E. A. MARTINELLI AND W. K. H. PANOFSKY
Radiation Laboratory, Department of Physics, University of California, Berkeley, California
(Received November 7, 1949)

The lifetime of the positive π-meson has been measured using a method similar to that used by Richardson in his measurement of the negative π-meson. The lifetime obtained is $\tau=1.97\pm\times10^{-8}$ sec. or $\tau_{\frac{1}{2}}=1.37\pm\times10^{-8}$ sec. These values are about 2.5 probable errors from Richardson's value of $\tau=7.7\pm\times10^{-9}$ sec. The method has been extended so that two points on a decay curve could be determined and the geometry of the system determined to better accuracy. The geometry of the apparatus was checked by measuring the effective "lifetime" of the α-particles in the same configuration; this was found to be greater than 0.5×10^{-8} sec.

INTRODUCTION

THE measurement of the lifetime of the negative π-meson was made by Richardson.[1] Richardson's work was done in the α-particle beam of the 184-in. cyclotron. Since the yield of mesons for 380-Mev α-particles is less by about a factor of 10 than the yield of mesons with the 350-Mev proton beam now available, it was decided to improve the data by taking several points on the decay curve and to improve the statistical reliability.

EXPERIMENTAL METHOD

The method used to determine the lifetime of the π^+-meson consists of measuring the attenuation, beyond geometrical losses, of a beam of mesons as a function of the number of cyclotron orbits it has traversed. In Richardson's experiment the number of turns over which the attenuation was measured was 1. This has been increased to 2 and therefore enables one to determine 2 points on the decay curve.

Figure 1 shows schematically the experimental arrangement. The cyclotron beam strikes the carbon target, thus producing mesons which are emitted in all directions and with various energies. These then move along helical paths in the magnetic field of the cyclotron. Channels provided in the copper shielding select positive mesons within a small angular interval about 180° from the beam direction, and in an energy interval of from 8 Mev to 14 Mev. One channel accepts a bundle of helical paths which are rising from the target, while the other accepts the equivalent paths which descend from the target. Since the mesons are focused in one dimension, the geometrical loss from the channel is linear. The helical channels have been approximated with a plane, as can be seen in Figs. 2 and 3. Figure 4 shows the developed channel, the solid lines representing the situation of the 14-Mev mesons while the dotted lines refer to the channel as seen by 8-Mev mesons. Appropriate wedges were placed at the 180° position to prevent cross talk between the various channels.

Photographic plates are placed at 180° from the target in the copper channel and at either 540° or 900° in the lower spiral. The ratio of π^+-mesons found at 180° to those at either one of the other angles determines two points on the decay curve for the meson.

In the earlier experiment of Richardson only the 380-Mev alpha-particle beam of the 184-in. cyclotron was available for producing mesons. His choice of fairly low energies was dictated by the success of other exposures with the same energy interval. However, when the 350-Mev proton beam came into operation it was estimated that the number of mesons produced would greatly increase and that the peak of the energy distribution would be at quite a high energy. It therefore appeared desirable to measure the lifetime at higher meson energies than those used by Richardson.

Early experiments with the proton beam indicated that much better ratios of the number of meson tracks to the number of unwanted tracks were obtained by exposing the plates at larger distances from the target and therefore at higher energies. However, an upper limit to the meson energy which can be used for this experiment is imposed by the available space in the cyclotron air lock. The energy that was chosen is the maximum allowed by this restriction.

The type of plates used for this experiment were Ilford C-3 100μ plates. These are slightly more sensitive than the Ilford C-2 plates and therefore facilitate finding the μ-meson in the $\pi-\mu$-decay. This aids considerably in identifying a meson as a π-meson.

In Richardson's experiment the emulsion was sand-

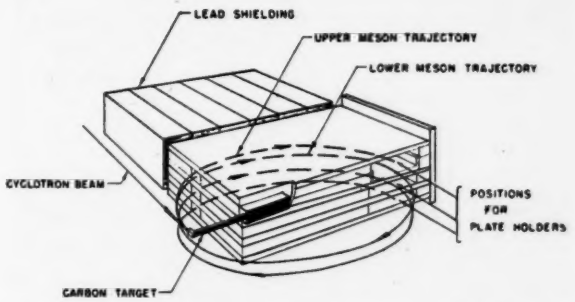

FIG. 1. Schematic diagram of meson trajectories in lifetime apparatus. Note that the "upper trajectory" is a 180° orbit while the "lower trajectory" mesons can be observed either at 540° or 900°.

[1] J. R. Richardson, Phys. Rev. **74**, 1720 (1948). See also Camerini, Muirhead, Powell, and Ritson, Nature **162**, 433 (1948) for a very approximate evaluation of the lifetime of the π-meson in cosmic rays.

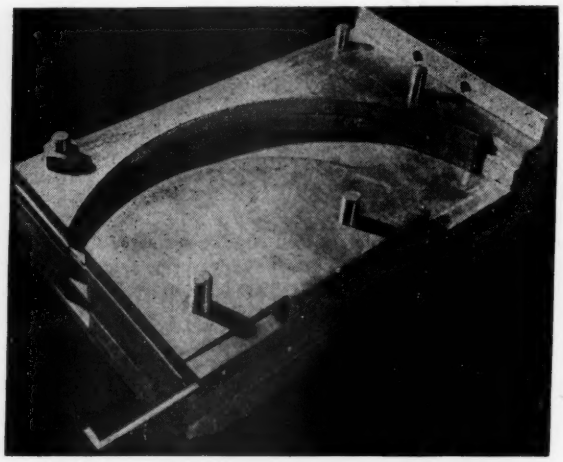

FIG. 2. Photograph of lifetime apparatus with 180° channels exposed.

wiched between glass and the edge of the plate was exposed to the mesons. This procedure is fairly good only if precise measurements are not wanted since there is a variation in the thickness of the emulsion of around ±16 percent. To avoid this error, plate holders which held two plates as shown in Fig. 5 were made. The solid angle accepted by such a device is independent, to the first order, of its orientation.

Since it is necessary to have the mesons stop in the emulsion, so that they may be identified as π-mesons, the method of using tilted plates requires an absorber in front of the plate holder which will slow down the mesons to an appropriate energy. In view of the fact that the energy varies from 8–14 Mev across the plate it is necessary to use a tapered absorber. This is allowed since the plates are exposed at odd multiples of 180° from the target where the magnetic field focuses each energy at a definite position. The thickness of the absorber was chosen by using the range-energy curves of Aron, *et al.*[2] and the range-energy curves for mesons in emulsion.[3] A residual range of approximately 300 microns was left near the center of the plates and this increased at both ends. Only the center regions of the plates were scanned for this measurement.

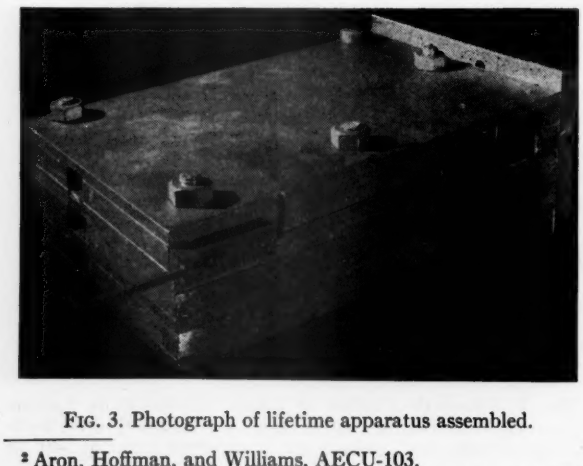

FIG. 3. Photograph of lifetime apparatus assembled.

[2] Aron, Hoffman, and Williams, AECU-103.
[3] Bradner, Smith, Barkas, and Bishop, Phys. Rev. **77**, 462 (1950).

This absorber introduces some difficulties since mesons scatter in it and some mesons therefore leave the emulsion which otherwise would have stopped. However, since the geometries of the plates at the 180° and farther positions are identical, it was felt that with a reasonably large number of mesons counted in each position, the fraction lost would be independent of position.

The experiment, till now, has been discussed as though the magnetic field of the cyclotron were completely uniform; this, of course, is not the case. In order to provide magnetic focusing for the cyclotron beam the field is made to fall off slowly with increasing radius. This decreasing field has the effect of distorting the helical paths of the mesons. Since the mesons spiral in small circles at the edge of the cyclotron field, an investigation of the motion of charged particles in a non-uniform magnetic field was undertaken.

The motion was analyzed in two ways. In the horizontal plane the non-uniform field causes the small circular orbits to precess about the center of the cyclotron. The effect on the vertical motion is to introduce some vertical focusing, so that the particle instead of maintaining its vertical component of velocity will oscillate about the central plane of the magnetic field. The calculations indicated that these effects were small if one performed the experiment with the target at 65-in. radius in the cyclotron.

Since the motion of a particle in a magnetic field is characterized by its $H\rho$, it is possible to check the geometrical decay of the channel experimentally by replacing the target with a thick alpha-particle source. An alpha-particle source (Am^{241}) of approximately 10^7 alphas/sec. was constructed by Mr. William Crane for this purpose. It was necessary to have the activity concentrated in an area the size of the target ($\frac{1}{8}$ in.$\times\frac{1}{8}$ in.) since with larger sizes part of the source would be blocked from the far positions.

Only the 900° point was checked in this way. The data contained in Table I show that the ratio of the number of alpha-particles which arrive at the 180° position to the number which arrive at the 900° position is uniform across the plate and that the deviation from the expected ratio 5.00 is within the probable error.

For the computation of the lifetime the geometrical factors of 3.00 for the 540° and 5.00 for the 900° position were used.

In order to make exposures it was necessary to provide additional shielding. Figure 6 shows the arrangement of the shielding in the cyclotron.

Since the target is very small compared to the beam height, it was necessary to provide a stop for the beam on the other side of the cyclotron. After the beam strikes this block some of the protons are scattered into the

copper channel holder. It was found from other experiments that these protons were the cause of a great deal of the background tracks in the plates. To eliminate them, a large carbon block was placed in the "dee" approximately 90° away from the target inside the cyclotron "dee." As an additional precaution about 8 in. of lead were mounted in the cyclotron on the beam side of the channel. With these measures it was possible to get readily readable plates.

In order to find out how many mesons were capable of getting to the plates without going through the prescribed channel, identical exposures to those determining the lifetime were made with the downward channel blocked at 180°. The ratios of the numbers of mesons at 180° to that at 540° and that at 900° in these runs give a measure of the background.

EVALUATION OF DATA

Since the energies of the mesons are in the neighborhood of 10 Mev whereas the rest mass is 145 Mev relativistic effects will be small.

It is simple to show, however, that using a large energy interval will not affect the lifetime measurement.[4] This is a consequence of measuring the lifetime in terms of the decay per revolution in the field. Thus, although it is true that an observer would see the lifetime lengthened for the higher energy mesons by a factor $(1-\beta^2)^{-\frac{1}{2}}$ it is equally true that the period per revolution as seen by the observer would also be lengthened by $(1-\beta^2)^{-\frac{1}{2}}$. Thus, the fraction decaying per revolution would be independent of β.

It is interesting to note that if the experiment were carried out to higher accuracy for both fast and slow mesons, it constitutes the experimental equivalent of the clock paradox.[5] It would be observed that the fast meson returning to its starting point has actually lived longer in the laboratory frame as compared to a slow one. This experiment therefore in principle depends on the fact that the laboratory frame is a preferred one in relation to the masses in surrounding space. It is also of interest to note that the mean life measured in terms of number of turns is independent of relativistic considerations; this fact is a reasonable one since it is a pure counting operation and not an experiment involving physical measurement.

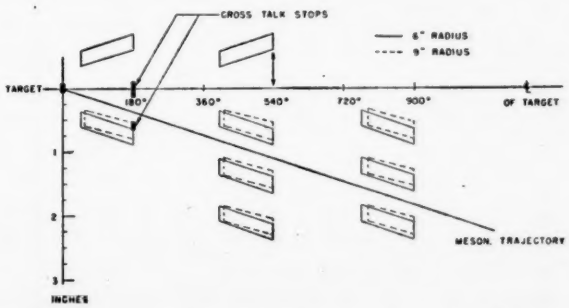

FIG. 4. Developed view of lifetime apparatus; i.e., a plot of the meson trajectory and channel walls in vertical coordinates *vs.* angular position. Solid parallelograms show the channel walls as "seen" by a 14 Mev—π^+-meson while dotted parallelograms show the walls as "seen" by an 8-Mev meson. Note the "cross-talk stops" which prevent mesons from reaching the 180° position after 540° travel and from reaching the 900° position after 540° travel.

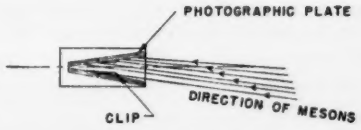

FIG. 5. Geometry of plate holder showing meson incident on inclined surfaces of photographic plates. The sum of tracks on the two plates is virtually independent of the inclination of the plate holder assembly toward the beam direction.

The plates were scanned using a Spencer microscope with a 1.8-mm oil immersion achromatic objective and 6-power eyepiece. This results in a field of view of approximately 250 micron in diameter.

Two methods of measuring the scanned area were used depending on the meson density in the plate. For the plates exposed at 180° a reticule with 2 parallel rulings which marked a region 73 microns wide in the field of view was used. The plate was scanned parallel to the direction of the mesons and only mesons stopping in the 73-micron swath were tabulated. In this way the area is found by measuring the total length of scan. For the plates at 540° and 900° it was desirable to utilize all of the mesons in a given area. This was especially true of the 900° plates where the total number of mesons available was not very great. In these cases the observation was done by taking overlapping scans. At the end of each swath the plate was moved 100 microns so that there was an overlap of about 150 microns. The area was then obtained from the vernier on the microscope stage. For the 180° plates this method would have lead to confusion as to which mesons had already been tabulated.

Table II shows the data which were obtained from the background plates.

These data give the following ratios:

$$\text{(Density at 540°)/(density at 180°)} = 0.0197 \pm 0.009$$

and

$$\text{(density at 900°)/(density at 180°)} = 0.00320 \pm 0.0012.$$

The shielding for the background runs was not as good as in the lifetime runs and hence this background is considered as an upper limit and will not be used for correction but will be incorporated in the probable error of the final result.

Among the meson tracks observed, those were counted which showed a definite $\pi-\mu$-decay and were therefore certain to be due to π^+-mesons. Also counted were those tracks which could be identified as mesons

[4] See, e.g., W. F. G. Swann, Phys. Rev. **76**, 157 (1949).
[5] R. C. Tolman, *Relativity, Thermodynamics and Cosmology* (Oxford University Press, New York, 1934), p. 194.

TABLE I. Ratio of the number of alpha-particles which at the 180° position to the number which arrive at the 900° position.

Distance along plate from the low energy side (cm)	Ratio α's at 180 To α's at 900
2	5.07±0.25
3	5.62±0.28
4	5.04±0.25
5	4.99±0.25
6	5.23±0.25
Weighted average	5.16±0.11

but which did not stop in the emulsion, and those meson tracks which stopped in the emulsion but for which no decay track could be found. Table III gives a summary of the data.

The reliability of the count for mesons which did not stop in the emulsion is not very high since the identification is not certain in many cases, and such tracks are easily overlooked if one is intent on observing mesons that stop. In view of the uncertainty of this number, the data appear to be quite consistent as to the fraction which stops in the emulsion. The mesons going through the emulsion were not included in the computation of the lifetime since some of them might very well be μ-mesons. Those meson tracks which did not appear in conjunction with decay meson tracks are probably due to μ-mesons, π^+-mesons which do not decay by $\pi-\mu$-decay or mesons which stopped in a

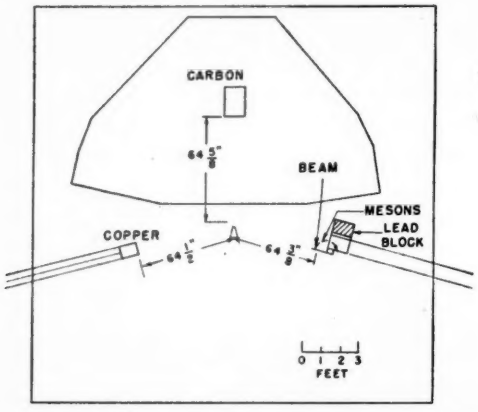

FIG. 6. Disposition of shielding in the tank of the 184-inch cyclotron. The copper block shown is slotted to limit the vertical oscillation amplitude of the beam. The carbon block inside the "dee" serves to stop protons scattered by the target from striking the shielding (lead blocks) behind the lifetime apparatus.

region of the plate which would not record a μ-meson of 4 Mev.

Considering only the $\pi-\mu$-decays recorded in Table III, the density of mesons at the various positions may be computed. These are recorded in Table IV.

These values give the following ratios:

(Meson density 540°)/(meson density 180°)
$=0.862/348=0.248\pm0.014$,
(meson density at 900°)/(meson density at 180°)
$=0.288/3.02=0.0954\pm0.0052$.

TABLE II. Data from the background plates.

Position	Number of decays	Area scanned mm²	Density of mesons/No./mm²
180°	21	20	0.953
540°	3	160	0.0187
180°	70	60	1.17
900°	3	800	0.00375

If the lifetime were infinite, the expected ratios would be 0.333 and 0.200 respectively. The decrease in density due to decay in flight if normalized to 1 at 180° is then given by Table V. All of the errors recorded are purely statistical.

In order to average the 540° and 900° points in such a way that the errors could be computed, the 540° point was extrapolated to 900° by using the mean life computed from the 540° point. The probable error at the extrapolated point was doubled. Thus from Table V the ratio R at 540° is:

$$R_{540°}=0.743\pm5.6 \text{ percent.}$$

Extrapolated to 900° this gives:

$$R_{540°}=0.564\pm11.3 \text{ percent.}$$

The rotio obtained from the 900° data is:

$$R_{900°}=0.476\pm5.45 \text{ percent.}$$

Averaging these two 900° points by weighting inversely

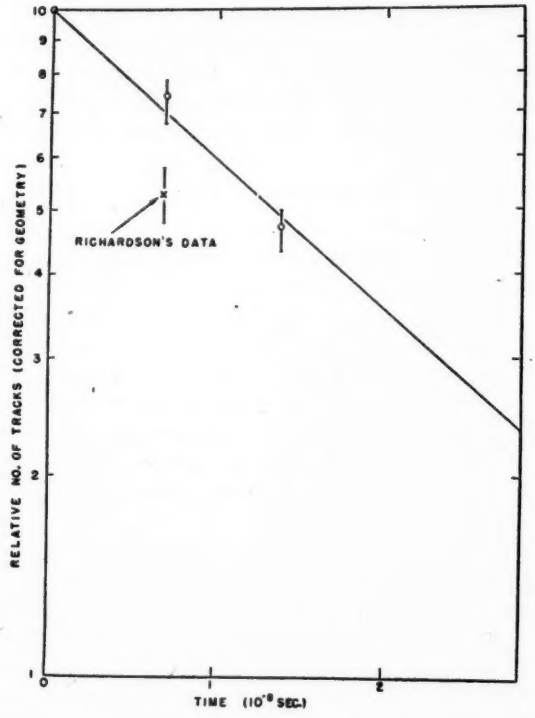

FIG. 7. Decay curve of the π^+-meson. The point of Richardson (see reference 1) is shown also. Ordinates plotted represent the fall-off in intensity other than due to geometry, plotted relative to the 180° position.

TABLE III. Summary of the data.

Plate No.	Position	No. of decay	No. scattered out of the emulsion	No showing No decay	Area scanned mm²
6603	180°	166	41	4	43.8
6602		130	37	3	43.8
6601	540°	114	45	6	140
6600		127	51	5	140
6571	180°	204	73	10	58.4
6570		148	50	7	58.4
6569	900°	116	42	7	400
6568		114	45	6	400

TABLE IV. Density of the mesons in various positions.

Position	Density of mesons in plates No./mm³
180°	3.48 ±0.14
540°	0.862±0.036
180°	3.02±0.10
900°	0.288±0.012

TABLE V. Decrease in density of mesons due to decay in flight.

Position	Relative density R (due to decay in flight)
180°	1.00
540°	0.743±0.042
900°	0.476±0.026

with the square of the probable errors gives:

$$R_{900°_{Au}}=\frac{0.476(4.32)+0.564}{5.32}=0.492\pm0.024,$$

the probable error being computed by weighting in the same way.

From this value the mean life in cyclotron revolutions at a magnetic field of 14,300 gauss is easily computed to be:

$$=2.84\pm0.20 \text{ revolutions.}$$

Using the magnetic field data obtained recently by Bradner and Bishop[5] with the proton magnetic moment resonance method we obtain $H=14{,}295$ gauss for the mean field over the orbit. Using adopted values of the atomic constants[6] we thus obtain a period per revolution of

$$\tau=0.6945\times10^{-8} \text{ sec.}$$

Using this number we obtain for the mean and half-lives

$$\tau=1.97\pm0.139\times10^{-8} \text{ sec.}$$
$$\tau_{\frac{1}{2}}=1.37\pm0.095\times10^{-8} \text{ sec.}$$

In addition to these statistical errors there is a probable error in the geometrical ratio of approximately 3 percent, and the effects of background to lengthen the lifetime. On combining the errors one arrives at the following limits:

1. In the upward direction,

$$\Delta\tau/\tau=[(0.07)^2+(0.03)^2]^{\frac{1}{2}}=0.076.$$

2. In the downward direction,

$$\Delta\tau/\tau=[(0.07)^2+(0.03)^2+(0.05)^2]^{\frac{1}{2}}=0.086.$$

Using these errors one has as the final result.

$$\tau=1.97\pm\begin{matrix}0.14\\0.17\end{matrix}\times10^{-8} \text{ sec.}$$

$$\tau_{\frac{1}{2}}=1.37\pm\begin{matrix}0.10\\0.12\end{matrix}\times10^{-8} \text{ sec.}$$

Although this result is somewhat outside of Richardson's published value,

$$\tau_{\frac{1}{2}}=7.7\pm\begin{matrix}0.21\\0.16\end{matrix}\times10^{-9} \text{ sec.},$$

it can be seen from Fig. 7 that the disagreement is not as extreme as is implied. Certainly one could not say that the experiment shows a difference between the π^+- and π^--mesons. However, the discrepancy is enough so that it might warrant investigation.

ACKNOWLEDGMENTS

We should like to acknowledge our indebtedness to Dr. J. Reginald Richardson from whose experiment this work has grown. We should also like to express our gratitude to Professor E. O. Lawrence for interest, encouragement, and advice concerning the performance of the experiment. We also have benefited greatly from the previous experiment of the photographic film group at the Radiation Laborotory, particularly H. Bradner, E. Gardner, and C. M. G. Lattes. The bombardments were carried out by the cyclotron crew under direction of J. Vale.

This work was performed under the auspices of the AEC.

[6] J. W. M. DuMond and E. R. Cohen, Rev. Mod. Phys. **20**, 82–108 (1948).

The Production of Fast Deuterons in High Energy Nuclear Reactions*

G. F. CHEW AND M. L. GOLDBERGER†
Radiation Laboratory, University of California, Berkeley, California
(Received October 11, 1949)

It is proposed that the fast deuterons observed among the products of high energy nuclear reactions are to be understood in terms of a "pick-up" or sudden rearrangement process. A theoretical treatment of such a process is given which suffices to interpret presently existing data. Further experiments are proposed to test the hypothesis critically, and a possible application of this type of experiment to the determination of nuclear wave functions is pointed out.

I. INTRODUCTION

PROPORTIONAL counter experiments by York[1] and cloud-chamber measurements by Brueckner and Powell[2] have revealed a substantial number of fast deuterons among the reaction products from nuclear bombardments by 90-Mev neutrons. Analogous experiments with high energy protons seem to be giving similar results.[3] Since the energy of these deuterons is of the same order as the incident neutron energy and since they are strongly peaked forward in angular distribution, they cannot be the result of an evaporation which follows the formation of a compound nucleus. They might be understood, instead, on the basis of a sudden rearrangement, in which a proton is transferred from the target nucleus to the passing neutron. This process would be almost the inverse of deuteron stripping, which Serber[4] and Peaslee[5] have discussed.

In this paper, a calculation of the high energy "pick-up" cross section is made in Born approximation. This neglects all processes involving more than the incident nucleon and the partner with which it is to join. It is a reasonable procedure for light nuclei, which are relatively transparent to neutrons and protons with energies of the order of 100 Mev. It is hoped that any opacity may lower the over-all probability of the process without seriously changing the energy and angular dependence. Experimental data will be cited to support this point of view. The Born approximation, of course, can also fail badly in describing the elementary neutron-proton interaction, even at high energies.[6] An attempt is made to remedy this situation by separating the elementary matrix element from the rest of the calculation and making sure that this matrix element is consistent with the known facts about high energy neutron-proton scattering. The separation will become clear in Section II as the calculation is performed.

It should be pointed out that the pick-up process must not be thought of as taking place within the nucleus, following a real collision of the neutron and proton. The period of the deuteron is considerably longer than the time required for a 100-Mev neutron or proton to cross the nucleus, and the "radius" of the deuteron is as large as the mean separation of the constituents of a heavier nucleus. The "scattering" is virtual, with different energy-momentum requirements from a free neutron-proton collision, and the part of the wave function corresponding to the outgoing deuteron does not materialize as such until long after the nuclear event.

II. DERIVATION OF THE CROSS-SECTION FORMULA

It is necessary to estimate the value of a matrix element which connects an initial state consisting of an incoming free neutron, nucleus in state Ψ_i, to a final state consisting of a free deuteron, nucleus in state Ψ_f. In first approximation, we need consider only the triplet interaction between the neutron and that proton with which it is to join. Let us designate this interaction by $V(\mathbf{r}_n, \mathbf{r}_p)$ where $\mathbf{r}_n$ and $\mathbf{r}_p$ are the neutron and proton coordinates, respectively. The required matrix element is then

$$\mathcal{H}_f = (e^{i\mathbf{K}\cdot(\mathbf{r}_n+\mathbf{r}_p)/2}\varphi(\mathbf{r}_n-\mathbf{r}_p)\Psi_f,\ V(\mathbf{r}_n,\ \mathbf{r}_p)e^{i\mathbf{k}\cdot\mathbf{r}_n}\Psi_i) \quad (1)$$

where $\mathbf{k}$, $\mathbf{K}$ are the wave number vectors of the incident neutron and center of mass of the outgoing deuteron, respectively, and $\varphi(\mathbf{r}_n-\mathbf{r}_p)$ is the internal wave function of the deuteron. The cross section per proton for emission of a deuteron into the solid angle $d\Omega$, leaving the nucleus in the state Ψ_f, is

$$\sigma_f d\Omega = \frac{3}{4}\frac{M^2}{2\pi^2\hbar^4}\frac{K}{k}|\mathcal{H}_f|^2 d\Omega, \quad (2)$$

where M is the mass of a nucleon. The magnitude of K is determined by energy conservation:

$$\frac{\hbar^2K^2}{4M} - B_D = \frac{\hbar^2k^2}{2M} - B_{if}, \quad (3)$$

where B_{if} is the energy difference of initial and final nuclear levels and B_D is the deuteron binding energy.

* Originally reported at the meeting of the Am. Phys. Soc. (February 1949) at Berkeley.
† Now at M.I.T., Cambridge, Massachusetts.
[1] H. York, Phys. Rev. **75**, 1467A (1949). A complete report of this work will be submitted for publication in the Phys. Rev.
[2] K. Brueckner and W. Powell, Phys. Rev. **75**, 1274 (1949).
[3] W. Crandall (private communication).
[4] R. Serber, Phys. Rev. **72**, 1008 (1947).
[5] D. C. Peaslee, Phys. Rev. **74**, 1001 (1948).
[6] See, for example, M. Camac and H. Bethe, Phys. Rev. **73**, 191 (1948).

If the target nucleus is very light its recoil will introduce an additional angular dependent term into (3). The factor of $\frac{3}{4}$ in (2) represents the *a priori* probability for the neutron and proton to have parallel spins.

If the relative coordinate, $\mathbf{r}=\mathbf{r}_n-\mathbf{r}_p$, is introduced in place of $\mathbf{r}_n$, the matrix element, $\mathcal{H}_f$ may be factored:

$$\mathcal{H}_f=(e^{i(\mathbf{K}-\mathbf{k})\cdot\mathbf{r}_p}\Psi_f,\ \Psi_i)(\varphi(\mathbf{r}),\ V(\mathbf{r})e^{i(\mathbf{k}-\mathbf{K}/2)\cdot\mathbf{r}}). \quad (4)$$

The final deuteron momentum, $\hbar K$, depends only weakly on the state f of the residual nucleus if the incident neutron momentum is high. We shall neglect this dependence, taking the constant value corresponding to an average B_{if} (Eq. (3)). The sum over all final nuclear states can then be performed, since

$$\sum_f |(e^{i(\mathbf{K}-\mathbf{k})\cdot\mathbf{r}_p}\Psi_f,\ \Psi_i)|^2 = \int d\mathbf{R}\left|\int e^{-(\mathbf{K}-\mathbf{k})\cdot\mathbf{r}_p}\Psi_i d\mathbf{r}_p\right|^2. \quad (5)$$

$\mathbf{R}$ represents the coordinates of all particles in the initial nucleus except the one proton which is picked up. The right-hand side of (5) can obviously be interpreted as the probability of finding the proton with the momentum, $\hbar(\mathbf{K}-\mathbf{k})$, in the initial nucleus. Let this probability be designated by $N(\mathbf{K}-\mathbf{k})$. The proton momentum in question is, of course, just that required to lead to a deuteron of momentum $\hbar\mathbf{K}$.

The second factor of (4) may be treated in two ways. To understand its meaning, let us first rewrite it as follows:

$$(\varphi(\mathbf{r}),\ V(\mathbf{r})e^{i(\mathbf{k}-\mathbf{K}/2)\cdot\mathbf{r}}) = \frac{1}{(2\pi)^3}\int d\mathbf{q}(\varphi(\mathbf{r}'),\ \exp(i\mathbf{q}\cdot\mathbf{r}')) \times(\exp(i\mathbf{q}\cdot\mathbf{r}),\ Ve^{i(\mathbf{k}-\mathbf{K}/2)\cdot\mathbf{r}}). \quad (6)$$

The second factor of the integrand on the right-hand side of (6) is essentially the probability *amplitude* for the initial neutron-proton pair to be scattered from the relative momentum, $\mathbf{k}-\mathbf{K}/2$, to the relative momentum, $\mathbf{q}$. The first factor is the probability *amplitude* for the relative momentum $\mathbf{q}$ to be found in a deuteron. Since the relative momentum is unobservable, one sums over all possible values *before* squaring to get the probability of deuteron formation. Now instead of choosing a particular interaction $V(r)$ as a starting point, one might insert for the scattering matrix element in (6) a function of $\mathbf{q}$ and $\mathbf{k}-\mathbf{K}/2$ which correctly represents the known triplet scattering cross section. This ought to eliminate much of the error of the Born approximation and also the uncertainty due to not knowing the interaction $V(r)$. Unfortunately, as mentioned above, the free neutron-proton scattering involves different pairs of momenta than occur in this problem and some kind of extrapolation has to be made. $V(r)$ can be eliminated in a different way, however, without sacrificing the desired property of the scattering matrix. The second way leaves no ambiguity as to how the extrapolation must be made.

If we remember that $V(r)$ and $\varphi(\mathbf{r})$ are connected through the Schrödinger equation for the ground state of the deuteron, then the left-hand side of (6) may be written as:

$$(V(r)\varphi(\mathbf{r}),\ e^{i(\mathbf{k}-\mathbf{K}/2)\cdot\mathbf{r}})=\left[\left(\frac{\hbar^2}{M}\Delta_r-B_D\right)\varphi(\mathbf{r}),\ e^{i(\mathbf{k}-\mathbf{K}/2)\cdot\mathbf{r}}\right].$$

The operator can be thrown back onto the exponential function, giving

$$-\left[B_D+\frac{\hbar^2}{M}(\mathbf{k}-\mathbf{K}/2)^2\right](\varphi(\mathbf{r}),\ e^{i(\mathbf{k}-\mathbf{K}/2)\cdot\mathbf{r}}) \quad (7)$$

and the neutron-proton interaction has been completely eliminated. Instead of high Fourier components of the interaction, V, one now has only to guess about high Fourier components of the deuteron wave function. There need be no concern about the nature of the force. If it is possible to choose a wave function, $\varphi(r)$, corresponding to a potential with high Fourier components which actually do agree with the observed neutron-proton scattering, then one may have confidence in the approximation. This can be done, although it actually turns out to be not very important. The two factors of (7) compensate each other to such a large extent that the function $N(\mathbf{K}-\mathbf{k})$ completely dominates the calculation.

The results of this section are that the square of the matrix element, summed over all final states of the residual nucleus, may be written as

$$\sum_f |\mathcal{H}_f|^2=N(\mathbf{K}-\mathbf{k}) \times\left[B_D+\frac{\hbar^2}{M}(\mathbf{k}-\mathbf{K}/2)^2\right]^2|(\varphi(\mathbf{r}),\ e^{i(\mathbf{k}-\mathbf{K}/2\cdot\mathbf{r})})|^2. \quad (8)$$

The unknown quantities are the initial momentum distribution of the proton to be picked up, the deuteron wave function, and the appropriate average value of B_{if}, which determines the magnitude of K.

III. DISCUSSION OF THE CROSS-SECTION FORMULA

The distribution of final energy levels is determined chiefly by the overlap of the nuclear wave functions, Ψ_i and Ψ_f. The residual nucleus is not likely to be found in its ground state, for even if the proton removed was the one most loosely bound, the wave function of the remaining nucleons will not exactly correspond to the new potential which they feel. The most probable value of B_{if}, therefore, will be greater than the energy difference between ground states of initial and final nuclei. This makes the effective threshold correspondingly higher than one would expect for an $n-d$ reaction in which a compound nucleus is formed.

UNIVERSITY OF MICHIGAN LIBRARIES

An empirical average value of B_{if} can be obtained from the observed energy of the deuterons, and there may be different values for different protons within the initial nucleus. This point will be discussed further in connection with specific experiments.

The ground state of the deuteron, neglecting the small amount of d wave, may be written

$$\varphi(\mathbf{r})=A/r[e^{-\alpha r}-h(r)], \tag{9}$$

where $\alpha=[(MB_D)/\hbar^2]^{\frac{1}{2}}$, $h(r)$ is a function which is unity at the origin and vanishes outside the range of the force, and A is a normalization factor. In terms of the effective range,[7] ρ, of the triplet neutron-proton force, A may be written

$$A=\left[\frac{\alpha}{2\pi(1-\alpha\rho)}\right]^{\frac{1}{2}} \tag{10}$$

since the definition of the effective range is

$$\rho=2\int_0^\infty dr[e^{-2\alpha r}-(e^{-\alpha r}-h(r))^2]. \tag{11}$$

A simple assumption as to the form of $h(r)$ is $h(r)=e^{-\beta r}$. Then

$$\rho=4/\alpha+\beta-1/\beta. \tag{12}$$

The best value of ρ known at present is 1.6×10^{-13} cm,[7] which corresponds to $\beta=7\alpha$.

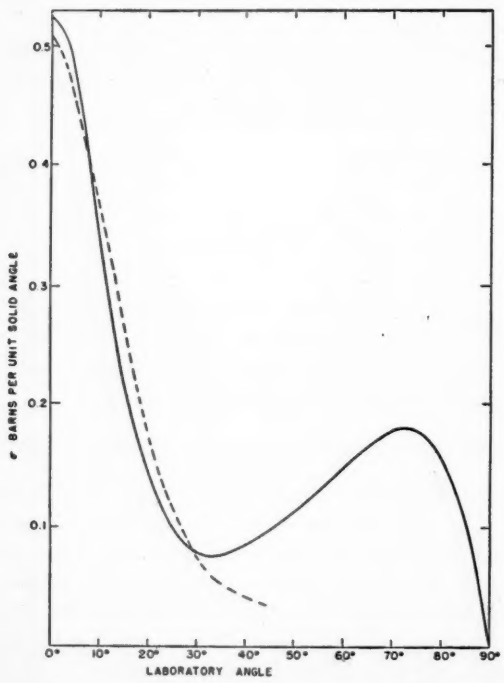

FIG. 1. Recoil deuterons from 14-Mev neutrons. Solid curve represents measurement of Coon, Taschek, and Forbes. Dotted curve follows from momentum distribution (14), normalized arbitrarily.

[7] J. Blatt and J. D. Jackson, Phys. Rev. **76**, 18 (1949).

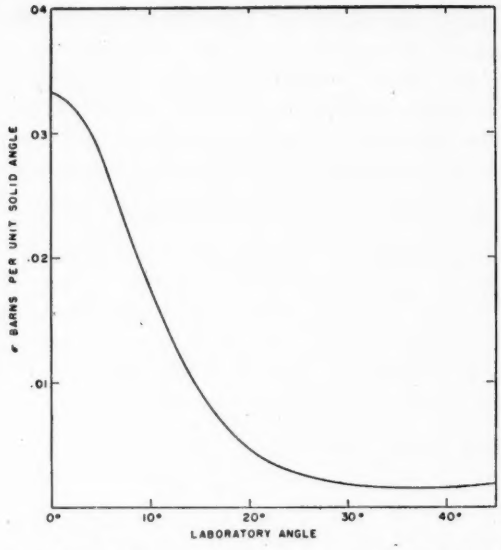

FIG. 2. Pick-up deuterons theoretically expected in the elastic scattering of 90-Mev neutrons by deuterons.

The wave function,

$$\varphi(\mathbf{r})=A(e^{-\alpha r}-e^{-\beta r})/r, \tag{13}$$

is very close to the form corresponding to a Yukawa potential.[8] It is known[8] that the Yukawa potential with a half-ordinary half-exchange character gives in Born approximation a satisfactory representation of high energy neutron-proton scattering. This is a purely fortuitous situation but is nonetheless reassuring. We believe therefore that the function (13) may be used in this particular problem with considerable confidence.

The Fourier transform of (13) is

$$4\pi A\frac{\beta^2-\alpha^2}{[\alpha^2+(\mathbf{k}-\mathbf{K}/2)^2][\beta^2+(\mathbf{k}-\mathbf{K}/2)^2]} \tag{14}$$

so that the product of the second and third factors of (8) depends on $\mathbf{K}$ only as $[\beta^2+(\mathbf{k}-\mathbf{K}/2)^2]^{-2}$. Now β^2 corresponds to about 50 Mev, while the relative energies which must be accommodated are rarely more than half this. Thus the variation of this factor over the range of interest is weak. It would be a constant if the $n-p$ force were of zero range.

The momentum distribution of the target proton, $N(k_p)$ will depend on the nucleus under bombardment. The one case where it is fairly well known is when the target nucleus is actually a deuteron. In this case, the pick-up process is simply a part of the $n-d$ elastic scattering, but it is distinguishable from the "collision part" by its forward angular distribution. In Fig. 1 is shown the angular distribution of recoil deuterons observed from 14-Mev incident neutrons.[9] The pick-up peak is evident, and the width agrees with the momentum distribution (14), even though 14 Mev is too low

[8] G. F. Chew, Phys. Rev. **74**, 809 (1948).

[9] J. H. Coon and R. F. Taschek, Phys. Rev. **76**, 710 (1949).

an energy for our calculation to apply. This is perhaps confirmation that multiple processes decrease the pick-up probability without distorting violently the angular distribution.

The corresponding experiment with 90-Mev neutrons is now being planned at the Radiation Laboratory. The theoretical prediction for the forward deuteron peak is shown in Fig. 2. This result was calculated earlier by Chew,[8] although the significance of the pick-up process was not emphasized in the earlier paper. The probability of multiple effects should be quite small in this case, so one has the opportunity of quantitatively testing the pick-up hypothesis. The expected intensity of deuterons in the forward direction is 30 mb per unit solid angle.

Experiments, however, have been and presumably will be done with targets heavier than deuterons. It is, therefore, necessary to have some idea of the momentum distribution of the protons in a complex nucleus. The simplest estimate is given by assuming the nucleus to consist of a degenerate Fermi gas of neutrons and

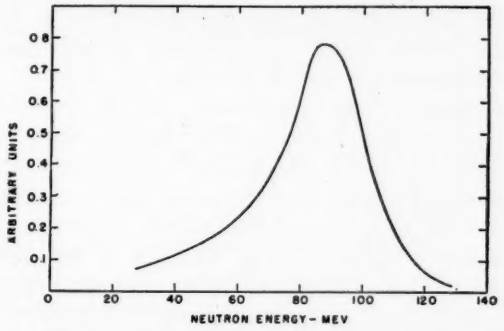

FIG. 3. The neutron spectrum obtained by stripping 190-Mev deuterons with a half-inch beryllium target in the 184-inch cyclotron.

protons, non-interacting but confined to the nuclear volume. This suffices to estimate the total cross section. The Fermi distribution, however, inevitably predicts a peculiar angular distribution, due to its sharp upper limit. For example, if this limit corresponded to 25 Mev, there could be no pick-up deuterons at angles greater than 22° for 90-Mev incident neutrons. Below this limit the angular dependence would be weak, coming entirely from the second and third factors of (8). Such a square distribution has not been observed.

In the absence of supplementary information, such as one has about the deuteron, we believe the most reasonable procedure is to read the existing proton *momentum* distribution out of the observed deuteron *angular* distribution. This same distribution should then suffice, with formula (2), to *predict* the dependence of the pick-up cross section on the *energy* of the incident neutron. The latter measurement would constitute a second critical test of the pick-up hypothesis and our treatment of it.

If these tests are passed, one would have a direct method of examining nuclear wave functions. In especially simple cases where there are only one or two neutrons or protons present so that only the first level is occupied, the energy or angular dependence of the pick-up cross section would give directly the square of the Fourier analysis of that state. These experiments should be done with monoenergetic projectiles, of course, so that the role of proton and neutron in all that has been said ought probably to be reversed.

One nucleus may be accessible even to fairly low energy measurements. This is Be^9. If there is any truth to the alpha-particle model for light nuclei, it should be possible to pick-up the odd neutron from Be^9 and still not excite the residual Be^8 by more than one or two Mev. Pick-up deuterons might therefore be produced by any accelerator which can reach a proton energy of 3 or 4 Mev. The Born approximation is not valid at low energies but the excitation function and angular distribution of these deuterons is still of interest. Be^9 should produce two distinct groups of pick-up deuterons when bombarded by protons of an energy greater than 30 or 40 Mev, since the four tightly bound neutrons could then be picked up. Again using the alpha-particle model as a guide, a B_{ij} somewhat greater than 21 Mev would be expected for this second group, since this is the binding energy difference between He^3 and He^4.

IV. COMPARISON WITH EXISTING EXPERIMENTS

The most complete experimental data which is at present available is that of York.[1] He employed the neutron beam produced by deuteron stripping in the 184-inch cyclotron.[10] These neutrons are not monoenergetic, their spectrum being shown in Fig. 3, as measured in the neutron-proton scattering experiments.[11]

Most of York's results were obtained with a carbon target, for which he measured both the energy and the angular distribution of the fast deuterons. Since the dependence of the process on neutron energy has only been observed in a very crude way in this experiment,

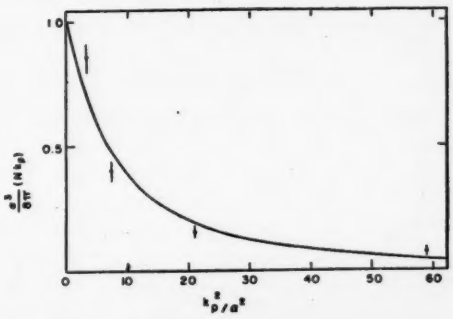

FIG. 4. Assumed distribution of proton momenta in C^{12}, normalized to unity at the origin. The four points are based on York's measurement of the deuteron intensity at 0°, 12°, 25°, 45°.

[10] Helmholz, McMillan, and Sewell, Phys. Rev. **72**, 1003 (1947).
[11] Hadley, Kelly, Leith, Segrè, Wiegand, and York, Phys. Rev. **75**, 351 (1949).

UNIVERSITY OF MICHIGAN LIBRARIES

and since carbon is not very transparent, it cannot be said that the pick-up hypothesis has been verified. The most that can be done is to show that with reasonable assumptions about the carbon nucleus, York's results are understandable.

One of the most striking observations made in the $C^{12}(n, d)B^{11*}$ experiment was that the spread of possible final states in B^{11} is small. Both York and Brueckner and Powell found that the high energy end of the forward deuteron distribution gave a close reproduction of the incident neutron spectrum. It is possible to assume, therefore, that only one distinct type of proton state in the carbon is contributing, and that a single value of B_{if} is sufficient. This simplifies the problem enormously, since one can then identify the energy of a neutron by the energy of the deuteron which it produces. It is merely necessary to add 25 Mev, the difference in position of the deuteron and neutron peaks. (See Figs. 3 and 5.) According to the alpha-particle model of carbon, all six protons are equivalent, so the experimental result is perhaps not surprising.

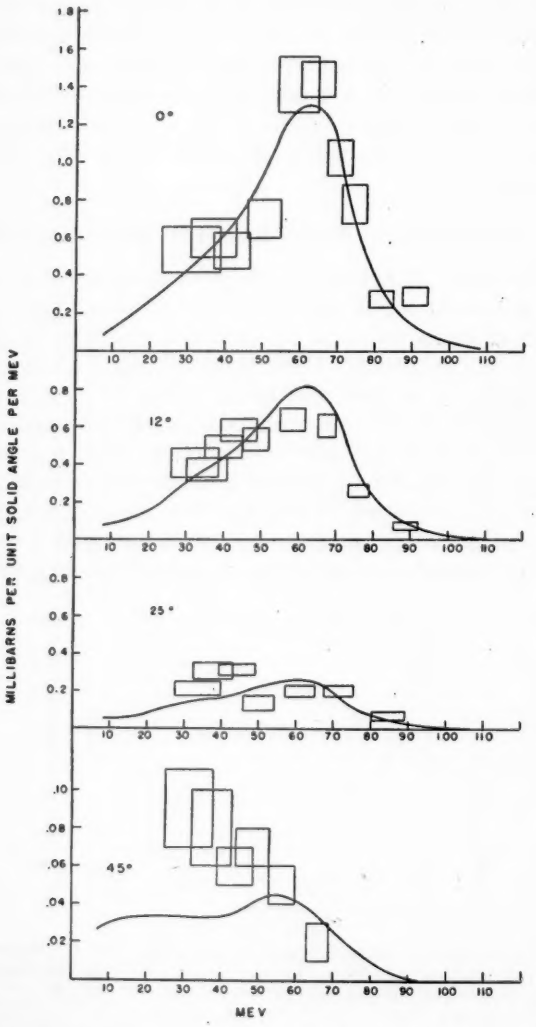

FIG. 5. Fast deuterons ejected from carbon at various angles by the stripped neutrons. Blocks represent the results of York. Solid curves are theoretical.

Let us begin the analysis by determining the initial proton momentum distribution $N(k_p)$ from the angular distribution of 60–65-Mev deuterons, those at the peak. A reasonable fit over the relevant range, shown in Fig. 4, is obtained with

$$N(k_p)=\frac{8\pi\alpha_p}{(\alpha_p^2+k_p^2)^2}, \tag{15}$$

where $\mathbf{k}_p=\mathbf{K}-\mathbf{k}$, and $\alpha_p=4\alpha$. This value of α_p^2 corresponds to a proton energy of 18 Mev so that for momenta of this order of magnitude, the distribution is not surprising. At very high momenta, however, where there is as yet no evidence, this function should certainly not be believed.

Having $N(k_p)$, the problem is completely determined except for the over-all normalization. A carbon nucleus stops two-thirds of the 90-Mev neutrons entering it, so we must expect a sizeable attenuation coefficient. Choosing a value of 0.76 for the effective number of protons, and using the neutron spectrum of Fig. 3, one calculates the energy and angular distribution of deuterons shown in Fig. 5.

The agreement with experiment is satisfactory except for a group of low energy deuterons whose relative number increases with angle. These could easily be of a secondary origin, i.e., the result of interactions between three or more particles. A typical process of this type, which seems fairly likely, is to have a fast proton, produced in an exchange collision, pick up a neutron from the same nucleus. Since the incident neutron will not have lost all its energy in the initial collision, the emerging deuteron will have a smaller momentum than those considered in this paper. Such secondary deuterons should be smaller in number than the fast protons observed in the same bombardment and be less peaked in angular distribution. The data is inadequate at present to check such facts. Practically all of York's 45° deuterons could be secondary, and we may have seriously overestimated the high momentum components of the proton wave function in attempting to fit at this angle.

It should be emphasized that the agreement between theory and experiment did not follow automatically from our choice of $N(k_p)$. It is true that the heights of the deuteron peaks at various angles were forced to come out right. However, the shapes of the peaks, whose breadths increase with angle, could not be adjusted. They followed directly from the independently determined $N(k_p)$.

It is evident, nevertheless, that a really convincing experiment can only be done with a monochromatic beam, which means protons. The relatively well-defined energy of the primary pick-up deuterons should then distinguish them from secondary particles of a more complicated origin. The energy and angular de-

pendence should also be tested in a differential rather than in an integral manner.

Two last experimental facts are worthy of mention. One is that bombardments of copper and lead targets show that the number of fast deuterons increases with atomic number less rapidly than the number of fast protons.[1] This may be an indication that the pick-up process is more confined to the surface of the nucleus than is a knock-out process. The second fact is that fast tritons have also been observed with perhaps one-tenth the probability of deuterons. If the pick-up hypothesis is correct, more complicated rearrangements are expected also to occur, but, of course, less often.

The authors wish to thank Professors Serber and Wick for helpful theoretical discussions. We are also grateful to H. York and K. Brueckner for their aid in interpreting the experiments. Work described in this report was performed under the auspices of the AEC.

PHYSICAL REVIEW VOLUME 77, NUMBER 4 FEBRUARY 15, 1950

X-Ray and Gamma-Ray Reflection Properties from 500 X Units to Nine X Units of Unstressed and of Bent Quartz Plates for Use in the Two-Meter Curved-Crystal Focusing Gamma-Ray Spectrometer*

D. A. LIND, W. J. WEST,† AND J. W. M. DUMOND
California Institute of Technology, Pasadena, California

(Received October 6, 1949)

The x-ray and gamma-ray reflection properties of the (310) planes of quartz have been investigated over the wave-length range 500 to 9 x.u. for the Laue or transmission case. The plates were inhomogeneously stressed by bending to a cylinder with a radius of 200 cm. The value of the integrated reflection coefficient was deduced from the luminosity properties of the curved-crystal spectrometer for seven different wave-lengths. The data indicate that the integrated reflection coefficient R_θ for a bent crystal varies as λ^2 over the range of wave-lengths studied. This behavior is in accord with that of a mosaic crystal. The reflection properties of the (310) planes of an unstressed crystal plate cut from the same sample were measured over the range 700 to 120 x.u. by the two-crystal spectrometer technique. These results indicate that the unstressed quartz plates behave more nearly as perfect crystals. Data are given on the integrated reflection coefficient, the peak value of Laue reflection coefficient, and the width at half-maximum of the diffraction curve for the unstressed case.

INTRODUCTION

DURING the development of the curved-crystal gamma-ray spectrometer,[1] it became apparent that a careful determination of the reflection properties of the (310) planes of the elastically curved-quartz plates used in the spectrometer would have to be made. At the same time, a thorough analysis of the intensity problem of the spectrometer was carried out. This analysis showed that the determination of the integrated Laue reflection coefficient of the curved crystal was possible from the experimental reflection properties.

While this determination is of particular interest for the design and operation of the curved-crystal spectrometer, it has additional importance because, in the past, other observers[2,3] have noted that the x-ray reflections from inhomogeneously stressed quartz plates show rather marked anomalies not present in unstressed or homogeneously stressed plates. Our experimental results confirm these qualitative observations but, in addition, we offer some quantitative data which may be useful for interpreting the observations.

THEORY

The theory of x-ray diffraction has been completely worked out for a great many conditions. From the character of the diffraction it is possible to deduce some information concerning the perfection of the lattice structure and the nature of its imperfections. A perfect lattice is one in which there exist no disorders of any kind in the atomic arrangement throughout the complete crystal. A mosaic structure, on the other hand, is one in which disorders do exist. It is convenient to describe a mosaic crystal as consisting of small domains each with perfect internal lattice structure which are more or less disarranged in the macroscopic crystal. The essential effect of the domain structure is to cause the scattering from separate domains to be incoherent. For the perfect crystals, two cases are of interest. A "thick" crystal is one for which the primary extinction distance is much smaller than the thickness of the crystal; a "thin" crystal is one for which the extinction distance is much greater than the thickness of the crystal. In a mosaic crystal, the situation is somewhat

* This work was supported by funds supplied through the joint cooperation of the ONR and AEC.

† Now with California Research Corporation, La Habra, California.

[1] J. W. M. DuMond, Rev. Sci. Inst. 18, 626 (1947).

[2] Y. Sakisaka and I. Sumato, Proc. Phys. Math. Soc. Japan III 13, 211 (1931).

[3] C. S. Barrett and C. E. Howe, Phys. Rev. 39, 889 (1932).

UNIVERSITY OF MICHIGAN LIBRARIES

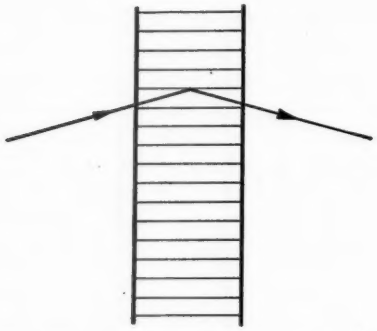

FIG. 1. This figure shows the orientation of the crystal planes and the incident and diffracted beams for the symmetrical Laue case.

more complicated because there are two types of extinction, primary and secondary. "Primary" refers to extinction in the individual mosaic units while "secondary" refers to the extinction which occurs in the macroscopic crystal. The "dynamical theory" of x-ray reflection has been developed first by Darwin[4] and later by Ewald[5] and von Laue.[6] The details of the scattering behavior of real crystals have been given by Zachariasen[7] who follows the developments of Ewald and of Von Laue. The cases which are of most interest for this work are: (1) Negligible primary extinction in the coherent domains and small secondary attenuation in the crystal plate, (2) large primary extinction but small secondary attenuation.

In the curved-crystal spectrometer used at short wave-lengths, only the Laue or transmission case is employed because it is possible thus to realize much greater luminosity than with the Bragg or reflection case. The results of the dynamical theory of x-ray reflection have been completely worked out for these cases.[4,5] It is of interest to examine the theoretical results to see what may be expected when the range of wave-lengths is extended down to wave-lengths of the order of 10 x.u., for at short wave-lengths the effects of much smaller lattice imperfections manifest themselves. The theory leads us to expect that such small lattice imperfections will be masked at longer wave-lengths where the diffraction pattern for an ideal crystal is broader than the angular disturbances in question.

In what follows, the (310) planes of the quartz crystal lay very nearly normal to the plane of the 1-mm thick crystalline slab (symmetrical Laue case), see Fig. 1. The discussion which follows refers therefore to the particular geometry which was employed, namely, that of the symmetrical Laue case exclusively.

[4] C. G. Darwin, Phil. Mag. **27**, 325 (1914); **27**, 675 (1914).
[5] P. P. Ewald, Ann. d. Physik **54**, 519 (1917); **54**, 577 (1917); Zeits. f. Physik **2**, 232 (1920); **30**, 1 (1924); Physik. Zeits. **26**, 29 (1925).
[6] M. von Laue, Ergeb. d. exakt. Naturwiss. Bd. X, 137–158 (1931); *Rontgenstrahl-interferenzen* (Akademische Verlagsgesellschaft, Leipzig, 1941).
[7] W. H. Zachariasen, *Theory of X-Ray Diffraction in Crystals* (John Wiley and Sons, Inc., New York, 1945).

The rigorous development of the dynamical theory of x-ray reflection tends to obscure rather than reveal the physical interpretation. We, therefore, here give a brief non-rigorous physical argument leading to the required results.

The Ewald construction (Fig. 2) of the propagation sphere inside the crystal lattice serves to determine the allowable propagation vectors. Except for the dispersion effects‡ the Bragg equation must be satisfied,

$$\mathbf{k}_H - \mathbf{k}_0 = 2\pi \mathbf{B}_H. \tag{1}$$

The Ewald construction is the graphical representation of Eq. (1). $\mathbf{k}_H$, $\mathbf{k}_0$ are propagation vectors outside the crystal for the diffracted and incident beams, respectively, and have identical magnitudes $2\pi/\lambda$; $\mathbf{B}_H$ is a vector of the reciprocal lattice with magnitude $1/d_H$ where d_H is the interplanar spacing for the (H) set of

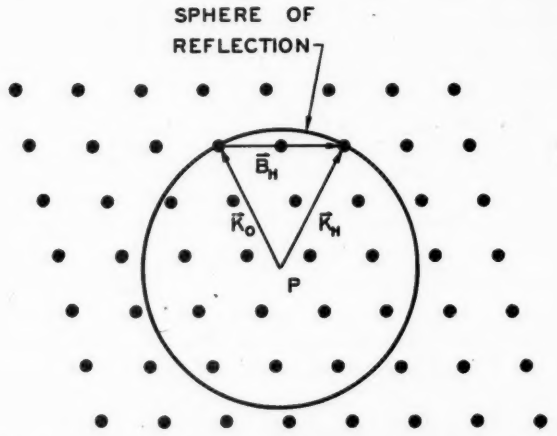

FIG. 2. Ewald's construction of the Bragg relation. The vectors connecting the lattice points of this figure constitute the family of reciprocal lattice vectors one of which $\mathbf{B}_H$ is shown. $\mathbf{K}_0$ and $\mathbf{K}_H$ are the propagation vectors for the incident and scattered radiations, respectively. Only those lattice points lying on or very near the propagation sphere will define the allowable propagation vectors.

planes. We shall only be concerned with the case where two propagation vectors are present.

In passage through the crystal the primary beam will suffer extinction until the diffracted beam contains most of the energy. Then, the roles of diffracted beam and incident beam become reversed. Actually, (see Fig. 3) there is a periodic exchange of energy between the two allowed beams; the periodicity in space will be closely related to the distance in the crystal medium which corresponds to an attenuation of the primary beam of the order of $1/e$. This attenuation will be here assumed to take place entirely by diffraction, absorption being neglected. The dynamical theory gives for this

‡ It can be shown that for the symmetrical Laue case when the incident and diffracted beams make equal angles with the crystal plate Eq. (1) for the determination of the center of the diffraction maximum is exact. λ is in this case the wave-length in vacuum, hence there is no correction for refractive index.

extinction distance the following result[8] under the assumption that for Laue

$$t_x=[2r_0(|F_H|/V)Kd_H\tan\theta_B]^{-1}, \qquad (2)$$

reflection the two propagation directions make equal angles with the face of the crystalline slab. K is the polarization factor, F_H the crystal structure factor,¶ V the volume of the unit cell and r_0 equals $e^2/(mc^2)$. The distance t_x is measured normal to the face of the slab. See Fig. 3. If it is measured instead in terms of the number of atomic reflecting planes effective for extinction, then

$$N_H=t_x\tan\theta_B/d_H \qquad (3)$$

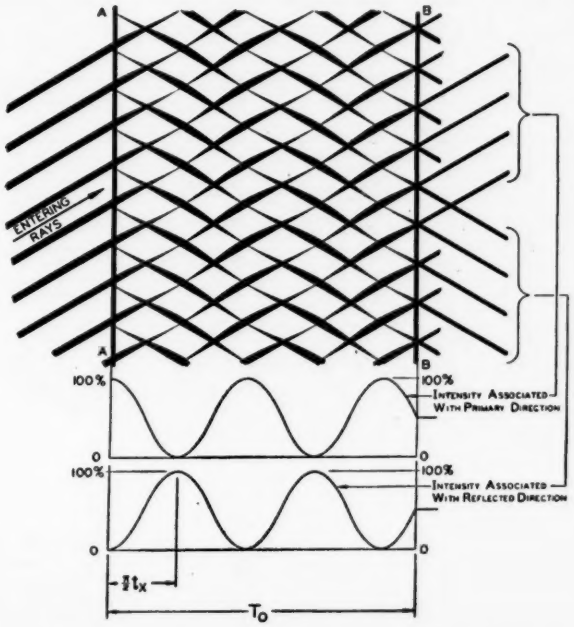

FIG. 3. The intensities of the two propagated beams are shown by the relative breadths of the corresponding rays. A periodic exchange of the energy from the one to the other beam takes place in the crystal. The distance which corresponds to a complete exchange of the energy from one beam to the other is $\pi/2t_x$. t_x is the extinction distance. Because of the surface irregularities, the two beams emerging will on the average each contain one-half the energy. For this reason, the emerging rays are shown with a breadth one-half the maximum.

[8] See reference 7, pp. 123–135.

¶ It might at first be thought that for the very short nuclear gamma-ray wave-lengths whose reflection coefficients are here measured, the coherent scattering would be completely negligible, and since only the coherent part of the scattered radiation can contribute to the selective diffraction by the crystal, one would be tempeted to expect no selective reflection whatever. The Compton shifted scattering is incoherent and plays no role in selective diffraction.

In order that coherent scattering shall occur, the final state of the atom after scattering must be the same as its initial state. The probability that an atom will scatter a photon and return to its initial state (coherent scattering) is a function only *of the change in momentum of the radiation* before and after scattering. So long as the scattering takes place at the Bragg angle, the change in momentum is constant independent of the wave-length. In calculating the structure factor F_H no account therefore need be taken of any variation with wave-length in the probability of coherent scattering. See A. H. Compton and S. K. Allison, *X-Rays in Theory and Experiment* (D. Van Nostrand Company, Inc., New York, 1935), pp. 252–253.

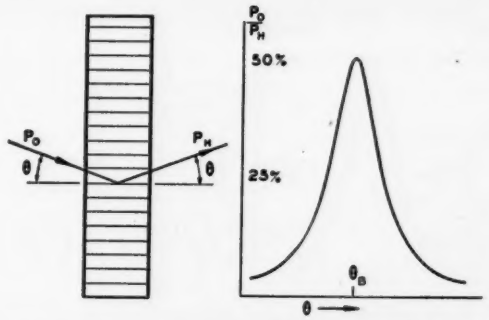

FIG. 4. This figure illustrates an idealized experiment to determine the reflection power of a crystal. P_0 and P_H represent the intensities, respectively, in the incident and diffracted beams. It is assumed that the radiation is *strictly* monochromatic and that the incident beam is a plane-parallel wave. The curve represents the fraction of the power which is diffracted as a function of the angle of incidence in the neighborhood of the Bragg angle θ_B. The equality of angles of incidence and diffraction is true only when the angle of incidence is θ_B in this Laue case.

so

$$N_H=[2r_0K(|F_H|/V)d_H^2]^{-1}. \qquad (4)$$

This is a good measure of the maximum number of planes which can at any setting contribute coherently to the scattered amplitude. It is well known that the resolving power $d\lambda/\lambda$ of a grating in the first order is proportional to $1/N$ where N is the total number of lines in the grating. In the case of a crystal grating, this relation is

$$d\lambda/\lambda=1/(\pi N_H). \qquad (5)$$

From the Bragg relation, we have $d\lambda/\lambda=d\vartheta/\tan\theta_B$ so $d\theta=\tan\theta_B/(\pi N_H)$. Set the width w of the diffraction pattern at half-maximum in radians equal to $d\theta$, then

$$w=2r_0K(|F_H|/V)d_H^2\tan\theta/\pi, \qquad (6)$$

$$w=r_0Kd_H(|F_H|/V)\lambda/(\pi\cos\theta_B). \qquad (6.1)$$

This is the same result which follows from the rigorous theory.

To define the "diffraction pattern," we must describe a somewhat idealized but not conceptually impossible experiment. Referring to Fig. 4, we think of a beam of extremely monochromatic and extremely parallel x-rays falling on a set of crystal planes at glancing angle θ. We then vary θ over a region of values in the neighborhood of the Bragg angle and we plot *the ratio of the power in the diffracted beam to the power in the incident beam* as a function of θ. The resulting curve exhibiting a maximum at say θ_B and falling rapidly on either side to very low values is called the "diffraction pattern." The words "extremely monochromatic" and "extremely parallel" used are to be interpreted as meaning that these qualities are pushed sufficiently far so that the effect of any residual inhomogeneity on the shape of the observed diffraction pattern becomes negligible. The diffraction pattern can be roughly characterized by giving its width at half-maximum height and the maximum value of the reflection coefficient at the peak of the

UNIVERSITY OF MICHIGAN LIBRARIES

TABLE I. Summary of results for the four cases of special interest.

Type		Integrated reflection coefficient (Laue case)	Half-width of diffraction pattern at half-maximum
Perfect	Thick	$\frac{r_0 d_H K(\lvert F_H\rvert/V)\lambda}{2\cos\theta_B}$	$\frac{r_0 d_H K(\lvert F_H\rvert/V)\lambda}{\pi\cos\theta_B}$
	Thin	$\frac{r_0^2 d_H K^2(\lvert F_H\rvert/V)^2\lambda^2 T_0}{(\cos\theta_B)^2}$	$\left(\frac{\ln 2}{\pi}\right)^{\frac{1}{2}}\frac{d_H}{T_0}$
Mosaic	Low primary and secondary extinction	$\frac{r_0^2 d_H K^2(\lvert F_H\rvert/V)^2\lambda^2 T_0}{(\cos\theta_B)^2}$	$(\ln 4)^{\frac{1}{2}}$
	Primary extinction present. Low secondary extinction	$\frac{r_0 K(\lvert F_H\rvert/V)\lambda T_0 d_H}{2\cos\theta_B t_0}$	$\eta(\ln 4)^{\frac{1}{2}}$

pattern. Another very important quantity derived from the diffraction pattern is the *total area under the curve*. This we shall call the integrated reflection coefficient. Since the ordinates of the diffraction pattern are pure numbers (reflection coefficients) and the abscissas are angles, it follows that the integrated reflection coefficient is an angle. It is generally and will here be expressed in radians. It is in fact the equivalent angular range over which at 100 percent efficiency the same total amount of reflection would occur. The diffraction pattern widths of many crystals of perfect type are so small (of the order of a second of arc or less) that in practice x-ray beams are seldom defined in direction (at least by means of slits) with comparable homogeneity. The integrated reflection coefficient therefore is a very important factor in determining the power which will be associated with an x-ray reflection since it essentially determines the usable solid angle into which an emitting atom in an x-ray source can shine in order to be selectively reflected by the crystal planes.

If P_0 and P_H are intensities in the incident and diffracted plane parallel beams, respectively, then the integrated reflection coefficient is defined by

$$R_\theta=\int_{-\infty}^{\infty}[P_H(\theta-\theta_B)/P_0]d\theta. \tag{7}$$

Ewald's theory shows that for symmetrical Laue reflection in an ideally perfect crystal lattice, the shape of the diffraction pattern is that of a "witch" or resonance curve if the slab is sufficiently thick to include a large number of the intensity oscillations illustrated in Fig. 3. Since the distance t_x corresponding to the "wavelength" of one such oscillation is in most cases extremely small in comparison to the thickness of the slab, T_0, the assumption usually made is that the diffracted beam in different parts of the exit surface emerges *in all different phases* of the intensity oscillation. Therefore, for the case of a thick slab, the observed intensity is taken (by averaging uniformly over all phases) to be *half* the value occurring at the maximum intensity of the oscillations. These considerations show that for a thick crystal the maximum of the diffraction pattern will be a constant, $\frac{1}{2}$, independent of λ. For this case, only the width w will therefore depend on λ. The integrated reflection coefficient for the Laue case is:

$$R_\theta=\tfrac{1}{2}\pi w=r_0 K d_H(\lvert F_H\rvert/V)\lambda/2\cos\theta. \tag{7.1}$$

This is the value given in Table I.

The distinction between "thick" and "thin" crystals can only be made in terms of the extintion distance t_x. A thin crystal is one whose thickness T_0 is much less than t_x. In this case, the number of scattering planes is given by

$$N_H=T_0\tan\theta/d_H. \tag{8}$$

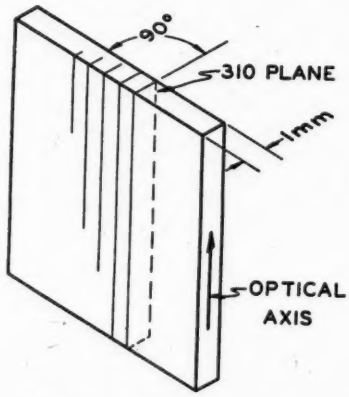

FIG. 5. The (310) lattice planes of quartz lie so that they are parallel to the edge of the crystal wafer and normal to the major faces of the wafer. The crystal was bent elastically so that the "c" or optic axis, and therefore the (310) planes, lay parallel to the generators of a right circular cylinder.

Again $d\lambda/\lambda$ is proportional to $1/N_H$ so

$$d\lambda/\lambda=kd_H/(T_0\tan\theta),$$

where k is a proportionality constant of order one-half, from which it follows that the width of the diffraction pattern w is given by

$$w=kd_H/T_0. \tag{9}$$

The theory predicts $k=(\pi^{-1}\ln 2)^{\frac{1}{2}}$. The angular width of the diffraction pattern is now independent of the wave-length. The intensity diffracted by the crystal is proportional to the square of the diffracted amplitude. The amplitude will be given by

$$r_0 K(\lvert F_H\rvert/V)\lambda T_0/\cos\theta_B.$$

The integrated reflection coefficient will then be proportional to the square of the amplitude and to the diffraction pattern width. That is,

$$R_\theta\propto[r_0 K(\lvert F_H\rvert/V)\lambda T_0/\cos\theta_B]^2 d_H/T_0.$$

The dynamical theory predicts the integrated reflection

coefficient to be

$$R_\theta = r_0^2 d_H K^2 (|F_H|/V)^2 \lambda^2 T_0 / \cos^2\theta_B. \quad (10)$$

Thus, our simple considerations lead to the same result as the more rigorous theory. The conditions in a mosaic crystal can be understood in terms of these two results (7.1) and (10) for a perfect crystal. If the mosaic units are perfect and of such size that the primary extinction is small, then each unit will scatter an intensity proportional to

$$[r_0 K (|F_H|/V) \lambda t_0 / \cos\theta_B]^2,$$

where t_0 is an appropriate mosaic unit dimension. The integrated reflected intensity per mosaic unit will be

$$R_\theta' = r_0^2 K^2 (|F_H|/V)^2 \lambda^2 d_H t_0 / \cos^2\theta. \quad (11)$$

Now the further assumption is made that in every layer of crystal dx there exists a distribution function for the orientation of these individual units in that layer. The number of mosaic units in the layer dx will be proportional to dx/t_0. The angular orientations of the blocks are assumed to be distributed about a mean orientation as given by

$$w(\Delta) = (2\pi\eta)^{-\frac{1}{2}} \exp(-\Delta^2/2\eta^2), \quad (12)$$

where Δ is the deviation from the mean and η is the distribution parameter. Hence, the total integrated reflected intensity from the layer dx will be given by

$$r_0^2 K^2 (|F_H|/V)^2 \lambda^2 d_H dx / \cos^2\theta_B, \quad (13)$$

provided we explore a sufficient angular breadth to accommodate all the orientations covered under (12). Thus, the intensity reflected by the crystal will be

$$R_\theta = r_0^2 K^2 (|F_H|/V)^2 \lambda^2 d_H T_0 / \cos^2\theta_B. \quad (14)$$

The width of the diffraction pattern will be given by $\eta(\ln 4)^{\frac{1}{2}}$ provided the diffraction width for the individual units, $(\pi^{-1} \ln 2)^{\frac{1}{2}} d_H/t_0$ is less than $\eta(\ln 4)^{\frac{1}{2}}$. The integrated reflection coefficient as written assumes that secondary attenuation, as well, is negligible. The expression for the case of large primary extinction but small secondary attenuation follows by similar arguments. Since the primary extinction is large, one may substitute the expression (7.1) for Eq. (11) in the development just preceding.

The results for the four cases of special interest are tabulated in Table I. It is recognized that the interpretation of the experimental results for the curved crystal by the formulas derived for an unstressed crystal may not be valid but the comparison will be useful toward understanding the phenomena.

The method of the curved-crystal spectrometer described in this paper *permits only measurements of R_θ, the integrated reflection coefficient*, but unfortunately *does not afford any means with our present facilities of estimating t_0 the size of the domains* in the crystal over which coherent reflection can take place. Reference to formula (14) shows that R_θ is independent of t_0. A study of the structure of the undoubtedly very narrow intrinsic diffraction pattern of the quartz lattice is at present beyond the reach of even the very high resolving power attained in our two-meter curved-crystal instrument. We have in fact no clear-cut experimental evidence that any mosaic structure exists at all in elastically bent quartz save that to date this assumption is the only one we have found to explain the observed fact that for such quartz R_θ is proportional to λ^2 over the wide range of wave-lengths we have covered. Unstressed quartz, on the other hand, for which R_θ is more nearly proportional to λ, turns out to behave more nearly like an ideally perfect lattice over the limited range of wavelengths with which we have been able to study it by the two-crystal spectrometer method. Our reason therefore for presenting here brief accounts of the results of the dynamical theories of x-ray reflection for both ideally perfect and mosaic crystals is merely to permit a comparison of these with our observed results. We make no claim that any such theories satisfactorily fit the observed facts.

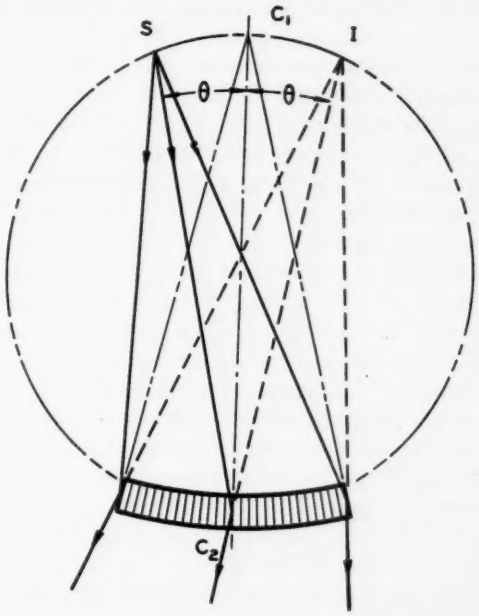

FIG. 6. The fundamental geometry of the curved-crystal focusing spectrometer used in transmission is shown. The crystal lamina is bent to a radius equal to the diameter of the focal circle. S represents the source position, C, the intersection of the atomic planes on the focal circle, and I the virtual source of the radiation after diffraction by the lattice. The neutral axis of the bent crystal is tangent to the focal circle at C_2. This geometry is not exact because the neutral axis should coincide with the focal circle over the whole crystal.

EXPERIMENTAL TECHNIQUE

Entirely different experimental methods were used for measuring the integrated reflection coefficients for the stressed and unstressed quartz plates. The quartz crystals used in this investigation were cut so that the (310) planes lay parallel to one edge and normal to the plane of the plate (Fig. 5). These are the same crystals which are used in the gamma-ray spectrometer de-

UNIVERSITY OF MICHIGAN LIBRARIES

scribed by DuMond.[1] The plates were polished to an optically flat finish on the major faces. When used in the curved-crystal spectrometer, the crystal plate is bent elastically so that it has with extremely high accuracy the shape of a right circular cylinder with a radius of approximately two meters. This bending is accomplished by clamping the crystal between two blocks of stainless steel provided with holes for the passage of the radiation.

The vise-like jaws so formed are cylindrically profiled, one convex, the other concave, with a radius of curvature of two-meters. Only the convex surface is profiled to high precision, the crystal being held in intimate contact with it by means of a rubber cushion placed between the crystal and the concave vise jaw.

Figure 6 shows the essential geometry of the focusing curved-crystal spectrometer. The crystal shown at C_2 is elastically deformed so that the crystal planes intersect at the point C_1. Since the point S lies on the circle through C_1 and C_2 having C_1C_2 as a diameter, all rays leaving S and striking the crystal will make the same angle with the atomic planes. In order to have exact focusing, it is necessary that the crystal lamina lie on the focal circle. This condition is not exactly satisfied in the present spectrometer but the aberrations introduced by failure to meet the condition are entirely negligible. The diffracted rays will appear to come from the virtual source I. It is readily seen that this arrangement affords a tremendous gain in luminosity over the usual flat-crystal spectrometer. The aperture angle available to the source is just the angle which the crystal subtends at the source.

Figure 7 shows schematically just enough of the essential elements of the instrument to clarify the method of measuring reflection coefficients with it. In the gamma-ray case, the source at S consists of a thin strip of neutron-activated material while in the x-ray case a thin metal strip at the same point is exposed (from the side) to primary x-radiation which causes it to emit its characteristic fluorescent x-radiation. This radiation emerges from the radiator surface at a small grazing angle and passes to the curved crystal at C_2. Here the radiation, diffracted at the Bragg angle θ on the crystal planes, is deviated through an angle 2θ and emerges as a divergent beam with the image point I as its virtual source. It then passes through the diverging collimator whose function is to arrest the strong direct radiation from S transmitted without deviation through the crystal. By mechanical means not here shown, both S and C_2 are moved so as to explore the spectrum but maintain the diffracted beam always strictly aligned with the collimator. The intensity of the diffracted beam is then measured in a special "multicellular" Geiger counter.[9] As S approaches I a point P determined by the collimator geometry will be reached at which the directly transmitted beam will start to leak through the collimator channels to the counter. Beyond this point, the spectrometer cannot be used as such. However, by setting the source S exactly at I, a good measure of the intensity of the entire direct undiffracted beam can be made and this is very useful in the determination of reflection coefficients. Such a direct measurement is so many thousands of times stronger than the reflected beam that it is necessary to attenuate the direct beam with a series of absorbing plates or foils. The true unabsorbed intensity of the line radiation in question can then be obtained by extrapolating on a semilogarithmic absorption plot back to the counting rate for zero absorber.

It would be a mistake, however, to suppose that the ratio of direct to diffracted intensities observed in the way roughly indicated can be taken directly as the

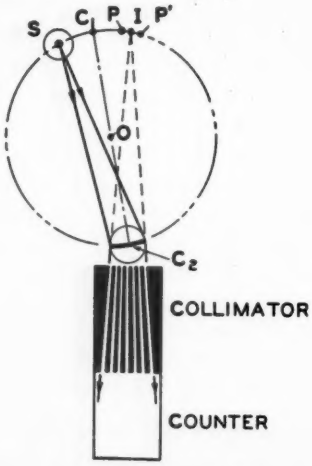

FIG. 7. The essential elements of the curved-crystal focusing spectrometer as used for the study of the reflection properties of the (310) planes of quartz. The source is placed on the focal circle at S, and the radiation diffracted by the crystal appears to come from the point I. The collimator only serves to prevent the directly transmitted beam from detection by the counter placed behind the collimator. PP' is the arc inside of which the source S can radiate directly through the collimator into the counter.

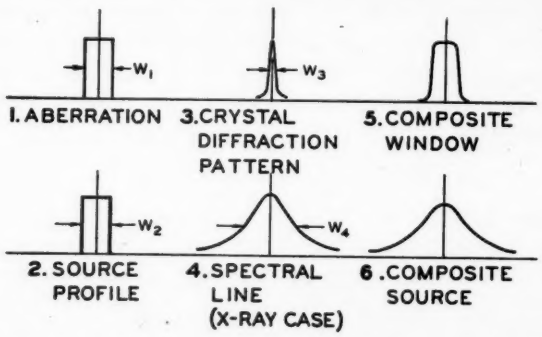

FIG. 8. This figure shows the form of the four profiles which determine the nature of the experimentally observed line profile in the curved-crystal spectrometer, (1) the assumed focal aberration of the curved crystal, (2) the finite source size, (3) the intrinsic diffraction pattern of the crystal, and (4) the spectral distribution of the x-ray or gamma-ray line. The composite window 5, (fold of 1 and 3) may be considered the tool which is used to explore the composite source 6, fold of (2 and 4).

[9] D. A. Lind, Rev. Sci. Inst. 20, 233 (1949).

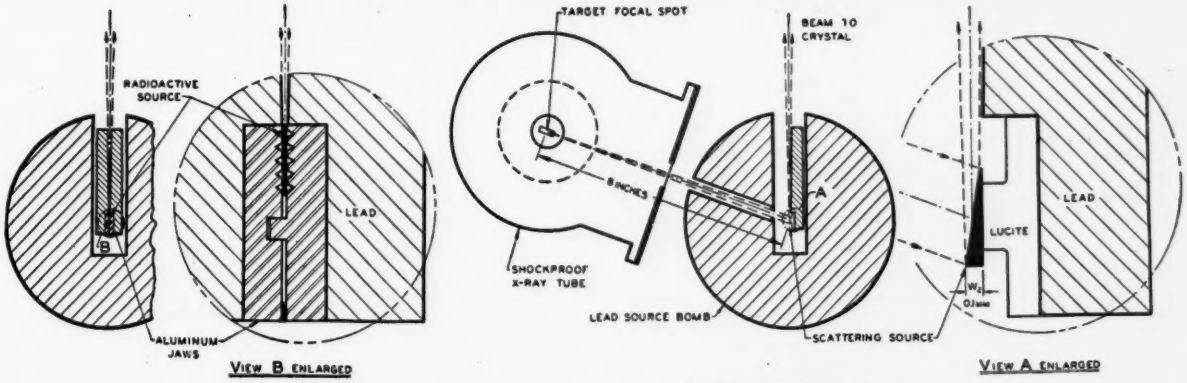

FIG. 9. Source geometry for x-ray and nuclear gamma-radiation sources. The x-ray source is a piece of metal foil ground to the shape of a thin wedge and placed at the center of the lead source bomb. This foil is irradiated with the continuous radiation from a tungsten target x-ray tube at the left. The nuclear gamma-sources are metal foils activated by neutron bombardment. These foils are clamped between the aluminum jaws of the holder to define the source geometry accurately. The surrounding lead defines the angular divergence of the beam so that it will just fill the crystal aperture. This source assembly is mounted in the lead source bomb in place of the x-ray scattering source holder.

reflection coefficient. A number of instrumental factors in addition to the reflection properties of the crystal determine this observed ratio as follows:

(1) The bending of the crystal in the profiled vise never succeeds in focusing the atomic planes with absolute perfection at C_1. Instead a small aberration pattern of finite width w_1 in the focal circle is formed. (2) The source is not an infinitesimal line but has also a finite width w_2 on the focal circle. Furthermore, (3) the intrinsic diffraction pattern of the crystal, as we have already pointed out, has an angular width w which may be translated into linear measure w_3 on the focal circle, and finally (4) the spectral line under study has a natural spectral width $\delta\lambda$ which may also be translated into linear units giving a width w_4 on the focal circle. Figure 8 gives an idea of the shapes of these different patterns. The "shape" of an observed spectral line is then explored with the spectrometer by plotting the counting rate for successive closely spaced positions of the source S on the focal circle relative to the crystal C. Actually, this process can be thought of as a superposition of all four of the above patterns. Patterns (1) and (3) associated with the crystal can be thought of as folded together to form a composite exploring "tool" or "window" (pattern 5 in Fig. 8) while patterns (2) and (4) are folded together to form a composite source profile (pattern 6 in Fig. 8). As this tool explores across the source profile, the maximum intensity will be observed when the product integral of the two composite profiles has its maximum value, i.e., at the point where all four separate profiles overlap most advantageously. Clearly then, the modus of this overlapping is of great importance in determining the observed intensity whereas R_θ the integrated reflection coefficient which we seek to measure depends on only one of the four patterns.

By an analysis of the four pattern shapes, one of us[10] has derived formulas which permit the calculation of R_θ the integrated reflection coefficient of the crystal from a quantity Γ_λ which is easy to obtain from the direct observations and which has the following definition. Γ_λ is the ratio of two quantities, in the numerator, (1) the peak line intensity (counting rate), $R_A(0)$, observed in the diffracted beam as the spectrometer explores across a given spectral line of wave-length λ with the source in position S (Fig. 7) and (2) in the denominator that fraction, γ_λ, of the peak primary intensity (counting rate), R_D, which is associated with the same line λ and which is observed in the divergent direct beam transmitted through the crystal with the source in position I (Fig. 7). The spectral composition of the entire measured radiation in the direct neam must, of course, be known in order to determine the fraction γ_λ associated with the line λ. The formula for Γ_λ as defined above is then

$$\Gamma_\lambda = R_A(0)/(\gamma_\lambda R_D). \tag{15}$$

In order to compute R_θ from Γ_λ, the following reasonable assumptions were made regarding the four profiles of Fig. 8. (1) The linear extension w_1 of the focal aberration pattern and the width w_2 of the source on the focal circle are approximately equal and they are large compared to the width w_3 of the intrinsic crystal diffraction pattern. The focal aberration pattern was carefully studied by observing with the spectrometer the exact positions of the centers of line-profiles formed by utilizing different portions of the curved crystal (isolated with a stop), a method analogous to the Hartmann test in optics. This aberration pattern had a width** $w_1 = 0.1$ mm on the focal circle. The widths, w_2, of the sources were purposely made as nearly as possible

[10] D. A. Lind, thesis, California Institute of Technology (1948).

** By improvements in the crystal clamp profiling, we have subsequently succeeded in reducing w_1 to 0.05 mm.

UNIVERSITY OF MICHIGAN LIBRARIES

TABLE II. Table of data and derived results from R_θ.

Line	λ x.u.	E Mev	Γ_i[a]	Γ_i/R_θ from theory	R_θ x.u.[b]	R_θ radians
Sn $K\alpha_1$	489.57	0.0253	0.175 ± 0.023	2.27	7.70×10^{-2}	$(3.28\pm0.43)\times10^{-5}$
Ta $K\alpha_1$	214.88	0.0506	0.050 ± 0.002	3.20	1.56×10^{-2}	$(6.63\pm0.27)\times10^{-6}$
Au $K\alpha_1$	179.96	0.0688	0.044 ± 0.004	3.39	1.30×10^{-2}	$(5.52\pm0.50)\times10^{-6}$
Th $K\alpha_1$	132.3	0.0936	0.017 ± 0.004	3.62	4.69×10^{-3}	$(1.99\pm0.47)\times10^{-6}$
Au^{198}	30.09	0.411	0.0030 ± 0.0001	8.33	3.60×10^{-4}	$(1.53\pm0.05)\times10^{-7}$
Co^{60}	10.578	1.172	$(4.97\pm0.50)\times10^{-4}$	8.33	5.97×10^{-5}	$(2.54\pm0.25)\times10^{-8}$
	9.308	1.332	$(4.12\pm0.50)\times10^{-4}$	8.33	4.95×10^{-5}	$(2.11\pm0.25)\times10^{-8}$

[a] Γ_i is the ratio of the peak counting rate at the line to the counting rate in the incident beam, and hence, represents the fraction of incident quanta which is selectively diffracted at the maximum of the line profile. Γ_i is not a constant of the crystal but depends on instrumental factors as well.
[b] In this column the angle R_θ which is usually expressed in radians is instead expressed in x units.

equal to the aberration width w_1. (2) The wave-length distribution (spectral line profile) of the line of wave-length λ under observation must be assumed to be known. In the x-ray cases, the spectral profiles can safely be assumed to be "witches" and the widths can be found from previous two-crystal spectrometer data. In the gamma-ray cases, there are good reasons for believing that the spectral line widths w_4 used in these observations are far too narrow for detection, a condition which simplifies the calculations of R_θ from Γ_λ. For brevity, most of these calculations and the derivations of the formulas on which they are based are here omitted. As an example, however, take the gamma-ray case of a line of negligible spectral width w_4.

If one focuses attention on an infinitesimal areal element of the crystal and asks what fraction of the source will radiate quanta which will pass through this element so as to make angles of incidence with the (310) planes lying within the crystal diffraction pattern, one will see that this fraction is proportional to $R_\theta D_f/l$, where R_θ is the integrated reflection coefficient, D_f the focal circle diameter and $l=w_1=w_4$ is the linear extension of the source (and also the focal aberration) at the focal circle. This follows because $R_\theta D_f$ is the width on the focal circle of that part of the source from which radiation can be selectively diffracted by any given element of crystal. This is just the result which is derived from a more general and exact analysis. By a similar analysis any case can be reduced to give an expression for Γ_λ in terms of R_θ provided the above-stated assumptions are fulfilled.

To make a reliable determination of Γ_λ, a source of known spectral composition is needed so that γ_λ shall be known. In the x-ray region, the fluorescent K radiation from an element of high atomic number is satisfactory since the continuous background from Compton scattering can be kept very small. Figure 9 shows a schematic drawing of the source arrangement. The x-ray tube excites in the scatterer its characteristic fluorescent radiation as well as Compton-scattered radiation. However, very little of the Compton scattering is directed toward the crystal because the scattering angle is about 110° and the atomic number is high. Nevertheless, to eliminate all question as to the effect of continuous scattered background, a procedure utilizing the Ross method of "balanced filters"[11] was employed. By this procedure, the direct beam was observed with a pair of filters which were designed so that their K edges bracketed the line under study. The *difference* between these readings then represented the sum of the fluorescent radiation *plus only the Compton scattering which lay in the small wave-length interval bracketed by the filters*. At the same time, the peak reading at the line was also made with the same transmission filters.

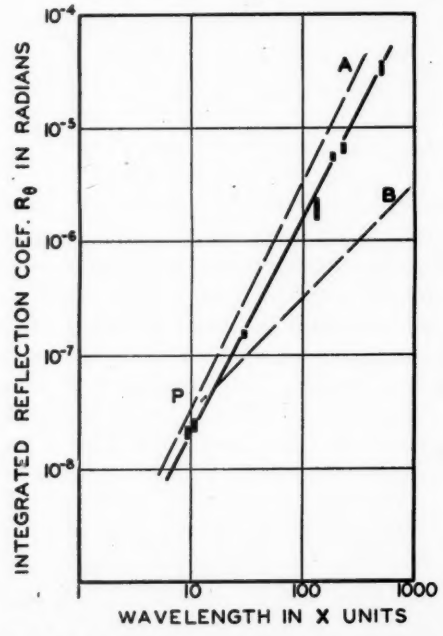

FIG. 10. Reflection properties of elastically curved-quartz plate. The full line is a plot of the measured integrated reflection coefficient R_θ for the (310) planes of quartz in the Laue or transmission case as a function of the wave-length λ. The ordinate scale is in radians and the abscissa scale is in x.u. The experimental points are shown with their probable errors (vertical heights of the rectangles). (The probable error of the wave-length is completely negligible on this plot.) Curve A represents the theoretical behavior of a similar quartz plate if the crystal behaved as a mosaic with small primary and secondary extinction. The curve B represents its behavior if it were perfect. In the region of the intersection P of the curves A and B, the primary extinction distance is of the same order as the plate thickness. Below this point, curve B should coincide with curve A.

[11] P. A. Ross, J. Opt. Soc. Am. and Rev. Sci. Inst. **16**, 433 (1928); P. Kirkpatrick, Rev. Sci. Inst. **10**, 186 (1939).

The actual source mounted in the spectrometer was the scattering foil. See Fig. 9. This was prepared of pure metal foil 0.004 in. thick by grinding to the shape of a thin wedge. Foils of Sn, Ta, Au, and Th were used. Great care was taken to make the sources identical in projected geometrical width w_2 as seen by the curved crystal. This required mounting them so that their projected width on the focal circle was 0.1 mm and no more. The width of 0.1 mm represented also the linear extent of the focal aberration of the curved crystal at the focal circle. The foils were mounted on a Lucite support by means of stopcock grease which was sufficiently tacky to hold them, yet did not dry and distort their shape. The x-ray tube was mounted so that the target-source distance remained always at 8 in. Preliminary calculations had shown that a tungsten tube operating at 150 kvp and 10 ma would generate sufficient fluorescent radiation for these measurements, thanks to the high luminosity of the curved-crystal instrument with the source at the focus.

The peak intensity in the diffracted $K\alpha_1$ line from each source and the intensity of the incident beam were measured with the Ross filters. In the case of thorium $K\alpha_1$, no filter was available but an extrapolation of the corrections to the measurements at gold showed this correction for Compton-scattered continuous radiation to be negligible. The relative intensities of the lines of the K spectra have been measured.[12] From these data it is possible to determine the factor γ_λ in Eq. (15).

In the determination of the values of Γ_λ for the nuclear gamma-radiations[13,14] from Au^{198} and Co^{60}, the only difference from the x-ray measurements was that in each case the source was a piece of a pure activated metal foil mounted as shown at B in Fig. 9. The foil was 5 mm wide by 30 mm long by 0.1 mm thick and was activated by neutron bombardment at Oak Ridge. It was necessary in these cases to know the decay scheme so that the values of γ_λ could be evaluated. In gold, only the 0.41-Mev gamma-line was assumed to be present while in cobalt it was assumed that the 1.17- and 1.33-Mev lines were in cascade.†† In every case the data were corrected for background counting rate.

In the gamma-ray cases, lead defining jaws were used to limit the angular dimensions of the beam transmitted from the source to the crystal. The width w_2 of the source on the focal circle was however determined by the thickness of the source foil itself.

The experimental determinations of Γ_λ were reduced to R_θ by the expressions relating Γ_λ and R_θ which are found by Lind.[10] They take slightly different forms for the x-ray and gamma-ray lines because the inherent spectral line widths are different for the two cases. The spectral line widths for the $K\alpha_1$ lines of tungsten and silver were taken from Compton and Allison.[15] By linear interpolation, the values for the other elements were obtained. The line widths for the nuclear gamma-lines were assumed to be very much smaller than any other factors contributing to the diffracted line profile; hence, it was not necessary to know these values. Table II contains the data which were obtained, together with the derived results for R_θ.

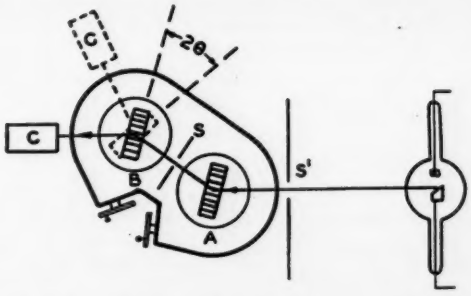

FIG. 11. Schematic illustration of the two-crystal x-ray spectrometer employing the (310) planes (transmission or Laue case) of two identical quartz plates, 1 mm thick. The full lines show the general position for the parallel rocking curve. The dotted lines show the position for the antiparallel rocking curve. The slits or stops are at S and S'. The xenon-filled counter is at C.

INTERPRETATION OF THE EXPERIMENTAL RESULTS

Table II shows the experimental results on the measurement of Γ_i and their reduction to R_θ. In Fig. 10 is shown the plot of the resulting data. The slope of the curve of R_θ *versus* λ on a logarithmic plot is slightly less than two. However, the discrepancy when compared with the curve of slope 2 is not outside deviations which might be accounted for by experimental errors. The probable errors which are shown *represent only the statistical errors in the observed data.* It must be pointed out that there are a number of other factors which could influence the exact value of R_θ. The presence of scattering from certain parts of the instrument when the intensity of the direct beam was measured would have the effect of depressing the curve more at short wave-lengths than at long wave-lengths. The assumptions involved in the reduction of the experimental value Γ_λ to R_θ introduce, perhaps, the largest uncertainties. It is believed that the additional uncertainty introduced by all such factors would probably not exceed plus or minus 25 percent. On the logarithmic scales shown, this would not greatly modify the data.

A calculation of the theoretical value of R_θ for the (310) planes of quartz is made as follows. From Table I the value of R_θ for a mosaic-like crystal is

$$R_\theta = r_0^2(|F_H|/V)^2K^2\lambda^2 d_H T_0/(\cos\theta_B)^2. \qquad (14)$$

Because the radiation is unpolarized, the value $\langle K^2\rangle_{Av}=\frac{1}{2}(1+\cos^2 2\theta_B)$ is substituted for K^2.

[12] Compton and Allison, see reference ¶, pp. 638–641.
[13] DuMond, Lind, and Watson, Phys. Rev. **73**, 1392 (1948).
[14] Lind, Brown, and DuMond, Phys. Rev. **76**, 1838 (1949).
†† Direct measurements on Co^{60} with this instrument have confirmed the equality of intensity of the two lines.

[15] Compton and Allison, see reference ¶, pp. 745–746.

TABLE III. Observations on the transmission diffraction patterns from the (310) planes of quartz. The factor $\exp[\mu_0 t_0/\gamma_0]$ corrects the specified data for the absorption of the beam in the crystal plate since the crystals are used in transmission throughout.

(A)	$R\exp[\mu_0 t_0/\gamma_0]\times10^6$ (radians)			$P(0)\exp[\mu_0 t_0/\gamma_0]$			W_θ (seconds of arc)		
	Obs.		Calc.	Obs.		Calc.	Obs.		Calc.
	(310)	$(\bar{3}\bar{1}0)$	(310) or $(\bar{3}\bar{1}0)$	(310)	$(\bar{3}\bar{1}0)$	(310) or $(\bar{3}\bar{1}0)$	(310)	$(\bar{3}\bar{1}0)$	(310) or $(\bar{3}\bar{1}0)$
0.710±0.0020[a]	2.58	2.77	2.30	0.172	0.161	0.246	1.1	1.3	0.53
0.530±0.0074[a]	2.02	2.12	1.65	0.134	0.136	0.250	1.2	1.2	0.42
0.320±0.0076[a]	1.50	1.51	1.00	0.116	0.111	0.250	1.1	1.0	0.26
0.210±0.002[b]	1.30	1.63	0.657	0.123	0.128	0.250	0.73	0.92	0.17
0.123±0.0084[b]	0.89	1.04	0.389	0.115	0.890	0.250	0.54	0.88	0.10

[a] Molybdenum tube used for the x-ray source.
[b] Tungsten tube used for the x-ray source.

The maximum value of θ_B is about 12° so, one may set $\langle K^2\rangle_{Av}/\cos^2\theta_B=1$ with an error of 10 percent or less. Hence,

$$R_\theta\cong r_0^2(|F_H|/V)^2\lambda^2 d_H T_0.$$

Substituting the following data:

$$T_0=1\text{ mm},\quad d_{310}=1.178\text{A},\quad |F_{310}|=21.0,$$
$$V=112\text{A}^3,\quad r_0=2.82\times10^{-5}\text{A},$$

hence, we obtain the result

$$R_\theta=3.29\times10^{-4}\lambda^2.$$

R_θ is in radians and λ in A. This result is graphically plotted as curve A in Fig. 10 for comparison with the experimental results. The corresponding formula for a perfect thick crystal is

$$R_\theta=r_0(|F_H|/V)K\lambda d_H/(2\cos\theta_B). \qquad (7.1)$$

Again set

$$\langle K\rangle_{Av}/\cos\theta_B=1,$$

we obtain for the result

$$R_\theta\cong3.14\times10^{-6}\lambda.$$

This is plotted as curve B in Fig. 10.

It should be noted that for the range of λ for which $T_0<t_x$, i.e., for which the primary extinction distance is greater than the thickness of the plate, the "perfect" crystal behaves as would the "mosaic" as far as integrated reflection is concerned. It is interesting to note that for every thickness of crystal, the mosaic crystal will have the *higher reflection coefficient* until the perfect crystal no longer may be considered thick. The numerical agreement of the observed results with the "mosaic model" (curve A, Fig. 10) is quite good considering the nature of these measurements. The mosaic-like behavior of the stressed- (curved-) quartz plates was a source of some surprise. There is no reason to think that bending the quartz plate introduces any *permanent* irreversible disorder in the structure since the crystalline quartz behaves perhaps more nearly perfectly elastically than any other known substance.

These results prompted one of us (W.J.W.) to carry out determinations of the integrated reflection coefficients and diffraction pattern widths over a part of the same range of wave-lengths for the (310) planes of identical *unstressed* quartz crystals.

MEASUREMENTS OF THE REFLECTION PROPERTIES OF UNSTRESSED-QUARTZ PLATES

The two-crystal spectrometer designed by DuMond[16] was used to measure the reflection properties of the (310) planes of unstressed quartz over a wave-length range from 0.123 to 0.707A. The great flexibility of this high precision instrument afforded by its four separate worm-wheel adjustments permitted the easy realization of many of the requisite conditions which would have been made much more difficult or impossible with other less flexible designs. The two-crystal method has been adequately described.[17] It is well known that the "parallel" position curves give information concerning the crystal properties independent of the spectral distribution of the radiation. Figure 11 shows the two-crystal arrangement. The usual procedure is to set the crystal A so that a wave-length λ is reflected through the slit S to the crystal B. The crystal B is rocked about the position of parallelism with crystal A and the intensity as detected by the counter C is plotted as a function of the angle. Since this arrangement allows all wave-lengths to be transmitted, the wave-length band which is used is controlled by the slit system at S^1 which limits the horizontal (and also the vertical) angular divergence of the beam incident on crystal A. It can be shown that the power received by the detector, as crystal B is rotated through small angles, is a function only of the properties of the crystals and not of the spectral distribution or the geometry of the slit system.

The quantities which one can obtain are the integrated reflection coefficient R_θ, the half-value width of the diffraction curve and the peak Laue reflection of the crystal planes. (Peak value of the diffraction pattern of Fig. 4.) If a plane-parallel beam of monochromatic radiation falls on the crystal, the ratio of the intensity in the diffracted beam to that in the incident beam will be the ordinate of the diffraction pattern of Fig. 4 or the reflection factor. It is the maximum ordinate of this function and its half-maximum width which one can

[16] J. W. M. DuMond and D. Marlow, Rev. Sci. Inst. 8, 112 (1937).
[17] See reference 7, pp. 147–155.

measure. It has been shown that it is impossible however to obtain the *shape* of the diffraction profile from the parallel position rocking curve. The two-crystal spectrometer results cannot be reduced so as to give exactly these quantities, unless it can be proved by some other means that the diffraction pattern sought *is symmetrically distributed about a central point.* The usual procedure is to observe the ratio of the total power reflected by the internal planes of crystal B to the power incident upon it. If this quantity is designated by $P(\beta)$, the *two-crystal integrated reflection coefficient is* defined by

$$R'=\int_{-\infty}^{\infty}P(\beta)d\beta. \tag{16}$$

where β is the angle by which the atomic planes of crystal B deviate from parallelism with those of A. Equation (16) is analogous to the definition for R_θ, the integrated reflection coefficient for a single crystal. It can be shown that

$$R'=\frac{[^pR_\theta]^2+[^nR_\theta]^2}{^pR_\theta+{}^nR_\theta} \tag{17}$$

in the case that the incident radiation may be considered unpolarized. The superscripts p and n refer to the orientation of the plane of polarization of the incident radiation, p refers to the electron vector parallel to the plane of scattering and n, normal to said plane. If other absorption processes are present as well as anomalous dispersion, then

$$\exp[\mu_0 l_0/\gamma_0]R'=\left[\frac{1+\cos^2 2\theta_B+2l_0^2(1+\cos^4 2\theta_B)}{1+\cos 2\theta_B+l_0^2(1+\cos^3 2\theta_B)}\right]. \tag{18}$$

The terms in l_0 occur because of anomalous dispersion and are important only at wave-lengths in excess of about 400 x.u. The term $\exp[\mu_0 l_0/\gamma_0]$ is an attenuation factor. μ_0 is the total absorption coefficient while l_0/γ_0 is the true path length in the crystal. γ_0 is the cosine of the angle of incidence measured with the normal to the crystal plate.

W_θ, the half-maximum width of the two-crystal rocking profile, is given by

$$W_\theta=2w_\theta. \tag{19}$$

w_θ is the half-maximum width of the single crystal Laue diffraction pattern.‡‡ Finally, the peak transmission $P(0)$ is given by

$$P(0)\exp[\mu_0 l_0/\gamma_0]=\frac{1}{4}\left[\frac{1+\cos 2\theta_B+(3/4)l_0^2(1+\cos^3 2\theta_B)}{1+\cos 2\theta_B+l_0^2(1+\cos^3 2\theta_B)}\right]. \tag{20}$$

It must be noted that if unpolarized radiation is used, it is impossible from the two-crystal rocking curves to

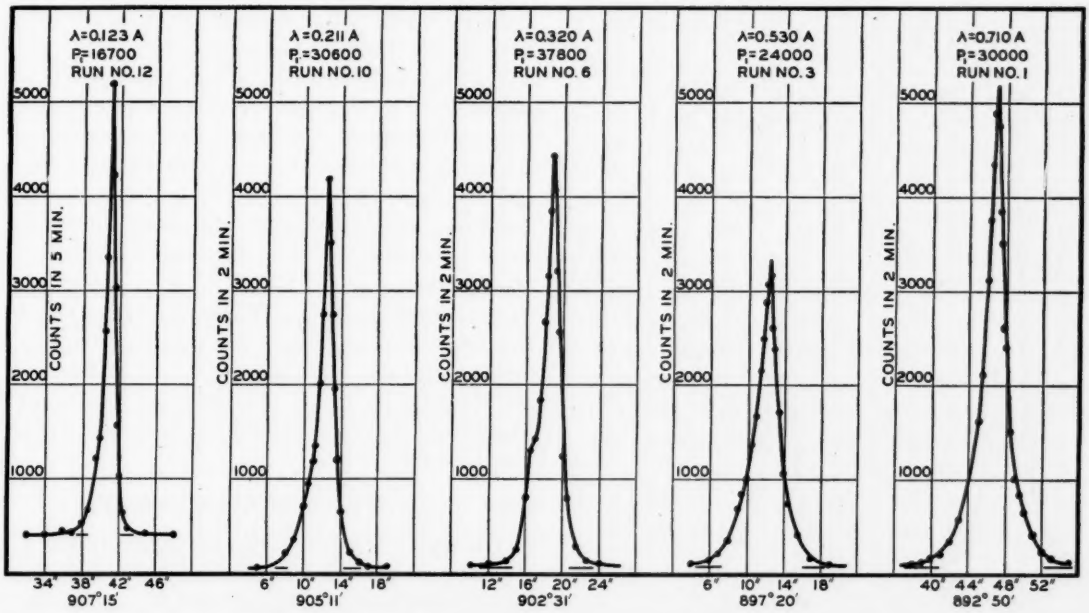

FIG. 12. Experimental Laue reflection rocking curves of the two-crystal x-ray spectrometer using the (310) planes of quartz in the first-order parallel position. P_i (given above each curve) is the number of counts in 2 min. for the "straight through" beam (off parallel setting) used for "normalizing" the curves. The angular positions indicated below each curve refer to the nominal setting of the spectrometer worm wheels. The points were taken at ¼ second intervals.

‡‡ The result Eq. (19) follows from the fact that the single-crystal Laue diffraction pattern for the symmetrical case has the profile of a witch or resonance curve. The half-maximum width of the fold of two witches is just the sum of the individual half-maximum widths.

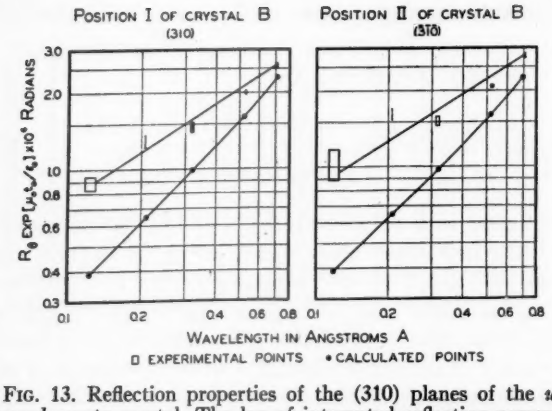
POSITION I OF CRYSTAL B
(310)
POSITION II OF CRYSTAL B
(3$\bar{1}$0)
$R_\theta \exp[\mu_0 t_0/\gamma_0] \times 10^4$ RADIANS
WAVELENGTH IN ANGSTROMS A
□ EXPERIMENTAL POINTS • CALCULATED POINTS

FIG. 13. Reflection properties of the (310) planes of the *unstressed*-quartz crystal. The log of integrated reflecting power is plotted *versus* the log of the wave-length to determine the dependence of the integrated reflecting power on the wave-length. These data were obtained on the two-crystal spectrometer. The widths of the rectangles, where these are used to locate the experimental points, give the ranges of wave-lengths transmitted by the spectrometer at each wave-length setting. The height of the rectangle gives the spread in the experimental intensity data. The position *II* of crystal *B* was obtained by rotating the crystal through 180° so that the ($\bar{3}\bar{1}0$) planes were used.

calculate separately ${}^{p}R_\theta$ and ${}^{n}R_\theta$. The usual procedure is to make an assumption concerning the model and calculate the two-crystal quantities. $R'\exp[\mu_0 t_0/\gamma_0]$, $P(0)\exp[\mu_0 t_0/\gamma_0]$ and W_θ were calculated for perfect thick crystals to compare with the experimental data.

The x-ray source consisted of a molybdenum target tube driven by a full-wave rectified filtered supply, or a tungsten tube driven by a half-wave rectified supply. Manual control was used except in the filament circuit where a saturable core stabilizer was used.

The two quartz plates were carefully mounted so that both the (310) planes and the large flat faces of the slabs were accurately parallel¶¶ to the axes of rotation and so that the centers of the thickness of the plates were centered on these axes. Great care was taken to avoid introducing any stress in the quartz by the supporting means. The quartz plates were optically polished and parallel to several fringes, but the surfaces were not etched. Subsequent experience has shown that even with the most careful polishing technique, the surfaces should be etched to remove submicroscopic material wedged into the minute cracks. The wave-length band which the instrument accepts was adjusted by the setting of the jaws of the defining slit (placed midway between crystal pivots *A* and *B*, Fig. 11). It is, of course, easy to ascertain this setting by turning crystal *B* and the arm supporting the counter through the appropriate angles to permit study of the anti-parallel rocking curve which gives the spectrum of the radiation being used. The x-ray beam was 4 mm wide and 5 mm high at crystal *B*. The slits were always wide enough to permit the $K\alpha_1-\alpha_2$ doublet to pass. Certain curves were taken using a band of the continuous spectrum of approximately this same width.

The use of a xenon-filled thin window counter made it possible to use rather low intensity from the x-ray tube. The efficiency of the counter ranged from about one to 20 percent over the range of wave-lengths used. The counters, made with a cylindrical copper cathode, and a 7-mil tungsten wire anode, were filled to a pressure of 10 cm of Hg with a two to three percent mixture of petroleum ether in xenon.

The center of the wave-length band was selected by setting the crystal *A*. Crystal *B* was then set "off parallel" by a very small angle and the total radiation transmitted by the plate was measured. This datum was used to normalize the parallel rocking curve appropriately. The parallel position rocking curves were made first with crystal *B* as shown and then with *B* rotated through an angle of 180°. Since the reference datum is the beam transmitted "off parallel" by the crystal *B*, the absorption factor $\exp[-\mu_0 t_0/\gamma_0]$ is taken into account and one can compare $R'\exp[\mu_0 t_0/\gamma_0]$ and $P(0)\exp[\mu_0 t_0/\gamma_0]$ directly with the experimental data.

COMPARISON OF THEORETICAL AND EXPERIMENTAL DIFFRACTION PATTERNS

Rocking curves were taken for five different wave-length bands from 0.710 to 0.123A. The data are collected in Table III and the rocking curves are plotted in Fig. 12. Their extreme narrowness is remarkable. The curves are not entirely reproducible when various portions of the crystal plate are used. Variations as large as 30 percent may occur. This may account for the discrepancy between the points above 0.25A taken with the molybdenum tube. The smallest incremental setting available was $\frac{1}{4}$-second of arc. Some of the patterns were so narrow that difficulty was experienced in obtaining good profiles. Figure 13 is a log-log plot of the data given in Table III. Where boxes are shown about the experimental points, these represent both the wave-length band and the probable errors of intensity to be associated with each point. The theoretical curves are calculated on the assumption that the crystals are ideally perfect.

DISCUSSION OF RESULTS

The first result which can be deduced from these observations on stressed and unstressed quartz is that the unstressed crystalline quartz behaves more nearly like a perfect crystal than does the bent crystal. The integrated reflection coefficient for the flat specimen falls off certainly less rapidly than λ while for the bent crystal it falls off as λ^2. For the flat crystal, the behavior of $P(0)\exp[\mu_0 t_0/\gamma_0]$ and W_θ is in qualitative agreement with what one might expect if the specimen were nearly but not completely perfect.

¶¶ The parallelism of the internal (310) planes of the quartz slab (which exhibit no cleavage or other developed faces) with the axis of rotation of the pivot was established first by photographing the reflections from both sides of the planes of crystal *B* at a distance of 100 cm and adjusting the crystal on its support till these images occurred at the same height. The final fine adjustment was made so as to yield the narrowest possible parallel rocking curve.

Let us consider an almost perfect crystal in which there exist domains over which the lattice is perfect. Assume, however, that these domains are not perfectly oriented in the macroscopic crystal, but are randomly rotated relative to one another through *very small* angles. If very long wave-length radiation is scattered by this crystal, it can appear to behave as a perfect crystal only so long as the slight angular misorientation is small compared with the diffraction pattern width. Reference to Table I shows that the width w of a perfect crystal pattern varies as λ to the first power. The effect of absorption will be neglected throughout this discussion. The integrated reflection coefficient R_θ and half-width w for this perfect case decrease linearly with λ. The peak of the single crystal Laue diffraction pattern for this case will remain constant (at 50 percent, as we have already shown).

As the wave-length decreases, the case we have just outlined is the first of three cases which we may distinguish in order as follows:

Case I. Angular misorientation η of the mosaic domains is small compared to the single-crystal diffraction pattern width, w. Ideal crystal extinction distance t_x small in comparison to domain size t_0. For this case, w should be proportional to λ, $P(0)$ the peak reflection coefficient should stay constant at 50 percent and R_θ the integrated reflection coefficient should be given by $\frac{1}{2}\pi w$ (witch-like diffraction pattern).

Case II. As the wave-length decreases the ideal single crystal diffraction pattern width w decreases proportionally thereto until w becomes much smaller than η the mosaic misorientation parameter. Also, with decrease in wave-length λ the ideal crystal extinction distance t_x *increases* in inverse proportion to λ. (This can be seen by referring back to Eq. (2) which takes the form $t_x \cong [r_0(|F_H|/V)K\lambda]^{-1}$, if we substitute λ for $2d\sin\theta$ and recall that $\cos\theta$ is essentially unity for the small angles here involved.) For case II, however, we shall assume that t_x has still not increased to the point where it is larger than t_0, the size of the mosaic domains.

For this case, w the diffraction pattern width should remain constant but because of the mosaic misorientation it should of course be broader than the ideal single crystal diffraction pattern width, w, for the same wave-length. $P(0)$, the peak reflection coefficient of the diffraction pattern, should stay constant at the value 50 percent. R_θ the integrated reflection coefficient should be greater than it would be for an ideally perfect crystal (because of the broadening of the pattern).

Case III. As the wave-length decreases still more, we come to the case where both the inequalities $\eta \gg w$ and $t_x > t_0$ hold so that now complete extinction does not occur in any of the domains.

For this case we shall tend to have w the width of the diffraction pattern constant (since it is now fixed by the mosaic misorientation) but the peak reflection coefficient $P(0)$ should diminish as λ^2 because the amplitude which is scattered will vary as λ. Since the pattern width remains constant R_θ should also vary as λ^2.

With ever-decreasing wave-length this λ^2 behavior is then the terminal behavior for the mosaic crystal. In an ideally perfect crystal, on the other hand, the transition between $R_\theta \sim \lambda$ and $R_\theta \sim \lambda^2$ would take place only when the extinction distance became comparable with the total plate thickness. But, in this case also the λ^2 behavior is the terminal behavior at short wave-lengths.

In Fig. 10, the dashed curve, A, represents the theoretical behavior of a mosaic crystal. Curve B represents theoretically the behavior of a perfect crystal. All crystal models should approach in behavior the curve A below the junction P because below this wave-length the extinction distance is greater than the plate thickness. It is of interest to note that in the region of about 500 x-units the observed integrated reflection coefficient for the bent crystal is about twenty times what the theory for a perfect crystal (curve B) would predict. This is in accord with results privately communicated to us which were obtained by B. E. Warren, at M.I.T.

The diffraction pattern width w should vary as λ down to wave-lengths corresponding to the junction P in a perfect crystal and then show a constant width. If the crystal is imperfect, the transition from the linear behavior with wave-length should take place at longer wave-lengths (transition between cases I and II) and the width should tend to become constant at greater widths. It was impossible to obtain any information on w for the bent crystal case except at 30 x.u. where the width of the diffraction pattern appears to be of the order of 5 sec. of arc.

The results obtained for unstressed quartz are in qualitative agreement with Parratt's finding for the (110) planes.[18] There remains a slight uncertainty concerning the effect of the unetched surface layers. The extremely narrow two-crystal rocking curves indicate their effect to be small however. Also, there has never been any indication that they contribute appreciably to the scattering in the two-meter curved-crystal case.

For the unstressed crystals, the wave-length range 0.12 to 0.71A of this study may quite possibly represent the transition from case I to case II mentioned where the ideal crystal diffraction pattern width just becomes comparable with the angular misorientation η. Here the diffraction pattern width w will remain constant but the peak reflection coefficient $P(0)$ will start to diminish slowly with diminishing λ in preparation for its eventual behavior proportional to λ^2.

In the case of the elastically curved crystal, the observed R_θ behavior (Fig. 10) *over the entire wave-length range from 500 x units to nine x units* is like that of the predicted terminal behavior at short wave-lengths for either an ideally perfect or a mosaic crystal.

We have as yet no good explanation for this behavior

[18] L. G. Parratt, Rev. Sci. Inst. 5, 395 (1934).

of the curved-quartz crystals when used in the focusing gamma-ray spectrometer. It seems very unlikely that bending the quartz plate creates permanent misorientation of mosaic blocks in the way in which this is supposed to occur when a rocksalt crystal for example is bent. In fact, we have no evidence that the quartz undergoes any permanent change either in its macroscopic geometry or otherwise as a result of bending. The quartz might, however, become mosaic-like in structure in some elastically reversible way not now understood. Such a division into mosaic domains when under stress could be either by reason of misorientation between domains or by reason of translational displacements between domains of such a nature as to destroy the coherence of the reflections from adjacent domains. Unfortunately, it is very difficult to study reliably such things as the width of the two-crystal spectrometer parallel rocking pattern utilizing a curved crystal for either of the specimens because this would require a beam so narrow that the arc of curvature of the plate over the region of reflection would be less in angular measure than the intrinsic diffraction pattern width, a matter of a second or so of arc only. At the very short gamma-ray wave-lengths studied here, it would be next to impossible to get sufficient intensity to work with the two-crystal spectrometer even with flat crystals and broad beams.

APPENDIX

The authors are indebted to the editors of the *Physical Review* whose remarks have brought out the need for further clarifying certain points in the description of our method of measuring the integrated reflection coefficients, R_θ, by means of the two-meter focusing curved-crystal spectrometer. One editorial remark was that we had made no attempt in our theoretical treatment of the problem to take into account *the effect of the bending of the crystal lattice on the reflection coefficient*. Now this criticism is, in the strict sense, *true*. We are as yet unable to formulate a rigorous *dynamical* theory of x-ray reflection for a curved lattice. Obviously all the well-recognized methods of attack (depending for example on Ewald's reciprocal lattice representation) break down because we no longer have to do with a strictly periodic structure. But we suspect that the editors (and, hence, probably many readers also) may have, as a result of reading the foregoing paper, erroneously imagined a much grosser defect than the lack of a rigorous dynamical theory for bent lattices. This is revealed by the next editorial remark to the effect that a beam of x-rays scattered in one layer of such a bent crystal slab can only go a certain distance before it encounters planes of different orientation (because of the bending) which therefore fail to satisfy the Bragg condition for the wave-length in question. Thus, it is asserted, the distance over which reflection is possible will be limited. This, it is stated, would be a direct effect of the bending which would tend to increase R_θ.

This argument we believe overlooks the fact that for source points on the focal circle of the instrument (when used as ours is in transmission), *the bending stresses change the lattice constant of the crystal in exactly the right manner through its thickness as to nullify the above supposed effect*. Y. Cauchois was the first to point out that on the convex side of the bent crystal slab, the grating constant (for the planes normal to the slab and parallel to the cylindrical generators) is increased by the tension in that region so that the Bragg angle for reflection is *decreased* while on the concave side the reverse is true. It is easy to prove that so long as Bernoulli's assumption for the bending of beams applies (that initially plane sections remain plane after bending) this effect will be just such that *rays emanating from one and the same point on the focal circle will encounter the crystal slab so as to satisfy the Bragg condition at all points throughout its entire thickness for one and the same wave-length*. As far as the geometrical optics of the selective reflection is concerned (ignoring multiple reflections to-and-fro between planes), the case seems thus to be beyond criticism. We propose to show here that this holds even for to-and-fro reflections. It is true of course that in our instrument an extremely minute and easily calculable aberration exists* because the design is of the approximate focusing type. This effect is

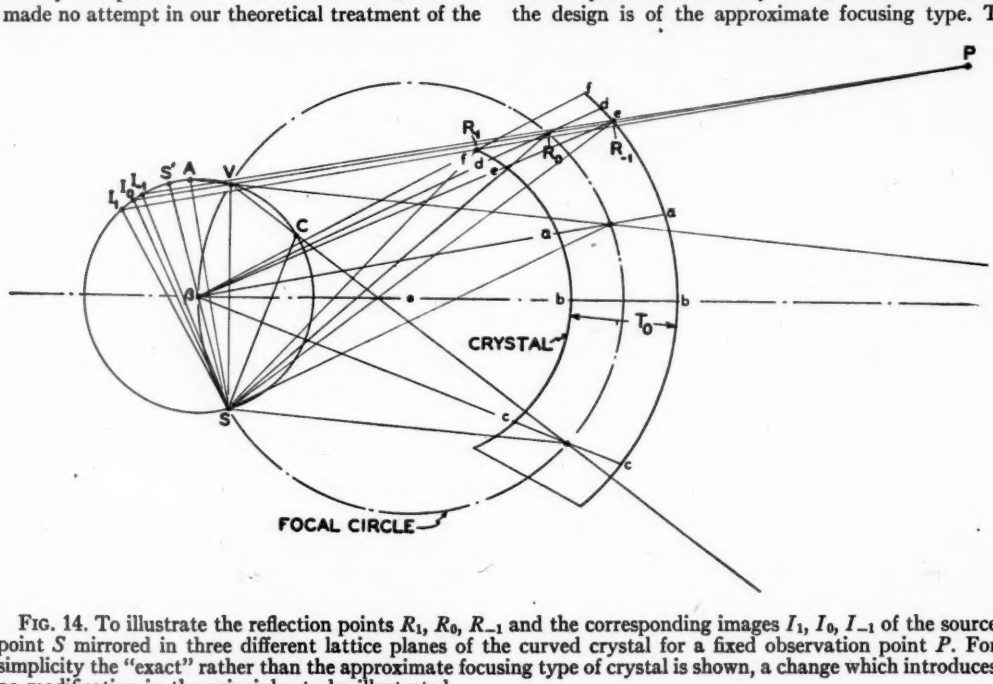

FIG. 14. To illustrate the reflection points R_1, R_0, R_{-1} and the corresponding images I_1, I_0, I_{-1} of the source point S mirrored in three different lattice planes of the curved crystal for a fixed observation point P. For simplicity the "exact" rather than the approximate focusing type of crystal is shown, a change which introduces no modification in the principles to be illustrated.

* See Fig. 3 and related text in our paper, Rev. Sci. Inst. 18, 629 (1947).

however far smaller even than the perfection of focusing we have so far been able to attain with our best curved-crystal holder would permit us to detect. All such minor effects are completely taken into account in our method of reducing our data (see Fig. 8 and related text for a summary of the factors involved in translating the observed quantity Γ_i into the desired reflection coefficient R_θ).

We have in a geometrical sense made a certain start in the direction of a more rigorous treatment of diffraction (by an accurately bent ideal crystal) which seems to indicate that the effect of such bending in limiting the domain of coherent interference in the crystal lattice must be practically quite beyond detection. In Fig. 14 the thickness T_0 of the bent crystal slab is enormously exaggerated relative to the radius of curvature for better clarity. The Bragg angle is also exaggerated for the same reason and for simplicity the exact focusing instrument is the one shown (neutral axis of the bent slab coinciding with the focal circle). The source is at S and the virtual focus for the selectively reflected rays leaving the crystal is at V. β is the convergence point of the reflecting crystal planes. Let us construct the image points of the source S for reflection by different atomic planes in the bent crystal. Simple geometrical considerations show that for the plane bb, which coincides with a diameter of the focal circle, the image of S is at V. For other crystal planes, such as aa or cc, the images of S lie in various positions such as A or C on the *circle* $SCVAS'$ whose center is at β, whose radius is βS, and whose diameter is $S\beta S'$. We shall call this circle the *image circle*. We are to think then of an arc of this circle (such as AC) as being closely studded with the image points of S mirrored in each and every one of the atomic lattice planes of the bent crystal slab. The lines SC and SA are the normals to the crystal planes projected from S. Furthermore, this geometry makes it clear that the multitude of image points of S mirrored in all the reflecting lattice planes of the curved crystal *are equidistantly spaced along that arc*. None of the geometrical results so far stated *involve any approximation whatever*. They are rigorous.

For the symmetrical Laue reflection of this type, as already pointed out in the preceding text, the very slight refractive bending of the rays at the entry and exit faces of the slab is just compensated by the change in wave-length inside the slab so that externally everything takes place as though the refractive index were strictly unity. It seems reasonable therefore to assume that the interference effects which will decide the intensity of the reflected beam leaving the convex side of the crystal will be essentially the same as though the crystal were removed and a multitude of coherent and equidistant sources studded along the arc AC were substituted for it. (This argument, for the moment, ignores multiple to-and-fro reflections in the crystal.) It is interesting to note how very different this set of virtual source points is from the set which would be observed *if the crystal were not bent*. For an unstressed crystal, the image points lie on a straight line, the common normal dropped from S to all of the (projected) lattice planes. Thus, the loci of images for the stressed and unstressed crystals lie roughly at right angles to each other. For the unstressed crystal the spacing between adjacent image points on the straight locus is $2d$ where d is the crystal grating space. For the curved crystal the spacing between adjacent image points on the circular arc AC can readily be shown to be $2d\sin\theta = n\lambda_B$ where d is the unstressed grating space, n is the order of reflection used (in all of our studies $n=1$) and λ_B is the wave-length satisfying the Bragg condition for reflection at angle θ.

Let us now consider classically how the rays actually interfere (constructively or destructively) so as to produce Bragg selective reflection in our curved crystal. Obviously we are dealing here with Fresnel rather than Fraunhofer diffraction. In order that reflections from a number of different atomic planes may cooperate coherently, it is necessary that rays starting from a source point S (an emitting atom), after reflection on different planes, shall, by different paths, eventually reunite at an observation point P (an absorbing atom in the detecting system). The "interference" (superposition of wavelets) *does not in reality occur in the crystal* but at the point of observation P. Neither S nor P are at infinity.

Let us consider how to construct the different rays arriving at P from different atomic mirror planes in the curved crystal. Clearly the fact that these mirror planes have *limited extension* (because of the limited thickness T_0 of the bent crystal slab) greatly restricts the number of such planes that can co-operate to send rays from S to any one given point P. Each plane will have one and only one geometrical reflection point R_i† for the given source and image points S and P. That mirror plane dd for which the geometrical reflection point R_0 *lies on the focal circle* (there can be not more than one such plane for specified positions of S and P) will furnish a ray to P directed as though it came from V. It will in general however *not* have V as its *image point*. The point I_0 where the line VP (or its extension) cuts the image circle again will be the image point. Now for other mirror planes such as ee or ff adjacent to the plane just referred to, the geometrical reflection points R_1 or R_{-1} will lie either inside or outside the focal circle and the corresponding image points from which the rays appear to arrive at P will be located as at I_1 or I_{-1} on a short arc of the image circle on either side of the point I_0. The range of image points I_i and geometrical reflection points R_i which can be operative to send rays to P is limited then by the thickness of the crystal slab, for when the reflection point R_i no longer lies inside the slab, reflection no longer occurs. The small range of different Bragg angles covered in this way corresponds to the above mentioned variation in grating constant as we pass through the thickness of the crystal slab resulting from the varying degrees of strain which the bending stress has set up on either side of the neutral axis. We have, of course, here selected a very exaggerated lateral position for P on purpose to clarify the geometry and as already stated the thickness of the crystal slab and other geometrical magnitudes such as the Bragg angle are also greatly exaggerated for the same reason. Clearly, however, in this idealized geometrical optical treatment the only specific effect of the bending which could place a limitation on the number of mirror planes cooperating coherently in sending wavelets to P *must come from the curvature of the short arc such as* I_1I_{-1} *on which the uniformly spaced image points lie* because this is the only effect of bending the crystal which introduces any important inhomogeneity in the otherwise uniformly increasing sequence of path lengths measured from the various image points I_i to P. Very simple considerations suffice to convince one that in the real geometry of our two-meter instrument the limited thickness of the crystal slab causes the number of image points clustering around I_0 to be far too limited to permit the accumulation of a phase change of order π through the curvature of the image locus. An order of magnitude for the number of co-operating image points can be found by computing how many planes a straight ray incident at the Bragg angle θ must cross in traversing the thickness of the unstressed slab. This is $T_0\tan\theta/d$ and in our two-meter instrument with a 1-mm thick crystal slab, for $\lambda = 8$ x.u. is about equal to 4×10^4. If we consider (see Fig. 15) the short arc of the image circle (on which the image points are clustered about I_0 with uniform spacing λ), then the projections of these image points on the ray direction furnish a means of closely approximating the successive path differences for the different paths I_iP. The angle α_0 between the image arc at I_0 and the ray direction can be approximated as x/D where x is the distance from the center of the curved crystal to the region in the crystal at which the reflection is occurring and D is the diameter of the focal circle. The difference of optical path for any

† As C. G. Darwin has pointed out in his remarkable early papers in 1914 on the dynamical theory of x-ray reflection, a reflection point such as R_i is in reality the center of a system of elliptical Fresnel zones, laid out on the atomic lattice plane and the explanation of the mirror reflection in terms of classical physical optics involves the coherent co-operative scattering of the entire pattern of atoms studded over these Fresnel zones which are the loci of points of equal path difference. C. G. Darwin, Phil. Mag. 27, 325; 675 (1914).

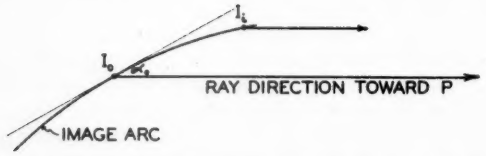

FIG. 15. To illustrate the geometry involved in the derivation of the dephasing of the interference from the array of images I_0 to I_i, by reason of the curvature of the locus on which they lie.

two image points on the arc will be $\lambda\cos\alpha$ where α is the angle with the ray direction at that point on the arc. Relative to the path I_0P the cumulative path difference δ_i for any image point I_i is found to be

$$\delta_i=\lambda[\cos\alpha_0+\cos(\alpha_0+\mu)+\cos(\alpha_0+2\mu)\cdots\cos(\alpha_0+i\mu)],$$

where $\mu=2d/D$ is the angular change in the direction of the image arc between adjacent image points. On the other hand, the cumulative path difference δ_i' if the image point locus had been a *straight* tangent to the arc at I_0 would have been

$$\delta_i'=\lambda i\cos\alpha_0.$$

By expanding the cosine terms in the expression for δ_i, the difference $\delta_i-\delta_i'$ can be readily shown to be

$$|\delta_i-\delta_i'|=\lambda i^2 d\sin\alpha_0/D.$$

This formula permits us to compute how many image points i must be included before $|\delta_i-\delta_i'|$ amounts to the order of a whole wave-length λ. The requisite number i_p is $i_p=D^{\frac{1}{2}}/(d\sin\alpha_0)^{\frac{1}{2}}$ or since α_0 is small and can be approximated by x/D we can write

$$i_p\cong D/(xd)^{\frac{1}{2}}.$$

For our two-meter spectrometer and with $x=4$ cm, $i_p=10^6$. Thus, 25 times as many image points are required (before dephasing from curvature becomes important) than the number actually available. The value of $\cos\alpha_0$ for our assumed case turns out to differ from unity by about $2\cdot10^{-4}$.

Now, in order to include in our discussion the case of repeated to-and-fro reflections between lattice planes in the crystal, we must consider not only the primary image points I_i (which we shall now distinguish as *primary* by calling them I_i') but also the images of these images I_{ij}'' each mirrored in an appropriately selected restricted set of atomic planes, the tertiary images I_{ijk}''' of each of these in turn mirrored in another appropriately selected restricted set of planes, etc.,‡ obviously only primary, tertiary, quinary and in general the images of *odd* ordinal number, I_i', I_{ijk}''', I_{ijklm}''''', etc. (lying on the same side of the central axis, $b\beta$, as the point V), operate as coherent image points to determine the intensity at P. Now a little thought will convince the reader *that all image points*, whether they be primary, secondary, tertiary, or of whatever ordinal number, *lie somewhere on the image circle*. Furthermore, it is not difficult to prove that all the cooperating image points *of odd ordinal number* lie at points on the image circle which belong to the same set as the primary image points, namely the set (of which I_0' is a member) consisting of points uniformly spaced along the arc with constant angular spacing μ between adjacent points. Thus, what we have proved for the primary image points (that the dephasing from curvature of the locus is negligible) will be equally true for the image points of higher ordinal number and in fact these will in general not lie as remote from I_0 as extreme members of the primary set for it can be shown that the sum of all subscripts without regard to algebraic signs,¶ $|i|+|j|+|k|\cdots$ for a given higher (odd) ordinal image point must have an upper bound of order of magnitude $T_0\tan\theta/d$ (or approximately $10^7\tan\theta$ in our instrument) whereas, for a higher odd ordinal image, the most remote position on the image arc from the origin I_0 will be given merely by the sum of the *alternate* subscript numbers $|i|+|k|\cdots$ (with the subscript numbers for the even ordinal reflections omitted from the summation). We arrive then at the conclusion *which holds rigorously, either for primary reflections or higher ordinal to-and-fro reflection in the crystal, that the dephasing effect of locus curvature cannot place a limit on the number of planes which cooperate coherently*. This holds for an ideally perfect crystal slab ideally bent so that its atomic planes pass through a common point β, so long as the lateral position of the observation point P from the central axis of the instrument defines an angle $\alpha_0\cong x/D$ as small as we have in our two-meter spectrometer. The conclusion seems inescapable that, for the ideal crystal case as stated, the above limitation must be placed by the thickness T_0 of the slab only.

‡ Each subscript after the first indicates the number of atomic planes traversed between two successive reflections.

¶ Note that, save for the first subscript, i, which may be either positive or negative, the series of subscripts, j, k, $l\cdots$, must have terms whose algebraic signs alternate because of the to-and-fro reflection.

The Structure of Atoms from Diffraction Studies

H. HAUPTMAN AND J. KARLE
Naval Research Laboratory, Washington, D. C.
(Received October 31, 1949)

A method is given for obtaining the electron distribution in atoms from diffraction data which makes use of the fact that the distribution function is positive. The property of positiveness affords a basis for extrapolating the scattering data which are determined experimentally over only a finite range. This extrapolation is needed since the formula relating the electron distribution to the scattering function requires that the latter be known over an infinite range. A procedure for the extrapolation is given and the nature of the error is discussed.

THE amplitude of x-rays scattered coherently by free atoms may be expressed according to theory in terms of the electron distribution about the nuclei of these atoms. By means of an inversion procedure the electron distribution may be in turn expressed explicitly in terms of the scattered x-ray amplitude. This suggestive form has lead to several investigations[1–7] with rare gas atoms in which attempts were made to determine the electron distribution. In these experiments scattering data were obtained only over a small range whereas the theory requires that the scattered intensity be known from zero to infinity. A procedure has been developed for extrapolating the data beyond the range covered by experiment which makes use of the fact that the electron distribution about a nucleus is a positive function. Extrapolation procedures used previously had no theoretical basis and caused errors in the final result. It will be shown that exact data known only in a restricted range of angle are sufficient to uniquely determine the positive electron distribution of an atom; the only requirement on the function represented by the data being the existence of all of its derivatives at the origin. If the scattering function is assumed to be analytic, then any finite length determines the remainder of the curve by the principle of analytic continuation, and the concept of positiveness need not be introduced. In practice, of course, experimental data are always obtained with some degree of uncertainty. In this case analyticity offers no useful criterion for extrapolating the data beyond the experimental range. On the other hand, the positiveness of the sine transform of the function does offer a basis for extrapolating the data within a limited range of uncertainty. The uncertainty in the resulting electron distribution will therefore fall within limited bounds which may be evaluated in terms of the uncertainty in the experimental data. In this paper a practical procedure will be developed for extrapolating experimental data which insures that its Fourier sine transform will be positive, and also an evaluation will be made of the error in the final results.

THEORY

The total x-ray intensity scattered by a free atom[8] at an angle θ to the main beam at a distance R is,

$$I_i = I_0 \frac{e^4}{m^2c^4R^2} \cdot \frac{1+\cos^2\theta}{2} [f^2(s)+QZS], \tag{1}$$

where

$$f(s) = \int_0^\infty D(r) \frac{\sin sr}{sr} dr \tag{2}$$

and $Q=1/[1+h(1-\cos\theta)/mc\lambda]^3$. The quantity I_0 is the incident intensity, $(1+\cos^2\theta)/2$ is the polarization factor, S is the incoherent scattering function tabulated by Bewilogua,[9] Q is the relativistic correction, Z is the atomic number, $s=(4\pi \sin\theta/2)/\lambda$, and the quantities e, m, c, h, and λ have their usual definitions. In this paper we are mainly concerned with the quantity $f(s)$ which is called the atomic scattering factor. It is defined in terms of $D(r)=4\pi r^2\rho(r)$ where $\rho(r)$ is the number of electrons per unit volume at a distance r from the atomic nucleus. The square of the scattering factor multiplied by the quantity in front of the bracket in (1) represents the coherent scattered intensity.

A Fourier inversion may be performed on (2) giving,

$$D(r) = \frac{2r}{\pi} \int_0^\infty sf(s) \sin rs ds. \tag{3}$$

The atomic scattering factor, $f(s)$, may be determined experimentally for only a restricted range of s. The practical lower limit of the range is some small value larger than zero and the upper limit is determined by many factors including the wave-length, the sensitivity of the measurements, and the relative magnitudes of the incoherent and coherent scattering. It is evident that $D(r)$ may be reliably obtained from (2) only if $f(s)$ is correctly extrapolated beyond the range in which it has been experimentally determined. The extrapolation

[1] A. H. Compton, Phys. Rev. **35**, 925 (1930).
[2] E. O. Wollan, Phys. Rev. **37**, 862 (1931).
[3] E. O. Wollan, Phys. Rev. **38**, 15 (1931).
[4] G. Herzog, Helv. Phys. Acta **2**, 169, 217 (1929).
[5] G. Herzog, Zeits. f. Physik **69**, 207 (1931).
[6] G. Herzog, Zeits. f. Physik **70**, 583, 590 (1931).
[7] G. Herzog, Helv. Phys. Acta **6**, 508 (1933).

[8] M. H. Pirenne, *The Diffraction of X-Rays and Electrons by Free Molecules* (Cambridge University Press, London, 1946).
[9] L. Bewilogua, Physik. Zeits. **32**, 740 (1931).

TABLE I. Witches of several orders, their cooresponding distribution functions, $D(r)$, and the coordinates of the maxima.

$f(s)$	$D(r)$	r_M	$D(r_M)$
$\frac{1}{(1+bs^2)^2}$	$\frac{r^2}{2b^{3/2}}\exp[-r/(b)^{1/2}]$	$2.0000(b)^{1/2}$	$0.2707/(b)^{1/2}$
$\frac{1}{(1+bs^2)^3}$	$\left(\frac{r^2}{8b^{3/2}}+\frac{r^3}{8b^{4/2}}\right)\exp[-r/(b)^{1/2}]$	$2.7321(b)^{1/2}$	$0.2266/(b)^{1/2}$
$\frac{1}{(1+bs^2)^4}$	$\left(\frac{r^2}{16b^{3/2}}+\frac{r^3}{16b^{4/2}}+\frac{r^4}{48b^{5/2}}\right)\exp[-r/(b)^{1/2}]$	$3.3369(b)^{1/2}$	$0.1991/(b)^{1/2}$
$\frac{1}{(1+bs^2)^5}$	$\left(\frac{5r^2}{128b^{3/2}}+\frac{5r^3}{128b^{4/2}}+\frac{r^4}{64b^{5/2}}+\frac{r^5}{384b^{6/2}}\right)\exp[-r/(b)^{1/2}]$	$3.8622(b)^{1/2}$	$0.1797/(b)^{1/2}$
$\frac{1}{(1+bs^2)^6}$	$\left(\frac{7r^2}{256b^{3/2}}+\frac{7r^3}{256b^{4/2}}+\frac{3r^4}{256b^{5/2}}+\frac{r^5}{384b^{6/2}}+\frac{r^6}{3840b^{7/2}}\right)\exp[-r/(b)^{1/2}]$	$4.3317(b)^{1/2}$	$0.1650/(b)^{1/2}$
$\frac{1}{(1+bs^2)^n}$	$\frac{1}{\Gamma(n)}\left(\frac{\Gamma(2n-3)}{2^{2n-3}\Gamma(n-1)}\cdot\frac{r^2}{b^{3/2}}+\frac{\Gamma(2n-4)}{2^{2n-4}\Gamma(n-2)}\cdot\frac{r^3}{1!b^{4/2}}+\frac{\Gamma(2n-5)}{2^{2n-5}\Gamma(n-3)}\cdot\frac{r^4}{2!b^{5/2}}+\cdots\right)\exp[-r/(b)^{1/2}]$		

procedure given here depends upon the use of a special type of analytic function. It will be indicated, although no formal mathematical proof will be offered, that the uncertainty in the final result for the electron distribution does not depend in the region of interest upon the special type of analytic function used but rather on the restrictiveness of the condition that the Fourier sine transform be positive. The restrictiveness will be shown by developing the formal theory of positive Fourier sine transforms and also by deriving certain of their special properties. The formal theory offers in principle a direct procedure for extrapolating numerical data without resorting to special functions. At its present stage of development, though, this procedure seems to be prohibitively laborious. The evaluation of the error is based on a numerical study involving a large class of examples using two different types of functions. Again the formal theory of positive Fourier sine transforms affords a basis in principle for studying the errors in the resulting electron distribution without resorting to special functions but requires considerable development to make it useful in practice.

NON-NEGATIVE SINE TRANSFORMS

The theory of non-negative Fourier sine transforms may be developed in terms of non-negative Hermitian forms in a manner entirely analogous to that for non-negative Fourier integrals of complex integrand[10] and non-negative Fourier series.[11,12] We define

$$(d/ds)[sf(s)]=\varphi(s)$$

whose value may be obtained from (2) by differentiating with respect to s, giving

$$\varphi(s)=\int_0^\infty D(r)\cos srdr. \tag{4}$$

From (4) we may write

$$\sum_i^m\sum_j^m \varphi(s_i-s_j)X_i\bar{X}_j = \int_0^\infty D(r)\sum_i^m\sum_j^m X_i\bar{X}_j\cos(s_i-s_j)rdr, \tag{5}$$

where X_i is an independent variable and $\bar{X}_i$ is its complex conjugate. The right side may be rewritten

$$\int_0^\infty D(r)[\sum_{i=1}^m X_i\cos s_ir\sum_{i=1}^m \bar{X}_i\cos s_ir + \sum_{i=1}^m X_i\sin s_ir\sum_{i=1}^m \bar{X}_i\sin s_ir]dr, \quad m=1,2,\cdots \tag{6}$$

which becomes, since each sum is multiplied by its complex conjugate,

$$\int_0^\infty D(r)[|\sum_{i=1}^m X_i\cos s_ir|^2+|\sum_{i=1}^m X_i\sin s_ir|^2]dr\geq 0. \tag{7}$$

Since $D(r)$ is a non-negative function, the integral is non-negative. We therefore obtain from (5) and (7) the infinite set of non-negative Hermitian forms characterizing the positive Fourier sine transform,

$$\sum_i^m\sum_j^m \varphi(s_i-s_j)X_i\bar{X}_j\geq 0, \quad m=1,2,\cdots. \tag{8}$$

The necessary and sufficient condition for the Hermitian forms to be non-negative is that the following set of determinants on the coefficients $\varphi(s_i-s_j)$ be non-negative,[13]

$$D_n=\begin{vmatrix} \varphi_0 & \varphi_{-1} & \varphi_{-2} & \cdots & \varphi_{-n} \\ \varphi_1 & \varphi_0 & \varphi_{-1} & \cdots & \varphi_{-(n-1)} \\ \varphi_2 & \varphi_1 & \varphi_0 & \cdots & \varphi_{-(n-2)} \\ \cdots & \cdots & \cdots & \cdots & \cdots \\ \varphi_n & \varphi_{n-1} & \varphi_{n-2} & \cdots & \varphi_0 \end{vmatrix}\geq 0, \quad n=0,1,2,\cdots, \tag{9}$$

[10] M. Mathias, Math. Zeits. **16**, 103 (1923).
[11] N. A. Achyeser and M. Krein, Comm. Soc. Math. Kharkoff **4**, 9 (1934).
[12] J. Karle and H. Hauptman, Acta Crystallograph. **3**, 181 (1950).
[13] For fixed m, n ranges from zero to $m-1$.

where $\varphi_{ij}=\varphi_{i-j}=\varphi(s_i-s_j)$ is the element in the ith row and jth column and satisfies $\varphi_{ij}=\varphi_{ia}+\varphi_{aj}$. Since φ is an even function, $\varphi_{ij}=\varphi_{ji}$. The determinants (9) may be rewritten to give a bound on φ_n in terms of the other elements. This bound may be written

$$|\varphi_n-\delta_n|\leq r_n, \tag{10}$$

where

$$r_n=D_{n-1}/D_{n-2}, \quad \delta_n=d_n/D_{n-2} \tag{11}$$

and

$$d_n=(-1)^n\begin{vmatrix} \varphi_1 & \varphi_0 & \varphi_{-1} & \cdots & \varphi_{-(n-2)} \\ \varphi_2 & \varphi_1 & \varphi_0 & \cdots & \varphi_{-(n-3)} \\ \cdots & \cdots & \cdots & \cdots & \cdots \\ \varphi_{n-1} & \varphi_{n-2} & \varphi_{n-3} & \cdots & \varphi_0 \\ 0 & \varphi_{n-1} & \varphi_{n-2} & \cdots & \varphi_1 \end{vmatrix}. \tag{12}$$

The element φ_n is real and is therefore bounded within an interval on the real axis whose center is δ_n and whose length is $2r_n$. It will be shown for a function $f(s)$ whose derivatives exist at the origin that the function known in a finite interval including the origin uniquely determines a positive electron distribution. It is therefore apparent that φ_n, which may be an element beyond the experimental range of s values, is bounded with greater and greater restriction as n and therefore the order of the determinants increases. As n approaches infinity, r_n approaches zero and φ_n becomes a definite point defined as

$$\varphi_\infty=\lim_{n\to\infty}\delta_n. \tag{13}$$

With experimental data there is some uncertainty in the extrapolation owing to the uncertainty in the data. However, the extrapolation of any experimental function consistent with the range of uncertainty of the data must obey the restrictions of (10).

In principle, numerical data can be extrapolated beyond the experimental range by means of (10). The elements $\varphi(s_i-s_j)$ in the experimental range are obtained by finding $(d/ds)[sf(s)]$, $s=s_i-s_j$, from the numerical data. These are used with (10) to extend the function φ. The extension on $f(s)$ may then be found by evaluating

$$sf(s)=\int_0^s \varphi(y)dy. \tag{14}$$

This procedure is quite formidable in its present stage of development. We have therefore devised an extrapolation method which is based upon the application of special functions.

UNIQUENESS PROPERTY

The question of uniqueness may be discussed by means of the Hamburger moment problem[14] which concerns the conclusions that may be drawn about an increasing monotonic function, $\Psi(r)$, given the moments,

$$\mu_n=\int_{-\infty}^{\infty} r^n d\Psi(r), \quad n=0, 1, 2, \cdots. \tag{15}$$

The identification of the moment problem with the problem of non-negative sine transforms may be made by successively differentiating both sides of (2) and then setting s equal to zero. Since $D(r)$ is an even function of r, we obtain

$$\int_{-\infty}^{\infty} r^n D(r)dr=\int_{-\infty}^{\infty} r^n d\Psi(r) =(-1)^{\frac{1}{2}(n^2-n)}\cdot 2(n+1)f^{(n)}(0) \tag{16}$$

where

$$(d/dr)\Psi(r)=D(r). \tag{17}$$

The moments of $D(r)$ are seen to be simply related to the successive derivatives of $f(s)$ at the origin. The function, $\Psi(r)$, according to (17) must be an increasing monotonic function since $D(r)$ is positive for all r. As a corollary to a result of Riesz[15] who studied the Hamburger moment problem, it can be shown that if $D(r)$ drops off at least as fast as $\exp(-kr)$ for some positive k (i.e., $\lim_{r\to\infty}D(r)/\exp(-kr)=0$), $D(r)$ is uniquely determined by its moments. This condition of Riesz may be readily assumed to hold. It may therefore be concluded that the derivatives at the origin of a function, $f(s)$, uniquely determine a positive electron distribution. Since $f(s)$, known in any interval including the origin, determines all its derivatives at the origin, it therefore determines the positive electron distribution. It follows too that any finite portion of the $f(s)$ curve which is connected to a region including the origin by analytic continuation will uniquely determine a positive electron distribution. These conclusions, which relate to functions known exactly, have been drawn without assuming that $f(s)$ is analytic everywhere. They serve to illustrate that positiveness affords extra restrictiveness on exact functions and imply that this restrictiveness may have applications to experimental functions which possess some degree of uncertainty.

EXTRAPOLATION PROCEDURE

The extrapolation method used involves fitting the experimental $f(s)$ data with a function of the type,[16]

$$\sum_{i=1}^{p}\frac{a_i}{(1+b_is^2)^{n_i}}. \tag{18}$$

This function is used to define $f(s)$ for all s from zero to infinity. The quantities a_i, b_i, and n_i are positive numbers and the value of p depends upon the accuracy de-

[14] J. Shohat and J. Tamarkin, *The Problem of Moments* (American Mathematical Society, New York, 1943).

[15] M. Riesz, Arkiv. f. Mat. Astr. o. Fys. **17**, 1 (1923), (see p. 46).

[16] The function $a/(1+bs^2)$ is known as the witch of Agnesi. We call the function $a/(1+bs^2)^n$ a witch of nth order.

sired and the complexity of the atom being studied. Generally the heavier atoms require more terms in the summation. The values of b_i and n_i must be positive for (18) to remain finite for all values of s. If, in addition, the coefficients a_i are positive, function (18), substituted for $f(s)$ in (3), must give a $D(r)$ which is positive for all values of r. Listed in Table I are examples of some of the simpler functions (18) together with the corresponding functions $D(r)$. In the third and fourth columns the abscissas and ordinates of the maxima of the $D(r)$ are tabulated since these are useful in plotting $D(r)$. If $b_i>0$, each $D(r)$ is seen to be positive for all values of r. Therefore the $D(r)$ which corresponds to any linear combination of the functions $1/(1+b_is^2)^{n_i}$ with positive coefficients will certainly be positive.

The types of functions found to be satisfactory and convenient for lighter atoms have p values up to about five in expression (18) and n_i values equal to integers, none less than two.

The curve fitting procedure which has been developed is divided into two steps. The first step is to approximate the experimental data with a function of the type (18) with all the n_i equal to the same positive integer n. In the second step this approximation is improved by the decomposition of some of the witches into a linear combination of witches of different orders.

The fitting of witches with all the n_i equal to a positive integer n can be reduced to the problem of fitting first-order witches. The experimental $f(s)$ is replaced by the function,

$$\varphi_n(s)=2(n-1)\sum_{i=0}^{n-2}(-1)^i\frac{\binom{n-2}{i}}{(s^2-s_0^2)^{i+1}}\times\int_{s_0}^{s}x(x^2-s_0^2)^i f(x)dx, \quad (19)$$

where $\binom{n-2}{i}$ are the binomial coefficients, $\binom{n-1}{0}=1$, and s_0 is the smallest value of s for which $f(s)$ is known. The function $\varphi_n(s)$ is fitted with first-order witches by a procedure which guarantees that the parameters a_i' and b_i' of the first-order witches will be positive. Multiplying a_i' by $(1+b_i's_0^2)^{n-1}$ and leaving b_i' unchanged, we obtain new parameters $a_i=a_i'(1+b_i's_0^2)^{n-1}$ and $b_i=b_i'$ which when substituted into (18) with each n_i equal to n yield a function which is an approximation to $f(s)$. This may be shown by substituting (18) with n_i equal to n for $f(s)$ into (19) and noting that the right-hand side then reduces to a sum of first-order witches with the same b_i but with the a_i replaced by $a_i'=a_i/(1+b_is_0^2)^{n-1}$:

$$\varphi_n(s)=\sum_{i=1}^{p}a_i/[(1+b_is_0^2)^{n-1}(1+b_is^2)]. \quad (20)$$

We note that

$$\varphi_n(s_0)=\sum_{i=1}^{p}a_i/(1+b_is_0^2)^n=f(s_0)=f_0 \quad (21)$$

so that $f(s)$ and every $\varphi_n(s)$ have the point (s_0, f_0) in common. Finally, if a_i' and b_i' are positive, then so are a_i and b_i.

The procedure for fitting first-order witches to a set of points (s_i, f_i), which guarantees that the a_i and b_i will be positive, has been developed as follows. If the sum of p witches

$$\sum_{i=1}^{p}a_i/(1+b_is^2)$$

passes through the p points (s_i, f_i), we have a set of p equations

$$\sum_{j=1}^{p}\frac{a_j}{1+b_js_i^2}=f_i, \quad i=1, 2, \cdots, p \quad (22)$$

which are linear in the a_j. These equations may be readily solved for the a_j, giving

$$a_j=\frac{[\prod_{i=1}^{p}(1+b_js_i^2)][(-1)^{\frac{1}{2}(p^2+p)+j}\sum_{i=0}^{p-1}A_i\hat{S}_i(b_j)]}{[(-1)^{\frac{1}{2}(p^2-p)}(s_1^2, s_2^2, \cdots, s_p^2)][(-1)^{j-1}\prod_{i\neq j}(b_j-b_i)]}, \quad j=1, 2, \cdots, p \quad (23)$$

where

$$(s_1^2, s_2^2, \cdots, s_p^2)=\prod_{k=i+1}^{p}\prod_{i=1}^{p}(s_i^2-s_k^2)$$
$$=(s_1^2-s_2^2)(s_1^2-s_3^2)\cdots(s_1^2-s_p^2)(s_2^2-s_4^2)$$
$$\times(s_2^2-s_4^2)\cdots(s_2^2-s_p^2)\cdots(s_{p-1}^2-s_p^2) \quad (24)$$

$$A_i=(s_2^2, s_3^2, \cdots, s_p^2)s_1^{2i}f_1$$
$$-(s_1^2, s_3^2, s_4^2, \cdots, s_p^2)s_2^{2i}f_2$$
$$+(s_1^2, s_2^2, s_4^2, \cdots, s_p^2)s_3^{2i}f_3-\cdots,$$
$$i=0, 1, 2, \cdots, p-1 \quad (25)$$

and $S_i(b_j)$ is the elementary symmetric function of degree i of all the b_k except b_j, e.g.,

$$S_0(b_j)=1,$$
$$S_2(b_2)=b_1+b_3+b_4+\cdots+b_p,$$
$$S_2(b_1)=b_2b_3+\cdots+b_2b_p+b_3b_4+\cdots+b_3b_p+\cdots+b_{p-1}b_p, \quad (26)$$
$$S_{p-1}(b_3)=b_1b_2b_4b_5\cdots b_p.$$

Since the b_i occur symmetrically in (22), we assume without loss of generality that $b_i>b_j$ if $i<j$. Similarly, we assume that $s_i<s_j$ if $i<j$. Since, if we require the b_i

to be positive each of the expressions

$$\left.\begin{aligned} &\prod_{i=1}^{p}(1+b_j s_i^2)\\ &(-1)^{\frac{1}{2}(p^2-p)}(s_1^2, s_2^2, \cdots, s_p^2)\\ &(-1)^{j-1}\prod_{i\neq j}(b_j-b_i)\end{aligned}\right\} \tag{27}$$

appearing in (23) is evidently positive, and since we desire to restrict the b_j so that a_j are positive, we conclude that the only remaining expression appearing in (23) must also be positive:

$$(-1)^{\frac{1}{2}(p^2+p)+j}\sum_{i=0}^{p-1}A_i S_i(b_j)>0, \quad j=1, 2, \cdots, p. \tag{28}$$

We have to determine the b_i, subject to

$$b_1>b_2>\cdots>b_p>0, \tag{29}$$

such that (28) is satisfied. The system of inequalities (28) and (29) has been completely solved for several small values of p. We give solutions sufficient to satisfy (28) and (29) (and therefore $a_i>0$) for $p=3, 4, 5$.

If $p=3$, the necessary and sufficient condition for (28) and (29) to have solutions is that the inequalities

$$\left.\begin{aligned} &(-1)^{i+1}A_i>0, \quad i=0, 1, 2\\ &A_1^2-A_0A_2<0\end{aligned}\right\} \tag{30}$$

be satisfied. If (30) is not fulfilled, then (28) and (29) have no solutions and it is impossible for a sum of three first-order witches with positive parameters to pass through the three points (s_i, f_i). If (30) is fulfilled, then the complete solution of (28) and (29) is given by:

$$\left.\begin{aligned} &0<b_3<-\frac{A_1}{A_2}\\ &b_3<b_2<-\frac{A_0+b_3A_1}{A_1+b_3A_2}\\ &-\frac{A_0+b_3A_1}{A_1+b_3A_2}<b_1<-\frac{A_0+b_2A_1}{A_1+b_2A_2} \quad \text{if} \quad b_2<-\frac{A_1}{A_2}\\ &-\frac{A_0+b_3A_1}{A_1+b_3A_2}<b_1 \quad \text{if} \quad b_2\geq-\frac{A_1}{A_2}\end{aligned}\right\}. \tag{31}$$

If $p=4$, the necessary and sufficient condition for (28) and (29) to have solutions is that the inequalities

$$\left.\begin{aligned} &(-1)^{i+1}A_i>0, \qquad i=0, 1, 2, 3\\ &A_i^2-A_{i-1}A_{i+1}<0, \quad i=1, 2\end{aligned}\right\} \tag{32}$$

be satisfied. If (32) is not fulfilled, then (28) and (29) have no solution and it is impossible for a sum of four first-order witches with positive parameters to pass through the four points (s_i, f_i). If (32) is fulfilled then the complete solution of (28) and (29) is given by:

$$\left.\begin{aligned} &0<b_4<\alpha\\ &b_4<b_3<-\frac{A_1+b_4A_2}{A_2+b_4A_3}\\ &\alpha<b_2<-\frac{A_1+b_3A_2}{A_2+b_3A_3} \quad \text{if} \quad b_3\leq\alpha\\ &b_3<b_2<-\frac{A_0+(b_3+b_4)A_1+b_3b_4A_2}{A_1+(b_3+b_4)A_2+b_3b_4A_3} \quad \text{if} \quad b_3\geq\alpha\\ &-\frac{A_0+(b_2+b_3)A_1+b_2b_3A_2}{A_1+(b_2+b_3)A_2+b_2b_3A_3}<b_1\\ &\qquad<-\frac{A_0+(b_2+b_4)A_1+b_2b_4A_2}{A_1+(b_2+b_4)A_2+b_2b_4A_3}\\ &\qquad\text{if} \quad b_3\leq\alpha, \quad \text{and} \quad b_2<-\frac{A_1+b_4A_2}{A_2+b_4A_3}\\ &-\frac{A_0+(b_2+b_3)A_1+b_2b_3A_2}{A_1+(b_2+b_3)A_2+b_2b_3A_3}<b_1\\ &\qquad\text{if} \quad b_3\leq\alpha, \quad \text{and} \quad b_2\geq-\frac{A_1+b_4A_2}{A_2+b_4A_3}\\ &-\frac{A_0+(b_3+b_4)A_1+b_3b_4A_2}{A_1+(b_3+b_4)A_2+b_3b_4A_3}<b_1\\ &\qquad<-\frac{A_0+(b_2+b_4)A_1+b_2b_4A_2}{A_1+(b_2+b_4)A_2+b_2b_4A_3}\\ &\qquad\text{if} \quad b_3\geq\alpha, \quad \text{and} \quad b_2<-\frac{A_1+b_4A_2}{A_2+b_4A_3}\\ &-\frac{A_0+(b_3+b_4)A_1+b_3b_4A_2}{A_1+(b_3+b_4)A_2+b_3b_4A_3}<b_1\\ &\qquad\text{if} \quad b_3\geq\alpha, \quad \text{and} \quad b_2\geq-\frac{A_1+b_4A_2}{A_2+b_4A_3}\end{aligned}\right\} \tag{33}$$

where α is the smaller root of the quadratic

$$(A_1^2-A_0A_2)+(A_1A_2-A_0A_3)x+(A_2^2-A_1A_3)x^2=0. \tag{34}$$

If $p=5$, the necessary and sufficient condition for (28) and (29) to have solutions is that the inequalities

$$\left.\begin{aligned} &(-1)^iA_i>0, \qquad i=0, 1, 2, 3, 4\\ &A_i^2-A_{i-1}A_{i+1}<0, \quad i=1, 2, 3\\ &\alpha_2<\alpha_1\end{aligned}\right\} \tag{35}$$

be satisfied where α_i are the smaller roots of the quad-

ratics

$$(A_i^2-A_{i-1}A_{i+1})+(A_iA_{i+1}-A_{i-1}A_{i+2})x+(A_{i+1}^2-A_iA_{i+2})x^2=0, \quad i=1,2. \quad (36)$$

If (35) is not fulfilled, then (28) and (29) have no solution and it is impossible for a sum of five first-order witches with positive parameters to pass through the five points (s_i, f_i). If (35) is fulfilled, then solutions of (28) and (29) are given by:

$$\left.\begin{array}{l} 0<b_5<b_4<b_3<\alpha_2 \\ \alpha(b_5)<b_2<\alpha(b_4), \quad \alpha(b_5)<b_2<-(A_2+b_5A_3)/(A_3+b_5A_4) \\ -\dfrac{A_0+(b_2+b_3+b_5)A_1+(b_2b_3+b_2b_5+b_3b_5)A_2+b_2b_3b_5A_3}{A_1+(b_2+b_3+b_5)A_2+(b_2b_3+b_2b_5+b_3b_5)A_3+b_2b_3b_5A_4}<b_1< \\ \qquad -\dfrac{A_0+(b_2+b_4+b_5)A_1+(b_2b_4+b_2b_5+b_4b_5)A_2+b_2b_4b_5A_3}{A_1+(b_2+b_4+b_5)A_2+(b_2b_4+b_2b_5+b_4b_5)A_3+b_2b_4b_5A_4} \end{array}\right\} \quad (37)$$

where $\alpha(b_5)$ is the smaller root of the quadratic

$$[(A_1^2-A_0A_2)+(A_1A_2-A_0A_3)b_5+(A_2^2-A_1A_3)b_5^2]+[(A_1A_2-A_0A_3)+(A_2^2-A_0A_4)b_5+(A_2A_3-A_1A_4)b_5^2]x+[(A_2^2-A_1A_3)+(A_2A_3-A_1A_4)b_5+(A_3^2-A_2A_4)b_5^2]x^2=0. \quad (38)$$

The method just described for fitting $f(s)$ by a sum of witches of order n will in general not yield solutions for every n since the system of inequalities (28) and (29) may have no solution. This is another indication of the restrictions imposed by positiveness since a solution has been found not to exist in cases where ten arbitrary parameters are available for fitting five points. We have found in practice, however, that if n is chosen sufficiently large then a solution can be found. For convenience n is chosen to be the smallest value for which a solution exists. In this way an approximation to $f(s)$ is obtained which is very good except possibly for the larger values of s and which may be improved as indicated below. If it is desired to improve the approximation use may be made of a set of formulas which permits a witch of any order to be replaced either by a witch of any other order or by a sum of witches of any higher order. These are obtained by writing the Maclaurin expansion for the given witch and also the Maclaurin expansion for the linear combination of higher order witches chosen to approximate the given witch. The first few terms in the expansions are then equated in order to evaluate the coefficients. Typical examples of these formulas are:

$$\left.\begin{array}{l} \dfrac{1}{1+bs^2}\sim\dfrac{1}{(1+\frac{1}{2}bs^2)^2}\sim\dfrac{1}{(1+\frac{1}{3}bs^2)^3}\sim\cdots \\ \dfrac{1}{(1+bs^2)^2}\sim\dfrac{\frac{1}{2}-(1/18)(6)^{\frac{1}{2}}}{[1+(\frac{3}{5}-(1/10)(6)^{\frac{1}{2}})bs^2]^3} \\ \qquad +\dfrac{\frac{1}{2}+(1/18)(6)^{\frac{1}{2}}}{[1+(\frac{3}{5}+(1/10)(6)^{\frac{1}{2}})bs^2]^3}\cdots \\ \dfrac{1}{1+bs^2}\sim\dfrac{5/18}{[1+(\frac{1}{2}-(15)^{\frac{1}{2}}/10)bs^2]^2}+\dfrac{8/18}{[1+\frac{1}{2}bs^2]^2} \\ \qquad +\dfrac{5/18}{[1+(\frac{1}{2}+(15)^{\frac{1}{2}}/10)bs^2]^2} \end{array}\right\} \quad (39)$$

It can be readily seen that the leading terms in the Maclaurin expansions of the left and right sides of these expressions are the same. In these formulas and in several others which have been derived the parameters are positive. In order to make efficient use of this adjustment procedure, it is necessary to have a large number of relations such as (39) with an evaluation of the deviation between the left and right sides as a function of s. The particular formula (39) which is chosen is then determined by matching the deviation of the first approximation to $f(s)$ with the deviations of relations (39).

By decomposing a given witch into a sufficiently large number of higher order witches, the given witch may be approximated as accurately as desired over any range. This type of approximation is very accurate for small values of s, but becomes poorer and poorer as s increases, eventually falling off too rapidly or too slowly according as we replace the given witch by higher order ones or by one of lower order. Due to this property, the method is well suited to adjusting the initial approximation which is poor only for large

TABLE II. Wollan's data for neon, $f_N(s)$ (obtained by interpolation from his results), and the fitted functions, $f_1(s)$ and $f_2(s)$.

s	$f_N(s)$	$f_1(s)$	$f_2(s)$
0	10.00	10.00	10.00
1	9.58	9.49	9.54
2	8.41	8.26	8.37
3	6.86	6.81	6.93
4	5.50	5.50	5.57
5	4.51	4.43	4.47
6	3.69	3.62	3.64
7	3.08	3.03	3.04
8	2.59	2.60	2.61
9	2.30	2.28	2.31
10	2.10	2.05	2.09
11	1.90	1.87	1.94
12	1.79	1.74	1.82

values of s if at all. Due to the large number of decompositions of a given witch this method is very flexible and with practice should permit adjustments leading to any desired degree of accuracy.

ERRORS

The examination of 22 different $f(s)$ curves, each with characteristic errors of varying magnitudes as compared to a reference $f(s)$ curve, and their corresponding positive $D(r)$ curves, has permitted an evaluation of the uncertainty in $D(r)$ to be expected from the uncertainties in an experimental $f(s)$. Two different types of functions were used to represent $f(s)$:

$$\sum_i a_i/(1+b_i s^2)^{n_i} \tag{40}$$

and

$$\sum_i a_i \exp(-k_i^2 s^2). \tag{41}$$

In both cases the corresponding $D(r)$ are positive if the parameters in (40) and (41) are positive. It was found that the nature and magnitude of the error in $D(r)$ depended essentially upon the nature and magnitude of the error in $f(s)$ over the interval for which experimental data are obtained, $0<s<s_0$ where s_0 ranges from about 30 to 40. The restriction imposed by the requirement that $D(r)$ be positive is indicated by the fact that the error in $D(r)$ was not sensitive to the form of the functions used. This is further born out by the fact that if an experimental $f(s)$ is extrapolated without the requirement that the associated $D(r)$ be positive, then no general conclusions concerning the character of the error in $D(r)$ may be drawn from an examination of $f(s)$ in the experimental range.

On the basis of our empirical evidence, the following estimates of the error in $D(r)$ as a function of the error in $f(s)$ were obtained:

I. If

$$\left.\begin{array}{lll} |\delta f|<\eta & \text{when} & 0<s<10 \\ \text{and} & & \\ |\delta f|<\epsilon & \text{when} & 10<s<30 \\ \text{then} & & \\ |\delta D|<2\epsilon+2\eta & \text{when} & 0.15<r<1.0 \\ |\delta D|<5\epsilon+2\eta & \text{when} & 0.10<r<1.0 \\ |\delta D|<10\epsilon+2\eta & \text{when} & 0.08<r<1.0 \end{array}\right\}. \tag{42}$$

II. If

$$\left.\begin{array}{lll} |\delta F|<\eta & \text{when} & 0<s<10 \\ \text{and} & & \\ |\delta F|<\epsilon & \text{when} & 10<s<40 \\ \text{then} & & \\ |\delta D|<\epsilon+2\eta & \text{when} & 0.08<r<1.0 \\ |\delta D|<2\epsilon+2\eta & \text{when} & 0.07<r<1.0 \\ |\delta D|<5\epsilon+2\eta & \text{when} & 0.05<r<1.0 \end{array}\right\}. \tag{43}$$

The quantity δF is the relative error in $F(s)$, δD is the relative error in $D(r)$, and $0<\eta<0.03$, $0.01<\epsilon<0.10$. It is assumed that as s approaches zero η approaches zero at least as rapidly as s^2. In this connection it should be noted that the value and first derivative of $f(s)$ are known at $s=0$. In order that the error in $D(r)$ for $r\leq 0.08$ be of the same order of magnitude as the experimental error, it is seen from (42) and (43) that data are required to $s=40$ and beyond.

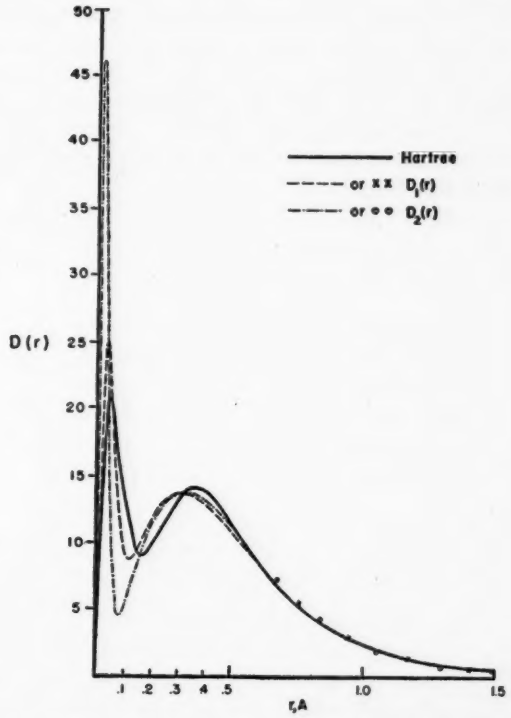

FIG. 1. The two distributions, $D_1(r)$ and $D_2(r)$, corresponding to the functions, $f_1(s)$ and $f_2(s)$, respectively, and the Hartree distribution for neon.

RESULTS

Neon

The application of this method to neon concerns the computation of the electron distribution from the ex-

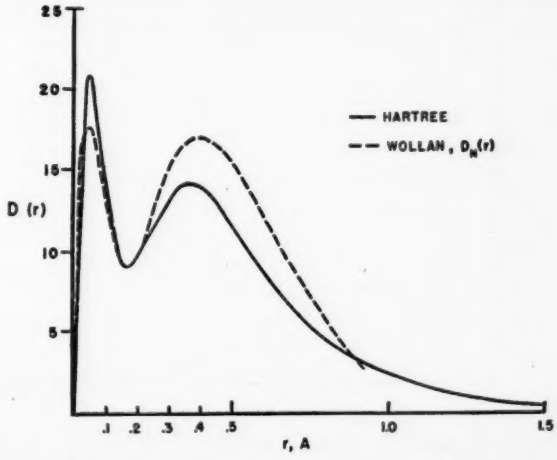

FIG. 2. Wollan's computation of the distribution, $D_N(r)$, corresponding to his data, $f_N(s)$, extrapolated to infinity using the function, $a\exp(-ks)$, and the Hartree distribution for neon.

perimental data of Wollan, although little accuracy can be expected for the inner region from experimental data which extends only to $s=12$. These results were compared with the Hartree distribution for neon.[6,17] The $f(s)$ data obtained by Wollan are given in the second column of Table II. The following functions were fitted to this data:

$$f_1(s)=\sum_{i=1}^{6}\frac{a_i}{(1+k_is^2)^2} \tag{44}$$

$a_1=1.4612$	$k_1=0.000\,28$
$a_2=0.1581$	$k_2=0.011\,00$
$a_3=6.0933$	$k_3=0.022\,60$
$a_4=0.4031$	$k_4=0.039\,899$
$a_5=1.5887$	$k_5=0.058\,40$
$a_6=0.2956$	$k_6=0.065\,00$

$$f_2(s)=\sum_{i=1}^{5}\frac{a_i}{(1+k_is^2)^2} \tag{45}$$

$a_1=1.509\,839$	$k_1=0.000\,077\,778$
$a_2=0.145\,649$	$k_2=0.013\,211$
$a_3=7.886\,528$	$k_3=0.027\,400$
$a_4=0.425\,280$	$k_4=0.042\,178$
$a_5=0.032\,704$	$k_5=0.111\,111.$

The functions $f_1(s)$ and $f_2(s)$ are tabulated in Table II. The two $D(r)$ corresponding to $f_1(s)$ and $f_2(s)$ are plotted in Fig. 1 along with the Hartree distribution. The result obtained from Wollan's data when extrapolated with the function $a\exp(-ks)$, where a and k are determined by the slope and magnitude of the data at the point of joining, is shown in Fig. 2.

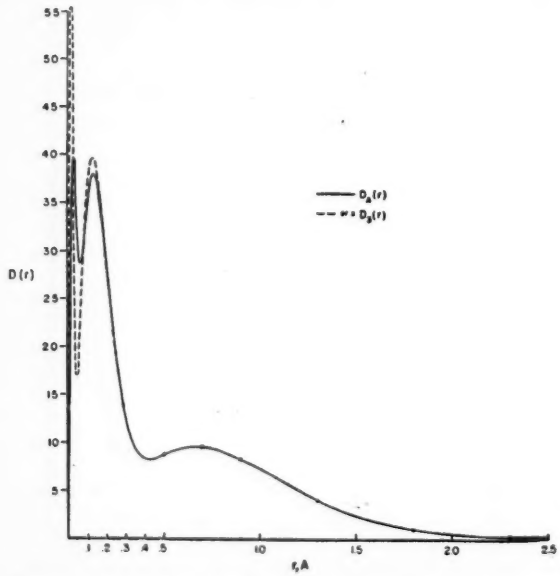

FIG. 3. An analytic distribution, $D_A(r)$, corresponding to the assumed scattering factor for argon, $f_A(s)$, and the distribution, $D_3(r)$, corresponding to the fitted function, $f_3(s)$.

[17] D. R. Hartree, Reports Prog. Phys. **11**, 113 (1946–47).

On the basis of the discussion of errors, it can be expected that very large errors may occur below $r=0.15$, since the experimental data are limited to $s<12$. This is in fact the case as may be seen in Fig. 1. The positive distributions, $D_1(r)$ and $D_2(r)$, however show a uniformly increasing accuracy with increasing r in agreement with the expected behavior of the error. A similar remark concerning $D_N(r)$ in Fig. 2, obtained using the $a\exp(-ks)$ extrapolation, cannot be made. In addition, a computation of the area under $D_N(r)$ shows an excess above the atomic number, 10, and therefore $D_N(r)$ must become negative for larger r in order that the total area be equal to the atomic number.

Argon

In order to study the application of the method to a more complicated atomic structure, a theoretical model for argon closely approximating the Hartree distribution was defined by means of an analytic function,[18]

$$\begin{aligned}D_A(r)=a_1r^2\exp[-r/(k_1)^{1/2}]/2k_1^{3/2}\\+a_2\left[\frac{7r^2}{256k_2^{3/2}}+\frac{7r^3}{256k_2^{4/2}}+\frac{3r^4}{256k_2^{5/2}}\right.\\\left.+\frac{r^5}{384k_2^{6/2}}+\frac{r^6}{3840k_2^{7/2}}\right]\exp[-r/(k_2)^{1/2}]\\+a_3\left[\frac{5r^2}{128k_3^{3/2}}+\frac{5r^3}{128k_3^{4/2}}+\frac{r^4}{64k_3^{5/2}}\right.\\\left.+\frac{r^5}{384k_3^{6/2}}\right]\exp[-r/(k_3)^{1/2}]\end{aligned} \tag{46}$$

$a_1=1.59$	$k_1=0.000\,144$
$a_2=6.95$	$k_2=0.000\,971$
$a_3=9.46$	$k_3=0.030\,999.$

By means of (2) the $f(s)$ corresponding to (46) has been computed. Values of this function $f_A(s)$ are given in the second column of Table III. This function was fitted

TABLE III. A theoretical scattering factor for argon [derived from (46)], and the fitted function $f_3(s)$.

s	$f_A(s)$	$f_3(s)$
0	18.000	18.000
2	13.651	13.652
4	9.181	9.183
8	6.441	6.442
12	4.696	4.698
16	3.313	3.313
20	2.391	2.390
24	1.839	1.842
30	1.406	1.437

[18] Experimental results for the scattering factor for argon have been neither sufficiently accurate nor sufficiently extensive to afford very much instructive information.

with six witches of the fifth order, giving,

$$f_3(s)=\sum_{i=1}^{6}\frac{a_i}{(1+k_i s^2)^5} \qquad (47)$$

$a_1=0.006$ $k_1=0.041\,667$
$a_2=9.436$ $k_2=0.031\,033$
$a_3=0.023$ $k_3=0.009\,167$
$a_4=7.217$ $k_4=0.001\,131$
$a_5=0.003$ $k_5=0.000\,833$
$a_6=1.315$ $k_6=0.000\,016\,667.$

The function $f_3(s)$ is tabulated in Table III. The agreement between the two functions is seen to be excellent for the smaller values of s. As s increases, the discrepancy increases to two percent at $s=30$. In Fig. 3 are shown the theoretical $D_A(r)$ and the distribution $D_3(r)$, obtained from the fitted function. It is seen that the two distributions agree very closely except at small values of r in accordance with the expected nature of the error.

In Fig. 4 is shown the result of computing an electron distribution from $f_A(s)$ in the range, $0\leq s\leq 24$, and extrapolating the curve to infinity by means of the function, $a\exp(-ks)$. Again the parameters a and k were chosen so that $a\exp(-ks)$ would agree in magnitude and slope with $f_A(s)$ at $s=24$. It is seen that the two inner maxima are not resolved, the error is relatively large, even for large r and a measurement of the area shows that the curve will eventually become negative.

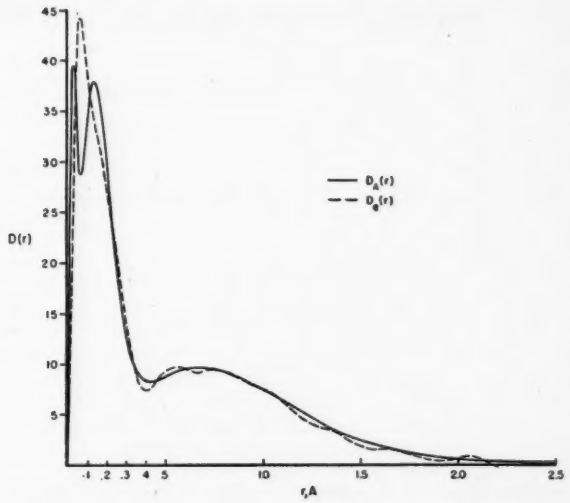

FIG. 4. An analytic distribution, $D_A(r)$, corresponding to the assumed scattering factor for argon, $f_A(s)$, and the distribution, $D_e(n)$, obtained from $f_A(s)$ extrapolated from $s=24$ to infinity by means of the function $a\exp(-ks)$.

CONCLUDING REMARKS

The method presented can be used with x-ray scattering from atoms. It should also prove fruitful with electron scattering but may require further theoretical investigation to improve the atomic scattering formulas. The application of atomic structure studies by the diffraction method to atoms in molecules is also an interesting possibility. It may determine the changes that occur in the electron distributions about atoms when they bind together to form a molecule.

The idea that there are special relationships between the scattering function and the structure of a scatterer which may be represented by a function of one sign is a concept whose usefulness extends beyond the particular application in this paper. Investigations have been in progress applying this idea to scattering experiments involving the determination of particle size and the structure of crystals.[12] In all cases the diffraction experiments yield a limited amount of data. The adjustment and extrapolation of these data consistent with the restrictions imposed by the positiveness of the function describing the structure increases the accuracy and detail of the conclusions that may be drawn.

We wish to thank the Computing Laboratory of the National Bureau of Standards for performing the numerical computations. We also wish to thank Mr. Walter Lynch for drawing the figures.

Molecular Dipole Moments and Stark Effects.* II. Stark Effects in OCS†

R. G. SHULMAN‡
Chemistry Department, Columbia University, New York, New York

AND

C. H. TOWNES
Physics Department, Columbia University, New York, New York

(Received October 3, 1949)

The dipole moments of OCS for several isotopic species and vibrational states have been determined from the Stark splitting of the $J=1\rightarrow 2$ rotational transition. The value of the $O^{16}C^{12}S^{32}$ moment is 0.7085 ± 0.004 debye units. The $O^{16}C^{12}S^{34}$ and $O^{16}C^{13}S^{32}$ moments differ from this by less than 0.2 percent. The $O^{16}C^{12}S^{32}$ molecule in the excited bending mode ($v_2=1$) is treated formally as a slightly asymmetric top which produces a doublet. Measurement of Stark effect for these lines gives a dipole moment of 0.700 ± 0.004 debye. Upon introduction of a Stark voltage, two weak lines appear on either side of the doublet $v_2=1$. They are explained as transitions involving the doublet levels which are forbidden in zero field, but allowed upon the introduction of a perturbing field.

INTRODUCTION

THE dipole moments of various vibrational states and isotopic species of OCS were determined as the first step in the investigation of the dipole moments of a number of other molecules. The dipole moments of OCS were measured partly because they could be compared with previous measurements[1,2] and because OCS is a linear molecule uncomplicated by nuclear quadrupole effects. It is hoped that the OCS dipole moment can conveniently be used as a standard for future dipole moment determinations.

The method employed was the splitting into components of the pure rotational transitions in the microwave region by the application of an external electric field. Upon applying the external field, the total angular momentum vector of the molecule is oriented at various discrete angles with respect to the field. The potential energy differences of the allowed orientations split the rotational energy levels and transitions.

This splitting for a linear molecule is:[3]

$$\Delta\nu=\frac{3M^2(16J^2+32J+10)-8J(J+1)^2(J+2)}{J(J+2)(2J-1)(2J+1)(2J+3)(2J+5)}\frac{\mu^2E^2}{h^2\nu_0}, \quad (1)$$

where the transition is from $J\rightarrow J+1$, M is the magnetic quantum number, μ is the permanent dipole moment of the molecule, ν_0 is the frequency of the pure rotational transition, E is the applied electric field, and $\Delta\nu$ is the difference in frequency between ν_0 and the frequency of the Stark component. Expression (1) assumes that $\Delta M=0$ for the transition, which is true in the convenient case where the applied electric field and the electric vector of the microwave radiation are parallel.

APPARATUS

The apparatus was a Stark modulation-type microwave spectroscope[4] of which Fig. 1 is a block diagram. The sweep from scope No. 1 is the controlling sweep of the equipment, being fed into scope No. 2 and the signal klystron repeller. The absorption cell is a 10-ft. section of wave guide immersed in a trough for temperature control. After passing through the absorption cell the signal is detected by the crystal detector, which can be biased by a small d.c. voltage to improve its performance, and from there fed into a transformer turned to the frequency of the modulating square wave, i.e., 50–200 kc. The signal is then amplified by a wide band Hewlitt Packard amplifier followed by a narrow band amplifier consisting of the r-f stage of a CWQ-46161-A TRF Navy receiver into the phase detector with a band width variable from 5 c.p.s. to about 200 c.p.s. The phase detector output is displayed on an oscilloscope.

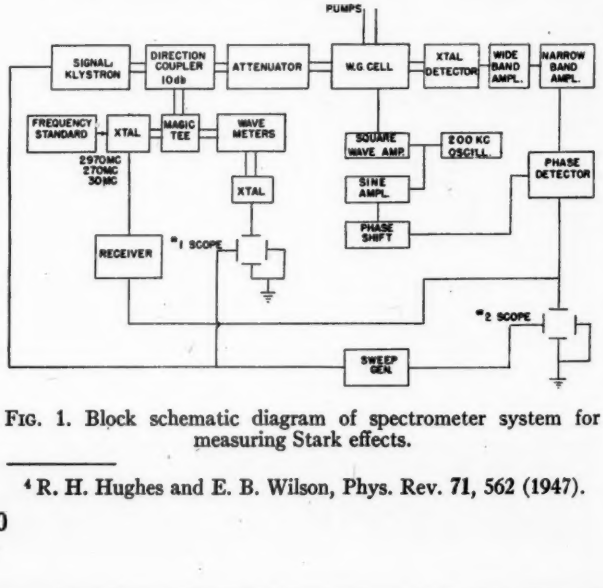

FIG. 1. Block schematic diagram of spectrometer system for measuring Stark effects.

* Work supported jointly by the Signal Corps and the ONR.

† Part of a dissertation submitted by R. G. Shulman in partial fulfillment of the requirements for a Ph.D. at Columbia University.

‡ Present address: Department of Chemistry, California Institute of Technology, Pasadena, California.

[1] Strandberg, Wentink, and Kyhl, Phys. Rev. **75**, 270 (1949).

[2] Dakin, Good, and Coles, Phys. Rev. **71**, 640 (1947).

[3] R. De E. Kronig, Proc. Nat. Acad. Sci. **12**, 488 (1926).

[4] R. H. Hughes and E. B. Wilson, Phys. Rev. **71**, 562 (1947).

Frequencies were measured at first by beating the output of a d.c. Pound stabilizer[5] with the source klystron.[6] Subsequently, the stabilized frequency was replaced by the harmonic output of a 2K47 frequency multiplier klystron supplied by 270 Mc multiplied up from a 7.5-Mc crystal.

The modulating Stark voltage is connected to an electrode in the guide so that the electric field is parallel to the electric field of the radiation being transmitted through the guide in the prevailing TE_{01} mode (see Fig. 2).

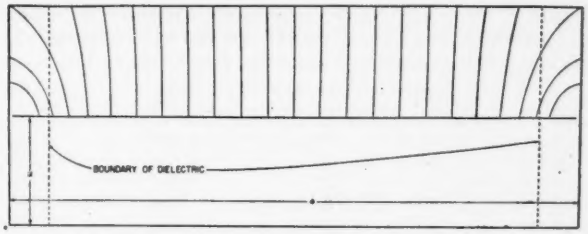

FIG. 2. Cross section of Stark wave guide and applied electric field.

EXPERIMENTAL METHOD

Examination of Eq. (1) shows that in order to determine μ for a rotational transition where J and ν_0 are known, it is necessary to measure $\Delta\nu$ and E.

The field strength, E, in volts/cm, is a function of the applied voltage and the spacing between the electrode and the walls of the guide. A cross section of the wave guide absorption cell is shown in Fig. 2.

A variable d.c. voltage with a superimposed 50-kc square wave of variable amplitude was applied to the guide electrode. The resulting scope presentation is shown in Fig. 3. The components above the line correspond in phase to the lower half of the 50-kc square wave and the components below correspond to the upper half of the square wave. When the lower half of the square wave is at zero volts with respect to the wave guide walls, then the upward deflection on the oscilloscope corresponds to the undisplaced frequency, ν_0, of the transition.

When the d.c. was increased, the separation was increased until it was possible to measure the frequency of the top and bottom components. The average of the top displacement and the bottom displacement was considered as a first and usually good approximation to be the displacement corresponding to the d.c. voltage.

The $O^{16}C^{12}S^{32}$ $J=1\rightarrow2$ rotational transition of the ground vibrational state had been measured at 24,325.92 Mc.[2] The dipole moment for this transition was determined by measuring the frequency difference between the $M=0$ component which splits to lower frequencies and the $M=\pm1$ component which splits to higher frequencies. This difference is called $\Delta\nu$ in Table I.

A weighted average of the dipole moment is $\mu=0.7119$ debye units and applying corrections for field inhomogeneities, voltage measurement, and electrode slippage, as noted below, $\mu=0.7085$ debye units.

A change of dipole moment of OCS with change of isotopic species has previously been reported.[1] $O^{16}C^{12}S^{34}$ has an abundance of four percent and its $J=1\rightarrow2$ transition occurs at 23,731.33 Mc.[2] The splitting of this line relative to the splitting of the $O^{16}C^{12}S^{32}$ line was measured at several fixed values of Stark voltage. If the dipole moments for both transitions were equal then for the same voltage from Eq. (1),

$$\frac{\Delta\nu_{O^{16}C^{12}S^{34}}}{\Delta\nu_{O^{16}C^{12}S^{32}}}=\frac{\nu_{0O^{16}C^{12}S^{32}}}{\nu_{0O^{16}C^{12}S^{34}}}=1.0251. \quad (2)$$

The experimental results of Table II indicate that within 0.2 percent (the accuracy of these measurements), the dipole moments are equal.

The isotopic species $O^{16}C^{13}S^{32}$ has a natural abundance of 1.1 percent and its $J=1\rightarrow2$ transition occurs[5] at 24,247.76 Mc. If the dipole moment of this transition equals the dipole moment of the $O^{16}C^{12}S^{32}$ transition, then from (1),

$$(\Delta\nu_{O^{16}C^{13}S^{32}})/(\Delta\nu_{O^{16}C^{12}S^{32}})=1.0032. \quad (3)$$

The experimental results of Table III show that the dipole moments are equal to within 0.2 percent.

Strandberg, Wentink, and Kyhl,[1] using a similar method, have reported that $\mu_{O^{16}C^{12}S^{32}}=0.732$ and $\mu_{O^{16}C^{13}S^{32}}=0.722$. This rather large (1.4 percent) change of dipole moment with change of isotopic species is hence in disagreement with the present experiments. Variations of several percent in dipole moment values have been reported by Strandberg *et al.* for changes of vibrational state in OCSe[7] and for OCS as discussed below. The variation of dipole moment with nuclear mass can be attributed to different amplitudes of

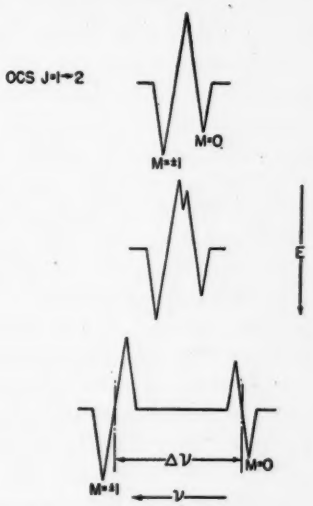

FIG. 3. Appearance on oscilloscope of microwave absorption line split into two Stark components.

[5] R. V. Pound, M.I.T. Rad. Lab. Report No. 837 (October, 1945).

[6] Townes, Holden, and Merritt, Phys. Rev. 74, 1113 (1948).

[7] Strandberg, Wentink, and Hill, Phys. Rev. 75, 827 (1949).

TABLE I. Stark splitting $\Delta\nu$ between $M=0$ and $M=\pm1$ components of $J=1\rightarrow2$ transition as a function of field strength.

$\Delta\nu$ (Mc)	Guide No.	Volts applied (practical units)	Volts e.s.u./cm	Debye units
5.13	1	251.2	4.398	0.7160
8.14	1	317.5	5.558	0.7135
19.23	1	487.6	8.536	0.7140
19.98	1	493.2	8.634	0.7195
20.49	1	501.4	8.778	0.7167
27.09	1	576.8	10.098	0.7163
32.10	1	630.1	11.031	0.7137
				Average=0.7157
4.01	2	503.9	3.947	0.7061
12.54	2	885.0	6.932	0.7123
15.05	2	958.5	7.508	0.7201
15.60	2	994.9	7.793	0.7067
18.02	2	1071.4	8.393	0.7054
				Average=0.7101
12.34	3	363.9	6.920	0.7065
23.55	3	503.1	9.567	0.7049
23.60	3	503.0	9.565	0.7060
24.56	3	509.1	9.681	0.7113
29.88	3	564.4	10.733	0.7077
36.27	3	618.3	11.758	0.7120
				Average=0.7079

TABLE II. Stark splitting of $O^{16}C^{12}S^{32}$ and $O^{16}C^{12}S^{34}$ lines for identical fields.

$\Delta\nu_{O^{16}C^{12}S^{32}}$	$\Delta\nu_{O^{16}C^{12}S^{34}}$	Ratio
30.81	31.76	1.0308
49.98	51.12	1.0228
57.45	58.79	1.0233
83.13	85.13	1.0241
		Average=1.0252

TABLE III. Stark splitting of $O^{16}C^{12}S^{32}$ and $O^{16}C^{12}S^{32}$ lines for identical fields.

$\Delta\nu_{O^{16}C^{12}S^{32}}$	$\Delta\nu_{O^{16}C^{12}S^{32}}$	Ratio
24.56	24.59	1.0012
33.33	33.48	1.0045
44.13	44.15	1.0005
43.33	43.51	1.0042
52.69	53.11	1.0080
56.21	56.49	1.0050
		Average=1.0047

vibration in the ground state. Since the change of dipole moment with vibrational excitation and also the change with different isotopic species are both caused by the same type of distortion of the molecule, it seems reasonable to expect the more violent changes of vibrational state to have considerably more effect than a 10 percent difference of nuclear mass.

DISCUSSION OF ERRORS

Five possible sources of error were considered. Two of these sources produce only negligible errors, but the other three required the introduction of small corrections. The errors considered are listed.

First, the measurement of the d.c. voltage. The a.c. component of the Stark voltage was by-passed to ground by an L-C filter. The d.c. was then led to a voltage divider network, and thence into a Leeds and Northrup Type K potentiometer. The accuracy of this measurement was better than 0.01 percent and errors from this source are negligible.

Second were errors in the determination of the spacing between the electrode and the walls of the wave guide. Three different wave guides with different electrode spacings were used in order to minimize this error. Two X-band guides with internal dimensions 1.016×2.286 cm and one K-band guide with dimensions 0.4318×1.067 cm were used. The electrode thicknesses were 0.6350 cm, 0.1651 cm, and 0.0813 cm, respectively, and the average distances between the electrodes and the walls were 0.1904 ± 0.0005 cm, 0.4255 ± 0.0005 cm, and 0.1753 ± 0.0005 cm (see Table IV). The internal dimensions of guides were only measured at the ends. However, the dimensions at the ends of various sections of guides from the same lot were also measured and in all cases the average dimensions were within 0.07 percent of the values given above.

The third source of error considered was unequal spacing between the electrode and the top and bottom walls of the wave guide. This would arise if the polystyrene runners supporting the electrode in the guide were not centered (see Fig. 2). If the polystyrene were at all points snug along the bottom of the guide, the difference between the top and bottom septum to guide spacings would be 0.01 cm. For an average difference of displacement which is two percent of the spacing, the true value of the dipole moment is 0.12 percent smaller than the measured value. A correction of -0.08 percent was made to the measured value of the dipole moment to allow for a possible error from this source.

The fourth source of error was the assumption that by averaging the displacements caused by the top and bottom of the applied square wave, a splitting corresponding to the d.c. voltage was measured. Since the displacement is proportional to the square of the voltage, this introduces a consistent second-order error which can be corrected. Let the d.c. volts$=E_0$ and the peak-to-peak square wave voltage equal $2E$. We have measured a displacement which equals

$$\tfrac{1}{2}K[(E_0+E)^2+(E_0-E)^2]$$

and called this $=KE_0^2$. The difference in displacement is KE^2 and the fractional difference is E^2/E_0^2. Since experimentally, $E/E_0\approx1/30$, then the average correction applied to the dipole moment is 0.11 percent with the true value smaller than the measured by this amount.

The fifth error was due to field inhomogeneities in the wave guides. A first look at Fig. 2, showing the variation of electric field in the guide, may give the

impression that an accurate determination of dipole moments in such an inhomogeneous field is impractical. However, since the microwave intensity is greatest in the center of the guide and decreases to zero at the outer walls, a large majority of the absorption processes take place in the more homogeneous central region of the field. In addition, it will be shown that the primary effect of inhomogeneities is to broaden the Stark component lines but not to shift their centers of gravity. As long as the absorption line is nearly symmetric in shape, only changes of the centers of gravity will produce errors in the dipole moments. Corrections to dipole moments due to field inhomogeneities were calculated and applied but were less than one percent for each of the three guides used.

In order to find the field strength of the applied Stark voltages, conformal transformations were used which give an exact solution for the field in a wave guide of the same general construction as that used, but without the thin strips of supporting dielectric, and with the wide dimension of the wave guide cross section infinitely large compared with the narrow dimension ($a \gg d$).

Figure 4 shows the nature of the transformations and the configuration actually solved.

If $c_1=\exp[\frac{1}{2}\pi(U+iV)]$, where V is the potential and U the stream function, then the positive x_1 axis is at potential and the positive y_1 axis is at unit potential. The z_1 plane is transformed into the z_2 plane by the Schwarz transformation[8] $z_2=2\pi \sin^{-1}z_1$ which gives

$$E_x=-\partial V/\partial x = 1/[\coth\pi y/2 \sin^2\pi x/2+\tanh\pi y/2 \cos^2\pi x/2] \quad (4)$$

$$E_y=-\partial V/\partial y -1/[\tan\pi x/2 \cosh^2\pi y/2+\cot\pi x/2 \sinh^2\pi y/2]. \quad (5)$$

E_x approaches the constant value one, and E_y approaches zero, when y is large. If the large cross-sectional dimension of the wave guide (along the y axis of z_2) is much greater than the small dimension ($a \gg d$), then Eqs. (4) and (5) give good approximations to the field from the edge of the wave guide to the center. In the case of the actual wave guide, E_y must be zero and E_x equal to one at the center. For the wave guides used $a>5d$ and the above equations give $|E_y|<0.003$ and $1.000>E_x>0.993$ at the center of the guide

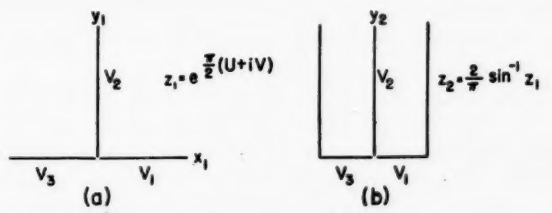

FIG. 4. (a) Configuration for which the electric field distribution is solved and (b) conformal transformation used.

[8] W. R. Smythe, *Static and Dynamic Electricity* (McGraw-Hill Book Company, Inc., New York, 1939), p. 80.

TABLE IV. Dimensions of wave guides used.

Guide	Int. dimensions	Electrode thickness	Electrode spacing	1/electrode spacing
1	1.016 ×2.286 cm	0.6350 cm	0.1904±0.0005	5.252
2	1.016 ×2.286 cm	0.1651 cm	0.4255±0.0005	2.350
3	0.4318×1.067 cm	0.0813 cm	0.1753±0.0005	5.705

($y=1/2a$), so that they represent a very good approximation to the case of a wave guide without supporting dielectric material.

Now consider the effect on the center of a Stark component of the deviations from a uniform field ($E_x=1$, $E_y=0$). For a second-order Stark displacement, the frequency shift, $\Delta\nu$, produced by a field E, is $\Delta\nu=CE^2$, where C is some constant. The intensity of the microwave energy in the TE_{01} mode varies with y as $\sin^2\pi y/a$. The transitions of primary importance are those which the angular momentum about the x axis does not change ($\Delta M=0$). The number of such transitions is proportional to the microwave intensity and the square of the cosine of the angle between the microwave electric field (always parallel to the x axis) and the Stark electric field, or proportional to $(\sin^2\pi y/a)(E_x^2)/(E^2)$. Hence, the average displacement of a Stark component of this type is

$$\langle\Delta\nu\rangle_{Av}=\frac{\int CE^2 \sin^2\pi y/a(E_x^2/E^2)dxdy}{\int \sin^2\pi y/a(E_x^2/E^2)dxdy}, \quad (6)$$

where the integration need be taken only over one-quarter of the cross-sectional area of the guide, on one side of the septum and between the center and one wall.

Setting $E_x=E_{x0}+\delta E_x$ where E_{x0} is the field strength in the center of the guide, $(\delta E_x)/(E_{x0})\ll 1$ and $(E_y)/(E_{x0})\ll 1$, Eq. (6) may be approximated as

$$\langle\Delta\nu\rangle_{Av}=CE_{x0}^2\Big[1+2E_{x0}\int\delta E_x dx + \frac{4}{aE_{x0}^2}\Big\{\int \sin^2\pi y/a\,\delta E_x^2 dxdy + \int \sin^2\pi y/a\,E_y^2 dxdy\Big\}\Big]. \quad (7)$$

Since the potential between the septum and the wave guide is fixed, $\int(E_{x0}+\delta E_x)dx=$ constant and hence $\int\delta E_x dx=0$, and the fractional error in $\langle\Delta\nu\rangle_{Av}$ produced by field inhomogeneities is

$$\frac{4}{aE_{x0}^2}\Big\{\int \sin^2\pi y/a\,\delta E_x^2 dxdy+\int \sin^2\pi y/a\,E_y^2 dxdy\Big\}. \quad (8)$$

The dimension d of the wave guide is taken to be one in these expressions. It should be noted that the field

TABLE V. Stark splitting and resulting dipole moment of OCS excited state $v_2=1$.

$\Delta\nu$ meas. Mc	μdebye units
− 6.98	0.6984
−18.60	0.7037
−28.08	0.7033
−28.52	0.6974

Average = 0.7007±0.0014 debye units and the corrected value is 0.7000±0.004 debye. This agrees with the value of 0.701±0.007 debye found by Hill *et al.*[8] for this vibrational state.

[8] A. G. Hill, M.I.T. Research Lab. of Electronics Quarterly Progress Report (October 15, 1948).

variation qE_x produces a broadening of the Stark line, but according to (8) does not in first-order approximation shift the line's center. E_y and δE_x may be obtained from (4) and (5) and the integrals of (8) evaluated numerically. δE_x can be expressed in the rather simple form

$$\delta E_x=\frac{e^{-\pi y}-\cos\pi x}{\cosh\pi y-\cos\pi x}. \tag{9}$$

Similarly, for a first-order Stark component where $\Delta\nu=C'E$, the fractional error in $\langle\Delta\nu\rangle_{Av}$ may be found to be

$$\frac{2}{aE_{x_0}^2}\int \sin^2\pi y/aE_y^2dxdy. \tag{10}$$

As confirmation that these integrals are not large, it may be observed that the relative intensity of Stark components with change of M ($\Delta M=\pm1$) to those with no change of M ($\Delta M=0$) is given by the same type of integral. Since no components associated with a change in M have been observed in the guides used, their intensities are small.

The presence of the thin strip of supporting dielectric material at the wave guide walls was partially allowed for by solving exactly for the microwave intensity instead of using the simple form $\sin^2\pi y/a$ of the above formulas. The effect of the dielectric on the Stark field, which was not considered, is probably small.

Numerical integration of the two terms of (8) over y shows that for each value of x the integrals are almost exactly equal. No general proof of this could be found, however.

For second-order Stark components, the fractional correction to the dipole moments is just one-half of that for the displacement $\Delta\nu$. The dipole moment correction was found to be −0.1 percent for guide No. 3 and −0.6 percent for guide No. 2. For guide No. 1 a correction of −0.1 percent was estimated.

VIBRATIONAL-ROTATION INTERACTION

The rotational transitions discussed above are due to changes of rotational level where both initial and final levels are in the ground vibrational state. At room temperature, about eight percent of the OCS molecules are in the first excited state of the perpendicular vibration ν_2. The spectrum due to the $J=1\rightarrow2$ rotational transition of $O^{16}C^{12}S^{32}$ in this state consists of two lines at 24,355.50 Mc and 24,380.84 Mc.[2] These lines, the so-called l-type doublets, are not at the same frequency as the ground state line because of vibration rotation interaction.

The frequency of a rotational transition $J-1\rightarrow J$ of a linear molecule is

$$\nu=2B_vJ, \tag{11}$$

where

$$B_v=B_e-\sum_i\alpha_i(v_i+d_i/2), \tag{12}$$

and B_e = rotational constant if the nuclei were stationary at their equilibrium positions. α_i is a coefficient of the change of rotational constant per quantum of excitation of the ith vibrational state and v_i and d_i are the corresponding quantum number and degree of degeneracy of the vibration.

The change in vibrational state therefore produces a shift in frequency of the line. However, for the explanation of the doublet structure, the vibration-rotation interaction Hamiltonian of this type of degenerate vibration must be considered.

The total wave function, to a first order of approximation, which is a solution of the rotation-vibration interaction Hamiltonian is, according to Nielsen[9]

$$\psi=\Pi_S\exp(-q_s^2/2)H_{v_s}(q_s)\Pi_R \times\exp(-\rho_r^2/2)F_{\rho_r}{}^{l_r}(\rho_r)\exp(\pm il_r\phi_r)\psi_R{}^0, \tag{13}$$

where $\Pi_S\exp(-q_s^2/2)H_{v_s}(q_s)$ and $\Pi_R\exp(-\rho_r^2/2)\times F_{\rho_r}{}^{l_r}(\rho_r)$ are the contributions of the normal vibrations, $l_rh/2\pi$ is the angular momentum about the symmetry axis due to vibration and $\psi_R{}^0$ is the pure rotational part of the wave function.

The angular dependence or what may be considered the rotational part of this wave function is identical with the rotational wave function for the slightly asymmetric top. This may be expected since the degenerate vibration introduces an angular momentum around the molecular symmetry axis similar to the angular momentum K for a symmetric top. In addition, the vibration-rotation interaction splits the degenerate bending modes in a way similar to the splitting of symmetric top levels by a slight asymmetry.

If the amount of splitting is calculated from the rotation-vibration interaction, or empirically evaluated, a linear molecule in an excited bending mode may thus be treated as a slightly asymmetric rotor.

Since notation, matrix elements, and Stark effects have been well established for the asymmetric top, we shall treat the OCS molecule as a slightly asymmetric prolate rotor. Using the asymmetric rotor notation $J_{\tau M}$, where τ is a pseudo-quantum number, the l-type doublets correspond to the transitions $1_{0M}\rightarrow2_{-1M}$ and $1_{1M}\rightarrow2_{0M}$.

[9] H. H. Nielsen, Phys. Rev. 60, 794 (1941).

EXCITED STATE DIPOLE MOMENT

The Stark effect for the slightly asymmetric top has been derived[10] as a function of the energy difference between the near degenerate levels, the matrix element of transition between these levels, and the dipole moment of the molecule. Using the $J\tau M$ notation, upon the application of an external field E, the energy levels are

$$W=\tfrac{1}{2}[H(J\tau M)+H(J\tau' M) \pm([H(J\tau M)-H(J\tau' M)]^2+4\mu^2E^2\Phi^2)^{\frac{1}{2}}], \quad (14)$$

where

$$H_{(J\tau M)}=W_{J\tau}{}^0+E^2\sum_{J\tau\varrho}{}' \frac{\mu_\varrho{}^2[(\Phi_{z\varrho})_{J\tau M,\ J'\tau' M}]^2}{W_{J\tau}{}^0-W_{J'\tau'}{}^0}.$$

The summation is over all levels where $W_{J\tau}{}^0\neq W_{J'\tau'}{}^0$ and $\Phi_{z\varrho}$ is the matrix element of direction cosine.

If we let ν_0 be the frequency of the hypothetical transition between the center of the doublet levels for $J=1$ and the center for $J=2$, then for any value of E

$$\nu_0=\frac{\tfrac{1}{2}[H(20M)+H(2-1M)-H(11M)-H(10M)]}{h}. \quad (15)$$

The separation between the two doublet lines is

$$\Delta\nu=\{(H(20M)-H(2-1M))^2+4\mu^2E^2\Phi_{22}{}^2\}^{\frac{1}{2}} -\{(H(11M)-H(10M))^2+4\mu^2E^2\Phi_{11}{}^2\}^{\frac{1}{2}}. \quad (16)$$

Using this formula, Table V shows the values of dipole moment measured for this transition.

In measuring $\Delta\nu$, the interval between the components was measured. In this way the second-order shifting of the levels is negligible.

ANOMALOUS LINES

Two weak lines symmetrically situated on either side of the l-type doublets were observed upon the application of a Stark field. The lines first appear, with very weak fields, separated by about twice the separation of the doublets themselves. With increasing voltage these lines move apart in frequency and increase in intensity, passing through a maximum intensity and eventually fading out.

These lines are explained by considering them as corresponding to the transitions of the perturbed $1_{0M}\rightarrow 2_{0M}$ and $1_{1M}\rightarrow 2_{-1M}$ levels, forbidden in the absence of a field but allowed in the presence of a field.

Consider the unperturbed wave functions to be $A_{20}{}^0$, $A_{2-1}{}^0$, $A_{11}{}^0$, and $A_{10}{}^0$ and the perturbed functions

$$\begin{aligned}\psi_1&=a_1A_{20}{}^0+b_1A_{2-1}{}^0\\ \psi_2&=a_2A_{20}{}^0-b_2A_{2-1}{}^0\\ \psi_3&=a_3A_{11}{}^0+b_3A_{10}{}^0\\ \psi_4&=a_4A_{11}{}^0-b_4A_{10}{}^0.\end{aligned} \quad (17)$$

The Hamiltonian including the field is $H_0-E\sum_\varrho\Phi_{z\varrho}\mu_\varrho$ ignoring the contribution of polarization by the field.

[10] S. Golden and E. B. Wilson, J. Chem. Phys. 16, 669 (1948).

Since the wave function of the original level can be considered as comprising two complete orthonormal sets of two members each then

$$\begin{aligned}b_1&=a_2 \quad a_1=b_2\\ b_3&=a_4 \quad a_3=b_4\end{aligned} \quad (18)$$

and the complete solution yields

$$a_1=\left[\frac{(W_1-W_{2-1}{}^0)^2}{(\mu^2E^2/36)+(W_1-W_{2-1}{}^0)^2}\right]^{\frac{1}{2}}$$

$$b_1=\left[\frac{\mu^2E^2/36}{(\mu^2E^2/36)+(W_1-W_{2-1}{}^0)^2}\right]^{\frac{1}{2}}$$

$$a_3=\left[\frac{(W_3-W_{10}{}^0)^2}{(\mu^2E^2/4)+(W_3-W_{10}{}^0)^2}\right]^{\frac{1}{2}}$$

$$b_3=\left[\frac{\mu^2E^2/4}{(\mu^2E^2/4)+(W_3-W_{10}{}^0)^2}\right]^{\frac{1}{2}}$$

where

$$W_1=\tfrac{1}{2}[W_{20}{}^0+W_{2-1}{}^0+\{(W_{20}{}^0-W_{2-1}{}^0)^2 +4\mu^2E^2\Phi^2_{20M,\,2-1M}\}^{\frac{1}{2}}]$$
$$W_3=\tfrac{1}{2}[W_{11}{}^0+W_{10}{}^0+\{(W_{11}{}^0-W_{10}{}^0)^2 +4\mu^2E^2\Phi^2_{11M,\,10M}\}^{\frac{1}{2}}] \quad (19)$$

and where

$$\Phi^2_{20M-1,\,2-1M-1}=1/36, \quad \Phi^2_{11M-1,\,10M-1}=\tfrac{1}{4}.$$

The separation of these anomalous lines from each other then is

$$\Delta\nu=\{(W_{20}{}^0-W_{2-1}{}^0)^2+(\mu^2E^2/9)\}^{\frac{1}{2}} +\{(W_{11}{}^0-W_{10}{}^0)^2+\mu^2E^2\}^{\frac{1}{2}}, \quad (20)$$

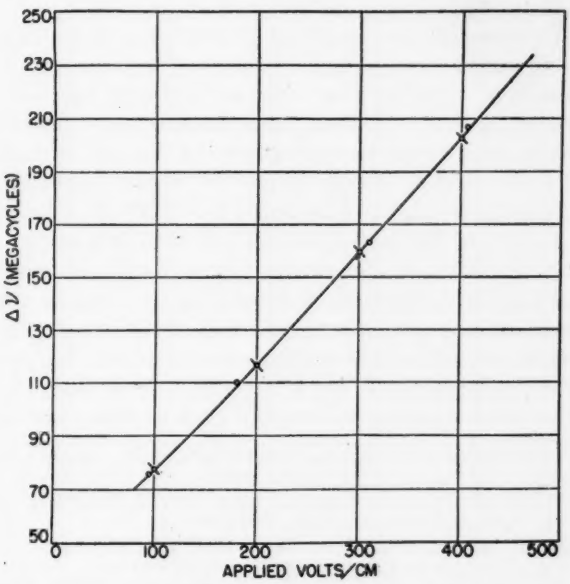

FIG. 5. Frequency difference between anomalous lines as a function of field strength.

where $W_{20}^0-W_{2-1}^0=37.82$ mc, $W_{11}^0-W_{10}^0=12.60$ mc, and $\mu=0.700$ debye units.

The plot of theoretical separation *vs.* field strength (see Fig. 5) agrees with the plot of experimental separation *vs.* field strength to within 0.5 percent. The intensities of both components are the same and are proportional to $[a_1^2a_4^2-2a_1a_4b_1b_4+b_1^2b_4^2]$. This expression varies from zero when the field is zero through a maximum as the field increases and decreases to zero again for large fields. Rough intensity measurements showed that the intensity followed the theoretical expectations.

ACKNOWLEDGMENT

The spectrometer described above was built through the combined efforts of a number of people. The authors wish to acknowledge especially the assistance of Messrs. K. Rusinow, S. Geschwind, A. W. Costello, and E. Richter.

PHYSICAL REVIEW VOLUME 77, NUMBER 4 FEBRUARY 15, 1950

Some General Properties of Nuclear Reaction and Scattering Cross Sections*

T. TEICHMANN
Princeton University, Princeton, New Jersey
(Received October 21, 1949)

This paper deals with some general properties of nuclear reaction and scattering cross sections which can be derived from the dispersion-theoretic treatment of nuclear reactions as given, for example, by Wigner and Eisenbud. The form of the cross section near the resonances is found to satisfy the Breit-Wigner formula with corrections of the order Γ^2/D^2, Γ=level width, D=level spacing. In the region between the resonances, the behavior is found to be of three types. In the first two types, simple minima occur differing in order of magnitude in the two cases by a factor Γ^2/D^2. In the third type, a flat non-resonance maximum occurs between the resonances considered, accompanied by two minima. This type of behavior may be associated with a large fluctuation of Γ or D at some of the neighboring levels. The cross sections are explicitly calculated for some special choices of the Γ and D, and the averages compared with those of the statistical theory. The effect of the potential scattering on the scattering cross sections is briefly discussed.

I. INTRODUCTORY REMARKS

IT is the purpose of this paper to investigate in a more or less quantitative manner the behavior of nuclear reaction and scattering cross sections both near and between the resonances, using as a basis the results of the formal (dispersion) theory of nuclear reactions.[1–5]

These results are concerned first with the estimation of the maxima and minima of the cross sections (corresponding to the behavior near and between the resonances), both of which may be derived from the general theory, even when the explicit form of the cross section as a function of energy cannot be easily calculated, provided only that it is assumed that $\Gamma/D\ll1$, Γ being the width of the resonance lines and D their spacing.

On the basis of more far-reaching assumptions about the nuclear parameters, it is possible to calculate the cross sections explicitly as functions of the energy; the results so obtained serve to indicate what may happen if the assumption $\Gamma/D<1$ is relaxed. It is then also possible to calculate the average cross sections, and to compare the results thus obtained with those obtained from the statistical theory,[6] which serves to clarify the connection between the quantities occurring in the latter and the parameters of nuclear dispersion theory.

II. NOTATION

The following results or definitions are used in the remaining sections:

σ_{st} denotes the cross section for the reaction in which the pair of particles denoted by "s" collide to form the pair "t." In particular, σ_{ss} denotes the scattering cross section for the collision of the pair "s." As is usual in this work, "s," "t," etc., denote not only the type of particles, but also their internal states, their spin orientation, and their relative angular momentum. If there are n such possible reactions "st" associated with the same compound nucleus in a given energy range, then σ_{st} may be expressed, in this energy range, in terms of the n-dimensional, symmetric, unitary collision matrix U by the formula

$$\sigma_{st}=(\pi/k_s^2)\,|(U-1)_{st}|^2. \tag{2.1}$$

k_s is the relative (reduced) wave number of the pair "s" in their center-of-mass system. U itself may be expressed in terms of the diagonal "potential" matrices B, C, and ω, and the real symmetric "derivative"

* This paper contains some results of a Ph.D. dissertation submitted to Princeton University (1949).
[1] E. P. Wigner and L. Eisenbud, Phys. Rev. **72**, 29 (1947).
[2] E. P. Wigner, Phys. Rev. **73**, 1002 (1948).
[3] E. P. Wigner, Am. J. Phys. **17**, 99 (1949).
[4] E. P. Wigner and T. Teichmann (unpublished).
[5] T. Teichmann, Ph.D. dissertation, Princeton (1949). This reference contains further details of the methods described in this paper.
[6] V. F. Weisskopf, Phys. Rev. **52**, 295 (1937).

matrix R, by[7]

$$U=\omega\frac{1-iC+iBRB}{1+iC-iBRB}\omega. \tag{2.2}$$

Here the diagonal matrices B, C, and ω are determined by the behavior of the relative wave functions of the pairs "s," etc., in the external (separated) region. If $r_s\varphi_s$ denotes the relative wave function for the pair "s" in the external region (r_s being the separation of the pair), then

$$\omega_s=(i\varphi_s')/|\varphi_s'|, \tag{2.3}$$

$$1/B_s^2=Im(\varphi_s/\varphi_s'), \tag{2.4}$$

and

$$C_s=B_s^2Re(\varphi_s/\varphi_s'), \tag{2.5}$$

all these quantities being evaluated at $r_s=a_s$, where a_s is the approximate range of the nuclear force between the pair "s." The prime denotes differentiation with respect to r_s. Tables of these quantities are given, for example, by Wigner[2] and Wigner and Eisenbud.[4]† ω_s may be written in the form

$$\omega_s=\exp(ix_s) \tag{2.6}$$

and for zero angular momentum neutrons x_s is simply given by

$$x_s=k_sa_s, \tag{2.7}$$

while

$$B_s^2=k_s, \quad C_s=0. \tag{2.8}$$

In general, $B_s^2/(1+C_s^2)$ is simply k_s times the barrier penetration factor P_s for the combined Coulomb and centrifugal potentials for the pair "s."

The symmetric matrix R is determined purely by intranuclear effects (i.e., by properties of the compound state). Its elements have the form

$$R_{st}=\sum_\lambda\gamma_{\lambda s}\gamma_{\lambda t}/(E_\lambda-E), \tag{2.9}$$

E being the energy. The (constant) parameters $\gamma_{\lambda s}$ and E_λ have been discussed elsewhere.[4]

The quantities

$$\Gamma_{\lambda s}=2B_s^2\gamma_{\lambda s}^2/(1+C_s^2) \tag{2.10}$$

and

$$\Gamma_\lambda=\sum_s\Gamma_{\lambda s} \tag{2.11}$$

are defined to be the partial width for the process "s" and the total width, respectively, at the level λ (i.e., $E=E_\lambda$), while

$$\Delta_{\lambda s}=-C_sB_s^2\gamma_{\lambda s}^2/(1+C_s^2) \tag{2.12}$$

and

$$\Delta_\lambda=\sum_s\Delta_{\lambda s} \tag{2.13}$$

may be regarded, respectively, as the partial level shift for the process "s" and the total level shift at the level λ. D denotes the level spacing

$$D=\langle E_{\lambda+1}-E_\lambda\rangle_{Av}. \tag{2.14}$$

For many purposes it is convenient to use the matrix

$$V=\frac{2i(BRB-C)}{1+iC-iBRB}. \tag{2.15}$$

The cross sections then become

$$\sigma_{st}=(\pi/k_s^2)\{|V_{st}|^2+4\delta_{st}[\sin^2x_s+|V_{ss}|\sin x_s\sin(x_s+\theta_{ss})]\}, \tag{2.16}$$

where

$$V_{st}=|V_{st}|\exp(i\theta_{st}).$$

Equation (2.16) corresponds to an approximate division of the cross section into the contribution due to purely nuclear reaction or scattering [*viz.*, $(\pi/k_s^2)|V_{st}|^2$], that due to purely potential scattering [$(4\pi/k_s^2)\sin^2x_s\cdot\delta_{st}$], and the interference between potential and nuclear effects

$$[(4\pi/k_s^2)|V_{ss}|\sin x_s\cdot\sin(x_s+\theta_{ss})\cdot\delta_{st}].$$

This separation is not exact because of the part played by the potential matrix C in V; its effect on the reaction cross sections is, however, not very significant, especially at the lower energies at which C is very small. It is clear that even if V_{ss} has a simple form, the scattering cross section itself need not be simple due to the interference between potential and nuclear (resonance) scattering.

III. MAIN RESULTS

The general results which are obtained may be stated briefly as follows.

A. Maxima

In a region in which the total width Γ_λ and level shift Δ_λ of the lines at E_λ is small compared to the level spacing D, the form of the reaction cross sections σ_{st} near the resonances E_λ is

$$\sigma_{st}=\frac{4\pi}{k_s^2}\cdot\frac{\Gamma_{\lambda s}\Gamma_{\lambda t}}{\Gamma_\lambda^2}\left\{\frac{\frac{1}{4}\Gamma_\lambda^2}{(E_\lambda+\Delta_\lambda-E)^2+\frac{1}{4}\Gamma_\lambda^2}+\text{terms of the form } O\left(\frac{E_\lambda+\Delta_\lambda-E}{D}\right)\right.$$
$$\left.\text{and } O\left(\frac{|\Gamma_\lambda+2i\Delta_\lambda|^2}{D^2}\right)\right\}. \tag{3.1}$$

The terms $O[(E_\lambda+\Delta_\lambda-E)/D]$ vanish for $E=E_\lambda+\Delta_\lambda$, and the cross section then becomes[8]

$$\sigma_{st}^{(max)}\simeq\frac{4\pi}{k_s^2}\cdot\frac{\Gamma_{\lambda s}\Gamma_{\lambda t}}{\Gamma_\lambda^2}. \tag{3.2}$$

[7] The notation used here in discussing applications of (2.1) most conveniently follows that of reference 1, instead of that of references 2 and 5, which is more convenient for the purposes of derivation.

† See also Breit, Yost, and Wheeler, Phys. Rev. **49**, 174 (1936)

[8] Here, as in the remainder of this discussion, the energy variation of the Δ_λ, Γ_λ, and k_s is disregarded as compared to the

The correction terms[9] may be attributed to the contribution from other levels, and, in particular, even the term $O[(E_\lambda+\Delta_\lambda-E)/D]$ may remain unimportant at a given level E_λ if the contributions from other levels on both sides of E_λ tend to annul each other. If this is not so, the approximation

$$\sigma_{st}\simeq\frac{4\pi}{k_s^2}\cdot\frac{\Gamma_{\lambda s}\Gamma_{\lambda t}}{\Gamma_\lambda^2}\cdot\frac{\frac{1}{4}\Gamma_\lambda^2}{(E_\lambda+\Delta_\lambda-E)^2+\frac{1}{4}\Gamma_\lambda^2} \tag{3.3}$$

is only valid in an energy region determined by $|(E_\lambda+\Delta_\lambda-E)/D|\ll 1$. In all cases the approximation breaks down as soon as $|(E_\lambda+\Delta_\lambda-E)/2D|$ becomes appreciable compared with 1.

Thus in a region where the lines are narrow (Γ_λ/D small) and the level shifts small (Δ_λ/D small), the reaction cross sections have the usual Breit-Wigner form (3.3) near the levels E_λ. The scattering cross sections do not behave in quite the same way, because of the complications introduced by the potential scattering, and it is necessary to treat them separately (see Section V).

B. Minima

If the lines are narrow, three different types of behavior must be distinguished in the form of the cross sections between the resonances (i.e., near the minima). In the first two cases the cross section varies rather slowly in the intermediate region, and may be represented over a large part of this region by a formula of the type

$$\sigma_{st}=\sigma_{st}^{(\min)}+C_{st}(E-E_{\min})^2, \tag{3.4}$$

i.e., by a parabolic approximation. The distinction between these two types is then mainly exhibited by the fact that for the minima of type (i)

$$\sigma_{st}^{(\min)}\simeq(4\Gamma_\lambda^2/D^2)\sigma_{st}^{(\max)}$$

if only two adjoining levels are considered, or

$$\sigma_{st}^{(\min)}\simeq(\pi\Gamma_\lambda/D)^2\sigma_{st}^{(\max)} \tag{3.5}$$

in general, $\sigma_{st}^{(\max)}$ having the value given by (3.2), while for the minima of type (ii)

$$\sigma_{st}^{(\min)}\simeq(4\Gamma_\lambda^4/D^4)\sigma_{st}^{(\max)}$$

if only the two adjoining levels are considered, or

$$\sigma_{st}^{(\min)}\simeq(\pi\Gamma_\lambda/D)^4\sigma_{st}^{(\max)} \tag{3.6}$$

in general. There is also a slight difference in the curvature (i.e., in the constant C_{st} above), due partly to the different ratio $\sigma^{(\min)}/\sigma^{(\max)}$ in the two cases. This may be best expressed by introducing the quantity W, the "width of the minimum," defined as the distance between the points at which the cross section has a value $8\Gamma^2/D^2$ times the maximum. This definition coincides with the natural definition of width for the minima of type (i). One then finds

$$W_{(i)}\simeq 0.55D \tag{3.7}$$

$$W_{(ii)}=0.71D. \tag{3.8}$$

There is a third type of behavior, (iii), related to both the above types, but of a rather pathological nature, in that there are two minima and one spurious, i.e., non-resonance, maximum in the intermediate region. It is illustrated, as are types (i) and (ii), in Fig. 1. The shape of the curve in the middle region is again mildly parabolic, but is now concave downward (toward the E axis), so that such a maximum should be clearly distinguishable by its shape from the resonance maxima of Section A. This type of pathological behavior may only be expected (in the case of thin lines) if there is some violent fluctuation of the quantities $\gamma_{\lambda s}^2$ (the reduced widths) or of the level spacing D in the energy region considered (e.g., if the value of $\gamma_{\lambda s}^2$ suddenly becomes large at the next level but one, or if D suddenly becomes small there). The two minima thus obtained resemble those of type (ii) in size, and are thus given in order of magnitude by $(\Gamma_\lambda/D)^4\sigma_{st}^{(\max)}$. The maximum is determined by the difference of an expression of type (i) and the contribution of the adjoining levels. As a rough estimate, the ratio of this maximum to the resonance maximum is given in order of magnitude by

$$(\Gamma^2/D^2)(\delta\Gamma/\Gamma)^2 \quad \text{or} \quad (\Gamma^2/D^2)(\delta D/D)^2 \tag{3.9}$$

depending on whether the fluctuation responsible is in the width ($\delta\Gamma$) or in the level spacing (δD).

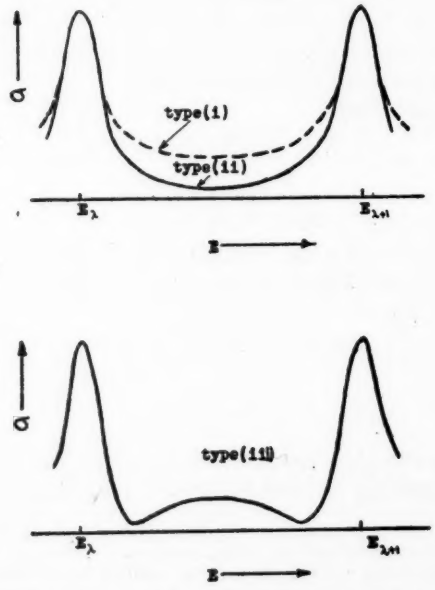

FIG. 1. Different types of behavior in the intermediate region.

resonance variation. Their variation is only important at very low energies (where it gives rise to the $1/v$ cross section for slow neutrons), and at very high energies where the resonance variation may be washed out due to large values of Γ/D. In this latter case most of the above formulas are inapplicable. See Eq. (3.13).

[9] The exact correction terms are given in reference 5 for the case where $|C_s|\ll 1$.

C. General Behavior under Special Assumptions

If the assumption is made that the ratio of the partial widths for various processes is independent of the level, i.e.,

$$\Gamma_{\lambda s}\Gamma_{\mu t}=\Gamma_{\mu s}\Gamma_{\lambda t} \tag{3.10}$$

and, in addition, the signs of the $\gamma_{\lambda s}$ are restricted in a suitable way (see Section IV, C), it is possible to calculate explicitly the form of the σ_{st} as a function of the energy. Physically this assumption means that all the levels behave in substantially the same way as regards the relation between various processes. If further assumptions are made about the regularity of the Γ_λ and D in going from level to level (*viz.*, Γ_λ the same for all λ, and D constant), the cross sections take a particularly simple form, and the average values of the reaction cross sections can always be written as

$$\langle\sigma_{st}\rangle=\frac{4\pi}{k_s^2}\cdot\frac{\Gamma_s\Gamma_t}{\Gamma^2}\cdot\frac{\pi\Gamma}{2D}F\left(\frac{\Gamma}{D}\right), \tag{3.11}$$

where $F(x)\simeq 1$ for small x, and $xF(x)$ decreases (to some finite value) for large x. This form facilitates comparison with the formula of the statistical theory[10]

$$\langle\sigma_{st}\rangle=S_s\xi_s\eta_t. \tag{3.12}$$

In the cases considered here the reaction cross sections are found to have the form

$$M\frac{A^2\tan^2(\pi E/D)+1}{G^2+\tan^2(\pi E/D)} \tag{3.13}$$

where A, M, and G depend on the energy only weakly compared to the resonance variation $\tan\pi E/D$. Disregarding the energy variation of A, M, and G, in order to obtain a qualitative picture of the behavior of (3.13), it is immediately clear[11] that there is a fundamental change of character depending on whether

$$AG<1 \tag{3.14}$$

or

$$AG>1. \tag{3.15}$$

The former case, which occurs for small Γ/D, corresponds to the usual state of affairs, in which the maxima occur at the resonances ($E_\lambda=\lambda D$) and the minima at points midway between ($E_{\min\lambda}=(\lambda+\frac{1}{2})D$). If Γ/D becomes large, however (in which case the levels are said to overlap, since the half-width Γ exceeds the spacing between them), the second case may obtain, and the points E_λ then give the minima, while the maxima now occur at the points $E_{\min\lambda}$ between the "resonances," so that there is a "reversal" of the maxima and minima. Such an effect is only to be expected for rather high energies, at which the experimental resolution would probably be too low to detect the resonance structure at all. The ratio $\sigma(E_{\min\lambda})/\sigma(E_\lambda)$ is, of course, equal to

$$A^2G^2 \tag{3.16}$$

in each case. The values of A and G are given in Section IV, C. For small Γ/D the values obtained for the maxima and minima are in good agreement with those given in Section III, A and B, and in fact they remain so almost up to $\Gamma/D\sim 1$. For still larger Γ/D, AG increases more slowly, or decreases, depending on the type of reaction considered. The importance of the above results lies not in the detailed form of A and G, but in the indication that, at least with fairly reasonable assumptions, the values deduced for the minima in general for small Γ/D remain valid for a much larger range of Γ/D.

The above results can be applied to the scattering cross sections only if the so-called potential scattering is negligible. If this is the case, then all the above results, A, B, and C are valid, with the restriction that only minima of type (ii) occur for the scattering cross sections (see Section V).

IV. METHODS OF DERIVATION

It is clear from (2.1) and (2.2) that the fundamental mathematical problem in the calculation of the cross sections is the inversion of the matrix $1+iC-iBRB$. Since C and B are diagonal, this problem is defined by the properties of R. In any given energy range in which R is n-dimensional, this inversion is always possible, at least in principle, but it is a matter of prohibitive labor unless $n=2$, or R has some special simplifying properties; e.g., "smallness" in a suitable mathematical sense, so that $(1+iC-iBRB)^{-1}$ can be expanded in a formal power series, or if R is of rank one or two, in which case the inversion is algebraically straightforward. The first case applies in the calculation of the minima (Section IV, B), and the second in the explicit calculation of the cross sections (Section IV, C). A combination of the two cases applies in the calculation of the form of the cross sections near the maxima.

A. Maxima

Near the resonances $E=E_\lambda$, R is expressible as the sum of a matrix of rank one, and a small perturbing matrix, and the matrix V whose elements determine the cross sections may then be calculated by a formal power series expansion in terms of the latter matrix.

The procedure is as follows: Near $E=E_\lambda$ it is convenient to write

$$R=R_\lambda+R_\lambda', \tag{4.1}$$

where

$$R_\lambda=(\gamma_\lambda\times\gamma_\lambda)/(E_\lambda-E) \tag{4.2}$$

and

$$R_\lambda'=\sum_{\mu\neq\lambda}(\gamma_\mu\times\gamma_\mu)/(E_\mu-E). \tag{4.3}$$

[10] See Weisskopf, reference 6, and Section VI.

[11] The results stated here (as also the remarks in the latter part of Section IV, C hold for the case where the potential matrix C is zero. Except for a level shift as indicated in III, A, there is no essential difference when C is not zero, though the formulas are then much more complicated and less perspicuous.

The matrix $(\mathbf{a}\times\mathbf{b})$ has elements $(\mathbf{a}\times\mathbf{b})_{st}=a_s b_t$. The components of the vector γ_λ are simply the $\gamma_{\lambda s}$. R_λ' is a slowly varying function of E in the region $E\sim E_\lambda$, and remains finite for $E=E_\lambda$. R_λ has rank one, and the matrix $(1+iC-iBR_\lambda B)^{-1}$ is easily found. Then

$$V^{(0)}=\frac{2i(BR_\lambda B-C)}{1+iC-iBR_\lambda B}$$

$$=\frac{2i}{E_\lambda+\Delta_\lambda-E-i\Gamma_\lambda/2}(\alpha_\lambda\times\alpha_\lambda), \tag{4.4}$$

where

$$\alpha_\lambda=(1+iC)^{-1}B\gamma_\lambda, \tag{4.5}$$

that is,

$$\alpha_{\lambda s}=(B_s\gamma_{\lambda s})/(1+iC_s).$$

The quantities Γ_λ and Δ_λ are then defined in terms of α_λ and C by

$$\tfrac{1}{2}\Gamma_\lambda=(\alpha_\lambda^*\cdot\alpha_\lambda)=\sum_s|\alpha_{\lambda s}|^2 \tag{4.6}$$

and

$$\Delta_\lambda=-(\alpha_\lambda^*\cdot C\alpha_\lambda). \tag{4.7}$$

Even though R_λ has a pole for $E=E_\lambda$, it is not permissible to neglect R_λ' in the calculation of V, though if one does, one finds simply the expression $V^{(0)}$, which gives the correct leading term in an expansion in terms of R_λ' (i.e., in orders of Γ/D). In actual fact

$$\begin{aligned}\tilde{U}&=V+1\\&=[1+iBR_\lambda'B(1-iC+iBR_\lambda B)^{-1}][V^{(0)}+1]\\&\quad\times[1-iBR_\lambda'B(1+iC-iBR_\lambda B)^{-1}]^{-1}.\end{aligned} \tag{4.8}$$

In order that it be permissible to expand

$$[1-iBR_\lambda'B(1+iC-iBR_\lambda B)^{-1}]^{-1},$$

it is necessary that the elements of

$$BR_\lambda'B(1+iC-iBR_\lambda B)^{-1}=BR_\lambda'B(1+iC)^{-1}$$

$$+\frac{i}{E_\lambda+\Delta_\lambda-E-i\Gamma_\lambda/2}BR_\lambda'B(\alpha_\lambda\times\alpha_\lambda)$$

be small enough. These elements are of the order Γ/D, so that this condition is satisfied for narrow lines. More precisely, one finds that a sufficient condition for expansibility is

$$\|BR_\lambda'B\|=\sum_s\sum_t|B_sR_{\lambda;st}'B_t|^2\leq\tfrac{1}{2}. \tag{4.9}$$

The elements of $BR_\lambda'B$ are of the order[12] $\Gamma\nu/nD$, n being the dimension of R, and ν a number depending on how many levels contribute appreciably to the sum. A statistical consideration similar to that employed in Section B below shows that generally $\nu\sim\pi$. Thus, (4.9) requires that

$$\Gamma/D<1/2\nu\sim1/2\pi. \tag{4.10}$$

This is only a sufficient condition; it is quite conceivable that under various special circumstances the expansion may be permissible with less stringent restrictions.

A straightforward, if lengthy, computation then yields for V the expansion

$$V=V^{(0)}+V^{(1)}+V^{(2)}+\cdots, \tag{4.11}$$

the various terms being of the corresponding orders in the elements of R_λ', i.e., of Γ/D. $V^{(0)}$ is given by[13] Eq. (4.4) (see reference 5).

B. Minima

The discussion of the minima is more complicated than that of the maxima, and the results are necessarily less exact, mainly because there is a not inappreciable contribution to a given minimum from non-adjoining levels. The estimates here obtained require the assumption of narrow lines: The values (though not necessarily the behavior) are similar in general, as may be seen by considering the case of two levels only, or some specialized forms of the many-level case.

The cross sections σ_{st} are determined by the elements V_{st} of the matrix V. If the elements of BRB are small enough (i.e., if $\|BRB\|<1$, which implies narrow lines (cf. Section IV, A), then V may be expanded in a series

$$V=-\frac{2iC}{1+iC}+2i\frac{B}{1+iC}R\frac{B}{1+iC}$$

$$-2\frac{B}{1+iC}R\frac{B^2}{1+iC}R\frac{B}{1+iC}\cdots$$

or (4.12)

$$V_{st}=\frac{-2iC_s\delta_{st}}{1+iC_s}+2i\frac{B_sR_{st}B_t}{(1+iC_s)(1+iC_t)}$$

$$-2\sum_r\frac{B_sR_{sr}B_r^2R_{rt}B_t}{(1+iC_s)(1+iC_r)(1+iC_t)}.$$

If $s\neq t$, two possibilities must be distinguished. First, R_{st} may go to zero between the two resonances E_λ, $E_{\lambda+1}$ considered. $\gamma_{\lambda s}\gamma_{\lambda t}$ and $\gamma_{\lambda+1,s}\gamma_{\lambda+1,t}$ must, in general, have the same sign for this to happen. If this is not so, the vanishing of R_{st} requires the fortuitous annulment of the contribution of the terms at E_λ, $E_{\lambda+1}$ by the contribution of the totality of other terms on both sides of

[12] Actually it is the matrix $(1+iC)^{-1}BR_\lambda'B(1+iC)^{-1}$ whose elements are of order $\Gamma\nu/nD$. Since C is small in all the cases considered, the same statement may also be made for $BR_\lambda'B$.

[13] Note that the method here employed differs from that given by Wigner and Eisenbud (reference 1) in that the widths Γ_λ and level shifts Δ_λ here defined depend only on the $\gamma_{\lambda s}$ at the level considered, and on potential factors which are known from the behavior of the system in the external (separated) region. The effect of the other levels is embodied in the correction factors. In reference 1 the Γ_λ and Δ_λ depend also on the contribution of the adjoining levels, and the separation between potential effects and those of other levels is not so clearly maintained.

this point. It may indeed happen that this contribution is more than enough to annul the contribution of the two adjoining levels, and in that case $|R_{st}|^2$ goes to zero twice between E_λ and $E_{\lambda+1}$, and has a maximum between the two zeros. This maximum has the same shape as the minimum which occurs when $R_{st}\neq 0$ between E_λ and $E_{\lambda+1}$. If Γ/D is small, it is clear that such an occurrence requires an anomalously high value of $\gamma_{\mu s}^2$ (i.e., Γ) at a nearby level, or a rather sudden decrease in the level spacing D.

If $R_{st}=0$ the minimum is closely approximated by

$$V_{st}\simeq -2\sum_r \frac{B_s R_{sr} B_r^2 R_{rt} B_t}{(1+iC_s)(1+iC_r)(1+iC_t)}. \quad (4.13)$$

This always occurs for $s=t$, because R_{tt} goes to zero between each adjoining pair of resonances; thus

$$V_{tt}\simeq \frac{-2iC_t}{1+iC_t}-\frac{2B_t^2}{(1+iC_t)^2}\sum_r \frac{R_{tr}^2 B_r^2}{1+iC_r}. \quad (4.14)$$

If R_{st} does not vanish, but is nevertheless small, then V_{st} may be approximated by

$$V_{st}\simeq \frac{2iB_s R_{st} B_t}{(1+iC_s)(1+iC_t)}. \quad (4.15)$$

These various types of behavior, which are labeled as type (i) [$R_{st}\neq 0$ (4.15)], type (ii) [$R_{st}=0$ (4.13)], and type (iii) ($R_{st}=0$ twice) are illustrated in Fig. 2.

If only two adjoining levels E_λ, E_μ are considered, it is not necessary to use the approximate formulas given above, for it is then possible to use exact formulas given elsewhere,[14] which do not involve the assumption $\Gamma/D\ll 1$. Direct substitution then yields in the two cases sign $(\gamma_{\lambda s}\gamma_{\lambda t}/\gamma_{\mu s}\gamma_{\mu t})=-1$ [type (i)], $+1$ [type (ii)], respectively,

$$\sigma_{st}^{(\min)}\simeq\sigma_{st}^{(\max)}[(4\Gamma^2/D^2)+(4\Gamma^2/D^2)^2] \quad \text{type (i)}$$
$$\simeq\sigma_{st}^{(\max)}4\Gamma^2/D^2 \quad \text{for } \Gamma/D\ll 1 \quad (4.16)$$

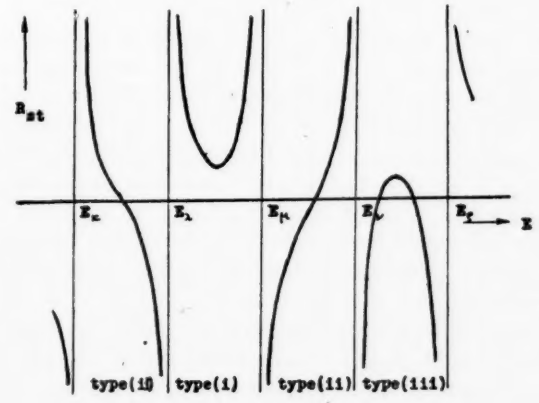

FIG. 2. Behavior of R in the intermediate region.

and

$$\sigma_{st}^{(\min)}\simeq\sigma_{st}^{(\max)}4\Gamma^4/D^4 \quad \text{type (ii)}. \quad (4.17)$$

Here $D=E_\mu-E_\lambda$ and Γ is an average of Γ_λ and Γ_μ lying between their geometric and arithmetic means. This shows that the two types of minima differ by a factor of the order Γ^2/D^2.

The same formulas may be used to calculate the width W as defined in Section III, and yield easily

$$W_{(i)}\simeq 0.55D(1+0.7\Gamma^2/D^2\cdots) \quad \text{type (i)} \quad (4.18)$$

and

$$W_{(ii)}\simeq 0.71D(1-4\Gamma^2/D^2\cdots) \quad \text{type (ii)}. \quad (4.19)$$

The above estimates involve the tacit neglect of levels other than those immediately adjoining the minimum in question, on the grounds that these levels on both sides of the point considered tend to annul each other. This certainly seems plausible if all the $\gamma_{\lambda s}\gamma_{\lambda t}$ have the same sign, and if the levels considered are not near the lower end of the spectrum. Even then, the fact that the sum for R_{st} has an infinity of terms requires an investigation of convergence, which, in turn, requires knowledge of the variation of the $\gamma_{\lambda s}$ and E_λ with λ. The results of reference 4 do ensure convergence, but do not render the evaluation of the sum much easier. If all the $\gamma_{\lambda s}\gamma_{\lambda t}$ do not have the same sign, the annulment argument breaks down, and the evaluation of the sum is then still more complicated. It is then no longer clear that the result, Eq. (4.16) say, is not substantially altered by some large additive term, or multiplicative factor, which takes account of the contribution of non-adjoining terms.

It is possible to resolve this problem fairly satisfactorily from the statistical point of view, by considering the totality of expressions

$$\sum_\lambda (\pm)|\gamma_{\lambda s}\gamma_{\lambda t}/(E_\lambda-E)|. \quad (4.20)$$

This certainly includes all the possibilities for R_{st}. Rademacher's theorem on random functions[15] then asserts that the mean square of (4.20) taken over all possible choices of sign, is equal to

$$\sum_\lambda |(\gamma_{\lambda s}\gamma_{\lambda t})/(E_\lambda-E)|^2 \quad (4.21)$$

provided this last expression converges. This result gives, as it were, a survey of all the possibilities, and a typical term may therefore be regarded as satisfying

$$|R_{st}|^2=\sum_\lambda |(\gamma_{\lambda s}\gamma_{\lambda t})/(E_\lambda-E)|^2 \quad (4.22)$$

at least on the average. The convergence is now manifest for any reasonable variation of the parameters with λ. The subsequent determination of the minimum depends on the approximations (4.13) and (4.15) and involves the Taylor expansion of $|R_{st}|^2$ up to terms of

[14] E. P. Wigner, Phys. Rev. **70**, 606 (1946), formula (46); also reference 5.

[15] See Kaczmarz and Steinhaus, *Theorie der Orthogonalreihen;* also reference 5, Appendix.

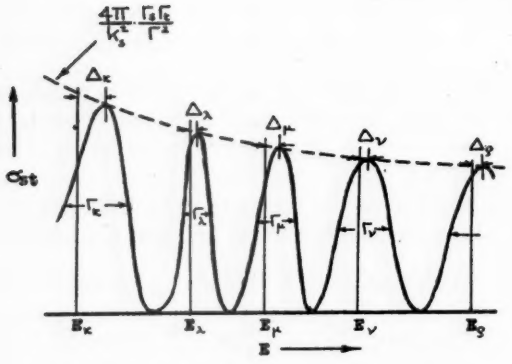

FIG. 3. The form of the cross section under simplifying assumptions.

the second degree about some point between the two maxima considered. The details, though lengthy, are neither difficult nor terribly instructive, and are not reproduced here (see reference 5).

The upshot of the calculation is that in the case of minima of type (i), for which $R_{st}\neq 0$, the ratio $\sigma_{st}^{(\min)}/\sigma_{st}^{(\max)}$ becomes

$$(\pi\Gamma/D)^2 \tag{4.23}$$

so that the factor 4 of (4.16) is replaced by π^2. [This result (4.23) depends on the assumption $\Gamma/D\ll 1$.] A similar calculation may be applied to the case where $R_{st}=0$ and here the ratio $\sigma_{st}^{(\min)}/\sigma_{st}^{(\max)}$ becomes

$$\sim(\pi\Gamma/D)^2[\pi(\Gamma-\Gamma_s-\Gamma_t)/D]^2. \tag{4.24}$$

If the potential scattering may be neglected, the relation for the scattering cross sections is

$$\sigma_{ss}^{(\min)}/\sigma_{ss}^{(\max)}\simeq(\pi\Gamma/D)^2(\pi\Gamma_{As}/D)^2, \tag{4.25}$$

$\Gamma_{As}=\Gamma-\Gamma_s=$absorption width for the process "s." The appearance of an additional factor π^2 may be ascribed mathematically to the fact that an extra order of $|R_{st}|^2$ appears in this calculation.

The above method of parabolic approximation to $|R_{st}|^2$ may also be used to give a rough estimate of the width of the minimum W in the case of minima of type (i). The distance $W/2$ from the minimum point to a point having double this minimum value [i.e., $2(\pi\Gamma/D)^2\sigma^{(\max)}$] is found to be

$$W/2\simeq D/\pi \quad \text{[see (4.18)]}. \tag{4.26}$$

[This method is not suitable for the calculation of the widths of minima of type (ii).]

C. Special Assumptions

In order that the elements of the matrix V have a simple form, it is necessary that the matrix $1+iC-iBRB$ be easily inverted, and this can generally only be the case if R is of rank one or two. This means essentially that BRB may be put in the form

$$BRB=\frac{1}{t}(\mathbf{x}\times\mathbf{x}) \tag{4.27}$$

or

$$BRB=\frac{1}{t'}(\mathbf{x}'\times\mathbf{x}')+\frac{1}{t''}(\mathbf{x}''\times\mathbf{x}''). \tag{4.28}$$

Equation (4.27) (R of rank one) is, of course a special case of (4.28) (R of rank two). Because of the multiplication rules for the matrices $(\mathbf{x}'\times\mathbf{x}')$, $(\mathbf{x}''\times\mathbf{x}'')$ etc., V (and, indeed, any similar function of R) may be written in the form

$$V=\frac{2}{1+iC}\{A'(\mathbf{x}'\times\mathbf{x}')+A''(\mathbf{x}''\times\mathbf{x}'')+A'''(\mathbf{x}'\times\mathbf{x}'')+A'''(\mathbf{x}''\times\mathbf{x}')\}\frac{1}{1+iC}. \tag{4.29}$$

The (scalar) coefficients A', A'', and A''' may be evaluated by multiplying both sides of the equation for V by $1+iC-iBRB$.

By special choices of the $\gamma_{\lambda s}$ it is indeed possible to get BRB into the form (4.27) or (4.28). For instance, if $\gamma_{\lambda s}=a_\lambda b_s$, then

$$x_s=B_s b_s$$

and

$$\frac{1}{t}=\sum_\lambda\frac{a_\lambda^2}{E_\lambda-E}, \tag{4.30}$$

whence

$$V=\frac{2i}{(t+\Delta)-i\Gamma/2}\left(\frac{\mathbf{x}}{1+iC}\times\frac{\mathbf{x}}{1+iC}\right)$$

where

$$\tfrac{1}{2}\Gamma=\sum_s B_s^2 b_s^2/(1+C_s^2) \quad\text{and}\quad \Delta=-\sum_s C_s B_s^2 b_s^2/(1+C_s^2)$$

[see Eqs. (2.10) and (2.12)]. The reaction cross sections then become

$$\sigma_{sr}=\frac{4\pi}{k_s^2}\cdot\frac{\Gamma_s\Gamma_r}{\Gamma^2}\cdot\frac{\Gamma^2/4}{(t+\Delta)^2+\Gamma^2/4}. \tag{4.31}$$

$\Gamma_s\Gamma_r/\Gamma^2=\Gamma_{\lambda s}\Gamma_{\lambda r}/\Gamma_\lambda^2$ is constant for given s and r and independent of λ. This form of the cross section is illustrated in Fig. 3. If Γ and Δ are small compared to the level spacing D, then the widths and level shifts are given quite accurately by the quantities $\Gamma_\lambda=a_\lambda^2\Gamma$ and $\Delta_\lambda=a_\lambda^2\Delta$. Zeros occur between each pair of resonances because $t(E)$ becomes infinite between each pair of zeros. The reaction cross sections all have the same type of energy variation and differ only in their relative amplitudes.

A special case of interest in which the formulas become very simple occurs when the levels are uniformly spaced, with spacing D, and the total widths are the same at the various levels (i.e., $\Gamma_\lambda=\Gamma_\mu=\cdots=\Gamma$, $a_\lambda^2=a_\mu^2=\cdots=1$). $t(E)$ then becomes

$$t(E)=-(D/\pi)\tan(\pi E/D) \tag{4.32}$$

and thus

$$\sigma_{sr}=\frac{4\pi}{k_s^2}\cdot\frac{\Gamma_s\Gamma_r}{\Gamma^2}\cdot\frac{(\pi\Gamma/2D)^2}{[\tan(\pi E/D)-(\pi\Delta/D)]^2+(\pi\Gamma/2D)^2}. \quad (4.33)$$

The maxima and minima, as for (4.31), are, respectively, $(4\pi/k_s^2)\cdot(\Gamma_s\Gamma_r/\Gamma^2)$ and 0. The actual line width is given by $(D/\pi)\tan^{-1}\pi\Gamma D/[D^2+\pi^2(\Delta^2-\Gamma^2/4)]$ which $\simeq\Gamma$ for small Γ/D. For narrow lines the width of the minima becomes $0.64D$ in good agreement with the previous results.

The remaining results of this subsection are clearer if they are only considered for the case $C=0$ (i.e., $\Delta=0$). Since the C_s (and Δ) are generally small, this assumption is justified. If it is not made, the results are much more complicated, though unchanged in their essence. For instance, if $\Delta=0$, the average $\langle\sigma_{st}\rangle$ is found to be

$$\langle\sigma_{st}\rangle=\sigma_{st}^{(\max)}\cdot\frac{\pi\Gamma/2D}{1+(\pi\Gamma/2D)} \quad (4.34)$$

which has the general form of (3.11). If $\Delta\neq0$ (but Δ/D is still small) then (4.34) must be multiplied by the correction factor

$$1-[\Delta/(\pi D-\Gamma/2)]^2. \quad (4.35)$$

It seems natural to try to generalize the assumption (4.30) in such a way that the ratios of the partial widths for different processes remain independent of the level, but without restricting the signs of the $\gamma_{\lambda s}$ so severely, *viz.*, to require only

$$\gamma_{\lambda s}^2\gamma_{\mu t}^2=\gamma_{\mu s}^2\gamma_{\lambda t}^2$$

which leaves the signs of the $\gamma_{\lambda s}$ arbitrary, but not

$$\gamma_{\lambda s}\gamma_{\mu t}=\gamma_{\mu s}\gamma_{\lambda t}$$

as is done above. Quite arbitrary variations of the signs[16] cannot be dealt with by the above method, but certain special types of sign changes lead to *BRB* being of rank two: to wit, if

$$\gamma_{\lambda s}=(1-2\sum_{\alpha}\delta_{\alpha\lambda}\sum_{a}\delta_{as})a_\lambda b_s \quad (4.36)$$

where the α, a run only over some of the λ, s, respectively. Thus the sign of $\gamma_{\lambda s}$ is reversed only for processes $a, b, \cdots$, and then only at the levels $\alpha, \cdots$. *BRB* then has the form (4.28).

The general features of the results are shown most clearly by considering a rather more special case on the lines of (4.32). Again the levels are supposed equally spaced with spacing D, and the width the same at all the levels, but it is now assumed that for processes $a, b, \cdots$ etc., the $\gamma_{\lambda s}$ have alternate signs at alternate levels. Then

$$\sigma_{st}=\frac{4\pi}{k_s^2}\cdot\frac{\Gamma_s\Gamma_t}{\Gamma^2}\cdot\frac{\left(\frac{\pi\Gamma}{2D}\right)^2\left[1+\left(\frac{\pi\Gamma''}{2D}\right)^2\tan^2\frac{\pi E}{D}\right]}{\left(\frac{\pi\Gamma}{2D}\right)^2+\left[1+\frac{\pi\Gamma'}{2D}\cdot\frac{\pi\Gamma''}{2D}\right]^2\tan^2\frac{\pi E}{D}} \quad (4.37)$$

and

$$\sigma_{sa}=\frac{4\pi}{k_s^2}\cdot\frac{\Gamma_s\Gamma_a}{\Gamma^2}\cdot\frac{\left(\frac{\pi\Gamma}{2D}\right)^2\sec^2\frac{\pi E}{D}}{\left(\frac{\pi\Gamma}{2D}\right)^2+\left[1+\frac{\pi\Gamma'}{2D}\cdot\frac{\pi\Gamma''}{2D}\right]^2\tan^2\frac{\pi E}{D}}. \quad (4.38)$$

Here Γ is the total width, $\Gamma=\sum_s\Gamma_s$, while Γ', Γ'' are the respective partial widths for processes with given sign, i.e.,

$$\Gamma'=\sum_{s\neq a}\Gamma_s \quad \text{and} \quad \Gamma''=\sum_a\Gamma_a.$$

σ_{ab} has a similar form to σ_{st} with Γ' and Γ'' interchanged.

A distinction must be made between the possibilities $\pi\Gamma/2D<1$ and $\pi\Gamma/2D>1$. It may be supposed that the former case applies, the latter having been discussed in Section III. The ratio $\sigma^{(\min)}/\sigma^{(\max)}$ is then given, respectively, by the expressions

$$\frac{(\pi\Gamma/2D)^2(\pi\Gamma''/2D)^2}{[1+(\pi\Gamma'/2D)\cdot(\pi\Gamma''/2D)]^2} \quad (4.39)$$

and

$$\frac{(\pi\Gamma/2D)^2}{[1+(\pi\Gamma'/2D)\cdot(\pi\Gamma''/2D)]^2} \quad (4.40)$$

for the two types of cross section and σ_{st} and σ_{sa}. These results are in agreement with the more general results of Section V, A and B. The minima are of two types, being, respectively, of order Γ^4/D^4 and Γ^2/D^2 times the maxima (if Γ/D is small). The latter case occurs only for reactions of the type "sa" which are just those whose matrix elements never vanish.

These distinctions do not, in general, play a role in the absorption cross sections

$$\sigma_{sA}=\sum_{t\neq s}\sigma_{st}, \quad \sigma_{aA}=\sum_{t\neq a}\sigma_{at},$$

because the summation substantially averages over the various possibilities. For small Γ/D

$$\frac{\sigma_{sA}^{(\min)}}{\sigma_{sA}^{(\max)}}\simeq\left(\frac{\pi\Gamma}{2D}\right)^2\frac{\Gamma''}{\Gamma-\Gamma_s} \quad \text{and} \quad \frac{\sigma_{aA}^{(\min)}}{\sigma_{aA}^{(\max)}}\simeq\left(\frac{\pi\Gamma}{2D}\right)^2\frac{\Gamma'}{\Gamma-\Gamma_a},$$

that is,

$$\sigma^{(\min)}/\sigma^{(\max)}\sim(\pi\Gamma/2D)^2, \quad (4.41)$$

the other factor on the right being of the order $\frac{1}{2}$ and taking account of the number of processes of each type.

[16] See reference 5 for a fuller discussion of this point.

The averages may also be calculated and are found to be

$$\langle\sigma_{st}\rangle=\sigma_{st}^{(\max)}\cdot\frac{\pi\Gamma}{2D}\cdot\frac{1+\frac{\pi\Gamma'}{2D}\cdot\frac{\pi\Gamma''}{2D}+\frac{\pi\Gamma}{2D}\left(\frac{\pi\Gamma''}{2D}\right)^2}{\left[1+\frac{\pi\Gamma'}{2D}\cdot\frac{\pi\Gamma''}{2D}\right]\left[1+\frac{\pi\Gamma}{2D}+\frac{\pi\Gamma'}{2D}\cdot\frac{\pi\Gamma''}{2D}\right]} \tag{4.42}$$

and

$$\langle\sigma_{sa}\rangle=\sigma_{sa}^{(\max)}\frac{\pi\Gamma}{2D}\cdot\frac{1}{\left[1+\frac{\pi\Gamma'}{2D}\cdot\frac{\pi\Gamma''}{2D}\right]} \tag{4.43}$$

both of which have the form (3.11).

V. SCATTERING CROSS SECTIONS

In order to extend the discussion to scattering cross sections it is necessary to consider the effect of the potential scattering term, and the interference between the potential scattering and the resonance (nuclear) scattering (see Section II). If these terms are comparatively small, which is the case at low energies where $x_s=k_sa_s$ is small, then the scattering cross sections behave just like reaction cross sections, and nothing further need be said. In general, however, the behavior is very complicated unless the discussion is confined to the vicinity of a resonance, in which case may be approximated by a single term of rank one (*viz.*, the $R_\lambda=(\gamma_\lambda\times\gamma_\lambda)/(E_\lambda-E)$ of Section IV, A. The calculation is then formally equivalent to that following from the simplifying assumption (4.27); thus the result is not only applicable to the scattering cross sections near the resonances of thin lines, but may also be used to give a rough indication of what happens between the resonances when the lines are not thin.

Using τ to denote $E_\lambda+\Delta_\lambda-E$ when single resonances are considered, or $\Delta-(D/\pi)\tan(\pi E/D)$ when the simplifying assumptions (4.27) and (4.32) are used,

$$V_{sc}=-\frac{2iC_s}{1+iC_s}+\frac{2i}{\tau-i\Gamma/2}\frac{B_s^2\gamma_s^2}{(1+iC_s)^2}. \tag{5.1}$$

The second term is the analog of what has already been obtained for $V^{(0)}$ in Section IV, A, or for V in Section IV, C. The first term is due to the contribution of the diagonal matrix C which appears in the expression (2.5) for V, and appears only in the diagonal elements of V. Its main effect is that in the final expression for the cross section it is not x_s but

$$y_s=x_s-\tan^{-1}C_s \tag{5.2}$$

which appears. Reference to (2.3) and (2.5) shows that $-y_s$ is simply the complex argument of the relative external wave function φ_s, i.e.,

$$e^{-iy_s}=\varphi_s/|\varphi_s|. \tag{5.3}$$

A straightforward calculation then yields for the cross section the expression

$$\sigma_{ss}=\sigma_{ss}^{(0)}+\delta\sigma_{ss}\cdot\sin^2(\theta+\zeta_s) \tag{5.4}$$

where

$$\sigma_{ss}^{(0)}=\frac{4\pi}{k_s^2}\left\{\frac{\Gamma_s^2}{2\Gamma^2}+\frac{\Gamma-\Gamma_s}{\Gamma}\sin^2y_s-\frac{\Gamma_s}{2\Gamma}\left(\frac{\Gamma_s^2}{\Gamma^2}+4\frac{\Gamma-\Gamma_s}{\Gamma}\sin^2y_s\right)^{\frac{1}{2}}\right\} \tag{5.5}$$

and

$$\delta\sigma_{ss}=\frac{4\pi}{k_s^2}\cdot\frac{\Gamma_s}{\Gamma}\left(\frac{\Gamma_s^2}{\Gamma^2}+4\frac{\Gamma-\Gamma_s}{\Gamma}\sin^2y_s\right)^{\frac{1}{2}}. \tag{5.6}$$

Here

$$\tan\theta=\frac{\Gamma}{2\tau}\left(=\frac{\Gamma_\lambda}{2(E_\lambda+\Delta_\lambda-E)}\text{ near a resonance}\right) \tag{5.7}$$

and

$$\tan\zeta_s=\frac{2\sin y_s\cos y_s}{(\Gamma_s/\Gamma)-2\sin^2y_s}. \tag{5.8}$$

$\sigma_{ss}^{(0)}$ is independent of the energy (as far as the resonance variation is concerned), and is the minimum value of the cross section. It is the sum of the pure potential scattering

$$(4\pi/k_s^2)\sin^2y_s$$

and the energy independent part of the interference between potential and resonance scattering, *viz.*,

$$\frac{4\pi}{k_s^2}\left\{\frac{\Gamma_s^2}{2\Gamma^2}-\frac{\Gamma_s}{\Gamma}\sin^2y_s-\frac{\Gamma_s}{2\Gamma}\left(\frac{\Gamma_s^2}{\Gamma^2}+4\frac{\Gamma-\Gamma_s}{\Gamma}\sin^2y_s\right)^{\frac{1}{2}}\right\}.$$

The first part vanishes for $y_s=0$ (no potential scattering), while the second vanishes both for $y_s=0$ and for $\Gamma_s=0$ (no resonance scattering). $\delta\sigma_{ss}\sin^2(\theta+\zeta_s)$ is the sum of the pure resonance scattering and the energy dependent part of the interference between resonance and potential scattering: it vanishes identically only for $\Gamma_s=0$. For small y_s,

$$\sigma_{ss}^{(0)}\simeq(4\pi/k_s^2)[(\Gamma-\Gamma_s)/\Gamma_s]^2\sin^4y_s$$

while

$$\delta\sigma_{ss}\simeq(4\pi/k_s^2)(\Gamma_s^2/\Gamma^2)$$

which is the value obtained for the maximum if potential effects are neglected (see Section III, A).

VI. AVERAGE CROSS SECTIONS

It is of interest to correlate the expression here obtained for the average cross section

$$\langle\sigma_{st}\rangle=\frac{4\pi}{k_s^2}\cdot\frac{\Gamma_s\Gamma_t}{\Gamma^2}\cdot\frac{\pi\Gamma}{2D}F\left(\frac{\Gamma}{D}\right) \tag{6.1}$$

with that of the statistical theory

$$\langle\sigma_{st}\rangle=S_s\xi_s\eta_t=S_s\xi\Gamma_t/\Gamma=\langle\sigma_s\rangle\eta_t. \tag{6.2}$$

$\langle\sigma_s\rangle$, the cross section of formation of the compound system, is thus given by

$$\langle\sigma_s\rangle=\frac{4\pi}{k_s^2}\cdot\frac{\pi\Gamma_s}{2D}F\left(\frac{\Gamma}{D}\right). \tag{6.3}$$

Note that $\langle\sigma_s\rangle\leq\langle\sigma_{sT}\rangle$, $\sigma_{sT}=\sum_t\sigma_{st}$ being the total cross section for the colliding pair "s," including the potential effects. In the absence of any potential scattering, $\langle\sigma_s\rangle=\langle\sigma_{sT}\rangle$.

Introducing the expression $2k_sP_s\bar{\gamma}_{\lambda s}^2$ for Γ_s [see (2.8)] and noting the relation $\bar{\gamma}_{\lambda s}^2/D\simeq0.27\times10^{-13}$ cm (see reference 4)

$$\langle\sigma_s\rangle=\left(\frac{\pi}{k_s^2}P_s\right)(0.75(E)^{\frac{1}{2}}F), \tag{6.4}$$

E being the energy measured in Mev. Thus, S_s the penetration cross section of the nucleus may be placed equal to $(\pi/k_s^2)P_s$ and ξ_s, the sticking probability equated to $0.75F(E)^{\frac{1}{2}}$. Both these quantities then have the properties required of them by the statistical theory.

Proceeding to higher energies[17] it is necessary to take into account processes of higher angular momenta when computing $\langle\sigma_s\rangle$; this now becomes the sum of all partial $\langle\sigma_s\rangle$ with angular momenta

$$l\leq k_sa_s, \tag{6.5}$$

[17] The energy variation of the cross section in going from the low to the higher energies is discussed, for example, by Wigner, reference 3.

a_s being the radius of the compound system. Thus

$$\langle\sigma_s\rangle=\frac{4\pi}{k_s^2}\sum^{ka}(2l+1)\left\langle\left[\frac{\pi\Gamma_s}{2D}F\left(\frac{\Gamma}{D}\right)\right]\right\rangle_{Av}$$

$$=\pi a^2\left(1+\frac{1}{k_sa_s}\right)^2\left\langle\left[\frac{4\pi\Gamma_s}{2D}F\left(\frac{\Gamma}{D}\right)\right]\right\rangle_{Av}. \tag{6.6}$$

Since k_sa_s is now large, S_s may be equated to πa_s^2, while

$$\xi_s\simeq\langle(4\pi\Gamma_s/2D)F(\Gamma/D)\rangle_{Av}. \tag{6.7}$$

Because of the properties of F ($xF(x)\sim$constant for large x), $\xi_s\sim$constant in this region since $\Gamma_s\sim\Gamma$. At still higher energies ξ_s tends to decrease, because Γ_s/Γ decreases due to more modes of disintegration of the compound system coming into play (i.e., the dimension of U increases, see reference 2). With these assignments, S_s, ξ_s again have the properties demanded by the statistical theory.

The absorption cross section $\sigma_{sA}=\sum_{t\neq s}\sigma_{st}$ is given by

$$\langle\sigma_{sA}\rangle\simeq\pi a_s^2\left(1+\frac{1}{k_sa_s}\right)^2\frac{\Gamma-\Gamma_s}{D}\cdot2\pi F\left(\frac{\Gamma}{D}\right). \tag{6.8}$$

Since $(\Gamma-\Gamma_s)/D=\Gamma_{As}/D$ is practically constant till new processes begin paying a role, (6.8) shows that in this part of the high energy region the energy dependence of the average cross section is determined mainly by the factor $F(\Gamma/D)$. In the simplest case F has the form

$$F\simeq1/[1+0.18(E)^{\frac{1}{2}}]\quad E\text{ in Mev} \tag{6.9}$$

and more generally this must be multiplied by a complicated but slowly varying function of E which is of the order 1 (see (4.42)).

ACKNOWLEDGMENT

The author is grateful to Professor E. P. Wigner for suggesting this problem, and for continued advice and encouragement.

The Spherical Shell Nuclear Model

H. A. WILSON
Rice Institute, Houston, Texas
(Received August 22, 1949)

The spherical shell nuclear model proposed by the writer in 1946 has vibration levels given by $E_n=\Delta E((n-1)(n+2))^{\frac{1}{2}}$ with $n=2, 3, 4\cdots$ and $\Delta E=Ze/4\pi(Am)^{\frac{1}{2}}r^{\frac{1}{2}}$. Here Z is the atomic number, e the protonic charge, A the mass number, m the mass of a nucleon and r the nuclear radius. The values of E_n with $\Delta E=0.387$ Mev are found to agree approximately with the excitation levels of many nuclei.

With $\Delta E=0.387$ Mev the radius r is given by $r=4.65\times10^{-13}(Z^2/A)^{\frac{1}{3}}$.

Besides the vibration levels rotation vibration levels given by

$$E_{nj}=0.387((n-1)(n+2))^{\frac{1}{2}}+1.44(Z^4A)^{-\frac{1}{3}}j(j+1)$$

have been found with several nuclei.

The energy of the shell model is discussed and the shell is shown to be stable for uniform radial displacements.

The level spacing at high excitations on the shell theory is much larger than on current theories. It is shown that the experimental evidence on level spacing can be explained on the shell theory.

A DISCUSSION of the energies on the beta-, gamma- and alpha-rays from the naturally radioactive elements led the writer[1] in 1933 to suggest that the nuclei of these elements may have sets of equally spaced energy levels with spacings of 0.387 Mev.

Later in 1935 the writer suggested the same thing for the elements of low atomic weight. This suggestion was based on the energies released in nuclear reactions.

Recently Wiedenbeck[2] has reported nearly equally spaced nuclear levels in gold, silver, indium, cadmium, and rhodium with spacings about 0.4 Mev.

Nearly equally spaced levels with separations about 0.4 Mev have been reported for several other elements, for example, nitrogen, iron, beryllium, cobalt, phosphorus and sulfur.

It seems probable, therefore, that most atomic nuclei have a set of nearly equally spaced energy levels with separations near to 0.4 Mev.

The current nuclear models do not give equally spaced levels and for high excitation energies give level spacings less than 0.4 Mev decreasing rapidly with increasing excitation.[3]

For nuclei containing more than about 100 nucleons the liquid drop model may be used. A nucleon on the surface of the drop is supposed to interact with only about half as many other nucleons as one inside so that the drop has a large surface tension. The surface tension prevents the electrostatic repulsions between the protons causing the drop to get larger.

If we suppose that there is "saturation" of the nuclear forces so that one nucleon can only interact strongly with a small number of other nucleons then a nucleon on the surface could interact with the small maximum number so that there would be little or no surface tension. In this case we should expect the nucleons to get as far apart as possible with each nucleon interacting with the small maximum number. The nucleons would therefore get distributed uniformly over a spherical surface so forming a hollow spherical shell.

This argument suggested to the writer that it might be worth while to consider a uniform spherical shell as a simple nuclear model. It is found that such a model enables nuclear energy levels to be calculated in many cases so that it seems to be useful. This very unexpected result is difficult to explain on current ideas about nuclear structure and its meaning is not yet clear.

In order to calculate the frequencies of vibration of such a shell nucleus, we shall suppose the mass and charge uniformly distributed over the surface of the sphere so as to form a uniform flexible spherical shell. For a nucleus with mass number A the mass will be Am where m is the mass of one nuclear particle, and the charge will be Ze where Z is the atomic number and e the protonic charge.

The possible frequencies of vibration of the shell for very small amplitudes may be calculated by the method used by Rayleigh[4] to calculate the frequencies of vibration of a water drop.

Let the radius r of the shell be given by $r=a(1+\alpha P_n)$ where P_n is a zonal harmonic of order n and α a small fraction. Then as Rayleigh shows the volume V is given by

$$V=\frac{4}{3}\pi a^3\left(1+\frac{3}{2n+1}\alpha^2\right),$$

where $n=1, 2, 3, \cdots$, and the area S by

$$S=4\pi a^2\left(1+\frac{n^2+n+2}{2(2n+1)}\alpha^2\right),$$

neglecting higher powers of α.

[1] H. A. Wilson, Phys. Rev. **44**, 858 (1933); Proc. Roy. Soc. London **A144**, 280 (1934); **150**, 1 (1935); **150**, 241 (1935); **152**, 497 (1935).
[2] M. L. Wiedenbeck, Phys. Rev. **68**, 237 (1945).
[3] H. A. Bethe, Rev. Mod. Phys. **9**, 69 (1937).
[4] Lord Rayleigh, Proc. Roy. Soc. London **XXIX**, 71–97 (1879).

TABLE I. Energy levels for x-ray excitation found by Weidenbeck.

Element	Threshold	2nd level	3rd level	4th level	5th level
Rh^{103}	1.26	1.64	2.02	2.37	2.71
Ag^{108}	1.18	1.59	1.95	2.32	2.76
Cd^{112}	1.25	1.68	2.08	2.56	—
Au^{197}	1.22	1.68	2.15	2.56	2.97
Mean	1.23	1.65	2.05	2.45	2.81
Calculated	1.224	1.643	2.047	2.447	2.844

TABLE II. Calculated values for nuclear radii.

Element	A	Z	$a\times10^{13}$ cm	$2.47A^{\frac{1}{3}}$
Uranium	238	92	15.3	15.3
Gold	197	79	14.7	14.4
Silver	108	47	12.7	11.8
Cobalt	59	27	10.4	9.6
Aluminum	27	13	8.5	7.4
Beryllium	9	4	5.6	5.1

The potential energy due to the deformation of the shell will be equal to the work done against the tension in the shell less the work done by the electrical forces acting on the shell.

If the charge per unit area is σ, the force on unit area will be $2\pi\sigma^2$, and this will produce a tension T given by $2T/a=2\pi\sigma^2$. If the area increases by δS, the work done against the tension will be $T\delta S$ provided δS is so small that T may be supposed not to be changed appreciably.

The work done by the electrical forces per unit area is equal to the force per unit area multiplied by the increase in the radius provided the distortion is very small so that the surface remains practically spherical.

The distortion of the shell changes the charge per unit area. If we suppose that the charge on each element of area remains on that element then $\sigma=\sigma_0(1-2\alpha P_n)$ where σ_0 is the value of σ for the undistorted shell and terms in α^2 and higher powers of α are neglected. If the shell is supposed to act like a conductor of electricity, then, as is well known, $\sigma=\sigma_0(1+(n-1)P_n\alpha)$, again neglecting terms in α^2 and higher powers.

We shall therefore assume $\sigma=\sigma_0(1+k\alpha P_n)$ where k is a constant probably having a value between -2 and $n-1$. The value of k will depend on the interactions between the nucleons which are unknown so at present k can only be estimated by comparing experimental with calculated results.

The value of k in any case makes no difference to the calculated energy level spacings for large values of n so its value is not important.

The work done by the electrical forces for very small values of α for which the shell remains practically spherical with $\sigma=\sigma_0(1+k\alpha P_n)$ is equal to

$$\int_0^\alpha\int_0^\pi 2\pi a^2(1+2\alpha P_n)2\pi\sigma_0^2(1+2k\alpha P_n)\times aP_n\sin\theta d\alpha d\theta=8\pi^2a^3\sigma_0^2\frac{1+k}{2n+1}\alpha^2,$$

neglecting terms in α^3 and higher powers of α. The potential energy P is therefore given by

$$\mathrm{P}=4\pi a^2T\left(\frac{n^2+n+2}{2(2n+1)}\right)\alpha^2-8\pi^2a^2T\frac{1+k}{2n+1}\alpha^2,$$

since $8\pi^2a^3\sigma_0^2=8\pi a^2T$. This gives

$$\mathrm{P}=2\pi a^2T\left(\frac{n^2+n-2-4k}{2n+1}\right)\alpha^2.$$

The kinetic energy of the shell is

$$\frac{1}{2}\frac{Ama^2}{2n+1}\dot{\alpha}^2,$$

where Am is the mass of the shell.

The frequency of vibration ν_n for very small amplitudes is therefore given by

$$\nu_n=(T(n^2+n-2-4k)/\pi Am)^{\frac{1}{2}}.$$

For large values of n this gives nearly equal spaced frequencies with spacings $\Delta\nu$ given by

$$\Delta\nu=\nu_{n+1}-\nu_n=(T/\pi Am)^{\frac{1}{2}},$$

so that $\Delta\nu$ for large n is independent of k. It will be shown later that experimental values of ν_n for small n require k to be small. In what follows therefore we shall put $k=0$. This means that when the mass per unit area of the shell is changed slightly by the distortion the charge per unit area remains unchanged.

With $k=0$

$$\nu_n=(T(n-1)(n+2)/\pi Am)^{\frac{1}{2}}\cdots. \tag{1}$$

The tension T is due to the electrostatic forces, so that

$$2T/a=F^2/8\pi,$$

where $F=Ze/a^2$ is the electric field strength at the surface of the shell and Ze is the nuclear charge. This gives $4\pi T=Z^2e^2/4a^3$ so that Eq. (1) becomes

$$\nu_n=(Ze/4\pi a)((n-1)(n+2)/Ama)^{\frac{1}{2}}\cdots. \tag{2}$$

This makes $\nu_1=0$, as it should be, since P_1 gives a motion of the shell without any distortion when α is very small.

The formula for ν_n gives the possible frequencies for very small amplitudes with $n=2, 3, 4\cdots$.

The values of the energy levels for x-ray excitation found by Wiedenbeck[5] for Rh, Ag, Cd and Au are given in Table I. The values for these elements are equal within the limits of error so that the mean values may be used for comparisons with the theory.

The calculated values are those of

$$E_n=0.387((n-1)(n+2))^{\frac{1}{2}},$$

which is the value of $h\nu_n$ with $k=0$ and $h\Delta\nu=0.387$ Mev with n equal to 3, 4, 5, 6, and 7. The mean values agree

[5] M. L. Wiedenbeck, Phys. Rev. 68, 237 (1945). Wiedenbeck's levels for indium do not agree with the others and are not included.

TABLE III. Calculated and observed values of E_d in Mev.

N	J	Calculated	Observed
−1	1	0.95	0.93
−1	2	1.16	1.18
0	0	1.30	1.30
0	1	1.40	1.43
0	2	1.61	1.66
1	0	1.75	1.75
1	1	1.86	1.81
1	2	2.06	2.09
2	0	2.20	2.20
2	1	2.31	2.34
2	2	2.52	2.53
3	0	2.66	2.66
3	1	2.76	2.76
2	3	2.83	2.82
3	2	2.97	2.95
4	0	3.11	3.11
4	1	3.21	3.20
3	3	3.28	3.31

with the calculated within the limits of experimental error. The value of ΔE for these elements may therefore be taken to be 0.387 Mev. Since the calculated values are for very small amplitudes these results suggest that the vibrations are approximately harmonic. These results show that $k=0$ approximately for these elements so we assume $k=0$ for all elements.

The value of ΔE for the naturally radioactive elements and for the elements of small atomic weights also appears to be equal to 0.387, so we shall assume that ΔE is equal to 0.387 for most elements with $A>9$. This is an empirical result deduced from experimental measurements. With the present theory it enables the nuclear radii to be calculated.

Corresponding to the frequency ν_n the shell will have a ground state with energy $\frac{1}{2}h\nu_n$ and a series of excited states with energies $\frac{3}{2}h\nu_n$, $(5/2)h\nu_n$, $(7/2)h\nu_n\cdots$, or $(N+\frac{1}{2})h\nu_n$.

When the shell is exposed to x-rays of gradually increasing frequency, the ground state $\frac{1}{2}h\nu_n$ may absorb a photon of energy $h\nu_n$ when the frequency becomes equal to ν_n. As the frequency is increased, another photon of energy $h\nu_{n+1}$ may be absorbed when the frequency becomes equal to ν_{n+1} and so on.

The shell may therefore be said to have a series of energy levels with energies $h\nu_n$, $h\nu_{n+1}$, $h\nu_{n+2}\cdots$.

These levels are nearly equally spaced for large values of n, and we shall assume that the nearly equally spaced nuclear levels found experimentally correspond to them. The value of N is unity for these levels, so that higher values of N need not be considered.

Equation (2) gives $\Delta\nu=\nu_{n+1}-\nu_n=Ze/4\pi a(Ama)^{\frac{1}{2}}$, when n is large. This equation enables values of the nuclear radii to be calculated. The values of the radii so calculated depend on the known values of Z and A. The equation for $\Delta\nu$ gives

$$a=(Ze/4\pi\Delta\nu)^{\frac{1}{2}}/(Am)^{\frac{1}{2}}.$$

Putting in the numerical values of e and m and with $\Delta\nu=9.382\times10^{19}$ corresponding to $\Delta E=0.387$ Mev, this gives

$$a=4.65\times10^{-13}(Z^2/A)^{\frac{1}{2}}.$$

This expression for the radius a contains no arbitrary constants.

TABLE IV. Calculated and observed values in kev of resonances in iron bombarded by neutrons.

N	J	Calculated	Observed
0	$\frac{1}{2}$	15	15
0	$1\frac{1}{2}$	30	30
0	$2\frac{1}{2}$	55	—
0	$3\frac{1}{2}$	90	90
0	$4\frac{1}{2}$	135	150
0	$5\frac{1}{2}$	190	195
0	$6\frac{1}{2}$	255	280?
0	$7\frac{1}{2}$	330	325
1	$\frac{1}{2}$	409	405
1	$1\frac{1}{2}$	424	—
1	$2\frac{1}{2}$	449	445
1	$3\frac{1}{2}$	484	475
2	$\frac{1}{2}$	803	800
3	$\frac{1}{2}$	1197	1220?

Table II gives the values of the nuclear radii, given by this formula, for several elements. The last column gives the values of $2.47A^{\frac{1}{3}}$.

It appears that the radius does not vary exactly as $A^{\frac{1}{3}}$; but as A gets smaller, the radius gets smaller a little more slowly than $A^{\frac{1}{3}}$. This agrees with previous estimates of the way in which the radius depends on A.

The value of the radius of the uranium nucleus got from the many particle theory of alpha-ray disintegration is about 13×10^{-13} cm.[6] This agrees as well as could be expected with the shell theory radius 15×10^{-13} cm.

The nuclear radii got from the target areas for fast neutrons are smaller than the radii got from alpha-ray disintegration theory and the shell theory. This may be due to the nuclei being partially transparent for fast neutrons. The transparency would probably be much greater for a shell nucleus than for a liquid drop nucleus.

The spherical shell would be expected to have rotational energies approximately equal to $(h^2/8\pi^2K)j(j+1)$, where j is a quantum number with integral or half-odd integral values and K is the moment of inertia of the spherical shell about an axis through its center. The energy levels E_{nj} of the nucleus should therefore be equal to

$$h\Delta\nu((n-1)(n+2))^{\frac{1}{2}}+(h^2/8\pi^2K)j(j+1).$$

When the nuclear levels are observed with low resolving power, the rotational levels may not appear but with sufficient resolving power they should be found between the nearly equal spaced vibration levels.

Putting

$$K=\tfrac{2}{3}Amr^2,\quad r=4.65\times10^{-13}(Z^2/A)^{\frac{1}{2}}$$

[6] H. A. Bethe, Rev. Mod. Phys. 9, 166 (1937); M. A. Preston, Phys. Rev. 71, 865 (1947).

and $h\Delta\nu=0.387$ Mev, we get

$$E_{nj}=0.387((n-1)(n+2))^{\frac{1}{2}}+1.44(AZ^4)^{-\frac{1}{3}}j(j+1)$$

for the energy levels in Mev.

The resonances observed in the bombardment of carbon by deuterons[7] occur with deuteron energies E_d given by

$$E_d(12/14)=E_{nj}-E,$$

where E is the reaction energy which is about 10.26 Mev. With $n=29$ and $j=0$ E_{nj} is 11.40 Mev. There should therefore be a resonance with E_d equal to about $(14/12)(11.40-10.26)$ or about 1.33 Mev. A resonance is observed with $E_d=1.30$ which may therefore be assumed to correspond to E_{nj} with $n=29$ and $j=0$. The vibration levels with large values of n are equally spaced with separations 0.387 Mev so the corresponding resonances should be equally spaced with separations $0.387\times14/12=0.452$ Mev. $(14/12)1.44(AZ^4)^{-\frac{1}{3}}$ with $A=14$ and $Z=7$ is equal to 0.052 so the resonances should occur with deuteron energies in Mev given by

$$E_d=1.30+0.452N+0.052j(j+1)$$

where N is an integer.

Table III gives the calculated and observed values of E_d in Mev. The observed values are those adopted in a previous paper[8] where this case is discussed in detail.

The resonances observed when iron is bombarded by neutrons[9] should be given by a similar formula. With $A=57$ and $Z=26$ we get

$$15+394N+5(j(j+1)-\tfrac{3}{4})\text{ kev.}$$

Table IV gives the calculated and observed values in kev. The resolving power above 500 kev was not sufficient to show the rotation levels. This case is discussed in greater detail in a previous paper.[10] Several other examples of rotation levels are discussed in references 8 and 10.

The sulfur nuclear levels measured by Davison[11] are compared with values of $0.387((n-1)(n+2))^{\frac{1}{2}}$ in Table V. The resolving power in this case was not good enough to show the rotation levels. The probable error was estimated to be ±0.11 so that the differences between the observed and calculated values are probably due to experimental errors. In this case the level for $n=2$ was not absent as in Wiedenbecks experiments

The energy levels of several other nuclei have been measured but unfortunately most of the results are not sufficiently exact to make comparisons of the observed values and the calculated values of E_{nj} very significant.

[7] Hydenberg, Inglis, Whitehead, and Hafner, Phys. Rev. **75**, 1147 (1949); Bonner, Evans, Harris, and Phillips, Phys. Rev. **75**, 1401 (1949).
[8] H. A. Wilson, Phys. Rev. **76**, 687 (1949).
[9] Barschall, Bockelman, and Segondollar, Phys. Rev. **73**, 659 (1948).
[10] H. A. Wilson, Phys. Rev. **74**, 351 (1948).
[11] P. W. Davison, Phys. Rev. **75**, 757 (1949).

TABLE V. Calculated and observed values for nuclear levels in sulfur.

n	Calculated	Observed (Mev)
2	0.77	0.79
5	2.05	1.90
6	2.45	2.17
7	2.84	2.85
8	3.24	3.15
9	3.64	3.88
10	4.03	4.15
11	4.41	4.42
12	4.80	4.70
13	5.19	5.11
14	5.58	5.63
16	6.36	6.30

TABLE VI. Values of E calculated from the formula and compared with values obtained from the atomic weight.

Element	A	Z	E Calculated	E Found (Mev)
Uranium	238	92	1795	1776
Silver	109	47	894	920
Cobalt	59	27	497	507
Aluminum	27	13	225	224
Boron	11	5	78	76
Beryllium	9	4	59	58

Values of n and j can be found which make the calculated values agree with the observed values within the limits of error in nearly all cases.

Since it appears that the shell theory, at least in some cases, gives very exact values of the energy levels, the question arises as to how a uniform shell can be supposed to represent a small number of particles arranged on the surface of a sphere. For example, the N^{14} nucleus has only 14 nucleons and the value of n in $0.387((n-1)(n+2))^{\frac{1}{2}}$ for the 1.30-Mev resonance in Table III is 29. It is obvious that 14 particles cannot be supposed to vibrate so as to give even a rough representation of a uniform shell vibrating so that $r=a(1+\alpha P_{29})$ where P_{29} is the zonal harmonic of order 29. It seems therefore that the shell model makes it necessary to suppose that the nucleons are in some way fused together in the nucleus so that they actually form a uniform spherical shell or at any rate behave like such a shell. According to this idea then a nucleus may be regarded as consisting of a single uniform shell and not as a number of discrete particles.

Nuclei may be supposed formed by the combination of neutrons and protons. The energy released in such combinations is relatively small so that the mass of a nucleus is roughly a multiple of the mass of one nucleon. The shell theory seems to suggest that nuclei do not contain neutrons and protons. When a nucleus disintegrates with the emission of neutrons, protons or electrons these particles may be formed at the moment of disintegration.

The negative energy of formation E of a nucleus on the shell theory should be a function of A, Z and r. A simple expression for E which agrees approximately

TABLE VII. Energy levels between 0 and 5 Mev.

Observed levels	Mean values	n	$0.387((n-1)(n+2))^{\frac{1}{2}}$
0.453	0.453	—	—
0.7, 0.8, 0.845	0.78	2	0.77
1.2, 1.26, 1.07	1.18	3	1.22
1.5, 1.74, 1.77	1.67	4	1.64
2.0, 2.1, 2.2, 2.01	2.08	5	2.05
2.34, 2.55, 2.48	2.46	6	2.45
3.0, 3.0	3.0	7	2.84
3.18, 3.25	3.21	8	3.24
3.45, 3.61	3.53	9	3.64
3.95, 4.0, 4.2	4.05	10	4.03
4.4, 4.47,[a] 4.38	4.42	11	4.41
4.8, 4.8, 5.0, 4.8	4.85	12	4.80

[a] W. M. Gibson, Proc. Phys. Soc. London **62**, 586 (1949).

with the values of E got from the atomic weights is

$$E=cA-d-kAr^2-Z^2e^2/2r.$$

The last term is the electrostatic energy and c, d and k are constants.

The equilibrium value of r is got by putting $\partial E/\partial r=0$. This gives

$$2kAr=Z^2e^2/2r^2$$

or

$$r=(e^2/4k)^{\frac{1}{3}}(Z^2/A)^{\frac{1}{3}}.$$

This makes the shell stable for uniform radial displacements. Using the shell theory value

$$r=4.65\times10^{-13}(Z^2/A)^{\frac{1}{3}},$$

we get $k=5.7\times10^{17}$ with the energy in ergs.

With the equilibrium value of r kAr^2 is equal to $Z^2/e^2/4r$ so that

$$E=cA-d-\tfrac{3}{4}(Z^2e^2/r),$$

with

$$r=4.65\times10^{-13}(Z^2/A)^{\frac{1}{3}},\quad \tfrac{3}{4}(Z^2e^2/r)=0.232(Z^4A)^{\frac{1}{3}}\text{ Mev}.$$

Using the known values of E, we find $C=10.2$, $d=30$ so that

$$E=10.2A-30-0.232(Z^4A)^{\frac{1}{3}}\text{ Mev}.$$

Table VI gives values of E calculated with this expression and values got from the atomic weights.

According to the shell theory the average level spacing of observable levels is about 0.1 Mev for all elements and all excitations. This follows if we assume about four observable rotation levels associated with each vibration level.

According to current theories the level spacing depends on the excitation energy E and on the mass number A. For $E=8$ Mev and $A=120$ it is from 100 ev to 10 ev. Thus with $E=8$ and $A=120$ the level spacing on the shell theory is from 1000 to 10,000 times greater than on current theories.

The experimental evidence for the small level spacing is mainly that when elements are bombarded by neutrons with energies between 0 and 100 ev one or more resonances are observed in this range in many cases. Thus if one resonance is observed between 0 and 100 ev it is assumed that there will be on the average about one resonance per 100 ev so that the average spacing is about 100 ev.

On the shell theory the presence of a resonance between 0 and 100 ev shows that the energy of the reaction $A^N+n^1\rightarrow A^{N+1}$ is only slightly less than the energy of one of the levels E_{nj}. The energies of the reactions $A^N+n^1\rightarrow A^{N+1}$ can be calculated from the atomic weights and are in fact in most cases nearly equal to a value of $0.387((n-1)(n+2))^{\frac{1}{2}}$ within the limits of error. Unfortunately the atomic weights are not known with sufficient accuracy to check this conclusion very closely. For example the energy of the reaction $Li^6+n^1\rightarrow Li^7$ got from the atomic weights is 7.15 Mev and with $n=18$ $0.387((n-1)(n+2))^{\frac{1}{2}}$ is equal to 7.14 which is equal to 7.15 within the limits of error. Similar results are obtained in nearly all other cases where the atomic weights are known with sufficient accuracy to make the comparison at all significant.

As we have seen the resonances observed with nitrogen and iron and in other cases agree with the shell theory. The observed level spacing with iron is about 500 times greater than would be expected on current theories.

In some cases a group of several neutron resonances is found between 0 and 100 ev. On the shell theory this indicates that the levels E_{nj} may have a fine structure when examined with high resolving power. Such fine structure might be expected because there are $2n+1$ different modes of vibration of the shell for each value of n. Thus any slight departure of the shell from uniformity or any small disturbing cause could split the levels into groups.

APPENDIX

Table VII gives the energy levels of the light nuclei[12] Ne^{20}, N^{14}, C^{13}, N^{13}, C^{12}, C^{11}, B^{11}, B^{10}, Be^8, Li^7, and of Co[13] and Mn[14] between 0 and 5 Mev. The mean values and the values of $0.387((n-1)(n+2))^{\frac{1}{2}}$ are also given. The level 0.453 of Li^7 is probably a rotation level. Some of the other levels may be rotation vibration levels but the observed values are not exact enough to distinguish between vibration levels and rotation vibration levels.

[12] W. F. Hornyak and T. Lauritsen, Rev. Mod. Phys. **20**, 191 (1948).
[13] G. T. Seaborg, Rev. Mod. Phys. **16**, 7 (1944).
[14] A. B. Martin, Phys. Rev. **72**, 378 (1947).

Moderation of Negative Mesons in Hydrogen I: Moderation from High Energies to Capture by an H_2 Molecule

A. S. WIGHTMAN
Palmer Physical Laboratory, Princeton, New Jersey
(Received August 5, 1949)

The moderation of negative μ- and π-mesons, as well as of hypothetical negative particles of mass 1000 m and 1837 m is described for a hydrogen moderator and a meson energy range: 10 Mev→0 ev (capture by an H_2 molecule). In this energy range, there are three principal modes of energy loss by the mesons: 1. High energy ionization loss, describable by the ordinary stopping power theory. 2. Energy loss due to nuclear collisions. 3. Low energy ionization loss caused by non-adiabatic processes special to hydrogen. From estimates of the probability of these three processes, the moderation times of a meson in liquid hydrogen from 10 Mev to capture by an H_2 molecule are calculated:

	μ^-	π^-	τ^-	P^-
From 10 Mev to $v/c=5\times10^{-2}$	8.6×10^{-10} sec.	4.8×10^{-10}	2.9×10^{-10}	2.4×10^{-10}
From $v/c=5\times10^{-2}$ to $v/c=6\times10^{-3}$	7.4×10^{-11}	9.7×10^{-11}	3.4×10^{-11}	6.3×10^{-11}
From $v/c=6\times10^{-3}$ to $v/c=5\times10^{-4}$ in $^1H_2$	7.9×10^{-11}	7.4×10^{-11}	1.5×10^{-11}	2.4×10^{-11}
From $v/c=6\times10^{-3}$ to $v/c=5\times10^{-4}$ in $^2H_2$	9.0×10^{-11}	1.1×10^{-11}	2.2×10^{-11}	2.9×10^{-11}
From $v/c=6\times10^{-3}$ to $v/c=5\times10^{-4}$ in $^3H_2$	9.4×10^{-11}	1.2×10^{-11}	2.6×10^{-11}	3.4×10^{-11}

1. INTRODUCTION

THE absorption of negative mesons in hydrogen and deuterium can yield interesting information on the character of mesons and their coupling to nucleons.[1] However, the possibility of an experiment depends on an appreciable fraction of the negative mesons being absorbed before decay can take place. In this and a following paper we analyze the moderation of a negative meson in liquid hydrogen. Such an analysis might seem superfluous, because of the existence in the literature of detailed studies of the mechanism of slowing down of negative mesons.[2] However, so far as the present author knows, those studies were not intended to apply to the case of hydrogen and in part, at least, use approximations inappropriate to that case. In fact, as we shall see, a principal part of the moderation process takes place by molecular mechanisms peculiar to the case of hydrogen.[3]

In this first paper, we consider the moderation of a negative meson from 10 Mev down to energies less than 0 ev. At the low energy end of this range the meson is bound to a hydrogen molecule. This energy range can be divided into three parts according to the velocity of the meson.

1. Velocity of the meson $\gg e^2/\hbar \approx$ the velocity of electrons in a hydrogen atom or molecule. For this energy range the ordinary stopping power formula can be used.

2. Velocity of the meson of the same order of magnitude as $e^2/\hbar$, the velocity of the electrons in the hydrogen atom or molecule. For this energy range, the ordinary stopping power formula fails, but the exact Born approximation expression for the stopping power is valid.

3. Velocity of the meson $< e^2/\hbar$. Here the energy loss of the meson due to ionization drops off to zero very rapidly as calculated in Born approximation. However, the Born approximation is no longer valid for these meson velocities and other appropriate methods of calculation show that energy loss by ionization continues down to very low meson velocities. In addition to the ionization loss, there is energy loss by nuclear collision which is of the same order of magnitude as ionization loss in this velocity range. At higher velocities nuclear collisions yield an energy loss negligible in comparison to the ionization loss. We consider each of these three velocity ranges in turn in the following sections.

The calculations are carried out for the three hydrogen isotopes as moderators, and for four kinds of negative particles, μ^--mesons, π^--mesons and the hypothetical particles, τ^--meson (mass assumed to be 1000 m) and negative proton (mass assumed to be 1837 m). For brevity, we shall carry out our discussion for the case of π^--mesons in $^1H_2$.

2. ENERGY LOSS FOR MESON VELOCITY $v \gg e^2/\hbar$

The ordinary stopping power formula is:

$$-\frac{dE}{dx}=\frac{4\pi Ne^4}{mv^2}\ln(2mv^2/I), \qquad (1)$$

[1] See for example: B. Ferretti, "Report of an International Conference on Fundamental Particles and Low Temperatures," Phys. Soc. London (1947), p. 75. C. Marty and J. Prentki, J. de phys. et rad. **10**, 156 (1949). Irving Stein and L. I. Schiff, Phys. Rev. **76**, 461 (1949). R. E. Marshak and A. S. Wightman, Phys. Rev. **76**, 114 (1949). A. S. Wightman, Thesis, Princeton (1949).

[2] Fermi, Teller, and Weisskopf, Phys. Rev. **71**, 314 (1947). E. Fermi and E. Teller, Phys. Rev. **72**, 399 (1947). H. Fröhlich, Nature **160**, 255 (1947). Fröhlich, Huby, Kolodziejski, and Rosenberg, Nature **162**, 450 (1948). B. Ferretti, Nuovo Cimento **5**, 325 (1948). N. F. Mott, Proc. Phys. Soc. London **62**, 136 (1949).

[3] These mechanisms result from the formation and inelastic collisions of π^-H^+ atoms, and seem to have been mentioned first by Fermi and Teller, Phys. Rev. **72**, 406 (1947).

TABLE I. Time, t, in seconds, to moderate meson from 10 Mev to velocity $v/c=5\times10^{-2}$ according to the stopping power formula (1). Compare with mean lives for decay $\tau_\mu=2\times10^{-6}$ sec., $\tau_\pi=1.1\times10^{-8}$ sec. Liquid H_2 at $-253°C$, one atmosphere pressure. H_2 gas at 0°C, one atmosphere pressure.

	μ	π	τ	P
Liquid H_2	8.64×10^{-10}	4.78×10^{-10}	2.94×10^{-10}	2.42×10^{-10}
H_2 Gas	6.77×10^{-7}	3.79×10^{-7}	2.34×10^{-7}	1.92×10^{-7}

where I is the mean ionization energy of moderator; N is the number of atoms of moderator per unit volume; v is the velocity of incident meson; m is the electron mass. The moderation time of a meson calculated from (1) is given by:[4]

$$t=\int dE/v(dE/dx)=1/8\pi(\mu/m)(\bar{v}/c)^3[(m^2c^3)/(Ne^4)]\times[Ei(3\ln(v/\bar{v}))-Ei(3\ln(v_0/\bar{v}))].$$

$\mu\equiv$meson mass; $v\equiv$final meson velocity; $v_0\equiv$initial meson velocity, $\bar{v}/c=(I/2mc^2)^{\frac{1}{2}}=4.17\times10^{-3}$ for hydrogen $E=\frac{1}{2}\mu v^2$.

We tabulate this formula for several cases (see Table I): As moderators we take hydrogen gas at 0°C and one atmosphere pressure and liquid hydrogen. For the gas $N=2\times2.69\times10^{19}$ atoms/cm^3, for the liquid at 20°K and one atmosphere pressure $N=4.275\times10^{22}$ atoms/cm^3.

Comparing the times of Table I with the mean lives for decay of μ- and π-mesons, one sees that in liquid hydrogen a very small percentage of μ- and π-mesons will decay during this part of the slowing down. In order for a similar statement to hold for π-mesons in gaseous hydrogen one would have to compress it to a density within better than a factor ten of the density of liquid hydrogen.

Relativistic corrections to the above formula for the moderation time, t, come from two sources: The relativistic corrections to the stopping power formula $(\ln(2mv^2/I)$ is replaced by $\ln(2mv^2/I)-\ln(1-v^2/c^2)-v^2/c^2)$, and the relativistic variation of the mass of the meson with velocity. For mesons with initial velocities $v\approx0.4c$ the first correction is less than 0.1 percent. The second is then about 10 percent and so would have to be taken into account if very accurate moderation times were needed. There is no point in making this correction here because the uncertainties in the moderation time for later portions of the moderation are at least of this order of magnitude.

3. BORN APPROXIMATION CALCULATION OF THE ENERGY LOSS OF A MESON BY INELASTIC COLLISION IN A GAS OF HYDROGEN ATOMS

Bethe has derived a theoretical expression for the energy loss by ionization of a charged particle passing through hydrogen.[5] Hirschfelder and Magee have given a semi-empirical expression for the stopping power of hydrogen for protons based on an exact calculation by Bethe for elements with $Z\geqslant4$ in which outer screening is taken into account.[6] However, the formulas of Bethe for hydrogen do not seem to have been evaluated numerically for velocities of order of magnitude, e^2/h. In this section, we record the results of such a numerical evaluation.

According to reference 5, p. 367, the stopping power of hydrogen per atom per unit volume is given by

$$\frac{1}{(4\pi a_0^2)(e^2/2a_0)}\left(\frac{-dE/dx}{N}\right)=\frac{\int\Delta Ed\sigma\Delta E}{(4\pi a_0^2)(e^2/2a_0)}$$

$$=\left(\frac{e^2}{hc}\right)^2\left(\frac{c}{v}\right)^2\left\{\sum_{n=2}^{\infty}(\epsilon_n+1)\int_{Q\min}^{Q\max}\frac{dQ}{Q^2}|F_{1n}(Q)|^2+\int_0^{\epsilon-1}(w+1)dw\int_{Q\min}^{Q\max}\frac{dQ}{Q^2}|F_{1w}(Q)|^2\right\},\quad(2)$$

where v is the initial velocity of meson; ϵ is the initial energy of meson in Rydbergs. ϵ_n and w are the energy levels of hydrogen atom measured in Rydbergs from the ionization limit; Q is a measure of momentum transfer in Rydbergs. $-dE/dx$ is the stopping power;

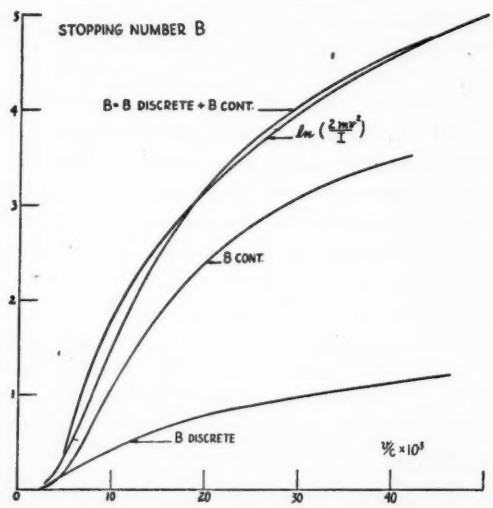

FIG. 1. Stopping number of hydrogen for negative particles. B_{discrete} gives the contribution to the stopping number due to excitation of discrete states of hydrogen atoms. B_{cont} gives the contribution due to ionization of hydrogen atoms. Their sum, B, can be approximated for $v/c\gg e^2/\hbar c$ by $\ln(2mv^2/I)$, where I, the mean ionization energy of hydrogen, is 17.6 ev.

[4] Yukawa and Okayama. Papers of the Inst. Phys. Chem. Research 36, 385 (1939) have calculated moderation times from (1) taking into account the relativistic variation of mass with velocity, but neglecting the variation of the logarithm in (1). For our purposes, it is more worth while to take into account the variation of the logarithm but to calculate non-relativistically.

[5] H. A. Bethe, Ann. d. Physik 5, 325 (1930).

[6] J. O. Hirschfelder and J. L. Magee, Phys. Rev. 73, 210 (1948).

N is the number of H atoms per unit volume.

$$Q_{\min}=(\bar{\mu}/m)(\epsilon^{\frac{1}{2}}-(\epsilon-(\epsilon_n+1))^{\frac{1}{2}})^2$$
$$Q_{\max}=(\bar{\mu}/m)(\epsilon^{\frac{1}{2}}+(\epsilon-(\epsilon_n+1))^{\frac{1}{2}})^2$$

where $\bar{\mu}$ is the reduced mass of meson. The definitions of the form factors F_{1n} and F_{1w} are given by Bethe.[7] The evaluation of the sum in Eq. (2) is carried out by him in reference 5. We have evaluated his expression for the sum and have carried out a numerical integration to subdue the integral. The results for the stopping number are shown in Fig. 1. (The stopping number is $-(dE/dx)/(4\pi Ne^4/mv^2)$.) The stopping power is shown in Fig. 2.

4. ESTIMATE OF ENERGY LOSS BY NUCLEAR COLLISION

For meson velocities large compared with electron velocities in hydrogen molecules, $e^2/\hbar$, the contribution of nuclear Coulomb scattering to the energy loss of a meson is less than the energy loss to electrons by a factor of order of magnitude (m/M_H)=(electron mass/nuclear mass). However, for meson velocities less than $e^2/\hbar$, the energy lost to electrons decreases precipitously and contribution of nuclear collisions becomes more important. Of course, for sufficiently low energies of the meson the energy loss from nuclear collisions also drops off very rapidly but this occurs at a meson energy of the order of magnitude of the binding energy of the nuclei in the molecule $\approx(1/3)e^2/2a_0 \ll 1/6\mu(e^2/\hbar)^2$.

To get a quantitative estimate of the energy loss of the meson due to nuclear collisions we use the Rutherford cross section for the scattering of the meson by a free nucleus. Only afterwards and then only approximately do we take account of the screening and binding of the nuclei, by limiting the possible energy transfers to greater than a certain minimum $\approx(1/3)e^2/2a_0$. The justification for this treatment is that over the energy range in which we are interested, the time of collision is short compared to the period of the vibrations of the nuclei in the ground state of the H_2 molecule.

The cross section for collision with energy loss between Q and $Q+dQ$ is given by the so-called knock-on formula

$$d\sigma_Q=(2\pi e^4/M_Hv^2)(dQ/Q^2).$$

The average energy loss is, in convenient units,

$$\frac{\int Qd\sigma_Q}{(4\pi a_0^2)(e^2/2a_0)}=\left(\frac{m}{M_H}\right)\left(\frac{e^2}{\hbar c}\right)^2\left(\frac{c}{v}\right)^2\ln\left(\frac{Q_{\max}}{Q_{\min}}\right). \quad (3)$$

$Q_{\max}$ is determined from the maximum possible energy transfer in head on collision

$$Q_{\max}=2[(\bar{\mu}^2v^2)/M_H],$$

where

$$\bar{\mu}=[(\mu M_H)/\mu+M_H],$$

while we take

$$Q_{\min}=(1/3)e^2/2a_0.$$

Equation (3) is plotted in Fig. 2, for representative meson and moderator masses.

5. ENERGY LOSS BY IONIZATION IN SLOW COLLISIONS

For meson velocities $<e^2/\hbar$ it is reasonable to try a different approach to the calculation of the energy loss, an adiabatic approach in which, as a first approximation, the meson and nuclei are regarded as standing still and the electrons moving in stationary states around them. The fact that the meson is moving can be taken into account approximately afterward. A special feature of the problem under consideration is the negative charge of the mesons. From this circumstance it follows that even in the adiabatic limit the meson may suffer energy loss. The presence of a negative meson in the interior of a hydrogen molecule may make it impossible for two electrons to be bound to the system. In this case, the collision between a negative meson and H_2 may result in ionization even though the negative meson moves infinitely slowly.

On the other hand, if the ground state of the molecule always binds two electrons regardless of the position

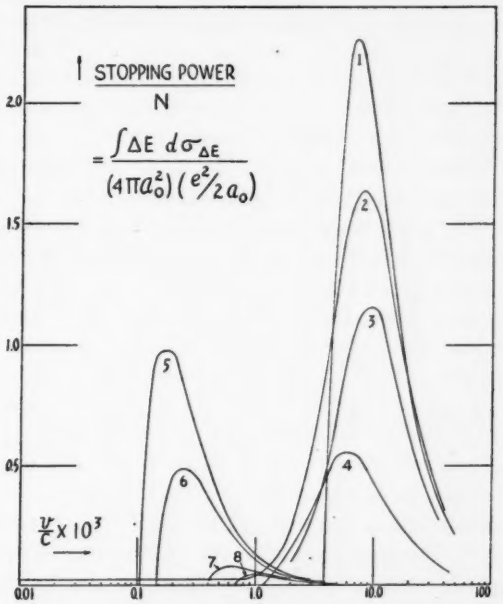

FIG. 2. Stopping power of hydrogen divided by number of hydrogen atoms per unit volume, in units of $(4\pi(\text{Bohr radius})^2)$ (Rydberg). **1**: According to ordinary stopping power formula, given by Eq. (1). **2**: For $v/c>10^{-3}$ this curve is calculated using Born's first approximation for $v/c<10^{-3}$, its magnitude is estimated in Section 5. **3**: Contribution to Born approximation stopping power due to ionization of hydrogen atoms. **4**: Contribution to Born approximation stopping power due to excitation of discrete states of H atoms. **5**: Due to nuclear collisions, for negative protons in $^1H_2$. **6**: Due to nuclear collisions for τ^--mesons in $^1H_2$. **7**: Due to nuclear collisions for π^--mesons in $^1H_2$. **8**: Due to nuclear collisions for μ^--mesons in $^1H_2$.

[7] H. A. Bethe, *Handbuch der Physik* Vol. 24–1, p. 503 (1933), Eqs. 52.11 and 52.13. Note missing Q in numerator of 52.13.

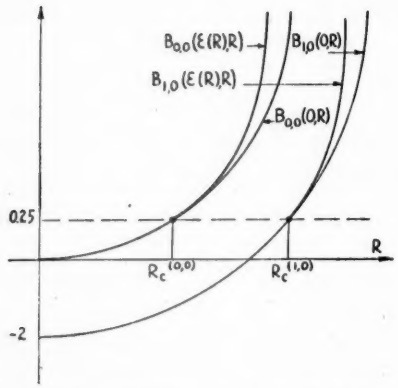

FIG. 3. Qualitative behavior of $B_{0,0}(\epsilon, R)$ and $B_{1,0}(\epsilon, R)$ for states of zero energy and for the two lowest bound states.

of the negative meson in its interior there will be no inelastic collisions at all in the adiabatic limit.

Suppose that the second situation occurs and the molecule always binds two electrons no matter what the position of the negative meson, but suppose, in addition, there are locations in the molecule for which the binding energy of an electron is very close to zero. Then, the passage of the negative meson through those regions with a finite velocity makes the electron particularly vulnerable to non-adiabatic transitions to states of positive energy.

In order to understand more clearly the case of molecular hydrogen we have studied in some detail the case of atomic hydrogen. For atomic hydrogen the energy loss problem reduces to the study of the states of π^-H system. We summarize the results for atomic hydrogen in the following paragraphs.

In order to carry out the adiabatic approximation, we first examine the states of an electron moving in the field of a fixed meson and proton. The Schrödinger equation of this problem is separable and an exact solution can be found.

The qualitative nature of the electron wave function is evident from the fact that for large meson proton separations, R, it must be approximately the wave function of a hydrogen atom, and for small separations that of an electron moving in the potential of an electric dipole of moment eR. For sufficiently small R, such a dipole has no bound states. Consequently, it is clear that there exists a critical radius $R_c^{(0,0)}$ such that for $R<R_c^{(0,0)}$ no bound states exist.[8] For values of R large compared with $R_c^{(0,0)}$, the energy of the system can be calculated from the Stark Effect of the hydrogen atom.

The wave equation of the system is separable in prolate spheroidal coordinates,[9] and leads to the ordinary differential equations

$$(d^2\Phi/d\phi^2)-m^2\Phi=0,$$

$$d/d\xi((\xi^2-1)dM/d\xi)+[B+\epsilon\xi^2-(m^2/\xi^2-1)]M=0, \quad 1\leq\xi<\infty,$$

$$d/d\eta((1-\eta^2)dN/d\eta)+[-B-\epsilon\eta^2-2R\eta-(m^2/1-\eta^2)]N=0, \quad -1\leq\eta\leq1,$$

where, when energy is measured in units of a Rydberg ($=e^2/2a_0$) and distance in units of the Bohr radius, a_0; $\epsilon=R^2/4[E+(2/R)]$, $B\equiv$dimensionless separation constant, and $\psi=MN\Phi$.

The condition that the wave function be square integrable leads to the restrictions

$$\int_{-1}^{+1}d\eta|N|^2<\infty, \quad \int_{-1}^{+1}d\xi|M|^2<\infty.$$

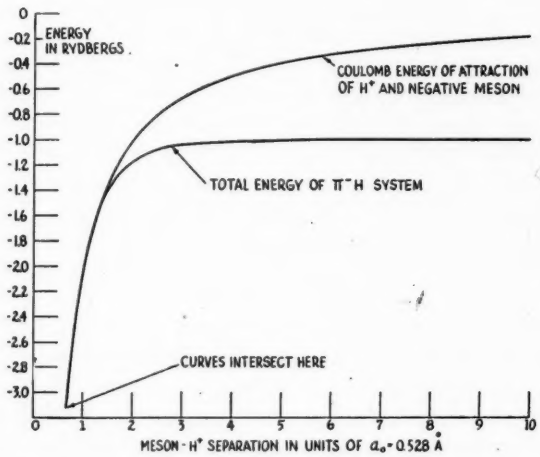

FIG. 4. Energy of π^-H system as a function of meson—H^+ separation. The system cannot bind its electron if the meson and H^+ get closer together than $0.639a_0$.

The first of these determines a denumerable set of B's:

$$B=B_{l,m}(\epsilon, R).$$

This denumerable set of $B_{l,m}$ is somewhat analogous to the square of the angular momentum which occurs in a central field problem. Just as in that case, the condition of square integrability of the angular wave function determines the possible separation constant for each value of the energy. Here, however, the separation constant B varies with the energy and, in addition, is a function of the nuclear separation. The values of $B_{l,m}$ can be computed by standard methods.[10]

The second condition applies to the solution, M, of the "radial" equation. This second condition also determines a family of B's:

$$B=B_{n,m}(\epsilon).$$

[8] This might be guessed from the fact that even the spherically symmetric potential $V=-e^2R/r^2$ has no bound states for $R<a_0/8$. See G. Shortley, Phys. Rev. 38, 120 (1931). The existence and size of the critical radius for our problem was pointed out by Fermi and Teller, Phys. Rev. 72, 406 (1947).

[9] For a general discussion of the solution of this equation, see G. Baber and H. R. Hassé, Proc. Camb. Phil. Soc. 31, 564 (1935).

[10] See reference 9 or the author's thesis. N is developed in a series of Legendre polynomials. The differential equation then leads to a three term recursion formula which can be solved in terms of continued fractions.

If we ignore the fact that this B must be the same as the B determined from the angular equation, then for every real value of ϵ we get a value of B. Finally by equating the B of the angular equation with the B of the radial equation we get

$$B_{n,m}(\epsilon)=B_{l,m}(\epsilon, R), \tag{4}$$

an equation which determines the possible values of the energy. The most convenient way to do the computation of the energy of the ground state as a function of R turned out to be

(1) to assume a value of ϵ and determine the corresponding value $B_{0,0}(\epsilon)$ from the radial equation;

(2) taking those values of $B_{0,0}$ and ϵ to compute for what value of R, Eq. (4) was satisfied.

The qualitative behavior of the B for the two lowest states is shown in Fig. 3. It is evident from Fig. 3 that with decreasing internuclear distance the B value for a given bound state approaches closer and closer to the B value for the corresponding state of zero energy until finally for $B=\frac{1}{4}$ the critical radius is reached and the bound state disappears into the continuum. The justification for this statement is obtained by studying the radial equation for zero electron binding energy, $E+2/R=0$. For simplicity, we consider the case of zero azimuthal quantum number, $m=0$. M satisfies

$$d/d\xi[(\xi^2-1)(dM/d\xi)]+BM=0.$$

The general solution of this, the Legendre equation, can be written

$$M=aP_\alpha(\xi)+bQ_\alpha(\xi),$$

where $-\alpha(\alpha+1)=B$ and P_α and Q_α are Legendre functions of the first and second kind. Now

$$\alpha=-\tfrac{1}{2}\pm\tfrac{1}{2}(1-4B)^{\frac{1}{2}},$$

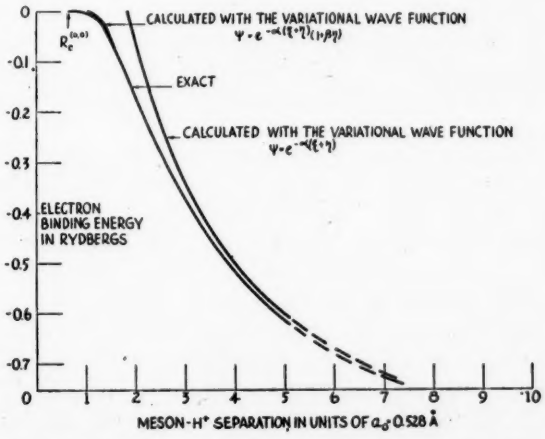
CALCULATED WITH THE VARIATIONAL WAVE FUNCTION
EXACT
CALCULATED WITH THE VARIATIONAL WAVE FUNCTION
ELECTRON BINDING ENERGY IN RYDBERGS
MESON-H+ SEPARATION IN UNITS OF a0=0.528 Å

FIG. 5. Binding energy of electron to π^-H system as a function of meson—H^+ separation. $R_c^{(0,0)}$ is the critical radius for which the electron becomes unbound. The exact curve is compared with approximate curves calculated by variational methods. Although the two-parameter variational wave function gives quite accurate values of the binding energy, it gives a misleading value of the critical radius.

and $P_\alpha(\xi)$ is asymptotically proportional to ξ^α while $Q_\alpha(\xi)\sim\xi^{-(\alpha+1)}$. Thus for $B>\frac{1}{4}$ the asymptotic form of M has in general an infinity of nodes while for $B<\frac{1}{4}$ it has at most a finite number and with proper choice of a and b, no nodes. These statements about the asymptotic form of M also hold for M itself. Now, if there is a zero energy state with no nodes, then there can exist no bound state, for the lowest state always has the smallest number of nodes, less than the number of nodes possessed by any other state.[11] Thus, no bound state can exist with $B<\frac{1}{4}$. At $B=\frac{1}{4}$ the state of zero energy suddenly acquires in infinity of nodes. Since the number of nodes of the lowest state is a continuous function of the parameter R, it must be for $B=\frac{1}{4}$ that a state with $\epsilon=0$ and no nodes breaks out of the continuum and becomes a bound state. Thus, the critical radius, $R_c^{(0,0)}$ for the lowest state can be found by solving the equation

$$\tfrac{1}{4}=B_{0,0}(0, R_c^{(0,0)}).$$

It turns out that $R_c^{(0,0)}=0.639a_0$.[8] A similar consideration can be carried out for the critical radius of the state specified by the quantum numbers l and m.

In Figs. 4 and 5 we have plotted for the lowest state the total energy E of the π^-H system and the binding energy E' of the electron as a function of the meson-proton separation. Note the binding energy of the electron is very close to zero for a considerable range of R greater than the critical radius, $R_c^{(0,0)}$.

With this information on the energy, E, of the system as a function of R, we can calculate the energy loss of the meson due to ionization in the adiabatic approximation as follows. Treat the motion of the meson as that of a classical particle moving in the potential $E(R)$. Compute the largest impact parameter, R, for which the orbit of the meson reaches the critical radius. Then the cross section for ionization is and the average energy loss satisfies the inequality

$$\int \Delta E d\sigma_{\Delta E} \geqslant (e^2/2a_0)\pi R^2.$$

We can get a lower limit to the right-hand side by replacing R by $R_c^{(0,0)}$. Then

$$\frac{\int \Delta E d\sigma_{\Delta E}}{(4\pi a_0^2)(e^2/2a_0)} \geqslant 0.102.$$

In this simple consideration we have treated the nucleus as infinitely heavy. Actually, there will be a large correction due to the motion of the nucleus. We will not discuss this correction, since it has already been taken into account for the molecular case by the calculations of Section 4. Thus it is clear that in a gas

[11] See, for example, Courant-Hilbert, Methoden der Math. Phys. I (Interscience Publishers, New York, 1943), Chapter 6.

TABLE II. Radial distribution of charge: Difference between density for H^- and H, as a function of distance from the nucleus.

r	$-[(dZ/dr)_{H^-}-(dZ/dr)_H]$
0.00	0.000
0.25	0.002
0.50	0.019
0.75	0.051
1.00	0.092
1.25	0.135
1.50	0.175
2.00	0.227
3.00	0.238
4.00	0.182
5.00	0.119
6.00	0.062

of hydrogen *atoms* a negative meson of velocity $e^2/\hbar$ would be moderated rapidly toward zero velocity, due to ionization alone. For example a π^--meson might be expected to spend less than 10^{-11} second in the energy range 1000 ev to 5 ev.

The case of an atomic hydrogen moderator is particularly suited to the testing of approximate methods which one might use to treat the case actually met in the laboratory: H_2 molecules. We have tested variational methods for the determination of the wave function of the π^-H system. The wave functions used were

$$\psi=e^{-\alpha(\xi+\eta)} \quad \text{and} \quad \psi=e^{-\alpha(\xi+\eta)}(1+\beta\eta).$$

The results are shown in Fig. 5. It is clear that the two parameter wave function gives a rather good value of the energy over most of the range of R, accurate, indeed, to about 0.005 Rydberg. However it gives quite a misleading value for the critical radius: $R_c^{(0,0)}\approx 1.0a_0$, instead of $0.639a_0$. This gives an ominous sign of the difficulties to be expected in the case of a hydrogen molecule. There, it is impossible with present methods to solve the problem exactly and it appears that even if we calculate the energy to a thousandth of a Rydberg by variational methods, and find a value of the "critical position" where the second electron of H_2 becomes unbound, we may be completely wrong because the binding energy curve may well behave just as that of Fig. 5 for the hydrogen atom.

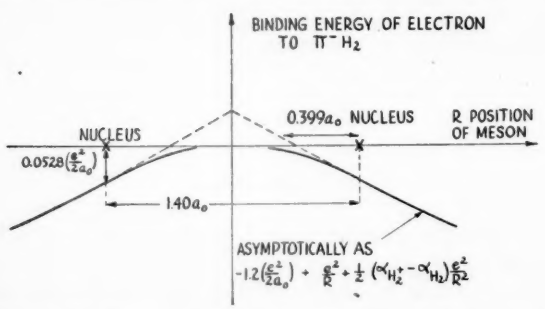

FIG. 6. Binding energy of electron to π^-H_2 as a function of meson position on H_2 internuclear axis. The H_+ nuclei are at the H_2 equilibrium separation. The position and slope of the binding energy curve at the nuclei are determined from existing information on the H^- atomic ion. The dashed lines are linear extrapolations of the slope at the nuclei. The solid line gives the expected behavior of the binding energy curve.

It is interesting to note how spread-out the wave function of the electron becomes as the meson approaches the critical radius. For example for $R=1.00a_0$, $\alpha=0.01$ so that the approximate wave function requires $50a_0$ in order to drop to $1/e$ of its value at the nucleus. This will mean that in a moderator composed of H atoms where the atoms are say $8a_0$ apart (the molecules of liquid hydrogen are about this far apart), the meson will already ionize the atom for $R\approx a_0$. However, as we will see later in the practical case of H_2 molecules, non-adiabatic effects will cause ionization as soon as the electron binding energy gets sufficiently small, so that the behavior of the electron in the adiabatic limit of zero meson velocity is not decisive for the meson moderation.

Now we turn from the case of a moderator of H atoms to one of H_2 molecules. The question then arises: is there a region within the hydrogen molecule where the presence of a negative meson will unbind one of the electrons of the molecule? This question is not answered in this paper, but, as will be seen, a considerable insight can be obtained on the basis of calculations already in literature.

The binding energy of an electron to the system π^-H_2 is the difference between the energy of π^-H_2 and the energy of $\pi^-H_2^+$. Consider first the energy of $\pi^-H_2^+$. If the distance between the nuclei be held fixed, then when the meson is far away the energy of the system is just the energy of H_2^+ plus the Coulomb attraction of the meson and H_2^+. When the meson gets closer the H_2^+ will have a Stark effect which will lower the energy of the system by an amount

$$\tfrac{1}{2}\alpha_{H_2^+}(e/R^2)^2,$$

where $\alpha_{H_2^+}$ is the polarizability of H_2^+ and (e/R^2) is the electric field at the position of H_2^+ due to the meson at a distance R. In the opposite case, when the meson is very close to one of the nuclei the Coulomb attraction of π^- and H^+ will give the greatest contribution to the energy.

The energy of interaction of a negative meson and a *neutral* H_2 molecule is quite similar to that of an H_2^+ ion, except that there is no Coulomb interaction between the meson and the neutral H_2. The difference between the energy of π^-H_2 and $\pi^-H_2^+$, which is the binding energy of an electron to π^-H_2 is indicated schematically in Fig. 6 for the case where the meson is on the internuclear axis. Since in the collisions of the meson with H_2, which we will have to consider, the nuclei do not have time to move very far, the internuclear distance in Fig. 6, has been taken as $1.4a_0$, the equilibrium internuclear separation for H_2; H_2^+ has an equilibrium separation of $2a_0$. In Fig. 6, the binding energy rises as:

$$e^2/R+\tfrac{1}{2}(\alpha_{H_2^+}-\alpha_{H_2})(e/R^2)^2$$

at large distances. On the other hand, when the meson is on top of one of the nuclei, the binding energy of an electron is very accurately equal to the electron affinity of hydrogen atom, since the charges of meson and nucleus cancel each other leaving a hydrogen atomic ion H^-. The hydrogen atomic ion has been studied very carefully by astrophysicists[12] so that we know not only the electron affinity, $0.0528(e^2/2a_0)$, very accurately but also the charge distribution. This information enables us to determine the slope of the binding energy curve as a function of mesonic displacement because that slope is the electric field at $R=1.4a_0$ for H^- minus the corresponding electric field for H.[13]

$$d/dR(E(\pi^-H_2)-E(\pi^-H_2^+))\,|_{R=1.4a_0}$$
$$=-\int_0^{1.4a_0}\left[\left(\frac{dZ}{dr}\right)_{H^-}-\left(\frac{dZ}{dr}\right)_{H}\right]dr/(1.4a_0)^2.$$

Now $-(dZ/dr)_H=4er^2e^{-2r}$ and taking the charge distribution from reference 12, we get the values in Table II.

We then have

$$-\int_0^{1.4}[(dZ/dr)_{H^-}-(dZ/dr)_H]dr=0.13e.$$

Slope$=0.13/(1.4)^2$ or $0.0664(e/2a_0^2)$ in Rydbergs per Bohr radius.

If the binding energy curve were continued as a straight line with this slope it would reach zero energy at a distance $0.399a_0$ from the nucleus. Thus if the linear approximation were correct there would be a stretch of length $0.6a_0$ of the internuclear axis, on which the presence of the meson would ionize the H_2 molecule. Provided that this result also held for the meson off the internuclear axis by a few tenths of a Bohr radius we could then conclude that the cross section for ionization loss in the adiabatic limit should be of the same order of magnitude in H_2 as in H. However, the linear approximation probably gives quite an incorrect answer (see the shape of the binding energy curve for H atoms, Fig. 5).

If one wishes to calculate the binding energy by variational methods, one must get the energy of H_2 and H_2^+ and take the difference. In that case, even though one would have an upper limit on the energy of H_2 and H_2^+ separately, one might get either too small or too large a value of the binding energy depending on the relative accuracy of the H_2 and H_2^+ calculations. To trust a determination of a point on the binding energy curve, one would have to calculate the energy of both H_2 and H_2^+ to an absolute accuracy considerably better than half the difference (which might be quite small, say 0.001 Rydberg for a point near the middle of the molecule). We thus conclude that to calculate the binding energy curve by variational methods would demand an inordinately high accuracy.

There are direct methods for determining the points at which the binding energy curve crosses the axis, analogous to the one used to determine the critical radii for π^-H. In fact, just as in the case of the hydrogen atom, one can answer the question of the existence of bound states solely from a knowledge of the solutions of the wave equation corresponding to zero energy; zero, that is, relative to the energy of meson $+H_2^+$ for the same configuration of the nuclei and meson. One needs only to look to see whether zero energy solutions of the wave equation exist which have no nodes; if so, no bound states exist. Unfortunately for the application of this method the investigation of the nodes of the zero energy wave function does not seem to be particularly straightforward.

Thus, our analysis so far does not answer the question: What is the cross section for ionizing an H_2 molecule in the limit of zero meson velocity?

However, it does show the existence of a region within the molecule of cross section of the order of magnitude a_0^2, where the presence of a meson makes the binding energy of the last electron smaller than $0.01e^2/2a_0=0.135$ ev if not zero. We now present arguments to show that even if the H_2 molecule is not ionized by the presence in its interior of a negative meson standing still, it probably will be ionized by non-adiabatic processes resulting from the finite velocity of the meson.

This proposal might seem unreasonable at first sight since in the collisions we have to consider the meson as moving very slowly, relative to the average velocity of the electrons in the undisturbed molecule. However, in order for a collision to be adiabatic the periods associated with transitions of the colliding system should all be short compared to the time of collision.

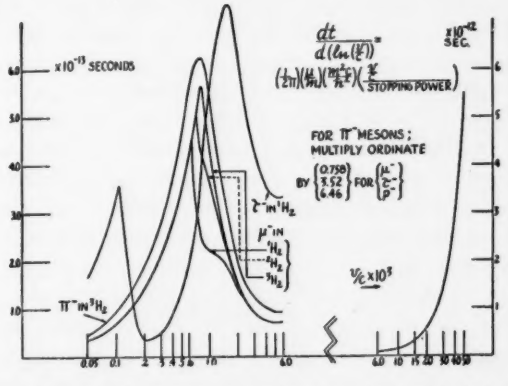

FIG. 7. Rate of change of moderation time with $\ln(v/c)$ of moderated particle. The right-hand curve describes the moderation from $v/c=5\times10^{-2}$ to $v/c=6\times10^{-3}$. Here the slowing down is independent of moderator. The left-hand curves represent the moderation in the velocity range $v/c=6\times10^{-3}$ to $v/c=5\times10^{-5}$ for selected meson masses and moderators.

[12] R. E. Williamson, Astrophys. J. **96**, 440 (1942).

[13] This calculation gives the slope of the binding energy curve *exactly*. To determine the binding energy of the electron when the meson is a finite distance away from the nucleus one must resort to perturbation theory.

TABLE III. Moderation times in seconds.

		μ^-	π^-	τ^-	P^-
From $v/c=5\times10^{-2}$ to $v/c=6\times10^{-2}$ these times are the same for $^1H_2$, $^2H_2$, and $^3H_2$ as moderator		7.4×10^{-12} sec.	9.7×10^{-12}	3.4×10^{-12}	6.3×10^{-12}
From $v/c=6\times10^{-2}$ to $v/c=5\times10^{-2}$	in $^1H_2$	7.9×10^{-12}	7.4×10^{-12}	1.5×10^{-12}	2.4×10^{-12}
	in $^2H_2$	9.0×10^{-12}	1.1×10^{-12}	2.2×10^{-12}	2.9×10^{-12}
	in $^3H_2$	9.4×10^{-12}	1.2×10^{-12}	2.6×10^{-12}	3.4×10^{-12}

Now, the collision time is of order of magnitude

$$a_0/v=\left(\frac{\mu}{m}\right)\frac{\frac{1}{2}\hbar^2/(me^4)}{\epsilon^{\frac{1}{2}}}$$

$$(=3.36\times10^{-16}/\epsilon^{\frac{1}{2}} \text{ sec. for a } \pi\text{-meson}),$$

where ϵ is the meson energy in Rydbergs. On the other hand, the separation of the bound state from the continuum is of the order of magnitude of 0.01 Rydberg (or less) and therefore the associated time is

$$\frac{\hbar}{0.01(e^2/2a_0)}=2\times10^2\left(\frac{\hbar^3}{me^4}\right)=4.18\times10^{-15} \text{ second.}$$

The shortness of the collision time in comparison with the equivalent period shows that the collision is not adiabatic and that transitions of an electron from the bound state to the continuum are likely in the collisions of a negative meson with an H_2 molecule. This conclusion holds for μ^-, π^-, τ^- and P^- having energies down to those considerably less than the binding energy of an electron to H_2.

In order to investigate the non-adiabatic processes more quantitatively, the following crude model was treated: An electron is bound in a well of depth V_0 and range, a_0. At time $t=0$ the depth of the well suddenly changes to V_1. Then, at time $t=T$, the depth of the well returns to its original value. The depths V_0 and V_1 are adjusted so that the binding energy of the electron is $\approx e^2/2a_0$ initially, and $\approx 0.01e^2/2a_0$ during the time interval $(0, T)$. T is adjusted to be $\approx$ the collision time for a meson H_2 collision. The model gave the result that in typical cases ionization resulted in 90 percent of the cases. There is another restriction on T which shows up clearly in this model: T must be not only shorter than ($\hbar$/binding energy of electron) but also longer than

$$a_0/e^2/\hbar=\hbar^3/me^4.$$

This latter restriction merely means that an electron which is knocked into the continuum by the approach of the meson must have time to get away before the collision is over. This condition is satisfied for meson velocities $<e^2/\hbar$.

On the basis of these arguments we may feel fairly secure in estimating that *in the velocity range $e^2/\hbar>v>5\times10^{-4}e^2/\hbar$ the cross section for ionization of a hydrogen molecule by a negative meson will be $>0.05\pi a_0^2$ and will probably be $\approx 0.1\pi a_0^2$. This holds for μ^-- and π^--mesons as well as the hypothetical τ^- and negative proton.*

The inelastic collisions which we have been discussing ought to yield an energy loss which goes over smoothly into the energy loss due to ionization and excitation as calculated in Born approximation. The result of fitting the two curves is shown in Fig. 2. In making the fit, it is assumed that in every inelastic collision the meson loses an energy $e^2/2a_0$. Actually, on the average the meson should lose more than this.

6. MODERATION TIMES FROM $v/c=5\times10^{-2}$ TO CAPTURE BY AN H_2 MOLECULE FOR μ^-, π^-, τ^-, P^- IN $^1H_2$ $^2H_2$ $^3H_2$

In Fig. 7, we have plotted the rate of change of moderation time with $\ln(v/c)$, for the various mesons and moderators. The moderation time between two velocities is the area under the curve between the abscissas corresponding to those two velocities. From these curves, the moderation times of Table III have been computed. The lower limit of meson velocity corresponds to an energy which is less than the binding energy of an electron to H_2. On its next ionizing collision the meson is captured by the struck H_2 molecule, forming a $\pi^-H_2^+$ system. Thus the times of Table III are the times taken by a meson to reduce its speed from $v/c=5\times10^{-2}$ to the point where it is captured by a hydrogen molecule. These times are two orders of magnitude smaller than the moderation times from 10 Mev to $v/c=5\times10^{-5}$. Thus the uncertainties involved in the low velocity stopping power of hydrogen are quite unimportant as far as the total moderation time is concerned once the order of magnitude of the low velocity stopping power is determined.

ACKNOWLEDGMENT

This work was carried out under the guidance of Professor J. A. Wheeler. It is a pleasure to thank him and also Professors R. E. Marshak and E. P. Wigner for helpful discussions. This work was assisted by the Joint Program of Office of Naval Research and the Atomic Energy Commission.

The Infra-Red Spectrum and Molecular Constants of HF and DF*,**

ROBERT M. TALLEY,† HOYT M. KAYLOR, AND ALVIN H. NIELSEN
Department of Physics, University of Tennessee, Knoxville, Tennessee
(Received September 26, 1949)

New high dispersion measurements on the infra-red absorption spectrum of HF and DF are reported. Discussion of the experimental details and analysis is given. Observed frequencies of the spectral lines, as well as observed and calculated constants, are tabulated. The principal constants for HF are $\omega_e=4138.52_2$ cm^{-1}, $x_e\omega_e=90.06_9$ cm^{-1}, $y_e\omega_e=0.980$ cm^{-1}, $z_e\omega_e=0.025$ cm^{-1}, $B_e=20.939_0$ cm^{-1}, $\alpha_e=0.770_5$ cm^{-1}, $\gamma_e=0.005_0$ cm^{-1}, $D_e=0.002_2$ cm^{-1}. The principal constants for DF are $\omega_e=3000.35_8$ cm^{-1}, $x_e\omega_e=47.33_6$ cm^{-1}, $y_e\omega_e=0.373$ cm^{-1}, $z_e\omega_e=0.006_8$ cm^{-1}, $B_e=11.004_5$ cm^{-1}, $\alpha_e=0.293_6$ cm^{-1}, $\gamma_e=0.001_4$ cm^{-1}, $D_e=0.0006_5$ cm^{-1}.

I. INTRODUCTION

THE infra-red spectrum of HF has been investigated by several workers, notably Imes,[1] who measured the fundamental ($v=1\leftarrow0$) vibration-rotation band; Schaeffer and Thomas,[2] who observed the first overtone ($v=2\leftarrow0$) band-center prismatically; and Kirkpatrick and Salant,[3] who photographed the rotational structure of the second ($v=3\leftarrow0$) and third ($v=4\leftarrow0$) overtone band in absorption. References to infra-red measurements on DF were not found in the literature.

In this paper the fundamental of HF has been remeasured, the rotational structure of the first overtone of HF and the fundamental and first overtone of DF have been observed. These data have been analyzed with a view to obtaining reliable molecular constants for both isotopic molecules.

II. EXPERIMENTAL DETAILS

HF and DF are very corrosive gases and present, therefore, a serious problem as regards cell and window materials. Sodium chloride and calcium fluoride windows were quickly etched by even the dry gas and, thus, scattered virtually all the incident light. It was found that fluorothene[4] (poly tri-fluorochloroethylene) could be used effectively for both absorption cells and windows. The cells were turned from solid cylinders of the material, and a metal valve was screwed into a thick section of side wall left for the purpose. Sheets of fluorothene of about $\frac{1}{16}$-inch thickness were found to transmit about 80 percent of the incident radiation in the spectral regions where HF and DF absorb. Windows of this material were sealed to the cell with a lower melting-point wax of fluorothene. Because the tensile strength of this wax is not great, the windows were also secured by end clamps drawn together by screws along the length of the cell.

Cells of 5-cm and 22-cm length, respectively, were used to observe the fundamental and first overtone of both HF and DF. The pressures, though not carefully observed, were approximately 15 cm of mercury for the fundamentals, and between 50 and 65 cm of mercury for the overtones. The gases were obtained as pure, dry, samples free from detectable impurities, except that the DF contained some HF which, however, did not interfere with the measurements because the spectra do not overlap.

For these measurements an automatically recording high dispersion prism-grating spectrograph[5] was used. The grating was a 7200 line-per-inch Wood replica used in first order for the fundamentals, and in second order for the overtones.

As the HF fundamental occurs in, and is virtually obscured by, the 2.7μ atmospheric water-vapor band, it was found necessary to place trays of P_2O_5 in the spectrograph, seal it carefully, and let it dry for several days before satisfactory records of HF could be made. When these precautions were taken the weaker water lines were reduced to background, and the most intense ones absorbed about 30 percent of the incident radiation at those frequencies. Excellent measurements on HF lines out to $P(6)$ were possible.

To ensure the greatest possible accuracy to these data, the graduated circle, with which grating angles were measured, was carefully calibrated.[6] Agreement between the present and other work, particularly the photographic work of Kirkpatrick and Salant, indicates that the frequencies given in Tables I to IV inclusive must be quite good. Successive angle readings under best conditions were repeated to ±1 second of arc. It is believed that, in general, the accuracy of the rotation line positions is about ±2 seconds. Angular positions of the spectral lines were obtained by interpolating between fiducial marks put on the record at intervals of one minute of arc. The frequencies given are the averages of at least four separate records across the

* This paper was presented at the Symposium on Molecular Structure and Spectroscopy, The Ohio State University, Columbus, Ohio, June 13–18, 1949.

** R. M. Talley and A. H. Nielsen, Phys. Rev. **74**, 123(A) (1948). H. M. Kaylor and A. H. Nielsen, Phys. Rev. **76**, 200(A) (1949).

† Frederick Gardner Cottrell Fellow.

[1] E. S. Imes, Astrophys. J. **50**, 251 (1919).

[2] C. Schaeffer and M. Thomas, Zeits. f. Physik **12**, 330 (1923).

[3] D. E. Kirkpatrick and E. O. Salant, Phys. Rev. **48**, 945 (1935).

[4] J. S. Kirby-Smith and E. A. Jones, J. Opt. Soc. Am. **39**, 780 (1949).

[5] A. H. Nielsen, J. Tenn. Acad. Sci. **XXII**, No. 4, 241 (1947).

[6] R. M. Talley and H. M. Kaylor, Phys. Rev. **74**, 123(A) (1948).

lines. All spectral lines given have been reduced to vacuum. The frequency standard used to calibrate the grating was the Mercury 10,139.976A[7] line observed in several orders.

III. EXPERIMENTAL RESULTS

Actual records of the fundamental and first overtone bands of HF and DF are shown in Fig. 1. The P branch of the fundamental of HF is normally completely obscured by atmospheric water vapor. Because of the great effort to dry the interior of the spectrograph, it is seen that these lines are easily measurable over the background. The background atmospheric absorption in the region of the overtone of HF and the bands of DF was easily cleaned up by the P_2O_5.

The records shown were made at a fairly fast recording speed. For actual measuring purposes the scanning speed was considerably slower.

Tables I to IV inclusive give the frequencies of the observed spectral lines of HF and DF in cm^{-1} with the J values in column 1, the observed frequencies in column 2, the frequencies computed from the new constants in column 3, and the differences in column 4.

IV. ANALYSIS

HF and DF are rather unusual among diatomic molecules because of their large anharmonicity. It was, therefore, necessary to use Dunham's[8] treatment of the vibrating-rotating diatomic molecule, in which contributions to the energy from potential energy terms through q^6 are calculated, in order to secure agreement among the six observed bands. The energy, expressed in the usual spectroscopic notation from Dunham's paper to the accuracy required, is given by

$$E/hc(\mathrm{cm}^{-1}) = E_0/hc + \{\omega_e - x_e\omega_e(v+1/2) + y_e\omega_e(v+1/2)^2 - z_e\omega_e(v+1/2)^3\}(v+1/2) + B_eJ(J+1) - D_vJ^2(J+1)^2 - \{\alpha_e - \gamma_e(v+1/2)\}(v+1/2)J(J+1). \quad (1)$$

E_0 represents a constant energy term which does not

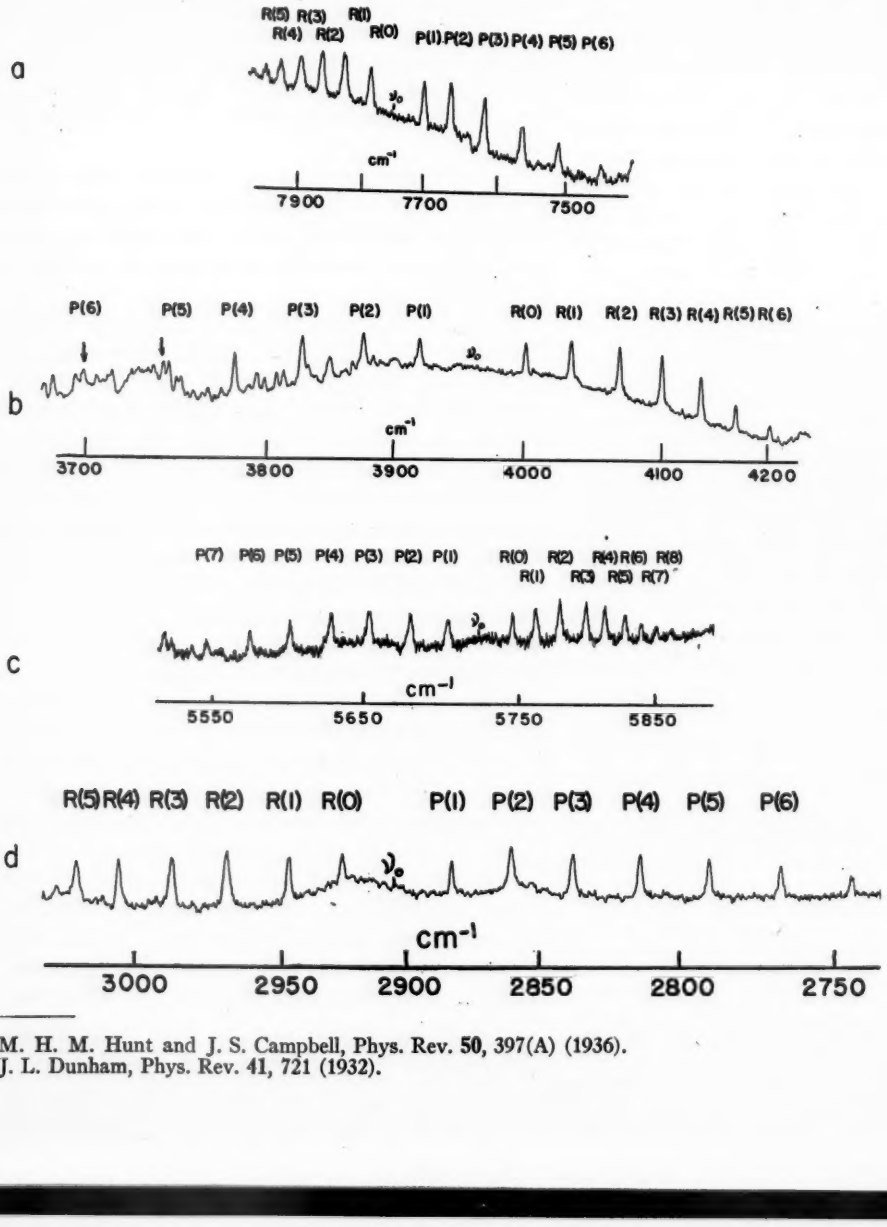

FIG. 1. Actual records of the fundamental and first overtone bands of HF and DF. (a) $v=2\leftarrow0$ (HF), (b) $v=1\leftarrow0$ (HF), (c) $v=2\leftarrow0$ (DF), (d) $v=1\leftarrow0$ (DF).

[7] M. H. M. Hunt and J. S. Campbell, Phys. Rev. **50**, 397(A) (1936).
[8] J. L. Dunham, Phys. Rev. **41**, 721 (1932).

TABLE I. Frequencies of observed rotation lines in $v=1\leftarrow0$ (HF).*

Line assignment	ν(obs.)	ν(calc.)	$\Delta\nu$
$R(5)$	4173.93	4174.25	+0.32
$R(4)$	4142.82	4142.85	+0.03
$R(3)$	4109.99	4109.84	−0.15
$R(2)$	4075.11	4075.18	+0.07
$R(1)$	4038.83	4038.89	+0.06
$R(0)$	4000.94	4000.96	+0.02
$P(1)$	3920.39	3920.30	−0.09
$P(2)$	3877.65	3877.63	−0.02
$P(3)$	3833.55	3833.50	−0.05
$P(4)$	3787.89	3788.00	+0.11
$P(5)$	3741.23	3741.21	−0.02
$P(6)$	3693.53	3693.25	−0.28

* All frequencies in cm^{-1} and corrected to vacuum.

TABLE II. Frequencies of observed rotation lines in $v=2\leftarrow0$ (HF).*

Line assignment	ν(obs.)	ν(calc.)	$\Delta\nu$
$R(5)$	7931.50	7931.54	+0.04
$R(4)$	7909.37	7909.39	+0.02
$R(3)$	7883.90	7884.09	+0.19
$R(2)$	7856.07	7855.60	−0.47
$R(1)$	7823.88	7823.87	−0.01
$R(0)$	7789.08	7788.94	−0.14
$P(1)$	7709.46	7709.56	+0.10
$P(2)$	7665.32	7665.31	−0.01
$P(3)$	7618.43	7618.14	−0.39
$P(4)$	7568.44	7568.23	−0.21
$P(5)$	7515.77	7515.73	−0.04
$P(6)$	7460.38	7460.88	+0.50

* All frequencies in cm^{-1} and corrected to vacuum.

appear in the frequency of the spectral lines. ω_e is the harmonic frequency for infinitesimal amplitudes. $x_e\omega_e$, $y_e\omega_e$, and $z_e\omega_e$ are anharmonic constants involving potential energy constants through terms in q^6. B_e is the equilibrium rotational constant, $h/8\pi^2cI_e$. $-D_v$ is the centrifugal stretching constant. α_e and γ_e are vibration-rotation interaction constants and depend upon the potential energy constants. v and J are the vibration and rotation quantum numbers. The frequency of the spectral lines may be determined by application of the Bohr frequency condition with the selection rules $\Delta v=\pm1$, 2, etc., and $\Delta J=\pm1$. Dunham also gives the expressions, to the same approximation, for the relations between the constants for the isotopic molecule.

The analysis of the experimental data was carried out by using combination relations between rotation lines of the P and R branches similar to those described by Herzberg.[9] This technique consists, essentially, of finding linear relationships between the frequencies of the P and R branch lines such that the values of the fundamental constants emerge as intercepts and slopes of these lines.

[9] G. Herzberg, *Molecular Spectra and Molecular Structure, I. Diatomic Molecules* (Prentice-Hall, Inc., New York, 1939).

TABLE III. Frequencies of observed rotation lines in $v=1\leftarrow0$ (DF).*

Line assignment	ν(obs.)	ν(calc.)	$\Delta\nu$
$R(6)$	3041.42	3041.10	+0.32
$R(5)$	3024.24	3024.29	−0.05
$R(4)$	3006.25	3006.25	0.00
$R(3)$	2987.62	2987.61	+0.01
$R(2)$	2968.38	2968.35	+0.03
$R(1)$	2948.41	2948.47	−0.06
$R(0)$	2928.01	2927.97	+0.04
$P(1)$	2885.08	2885.11	−0.03
$P(2)$	2862.79	2862.80	−0.01
$P(3)$	2839.99	2839.93	+0.06
$P(4)$	2816.51	2816.55	−0.04
$P(5)$	2792.69	2792.68	+0.01
$P(6)$	2768.25	2768.39	−0.14
$P(7)$	2743.05	2743.73	−0.68

* All frequencies in cm^{-1} and corrected to vacuum.

TABLE IV. Frequencies of observed rotation lines in $v=2\leftarrow0$ (DF).*

Line assignment	ν(obs.)	ν(calc.)	$\Delta\nu$
$R(8)$	5863.22	5863.89	+0.33
$R(7)$	5852.70	5852.29	+0.41
$R(6)$	5840.34	5840.40	−0.06
$R(5)$	5827.18	5827.24	−0.06
$R(4)$	5812.79	5812.81	−0.02
$R(3)$	5797.14	5797.14	0.00
$R(2)$	5780.09	5780.24	−0.15
$R(1)$	5761.98	5762.12	−0.14
$R(0)$	5742.78	5742.79	−0.01
$P(1)$	5700.22	5700.57	−0.35
$P(2)$	5677.55	5677.71	−0.16
$P(3)$	5653.87	5653.70	+0.17
$P(4)$	5628.55	5628.54	+0.01
$P(5)$	5602.30	5602.27	+0.03
$P(6)$	5574.79	5574.88	−0.09
$P(7)$	5546.47	5546.40	+0.07
$P(8)$	5516.89	5516.84	+0.05

* All frequencies in cm^{-1} and corrected to vacuum.

Rotational

Of the rotational constants, B_0 of HF is doubtless the most accurately known, because the state $v=0$ is the originating state for the four observed bands, and each band contributes a value of B_0. B_0 and D_0 were obtained from a graph in which the relation

$$(1/2)\{R(m-1)-P(m+1)\}/(2m+1) = (B_0-3D_0/2)-D_0(2m+1)^2/2, \quad (2)$$

where m is the ordinal number of the rotational line, was plotted with the left-hand side of the equation as ordinates *versus* $(2m+1)^2$ as abscissae, as shown in Fig. 2.†† Data from all four bands were plotted on the same graph. Points contributed by the bands $v=3\leftarrow0$ and $v=4\leftarrow0$ of HF were given somewhat more weight than those of $v=1\leftarrow0$ and $v=2\leftarrow0$, because, being

†† m is an index taking values 1, 2, 3, ⋯, etc., and thus the number in parenthesis, i.e., $R(m-1)$, is the J value of the lower state.

TABLE V. Rotational constants of HF and DF.*,**

	HF		DF		
B_0	20.555		10.857		
B_1	19.795		10.567		
B_2	19.035	obs.	10.263	obs.	
B_3	18.303				
B_4	17.573				
B_e	20.939_0	calc. from	11.007	calc. from	11.004_5 calc. from
α_e	0.770_5	obs. bands	0.293_5	observed	0.293_6 HF data
γ_e	0.005_0			DF bands	0.001_4
D_0	0.0022		0.0006_7		
D_1	0.001_9		0.0007		
D_2	0.003_2		0.0006		
D_3	0.002_2				
D_4	0.001_6				
D_e	0.002_2		0.0006_5		
I_e	$1.336_3\times10^{-40}$ g cm^2				
r_e	0.9170_1A				

* All constants are in cm^{-1} and reduced to vacuum.
** Constants for $v=3\leftarrow0$, $v=4\leftarrow0$ recalculated from Kirkpatrick and Salant's data.

photographic bands, it was believed that they were somewhat more accurately known. Had it been possible to observe rotation lines with larger m-values this graph would have been more accurate. B_0 from the intercept on this graph is 20.555 cm^{-1} and D_0, the slope of the line, is found to be 0.0022 cm^{-1} in perfect agreement with D_0 calculated from $4B_e^3/\omega_e^2$.

In Fig. 3 are shown plots of the relation

$$(1/2)\{R(m)-P(m)\} = (B_v-3D_v/2)(2m+1)-D_v(2m+1)^3/2 \quad (3)$$

with the left-hand side of the equation plotted as ordinates *versus* $(2m+1)$ as abscissae for the states $v=1, 2, 3, 4$. In these curves the effect of the D_v term pulling the points off a straight line is clear. In some diatomic molecules the term in D_v may be neglected. In Fig. 3 the straight lines are obtained when the parabolas are corrected appropriately using an average value of $D=0.0022$ cm^{-1}. This was considered proper inasmuch as D_v should not be appreciably different for the four observed states. The values of B_1, B_2, B_3, and B_4 may be obtained directly from Fig. 3.

The broken-line curve in Fig. 4 shows the relation

$$B_v=B_e-\alpha_v(v+1/2) \quad (4)$$

plotted with $B_v+0.77(v+1/2)$ as ordinates *versus* $(v+1/2)$ as abscissae. The coefficient 0.77 represents an approximate value of α_e used to expand the vertical scale. This curve clearly shows by its parabolic nature that α is a function of v. An additional term involving $\gamma_e(v+1/2)^2$ will produce linearity when a suitable choice of γ_e is made. It may be seen in Fig. 4 that all points, but one, fit very closely on the solid line, the intercept of which is $B_e=20.939_0$ cm^{-1}.

It should be pointed out, however that another method of determining α_e and γ_e, to be discussed in the next section, yields somewhat different values of these constants. It is believed that the α_e and γ_e of Fig. 4 give the best agreement among all the constants which depend on them. Using the expression given by Dunham for predicting DF constants from the HF constants, excellent agreement is achieved, as may be seen from Table V.

The left-hand side of Eq. (3) when divided by $(2m+1)$ and plotted as ordinates *versus* $(2m+1)^2$ as abscissae gives $(B_v-3D_v/2)$ as intercept and $-D_v/2$ as the slope. The B_v's determined this way are somewhat different from the B_v's determined from Fig. 3. As more consistent results in the B_v *versus* $(v+1/2)$ curve of Fig. 4 are obtained if the B_v's of Fig. 3 are used, these are the values used throughout.

Vibrational

The band-centers $\nu(v=v'\leftarrow v'')$ and vibration-rotation interaction constants α_v were obtained from graphs of

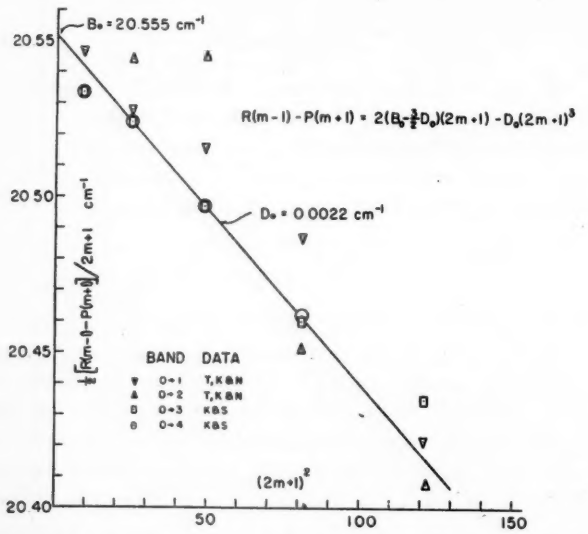

FIG. 2. Graph of $\frac{1}{2}\{R(m-1)-P(m+1)\}/(2m+1)$ *versus* $(2m+1)^2$ showing B_0 and D_0.

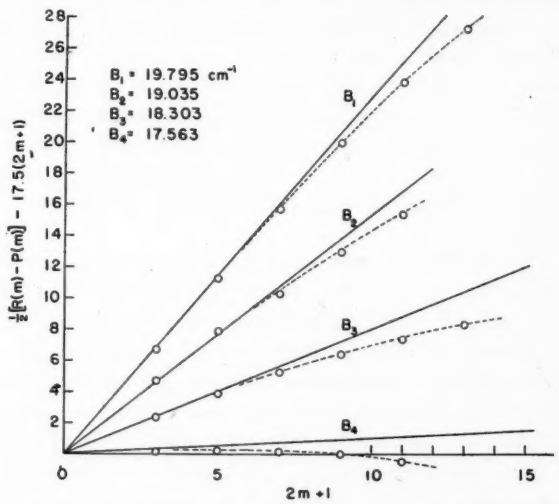

FIG. 3. Graph of $\frac{1}{2}\{R(m)-P(m)\}$ *versus* $(2m+1)$ showing effect of D_v term, and values of B_1, B_2, B_3, and B_4.

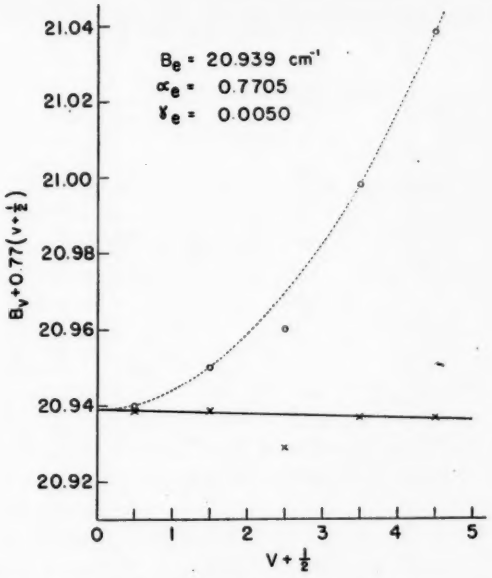

FIG. 4. Graph of B_v *versus* $(v+\frac{1}{2})$ showing effect of γ_e and giving values of B_e, α_e, and γ_e.

the equation

$$1/2\{R(m-1)+P(m)\}=\nu(v=v'\leftarrow v'')-\alpha_v m^2, \quad (5)$$

where m is the ordinal number of the rotation line, with the left-hand side plus $0.77m^2$ plotted as ordinates *versus* m^2 plotted as abscissae. Figure 5 shows the graph of the $v=1\leftarrow 0$ band of HF, and Fig. 6 shows the graph of the $v=3\leftarrow 0$ band of HF. It is worth noting that the dotted curve in Fig. 5 representing the experimental points clearly deviates from linearity, whereas in Fig. 6 for $v=3\leftarrow 0$ it does not. To ensure that no experimental errors in $v=1\leftarrow 0$ prevailed, the data for $v=1\leftarrow 0$ of Imes were plotted in the same way, and were found to deviate from linearity by about the same amount. Linearity may be achieved, as shown in the solid line of Fig. 5, by applying a correction term of fourth power in m. For the $v=2\leftarrow 0$ band, the coefficient of the fourth power term was twice the value (0.00065) for the $v=1\leftarrow 0$ band, whereas for the $v=3\leftarrow 0$ band the coefficient was zero, and for the $v=4\leftarrow 0$ band it was the same as for $v=1\leftarrow 0$. Theoretically, this coefficient is $\beta_e v$ and should change linearly with v. The value of β_e, from theoretical considerations, is 0.00009 cm^{-1} which is considerably smaller than is found experimentally in $v=1\leftarrow 0$, and $v=2\leftarrow 0$, but could, conceivably, agree within experimental error with the values found for $v=3\leftarrow 0$ and $v=4\leftarrow 0$. A similar correction of about the same magnitude is observed in the fundamental of DF but not in the first overtone. No explanation of this anomalous behavior of β_e is suggested. The band-centers used in the computations are the ones obtained from graphs like those in Figs. 5 and 6 when properly corrected for linearity.

When the values of α_v from these graphs are plotted as ordinates *versus* $(v+1/2)$ as abscissae, as shown in Fig. 7, the intercept, α_e, and the slope, γ_e, do not agree with the α_e and γ_e obtained and discussed in the previous section.

The data for DF were given similar analysis and the vibrational constants for both molecules are given in Table VI.

V. CONCLUSION

Four band-centers are required to compute ω_e, $x_e\omega_e$, $y_e\omega_e$ and $z_e\omega_e$. Just this number of observed bands is available in HF. By assuming that the potential energy constants for both HF and DF are identical and using the mass conversion expressions given by Dunham, the two bands in DF may be used as a check on the above constants. The band-centers for $v=1\leftarrow 0$ and $v=2\leftarrow 0$ for DF may thus be predicted to occur at 2906.86 cm^{-1} and 5722.17 cm^{-1} whereas they are observed at 2906.84 cm^{-1} and 5722.27 cm^{-1}, respectively. Other DF constants predicted from HF data are to be found in Tables V and VI.

It should be pointed out that the correction to the reduced mass by taking electron distribution into account following Hardy, Barker, and Dennison[10] is of

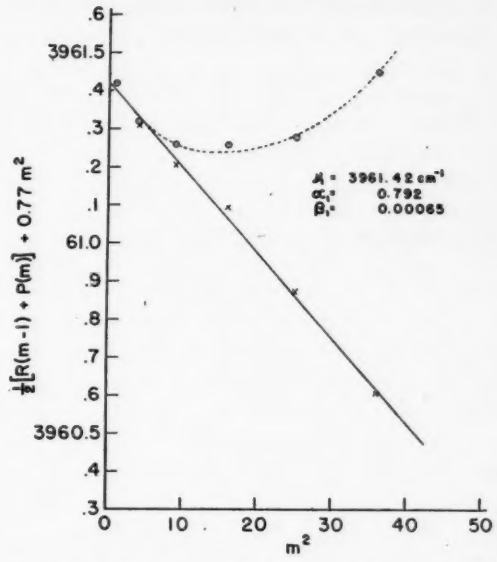

FIG. 5. Graph of $\frac{1}{2}\{R(m-1)+P(m)\}$ *versus* m^2 for $v=1\leftarrow 0$ showing effect of β_e and giving $\nu(v=1\leftarrow 0)$.

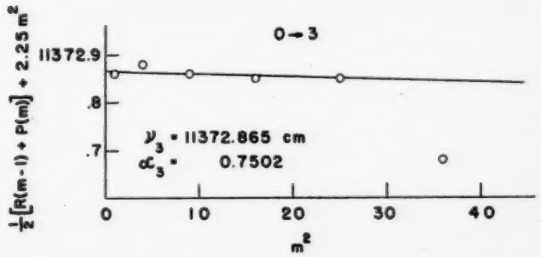

FIG. 6. Graph of $\frac{1}{2}\{R(m-1)+P(m)\}$ *versus* m^2 showing negligible β_e effect and giving $\nu(v=3\leftarrow 0)$.

[10] J. D. Hardy, E. F. Barker, and D. M. Dennison, Phys. Rev. 42, 279 (1932).

TABLE VI. Vibrational constants of HF and DF.*,**

	HF		DF		
$\nu(1\leftarrow 0)$	3961.42	obs.	2906.84	obs.	2906.86 calc. from
$\nu(2\leftarrow 0)$	7750.81		5722.27		5722.17 HF data
$\nu(3\leftarrow 0)$	11372.87				
$\nu(4\leftarrow 0)$	14831.71				
ω_e	4138.52$_2$	calc. from observed HF bands	3000.35$_8$	calc. from HF data	
$x_e\omega_e$	90.06$_9$		47.33$_6$		
$y_e\omega_e$	0.980		0.373		
$z_e\omega_e$	0.025		0.006$_8$		

* All constants are in cm^{-1} and corrected to vacuum.
** Constants for $v=3\leftarrow 0$, $v=4\leftarrow 0$ recalculated from Kirkpatrick and Salant's data.

the same order of magnitude as the difference between ω_e (DF) obtained by a direct reduced mass effect and the ω_e (DF) obtained when Dunham's formula is used. This effect is not included in the present paper. Furthermore, Dunham's correction depends critically on the value of α_e. As previously noted, two values of α_e are obtained from the present data. The value of α_e from Fig. 4 used here, for reasons previously stated, gives a Dunham correction of 0.145 cm^{-1} whereas the α_e from Fig. 7 gives a Dunham correction about twice as large.

It may further be seen by examining Fig. 7 that if a straight line should be drawn through the points contributed by $v=3\leftarrow 0$, and $v=4\leftarrow 0$, a value of α_e very near to the value used herein would be obtained. It appears, therefore, that there is something queer about $v=1\leftarrow 0$, and $v=2\leftarrow 0$, perhaps related to the anomalous β_e, which causes α_v to misbehave.

A Frederick Gardner Cottrell grant-in-aid from the Research Corporation of New York which provided one of the authors (Robert M. Talley) a fellowship and made possible the acquisition of various important items in connection with the instrumentation is gratefully acknowledged. Grants from the American Academy of Arts and Sciences and the Tennessee Academy of Science are also acknowledged. The authors also wish to thank Mr. Wilbur Simon of the K-25 Laboratory, Oak Ridge, Tennessee, for making the samples of DF used in these experiments.

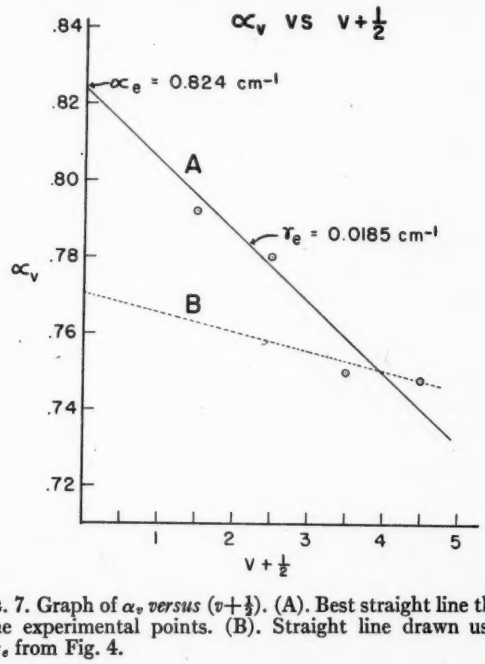

FIG. 7. Graph of α_v *versus* $(v+\frac{1}{2})$. (A). Best straight line through all the experimental points. (B). Straight line drawn using α_e and γ_e from Fig. 4.

Bernoulli's Theorem for Viscous Compressible Fluids

C. TRUESDELL
Applied Mathematics Branch, Mechanics Division, Naval Research Laboratory, Washington, D. C.
(Received October 14, 1949)

A BERNOULLI theorem is a statement that an expression of the type $v^2/2+P$, where P is a function of one or more dynamical variables, is constant, or is a function of time only, either (A) throughout a whole fluid motion, or (B) upon each of a certain family of surfaces (in previously known examples, the "Bernoullian surfaces" containing the stream-lines and vortex-lines) or (C) upon each of a certain family of curves (in previously known examples, the stream-lines or the vortex-lines). Long ago Craig[1] noticed that in the degenerate and physically improbable case of steady irrotational flow of a viscous incompressible fluid, and in the more general and important case of steady flow when the vorticity $\mathbf{w}\equiv\mathbf{curl}\,\mathbf{v}$ is itself irrotational ($\mathbf{curl}\,\mathbf{w}=0$), the classical Bernoulli theorem of type (A) still holds, and it has been pointed out by Sbrana[2] that in a flow such that the velocity $\mathbf{v}$ is perpendicular to $\mathbf{curl}\,\mathbf{w}$ the classical Bernoullian expression remains constant upon each stream-line. Castoldi[3] observed recently that in a flow such that the vorticity $\mathbf{w}$ is perpendicular to $\mathbf{curl}\,\mathbf{w}$, the classical Bernoullian expression remains constant upon each vortex-line. It had previously been noted by Masotti[4] that it is not steady flow but the weaker condition of steady vorticity, so that

$$\mathbf{v}(\mathbf{r},t)=\mathbf{grad}\int U(\mathbf{r},t)dt+\mathbf{u}(\mathbf{r}),\qquad \frac{\partial\mathbf{v}}{\partial t}=\mathbf{grad}\,U, \tag{1}$$

which is essential for the existence of any type of Bernoullian theorem. In the present note I shall exhibit a Bernoulli theorem of type (C) for any motion of a viscous fluid of uniform viscosity, provided the vorticity be steady. It is of course quite easy to write down a formula for the variation of $v^2/2$ along a stream-line in terms of a line integral, but I prefer to turn away from the stream-lines and instead to find curves $\mathcal{C}$ such that a *finite* expression containing $v^2/2$ and certain dynamical variables is a function of time only, or a constant, along them.

The relevant dynamical equation may be put into the form

$$\mathbf{w}\times\mathbf{v}+\mathbf{grad}(U+\tfrac{1}{2}v^2)=\mathbf{f}-(1/\rho)\,\mathbf{grad}\,p+\mathbf{grad}[(\lambda+2\mu)(\theta/\rho)]+(\lambda+2\mu/\rho)\theta\,\mathbf{grad}\log\rho-(\mu/\rho)\mathbf{curl}\,\mathbf{w}, \tag{2}$$

where $\mathbf{f}$ is the extraneous force per unit mass, ρ is the density, p is the pressure, $\theta\equiv\mathrm{div}\,\mathbf{v}=-D\log\rho/Dt$ is the expansion, and λ and μ are the constant coefficients of viscosity. Equivalently[5]

$$\mathbf{w}\times\mathbf{v}+\mathbf{grad}[U+\tfrac{1}{2}v^2-(\lambda+2\mu)(\theta/\rho)]=\bar{\mathbf{f}},\qquad \bar{\mathbf{f}}\equiv\mathbf{f}-(1/\rho)\mathbf{grad}\,\rho+(\lambda+2\mu/\rho)\mathbf{grad}\log\rho-(\mu/\rho)\,\mathbf{curl}\,\mathbf{w}. \tag{3}$$

Now if $\mathbf{w}\times\mathbf{v}\neq0$ the vectors $\mathbf{w}$ and $\mathbf{v}$ determine a plane at each point. Let $\mathbf{t}$ be a unit vector determined at each point by the intersection of this plane with the plane normal to the vector $\bar{\mathbf{f}}$. Then by taking the dot product of $(3)_1$ by $\mathbf{t}$ we obtain

$$\mathbf{t}\cdot\mathbf{grad}[U+\tfrac{1}{2}v^2-(\lambda+2\mu)(\theta/\rho)]=0. \tag{4}$$

Let the curves $\mathcal{C}$ be the trajectories of the field $\mathbf{t}$. Then we have the *general Bernoulli theorem:*

$$U+\tfrac{1}{2}v^2-(\lambda+2\mu)\theta/\rho=F(t) \tag{5}$$

on any one of the curves $\mathcal{C}$, *where the function* F *generally varies from one such curve to another.* In the special case when $\mathbf{w}\times\mathbf{v}=0$ throughout the motion, the Bernoulli Eq. (5) holds upon any curve normal to the field $\bar{\mathbf{f}}$, and if $\bar{\mathbf{f}}\cdot\mathbf{curl}\,\bar{\mathbf{f}}=0$ there are surfaces normal to $\bar{\mathbf{f}}$ and (5) holds upon each of these surfaces. In the special case when $\mathbf{w}\times\mathbf{v}\neq0$ but $\bar{\mathbf{f}}\times(\mathbf{w}\times\mathbf{v})=0$, the Bernoulli Eq. (5) holds upon any curve everywhere tangent to the planes of $\mathbf{w}$ and $\mathbf{v}$, and if moreover $\mathbf{w}\times\mathbf{v}\cdot(\mathbf{w}\cdot\mathbf{grad}\,\mathbf{v}-\mathbf{v}\cdot\mathbf{grad}\,\mathbf{w})=0$, then these planes are enveloped by "Bernoullian surfaces" upon each of which (5) holds.

It is unfortunate that in general the definition of the curves $\mathcal{C}$ is partially dynamical. In the special case of an incompressible fluid this objectionable quality disappears, however, if the extraneous force be conservative: $\mathbf{f}=-\rho\mathbf{grad}V$. Then (2) becomes

$$\mathbf{grad}[U+V+\tfrac{1}{2}v^2+(p/\rho)]=-\mathbf{w}\times\mathbf{v}-(\mu/\rho)\,\mathbf{curl}\,\mathbf{w}. \tag{6}$$

Now let $\mathbf{t}$ be a unit vector determined by the inter-

[1] T. Craig, "Motions of viscous fluids," J. Franklin Inst. **110**, 217–227 (1880). In this case, which includes Couette and Poiseuille flows, the acceleration $\mathbf{a}$ is irrotational, and hence Kelvin's theorem of conservation of circulation and the Helmholtz vorticity theorems, and in fact all general theorems of classical hydrodynamics except the energy theorems, remain valid also.

[2] F. Sbrana, "Sulla validità del teorema di Bernoulli per un fluido reale," Boll. Un. Mat. Ital. **10**, 77–78 (1931).

[3] L. Castoldi, "Superficie e linee di Bernoulli nel moto stazionario di un fluido reale," Atti Accad. Ligure **4** (1947), 21–25 (1948).

[4] A. Masotti, "Osservazioni sui moti di un fluido nei quali è stazionaria la distribuzione del vortice," Rend. Accad. Naz. Lincei (6^A) **6**, 224–228 (1927).

[5] The reader should be cautioned against accepting without qualification the results of a sequence of Italian papers [B. Caldonazzo, "Un' osservazione a proposito del teorema di Bernoulli," Boll. Un. Mat. Ital. **4**, 1–3 (1925); F. Sbrana, see reference 2; L. Castoldi, see reference 3] which purport to give results valid also for compressible viscous fluids, but are based upon a form of the dynamical equation valid only subject to the tacit requirement that $\rho=f(p-(\lambda+2\mu)\,\mathrm{div}\,\mathbf{v})$, a circumstance physically most improbable unless the fluid be incompressible ($\mathrm{div}\,\mathbf{v}=0$) or inviscid ($\lambda=\mu=0$).

section of the plane of **w** and **v** with the plane normal to **curl w**. Dot multiplication by **t** annuls the right-hand side, so that we obtain the following not inelegant theorem: *Let the curves* $\mathfrak{C}$ *be everywhere tangent to the plane of* **w** *and* **v**, *and everywhere normal to* **curl w**; *then along these curves*, which are determined by the instantaneous velocity field only, *in any flow of a viscous incompressible fluid of uniform viscosity if the vorticity be steady and the extraneous force be conservative Bernoulli's theorem in the classical form*

$$U+V+\tfrac{1}{2}v^2+(p/\rho)=F(t) \qquad (7)$$

is valid. Special cases when (7) holds for wider classes of curves or for special types of curves or for surfaces may be left to the reader; among these are the results of Sbrana and Castoldi.[6]

[6] In the case of plane or rotationally-symmetric flow the curves $\mathfrak{C}$ are the vortex-lines, as indeed is obvious from symmetry, and only if perchance the stream-lines and the curves of constant vorticity magnitude form an orthogonal net (Sbrana's case $\mathbf{v}\cdot\mathbf{curl}\,\mathbf{w}=0$) does (7) yield a non-trivial result, namely a theorem of type (*B*).

The foregoing theorem exhibits the non-uniformity of the limit $\mu\to 0$ in a strikingly simple dynamical form: since the curves **C**, along which the pressure obeys the relation (7), are determined by the instantaneous velocity field, they remain fixed as $\mu\to 0$, while at the limit $\mu=0$ of an inviscid fluid they spread out discontinuously into Lamb's Bernoullian surfaces.

The results given here constitute an application of a general theorem of pure kinematics, to be published elsewhere.[7]

[7] C. Truesdell, "The kinematics of vorticity," Mémorial des Sciences Mathématiques (to be published). I am obliged to Dr. P. Neményi for having suggested the problem of finding a kinematical generalization of Bernoulli's theorem valid in motions where Kelvin's circulation theorem does not hold, and for discussion of the present paper.

PHYSICAL REVIEW VOLUME 77, NUMBER 4 FEBRUARY 15, 1950

Fourth-Order Corrections in Quantum Electrodynamics and the Magnetic Moment of the Electron

ROBERT KARPLUS* AND NORMAN M. KROLL†‡
Institute for Advanced Study, Princeton, New Jersey
(Received October 17, 1949)

The covariant S matrix formalism of Dyson has been applied to the calculation of the fourth-order radiative correction to the magnetic moment of the electron. Intermediate results for the covariant Δ-functions which describe the interaction of virtual electrons and photons with the vacuum are given to order α. The addition to the magnetic moment to order α^3 is found to be finite after the charge of the electron is renormalized consistently. This correction amounts to $-2.97\alpha^3/\pi^3$ Bohr magneton so that the magnetic moment of the electron is $\mu=1.001147$ Bohr magnetons.

RECENT developments in the techniques of quantum electrodynamics, and in particular the general considerations of Dyson,[1] have shown that the radiative corrections to the motion of the electron can be made finite in all orders by the consistent use of the ideas of charge and mass renormalization. The renormalizations are, of course, infinite, so that one is forced to regard the present form of the theory as provisional. Still, the fact that one can give an unambiguous, consistent, and sensible prescription for dealing with this situation, and the excellent experimental verification accorded the second-order effects already computed, suggest that an investigation of a fourth-order effect might be of value: first, in order to make possible a sensitive test of the agreement of the theory in its present form with experiment and second, to demonstrate in a complete calculation of a particular example the feasibility of Dyson's program. The magnetic moment of the electron was chosen for investigation because it promised to present the least difficulties of computation while it does contain those points of theoretical interest which are relevant to the difficulties of quantum electrodynamics. Furthermore, in view of the success already achieved in the measurement of the anomalous moment of the electron,[2] it appears that the fourth-order effect may be accessible to experiment.

METHOD OF CALCULATION

We shall begin with a discussion of the fourth-order corrections to the elastic scattering of an electron by an an external electromagnetic field. The question of isolating that part of the scattering which may be attributed to an anomalous magnetic moment will be discussed in a later section.

In evaluating the matrix element describing the scattering, the methods of Dyson have been followed quite closely. We, therefore, require the fourth-order

* Frank B. Jewett Fellow.
† National Research Council Fellow.
‡ Now at Columbia University, New York, New York.
[1] F. J. Dyson, Phys. Rev. 75, 486, 1736 (1949), henceforth called I and II, respectively.
[2] P. Kush and H. M. Foley, Phys. Rev. 74, 250 (1948).

part, $U_1^{(4)}$, of the transformation matrix U_1 given by Dyson[3] as

$$U_1=\sum_{n=0}^{\infty}U_1^{(n)}=\sum_{n=0}^{\infty}\left(\frac{-i}{\hbar c}\right)^{n+1}\frac{1}{n!}\int_{-\infty}^{\infty}d^4x_0d^4x_1\cdots d^4x_n \times P[H^e(x_0),H^I(x_1)\cdots H^I(x_n)], \quad (1)$$

whence

$$U_1^{(4)}=\left(\frac{-i}{\hbar c}\right)^5\frac{1}{4!}\int_{-\infty}^{\infty}d^4x_0d^4x_1\cdots d^4x_4 \times P[H^e(x_0),H^I(x_1)_1\cdots H^I(x_4)]. \quad (2)$$

The variables x_i refer to particular space-time points and are thus to be understood to have four components; $P[\ ]$ is the chronological ordering operator of Dyson.[4]

In the above expression, $H^e(x_0)$ describes the interaction with the external electromagnetic field, whose vector potential is denoted by $A_\mu^e(x_0)$, and is given by

$$H^e(x_0)=-(1/c)j_\mu(x_0)A_\mu^e(x_0) =-ie\bar{\psi}(x_0)\gamma_\mu\psi(x_0)A_\mu^e(x_0), \quad (3)$$

while $H^I(x_i)$ describes the interaction with the photon field and is given by

$$H^I(x_i)=-ie\bar{\psi}(x_i)\gamma_\mu\psi(x_i)A_\mu(x_i)-\delta mc^2\bar{\psi}(x_i)\psi(x_i). \quad (4)$$

It is to be observed that the operator $-iec\bar{\psi}(x_i)\gamma_\mu\psi(x_i)$ is the usual unsymmetrized current density operator for the Dirac particle field. The term $-\delta mc^2\bar{\psi}\psi$ appearing in $H^I(x_i)$ implies that the interaction representation in which the theory was originally cast has been modified so that the mass appearing in the equation of motion of the electron states is the mass of the electron as corrected by its interaction with the radiation field (i.e., presumably the experimental mass) rather than the mass of a hypothetical uncharged electron.

The matrix U has the property that when it is applied to the state vector of the system at $-\infty$, it produces the state vector at $+\infty$. U_1 is the part of U corresponding to a first Born approximation and is the limiting form of U for a weak external field, while $U_1^{(4)}$ is that part of U_1 which describes processes involving four interactions between particles and photons and one interaction between a particle and the external potential. As such it describes a great many processes in addition to those in which we are interested. In particular, we shall be concerned with the "one electron" part of $U_1^{(4)}$, i.e., that part of $U_1^{(4)}$ connecting states consisting of a single electron and no photons. A simple and elegant method of extracting from U any portion in which one is interested has been given by Feynman and Dyson.[5] The matrix element in question is given by a sum of terms each of which may be described by a graphically represented transition scheme. The diagrams for our process appear in Fig. 1 and will be discussed in the next paragraphs. To each diagram there corresponds an integral over the variables $x_0, x_1\cdots, x_4$; the integrand can be written down by inspection and gives the contribution of the associated transition scheme to the matrix element. In these integrals the effect of the ordering operator $P[\ ]$ has been absorbed into the $S_F(x)$ and $D_F(x)$ functions, so that this operator no longer appears explicitly. These functions do of course contain an implicit dependence upon $P[\ ]$ in view of the relations

$$\tfrac{1}{2}S_{F\alpha\beta}(x_1-x_2)=\langle P[\bar{\psi}_\beta(x_1),\psi_\alpha(x_2)]\rangle_0\epsilon(x_1,x_2), \quad (5)$$

$$(\hbar c/2)D_{F\mu\nu}(x_1-x_2)=\langle P[A_\mu(x_1),A_\nu(x_2)]\rangle_0 =(\hbar c/2)\delta_{\mu\nu}D_F(x_1-x_2), \quad (6)$$

where $\langle\ \rangle_0$ denotes the vacuum expectation value.

To complete this summary of the method of calculation, it will be convenient to specialize the discussion to the problem at hand. For this reason we turn now to a discussion of the diagrams in Fig. 1 and the corresponding integrals.

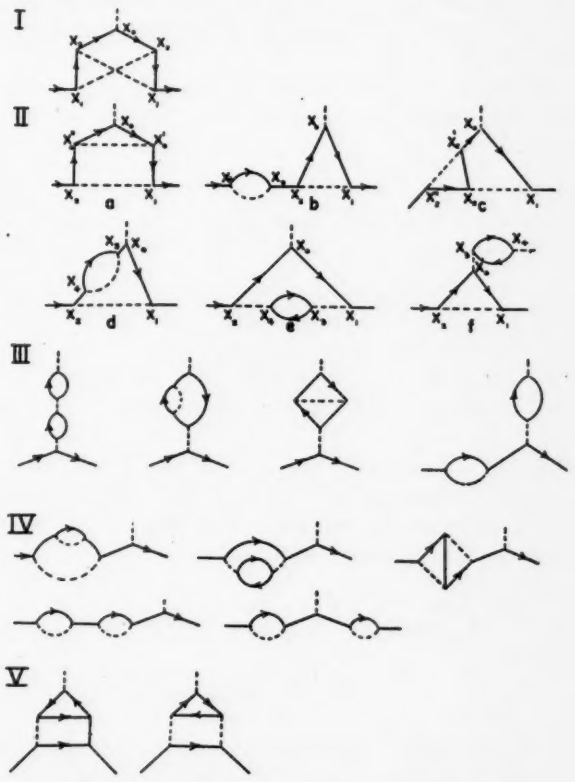

FIG. 1. Feynman diagrams for the fourth-order radiative corrections to the scattering of an electron by an electromagnetic field.

[3] See reference 1, II, Eqs. (6) and (7).
[4] See reference 1, I, Section V.
[5] See reference 1, II, Section II.

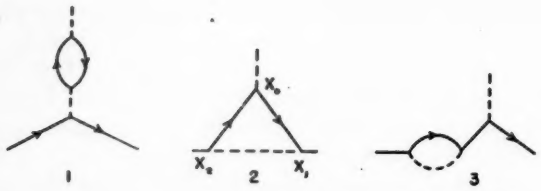

FIG. 2. Feynman diagrams for the second-order radiative corrections to the scattering of an electron by an electromagnetic field.

The diagram I gives rise to the integral

$$M^I=-\frac{e}{\hbar c}\frac{\alpha^2\pi^2}{4}\int_{-\infty}^{\infty}d^4x_0d^4x_1\cdots d^4x_4A_\mu{}^e(x_0)\bar{\psi}(x_1)\gamma_\nu$$
$$\times S_F(x_2-x_1)\gamma_\lambda S_F(x_0-x_2)\gamma_\mu S_F(x_3-x_0)\gamma_\nu$$
$$\times S_F(x_4-x_3)\gamma_\lambda\psi(x_4)D_F(x_3-x_1)D_F(x_4-x_2). \quad (7)$$

$$\left(\alpha=\frac{e^2}{4\pi\hbar c}=\frac{1}{137.0}\right).$$

This diagram is irreducible since it cannot be represented as a lower order process corrected by modified interaction functions. It contains a logarithmically divergent charge renormalization plus finite physical effects, of which the magnetic moment, to be extracted later, is one.

Integrals analogous to M^I can be written down for the diagrams grouped under II. For example, we might observe

$$M^{IIe}=\frac{e\alpha^2\pi^2}{4\hbar c}\int d^4x_0d^4x_1d^4x_2d^4x_3d^4x_4$$
$$\times\mathrm{Tr}[\gamma_\lambda S_F(x_3-x_4)\gamma_\nu S_F(x_4-x_3)]$$
$$\times A_\mu{}^e(x_0)\bar{\psi}(x_1)\gamma_\nu S_F(x_0-x_1)\gamma_\mu$$
$$\times S_F(x_2-x_0)\gamma_\lambda\psi(x_2)D_F(x_2-x_4)D_F(x_3-x_1), \quad (8)$$

where Tr[ ] indicates the trace of the bracketed expression. These diagrams are all reducible, however to the second-order diagram 2 in Fig. 2. Since the second-order diagram 2 is given by

$$-\frac{e}{\hbar c}\frac{\alpha\pi}{2}\int d^4x_0d^4x_1d^4x_2A_\mu{}^e(x_0)\bar{\psi}(x_1)\gamma_\nu S_F(x_0-x_1)\gamma_\mu$$
$$\times S_F(x_2-x_0)\gamma_\nu\psi(x_2)D_F(x_1-x_2), \quad (9)$$

all higher order corrections as well as (9) itself are included in

$$M^{II}=-\frac{e}{\hbar c}\frac{\alpha\pi}{2}\int d^4x_0d^4x_0'd^4x_0''d^4x_1d^4x_1'd^4x_1''$$
$$\times d^4x_2d^4x_2'd^4x_2''A_\mu{}^{e'}(x_0)D_F'(x_2-x_1)$$
$$\times\bar{\psi}'(x_1')\Gamma_\nu(x_1-x_1',x_1''-x_1)S_F'(x_0'-x_1'')$$
$$\times\Gamma_\mu(x_0-x_0',x_0''-x_0)S_F'(x_2'-x_0'')$$
$$\times\Gamma_\nu(x_2-x_2',x_2''-x_2)\psi'(x_2''), \quad (10)$$

where the primed functions and the current operator $\Gamma_\nu(x,x')$ are as defined by Dyson.[6] The presence of nine rather than five variables of integration is associated with the fact that (10) contains terms of all orders in α except the zeroth. The primed functions and Γ_μ are to be obtained as expansions in α, and inserted in Eq. (10). The terms of order α^2 will then include all of the diagrams in class II. When this is done, integration over four of the variables will be trivial, as these variables will appear only in the arguments of δ-functions.

We should like to emphasize that for the evaluation of the diagrams of class II, the use of the reduction Eq. (10), rather than expressions like Eq. (8), is of great assistance in the unambiguous elimination of the effects of charge renormalization. In any order, radiative corrections to scattering processes must be expected to include terms which merely renormalize the electronic charge occurring in lower order corrections. Thus, for example, a strightforward evaluation of M^{II} from expressions like Eq. (8) would yield infinite corrections to the magnetic moment for just this reason.[7] Were the charge renormalizations finite, this would cause no difficulty as these terms could then be readily subtracted out. They are, however, infinite and one would therefore have to exercise the greatest care to guarantee that no finite remains of charge renormalizations had been included in the true higher order correction. On the other hand, in using the reduced diagram method one explicitly separates out all renormalization effects, infinite and finite, at each order, so that the isolation and removal of the entire contribution of renormalization to the moment is simple and unambiguous. For the purpose of illustration the renormalization terms will be retained throughout so as to exhibit at the conclusion the renormalized second-order moment. This, of course, is not really necessary since the understanding that all effects be given in terms of the experimental charge allows one to drop renormalization terms as they appear.

FIG. 3. Feynman diagram for the second-order terms of $D_f'(x)$.

[6] See reference 1, II, Sections III and IV.

[7] One can avoid the use of the reduction Eq. (10) if one is willing to introduce Pauli regulators in such a way as to make all charge renormalizations finite. The application of regulators to higher order processes is discussed by J. Steinberger, Phys. Rev. 76, 1180 (1949). The true fourth-order correction obtained after the now finite contributions from charge renormalization are recognized and removed is the same as obtained by our procedure.

FIG. 4. Feynman diagram for the second-order terms of $S_F'(x)$.

Diagrams of class III are all reducible to the second-order diagram 1 of Fig. 2. Therefore, methods similar to those described in the last paragraph are to be used in their evaluation. These diagrams include corrections to the polarization of the vacuum by an external field and charge renormalizations applied to lower order vacuum polarizations. As such, the observable effects which they represent are modifications of the external potential and not of the properties of the electron. This implies that they cannot contribute to the magnetic moment, so they will not be considered in any further detail.

The diagrams of class IV can all be regarded as reducible to the second-order diagram 3 of Fig. 2, without including any modifications of the external potential at the vertex x_0. They can therefore contribute nothing but a charge renormalization of the zeroth-order scattering. They are of interest only if one wishes to investigate the actual form of the fourth-order renormalization.

Our discussion of the diagrams may be concluded with the remark that by the Furry[8] theorem diagram Va and Vb exactly cancel.[9]

The remainder of the paper will be concerned with the evaluation to order α of S_F', D_F', and Γ_μ and the extraction of the magnetic moment correction from the relevant integrals M^I and M^{II}. No error has been incurred by the neglect of the supplementary condition.[9a]

SECOND-ORDER FUNCTIONS

The function $D_F'(x)$, which describes the properties of a virtual photon as modified by its interaction with the electron-positron field, must be obtained to second order in e. The leading term, of course, is

$$D_F(x)=-\frac{2i}{(2\pi)^4}\int e^{-ipx}\frac{d^4p}{p^2}.$$

The corrections to this function arise from the ability of the virtual photon to create pairs. The first term is simply due to the creation and annihilation of one pair, as described by the Feynman diagram Fig. 3, or by the integral

$$\begin{aligned}D_{F\mu\nu}^{(2)}(x)=&(-1)(-i/\hbar c)^2\int d^4x_2d^4x_3\\&\times\langle P[A_\mu(x_1),A_\lambda(x_2)]\rangle_0\\&\times\langle P[(1/c)j_\lambda(x_2),(1/c)j_\sigma(x_3)]\rangle_0\\&\times\delta_{\sigma\nu}D_F(x_3-x_1+x)\\=&-(\alpha\pi/2)\int d^4x_2d^4x_3D_F(x_1-x_2)\\&\times\mathrm{Tr}[\gamma_\nu S_F(x_2-x_3)\gamma_\mu S_F(x_3-x_2)]\\&\times D_F(x_3-x_1+x)\\=&-\frac{\alpha\pi}{2}\left[\frac{-2i}{(2\pi)^4}\right]^4\int d^4pd^4kd^4k'd^4p'\\&\times\int d^4x_2d^4x_3e^{-ip(x_1-x_2)}e^{-ik(x_2-x_3)}\\&\times e^{-ik'(x_3-x_2)}e^{-ip'(x_3-x_1+x)}\frac{1}{p^2}\frac{1}{p'^2}\\&\times\mathrm{Tr}\left[\gamma_\nu\frac{i\gamma k-\kappa}{k^2+\kappa^2}\gamma_\mu\frac{i\gamma k'-\kappa}{k'^2+\kappa^2}\right]\\=&-\frac{\alpha}{2\pi^3}\frac{1}{(2\pi)^4}\int d^4pe^{-ipx}\frac{1}{(p^2)^2}\int d^4k\\&\times\mathrm{Tr}\left[\gamma_\nu\frac{i\gamma k-\kappa}{k^2+\kappa^2}\gamma_\mu\frac{i\gamma(k-p)-\kappa}{(k-p)^2+\kappa^2}\right].\end{aligned}\tag{11}$$

Here

$$px=p_\mu x_\mu=\mathbf{p}\cdot\mathbf{x}-p_0x_0;$$

$$S_F(x)=-\frac{2i}{(2\pi)^4}\int d^4pe^{-ipx}\frac{i\gamma p-\kappa}{p^2+\kappa^2}.$$

The integration over k must be carried out carefully, because the integral is divergent. This has been effectively carried out by Schwinger and yields[10]

$$\begin{aligned}&\int d^4k\,\mathrm{Tr}\left[\gamma_\nu\frac{i\gamma k-\kappa}{k^2+\kappa^2}\gamma_\mu\frac{-i\gamma(p-k)-\kappa}{(p-k)^2+\kappa^2}\right]\rightarrow\\&-\frac{8i\pi^2}{3}(\delta_{\mu\nu}p^2-p_\mu p_\nu)\left[\lim_{P\to\infty}\ln\frac{P+P_0}{\kappa}-1\right]\\&+i\pi^2(\delta_{\mu\nu}p^2-p_\mu p_\nu)\int_0^1 dv\frac{v^2(1-\frac{1}{3}v^2)p^2}{\kappa^2+p^2(1-v^2)/4}\end{aligned}\tag{12}$$

after the requirements of gauge invariance have been imposed. Since the electromagnetic potentials obey the

[8] Wendell H. Furry, Phys. Rev. **51**, 125 (1937).

[9] No reference has been made to diagrams and associated matrix elements arising from the term $-\delta mc^2\psi(x)\psi(x)$ in H^I. As described by Dyson, diagrams containing these interactions are to be placed in one-to-one correspondence with the diagrams containing self-energy parts. Their effect is taken into account in the evaluation of the S_F', $\psi'(x)$, and $\psi'(x)$ functions.

[9a] F. J. Dyson, "Longitudinal Photons in Quantum Electrodynamics," Phys. Rev. (to be published).

[10] Julian Schwinger, Phys. Rev. **76**, 790 (1949), Appendix; Schwinger's result has been multiplied by $2\pi i$ because of slightly different definitions of the singular functions.

Lorentz condition, the term $(p_\mu p_\nu)$ may be dropped. Then

$$D_{F\mu\nu}{}^{(2)}(x)=\delta_{\mu\nu}D_F{}^{(2)}(x),$$

and

$$\begin{aligned}D_F'(x)&=D_F(x)+D_F{}^{(2)}(x)\\&=-\frac{2i}{(2\pi)^4}\int e^{-ipx}d^4p\left\{\frac{1}{p^2}\left(1+\frac{\alpha}{2\pi}A\right)\right.\\&\qquad\left.+\frac{\alpha}{2\pi}\int_0^1 dv\frac{2v^2(1-\frac{1}{3}v^2)}{4\kappa^2+p^2(1-v^2)}\right\}\\&=\left(1+\frac{\alpha}{2\pi}A\right)D_F(x)+\bar{D}_F{}^{(2)}(x),\end{aligned}\tag{13}$$

where

$$A=-\frac{4}{3}\left[\lim_{P\to\infty}\ln\frac{P_0+P}{\kappa}-1\right].$$

This infinite constant, however, has no observable consequences because the term in which it occurs is indistinguishable from the original $D_F(x)$ function. It merely means that the matrix element in which $D_F(x)$ occurs is multiplied by a factor $[1+(\alpha/2\pi)A]$ and that the quantity which measures the intensity of the dynamical interaction described by the matrix element must be renormalized.

By a very similar calculation, the function $A^{e\prime}(x)$, the external electromagnetic field modified by second-order interaction with the pair field, may be calculated. Thus,

$$\begin{aligned}A_\mu{}^{e\prime}(x)&=\int e^{ipx}d^4pA_\mu{}^e(p)\left\{\left(1+\frac{\alpha}{2\pi}A\right)\right.\\&\qquad\left.+\frac{\alpha p^2}{2\pi}\int_0^1 dv\frac{2v^2(1-\frac{1}{3}v^2)}{4\kappa^2+p^2(1-v^2)}\right\}\\&=\left(1+\frac{\alpha}{2\pi}A\right)A_\mu{}^e(x)+\frac{\alpha}{2\pi}\bar{A}_\mu{}^{e(2)}(x).\end{aligned}\tag{14}$$

The function $S_F'(x)$ describes the behavior of a virtual electron as modified by its interaction with the electromagnetic field. The relevant diagrams, in this case, are in Fig. 4, while the appropriate integral is[11]

$$\begin{aligned}S_F{}^{(2)}(x)&=(-i/\hbar c)^2(-ie)^2\int\langle P[\psi(x_1),\bar{\psi}(x_2)]\rangle_0\gamma_\mu\\&\qquad\times\langle P[\psi(x_2),\bar{\psi}(x_3)]\rangle_0\gamma_\nu\langle P[A_\mu(x_2),A_\nu(x_3)]\rangle_0\\&\qquad\times S_F(x_1+x-x_3)d^4x_2d^4x_3\\&\qquad-(-i/\hbar c)\int d^4x_2\langle P[\psi(x_1),\bar{\psi}(x_2)]\rangle_0\\&\qquad\qquad\times\delta mc^2S_F(x_1+x-x_2)\\&=e^2/8\hbar c\int S_F(x_2-x_1)\gamma_\mu S_F(x_3-x_2)\\&\qquad\times\gamma_\nu S_F(x_1+x-x_3)\delta_{\mu\nu}D_F(x_3-x_2)d^4x_2d^4x_3\\&\qquad+i/2\hbar c\int d^4x_2S_F(x_2-x_1)\delta mc^2S_F(x_1+x-x_2)\\&=(\alpha/2\pi^3)(2\pi)^{-4}\int d^4pe^{-ipx}\frac{i\gamma p-\kappa}{p^2+\kappa^2}\\&\qquad\times\left\{\int d^4k\gamma_\mu\frac{i\gamma(p-k)-\kappa}{(p-k)^2+\kappa^2}\gamma_\mu\frac{1}{k^2+\lambda^2}\right.\\&\qquad\left.-(4i\pi^3/\alpha)(\delta mc^2/\hbar c)\right\}\frac{i\gamma p-\kappa}{p^2+\kappa^2}.\end{aligned}\tag{15}$$

Here again, the integral over k diverges and therefore must be evaluated carefully; furthermore, charge renormalization must be exhibited explicitly. This identification can only be done simply, however, after the integrand has been rearranged considerably so as to write it as a function of $i\gamma p+\kappa$. Thus,[12]

$$\begin{aligned}I(i\gamma p+\kappa)&=\int d^4k\gamma_\mu\frac{i\gamma(p-k)-\kappa}{(p-k)^2+\kappa^2}\gamma_\mu\frac{1}{k^2+\lambda^2}\\&=-2\int d^4k\int_0^1 du\frac{i\gamma(p-k)+2\kappa}{[(k-pu)^2+\kappa^2u^2+p^2u(1-u)+\lambda^2(1-u)]^2}\end{aligned}$$

$$\left(\text{by the use of } 1/ab=\int_0^1 du\frac{1}{[au+b(1-u)]^2}\right)$$

$$\begin{aligned}&=-2\int_0^1 du\int d^4k\frac{i\gamma p(1-u)-i\gamma k+2\kappa}{[k^2+\kappa^2u^2+(p^2+\kappa^2)u(1-u)+\lambda^2(1-u)]^2}\\&\qquad-2\int_0^1 du\int d^4kp_\mu u\frac{\partial}{\partial k_\mu}\frac{i\gamma k}{[k^2+\kappa^2u^2+(p^2+\kappa^2)u(1-u)+\lambda^2(1-u)]^2}.\end{aligned}\tag{16}$$

[11] The $D_F(x)$ function here is replaced by a $\Delta_F(x)$ function with mass $\hbar\lambda/c$ to avoid an anticipated infra-red catastrophe in the physically significant part of the $S_F'(x)$ function. $S_F{}^{(2)}(x)$ does not diverge in the infra-red.

[12] The Lorentz invariance of I assures that it is a function of $(i\gamma p)$, hence of $(i\gamma p+\kappa)$.

Here the second integral represents a surface term that must be added to take into account the effect of the displacement $k_\mu \to k_\mu + p_\mu u$ at large values of k^2, where the integrand does not tend to zero rapidly enough. It should be emphasized that all integrations are undertood to be symmetrical with respect to the origin of the variable of integration; i.e., the angular integrations are to be carried out first, and are followed by the integration over $|k|$.[13]

With these points in mind, the operator becomes

$$I(i\gamma p+\kappa)=-2\int_0^1 du\int d^4k\Big\{[(i\gamma p+\kappa)(1-u)+\kappa(1+u)]\Big[\frac{1}{[k^2+\Lambda^2]^2}-\frac{1}{[k^2+\Lambda_0{}^2]^2}\Big]$$
$$+\frac{(i\gamma p+\kappa)(1-u)+\kappa(1+u)}{[k^2+\Lambda_0{}^2]^2}+i\gamma pu\Big[\frac{1}{[k^2+\Lambda^2]^2}-\frac{k^2}{[k^2+\Lambda^2]^3}\Big]\Big\}, \quad (17)$$

where

$$\Lambda^2=\kappa^2u^2+\lambda^2(1-u)+(p^2+\kappa^2)u(1-u) \quad (18a)$$

and

$$\Lambda_0{}^2=\kappa^2u^2+\lambda^2(1-u). \quad (18b)$$

Using the facts that[14]

$$\int d^4k\frac{1}{(k^2+\mu^2)^3}=i\pi^2/2\mu^2 \quad (19)$$

and that

$$\int d^4k\Big[\frac{1}{(k^2+\Lambda^2)^2}-\frac{1}{(k^2+\Lambda_0{}^2)^2}\Big]=-2\int d^4k\int_0^1 dz\frac{(p^2+\kappa^2)u(1-u)}{[\Lambda_0{}^2+(p^2+\kappa^2)u(1-u)z]^3}=-i\pi^2\int_0^1 dz\frac{(p^2+\kappa^2)u(1-u)}{\Lambda_0{}^2+(p^2+\kappa^2)u(1-u)z} \quad (20)$$

one obtains

$$I(i\gamma p+\kappa)=-2\int_0^1 du\Big\{\int d^4k\frac{(i\gamma p+\kappa)(1-u)+\kappa(1+u)}{(k^2+\Lambda_0{}^2)^2}+u(i\gamma p+\kappa)\frac{i\pi^2}{2}-\kappa\frac{i\pi^2}{2}u$$
$$+i\pi^2[(i\gamma p+\kappa)(1-u)+\kappa(1+u)](i\gamma p+\kappa)(i\gamma p-\kappa)u(1-u)\int_0^1 dz\frac{1}{\Lambda_0{}^2+(p^2+\kappa^2)u(1-u)z}\Big\}. \quad (21)$$

Only the still remaining integral over momentum space is divergent here, and it will become apparent that it consists of renormalization terms only. After a slight rearrangement of the finite parts, the operator assumes the form

$$I(i\gamma p+\kappa)=-2\int_0^1 du\Big\{\Big[\int d^4k\frac{(1+u)\kappa}{(k^2+\Lambda_0{}^2)^2}-(i\pi^2/4)\kappa\Big]+(i\gamma p+\kappa)(1-u)\Big[\int d^4k\frac{1}{(k^2+\Lambda_0{}^2)^2}-2i\pi^2\frac{\kappa^2u(1+u)}{\Lambda_0{}^2}+\frac{i\pi^2}{2}\Big]$$
$$+i\pi^2(i\gamma p+\kappa)^2u(1-u)\Big[\int_0^1 dz\frac{\kappa(1+u)+(i\gamma p-\kappa)(1-u)\{1-[2\kappa^2u(1+u)z]/[u^2\kappa^2+\lambda^2(1-u)]\}}{\kappa^2u^2+\lambda^2(1-u)+(p^2+\kappa^2)u(1-u)z}\Big]\Big\}. \quad (22)$$

The first term in this expression is equal to $(4i\pi^3/\alpha)(\delta mc^2/\hbar c)$ and is therefore canceled by the mass renormalization term, Eq. (15). The rest of the integral can now be inserted into the expression for $S_F'(x)$,

$$S_F'(x)=S_F(x)+S_F{}^{(2)}(x)$$
$$=-2i/(2\pi)^4\int e^{-ipx}d^4p\Big\{\frac{i\gamma p-\kappa}{p^2+\kappa^2}\Big(1-\frac{\alpha}{2\pi}B\Big)+(\alpha/2\pi)\int_0^1 duu(1-u)$$
$$\times\int_0^1 dz\frac{\kappa(1+u)+(i\gamma p-\kappa)(1-u)\{1-[2\kappa^2u(1+u)z]/[\kappa^2u^2+\lambda^2(1-u)]\}}{\kappa^2u^2+\lambda^2(1-u)+(p^2+\kappa^2)u(1-u)z}$$
$$=[1-(\alpha/2\pi)B]S_F(x)+(\alpha/2\pi)\bar{S}_F{}^{(2)}(x), \quad (23)$$

[13] This implies $\int k_\mu f(k^2)d^4k=0$, $\int k_\mu k_\nu f(k^2)d^4k=\int \tfrac{1}{4}\delta_{\mu\nu}k^2f(k^2)d^4k$, etc.

[14] R. P. Feynman, Phys. Rev. 76, 769 (1949).

where B is an infinite constant,[15]

$$B=(1/i\pi^2)\int_0^1(1-u)du\int d^4k\frac{k^2+\Lambda_0^2-4\kappa^2u(1+u)+\Lambda_0^2}{[k^2+\Lambda_0^2]^3}$$
$$=(1/i\pi^2)\int_0^1 udu\int d^4k\frac{k^2-4\kappa^2(1-u-\frac{1}{2}u^2)}{[k^2+\kappa^2u^2+\lambda^2(1-u)]^3}. \quad (24)$$

The fact that B is infinite, however, is not a source of difficulty since it can be interpreted as a charge renormalization just as the constant A in the treatment of the $D_F'(x)$ function.

It must now be observed that the physically significant term of $S_F^{(2)}(x)$ diverges logarithmically as $\lambda\to 0$. Since this divergence is associated with the vanishing mass of a photon, it is an infra-red catastrophe. It is introduced by the separation of real and renormalization effects in $S_F^{(2)}(x)$. One must hope, of course, that the logarithmic dependence on λ will cancel when all contributions to a certain scattering process are added together. The work of Bloch and Nordsieck[16] indicates such a cancellation will actually occur.

We shall merely note now that the modification of the electron wave function brought about by virtual interaction with the electromagnetic field is obtained from the same diagram as the $S_F'(x)$ function, if one of the electron lines is taken to be an external line. Then, since the wave function obeys the Dirac equation,[17]

$$\psi'(x)=[1-(\alpha/4\pi)B]\psi(x) \quad (25a)$$

and

$$\bar\psi'(x)=[1-(\alpha/4\pi)B]\bar\psi(x). \quad (25b)$$

As pointed out by Dyson, the effect is merely one of renormalization so as to preserve the unitarity of the matrix U.

Some explanation is required for the necessity of replacing the renormalization factor Z_2 in Eq. (23) by $Z_2^{\frac{1}{2}}=Z_2/Z_2^{\frac{1}{2}}$ in Eq. (25), a substitution which is equivalent to dividing by Z_2^n the matrix element of U between states containing n electrons; for as long as the scattering matrix U is defined between two specific surfaces σ_1 and σ_2 in the remote past and distant future, its unitarity is guaranteed. Thus, it should not be necessary to apply an explicit renormalization. Furthermore, the use of the eigenstates of noninteracting fields to specify conditions at σ_1 and σ_2 must be justified, since experimental conditions would lead one to assume that the one-particle eigenstates (i.e., essentially the Bloch-Nordsieck states) of the interacting electron and photon fields (or combinations thereof for several particle problems) ought to be used. The replacement of σ_1 and σ_2 by $-\infty$ and $+\infty$, however, together with Dyson's computation rules imply a certain averaging of the matrix elements over long sequences of surfaces in the past and future. One can readily show that the averaged matrix element is just equal to the matrix element between Bloch-Nordsieck states, multiplied by a constant which depends only upon the number of real particles in the initial and final states.

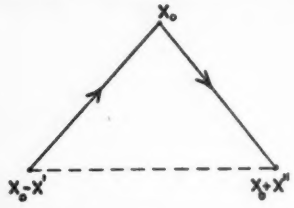

FIG. 5. Feynman diagram for the second-order terms of $\Gamma_\mu(x,x')$.

For simplicity, we confine our attention to the one-electron part of the scattering potential and restrict σ_1 and σ_2 to be surfaces of constant time, t_1 and t_2. The requirements that the state vector $\Phi_1(t)$ corresponds at time t_1 to an uncoupled or "bare" electron of momentum k_1 and that $\Phi_2(t)$ corresponds at t_2 to a bare electron of momentum k_2 are contained in the relations,

$$\psi_\sigma^+(x_\mu)\Phi_1(t_1)=a_{k_1\sigma}^+\exp[ik_{1\mu}x_\mu]\Phi_1(t_1),$$
$$\psi_\sigma^+(x_\mu)\Phi_2(t_2)=a_{k_2\sigma}^+\exp[ik_{2\mu}x_\mu]\Phi_2(t_2),$$

where the a^+'s are annihilation operators, together with the annihilation of $\Phi_1(t_1)$ and $\Phi_2(t_2)$ on application of $\bar\psi^-(x_\mu)$ and $A_\mu^+(x_\mu)$. The possibility that $\Phi_1(t_1)$ and $\Phi_2(t_2)$ have t_1 or t_2 dependent phase factors is eliminated by the requirement

$$(\Phi_2(t_2),\, a_{k_2}^+a_{k_1}^+\Phi_1(t_1))=1$$

for all t_1 and t_2. To interpret the procedure of calculation used it is convenient to expand Φ_1, and Φ_2 in the exact eigenstates, $\Psi_n(t)$, of the coupled electron and radiation fields thus,

$$\Phi_1(t_1)=\Sigma\, A_n(t_1)\Psi_n(t_1),$$
$$\Phi_2(t_2)=\Sigma\, B_n(t_2)\Psi_n(t_2).$$

We might observe that these relations serve to determine the behavior in time of the states Φ_i for zero external field. That is,

$$\Phi_1(t)=U_0(t,t_1)\Phi_1(t_1)=\Sigma_n A_n(t_1)\Psi_n(t),$$
$$\Phi_2(t)=U_0(t,t_2)\Phi_1(t_2)=\Sigma_n B_n(t_2)\Psi_n(t).$$

The important point is the fact that the t_1 and t_2 dependence of the A's and B's as determined by the boundary condition is given by

$$A_n(t_1)=a_n\exp[(i/\hbar)(E_n-E_1)t_1],$$
$$B_n(t_2)=b_n\exp[(i/\hbar)(E_n-E_2)t_2].$$

Thus the matrix elements of $U(t_2,t_1)$ between $\Phi_1(t_1)$ and $\Phi_2(t_2)$ are related to matrix elements between eigenstates of the coupled system by

$$(\Phi_2,\, U(t_2,t_1)\Phi_1=\Sigma\, b_na_m\exp[-(i/\hbar)(E_n-E_2)t_2]$$
$$\times\exp[(i/\hbar)(E_m-E_1)t_1](\Psi_n(t_2),\, U(t_2,t_1)\Psi_m(t_1)).$$

Since the matrix elements between the exact eigenstates will not depend upon t_1 and t_2 if these occur respectively before and after the application of the external field, we can average over these times explicity, thus obtaining

$$\langle(\Phi_2,\, U(t_2,t_1)\Phi_1)\rangle_{Av}=b_{n2}{}^*a_{m1}(\Psi_{n2}(t_2),\, U(t_2,t_1)\Psi_{m1}(t_1)),$$

where $E_{m1}=E_1$, $E_{n2}=E_2$. From

$$\langle(\Phi_2,\, U(t_2,t_1)\Phi_1)\rangle_{Av}=a_{m1}{}^*a_{m1}(\Psi_{m1},\, U_0(t_2,t_1)\Psi_{m1})=a_{m1}{}^*a_m,$$

where $k_{1\mu}$ is taken equal to $k_{2\mu}$, one finds $a_{m1}{}^*a_{m1}=Z_2$ and similarly $b_{m1}{}^*b_{m1}=Z_2$.

If there are n widely separated electrons in the initial and final states, the appropriate factor is clearly $Z_2{}^n$, because the state vectors Φ_1 and Φ_2 can be factored into states corresponding to the presence of a single electron, and for each of these the above analysis can be carried through.

[15] By the use of

$$\int_0^1 du\int d^4k\frac{(1-2u)k^2}{(k^2+\Lambda_0^2)^3}=\int_0^1 du\int d^4k\frac{-2u\Lambda_0^2+2\kappa^2u^2(2-u)}{(k^2+\Lambda_0^2)^3}$$
$$=\int_0^1 du\int d^4k\frac{-2(1-u)\Lambda_0^2+2\kappa^2u^2(2-u)}{(k^2+\Lambda_0^2)^3}$$

which is the result of an integration by parts.

[16] F. Bloch and A. Nordsieck, Phys. Rev. **52**, 54 (1937).

[17] See reference 1, II, Eq. (99). $Z_2=1-(\alpha/2\pi)B+\cdots$.

The vertex operator $\Gamma_\mu(x', x'')$ describes the scattering of a virtual electron by a potential. The second-order contribution to it is given by the diagram, Fig. 5, or by

$$\Lambda_\mu^{(2)}(x', x'')=(-i/\hbar c)^2(-ie)^2[\gamma_\lambda\langle P[\psi(x_0-x'), \bar\psi(x_0)]\rangle_0\gamma_\mu\langle P[\psi(x_0), \bar\psi(x_0+x'')]\rangle_0 \times\gamma_\nu\langle P[A_\lambda(x_0-x'), A_\nu(x_0+x'')]\rangle]$$

$$=(e^2/8\hbar c)\gamma_\nu S_F(x')\gamma_\mu S_F(x'')\gamma_\nu D_F(x''+x') \tag{26}$$

$$=(1/2\pi)^8\int d^4p'd^4p''e^{-ip'x'}e^{-ip''x''}L_\mu(p', p'')$$

where

$$L_\mu(p', p'')=\frac{i\alpha}{4\pi^3}\int d^4k\frac{\gamma_\nu(i\gamma(p'-k)-\kappa)\gamma_\mu(i\gamma(p''-k)-\kappa)\gamma_\nu}{[(p'-k)^2+\kappa^2][(p''-k)^2+\kappa^2][k^2+\lambda^2]}. \tag{27}$$

Thus one obtains the operator $L_\mu(p', p'')$.[18] This must now be rearranged so as to display explicitly renormalization terms. First the denominators of the three Δ-functions are combined,

$$L_\mu(p', p'')=(i\alpha/4\pi^3)\int_0^1 2udu\int_0^1 dv\int d^4k\frac{\gamma_\nu[i\gamma(p'-k)-\kappa]\gamma_\mu[i\gamma(p''-h)-\kappa]\gamma_\nu}{\{[k-u(p'v+p''(1-v))]^2+\Lambda'^2\}^3}$$

$$=(i\alpha/2\pi^3)\int_0^1 udu\int_0^1 dv\int d^4k\{\gamma_\nu[i\gamma(p'(1-uv)-p''v(1-u)-k)-\kappa]\gamma_\mu \times[i\gamma(p''(1-u+uv)-p'uv-k)-\kappa]\gamma_\nu\}/(k^2+\Lambda^2)^3, \tag{28}$$

where

$$\Lambda'^2=u^2[\kappa^2+(p'-p'')^2v(1-v)]+\lambda^2(1-u)+u(1-u)[(p'^2+\kappa^2)v+(p''^2+\kappa^2)(1-v)]; \tag{29}$$

a change of variables, $k_\mu\to k_\mu+u[p_\mu'v+p_\mu''(1-v)]$ has been made.

On extensive rearrangement, the numerator of the integrand can be brought into the form[19]

$$-\gamma_\mu[k^2-4\kappa^2(1-u-\tfrac{1}{2}u^2)]+2K_\mu(p', p''; u, v), \tag{30}$$

where

$$\begin{aligned}K_\mu(p', p''; u, v)=&(1-u)(i\gamma p'+\kappa)\gamma_\mu(i\gamma p''+\kappa)-(i\gamma p'+\kappa)[\kappa(1-u^2)\gamma_\mu+i(1-u)(1-uv)(p'+p'')_\mu\\&-i(1-u+2uv)(1-uv)(p'-p'')_\mu]-[\kappa(1-u^2)\gamma_\mu+i(1-u+uv)(1-u)(p'+p'')_\mu\\&+i(1-u+uv)(1+u-2uv)(p'-p'')_\mu](i\gamma p''+\kappa)+(1-u)\gamma_\mu[(p'^2+\kappa^2)(1-uv)\\&+(p''^2+\kappa^2)(1-u+uv)]-i\kappa(p'-p'')_\mu u(1+u)(1-2v)\\&+\gamma_\mu(p'-p'')^2[1-u+u^2v(1-v)]+\kappa\sigma_{\mu\nu}(p'-p'')_\nu u(1-u).\end{aligned} \tag{31}$$

Thus, with

$$\Lambda_0^2=\kappa^2u^2+\lambda^2(1-u), \tag{18b'}$$

$$L_\mu(p', p'')=(i\alpha/2\pi^3)\int_0^1 udu\int_0^1 dv\int d^4k\Big\{-\frac{\gamma_\mu[k^2-4\kappa^2(1-u-\frac{1}{2}u^2)]}{[k^2+\Lambda_0^2]^3}+\frac{2K_\mu}{[k^2+\Lambda'^2]^3}$$

$$+3\gamma_\mu\int_0^1 dz\frac{k^2(\Lambda'^2-\Lambda_0^2)}{[k^2+\Lambda_0^2+(\Lambda'^2-\Lambda_0^2)z]^4}-4\kappa^2(1-u-\tfrac{1}{2}u^2)\Big[\frac{1}{(k^2+\Lambda'^2)^3}-\frac{1}{(k^2+\Lambda_0^2)^3}\Big]\Big\}$$

$$=-(\alpha/2\pi)\Big[-B\gamma_\mu+\frac{K}{\Lambda'^2}+\gamma_\mu\int_0^1 dz\frac{\Lambda'^2-\Lambda_0^2}{\Lambda_0^2+(\Lambda'^2-\Lambda_0^2)z}-2\kappa^2\gamma_\mu(1-u-\tfrac{1}{2}u^2)\frac{\Lambda'^2-\Lambda_0^2}{\Lambda'^2\Lambda_0^2}\Big], \tag{32}$$

where B is defined by Eq. (24).

---

[18] See reference 1, II, Eq. (26).

[19] This expression may be compared with Julian Schwinger, Phys. Rev. 76, 790 (1949), Eq. (1.94). The expressions differ only in the definition of v and in the fact that certain terms, zero for a real electron, are included here.

Finally, therefore,

$$\begin{aligned}\Gamma_\mu(x', x'') &= \gamma_\mu\delta(x')\delta(x'')+\Lambda_\mu^{(2)}(x', x'')\\ &= \gamma_\mu\delta(x')\delta(x'')[1+(\alpha/2\pi)B]-(\alpha/2\pi)(1/(2\pi)^8)\int d^4p'd^4p''\exp[-ix'p'-ix''p'']\\ &\quad\times\left[\frac{K_\mu}{\Lambda'^2}+\gamma_\mu(\Lambda'^2-\Lambda_0^2)\left(\int_0^1 dz\frac{1}{\Lambda_0^2+(\Lambda'^2-\Lambda_0^2)z}-\frac{2\kappa^2(1-u-\frac{1}{2}u^2)}{\Lambda'^2\Lambda_0^2}\right)\right]\\ &= \gamma_\mu\delta(x')\delta(x'')[1+(\alpha/2\pi)B]+\bar{\Lambda}_\mu^{(2)}(x', x'').\end{aligned} \tag{33}$$

Here again the separation of the renormalization term B has made the physically significant correction divergent in the limit $\lambda\to 0$.

CALCULATION

Now that the singular functions have been calculated to second order, it is possible to proceed with the evaluation of the matrix elements written down earlier.

Thus,

$$\begin{aligned}M^{II} = -(e\alpha\pi/2\hbar c)\int d^4x_0d^4x_0'd^4x_0''d^4x_1d^4x_1'd^4x_1''d^4x_2d^4x_2'd^4x_2''A_\mu^e(x_0)D_F'(x_0-x_1)\bar{\psi}(x_1')\\ \times\Gamma_\nu(x_1-x_1', x_1''-x_1)S_F(x_0'-x_1'')\Gamma_\mu(x_0-x_0', x_0''-x_0)S_F(x_2'-x_0'')\Gamma_\nu(x_2-x_2', x_2''-x_2)\psi'(x_2'').\end{aligned} \tag{34}$$

On substitution of the last part of Eqs. (13), (14), (23), (25a), and (33) one obtains, to order α^2,

$$M^{II} = M^{II0}+\bar{M}^{IIa}+\bar{M}^{IIc}+\bar{M}^{IId}+\bar{M}^{IIe}+\bar{M}^{IIf},^{20} \tag{35}$$

where

$$\begin{aligned}M^{II0} &= -\left(1+\frac{\alpha}{\pi}A\right)\frac{e\alpha\pi}{2\hbar c}\int d^4x_0d^4x_1d^4x_2A_\mu^e(x_0)D_F(x_2-x_1)\bar{\psi}(x_1)\gamma_\nu S_F(x_0-x_1)\gamma_\mu S_F(x_2-x_0)\gamma_\nu\psi(x_2)\\ &= -\frac{e}{\hbar c}\left(1+\frac{\alpha}{\pi}A\right)\int d^4x_0d^4x_1d^4x_2A_\mu^e(x_0)\bar{\psi}(x_1)\Lambda_\mu^{(2)}(x_0-x_1, x_2-x_0)\psi(x_2),\end{aligned} \tag{36a}$$

$$\begin{aligned}\bar{M}^{IIa} = -\frac{e\alpha^2}{4\hbar c}\int d^4x_0d^4x_0'd^4x_0''d^4x_1d^4x_2A_\mu^e(x_0)D_F(x_2-x_1)\bar{\psi}(x_1)\gamma_\nu S_F(x_0'-x_1)\\ \times\bar{\Lambda}_\mu^{(2)}(x_0-x_0', x_0''-x_0)S_F(x_2-x_0'')\gamma_\nu\psi(x_2),\end{aligned} \tag{36b}$$

$$\begin{aligned}\bar{M}^{IIc} = -\frac{e\alpha^2}{2\hbar c}\int d^4x_0d^4x_1d^4x_2d^4x_2'd^4x_2''A_\mu^e(x_0)D_F(x_2-x_1)\bar{\psi}(x_1)\gamma_\nu S_F(x_0-x_1)\gamma_\mu S_F(x_2'-x_0)\\ \times\bar{\Lambda}_\nu^{(2)}(x_2-x_2', x_2''-x_2)\psi(x_2''),\end{aligned} \tag{36c}$$

$$\bar{M}^{IId} = -\frac{e\alpha^2}{2\hbar c}\int d^4x_0d^4x_1d^4x_2A_\mu^e(x_0)D_F(x_2-x_1)\bar{\psi}(x_1)\gamma_\nu S_F(x_0-x_1)\gamma_\mu\bar{S}_F^{(2)}(x_2-x_0)\gamma_\nu\psi(x_2), \tag{36d}$$

$$\bar{M}^{IIe} = -\frac{e\alpha^2}{4\hbar c}\int d^4x_0d^4x_1d^4x_2A_\mu^e(x_0)\bar{D}_F^{(2)}(x_2-x_1)\bar{\psi}(x_1)\gamma_\nu S_F(x_0-x_1)\gamma_\mu S_F(x_2-x_0)\gamma_\nu\psi(x_2), \tag{36e}$$

$$\bar{M}^{IIf} = -\frac{e\alpha^2}{4\hbar c}\int d^4x_0d^4x_1d^4x_2\bar{A}_\mu^{e(2)}(x_0)D_F(x_2-x_1)\bar{\psi}(x_1)\gamma_\nu S_F(x_0-x_1)\gamma_\mu S_F(x_2-x_0)\gamma_\nu\psi(x_2). \tag{36f}$$

Finally,

$$\begin{aligned}M^I = -\frac{e\alpha^2}{4\hbar c}\pi^2\int d^4x_0d^4x_1d^4x_2d^4x_3d^4x_4A_\mu^e(x_0)D_F(x_3-x_1)D_F(x_4-x_2)\bar{\psi}(x_1)\gamma_\nu S_F(x_2-x_1)\gamma_\lambda\\ \times S_F(x_0-x_2)\gamma_\mu S_F(x_3-x_0)\gamma_\nu S_F(x_4-x_3)\gamma_\lambda\psi(x_4).\end{aligned} \tag{37}$$

[20] The bar on $\bar{M}^{IIa}$, etc. indicates that the renormalization terms have been removed. These are incorporated in M^{II0}. Since M^{IIb} contains only renormalization, $\bar{M}^{IIb}$ is zero.

It is convenient to continue the calculation in momentum space. The momentum p_1 will be used to denote the momentum of the final state and p_2 the momentum of the initial state:

$$\psi(x)=\int e^{ip_2x}\psi(p_2)d^4p_2, \quad (i\gamma p_2+\kappa)\psi(p_2)=0, \tag{38a}$$

and

$$\bar{\psi}(x)=\int e^{-ip_1x}\bar{\psi}(p_1)d^4p_1, \quad \bar{\psi}(p_1)(i\gamma p_1+\kappa)=0. \tag{38b}$$

Then

$$M^I=\frac{e}{\hbar c}\frac{\alpha^2}{16\pi^6}(2\pi)^4\int d^4p_1d^4p_2A_\mu^e(p_1-p_2)\int d^4kd^4k'(1/k^2)(1/k'^2)\bar{\psi}(p_1)\gamma_\nu\frac{i\gamma(p_1-k)-\kappa}{(p_1-k)^2+\kappa^2}\gamma_\lambda\frac{i\gamma(p_1-k-k')-\kappa}{(p_1-k-k')^2+\kappa^2}$$
$$\times\gamma_\mu\frac{i\gamma(p_2-k-k')-\kappa}{(p_2-k-k')^2+\kappa^2}\gamma_\nu\frac{i\gamma(p_2-k')-\kappa}{(p_2-k')^2+\kappa^2}\gamma_\lambda\psi(p_2), \tag{39}$$

$$M^{II0}=\left(1+\frac{\alpha}{\pi}A\right)\left(+\frac{\alpha e}{2\pi\hbar c}\right)(2\pi)^4\int d^4p_1d^4p_2A_\mu^e(p_1-p_2)\int_0^1 udu\int_0^1 dv$$
$$\times\bar{\psi}(p_1)\left\{\frac{\sigma_{\mu\nu}(p_1-p_2)_\nu u(1-u)+(p_1-p_2)^2\gamma_\mu(1-u+u^2v(1-v))}{\kappa^2u^2+\lambda^2(1-u)+(p_1-p_2)^2u^2v(1-v)}-B\gamma_\mu+\gamma_\mu(p_1-p_2)^2u^2v(1-v)\right.$$
$$\times\left[\int_0^1\frac{dz}{\kappa^2u^2+\lambda^2(1-u)+(p_1-p_2)^2u^2v(1-v)z}\right.$$
$$\left.\left.-\frac{2\kappa^2(1-u-\frac{1}{2}u^2)}{[\kappa^2u^2+\lambda^2(1-u)][\kappa^2u^2+\lambda^2(1-u)+(p_1-p_2)u^2v(1-v)]}\right]\right\}\psi(p_2), \tag{40}$$

$$\bar{M}^{IIa}=\frac{ie\alpha^2}{8\pi^4\hbar c}(2\pi)^4\int d^4p_1d^4p_2A_\mu^e(p_1-p_2)\int d^4k\frac{1}{k^2+\lambda^2}\int_0^1 udu\int_0^1 dv$$
$$\times\bar{\psi}(p_1)\gamma_\nu\frac{i\gamma(p_1-k)-\kappa}{(p_1-k)^2+\kappa^2}\left\{\frac{K_\mu(p_1-k,\,p_2-k;\,u,\,v)}{\Lambda'^2(p_1-k,\,p_2-k;\,u,\,v)}+\gamma_\mu(\Lambda'^2-\Lambda_0^2)\left[\int_0^1\frac{dz}{\Lambda_0^2+(\Lambda'^2-\Lambda_0^2)z}\right.\right.$$
$$\left.\left.-\frac{2\kappa^2(1-u-\frac{1}{2}u^2)}{\Lambda'^2\Lambda_0^2}\right]\right\}\frac{i\gamma(p_2-k)-\kappa}{(p_2-k)^2+\kappa^2}\gamma_\nu\psi(p_2), \tag{41}$$

$$\bar{M}^{IIc}=\frac{ie\alpha^2}{4\pi^4\hbar c}(2\pi)^4\int d^4p_1d^4p_2A_\mu^e(p_1-p_2)\int d^4k\frac{1}{k^2+\lambda^2}\int_0^1 udu\int_0^1 dv\bar{\psi}(p_1)\gamma_\nu\frac{i\gamma(p_1-k)-\kappa}{(p_1-k)^2+\kappa^2}\gamma_\mu\frac{i\gamma(p_2-k)-\kappa}{(p_2-k)^2+\kappa^2}$$
$$\times\left\{\frac{K_\nu(p_2-k,\,p_2;\,u,\,v)}{\Lambda'^2(p_2-k,\,p_2;\,u,\,v)}+\gamma_\nu(\Lambda'^2-\Lambda_0^2)\left[\int_0^1\frac{dz}{\Lambda_0^2+(\Lambda'^2-\Lambda_0^2)z}-\frac{2\kappa^2(1-u-\frac{1}{2}u^2)}{\Lambda'^2\Lambda_0^2}\right]\right\}\psi(p_2), \tag{42}$$

$$\bar{M}^{IId}=-\frac{ie\alpha^2}{4\pi^4\hbar c}(2\pi)^4\int d^4p_1d^4p_2A_\mu{}^2(p_1-p_2)\int d^4k\frac{1}{k^2+\lambda^2}\int_0^1 u(1-u)du\int_0^1 dz\bar{\psi}(p_1)\gamma_\nu\frac{i\gamma(p_1-k)-\kappa}{(p_1-k)^2+\kappa^2}\gamma_\mu$$
$$\times\frac{(i\gamma(p_1-k)-\kappa)(1-u)(1-[2\kappa^2u(1+u)z]/[\kappa^2u^2+\lambda^2(1-u)])+\kappa(1+u)}{\kappa^2u^2+\lambda^2(1-u)+[(p_2-k)^2+\kappa^2]u(1-u)z}\gamma_\nu\psi(p_2), \tag{43}$$

$$\bar{M}^{IIe}=-\frac{ie\alpha^2}{8\pi^4\hbar c}(2\pi)^4\int d^4p_1d^4p_2A_\mu^e(p_1-p_2)\int d^4k\int_0^1 dv\frac{2v^2(1-\frac{1}{3}v^2)}{1-v^2}\frac{1}{k^2+(4\kappa^2/1-v^2)}$$
$$\times\bar{\psi}(p_1)\gamma_\nu\frac{i\gamma(p_1-k)-\kappa}{(p_1-k)^2+\kappa^2}\gamma_\mu\frac{i\gamma(p_2-k)-\kappa}{(p_2-k)^2-\kappa^2}\gamma_\nu\psi(p_2), \tag{44}$$

$$\bar{M}^{III}=-\frac{ie\alpha^2}{8\pi^4\hbar c}(2\pi)^4\int d^4p_1d^4p_2A_\mu^e(p_1-p_2)\int d^4k\frac{1}{k^2+\lambda^2}(p_1-p_2)^2\bar{\psi}(p_1)\gamma_\nu\frac{i\gamma(p_1-k)-\kappa}{(p_1-k)^2+\kappa^2}\gamma_\mu$$
$$\times\frac{i\gamma(p_2-k)-\kappa}{(p_2-k)^2+\kappa^2}\gamma_\nu\psi(p_2)\int_0^1 dv\frac{v^2(1-\frac{1}{3}v^2)}{\kappa^2+(p_1-p_2)^2(1-v^2/4)}. \quad (45)$$

Now, the interaction energy density of an anomalous magnetic moment $\mu e\hbar/2mc$ with the electromagnetic field is

$$H(x_0)=-\mu(e\hbar/2mc)\tfrac{1}{2}F_{\mu\nu}(x_0)\bar{\psi}(x_0)\sigma_{\mu\nu}\psi(x_0). \quad (46)$$

Since the calculation is being carried out in momentum space, it is convenient to have the Fourier transform of this expression. Its contribution to the scattering of an electron is

$$M=\frac{e}{2\hbar c\kappa}\mu(2\pi)^4\int d^4p_1d^4p_2A_\mu^e(p_1-p_2)\bar{\psi}(p_1)\sigma_{\mu\nu}(p_1-p_2)_\nu\psi(p_2). \quad (47)$$

In calculating the correction to the magnetic moment of the electron, therefore, one must seek to bring the matrix elements into this form by rearranging the Dirac matrices occuring in them and by using the Dirac equation to simplify the momentum dependence of the integrand. This, of course, can only be done after the integration over the directions of the virtual momenta has been made trivial, so that these variables no longer conceal a dependence on the initial and final momenta. In this process, any terms that contain a factor $(p_1-p_2)^2$ may be dropped from further consideration, because they represent derivatives of the quasi-constant electromagnetic fields. Hence, $\bar{M}^{III}$ does not contribute to the magnetic moment. Further, M^{II0} gives ($\lambda^2=0$)

$$M^{II0}\rightarrow\left(1+\frac{\alpha}{\pi}A\right)\left(+\frac{e\alpha}{2\pi\hbar c}\right)(2\pi)^4\int d^4p_1d^4p_2A_\mu^e(p_1-p_2)\bar{\psi}(p_1)\sigma_{\mu\nu}(p_1-p_2)_\nu\psi(p_2)\int_0^1 udu\int_0^1 dv\frac{u(1-u)\kappa}{u^2\kappa^2}$$
$$=\frac{e}{2\hbar c\kappa}\left(1+\frac{\alpha}{\pi}A\right)\frac{\alpha}{2\pi}(2\pi)^4\int d^4p_1d^4p_2A_\mu^e(p_1-p_2)\bar{\psi}(p_1)\sigma_{\mu\nu}(p_1-p_2)_\nu\psi(p_2). \quad (48)$$

The second-order part of this expression clearly is due to the well-known anomalous magnetic moment

$$(\alpha/2\pi)(e\hbar/2mc).^{21} \quad (49)$$

This quantity, however, depends on the "bare" charge e of the electron. The measured charge of the electron is $e_1=[1+(\alpha/4\pi)A]e$ to second order. Furthermore, the external potential A_μ^e, whose source is a current, must also be renormalized, $(A_\mu^e)_1=[1+(\alpha/4\pi)A]A_\mu^e$. Equation (48) may therefore be rewritten, to order α^2,

$$M^{II0}\rightarrow\frac{e_1}{2\hbar c\kappa}\frac{\alpha_1}{2\pi}(2\pi)^4\int d^4p_1d^4p_2(A_\mu^e(p_1-p_2))_1\bar{\psi}(p_1)\sigma_{\mu\nu}(p_1-p_2)_\nu\psi(p_2), \quad (50)$$

and is due to a magnetic moment

$$\mu^{II0}=\alpha_1/2\pi \text{ in units } e_1\hbar/2mc, \quad (51)$$

which depends on the renormalized charge.

$\bar{M}^{IIe}$ can be evaluated quickly by observing that the integration over d^4k and subsequent rearrangement of the matrix element is idential with that in $L_\mu(p_1, p_2)$, provided one sets $\lambda^2=4\kappa^2/(1-v^2)$. Hence,

$$\bar{M}^{IIe}\rightarrow\frac{e}{2\hbar c\kappa}\frac{\alpha^2}{2\pi^2}\int_0^1 udu\int_0^1 dv\frac{2v^2(1-\frac{1}{3}v^2)}{1-v^2}\frac{u(1-u)}{u^2+4/(1-u)/(1-v^2)}(2\pi)^4$$
$$\times\int d^4p_1d^4p_2A_\mu^e(p_1-p_2)\bar{\psi}(p_1)\sigma_{\mu\nu}(p_1-p_2)_\nu\psi(p_2). \quad (52)$$

The magnetic moment responsible for this scattering is

$$\mu^{IIe}=\frac{\alpha^2}{\pi^2}\int_0^1 du\int_0^1 dv\frac{u^2(1-u)v^2(1-\frac{1}{3}v^2)}{u^2(1-v^2)+4(1-u)}=\frac{\alpha^2}{\pi^2}\left(\frac{119}{36}-\frac{\pi^2}{3}\right)\cong 0.016\frac{\alpha^2}{\pi^2}. \quad (53)$$

[21] Julian Schwinger, Phys. Rev. 73, 415 (1948).

The expression for $\bar{M}^{IId}$ will be examined next. The first task now is to simplify the integration over k. The situation here again is very similar to that encountered in the evaluation of $L_\mu(p', p'')$; simplifications can be made, however, because of the equations satisfied by p_1 and p_2 and because $(p_1-p_2)^2$ may be neglected. The scattering becomes

$$\bar{M}^{IId}\rightarrow\frac{-ie\alpha^2}{2\hbar c\pi^4}(2\pi)^4\int d^4p_1d^4p_2A_\mu^e(p_1-p_2)\int_0^1 u(1-u)du\int_0^1 dz\int_0^1 vdv\int_0^1 dw\int d^4k\bar{\psi}(p_1)$$

$$\times\gamma_\nu\{i\gamma[p_1(1-vw)-p_2v(1-w)-k]-\kappa\}\gamma_\mu\frac{1}{u(1-u)z}$$

$$\times\frac{\{i\gamma[p_2(1-v+vw)-p_1vw-k]-\kappa\}(1-u)(1-[2u(1+u)z]/[u^2+(\lambda^2/\kappa^2)(1-u)])+\kappa(1+u)}{\{k^2+v^2\kappa^2+\lambda^2(1-v)+v(1-w)[\kappa^2u^2+\lambda^2(1-u)]/[u(1-u)z]\}^3}\gamma_\nu\psi(p_2). \quad (54)$$

Here, obviously, the k_λ vectors in the numerator contribute no magnetic moment, because the linear term vanishes and the quadratic one is independent of p_1 and p_2.

It is useful at this point to discuss the extraction of magnetic-moment terms from these more complicated momentum-dependent spinor matrices. Thus, with the neglect of charge renormalization terms (independent of p_1 and p_2) and terms representing higher derivatives than the first of $A_\mu^e(x_0)$,

$$\begin{aligned}
&i(p_1)_\mu\bar{\psi}(p_1)\psi(p_2)=i(p_2)_\mu\bar{\psi}(p_1)\psi(p_2)=-\tfrac{1}{2}\bar{\psi}(p_1)\sigma_{\mu\nu}(p_1-p_2)_\nu\psi(p_2)=-\tfrac{1}{2}m_\mu,\\
&\bar{\psi}(p_1)\gamma_\mu i\gamma p_1\psi(p_2)=\bar{\psi}(p_1)i\gamma p_2\gamma_\mu\psi(p_2)=-m_\mu,\\
&\bar{\psi}(p_1)\gamma_\nu i\gamma p_1\gamma_\mu\gamma_\nu\psi(p_2)=\bar{\psi}(p_1)\gamma_\nu i\gamma p_2\gamma_\mu\gamma_\nu\psi(p_2)=-2m_\mu,\\
&\bar{\psi}(p_1)\gamma_\nu\gamma_\mu i\gamma p_1\gamma_\nu\psi(p_2)=\bar{\psi}(p_1)\gamma_\nu\gamma_\mu i\gamma p_2\gamma_\nu\psi(p_2)=-2m_\mu,\\
&\bar{\psi}(p_1)\gamma_\nu i\gamma p_1\gamma_\mu i\gamma p_1\gamma_\nu\psi(p_2)=\bar{\psi}(p_1)\gamma_\nu i\gamma p_2\gamma_\mu i\gamma p_2\gamma_\nu\psi(p_2)=-2\kappa m_\mu,\\
&\bar{\psi}(p_1)\gamma_\nu i\gamma p_1\gamma_\mu i\gamma p_2\gamma_\nu\psi(p_2)=-4\kappa m_\mu,\\
&\bar{\psi}(p_1)\gamma_\nu i\gamma p_2\gamma_\mu i\gamma p_1\gamma_\nu\psi(p_2)=0.
\end{aligned} \quad (55)$$

The magnetic moment contribution to $\bar{M}^{IId}$ is due to a moment

$$\mu^{IId}=\left(-\frac{i\alpha^2}{\pi^4}\kappa\right)\int_0^1 u(1-u)du\int_0^1 dz\int_0^1 vdv\int_0^1 dw\cdot\frac{i\pi^2}{2}\frac{1}{u(1-u)z}$$

$$\times\frac{\begin{array}{l}2\kappa[2(1-v)(1-u)(1-[2u(1+u)z]/[u^2+(1-u)\lambda^2/\kappa^2])-(1+u)(1-v)]\\ -2\kappa(1-v)(2-v)(1-u)(1-[2u(1+u)z]/[u^2+(1-u)\lambda^2/\kappa^2])\end{array}}{\kappa^2v^2+\lambda^2(1-v)+v(1-w)[\kappa^2u^2+\lambda^2(1-u)]/u(1-u)z}$$

$$=\frac{\alpha^2}{\pi^2}\int_0^1 u(1-u)du\int_0^1 dz\int_0^1 vdv\int_0^1 dw\frac{(1-v)[v(1-u)(1-[2u(1+u)z]/[u^2+(1-u)\lambda^2/\kappa^2])-(1+u)]}{[v^2+(\lambda^2/\kappa^2)(1-v)]u(1-u)z+v(1-w)[u^2+(\lambda^2/\kappa^2)(1-u)]}. \quad (56)$$

As was already mentioned earlier, this expression may diverge logarithmically as $\lambda\rightarrow 0$. It is easy to verify that this catastrophe occurs only in the term which has two denominators, and that is associated with the integration over u. After integration over z, only one simple term is left which is afflicted with this difficulty. The photon mass may then be set equal to zero in all others, and the integration can be easily completed to yield

$$\mu^{IId}=\frac{\alpha^2}{\pi^2}\left(\frac{11}{24}-\frac{\pi^2}{18}+\frac{1}{2}\ln\frac{\lambda^2}{\kappa^2}\right)\cong\left(-0.090+\frac{1}{2}\ln\frac{\lambda^2}{\kappa^2}\right)\frac{\alpha^2}{\pi^2}. \quad (57)$$

The expressions for μ^{IIa}, μ^{IIc}, μ^I become successively more complicated and very much more tedious to evaluate and cannot be given in detail here. The contributions from group II are all treated in a manner similar to $L_\mu^{(2)}$. The presence of two virtual momenta in M^I, however, and the symmetry of the integrand suggest that this quantity

be evaluated by noting that

$$M^I=\frac{e}{\hbar c}\frac{\alpha^2}{16\pi^6}(2\pi)^4\int d^4p_1d^4p_2A_\mu^e(p_1-p_2)\left\{\bar\psi(p_1)\left[\gamma_\nu\left(\kappa+\left(\frac{i\gamma}{2}\frac{\partial}{\partial p}\right)\int_{\kappa^2}^\infty d\mu\right)\gamma_\lambda\left(\kappa+\left(\frac{i\gamma}{2}\frac{\partial}{\partial p'}\right)\int_{\kappa^2}^\infty d\mu'\right)\right.\right.$$
$$\times\gamma_\mu\left(\kappa+\left(\frac{i\gamma}{2}\frac{\partial}{\partial p''}\right)\int_{\kappa^2}^\infty d\mu''\right)\gamma_\nu\left(\kappa+\left(\frac{i\gamma}{2}\frac{\partial}{\partial p'''}\right)\int_{\kappa^2}^\infty d\mu'''\right)\gamma_\lambda\left.\left]\psi(p_2)\right.\right.$$
$$\left.\left.\times\int\frac{d^4kd^4k'/k^2k'^2}{[(p-k)^2+\mu][(p'-k-k')^2+\mu'][(p''-k-k')^2+\mu''][(p'''-k')^2+\mu''']}\right\}_{p=p'=p_1,\ p''=p'''=p_2}\tag{58}$$

and evaluating the integrals over k and k' before carrying out the other indicated operations.[22] The result will clearly involve five variables of the type of u, v, w, Eq. (54), to be integrated from zero to one. The other two remaining terms also involve five variables, but in these the variables tend to separate into two groups, because they were introduced in connection with two independent momentum integrations. The magnetic moments may now be deduced as before. They are integrals of rational functions of the auxiliary variables.[23]

After one trivial integration, μ^{IIa} involves the same type of functions as μ^{IId}. It is found, however, that the infra-red catastrophe introduced into the $\bar\Lambda_\mu^{(2)}$ operator is compensated by one that arises in the integration over k, Eq. (41). In other words, the terms depending on the photon mass all go to zero as this quantity is made to vanish. Thus

$$\mu^{IIa}=\frac{\alpha^2}{\pi^2}\left(\frac{11}{48}+\frac{\pi^2}{18}\right)\cong0.778\frac{\alpha^2}{\pi^2}\tag{59}$$

and no longer involves λ.

After a term $-(\alpha^2/2\pi^2)\ln(\lambda^2/\kappa^2)$ is separated from μ^{IIe}, this quantity is finite in the limit $\lambda\to0$, so that the integrand may be accordingly simplified. A typical term, which happens to involve only four variables, is

$$\int_0^1du\int_0^1dv\int_0^1dt\int_0^1dw\int_0^1dz\frac{2wt(1-t)(1-uv)}{\{vw[1-uv+ut(1-v)]^2+ut(1-uv)\}^2}.\tag{60}$$

If the first three integrations are carried out in the order indicated, each can be done analytically by virtue of simplifications that occur when the limits are inserted in the preceding integration. The order of the last two integrations must be determined by inspection for each term; with two exceptions they can be carried out with the help of well-known formulas. The value of μ^{IIe} is therefore given in terms of two integrals, L_1 and L_2:

$$\mu^{IIe}=\frac{\alpha^2}{\pi^2}\left(-\tfrac{1}{2}\ln\lambda^2/\kappa^2-13\frac{11}{24}+3\frac{4}{9}-\pi^2-8\frac{1}{6}\pi^2\ln2+\frac{49}{3}L_2+\frac{34}{3}L_1\right)\cong-3.178\frac{\alpha^2}{\pi^2}-\tfrac{1}{2}\ln\lambda^2/\kappa^2\frac{\alpha^2}{\pi^2}.\tag{61}$$

Here

$$L_1=\int_0^1[\ln(1-x)]^2dx/x=3\sum_{n=1}^\infty\frac{1}{n^3}=2.4041138\cdots\tag{62a}$$

and

$$L_2=\int_0^1[\ln(1+x)]^2dx/x=(\ln2)^2/2+(\ln2)^3/6+\sum_{n=1}^\infty(-1)^{n+1}\frac{B_n(\ln2)^{2n+2}}{(2n+2)(2n)!}=0.3005655....^{24}\tag{62b}$$

A typical term of μ^I is

$$\int_0^1du\int_0^1dv\int_0^1dt\int_0^1dwwt^2u^4v^2$$
$$\times\frac{1}{[1-wt(1-uv+u^2v^2)]\{u^2t-w[(1-t+tuv)^2-u^2t^2(1-uv)-2tu^2v(1-t+tuv)]\}^2},\tag{63}$$

[22] The integration over the virtual momenta is accomplished by combining the six denominators in the manner of Eq. (16). There are many equivalent ways of introducing the auxiliary variables; some of these, however, are much more convenient than others for carrying out the subsequent integrations.

[23] The details of two independent calculations which were performed so as to provide some check of the final result are available from the authors. The work is made lengthy by the large number of integrals over auxiliary variables.

[24] *Note added in proof:* Using the results of H. F. Sandham, J. Lon. Math. Soc. 24, 83 (1949), one can show that $L_2=\frac{1}{4}L_1$.

where a trivial integration over one variable has been carried out. After two integrations, which again can be carried out analytically by virtue of some remarkable simplifications, the functions of u and v obtained are very similar to those encountered in the calculation of μ^{IIe}. The final result, in terms of the integrals Eq. (62) is

$$\mu^{I}=\frac{\alpha^2}{\pi^2}\left[13/96+\frac{13}{36}\pi^2-\frac{5}{6}\pi^2\ln 2+(5/3)L_2+(5/12)L_1\right]\cong-0.499\frac{\alpha^2}{\pi^2}. \tag{64}$$

SUMMARY OF RESULTS

The five contributions to the fourth-order radiative correction to the electron's magnetic moment are, Eqs. (53), (57), (59), (61), and (64),

$$\mu^{I}=\frac{\alpha^2}{\pi^2}\left[\frac{13}{96}+\frac{13}{36}\pi^2-\frac{5}{6}\pi^2\ln 2+\frac{5}{3}L_2+\frac{5}{12}L_1\right]=-0.499\frac{\alpha^2}{\pi^2},$$

$$\mu^{IIa}=\frac{\alpha^2}{\pi^2}\left[\frac{11}{48}+\frac{1}{18}\pi^2\right]=0.778\frac{\alpha^2}{\pi^2},$$

$$\mu^{IIe}=\frac{\alpha^2}{\pi^2}\left[-13\frac{11}{24}+3\frac{4}{9}\pi^2-8\frac{1}{6}\pi^2\ln 2+\frac{49}{3}L_2+\frac{34}{3}L_1-\frac{1}{2}\ln\frac{\lambda^2}{\kappa^2}\right]$$

$$=-3.178\frac{\alpha^2}{\pi^2}-\frac{1}{2}\left(\ln\frac{\lambda^2}{\kappa^2}\right)\frac{\alpha^2}{\pi^2},$$

$$\mu^{IId}=\frac{\alpha^2}{\pi^2}\left[+\frac{11}{24}-\frac{1}{18}\pi^2+\frac{1}{2}\ln\frac{\lambda^2}{\kappa^2}\right]$$

$$=-0.090\frac{\alpha^2}{\pi^2}+\frac{1}{2}\left(\ln\frac{\lambda^2}{\kappa^2}\right)\frac{\alpha^2}{\pi^2},$$

$$\mu^{IIe}=\frac{\alpha^2}{\pi^2}\left[3\frac{11}{36}-\frac{\pi^2}{3}\right]=0.016\frac{\alpha^2}{\pi^2};$$

here L_1 and L_2 are the integrals of Eq. (62a) and (62b), respectively. Hence, the total radiative correction to the magnetic moment of the electron, to fourth order in e, is

$$\mu=\frac{\alpha_1}{2\pi}-\frac{\alpha_1^2}{\pi^2}\left[9\frac{95}{288}-3\frac{17}{36}\pi^2+9\pi^2\ln 2-18L_2-\frac{47}{4}L_1\right]$$

$$\cong\frac{\alpha_1}{2\pi}-2.973\frac{\alpha_1^2}{\pi^2}\cong 0.001147 \text{ in units } (e_1\hbar/2mc).$$

ACKNOWLEDGMENTS

It is a pleasure to acknowledge much helpful discussion with F. J. Dyson and to thank Professor Oppenheimer for his continual encouragement.

Bremsstrahlung for Heavy Elements at Extreme Relativistic Energies

L. BESS*
University of Illinois, Urbana, Illinois
(Received June 28, 1949)

The correction to the Born approximation has been found for high energy bremsstrahlung neglecting screening. The calculation involves using approximate Coulomb solutions to the Dirac equation which give the right phase and wave amplitude at large distances from the nucleus. The correction is found to decrease with increasing energies, and is less than 10 percent for 15-Mev electrons and a Pb target. Moreover, unlike the non-relativistic case, the correction is independent of the sign of charge of the projectile.

I. INTRODUCTION

UNTIL now, it has been possible to calculate bremsstrahlung from electrons of relativistic energies only within the Born approximation. If H is the total Hamiltonian, H_0 the Hamiltonian for a free particle and the radiation field, and H' the interaction between the particle and the radiation field, then near a point charge nucleus there will be the following relation

$$H=H_0+(Ze^2/\rho)+H'. \tag{1}$$

In the Born approximation H_0 is the unperturbed Hamiltonian and $(Ze^2/\rho)+H'$ is the perturbation. The calculation is then a second-order perturbation calculation with the condition for validity that $Ze^2/\hbar v(=a)$ be small compared to unity, where v is the velocity. Thus for heavy elements (large Z), this calculation would not be expected to be valid.

The work to be reported in this paper is the calculation of bremsstrahlung for arbitrary Z at high relativistic energies, assuming a pure Coulomb scattering field (i.e., screening is neglected). Here H_0+Ze^2/ρ is the Hamiltonian for the unperturbed state, and H' is the perturbation term. Bremsstrahlung, in this treatment, is then a first-order process.

In order to obtain the wave functions for the unperturbed states, it is necessary to solve the Dirac equation for an electron in a Coulomb field. Since it is essential that the magnitude and direction of the electron momentum be determinate at large distances from the nucleus, the requirement must be made on the wave function that it asymptotically approach a plane wave far from the nucleus. The simplest way to guarantee this requirement and have a solution in closed form would be to solve the Dirac equation in parabolic coordinates. Unfortunately this is not feasible since the equation is not separable. As a consequence, it is not possible to obtain a solution in closed form with the above asymptotic behavior. The only exact analytical solution possible is an infinite series.[1] It is therefore necessary to obtain some approximate solution. To do this, a variation of the method developed by Sommerfeld and Maue[2] will be used.

Notation

ϵ_1 = energy of incoming electron in units of mc^2;
ϵ_2 = energy of outgoing electron in units of mc^2;
$\mathbf{p}_1$ = momentum of incoming electron in units of mc;
$\mathbf{p}_2$ = momentum of outgoing electron in units of mc;
$\mathbf{k}$ = momentum of the quantum in units of mc;
$\mathbf{q}=\mathbf{p}_1-\mathbf{p}_2-\mathbf{k}$;
$s=-i(p_1-p_2-k)$; $t=-i(p_1-p_2+k)$;
$D_1=2k(\epsilon_1-p_1\cos\theta_1)$; $D_2=-2k(\epsilon_2-p_2\cos\theta_2)$.

The reference coordinate system is now chosen with the nucleus at the origin and $\mathbf{k}$ in the z direction.

θ_1 = angle between $\mathbf{p}_1$ and $\mathbf{k}$;
θ_2 = angle between $\mathbf{p}_2$ and $\mathbf{k}$;
ϕ_1 = angle between the y axis and the projection of $\mathbf{p}_1$ on the xy plane;
ϕ_2 = angle between the y axis and the projection of $\mathbf{p}_2$ on the xy plane;
$\boldsymbol{\varrho}$ = the radius vector;
$\mathbf{r}=\boldsymbol{\varrho}mc/\hbar$;
$a_1=(Ze^2/\hbar c)(\epsilon_1/p_1)$;
$a_2=(Ze^2/\hbar c)(\epsilon_2/p_2)$;
$Y=stq^2/D_1D_2$;
$X=1-Y$;
$\text{vs}\theta=1-\cos\theta$.

$F(a, b; c; X)$ = hypergeometric function in X;
$F(a; b; X)$ = confluent hypergeometric function in X, $\omega=k/\epsilon_1$;
$V(X)=F(ia, -ia; 1; X)$;
$W(X)=F(1+ia; 1-ia; 2; X)$;
$\mathbf{0}_\nu$ = unit vector in ν direction.

II. DETERMINATION OF UNPERTURBED WAVE FUNCTION

The matrix elements pertaining to bremsstrahlung are of the form

$$H_{12}'\sim\int\psi_2^*e^{-ik\cdot r}\psi_1 d^3r. \tag{2}$$

The subscript 1 refers to the initial state, and 2 to the final. It can be shown that at large distances from the nucleus the Coulomb solution to the Dirac equation can take the form:

$$\psi\sim e^{i\mathbf{p}\cdot\mathbf{r}+i\phi_p(\mathbf{r})}[c_0+c_1/pr+c_2/p^2r^2+\cdots], \tag{3}$$

where the c's are four component amplitudes which are functions only of θ and ϕ, and $\phi_p(\mathbf{r})$ is a phase factor. As will be seen later, H_{12}' becomes large for small θ_1 and θ_2. When the wave functions of the form of (3) are substituted in H_{12}', if one of the terms of the integrand in

* AEC Fellow.
[1] W. H. Furry, Phys. Rev. 46, 391 (1934).
[2] A. Sommerfeld and A. W. Maue, Ann. d. Physik 22, 629 (1935).

(2) is of the order of $1/r$ or lower, it can produce an integral of the order of $1/qD$; whereas it can be shown that if the integrand in (2) is of the order of $(1/r)^2$ or higher, the integral will at the most be of the order of $(1/q)\log q^2$.

A qualitative way of seeing this is to note that the region of space which contributes materially to the integral of (2) is a sphere with a radius of the order $1/q$. When θ_1 and θ_2 are small, $1/q$ will be large compared to $1/p$ for high energies. (It is assumed that the volume of the region beyond which the expansion of the form of (3) converges is of the order of $1/p^3$. Thus the contribution to the integral within this volume can be neglected compared to that within the sphere of radius $1/q$.) Over most of the sphere of radius $1/q$, terms in the integrand of the order $1/r^2$ will be very much smaller than terms of the order $1/r$ and unity. Therefore, if θ_1 and θ_2 are small, integrals produced by terms of the order $1/r^2$ and higher are very much smaller than integrals produced by integrands of the order $1/r$ and unity.

Since integrands in (2) of the order of $1/r$ and unity can only be produced by the c_0 and c_1 terms, it then follows that all c's beyond c_0 and c_1 can be neglected in calculating the high energy total cross section (i.e., the cross section after having done both angular integrations of the differential cross section). This is because the parts of the differential cross section of the order $(1/qD)^2$ will give rise to terms in the total cross section of the order $\log\epsilon^2$ and unity; whereas the $[(1/q)\log q^2]^2$ parts and cross terms between the $(1/q)\log q^2$ and the $1/qD$ parts can at the most produce terms of the order $(1/\epsilon)\log\epsilon^2$. Since for high energies $\epsilon\gg 1$, the second set of terms can be neglected in the total cross section.

Therefore in what follows, an approximate solution of the Dirac equation will be derived which is correct to the order $1/r$ inclusive at large distances from the nucleus (or if expanded in the form of (3), will give correct coefficients for c_1 and c_2 but not necessarily for higher c's).

In the development given below, the second-degree Dirac equation will be used although all the results obtained have been shown to be true for the more fundamental first-degree equation. The second-degree equation is:

$$\nabla_r^2\psi=[-(\epsilon-a/r)^2+1+i\alpha\cdot(\nabla_r a/r)]\psi, \tag{4}$$

where $\nabla_r\equiv(h/mc)$ grad. A solution will be assumed of the form:

$$\psi=Ne^{ip\cdot r}(1+\Omega)u(\mathbf{p})F, \tag{5}$$

where $F=F(ia;1;ipr-ip\cdot\mathbf{r})$, N is a normalization constant and $u(\mathbf{p})$ is the Dirac matrix coefficient of the free electron solution. The above form is very similar to the Sommerfeld-Maue solution except that Ω is to be considered a general operator which commutes with the gradient operators (in practice this necessitates that Ω consist essentially of space derivatives and Dirac operators, and be independent of θ, ϕ, and r).

When (5) is substituted in (4), the result obtained (after some cancellation) is:

$$\begin{aligned}-2[\Omega(ap/r)]uF=&-a^2/r^2(1+\Omega)uF\\&+i\alpha\cdot[\nabla_r(a/r)][1+\Omega]uF\\&-[2a(\epsilon-p)/r][1+\Omega]uF.\end{aligned} \tag{6}$$

For high relativistic energies the last term on the right-hand side of (6) becomes

$$[-2a(\epsilon-p)/r][1+\Omega]uF\cong-(a/\epsilon r)[1+\Omega]uF. \tag{7}$$

If the condition is imposed that $a/\epsilon\ll 1$, then this term can be neglected.

The terms on the right-hand side of (6) which are of the lowest order in $1/r$ (i.e., $1/r^2$) are $(-a^2/r^2)uF$ and $i\alpha\cdot(\nabla_r a/r)uF$. Ω is now chosen to that these terms are canceled out. This gives

$$\Omega=\alpha\cdot\nabla_r/2ip-(a/2p)(\partial/\partial r) \tag{8}$$

and

$$\psi_0\equiv Ne^{ip\cdot r}\left(1+\frac{\alpha\cdot\nabla_r}{2ip}-\frac{a}{2p}\frac{\partial}{\partial r}\right)uF \tag{9}$$

is then the approximate unperturbed wave function correct to the order $1/r$ inclusive at large distances from the nucleus provided $\epsilon\gg a$.

To check that this is so, assume that the exact solution to the Dirac equation ψ can be written in the form

$$\psi=\psi_0+e^{ip\cdot r}G(\mathbf{r}), \tag{10}$$

where G is a four component function. If (10) is then substituted in (4) there results

$$\begin{aligned}2ip\cdot\nabla_r G+(2a\epsilon/r)G+\nabla_r^2G+(a^2/r^2)(1+\Omega)G&\\-i\alpha\cdot(\nabla_r a/r)(1+\Omega)G&\\=-(a^2/r^2)\Omega uF+i\alpha\cdot(\nabla_r(a/r))\Omega uF.&\end{aligned} \tag{11}$$

It is to be noticed that ΩF is of the order $1/r$ since the derivative of F gives a hypergeometric function which (except for phase factors) varies as $1/r$ for large r. Since the lowest order in $1/r$ on the right of (11) is $1/r^3$, It can be seen from the left-hand side of (11) that G need not have a lower order than $1/r^2$. It then follows that ψ_0 is correct to the order $1/r$ inclusive.

III. DIFFERENTIAL CROSS SECTION

It has been shown[3] that the differential cross section for bremsstrahlung (in a box of volume L^3) is:

$$\begin{aligned}d^2\sigma=\frac{2\pi}{\hbar c}(mc^2)^4\left(\frac{p_1}{p_2}\right)\frac{\epsilon_1\epsilon_2L^9}{(2\pi\hbar c)^6}|H_{12}'|^2k^2dk&\\\times\sin\theta_1\sin\theta_2d\theta_1d\theta_2d\phi.&\end{aligned} \tag{12}$$

Wave functions of the form of (9) will be used in the

[3] See, for instance, W. Heitler, *The Quantum Theory of Radiation* (Oxford University Press, London, 1936), p. 163.

calculation of H_{12}'. The exact form of H_{12}' is:

$$H_{12}'=C_a\int \psi_2^*\boldsymbol{\alpha}\cdot\mathbf{0}_\lambda e^{-i\mathbf{k}\cdot\mathbf{r}}\psi_1 d^3\rho, \tag{13}$$

where $C_a=-e(2\pi\hbar^2c^2/L^3k)^{\frac{1}{2}}$ and $\mathbf{0}_\lambda$ is the unit polarization vector of the emitted quantum.

Substituting the wave functions in (13) and retaining only the integrals whose integrands is of the order $1/r$ or lower, the result is:

$$H_{12}'=[(u_2^{*T}\boldsymbol{\alpha}\cdot\mathbf{0}_\lambda u_1)I_1+(u_2^{*T}\boldsymbol{\alpha}\cdot\mathbf{0}_\lambda\boldsymbol{\alpha}\cdot\mathbf{I}_2u_1)+(u_2^{*T}\boldsymbol{\alpha}\cdot\mathbf{I}_3\boldsymbol{\alpha}\cdot\mathbf{0}_\lambda u_1)], \tag{14}$$

where

$$I_1=C_aN^2\Big[\int e^{i\mathbf{q}\cdot\mathbf{r}}F_2^*F_1d^3\rho-\frac{a}{2p_1}\int e^{i\mathbf{q}\cdot\mathbf{r}}F_2^*(\partial F_1/\partial r)d^3\rho-\frac{a}{2p_2}\int e^{i\mathbf{q}\cdot\mathbf{r}}(\partial F_2^*/\partial r)F_1d^3\rho\Big], \tag{14a}$$

$$\mathbf{I}_2=\frac{C_aN^2}{2ip_1}\int e^{i\mathbf{q}\cdot\mathbf{r}}F_2^*(\nabla_rF_1)d^3\rho, \tag{14b}$$

$$\mathbf{I}_3=-\frac{C_aN^2}{2ip_2}\int e^{i\mathbf{q}\cdot\mathbf{r}}(\nabla_rF_2^*)F_1d^3\rho, \tag{14c}$$

where

$$F_1\equiv F(ia_1;1;ip_1r-i\mathbf{p}_1\cdot\mathbf{r}),$$
$$F_2\equiv F(ia_2;1;ip_2r-i\mathbf{p}_2\cdot\mathbf{r}),$$
$$N^2=\{\exp[\pi(a_1+a_2)/2]\Gamma(1+ia_2)\Gamma(1-ia_1)\}[1/L^3].$$

As will be seen later, all of the above I's can be generated by means of differential operators from the integral

$$I_0=C_aN^2\int\frac{e^{i\mathbf{q}\cdot\mathbf{r}}}{r}F_2^*F_1d^3\rho. \tag{15}$$

Therefore, I_0 will first be evaluated. In performing the integration[4] of I_0 we use the following representation of F:

$$F(\alpha;1;z)=\frac{e^z}{\Gamma(1-\alpha)}\int_0^\infty e^{-x}x^{-\alpha}J_0(2(xz)^{\frac{1}{2}})dx. \tag{16}$$

The integration can further be facilitated by changing to parabolic coordinates, whose relation to spherical coordinates is:

$$z=(u-v)/2,\quad x=(uv)^{\frac{1}{2}}\cos\beta,\quad y=(uv)^{\frac{1}{2}}\sin\beta,$$
$$r=(u+v)/2,\quad d^3\rho=(\hbar/\mathrm{mc})^3\tfrac{1}{4}(u+v)dudvd\beta. \tag{17}$$

In the above relations, for large v the plane $v=$const. is perpendicular to the z axis. If it is required that the plane $v=$const. be at any arbitrary orientation with respect to the z axis (i.e., defined by θ_1 and ϕ_1), the relationship between the various u's and v's is:

$$u_1+v_1=u+v,$$
$$v_1=u\cos^2(\theta_1/2)+v\sin^2(\theta_1/2)-2(uv)^{\frac{1}{2}}\sin(\theta_1/2)\cos(\theta_1/2)\cos(\beta-\phi_1). \tag{18}$$

Written in parabolic coordinates, I_0 becomes:

$$I_0=\frac{C_b}{2\Gamma(1-ia_1)\Gamma(1+ia_2)}\int_0^\infty e^{-\xi}\xi^{-ia_1}d\xi\times\int_0^\infty e^{-\zeta}\zeta^{ia_2}d\zeta\int_0^\infty\int_0^\infty\int_0^{2\pi}dudvd\beta\times\exp^{-(su/2)-(tv/2)}J_0(2(ip_1v_1\zeta)^{\frac{1}{2}})\times J_0(2(-ip_2v_2\xi)^{\frac{1}{2}}), \tag{19}$$

where

$$s=-i(p_1-p_2-k),\quad t=-i(p_1-p_2+k),$$
$$C_b\equiv(h/\mathrm{mc})^3N^2Ca.$$

By using the well-known Bessel function theorem that:

$$J_0[(z_1^2+z_2^2-2z_1z_2\cos\phi)^{\frac{1}{2}}]=\sum_{\nu=-\infty}^{\infty}J_\nu(z_1)J_\nu(z_2)e^{i\nu\phi} \tag{20}$$

there results in view of (18) that:

$$I_0=\frac{C_b}{2\Gamma(1-ia_1)\Gamma(1+ia_2)}\int_0^\infty d\xi\xi^{-ia_1}e^{-\xi}\times\int_0^\infty d\zeta\zeta^{ia_2}e^{-\zeta}\int\int\int_0^{2\pi}dudvd\beta\times\sum_{\nu=-\infty}^{\infty}e^{i\nu(\beta-\phi_1)}J_\nu(2f_1(u\xi)^{\frac{1}{2}})J_\nu(2g_1(v\xi)^{\frac{1}{2}})\times\sum_{\mu=-\infty}^{\infty}e^{i\mu(\beta-\phi_2)}J_\mu(2f_2(u\zeta)^{\frac{1}{2}})J_\mu(2g_2(v\zeta)^{\frac{1}{2}}), \tag{21}$$

where

$$f_1=(ip_1)^{\frac{1}{2}}\sin\theta_1/2,\quad f_2=(-ip_2)^{\frac{1}{2}}\sin\theta_2/2,$$
$$g_1=(ip_1)^{\frac{1}{2}}\cos\theta_1/2,\quad g_2=(-ip_2)^{\frac{1}{2}}\cos\theta_2/2.$$

After the β-integration:

$$I_0=\frac{2\pi C_b}{2\Gamma(1-ia_1)\Gamma(1+ia_2)}\int_0^\infty d\xi\xi^{-ia_1}e^{-\xi}\times\int_0^\infty d\zeta\zeta^{ia_2}e^{-\zeta}\sum_{\nu=-\infty}^{\infty}A_\nu B_\nu e^{i\nu\phi}, \tag{22}$$

where

$$\varphi=\varphi_2-\varphi_1,$$
$$A_\nu=\int_0^\infty e^{-su/2}J_\nu(2f_1(u\xi)^{\frac{1}{2}})J_\nu(2f_2(u\zeta)^{\frac{1}{2}})du,$$
$$B_\nu=\int_0^\infty e^{-tv/2}J_\nu(2g_1(v\xi)^{\frac{1}{2}})J_\nu(2g_2(v\zeta)^{\frac{1}{2}})dv,$$

[4] The treatment of this integration in the initial stages is similar to that of A. Sommerfeld, Ann. d. Physik 11, 257 (1931).

and use has been made of

$$J_{-\nu}(z)=(-1)^{\nu}J_{\nu}(z).$$

Utilizing

$$\int_0^\infty e^{-\gamma x}J_\nu[\alpha(x)^{\frac{1}{2}}]J_\nu[\beta(x)^{\frac{1}{2}}]dx = \frac{(-i)^\nu}{\gamma}\exp[-(\alpha^2+\beta^2)/4\gamma]J_\nu(i\alpha\beta/4\gamma), \quad (23)$$

$$A_\nu=\frac{2(-i)^\nu}{s}\exp[-2(\xi f_1^2+\zeta f_2^2)/s]J_\nu(4if_1f_2(\xi\zeta)^{\frac{1}{2}}/s),$$
$$B_\nu=\frac{2(-i)^\nu}{t}\exp[-2(\xi g_1^2+\zeta g_2^2)/t]J_\nu(4ig_1g_2(\xi\zeta)^{\frac{1}{2}}/t). \quad (24)$$

Thus using (20) again

$$\sum_{\nu=-\infty}^{\infty}A_\nu B_\nu e^{i\nu\phi}=\frac{4}{st}\exp\left\{-\frac{2(\xi f_1^2+\zeta f_2^2)}{s} -\frac{2(\xi g_1^2+\zeta g_2^2)}{t}\right\}J_0(2R(\xi\zeta)^{\frac{1}{2}}). \quad (25)$$

Substituting in (22)

$$I_0=\frac{4\pi C_b}{st\Gamma(1-ia_1)\Gamma(1+ia_2)}\int_0^\infty d\xi\xi^{-ia_1}e^{-\xi d_1} \times\int_0^\infty d\zeta\zeta^{ia_2}e^{-\zeta d_2}J_0(2R(\xi\zeta)^{\frac{1}{2}}), \quad (26)$$

where

$$d_1=1+2f_1^2/s+2g_1^2/t,\quad d_2=1+2f_2^2/s+2g_2^2/t,$$
$$R=2i((f_1f_2)^2/s^2+(g_1g_2)^2/t^2+2f_1f_2g_1g_2\cos\phi/st)^{\frac{1}{2}}.$$

Letting $\zeta_1=\zeta d_2$ and $\xi_1=(d_1d_2+R^2/d_1)\xi$, in view of (16), (26) will become (after the ζ_1 integration):

$$I_0=\frac{4\pi C_b(d_1d_2)^{-1+ia_1}d_2^{-i(a_1+a_2)}}{st\Gamma(1-ia_1)}\left(\frac{d_1d_2+R^2}{d_1d_2}\right)^{-i+ia_1} \times\int_0^\infty d\xi_1\xi_1^{-ia_1}e^{-\xi_1}F\left(-ia_2;1;\frac{R^2\xi_1}{d_1d_2+R^2}\right). \quad (27)$$

A term by term integration of the hypergeometric expansion will verify that:

$$\int_0^\infty dx x^{-\alpha}e^{-x}F(\beta;1;zx)=\Gamma(1-\alpha)F(\beta;1-\alpha;1;z). \quad (28)$$

Thus:

$$I_0=\frac{4\pi C_b}{st}(d_1d_2+R^2)^{-1+ia_1}(d_2)^{-i(a_1+a_2)} \times F\left(-ia_2,1-ia_1;1;\frac{R^2}{R^2+d_1d_2}\right). \quad (29)$$

Now it can be verified that:

$$d_1\equiv D_1/st=\frac{2k(\epsilon_1-p_1\cos\theta_1)}{st},$$
$$d_2\equiv D_2/st=\frac{-2k(\epsilon_2-p_2\cos\theta_2)}{st},$$
$$d_1d_2+R^2=q^2/st,\quad st=k^2-(p_1-p_2)^2. \quad (30)$$

Then

$$I_0=4\pi C_b(st)^{ia_2}D_2^{-i(a_1+a_2)}(q^2)^{-1+ia_1} \times F\left(-ia_2,1-ia_1;1;1-\frac{D_1D_2}{stq^2}\right). \quad (31)$$

A more convenient form of I_0 involving a purely real hypergeometric function is obtained by using the connection formula:

$$F(\alpha,\beta;\gamma;z)=(1-z)^{-\alpha}F(\alpha,\gamma-\beta;\gamma;z/z-1). \quad (32)$$

I_0 then becomes:[5]

$$I_0=\frac{4\pi C_bD_1^{ia_2}D_2^{-ia_1}}{(q^2)^{1-ia_1+ia_2}}F\left(ia_1,-ia_2;1;1-\frac{stq^2}{D_1D_2}\right). \quad (33)$$

The integrals required in our calculation are derivable from I_0 as follows. Since

$$\nabla_r(pr-\mathbf{p}\cdot\mathbf{r})=p(\mathbf{0}_r-\mathbf{0}_p)=-(p/r)\nabla_p(pr-\mathbf{p}\cdot\mathbf{r}),$$

where

$$\nabla_p\equiv\mathbf{0}_x(\partial/\partial p_x)+\mathbf{0}_y(\partial/\partial p_y)+\mathbf{0}_z(\partial/\partial p_z),$$

then

$$\nabla_rF=-(p/r)\nabla_pF.$$

Similarly

$$(\partial/\partial r)F=(p/r)(\partial/\partial p)F. \quad (34)$$

Thus it can be shown that:

$$I_1=-(\partial/\partial s+\partial/\partial t)I_0(s,t,f_i,g_i,\phi) -(a/2)(\partial/\partial p_1+\partial/\partial p_2)I_0(p_i,q),$$
$$\mathbf{I}_2=(i/2)\nabla_{p_1}I_0(p_i,q),$$
$$\mathbf{I}_3=-(i/2)\nabla_{p_2}I_0(p_i,q), \quad (35)$$

where the arguments given for I_0 are the variables to be regarded as independent in performing the various partial differentiations.

After the differentiation has been carried out (a_1 is set $=a_2=a$ for relativistic energies) there results:

[5] This integral has also been evaluated by A. T. Nordsieck in a slightly more general way using contour integration.

$$I_1=4\pi aC_b\left(\frac{D_1}{D_2}\right)^{ia}\left\{\frac{V(x)}{q^2}\left(\frac{2\epsilon_2}{D_1}+\frac{2\epsilon_1}{D_2}\right)\right.$$
$$-\frac{a^2W(x)}{D_1D_2}\left[-(p_1+p_2)(1-\mathbf{0}_1\cdot\mathbf{0}_2)\right.$$
$$\left.+\mathbf{q}\cdot\mathbf{0}_1\left(1-\frac{st}{D_2}\right)-\mathbf{q}\cdot\mathbf{0}_2\left(1-\frac{st}{D_1}\right)\right]$$
$$-\frac{iaV(x)}{q^2}\left(\frac{\mathbf{q}\cdot\mathbf{0}_2}{D_1}+\frac{\mathbf{q}\cdot\mathbf{0}_1}{D_2}\right)$$
$$\left.-\frac{iaW(x)}{D_1D_2}\left[2\epsilon_1\left(1-\frac{st}{D_2}\right)-2\epsilon_2\left(1-\frac{st}{D_1}\right)\right]\right\},$$

$$\mathbf{I}_2=4\pi aC_b\left(\frac{D_1}{D_2}\right)^{ia}\left\{\frac{-\mathbf{q}V(x)}{q^2D_2}\right.$$
$$\left.+\frac{iaW(x)}{D_1D_2}\left[\mathbf{q}\left(1-\frac{st}{D_2}\right)-(\mathbf{p}_1p_2-p_1\mathbf{p}_2)\right]\right\},$$

$$\mathbf{I}_3=4\pi aC_b\left(\frac{D_1}{D_2}\right)^{ia}\left\{\frac{\mathbf{q}V(x)}{q^2D_1}\right.$$
$$\left.+\frac{iaW(x)}{D_1D_2}\left[\mathbf{q}\left(1-\frac{st}{D_1}\right)-(\mathbf{p}_1p_2-p_1\mathbf{p}_2)\right]\right\}, \quad (36)$$

where the $\mathbf{0}$'s are unit vectors and X, $V(x)$ and $W(x)$ are defined in Section I.

The absolute square of H_{12}' is now taken and the result is summed over both directions of radiation polarization and over outgoing electron spin, and averaged over the incoming electron spin. (It should be noticed that the spur and closure theorems of the free electron Dirac solution can be used here. This is because the spin sums involve the free electron spinor coefficients, $u(\mathbf{p})$.) Thus:

$$\sum|H_{12}'|^2=\frac{(4\pi aC_be^{-\pi a})^2}{\epsilon_1\epsilon_2}\sum_{\nu=1}^{2}\{(I_{2\nu}^2+I_{3\nu}^2)$$
$$\times(\epsilon_1\epsilon_2+1+p_1p_2\cos\theta_1\cos\theta_2)-2(I_{2\nu})_z(I_{3\nu})_z$$
$$\times(\epsilon_1\epsilon_2+1+\mathbf{p}_1\cdot\mathbf{p}_2)+I_{1\nu}^2(\epsilon_1\epsilon_2-1-p_1p_2\cos\theta_1\cos\theta_2)$$
$$+2[\mathbf{I}_{2\nu}-\mathbf{I}_{3\nu}]\cdot[\mathbf{p}_2(I_{3\nu})_z(p_1)_z-\mathbf{p}_1(I_{2\nu})_z(p_2)_z]$$
$$+2[(\mathbf{I}_{3\nu}\cdot\mathbf{p}_2)(\mathbf{I}_{2\nu}\cdot\mathbf{p}_1)-(\mathbf{I}_{2\nu}\cdot\mathbf{p}_2)(\mathbf{I}_{3\nu}\cdot\mathbf{p}_1)]$$
$$+2I_{1\nu}[\epsilon_2(\mathbf{I}_{2\nu}\cdot\mathbf{p}_1)-\epsilon_2(I_{3\nu})_z(p_1)_z$$
$$+\epsilon_1(\mathbf{I}_{3\nu}\cdot\mathbf{p}_2)-\epsilon_1(I_{2\nu})_z(p_2)_z]\}, \quad (37)$$

where

$$I_1=I_{11}+iI_{12}, \quad \mathbf{I}_2=\mathbf{I}_{21}+i\mathbf{I}_{22}, \quad \mathbf{I}_3=\mathbf{I}_{31}+i\mathbf{I}_{32}.$$

All of the $I_{\nu1}$'s and $I_{\nu2}$'s are real. In squaring the various I's, it should be noticed that $D_1>0$ while $D_2<0$; thus $|(D_1/D_2)^{ia}|^2$ is either $e^{2\pi a}$ or $e^{-2\pi a}$. However, certain known asymptotic behavior of I_0 requires that it be $e^{-2\pi a}$.

When the I's are substituted into (37) and (12), only those terms will be retained which will contribute to the order unity or $\log\epsilon^2$ to the total cross section. The result then is:

$$d^2\sigma=\left(\frac{\pi a}{\sinh\pi a}\right)^2\frac{a^2}{2\pi}\frac{(\hbar c)^2}{137}\left(\frac{p_1}{p_2}\right)\frac{dk}{k}\frac{\sin\theta_1\sin\theta_2d\theta_1d\theta_2d\phi}{(mc^2)^2}\left\{\frac{V^2(x)}{q^4}\left[\frac{4\epsilon_2^2p_1^2\sin^2\theta_1}{(\epsilon_1-p_1\cos\theta_1)^2}+\frac{4\epsilon_1^2p_2^2\sin^2\theta_2}{(\epsilon_2-p_2\cos\theta_2)^2}\right.\right.$$
$$\left.-\frac{(4\epsilon_1\epsilon_2+2k^2)2p_1p_2\sin\theta_1\sin\theta_2\cos\phi}{(\epsilon_1-p_1\cos\theta_1)(\epsilon_2-p_2\cos\theta_2)}+\frac{2k^2(p_1^2\sin^2\theta_1+p_2^2\sin^2\theta_2)}{(\epsilon_1-p_1\cos\theta_1)(\epsilon_2-p_2\cos\theta_2)}+\frac{a^2\epsilon_1^3\epsilon_2\,\mathrm{vs}^3\theta_1}{(\epsilon_2-p_2\cos\theta_2)^2}+\frac{a^2\epsilon_1\epsilon_2^3\,\mathrm{vs}^3\theta_2}{(\epsilon_1-p_1\cos\theta_1)^2}\right]$$
$$+\frac{8a^2V(X)W(X)}{q^2(\epsilon_1-p_1\cos\theta_1)(\epsilon_2-p_2\cos\theta_2)}\left[\frac{\epsilon_1^2\epsilon_2\,\mathrm{vs}^2\theta_1}{\epsilon_2-p_2\cos\theta_2}+\frac{\epsilon_1\epsilon_2^2\,\mathrm{vs}^2\theta_2}{\epsilon_1-p_1\cos\theta_1}+\frac{st}{k^2}\frac{\epsilon_1^3\epsilon_2\,\mathrm{vs}^2\theta_1}{(\epsilon_2-p_2\cos\theta_2)^2}+\left(\frac{st}{k^2}\right)\frac{\epsilon_1\epsilon_2^2\,\mathrm{vs}^2\theta_2}{(\epsilon_1-p_1\cos\theta_1)^2}\right]$$
$$+\frac{4a^2W^2(X)}{k^2(\epsilon_1-p_1\cos\theta_1)^2(\epsilon_2-p_2\cos\theta_2)^2}\left[\left(\frac{st}{k}\right)^2\frac{\epsilon_1\epsilon_2(\epsilon_1^2+\epsilon_2^2)\,\mathrm{vs}\theta_1}{(\epsilon_1-p_1\cos\theta_1)^2}+\left(\frac{st}{k}\right)^2\frac{\epsilon_1\epsilon_2(\epsilon_1^2+\epsilon_2^2)\,\mathrm{vs}\theta_2}{(\epsilon_2-p_2\cos\theta_2)^2}\right.$$
$$+\frac{k^2m^2c^4}{2\epsilon_1\epsilon_2}\left(k^2+\frac{2\epsilon_1\epsilon_2(st)^2}{k^2(\epsilon_1-p_1\cos\theta_1)(\epsilon_2-p_2\cos\theta_2)}+\frac{\epsilon_2^2(st)^2}{k^2(\epsilon_1-p_1\cos\theta_1)^2}+\frac{\epsilon_1^2(st)^2}{k^2(\epsilon_2-p_2\cos\theta_2)^2}+\frac{st}{\epsilon_2-p_2\cos\theta_2}\right.$$
$$\left.\left.+\frac{st}{\epsilon_1-p_1\cos\theta_1}\right)\right]+\frac{a^4W^2(X)}{k^2(\epsilon_1-p_1\cos\theta_1)^2(\epsilon_2-p_2\cos\theta_2)^2}\left[k^2\epsilon_1\epsilon_2(\mathrm{vs}^3\theta_1+\mathrm{vs}^3\theta_2)+\left(\frac{st}{k}\right)^2\frac{\epsilon_1^3\epsilon_2\,\mathrm{vs}^3\theta_1}{(\epsilon_2-p_2\cos\theta_2)^2}\right.$$
$$\left.\left.+\left(\frac{st}{k}\right)^2\frac{\epsilon_1\epsilon_2^3\,\mathrm{vs}^3\theta_2}{(\epsilon_1-p_1\cos\theta_1)^2}+\frac{2st\epsilon_1^2\epsilon_2\,\mathrm{vs}^3\theta_1}{\epsilon_2-p_2\cos\theta_1}+\frac{2st\epsilon_1\epsilon_2^2\,\mathrm{vs}^3\theta_2}{\epsilon_1-p_1\cos\theta_1}\right]\right\}, \quad (38)$$

where $\mathrm{vs}\theta=1-\cos\theta$; $st=k^2-(p_1-p_2)^2=-k^2/\epsilon_1\epsilon_2$ and $|\Gamma(1-ia)|^2=\sinh\pi a/\pi a$.

IV. TOTAL CROSS SECTION

Integrating (38) over θ_1, θ_2, and ϕ exactly is very difficult because of the presence of the hypergeometric functions $V(X)$ and $W(X)$. It should be noticed, however, that both $V(X)$ and $W(X)$ are real monotone increasing functions with $V(1)=1/|\Gamma(1-ia)|^2$ and $W(X)$ logarithmically infinite at $X=1$. For this reason, it was found that they could be treated with sufficient accuracy (i.e., the error in the deviation from the Born approximation would be less than 10 percent) if V^2, VW and W^2 were approximated by cubics. These cubics were so chosen that the one for $V^2(X)$ would agree with the function at $X=0$, 0.5, 0.75, and 1.0; and for all the other combinations of V and W they were fitted at $X=0$, 0.5, 0.75, and 0.9. It can be shown that having neglected the logarithmic infinity does not affect the accuracy, since the various combinations of $W(X)$ and $V(X)$ are only large over a very small part of the range of angular integration. ($W(X)$ never really becomes infinite since $X\leq 1-1/\epsilon$.) Thus in using any of the function combinations, $F_\nu^2(X)$, the approximation is

$$F_\nu^2(x)=b_0^{(\nu)}+b_1^{(\nu)}Y+b_2^{(\nu)}(Y-Y^2)+b_3^{(\nu)}(Y-3Y^2+2Y^3), \quad (39)$$

where

$$Y\equiv 1-X=stq^2/D_1D_2.$$

(The expansion in orthogonal functions in Y was used instead of the straight power series in order to facilitate the finding of coefficients and estimating errors.) The b's can now be determined from (39) and are functions of a only. Adopting the notation that

$$\begin{aligned} &F_1^2(X)=V^2(X), && F_4^2(x)=W^2(X),\\ &F_2^2(X)=V^2(X), && F_5^2(X)=W^2(X).\\ &F_3^2(X)=V(X)W(X), \end{aligned}$$

The result of making the necessary substitutions in (39) is then:

$$b_0^{(1)}=b_0^{(2)}=V_4^2;\quad b_2^{(1)}=b_2^{(2)}=-8[V_4^2-2V_1^2+1];$$

$$b_1^{(1)}=b_1^{(2)}=-V_4^2+1;$$

$$b_3^{(2)}=b_3^{(2)}=-(256/3)[3V_4^2-8V_2^2+6V_1^2-1]. \quad (40a)$$

$$b_0^{(3)}=\tfrac{1}{3}[5V_3W_3-2V_2W_2];$$

$$b_1^{(3)}=\tfrac{1}{3}[-5V_3W_3+2V_2W_2];$$

$$b_2^{(3)}=\tfrac{2}{3}[-5V_3W_3+2V_2W_2+6V_1W_1-3];$$

$$b_2^{(3)}=(4/3)[-5V_3W_3+10V_2W_2-6V_1W_1+1]; \quad (40b)$$

$$b_0^{(4)}=b_0^{(5)}=\tfrac{1}{3}[5W_3^2-2W_2^2];$$

$$b_1^{(4)}=b_1^{(5)}=\tfrac{1}{3}[-5W_3^2+2W_2^2+3];$$

$$b_2^{(4)}=b_2^{(5)}=\tfrac{2}{3}[-5W_3^2+2W_2^2+6W_1^2-3];$$

$$b_3^{(4)}=b_3^{(5)}=(4/3)[-5W_3^2+10W_2^2-6W_1^2+1]. \quad (40c)$$

where

$$\begin{aligned} &V_1\equiv V(0.5), && W_1\equiv W(0.5),\\ &V_2\equiv V(0.75), && W_2\equiv W(0.75),\\ &V_3\equiv V(0.9), && W_3\equiv W(0.9).\\ &V_4\equiv V(1.0), \end{aligned}$$

With the above simplification the integration of (38) becomes elementary and results in:

$$\begin{aligned}\sigma_k dk=\bar{\sigma}(dk/k)(\pi a/\sinh\pi a)^2\{&[(8/3)(1-\omega)+2\omega^2]\\ &\times[2\log 2\epsilon_1(1-\omega)/\omega-1]V^2(\eta_1)\\ &+2[(1-\omega)+\omega^2][a^2V^2(\eta_2)+4a^2V(\eta_3)W(\eta_3)]\\ &+a^2W^2(\eta_4)[(4/3)(1-\omega)+\omega^2]\\ &+a^4W^2(\eta_5)[((8/3)+\omega)(1-\omega)\\ &+(4/3)\omega^2+\omega]\}, \quad (41)\end{aligned}$$

where $\omega=k/\epsilon_1$ and $\bar{\sigma}=(Z^2/137)(e^2/mc^2)^2$. The η's are mean values defined as follows:

$$F_\nu^2(\eta_\nu)=b_0^{(\nu)}+b_1^{(\nu)}\langle Y_\nu\rangle+b_2^{(\nu)}\langle Y_\nu-Y_\nu^2\rangle+b_3^{(\nu)}\langle Y_\nu-3Y_\nu^2+2Y_\nu^3\rangle, \quad (42)$$

where $\nu=1, 2\cdots 5$,

$$\langle Y_\nu\rangle\equiv\frac{\int(Y)d^2\sigma_\nu d\Omega_1 d\Omega_2}{\int d^2\sigma_\nu d\Omega_1 d\Omega_2};$$

$$\langle Y_\nu-Y_\nu^2\rangle\equiv\frac{\int(Y-Y^2)d^2\sigma_\nu d\Omega_1 d\Omega_2}{\int d^2\sigma_\nu d\Omega_1 d\Omega_2};$$

$$\langle Y_\nu-3Y_\nu^2+2Y_\nu^3\rangle\equiv\frac{\int(Y-3Y^2+2Y^3)d^2\sigma_\nu d\Omega_1 d\Omega_2}{\int d^2\sigma_\nu d\Omega_1 d\Omega_2},$$

where

$$d\Omega_1 d\Omega_2\equiv\sin\theta_1\sin\theta_2 d\theta_1 d\theta_2 d\phi.$$

$d^2\sigma_\nu$ is that part of the differential cross section which is multiplied by $F_\nu^2(X)$. Note that the $\langle Y\rangle$'s are independent of a. In carrying out the indicated operations there results:

$$\langle Y_1\rangle=1/2L-1;\quad \langle Y-Y_1^2\rangle=1/4(2L-1),$$
$$\langle Y_1-3Y_1^2+2Y_1^3\rangle=1/6(2L-1), \quad (43a)$$

where $L=\log 2\epsilon_1(1-\omega)/\omega$.

$$\langle Y_2\rangle=\tfrac{1}{2};\quad \langle Y_2-Y_2^2\rangle=\tfrac{1}{6},$$

$$\langle Y_2-3Y_2^2+2Y_2^3\rangle=0, \tag{43b}$$

$$\langle Y_3\rangle=\tfrac{1}{3},\quad \langle Y_3-Y_3^2\rangle=\tfrac{1}{6},$$

$$\langle Y_3-3Y_3^2+2Y_3^3\rangle=1/30, \tag{43c}$$

$$\langle Y_4\rangle=\frac{6(1-\omega)+4\omega^2}{12(1-\omega)+9\omega^2},\quad \langle Y_4-Y_4^2\rangle=\tfrac{1}{6},$$

$$\langle Y_4-3Y_4^2+2Y_4^3\rangle=3\omega^2/320(1-\omega)+290\omega^2, \tag{43d}$$

$$\langle Y_5\rangle=\frac{1}{12}\left[\frac{(52+27\omega)(1-\omega)+26\omega^2+27\omega}{(8+3\omega)(1-\omega)+4\omega^2+3\omega}\right];$$

$$\langle Y_5-Y_5^2\rangle=\frac{1}{60}\left[\frac{(40+27\omega)(1-\omega)+20\omega^2+27\omega}{(8+3\omega)(1-\omega)+4\omega^2+3\omega}\right], \tag{43e}$$

$$\langle Y_5-3Y_5^2+2Y_5^3\rangle=-\frac{1}{60}\left[\frac{(4+9\omega)(1-\omega)+2\omega^2+9\omega}{(8+3\omega)(1-\omega)+4\omega^2+3\omega}\right].$$

Upon substituting (40a, b, c) and (43a, b, c, d, e) in (42) and that in (41), the final result for the total cross section then emerges as:

$$\begin{aligned}\sigma_k dk=\bar{\sigma}(dk/k)\{&[(8/3)(1-\omega)+2\omega^2][2\log(2\epsilon_1(1-\omega)/\omega)-1-(2/9)(\pi a/\sinh\pi a)^2(12V_4^2-8V_2^2-3V_1^2-1)]\\
&+(a^2/36)(\pi a/\sinh\pi a)^2[10V_4^2-4V_2^2+24V_1^2+6][2(1-\omega)+\omega^2]\\
&(4a^2/45)(\pi a/\sinh\pi a)^2[15V_3W_3+10V_2W_2+18V_1W_1+2][2(1-\omega)+\omega^2]\\
&+(a^2/9)(\pi a/\sinh\pi a)^2[5W_3^2-2W_2^2][4(1-\omega)+3\omega^2+(8+\omega)(1-\omega)a^2+4\omega^2a^2+3\omega a^2]\\
&+(a^2/54)(\pi a/\sinh\pi a)^2[-5W_3^2+2W_2^2+3][12(1-\omega)+8\omega^2+(26+(27/2)\omega)(1-\omega)a^2\\
&+13\omega^2a^2+(27/2)\omega a^2]+(a^2/27)(\pi a/\sinh\pi a)^2[-5W_3^2+2W_2^2+6W_1^2-3][4(1-\omega)+3\omega^2\\
&+(4+(27/10)\omega)(1-\omega)a^2+2\omega^2a^2+(27/10)\omega a^2]+(a^2/135)(\pi a/\sinh\pi a)^2[-5W_3^2+10W_2^2-6W_1^2+1]\\
&\times[(9/4)(1-\omega)-(4+9\omega)(1-\omega)a^2-2\omega^2a^2-9\omega a^2]\}.\end{aligned} \tag{44}$$

As a check, a will be allowed to approach zero in (44). σ_k then becomes:

$$\sigma_k dk=\bar{\sigma}(dk/k)[(8/3)(1-\omega)+2\omega^2]\times[2\log(2\epsilon_1(1-\omega)/\omega)-1], \tag{45}$$

which is just the Bethe-Heitler relativistic total cross section[3] derived under the Born approximation.

For a sample numerical value of the cross section, the operating conditions of a recent experiment[6] will be used. Here a (for Pb)$=0.6$, $E_1\cong 15$ Mev ($\epsilon_1=30$) and $\omega=0.8$. When these values are substituted in (44), σ_k is about 7.5 percent greater than the σ_k (given in (45)) of the Born approximation. This increase in the σ_k of (45) is in agreement with the experimental figure.

Since ω was fairly large, our neglect of screening would not be expected to affect the agreement with experiment because large ω implies deep penetration of the Coulomb field. For small ω's this is not so. Consideration of screening should give a smaller σ_k than given in (44). For ω nearly equal to unity, (44) is again invalid since this means that the energy of the outgoing electron is no longer high.

A qualitative study of (44) reveals some interesting facts. First, the correction to the Born approximation is always positive, and for $\epsilon_1>30$ it is always less than 10 percent. Furthermore as ϵ_1 increases the percentage correction decreases, so that the higher the energy the more nearly valid is the Born approximation answer. Finally it will be noticed that σ_k is independent of the sign of a. Thus the cross section is the same for both positrons and electrons, (a situation which is very different from the case where the kinetic energy of the incoming particle is low, as has been shown by Sommerfeld[7]).

V. ACKNOWLEDGMENT

The author wishes to express his indebtedness to Professor A. T. Nordsieck for his very valuable guidance and criticism, and to thank Professor S. M. Dancoff for his friendly interest. He is also very grateful to the AEC for its financial assistance.

[6] Lanzl, Laughlin, and Skaggs, Phys. Rev. **74**, 1261 (1948).

[7] A. Sommerfeld, Ann. d. Physik **11**, 257 (1931).

Letters to the Editor

PUBLICATION of brief reports of important discoveries in physics may be secured by addressing them to this department. The closing data for this department is five weeks prior to the date of issue. No proof will be sent to the authors. The Board of Editors does not hold itself responsible for the opinions expressed by the correspondents. Communications should not exceed 600 words in length.

The 5-Ev Neutron Resonance in Ag

W. SELOVE
Argonne National Laboratory, Chicago, Illinois, and Department of Physics, University of Chicago, Chicago, Illinois
January 3, 1950

UNTIL the past year or so, the resolution of slow-neutron spectrometers has been so low that it has not been possible to determine the exact shape and strength of resonances occurring much above 1 ev. Now, however, considerably higher resolution is available, and it is possible to determine resonance parameters for resonances up to 5 or 10 ev, if one assumes only that the one-level Breit-Wigner resonance formula gives the correct variation of cross section near an isolated resonance; this assumption is adequately supported by experimental data. The 5-ev resonance in Ag has been investigated, to give an example of the results possible, and the peak cross section σ_0 and natural width Γ have been determined to within about 10 percent.

The method used is basically independent of both the resolution and the Doppler effect. It consists of determining (1) $\sigma_0\Gamma$ from the "absorption integral" of a thin sample, and (2) $\sigma_0\Gamma^2$ from the cross section far from resonance. The "absorption integral," obtained by a transmission measurement, is defined as

$$A=\int(1-T)dE,$$

where T is the transmission of the sample, and E is energy. The integral, A, is simply related to the quantity $\sigma_0\Gamma$ and to the sample thickness, but only for very thin samples. For thicker samples, A no longer increases as fast as the sample thickness.

Unfortunately, for a very thin sample $(1-T)$ is small and the relative error in A is much greater than that in T. It would therefore be hard to determine A (and thus $\sigma_0\Gamma$) accurately from a measurement on a single very thin sample, because present spectrometers of the time-of-flight type have such low counting rates at high resolution that many hours are required to obtain a statistical accuracy of a few percent in T. Hence measurements were made with several sample thicknesses, A was plotted against the thickness, and $\sigma_0\Gamma$ determined from the slope of the curve at the origin. Figure 1 shows the results of the measurements on one of the four sample thicknesses used. These measurements were made with the new rotating-shutter time-of-flight spectrometer[1] at the Argonne Laboratory.

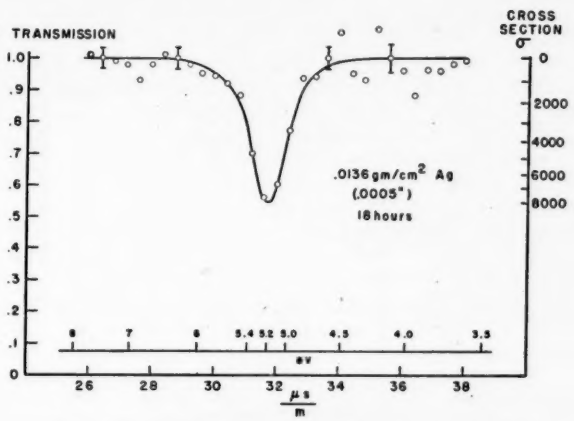

FIG. 1. Transmission of thin silver resolution ~1.0 μsec./m.

As mentioned, σ_0 and Γ, both uncorrected for Doppler effect, were determined without having to introduce the effect of the resolution, or even to assume its form. However, a simple rough calculation of the effect of resolution and Doppler broadening gave an excellent check with the experimental results, and permitted considerable reduction of the probable-error limits on σ_0. The resolution used was roughly triangular in shape, and of a base width about three times the separation between points in Fig. 1. The effect of the resolution, at the resonance peak, was to lower the apparent cross section to 8000 barns from a calculated true value of 10,000 (at room temperature).

The constants for this resonance, as measured in the normal element, are:

$E_r=(5.17\pm0.08)$ ev
$\Gamma=(0.17\pm0.02)$ ev
$\sigma_0=(12{,}000\pm1500)$ barns } uncorrected for Doppler effect
$(10{,}000\pm1300)$ barns—corrected for Doppler effect.

With values of this accuracy, and with values of Γ_n/Γ which have been obtained by other workers, it is easily possible to determine the neutron width Γ_n, and the spin of the compound nucleus, J. For the isotope having the 5-ev resonance, Ag^{109}, the value of Γ_n/Γ averaged over the resonances in a $1/E$ flux has been found[2] to be ~0.04. From this it can be shown that, for the 5-ev resonance, $J=1$, and $\Gamma_n\approx0.011$ ev.

[1] W. Selove, Phys. Rev. **76**, 187A (1949). A detailed description of this apparatus and a more detailed description of measurements made with it are in preparation.
[2] C. C. Muehlhause (unpublished).

Angular Correlation of Successive Internal Conversion Electrons

H. FRAUENFELDER, M. WALTER, AND W. ZÜNTI
Swiss Federal Institute of Technology, Zurich, Switzerland
December 27, 1949

AN effect similar to the now well-established angular correlation of successive gamma-rays is a correlation of the corresponding conversion electrons. Such measurements may be rather difficult due to unwanted beta-rays and to multiple scattering in the source and the air. Au^{197}, resulting from K-capture in 25h Hg^{197}, was selected for the experiment because it offers a cascade of two strong conversion lines without disturbance by a beta-spectrum (Fig. 1).

The source is prepared in the following way: A gold target is irradiated in the cyclotron with protons. The layer of gold containing the Hg^{197} is placed in a carbon crucible. By heating to ~900°C in a vacuum, the radioactive mercury atoms diffuse out of the gold, evaporate and are directed onto a thin aluminum film on a rocksalt backing. At the same time, a steady stream of inactive gold vapor from a second crucible falls on the aluminum, effectively fixing the mercury.

The aluminum film is then detached from the rocksalt by immersion in water and is transferred onto a collodion foil. The total thickness of source and backing was always less than 0.25 mg/cm².

Coincidences were measured in a vacuum vessel with two G-M counters at angular intervals of 45°. The window thickness of 6-mg/cm² mica cut off the beta-lines of 65h Hg^{197} and the K-electrons of 25h Hg^{197}, so that mostly coincidences between the

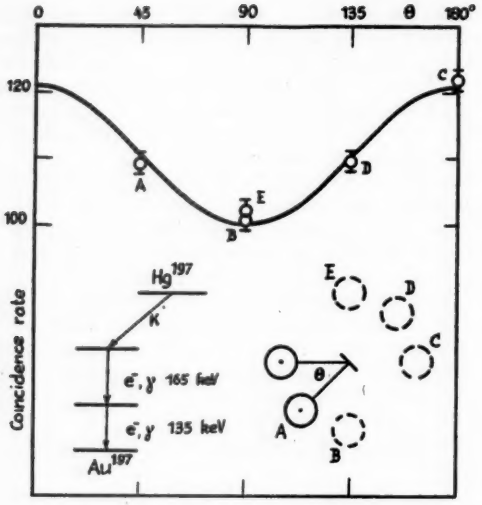

FIG. 1. Angular variation of coincidence rate of successive L-electrons from Au^{197}.

L-electrons were recorded. The contribution from M-electrons is relatively small. To diminish back-scattering the whole apparatus was lined with material of low Z. The points measured in three independent runs are shown in Fig. 1. Assuming a correlation function of the form $(1+A\cos^2\theta)$, with $A=0.24$, and taking into account multiple scattering and the finite solid angles of source and counters we find the solid curve of Fig. 1. The value of A mentioned above gives the best agreement with the measured points, the statistical accuracy being about 0.03.

A rather large contribution from a term of the form $\cos^4\theta$, with the same sign, cannot be excluded because the curve is very insensitive to such terms.

Detailed reports on the measurements and the preparation of the sources will appear in *Helvetica Physica Acta*.

We thank Professor P. Scherrer for his continuous interest and his valuable advice.

Physical Interpretation of Type A Transistor Characteristics

L. P. HUNTER
Westinghouse Research Laboratories, East Pittsburgh, Pennsylvania
December 27, 1949

A METHOD of analysis of a transistor characteristic is described which enables one to distinguish between the effects of the efficiency of current carrier injection by the emitter, the effects of the utilization of these carriers at the collector, and the effects of the current carrier mobility ratio. The fundamental assumption involved is that the back conductance of a crystal rectifying barrier is directly proportional to the number of current carriers in the neighborhood of the barrier which are of the type not impeded by the barrier in their passage from the semiconductor to the metal (holes in an N type crystal and electrons in a P type crystal).

The simple expression for hole injection efficiency, γ, in an N type semiconductor as given by Shockley[1] for a filamentary transistor is

$$\gamma=\frac{I_e+I_b}{I_e}\frac{1-G_0/G}{1+b}. \qquad (1)$$

For our case of a Type A transistor we will define: I_e+I_b is the collector current, I_c; I_e is the emitter current, I_e; G_0 is the d.c. conductance of the collector probe held at given negative voltage

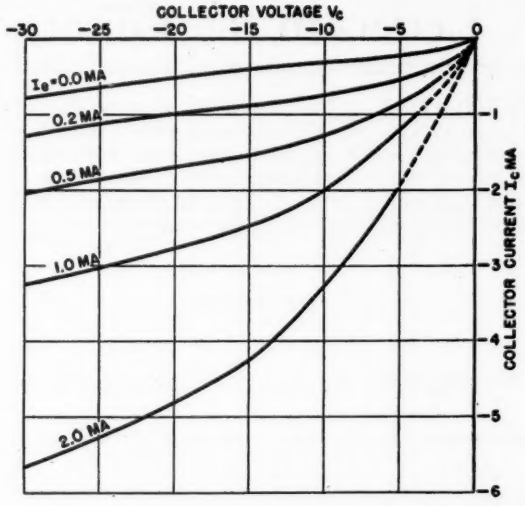

FIG. 1. Typical transistor output characteristics.

with no emitter current; G is the d.c. conductance of the collector probe at the same voltage but with emitter current flowing; b is the ratio of the electron mobility to the hole mobility; and γ is the fraction of the emitter current carried by holes.

From the typical transistor output characteristics of Fig. 1 the above quantities may be obtained, and the value of $\gamma(1+b)$ calculated from (1). A plot of $\gamma(1+b)$ against collector voltage (Fig. 2) produces a set of performance characteristics from which several interesting properties of the transistor may be deduced.

From Fig. 2 it can be seen that none of the performance characteristics exceed the value 2.5 for $\gamma(1+b)$. From a study of a number of good transistors it was found that the saturation value of the performance characteristics never exceeded 2.5. It seems reasonable to assume that this value of $\gamma(1+b)$ then represents a hole injection efficiency of 100 percent, or a γ of 1.0. The mobility ratio, b, for these samples of germanium is then seen to be about 1.5. This value of b is in good agreement with other measurements.[2]

Many poor transistors show saturation values of performance characteristics much lower than 2.5. In these cases the mobility ratio is probably still about 1.5 but the hole injection efficiency of the emitter is low and may be computed from the saturation value of $\gamma(1+b)$ by dividing by 2.5. These considerations would

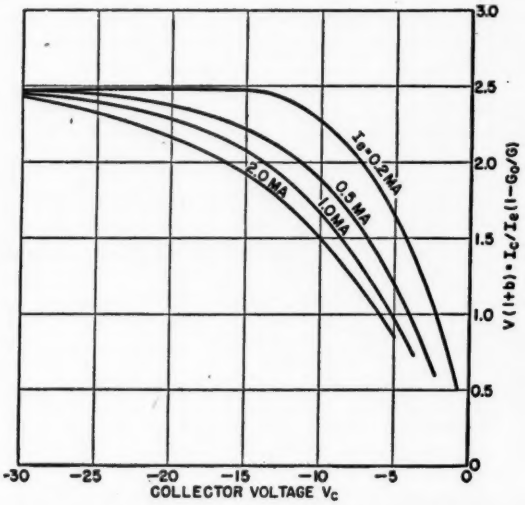

FIG. 2. Typical transistor performance characteristics.

lead one to believe that the maximum value of the small signal current gain, $\alpha=(\partial I_c/\partial I_e)_{V_c}$, for a Type A transistor is 2.5 as it is for a filamentary transistor.[1]

The region of a performance characteristic below saturation represents a combination of effects. Here the emitter may still be carrying a sufficiently large proportion of the total current that it must remove some electrons from the crystal as well as inject holes into it. Here also, the field set up in the crystal by the voltage on the collector may not be strong enough to bring all injected holes into the neighborhood of the collector before some of them disappear. This effect should only be noticed for collector voltages less than one or two volts however, since one would expect that the transit time of holes at higher collector voltages should be negligible in comparison with their average lifetime under these conditions. The performance characteristics are terminated on the low voltage end at the point where the collector and emitter currents are equal. (Only the solid portions of the output characteristics of Fig. 1 are used in plotting the performance characteristics.) At this point there is no current in the base lead of the transistor and the emitter efficiencies given by these points may approximate the hole injection efficiency of the emitter probe when it is carrying the total current.

In making measurements at power levels over 100 milliwatts it was found necessary to correct for the change in G due to heating. If the semiconductor temperature rises sufficiently in the neighborhood of the barrier to reach the range of intrinsic conductivity the number of holes present even in the absence of hole injection will rapidly increase and raise the value of G. This effect shows up in the performance characteristic as a failure to saturate at a constant $\gamma(1+b)$ value for high collector voltages.

[1] Shockley, Pearson, and Haynes, Bell Sys. Tech. J. **28**, 352 (1949).
[2] G. L. Pearson, Phys. Rev. **76**, 179 (1949).

Forbidden Lines in the Spectra of Impure Hg^{198}

K. G. Kessler
National Bureau of Standards, Washington, D. C.
January 9, 1950

Mrozowski[1] has shown that the observed structures of Hg 2967.5A ($6p\,^3P_0-6d\,^1D_2$) are explained as due to one line from Hg^{199} and three from Hg^{201}, the separations and intensities of all components being in complete agreement with the predicted pattern. Deloume and Holmes[2] have studied the lines 3320A ($5p\,^3P_0-5s\,^1S_0$) and 3141A ($5p\,^3P_2-5s\,^1S_0$) in natural and enriched Cd^{111} and found that the intensities of these forbidden lines increased in proportion to the increase in abundance of the odd isotope.

To corroborate Mrozowski's conclusion, three electrodeless discharge tubes were prepared, containing respectively natural Hg (17 percent Hg^{199}, 13 percent Hg^{201}, and remainder even-mass isotopes), Hg^{198} with a 3.6 percent contamination of Hg^{199}, and Hg^{198} with 0.3 percent Hg^{199} contamination. The last two were made by neutron bombardment of gold. Spectrograms were made with a large quartz spectrograph possessing at 2967A dispersive power of 1.7A/mm and practical resolving power exceeding 100,000. The forbidden lines from natural mercury could be photographed with exposures of two minutes duration. The resultant spectra show, in the case of natural Hg, clearly resolved components due to Hg^{199} and Hg^{201}. The component due to Hg^{201} is further resolved into three components corresponding to $\Delta F=-1, 0, +1$. In the spectrum of the 3.6 percent contaminated sample, the Hg^{201} components are almost absent and the Hg^{199} component has been greatly reduced in intensity. The 0.3 percent contaminated sample shows only a faint trace of the forbidden line ascribed to Hg^{199}. Spectrograms obtained with exposure times inversely proportional to the abundance of Hg^{199} show that the intensities of the forbidden lines are indeed proportional to the abundance of the odd isotopes, thus verifying the nuclear perturbational nature of the forbidden transitions.

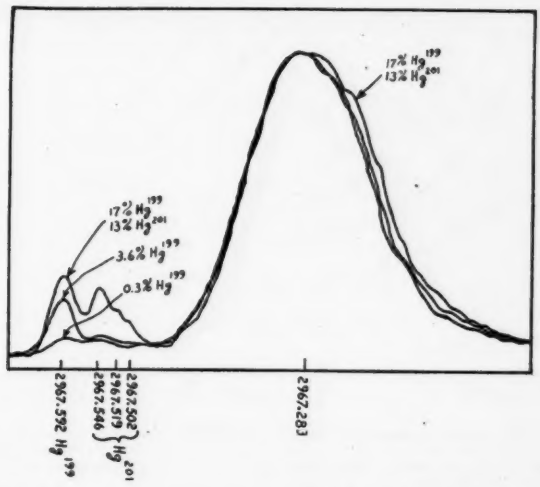

FIG. 1. Microphotometer traces of the 2967.5A forbidden lines and the allowed line 2967.3A for samples containing different concentrations of odd isotopes.

Microphotometer traces of the permitted line, 2967A ($6p\,^3P_0-6d\,^3D_1$) and for forbidden lines from three samples of impure Hg^{198} are reproduced in Fig. 1.

[1] S. Mrozowski, Phys. Rev. **67**, 161 (1945); Rev. Mod. Phys. **16**, 153 (1944).
[2] F. F. Deloume and J. R. Holmes, Phys. Rev. **76**, 174 (1949).

Temperature Effects in the Spurious Discharge Mechanism of Parallel Plate Counters*

Frank L. Hereford
Rouss Physical Laboratory, University of Virginia, Charlottesville, Virginia
December 27, 1949

An outstanding limitation of the parallel plate spark counter is the large spurious counting rate which thus far has been suppressed only through operation at inconveniently long recovery times (>0.05 sec.). Investigations of this phenomena[1,2] have been limited to the observation that the spurious rate is appreciably influenced by the cathode material and its preparation. It also was pointed out that the clearance time for positive ions should be at the most 10^{-4} sec., and hence that the necessity for longer recovery times must be due to some mechanism associated with the cathode surface rather than the state of the gas. Such a mechanism giving rise to delayed electron emission from a surface (described by Malter[3] and Paetow[4]) was cited as a possible process in this connection.

During the preparation and testing of a number of such counters for use in investigation of short time delay phenomena, a marked dependence of counting rate upon temperature has been observed. The counters used consisted of copper plates, 9 cm^2 in area, spaced at 0.2 cm separation, and mounted in glass envelopes. After washing with acid solution and rinsing with distilled water, the counters were baked in vacuum at 425°C for two hours and allowed to cool slowly with one-half atmosphere of hydrogen admitted during this period. After complete cooling a premixed filling of 85 percent argon and 15 percent ethyl ether was admitted, the total filling pressure being 70 cm Hg.

In obtaining the data reported here a conventional Neher-Harper quench circuit was employed (Fig. 1). The counters were operated at approximately 200 volts over-voltage and held at various temperatures in an oven. Figure 1 shows the variation of counting rate with recovery time, t_r, at various temperatures.

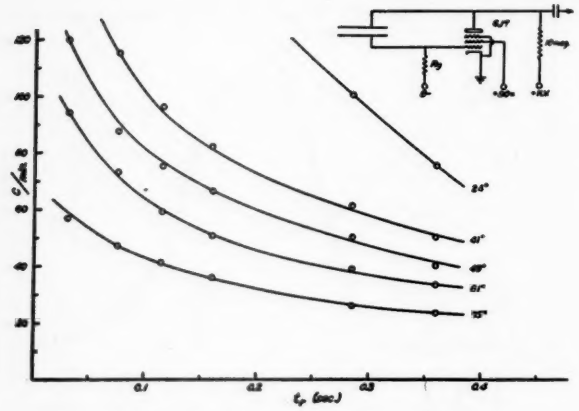

FIG. 1. The counting rate *vs.* recovery time at various temperatures. The spurious rate at room temperature is considerably higher than that reported in references 1 and 2 probably as a result of a less successful surface preparation.

It should first be pointed out that for constant gas density no variation of the sparking threshold with temperature is to be expected on the basis of the Paschen criterion or previous experimental work.[5] Neither is a variation of counter efficiency with temperature probable, since only the mass of material available for electron-ion pair production is pertinent in this connection. Hence, one is led to considerations concerning the spurious discharge mechanism and the possible influence of temperature variation there.

It does not seem possible to draw unambiguous conclusions concerning the mechanism of spurious breakdown on the basis of the results reported here or those reported elsewhere. However, it is worth while to point out several possibilities in this connection. With regard to a surface mechanism, small bits of insulating material on the cathode can be charged by positive ion bombardment during a count. This charge would remain until it either leaked off in a time dependent upon either the resistivity of the insulating material or the nature of the contact between the insulating material and the surface or until by some process it caused electron emission from the cathode surface leading to a spurious count. The question as to whether the resistivity or the contact influences the leakage time is important. In the event that the resistivity of the material is the determining factor, the temperature effects reported here could be understood. Substances such as SiO_2 which might be released in baking the glass envelope are known to exhibit high resistivity ($\sim 10^{14}$ ohm-cm) with a negative temperature coefficient. Hence, at high temperatures where their resistivity and the corresponding time required for neutralization of the charge are smaller, a shorter recovery time should be sufficient to prevent a spurious count. Consequently, one would expect that the recovery time necessary to reduce the spurious rate to a given value should decrease with increasing temperature. This behavior is exhibited in Fig. 1. It does not seem likely that through this process oxides of the cathode material could be responsible for spurious counts at intervals as great as 0.05 sec. after an initial count. Though the resistivity of such oxides exhibits the required temperature dependence, it is too small to hold the charge for intervals of the order of 0.05 sec. In the case of cuprous oxide, the resistivity of approximately 10^5 ohm-cm at room temperature[6] should allow charge neutralization in roughly a microsecond.

The above considerations hinge upon the assumption of an intimate contact between the insulating material and the cathode surface. In the event that the neutralization time depends most heavily upon the character of this contact rather than the resistivity of the insulating particle, no immediate interpretation of the temperature dependence seems evident.

Another possible mechanism involving the state of the gas rather than that of the cathode is worth mentioning. Minute droplets which are known to exist in a gas at any degree of supersaturation[7] could become charged during a count and liberate electrons upon striking the cathode, thus initiating a spurious count. The size of such droplets is known to decrease with increasing temperature.[7] Hence, their mobility would increase and shorter recovery times would be sufficient for their clearance at higher temperatures. In the case of the cylindrical type counter the weak field strength in the neighborhood of the cathode would probably enable the quenching vapor to suppress this mechanism through the well known pre-dissociation process.

In any case, it appears in view of the foregoing that operation at temperatures of 60°C to 70°C could appreciably enhance the usefulness of the parallel plate counter, allowing a considerable increase in the maximum counting rate attainable without dead time losses.

Frequent discussions with Drs. J. W. Beams and L. B. Snoddy contributed much to the success of the investigation reported. The counters employed were constructed by Mr. A. G. Nester of the Bartol Research Foundation.

* This work was partially supported by Contract NOrd-7873 with the Bureau of Ordnance of the Navy.

[1] J. W. Keuffel, Rev. Sci. Inst. **20**, 202 (1949).
[2] R. W. Pidd and L. Madonsky, Phys. Rev. **75**, 1175 (1949).
[3] L. Malter, Phys. Rev. **50**, 48 (1936).
[4] H. Paetow, Zeits. f. Physik **111**, 770 (1939).
[5] L. B. Loeb, *Fundamental Processes of Electrical Discharges in Gases* (John Wiley and Sons, Inc., New York, 1939), p. 534.
[6] W. Vogt, Ann. d. Physik **7**, 190 (1930).
[7] J. J. Thomson, *Conduction of Electricity Through Gases* (Cambridge University Press, London, 1906), pp. 183–187.

The Absorption Spectrum of Water Vapor between 900 and 2000 Angstroms

J. J. HOPFIELD
Applied Physics Laboratory, Johns Hopkins University, Silver Spring, Maryland*
January 3, 1950

THE solar spectrum has recently been extended in the ultraviolet region by spectrographs carried to heights of 100 to 130 km by the Aerobee and the German V-2 rockets. This extension of the solar spectrum brings into prominence the absorption of ultraviolet light by the constituents of the atmosphere. The u.v. absorption of the O_2 constituent is well known. In thicknesses of air of 1 meter or more it is the gas whose absorption in the Schumann-Runge bands limits observation of laboratory spectra in air to wave-lengths longer than about 1850A. Nitrogen absorption is also well known. Its u.v. absorption is not as great as that of oxygen in the region 1800A. It is also known that the absorption of u.v. light by 2 or 3 mm (S. T. P.) of atmospheric ozone (Hartley band) cuts off the solar spectrum, as observed from the ground, at about 2900A. On the other hand the u.v. absorption spectrum of water vapor is not well known. Yet the vapor exists in the atmosphere to heights as great as 90 km, for noctilucent clouds are observed at these heights. Any complete study of the absorption of sunlight at high altitudes may need to take this into account.

The accompanying absorption spectrum was obtained in the laboratory using a vacuum-grating-spectrograph. This spectrograph also served as an absorption cell of 100 cm equivalent thickness. The source of the continuous spectrum was a condensed discharge in an open-ended capillary glass tube which faced the slit of the spectrograph.

These absorption spectra (Figs. 1 and 2) are adjacent parts of the same spectrograms. In the reproduction they show a slight overlapping near 1500A. They are arranged from top to bottom in order of increasing pressure of water vapor. These pressures

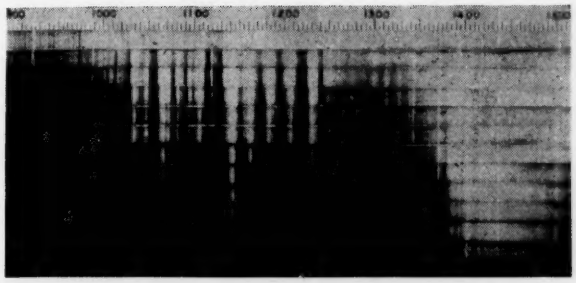

FIG. 1. Absorption spectra of water vapor.

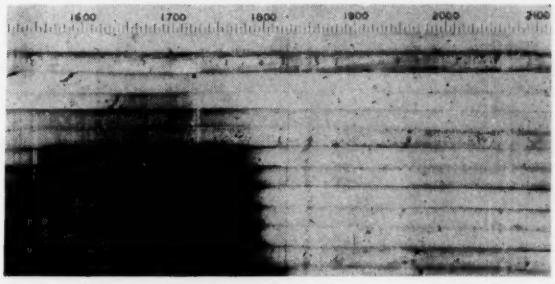

FIG. 2. Absorption spectra of water vapor.

were not measured, but they ranged from almost zero to perhaps 6 mm of Hg. A fairly accurate wave length scale is shown. Among the things these spectra show are:

(1) A region of continuous absorption between 1830A and 1500A (*A*-band).

(2) A region of relative transparency 1500A–1380A.

(3) A progression of diffuse absorption bands 1380A–1250A (*B*-bands).

(4) A progression of strong absorption bands 1240A–1150A (*C*-bands).

(5) Mixed progressions of strong bands starting with a strong one at 1125A, and others apparently starting at 1055A, 1028A, 1014A, 1007A, 1000A, etc. These bands together with the *C*-bands will be examined for possible series relations.

(6) A progression of diffuse bands in the region 950A and extending below 900A. These are more easily apparent on other plates.

This absorption spectrum needs more laboratory study, for it may be affecting the u.v. solar spectrum obtained from high altitudes. For example, the measurement of the absorption coefficients of these water vapor bands, and especially of the *A*-band, is one of these studies. If the coefficients of the *A*-band should be found comparable to those of atmospheric ozone (Hartley band), then water vapor might need to be considered as one of the atmospheric constituents that is limiting the solar spectrum at present observed from rockets to wave-lengths longer than 1800A.

As another item, a measurement of the absorption coefficients of the *C*-band is needed. The second and apparently the strongest member of this band covers the region of 1215A which is the wave-length of Lyman-α, the resonance line of atomic hydrogen. This band is also in a position to block a "window" in the absorption spectrum of air, and if its absorption coefficients are found large enough then water vapor at high altitudes might preclude the easy discovery of Lyman-α in solar or stellar spectra from rockets. When the above problems are solved in the laboratory then their solution can be applied to the related problem of u.v. solar absorption and the conversion by water vapor of a part of the u.v. light of the sun into heat at great altitudes.

* Supported by the Navy Bureau of Ordnance under Contract NOrd 7386.

The Distribution of Atomic and Molecular Oxygen in the Upper Atmosphere

RUDOLF PENNDORF
Geophysical Research Directorate, Air Materiel Command, Cambridge Field Station, Cambridge, Massachusetts
November 21, 1949

THE spectra from aurorae and from the night sky prove that atomic oxygen is permanently present in the ionosphere. Oxygen molecules are dissociated photochemically by ultraviolet radiation

$$O_2+h\nu\rightarrow O+O \quad (\lambda<2445). \tag{1}$$

The atoms recombine in a three-body collision

$$O+O+M-k_1\rightarrow O_2+M \quad (M=N_2, O_2, O).$$

The relative yield of M in reaction (2) presumably is

$$[M]=0.6[N_2]+[O_2]+0.1[O].$$

Formulas have been derived for the state of equilibrium as well as for changes of the oxygen concentration with time. A special case occurs during the night, when radiation is absent and only recombination takes place. Since the quantity M changes with height (concentration of O and O_2), the formulas become more complicated.

The numerical calculations have been carried through using different values for incoming radiation (effective temperature of a blackbody varying between 5000° and 6000°K), zenith distance of the sun, and rate constant k_1 of the three-body collision.[1] From the data obtained, it is concluded that the thickness of the transition layer is about 10 km. Due to the uncertainty of the

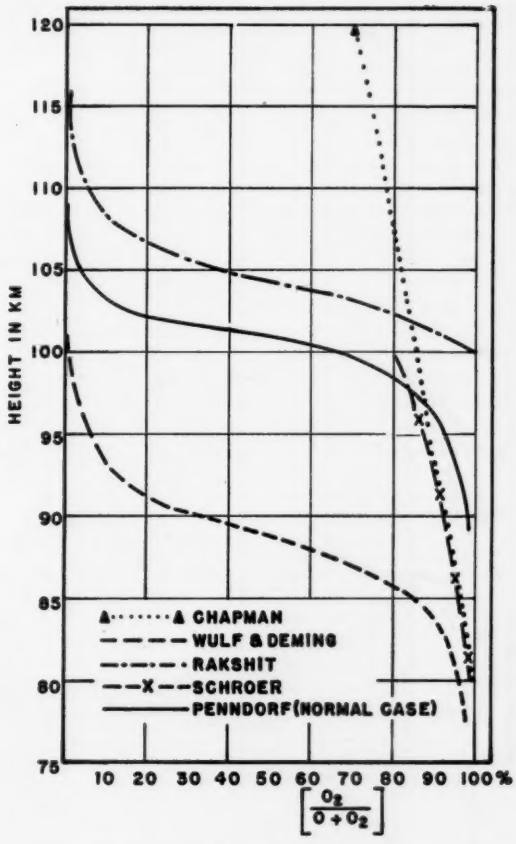

FIG. 1. Transition layer according to various investigators together with the "normal case." (Concentration of oxygen molecules in equilibrium state expressed as the percentage of the total amount of oxygen.)

TABLE I. Composition of the ionosphere and mean molecular weight.

Height in km	Concentration in percent by volume N_2	O_2	O	Mean molecular weight
110	69.4	0	30.6	24.33
105	69.9	0.4	29.7	24.45
100	76.9	10.9	12.2	26.97
95	81.2	16.2	2.6	28.34
90	81.6	17.3	1.1	28.56
85	82.0	18.0	0	28.73

constants involved, its mean height can be confined only between 100 and 110 km, no more accurate value can be given. The transition layer is definitely below the maximum ion and electron concentration of the E layer.

Differences caused by the use of different intensities of incoming radiation are large; variations of the rate constant k_1 have about the same influence, whereas different zenith distances are of little importance. Height and shape of the transition layer is more or less equal all over the globe. The assumed atmospheric density distribution influences the results considerably.

From the eight cases calculated only the results for the "normal case" (effective temperature of blackbody: 5300°K; zenith distance of the sun: 0°; $k_1=1.3\times10^{-33}T/To$) are given in Fig. 1, together with the results of earlier investigations. It can be seen that the transition from an all molecular to an all atomic state is very sharp. This does not mean, however, that no molecular oxygen will be found above the transition layer, but the concentration becomes very small compared with the amount of atomic oxygen. A few figures will be given for the above-mentioned "normal case." At 130 km 1.64×10^{7} oxygen molecules will be found compared with 7.84×10^{11} oxygen atoms. For 100 km the corresponding numbers are 1.26×10^{13} and 1.42×10^{13}, for 91 km 5.37×10^{13} and 3.44×10^{12}. Reaction (2) does not sufficiently describe the processes around 90 km or lower. Therefore, the calculations have been carried out for the interval 90–130 km.

During the night, when the dissociative agent is absent, the concentration of oxygen atoms undergoes small changes. It is negligible above 120 km, largest at about 100 km. Within 12 hr. the largest changes which occur are less than 16 percent with the equilibrium amount depending on the value of rate constant k_1. The amount of atoms recombined during the night is exactly formed anew during the day. Therefore, the equilibrium is maintained, and the assumptions made, justified. The height of the transition layer is constant during day and night. Recombination during the night has no appreciable influence on the vertical distribution of atomic oxygen.

From these data the composition of the atmosphere can be calculated. The results are given in Fig. 2. The percentage of O_2 at the surface is 20.95 percent. Separation occurs in the stratosphere and the amount of oxygen decreases; at 50 km the percentage is assumed to be 18 percent.[2] Above that height mixing will be strong again, and therefore no change in the volumetric percentage is assumed. In the above-mentioned transition layer, however, the composition changes. If the pressure is kept constant, the concentration of O increases to 30.6 percent by volume above the transition layer, whereas N_2 decreases to 69.4 percent by volume, as shown in Fig. 2. Such a change causes a considerable decrease in the mean molecular weight. All calculations of the temperature[3] and other properties in the ionosphere largely depend on the mean molecular weight (i.e., on the composition assumed). Since the composition of the atmosphere is the basic problem, a few values are tabulated in Table I for selected heights.

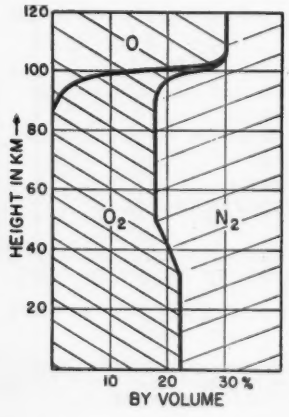

FIG. 2. Concentration of oxygen (O_2 and O) in percentage by volume between 0 and 120 km.

[1] R. Penndorf, J. Geophys. Research **54**, 7 (1949).
[2] R. Penndorf, Meteorolog. Zeits. **58**, 103 (1941); Bull. Am. Meteorolog. Soc. **27**, 343 (1946).
[3] A. Nazarek, Bull. Am. Meteorolog. Soc. (in press).

Mesons Produced by Neutrons from the Cyclotron*

F. M. SMITH, EUGENE GARDNER, AND HUGH BRADNER
Radiation Laboratory, Department of Physics, University of California, Berkeley, California
January 9, 1950

IN photographic plates exposed to high energy neutrons from the 184-inch Berkeley cyclotron, we have observed stars in which one of the outgoing particles is a meson. This type of star is well known from cosmic-ray studies,[1] and the only new feature is that the stars we are studying were initated by particles from the cyclotron. The arrangement of apparatus is shown in Fig. 1.

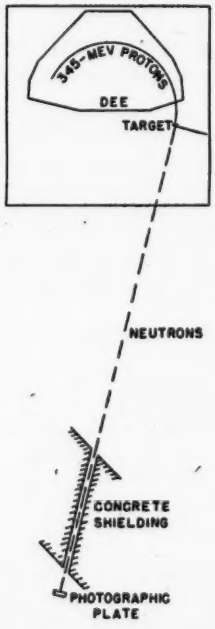

FIG. 1. Sketch showing position of photographic plate for exposure to neutrons from the cyclotron. (Not to scale.)

As indicated in the figure, the neutrons used for bombarding the plates are produced in the cyclotron when a beam of 345-Mev protons strikes an internal target. The plates are placed in a position similar to that used in cloud-chamber studies[2] of mesons produced by neutrons from the cyclotron.

An example of a photographic emulsion star in which one of the outgoing particles is a meson is shown at point A of Fig. 2. The star at A consists of two tracks, a proton (upper track) and a π^--meson (lower track). From the grain density changes along the tracks it is clear that both proton and meson were moving

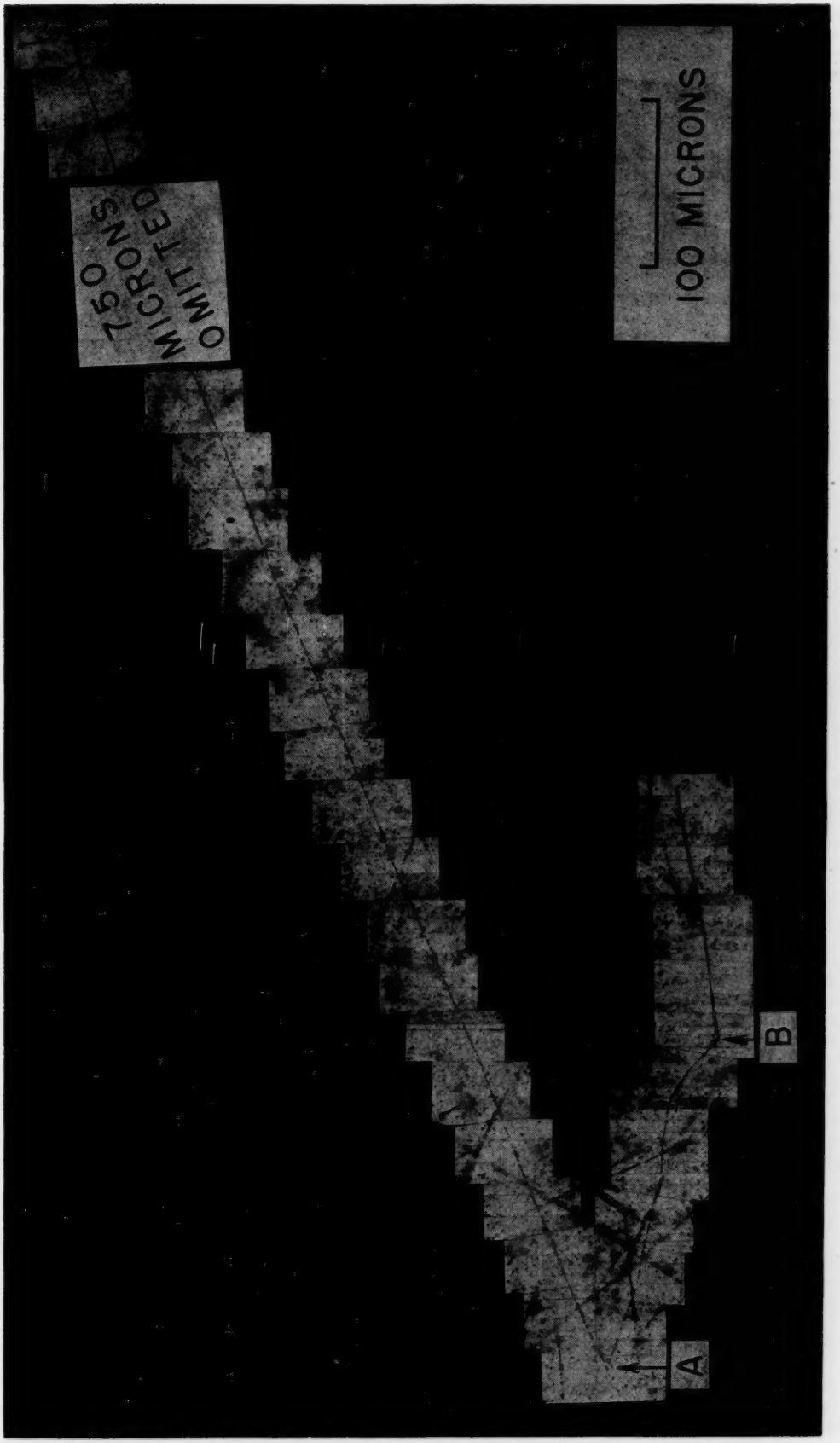

FIG. 2. Photographic emulsion star in which one of the outgoing particles is a π^--meson. Meson is formed at *A* and comes to rest at *B*.

from left to right. The meson came to rest in the emulsion at point B and initiated a one-prong star; the one prong is the straight heavy track which begins at B. This event was found in a preliminary survey of meson production by neutrons from the cyclotron. The survey indicated that the neutron beam offered excellent opportunities for meson work, and systematic studies are being planned. Inasmuch as it may be some time before any results are available from these studies, we shall give additional details of the preliminary survey. In this survey we scanned hastily an area of 8 sq. cm of one plate which was exposed as shown in Fig. 1. The plate used was an Ilford C2 unbacked emulsion with a thickness before development of 300 microns. The exposure time was about 5 minutes at a distance of about 60 feet from the target. We found a total of 5 stars in which one of the outgoing particles was a meson. In addition, there were 4 meson tracks which could not be followed back to the points at which the mesons were formed. In the same plate area we found 5×10^4 stars at which no meson tracks were observed. We hesitate to use these numbers to estimate the cross section for the production of mesons by neutrons because of the uncertainty in the meson count. In this survey we made no attempt to find all of the mesons or to estimate the fraction of the total that might have been missed. Even with a more careful search we would not expect to see the higher energy mesons with this plate, since the C2 emulsion does not record mesons of energy greater than about 10 Mev.

We are indebted to Professor Ernest O. Lawrence for his continued interest in this work. We also wish to thank Professor R. L. Thornton for many helpful discussions. The first work on this problem was done by Professor C. M. G. Lattes, who has kindly given us the benefit of his experience. The photo-micrograph shown in Fig. 2 was prepared by Mr. A. J. Oliver.

* This work was done under the auspices of the AEC.
[1] Lattes, Muirhead, Occhialini, and Powell, Nature **159**, 694 (1947).
[2] Hartsough, Hayward, and Powell, Phys. Rev. **75**, 905 (1949).

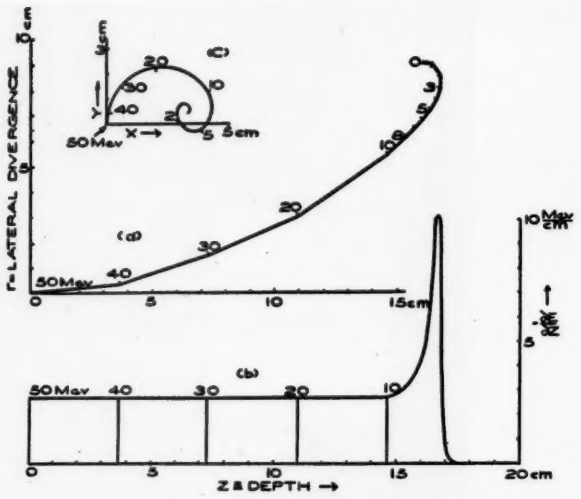

FIG. 1. (a) The calculated root-mean-square lateral displacement or divergence in cm *vs.* depth of penetration, Z, in cm for a 50-Mev electron entering tissue (water) in the Z direction. Energies in Mev of the electron at various points along its path are indicated.
(b) Loss of energy by ionization per unit length of depth, i.e., $-\partial E/\partial Z$, in Mev/cm *vs.* Z for the root-mean-square electron of (a).
(c) Scattered trajectory of the r.m.s. electron, as seen along the Z direction if a magnetic field of 10^4 oersteds is imposed in the Z direction.

Possible Techniques in Direct-Electron-Beam Tumor Therapy

W. H. BOSTICK
Research Laboratory of Physical Electronics, Department of Physics, Tufts College, Medford, Massachusetts
December 27, 1949

SINCE the invention of the betatron there has been some speculation concerning the merit of the use of a high energy electron beam instead of x-rays for tumor therapy because of a possible concentration of ionization at the end of the electron track in the tissue. The principal fault in this proposal is the fact that electrons once in the tissue change their direction markedly by elastic scattering[1,2] in the Coulomb field of the nuclei of atoms in the tissue. This scattering would cause the electrons, on the average, to "miss the mark."

The author has made approximate calculations, layer by layer, of the scattering of electrons in water (which is practically equivalent to tissue) with the use of the expression[2] for the mean-square scattering angle $\langle\theta_i^2\rangle=(K/E_i)^2 l_i$, where E_i is the energy of the electron in Mev, $K=21$ Mev, l_i the thickness of layer number i is measured in radiation units, and where the angle $(\langle\theta^2\rangle)^{\frac{1}{2}}$ is required to be small. The radiation unit for water is 43 cm. The resultant mean-square scattering angle for n layers of tissue is then $\langle\theta^2\rangle=(\langle\theta_1^2\rangle+\langle\theta_2^2\rangle+\cdots\langle\theta_n^2\rangle)$. These calculations assume that the energy loss of the electron occurs entirely by ionization and follows the well-known variation with energy given by Bloch.[3]

The results of these calculations of the mean-square scattering are given in Figs. 1a and 2a for 50-Mev and 20-Mev electrons incident on tissue in the Z or depth direction (abscissa, in cm); the ordinate is the lateral displacement or divergence from the original line of direction in cm. Figures 1b and 2b are plots of $-\partial E/\partial Z$, the ionization loss per cm depth in Mev/cm for the same mean electrons. From these plots it can be seen that although $-\partial E/\partial Z$ increases markedly toward the end of its penetration in depth, the root-mean-square lateral displacement from its original direction is so great that the position of the beam is no longer precisely known.

If, however, a magnetic field in the Z direction is applied to the patient the scattered electron beam will be confined approximately to spiral-helical orbits, whose radii are determined by the lateral component of momentum and the magnetic field applied. The approximate calculated root-mean-square scatterings from the Z axis for the 50-Mev and 20-Mev electrons in a magnetic field of 10^4 oersteds are shown in Figs. 1c and 2c which show the approximate orbits of the root-mean-square electrons as viewed along the Z axis. From these plots it can be seen that at the end of the track the radial excursion from the original line of direction Z is considerably reduced by the imposition of a magnetic field of 10^4 oersteds. A magnetic field of 10^4 oersteds could be readily achieved with the help of an iron yoke, and the electron beam could be shot through one pole piece of this iron-core electromagnet. If

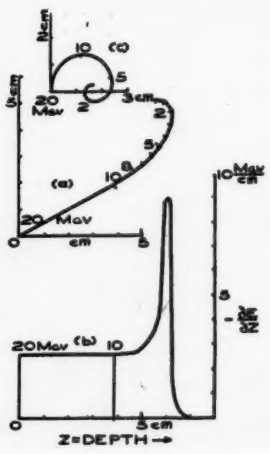

FIG. 2. (a), (b), (c), the same as Fig. 1 but for a 20-Mev incident electron.

intermittently operated magnetic field coils are used without an iron yoke, fields considerably higher than 10^4 gauss can be obtained, and the orbits diagrammed in Figs. 1c and 2c could be proportionally reduced in radius. The plot of $-\partial E/\partial Z$ remains essentially the same with or without a magnetic field.

One should not be too enamored of the apparently high sharp peaks in ionization loss (see Figs. 1b and 2b) at the end of the electron tracks. It should be remembered that since these plots are for the root-mean-square scattering of the electrons, approximately half of the electrons will scatter at larger angles and half at smaller angles than the root-mean-square value. This statistical distribution of scattering effectively smears out these peaks at the end of the electron tracks, and the resultant effective ionization as a function of Z cannot be elicited from the simple and approximate calculation made here.

With the external electron beam which has already been produced by the betatron and with the progress in the development of electron linear accelerators, relatively high current, monoenergetic electron beams in a usable energy range will soon be a reality. These machines might well be used for investigating the merit in the treatment of tumors by high energy electron beams projected parallel to a magnetic field into the patient. The electron beam treatment could, of course, follow the same technique used in x-ray treatments in which the patient is rotated in order to concentrate the tumor dosage but distribute the skin dosage.

Another possible technique in the use of electron beams in tumor therapy is to make a short (but, if necessary, deep) incision to the tumor, insert a tube about 1 cm in diameter to hold back the intervening tissue between skin and tumor and shoot the electron beam directly into the tumor (without the use of any magnetic field). Under these circumstances it should make little difference whether the electrons scatter because they will be in the tumor from the very start of their track in tissue. With this technique it should be possible to use a linear accelerator of fairly modest energy (4 Mev), length (4 feet), and cost. It should be possible to make ratio of tumor dose to surrounding-tissue dose exceedingly high because each 4-Mev electron can be made to lose practically all of its energy in the tumor. Hence the radiation dose given to the tumor can be made very large indeed without substantial radiation harm to the patient. It is then necessary for the patient to heal only a small incision instead of extensive radiation damage to blood and healthy tissue.

[1] E. J. Williams, Proc. Roy. Soc. **A169**, 531 (1938–1939).
[2] W. Heisenberg, Cosmic Radiation (Dover Publications, New York, 1946), p. 27.
[3] F. Bloch, Ann. d. Physik **16**, 285 (1933).

The Beta-Ray Distribution of Tc^{99}

B. H. Ketelle and John W. Ruch*
Chemistry Division, Oak Ridge National Laboratory, Oak Ridge, Tennessee
January 6, 1950

Lincoln and Sullivan[1] studied a long-lived activity which was believed to be a technetium isotope produced by uranium fission. They reported it to decay by emission of beta-rays with a maximum energy of 0.4 Mev and estimated the half-life to be between 10^3 and 10^6 years. R. P. Schuman[2] prepared a source of the same activity and established that it was a Tc isotope by a tracer technique. He reported the maximum beta-energy as 0.3 Mev and the half-life as 3×10^5 years. Motta, Boyd, and Larson[3] used improved chemical separations and obtained extremely pure technetium activity produced by radiative neutron capture on Mo. They report the half-life as 9.4×10^5 years and the maximum beta-energy to be 0.32 Mev. Parker[4] and associates have separated the activity from the fission product mixture, and it has been identified to be Tc from its x-ray spectrum.[5] They report the half-life to be 4.7×10^5 years. Inghram, Hayden, and Hess[6] used part of the latter source and assigned the activity to a mass number of 99.

The source material used for this measurement was isolated from an acid chloride solution of irradiated uranium by precipitating platinum sulfide which carries other insoluble sulfides. Further purification consisted of five cycles of sulfuric acid distillation and sulfide precipitation. The sample was probably a mixture of two or more oxides since it was the residue from the evaporation of an ammonium hydroxide hydrogen peroxide solution of the sulfide. A detailed discussion of this process has been given elsewhere.[7] The total mass of the sample was approximately 10 mg, though the mass of the Tc was probably not more than 6 mg. The mount consisted of a one-inch Formvar film supported on a copper ring. The total area of the sample was approximately one cm^2.

The beta-ray spectrum was determined on a thin lens spectrometer constructed and described by W. C. Peacock.[8] The Kurie plot of the data is shown in Fig. 1. The maximum beta-energy is 0.30 ± 0.01 Mev. Since no conversion lines were observed with the spectrometer and no gamma-radiation was detectable when the source was counted with a thin window G–M counter, this isotope appears to decay by simple beta-emission. Because of the thickness of the source and the window cut off at the low energy end of the spectrum, the fact that the Kurie plot appears to be linear is not considered significant.

Feenberg and Hammack[9] have predicted from shell theory that this transition probably involved a spin change of three units and no parity change. They have also stated that the ft value computed by the empirical method of Konopinski and Uhlenbeck would indicate that the transition is highly forbidden. We have computed the theoretical half-lives by the method of Greuling[10] using several assumed spin changes. On the assumption that the transition is second forbidden tensor interaction with a spin change of three units, the computed half-life is 10^5 years compared to the observed half-life of from 5×10^5 to 9×10^5 years. Any lower degree of forbiddeness gives computed half-lives many orders of magnitude shorter than the observed half-life whereas any higher degree of forbiddeness with spin change greater than three units gives excessively long computed half-lives. However, the minimum half-life computed upon the assumption that the transition is third forbidden with a spin change of three units and with a change of parity is 1.7×10^7 years. If the observed half-life should be as long as 10^6 years, this value, 1.7×10^7 years, would be in agreement within the uncertainties of the values of the Fermi constant and the nuclear radius. However, should the

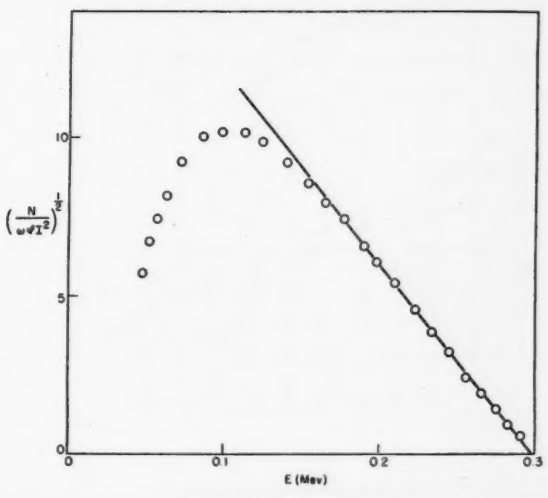

Fig. 1. Kurie plot of Tc^{99}.

observed half-life be as short as 10^8 years, one would conclude that the transition is second forbidden.

This document is based on work performed under Contract Number W-7405 eng 26 for the Atomic Energy Project at Oak Ridge National Laboratory.

* Formerly at Oak Ridge National Laboratory; now with Research Division, Atomic Energy Commission, Oak Ridge, Tennessee.

[1] D. C. Lincoln and W. H. Sullivan, Plutonium Project Report CN-3449 (January, 1946).
[2] R. P. Schuman, Plutonium Project Report, CC-3434 (February, 1946).
[3] Motta, Boyd, and Larson, Phys. Rev. **72**, 1270 (1947).
[4] Parker, Hebert, Lantz, Meredith, Reed, and Ruch, Mon-N-311, p. 60 (June, 1947).
[5] Peed, Saunders, and Burkhart, Phys. Rev. **73**, 347 (1948).
[6] Ingram, Hayden, and Hess, Jr., Phys. Rev. **72**, 1269 (1947).
[7] Parker, Reed, and Ruch, AECD-2043.
[8] W. C. Peacock, Phys. Rev. **72**, 1049 (1947).
[9] E. Feenberg and K. C. Hammack, Phys. Rev. **75**, 1877 (1949).
[10] E. Greuling, Phys. Rev. **61**, 568 (1942).

On Elastic Constants of Nickel Crystals

MIKIO YAMAMOTO
Research Institute for Iron, Steel, and Other Metals, Tohoku University, Sendai, Japan
December 27, 1949

IN the "Letters to the Editor" column of this journal, Bozorth and his collaborators[1] reported their data on the elastic constants of nickel crystals, determined by the dynamic pulsing method, and stated that these constants had not been measured previously. I would like to remark that two reports on this subject have been published by Japanese physicists. Young's moduli for various crystallographic directions were measured with a static method of torsion by Honda and Shirakawa[2] in 1937, and with a dynamic method of magnetostrictive vibration by Yamamoto[3] in 1942. They determined elastic constants by combining their data on Young's moduli as a function of crystal direction with the measured value of the cubic compressibility of polycrystalline nickel obtained by Bridgman[4] and afterward corrected by Slater,[5] since it has been verified for most metals (though not yet for nickel) that the cubic compressibility is the same for a single crystal as for a polycrystal if the effect of grain-boundaries in the polycrystal is negligible.

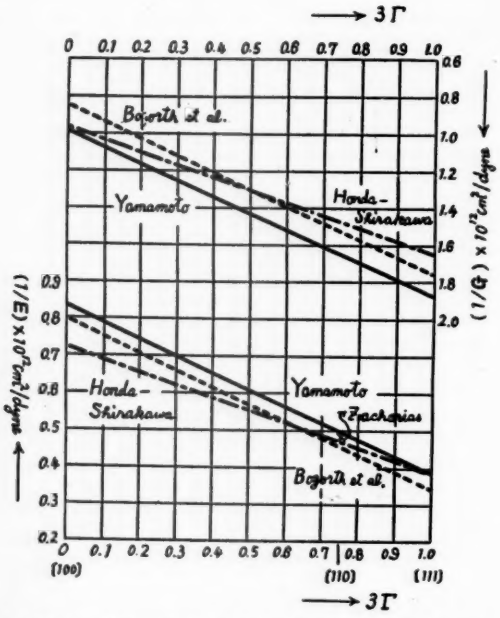

FIG. 1. Linear relations between the reciprocals of Young's and rigidity moduli, $1/E$ and $1/G$, and the orientation function, Γ, in nickel crystals.

TABLE I. Comparison among the three sets of data on the elasticity of nickel crystals.

Investigators	Elastic constant (10^{12} dynes/cm²)			Elastic anisotropy		Moduli for a polycrystal, computed with Voigt's theory (10^{12} dynes/cm²)	
	C_{11}	C_{12}	C_{44}	E_{111}/E_{100}	G_{100}/G_{111}	$\bar{E}$	$\bar{G}$
Honda-Shirakawa	2.52	1.51	1.04	1.90	1.72	2.16	0.82
Yamamoto	2.44	1.58	1.02	2.16	1.92	2.07	0.78
Bozorth *et al.*	2.50	1.60	1.185	2.35	2.09	2.32	0.89
						2.00[a]	0.74[a]

[a] Average of measured values for polycrystalline nickel.

Honda-Shirakawa's and Yamamoto's data are compared with those of Bozorth and others in Table I and Fig. 1. Table I contains the principal elastic constants, C_{ik}, elastic anisotropy expressed by ratios of Young's and rigidity moduli for [100] and [111] directions, E_{111}/E_{100} and G_{100}/G_{111}, and Young's and rigidity moduli for a pseudoisotropic polycrystal, $\bar{E}$ and $\bar{G}$, calculated by Voigt's[6] theory (under the assumption that strain components are uniform throughout every grain of a polycrystal). Averages of measured values of Young's and rigidity moduli for polycrystalline nickel are also added for comparison at the base of Table I. In Fig. 1 linear relations between both reciprocals of Young's and rigidity moduli, $1/E$ and $1/G$, and the orientation function $\Gamma=\gamma_1^2\gamma_2^2+\gamma_2^2\gamma_3^2+\gamma_3^2\gamma_1^2$ (γ_1, γ_2, and γ_3 are the direction cosines of a direction in reference to the crystal axes) are shown. Zacharias'[7] data on $1/E$ for the [100] direction, obtained with a dynamic method of piezoelectric excitation, is also plotted as a cross in Fig. 1.

No remarkable differences are seen among the three sets of data on elastic constants, but elastic anisotropy increases in the order of the data by Honda-Shirakawa, Yamamoto, and Bozorth *et al.* As to the values of Young's and rigidity moduli for a polycrystal, computed with the Voigt method of average, which usually gives values comparatively near to (but always slightly higher than) observed ones,[8] those computed from Yamamoto's data are nearest to, while those from Bozorth's data the farthest from observed values. Further, it is to be noted that the value of the cubic compressibility $\kappa=3/(C_{11}+2C_{12})$ computed from Bozorth's data, 0.526×10^{12} dynes/cm², is considerably lower than the measured value for a polycrystalline nickel (0.535×10^{12} dynes/cm²).

[1] Bozorth, Mason, Skimin, and Walker, Phys. Rev. **75**, 1954 (1949).
[2] K. Honda and Y. Shirakawa, Nippon Kinzoku Gakkai-si, J. Inst. Metals Japan **1**, 217 (1937) (in Japanese and with an English abstract). See also Sci. Rep. Res. Inst. Tohoku Univ. **1**, 9 (1949).
[3] M. Yamamoto, Nippon Kinzoku Gakkai-si, J. Inst. Metals Japan **6**, 331 (1942) (in Japanese and with an English abstract).
[4] P. W. Bridgman, Proc. Am. Acad. **58**, 165 (1923).
[5] J. C. Slater, Phys. Rev. **57**, 744 (1940).
[6] W. Voigt, *Lehrbuch der Kristallphysik*, Appendix II.
[7] J. Zacharias, Phys. Rev. **44**, 116 (1933).
[8] Voigt's method of average is an approximation for a case of small elastic anisotropy of Bruggeman's method which may be regarded as the most accurate one.

The Zenith Angle Variation of the Latitude Effect of Cosmic Rays

H. D. RATHGEBER
Physics Department, University of Melbourne, Australia
December 27, 1949

THE latitude effect of cosmic rays at sea level was measured with three different Geiger counter telescopes on a journey from Sydney (Australia) to Kure (Japan) and back.[1] Two telescopes subtended an angle of 26×33°, of which the first recorded the total radiation and the second the radiation filtered by 10 cm of lead. The third telescope consisting of two closely stacked trays

of Geiger counters subtended practically the whole hemisphere. The following uncorrected latitude effects were obtained; for the first and second, 20±1 percent, for the third telescope 13±1 percent.[1]

The first result exceeds the previous highest result of 15±1 percent obtained by Neher and Pickering,[2] while the third is of the same magnitude as ionization chamber measurements obtained at the same longitude.[3]

As the measurements under consideration were made simultaneously, longitude differences, atmospheric effects, and variations of primary cosmic-ray intensity are excluded. A quantitative calculation of the zenith angle sensitivity of several Geiger counter telescopes and of ionization chambers showed that after correction for seasonal and longitude effects all measurements except one,[4] which falls outside the range covered by the others, satisfy the relation: latitude effect averaged over all azimuths $=0.18\cos^3(1.2\zeta)$ in which ζ is the zenith angle. This is nearly the same zenith angle variation as that of the cosmic-ray intensity at latitudes above the knee. This coincidence appears to be fortuitous since the intensity variation is determined by absorption and decay only, whereas the variation of the latitude effect is mainly produced by deflection in the earth's magnetic field. Considering the uncertainty of the several effects[5] which affect the reduction to the geomagnetic latitude effect, no effort at such a correction is made.

It may be pointed out that the zenith angle variation found confirms the multiple production of mesons by the cosmic-ray primaries. If the whole energy of a primary particle were transferred to a single meson the latitude effect would disappear for a zenith angle at which the energy loss in the atmosphere becomes equal to the magnetic cut-off energy at the equator. The latitude effect would disappear first in the direction of the lowest cut-off energy, i.e., in the western direction. From Vallarta's[6] graphs this cut-off energy, which varies only slowly with zenith angle, is taken as 10 Bev for $\zeta>60°$. Thus, for $\cos\zeta=0.2$ or $\zeta=78.5°$ the latitude effect would disappear in the western direction, for $\zeta=84.5°$ in the north and south directions, and for $\zeta=88°$ in the eastern direction. The result of this calculation does not agree with the relationship which was deduced above from the experimental data; the latitude effect becomes 0.02 for $\zeta=60°$ and disappears practically for $\zeta=70°$.

Taking the latitude effect in the north and south directions as the same as the averaged effect, we may estimate the multiplicity in the energy range concerned. At $\zeta=70°$ the magnetic cut-off energy is 18 Bev and the energy loss 2 Bev/cos70°=6 Bev, i.e., about 18/6=3 mesons are produced on the average by each primary.

A detailed account of the calculation will appear in the *Australian Journal of Scientific Research.*

[1] Law, McKenzie, and Rathgeber, Australian J. Sci. Research **A2**, 495 (1949).
[2] H. V. Neher and W. H. Pickering, Phys. Rev. **53**, 111 (1938).
[3] R. A. Millikan and H. V. Neher, Phys. Rev. **50**, 15 (1936).
[4] Morris, Swann, and Taylor, Phys. Rev. **74**, 1102 (1948).
[5] A. Duperier, Nature **163**, 369 (1949).
[6] M. S. Vallarta, Phys. Rev. **74**, 1837 (1948).

The Internal Diamagnetic Field Correction in Measurements of the Proton Magnetic Moment

NORMAN F. RAMSEY
Harvard University, Cambridge, Massachusetts
December 27, 1949

IN recent high precision experiments[1,2] involving the proton magnetic moment, the internal diamagnetic field correction[3] to the measurements has become an important limitation to the accuracy of the results. This correction arises from the fact that the protons being measured are contained in a molecule, such as H_2, whose electrons to some extent magnetically shield the nucleus so that the magnetic field at the nucleus is not the same as the externally applied field. Approximations to this correction have been made either by using in the H_2 molecule the same correction as would be calculated for a single hydrogen atom[1] or by evaluating with Nordsieck wave functions in H_2 the contribution the electrons would make to the shielding if one could neglect the influence of the internuclear axis in preventing free diamagnetic motion of the electrons when the magnetic field is applied.[2] The latter approximation corresponds to neglecting the analog to the orbital moments' high frequency matrix elements in the theory of molecular diamagnetism.[4] These two methods of estimating the correction yield results which differ by almost a factor of two. An exact theoretical evaluation of the diamagnetic correction has been impossible because the term in the correction which is dependent on the orbital moments' high frequency matrix elements is numerically important and at the same time very difficult to evaluate since it depends on the wave function of the H_2 molecule in its various excited states.

The purpose of the present letter, however, is to point out that this difficult term is directly related to the spin-rotational interaction constant[5,6] of the molecule, which has been experimentally measured in certain cases, notably for H_2. This relationship can be seen by developing the theory for the internal diamagnetic field correction and comparing the results with the spin-rotational interaction theories of Foley and of Wick.[6] However, the results can be seen even more directly by adopting the point of view used once by Wick[7] in discussing rotational magnetic moments. From this point of view it is immediately seen that the internal diamagnetic field correction is a quantity entering directly into the theory of the spin-rotational magnetic interaction of diatomic molecule.

The result obtained from either of the above methods of analysis is that in a $^1\Sigma$-diatomic molecule the internal diamagnetic field $H'(O)$ at the nucleus in the presence of an external field H is given by

$$\frac{H'(O)}{H}=-\frac{e^2}{3\,mc^2}\int\frac{|\psi|^2}{r}d\tau+\frac{1}{6}\alpha^2\frac{a_0a^2}{(\mu_0m/M)}\left\{\frac{2Z(\mu_0m/M)}{a^3}-\frac{\mu}{M}H_p\right\},$$

where a is the internuclear distance in the molecule, μ is the reduced mass of the molecule, μ_0 is the Bohr magneton, M is the proton mass, and H_p is the spin-rotational interaction constant.[5]

The first term in the above has been evaluated by Anderson[3] to be -3.24×10^{-5} while $\mu H_p/M$ has been determined in the experiments of Kellogg, Rabi, Ramsey, and Zacharias with the result that

$$H'(O)/H=[-3.2_4+0.53]\times10^{-5}=-2.7_1\times10^{-5}.$$

[1] E. M. Purcell, Phys. Rev. **76**, 1262 (1949).
[2] H. L. Anderson, Phys. Rev. **76**, 1460 (1949).
[3] W. Lamb, Phys. Rev. **60**, 817 (1941).
[4] J. H. Van Vleck, *Electric and Magnetic Susceptibilities* (Oxford University Press, London, 1932), p. 275.
[5] Kellogg, Rabi, Ramsey, and Zacharias, Phys. Rev. **57**, 691 (1940).
[6] G. C. Wick, Phys. Rev. **73**, 51 (1948).
[7] G. C. Wick, Zeits. f. Physik **85**, 25 (1933).

Concerning W. P. Allis' Criticism of My Paper on Coulomb Interactions in a Plasma

L. LANDAU
Institute for Physical Problems, Academy of Sciences of the USSR, Moscow, USSR
December 2, 1949

IN a note entitled "An error in a paper by Landau on Coulomb interactions in a plasma,"[1] Allis asserts that there is an error in my kinetic equation for the case of Coulomb interaction.[2] However this assertion is a result of a calculational error made by Allis himself. In expanding the collision integral in powers of Δ,

Allis assumes that the first-order terms vanish on integration; this is incorrect because his probability function $w(p-p', \Delta)$ is *not* an even function of Δ's. The principle of detailed balancing gives merely $w(p-p', \Delta)=w(p-p'+2\Delta, -\Delta)$, and using this equality in order to evaluate the first-order terms, one obtains readily my original result.

It is to be noted that the differential kinetic equation must necessarily be of the form of a continuity equation in momentum space due to conservation of the particle number. The fact, that Allis obtains an opposite result is in itself sufficient to prove its incorrectness.

As to Allis' remark at the end of his note, it is based on a misunderstanding. The function w used in my paper is assumed to contain δ-functions which secure the conservation laws; therefore the integrations over p' and Δ can be performed independently.

[1] W. P. Allis, Phys. Rev. **76**, 146 (1949).
[2] L. Landau, Physik. Zeits. Sowjetunion **10**, 154 (1936).

Nuclear Saturation for $V=\frac{1}{2}(1+P)J(r, \sigma_1, \sigma_2)$

E. GERJUOY
Department of Physics, University of Southern California, Los Angeles, California
November 21, 1949

IT has been suggested recently[1] that the interaction between nucleons is of the form $V=\frac{1}{2}(1+P)J(\mathbf{r}, \boldsymbol{\sigma}_1, \boldsymbol{\sigma}_2)$, where P is the space exchange operator. The evidence for an interaction of this sort is the apparent symmetry or near symmetry about 90° of the angular distribution of np scattering and the small value ($\sim$3) of the observed isotropy ratio $R=\sigma(\pi)/\sigma(\pi/2)$, at 90 Mev.[2,3] R remains small ($\sim$6) at 280 Mev.[4] Calculations of the expected angular distribution and total cross section at 90 Mev based on the use of the above interaction V are reported to give results in fair agreement with experiment.[5] The more usual symmetrical, neutral, and "Majorana exchange" theories, using the potentials developed by Rarita and Schwinger[6] to fit the deuteron, are termed "unacceptable."[5] They do not predict symmetry about 90°, nor do they appear to yield the observed values of R and σ.[1,7]

We wish to point out that except for an unlikely possibility, discussed below, the above interaction V will not lead to saturation of heavy nuclei. If non-central forces are excluded, the most general form of V which is zero in odd states is (assuming all forces have the same well)

$$V=(W+MP+BQ+HPQ)J(r) \tag{1}$$

with $W=M$ and $B=H$. Q is the spin exchange operator and $J(r)$ is everywhere positive. In the notation of Rosenfeld,[8]

$$V=(a_0+a_\sigma\boldsymbol{\sigma}_1\cdot\boldsymbol{\sigma}_2+a_\tau\boldsymbol{\tau}_1\cdot\boldsymbol{\tau}_2+a_{\sigma\tau}\boldsymbol{\sigma}_1\cdot\boldsymbol{\sigma}_2\boldsymbol{\tau}_1\cdot\boldsymbol{\tau}_2)J(r) \tag{2}$$

with $a_0=3W/4$, $a_\sigma=B/2-W/4$, $a_\tau=-B/2-W/4$, $a_{\sigma\tau}=-W/4$. $2W+2B=-1$, while the observed value of the ^1S interaction requires $-1<2W-2B<0$. These relations imply $-\frac{1}{2}<W<-\frac{1}{4}$, $W<B$, $B<0$. It follows that (2) is compatible with none of the inequalities[8] required for saturation: $a_0\geqslant 0$, $a_0+a_\sigma\geqslant 0$, $a_0+a_\tau\geqslant 0$. An obvious difficulty of the proposed potential V is that it fails to satisfy the requirement that the ^3P interaction must be a repulsion amounting to at least one-third the magnitude of the ^3S interaction.[8]

Including non-central forces will not materially affect the above argument. In this event a term of the form $V_T=(\gamma/2)(1+P)S_{12}$ is added to (1), where γ is a numerical factor and S_{12} the customary tensor operator.[6] In the isotopic spin formalism $V_T=(\gamma/4)\times(1-\boldsymbol{\tau}_1\cdot\boldsymbol{\tau}_2)S_{12}$. The aforementioned condition $a_0\geqslant 0$ is obtained by considering a heavy nucleus having equal numbers of neutrons and protons and such that for every neutron (proton) state of positive spin direction there is a corresponding neutron (proton) state of negative spin direction.[8] But for such a nucleus V_T averages to zero.[9] Consequently the requirement $a_0\geqslant 0$ remains necessary even when non-central interactions are included. To conclude that saturation is not possible it is necessary only to verify that a_0 remains negative when tensor forces are included. Using the Rarita-Schwinger theory[6] we have now $2W-2B=-(1-2g)$, $2W+2B=-1$, with $g=0.0715$, so that $W=(-1+g)/2=\sim-\frac{1}{2}$, and $a_0<0$. If we abandon the Rarita-Schwinger constants and write simply $2W-2B=-\alpha$, $2W+2B=\beta$, where α is known to be positive from the ^1S interaction, we have $W=(\beta-\alpha)/4$, so that $a_0=3W/4$ is $\geqslant 0$ only if $\beta\geqslant\alpha$. But this means the central force part of the ^3S interaction is a repulsion. It is unlikely, to put it mildly, that such a repulsion could be made consistent with known information. However, this argument does not depend on any assumptions about the range of the tensor interaction, and the writer sees no immediate *proof* that a combination of a ^3S central repulsion and an attractive tensor interaction is not possible.

We may conclude that an interaction of the form $V=\frac{1}{2}(1+P)\times J(\mathbf{r}, \boldsymbol{\sigma}_1, \boldsymbol{\sigma}_2)$ is very difficult to reconcile with the requirement that heavy nuclei be saturated. The most likely inference, if further scattering experiments confirm the necessity for such a V, is that many body forces cannot be neglected in heavy nuclei.

[1] J. Ashkin and T. Wu, Phys. Rev. **73**, 973 (1948).
[2] Hadley, Kelly, Leith, Segrè, Wiegand, and York, Phys. Rev. **75**, 351 (1949).
[3] Brueckner, Hartsough, Hayward, and Powell, Phys. Rev. **75**, 555 (1949).
[4] Kelly, Leith, and Wiegand, Phys. Rev. **76**, 589 (1949).
[5] R. Christian and E. W. Hart, Phys. Rev. **75**, 1465 (1949).
[6] W. Rarita and J. Schwinger, Phys. Rev. **59**, 436 (1941).
[7] F. Rohrlich and J. Eisenstein, Phys. Rev. **75**, 705 (1949).
[8] L. Rosenfeld, *Nuclear Forces* (Interscience Publishers, Inc., New York, 1949), p. 225 ff.
[9] G. W. Volkoff, Phys. Rev. **62**, 134 (1942).

The Half-Life of Br^{82}

E. BERNE
Laboratory for Nuclear Chemistry, Chalmers Institute of Technology, Göteborg, Sweden
December 27, 1949

IN connection with tracer studies using Br^{82} the half-life of this nuclide has been re-examined. Earlier Snell[1] found a value of 33.9±0.1 hr., which is also the value given in the tables of isotopes of Seaborg and Perlman.[2]

Six series of measurement have been performed, where the decay of different bromine samples has been followed over periods of 100 to 150 hr. In five of these series the activity of one sample was measured at different times and the decay constant calculated according to the formula:

$$\lambda=-\ln(10)\Big(\sum_{i=1}^{n}\log I_i-\sum_{i=n+1}^{2n}\log I_i\Big/\sum_{i=1}^{n}t_i-\sum_{i=n+1}^{2n}t_i\Big), \tag{1}$$

where I=activity and t=time after zero-time. The number n was equal to 30 to 40 in the different series. The error in each decay constant arrived at by use of Eq. (1) was estimated from the formula:

$$\Delta\lambda=\Big[\sum_{j=1}^{n}\Delta_j^2/n(n-1)\Big]^{\frac{1}{2}}, \tag{2}$$

where $\Delta_j=|\lambda-\lambda_j|$ and

$$\lambda_j=-\ln(10)\frac{\log I_i-\log I_{i+n}}{t_i-t_{i+n}}.$$

In the last series 40 different bromine samples were prepared and measured twice. The time between the measurements was about 100 hr. A decay constant was calculated for each sample and the mean value of these constants determined.

Values for the half-life have been found and are listed in Table I. The mean value of the half-life is calculated to 36.0±0.1.

TABLE I. Experimental values of half-life of Br^{82}.

Series	Half-life (hr.)
1	36.1±0.1
2	36.5±0.2
3	35.0±0.3
4	35.9±0.2
5	36.7±0.4
6	35.7±0.2

The activities were measured by a G-M tube with a 1.8-mg/cm² mica window using a scale-of-64 amplifier. All measurements were started several days after the end of the irradiation in order to make sure that no Br^{80} activity was present. During every experiment a Pb^{210}(RaD) standard was measured three times an hour and the measured Br^{82} activity corrected for small changes in the counter.

The radio-bromine was prepared by irradiation of NH_4Br in the pile of the AERE, Harwell, England.

This work was performed under the auspices of Atomkommittén, Stockholm.

[1] A. H. Snell, Phys. Rev. **52**, 1007 (1937).
[2] G. T. Seaborg and I. Perlman, Rev. Mod. Phys. **20**, 585 (1949).

Spectroscopic Isotope Shift and Nuclear Polarization

G. BREIT, G. B. ARFKEN, AND W. W. CLENDENIN
Yale University, New Haven, Connecticut*
December 27, 1949

RELATIVE isotope displacements of spectroscopic terms of the heavier elements are known[1] to be approximately explicable by the nuclear volume effect theory. Observed shifts have been related, therefore, to changes in nuclear radii expected on the $A^{\frac{1}{3}}$ basis. Calculation indicates, however, that while it may be legitimate to replace the action of the nucleus by an effective central field in an approximation, the relative isotope displacements need not be simply related to the uniform changes in nuclear radii expected from the $A^{\frac{1}{3}}$ formula. The smallness of the fractional change in nuclear radius (1/600) between neighboring isotopes necessitates the consideration of differences in polarizability of nuclei by electrons. The occurrence of many low lying levels for odd isotopes of even elements[2] as well as theories of nuclear binding indicate a greater polarizability of such nuclei as compared with those of the even isotopes. The correspondingly greater effective attraction of the electron fits qualitatively the staggered position of Pb^{207} between Pb^{206} and Pb^{208}, and similar effects for Hg^{199}, Hg^{201}, Pt^{117}, Sm^{147}, Sm^{149}.

The probable bearing of the expected polarizability on observation is indicated by calculations making use of non-diagonal matrix elements, V, of the electrostatic energy of nuclear particles in the electron's field. The considerations are relativistic for the electron only. Three calculations have been carried through. In the first, V is approximated by a constant inside the nucleus and by zero outside. The coupled equations for the electron wave functions corresponding to the normal and excited condition of the nucleus are solved and an approximate value of $|V|=1.6$ in units mc^2 is found to make the polarization effect equal to about one-half of the nuclear volume effect. This calculation does not consider the Pauli exclusion principle. It shows that second-order perturbation theory is good enough.

In the second calculation perturbation theory is used, the exclusion principle is satisfied, the potential inside the nucleus is reproduced but the Coulomb field outside is neglected. The required $|V|$ is ~1.7 and important contributions arise from electronic excitations of ~50. In the third calculation the Coulomb field outside is taken into account, deviations from it inside are neglected, comparisons with the isotope shift are made on a relative basis. The main contributions are shifted to lower energies so that $|V|=3.8$ from E (electron)$=2$ to 10 and a nuclear level at 0.4 (200) kev account for the odd-even staggering.

The $|V|$ required for staggering are too large for a single proton central field nuclear model with monopole action; they come within range for alpha-particles with non-central field approximations to nuclear wave functions. Interaction of $s_{\frac{1}{2}}$ electrons with the p continuum and of $p_{\frac{1}{2}}$ electrons with the s continuum through dipole action of an α-particle is comparable with experimental indication.

The polarization of the nucleus may perhaps be responsible also for the smallness of the observed shifts and some of the irregularities for even isotopes. There may be other reasons for this effect but this appears to be one of them.

* Assisted by the Joint Program of the ONR and AEC.
[1] Experiment and theory summarized by H. Kopfermann, *Kernmomente* (Akademische Verlagsgesellschaft, Leipzig, 1940); and M. F. Crawford and A. L. Shawlow, Phys. Rev. **76**, 1310 (1949).
[2] Data of A. C. G. Mitchell (private communication).

Phase Transition and Vapor Pressures of Liquid Mixtures of He^4 and He^3

C. J. GORTER
Kamerlingh Onnes Laboratory, University of Leiden, Holland
AND
J. DE BOER
Institute for Theoretical Physics, University of Amsterdam, Holland
December 27, 1949

IN a recent Letter to the Editor[1] the liquid mixtures of He^4 and He^3 were treated by the methods of statistical thermodynamics, in accordance with Taconis' hypothesis,[2] starting from the Gibbs' function for an ideal mixture of He^3 and the normal component of He^4. In accordance with this procedure it was assumed that the internal properties of He^4, in particular the fraction (x) of He^4 which is "normal," are not functions of the concentration (X) of He^3. As was stressed recently by the first of the present authors at the M.I.T. Conference on very low temperatures,[3] it is reasonable to assume that at each temperature T and concentration X the value of the normal fraction of He^4 is adjusted to a new value which makes the total Gibbs' function of the mixture a minimum, and which will be higher than the value $x_0(T)$ at the same temperature and at concentration $X=0$. The physical consequences of both assumptions have been worked out and are compared in detail in a paper which is in press for the journal *Physica*.

The Gibbs' function is assumed to be the same in form as the expression given in reference 1:

$$G(T,X;x)=(1-X)G_4(T;x)+XG_3(T)+RT\cdot(X/X_e)\cdot[X_e\ln X_e+(1-X_e)\ln(1-X_e)], \quad (1)$$

where X_e is the effective concentration, $X/[x(1-X)+X]$, and x is the fraction of He^4 which is normal, being equal to $x_0(T)$ in pure He^4.

If $x=x_0(T)$, independently of concentration, the transition in the liquid mixture is a *first-order transition*,[1] with a splitting into two phases with an effective concentration X_e. If, on the contrary, $x(T,X)$ is determined at each T and X by the condition $[dG(T,X;x)/dx]_{T,X}=0$, the equation $x(T,X)=1$ determines the lambda-point $T_{\lambda X}$ at each concentration X, the transition now being a *transition of the second order* at all concentrations. Using a simple function for $G_4(T;x)$ [leading to Tisza's formula $x=S/S_\lambda=(T/T_\lambda)^6$], the equation for the lambda-point, $T_{\lambda X}$, at concentration X is

$$1-X=\exp[(S_\lambda/R)(1-T_\lambda/T_{\lambda X})]. \quad (2)$$

The partial vapor pressures p_3 and p_4 of He^3 and He^4 are given

in both cases, *below* the transition point by the formulas

$$p_3 = p_3^0 \cdot X_s, \tag{3}$$

$$p_4 = p_4^0 \cdot (1-X_s)^x \cdot \exp[G_4(T;x) - G_4(T;x_0)] \tag{4}$$

and *above* the transition point by the formulas

$$p_3 = p_3^0 X, \tag{5}$$

$$p_4 = p_4^0 \cdot (1-X) \cdot \exp[G_4(T;1) - G_4(T;x_0)] = p_4^{0\prime} \cdot (1-X). \tag{6}$$

In these formulas p_3^0 and p_4^0 are the vapor pressures of pure He^3 and He^4, and $p_4^{0\prime}$, for temperatures *below* the lambda-point of *pure* He^4, is the *extrapolated* vapor pressure of the phase *II*. When x is supposed to be independent of the concentration, X, one must substitute in (3) and (4) the relation $x=x_0(T)$, but when x is supposed to change with X one must substitute $x=x(T,X)$ as determined from the condition $dG/dx=0$ at constant values of T and X. For very small concentrations in both cases the vapor pressures become

$$p_3 = p_3^0 \cdot X/x, \quad p_4 = p_4^0. \tag{7}$$

[1] J. de Boer, Phys. Rev. **72**, 852 (1949).
[2] Taconis, Beenakker, Nier, and Aldrich, Physica **15**, 733 (1949).
[3] Communication at the M.I.T. Conference (September 6–10, 1949).

Regularization as a Consequence of Higher Order Equations

W. THIRRING
Dublin Institute for Advanced Studies, Dublin, Ireland
December 19, 1949

WE consider any invariant differential equation in space-time of finite order $2n$ and write it in the factorized form:

$$\prod_{i=1}^{n}(\Box^2 - m_i^2)\phi(x) = 0. \tag{1}$$

For simplicity we assume $\phi(x)$ to be a scalar field. The Green function of (1) which satisfies

$$\prod_i(\Box^2 - m_i^2)\bar{D}(x) = -\delta(x) \tag{2}$$

is given by:

$$\bar{D}(x) = \frac{(-1)^{n-1}}{(2\pi)^4}\int e^{ikx}\prod_i(k^2+m_i^2)^{-1}d^4k. \tag{3}$$

For quantization of ϕ we need the commutator function

$$D(x-x') = \frac{1}{i}[\phi(x), \phi^*(x')],$$

which is an odd invariant function obeying (1). This determines it to be

$$D(x) = -\frac{i(-1)^{n-1}}{(2\pi)^3}\int e^{ikx}\delta[\prod_i(k^2+m_i^2)]\epsilon(k)dk \tag{4}$$

(in Schwinger's notation), the numerical factor we get from the relation

$$\bar{D}(x) = -\tfrac{1}{2}D(x)\epsilon(x). \tag{5}$$

Developing the δ-function

$$\delta[\prod_i(k^2+m_i^2)] = \sum_i \frac{\delta(k^2+m_i^2)}{\prod_{j\neq i}(m_j^2-m_i^2)}$$

and the denominator

$$\prod_i(k^2+m_i^2)^{-1} = \sum_i(k^2+m_i^2)^{-1}\prod_{j\neq 1}(m_j^2-m_i^2)^{-1},$$

we obtain

$$D = c_i D_{m_i}; \quad \bar{D} = c_i \bar{D}_{m_i}; \quad c_i = \prod_{j\neq 1}(m_j^2-m_i^2)^{-1}(-1)^{n-1}. \tag{6}$$

D is a sum of ordinary D functions with different masses, the coefficients obey the following conditions:

$$\sum c_i = 0, \quad \sum_i c_i \sum_{j\neq i} m_j^3 = 0 \cdots \sum_i c_i \prod_{j\neq i} m_j^2 = (-1)^{n-1}. \tag{7}$$

Using (6), (7), and the well-known property of $\bar{D}_m$, we can again prove (2); (1) for D is trivial after (6).

The first condition of (7) is Pauli's regularization condition which cancels the δ-singularity of the D function. For more than one mass there cannot be a δ-singularity in D, as (4) is then a convergent integral. Corresponding to the regularization method there is a fourth-order equation sufficient to make the self-energy of the nucleus finite, if we use ϕ as the meson field, as (using the corresponding Feynmann's function)

$$\int \frac{\gamma_5[\gamma_i(p_i-k_i)-m]\gamma_5 d^4k}{[k^2+\mu_1^2][k^2+\mu_2^2][(p-k)^2+m^2]}$$

is a convergent integral. This shows that the equations of Podolsky, Bhabha, Born, and Green, etc., if quantized, lead automatically to regularization and give a simpler model of subtracting fields than the otherwise *ad hoc* assumed one.

The Photo-Disintegration of Nitrogen at Energies of 20 Mev to 100 Mev

E. R. GAERTTNER AND M. L. YEATER
Research Laboratory, General Electric Company, Schenectady, New York
December 30, 1949

THE photo-disintegration of several gaseous elements by x-rays from the 100-Mev betatron[1] is being studied in a cloud chamber, and the relative abundance of various modes of nuclear disintegration directly compared. The data obtained so far include about 5000 nuclear disintegrations in nitrogen. The energy dependence of some of these events is discussed in this note.

The cloud chamber[2] developed by the authors is suited for this type of investigation because it can be operated directly in a high energy x-ray beam of relatively strong intensity owing to its good clean-up characteristics,[3] and operation of the chamber at the rate of an expansion every five seconds permits the accumulation of adequate data in a relatively short time. The betatron is adjusted for an intensity level near its maximum output and is pulsed in synchronism with the cloud chamber. The x-ray beam, defined by thick sections of lead, is $\frac{1}{8}$ in.$\times\frac{3}{4}$ in. in cross section, and enters the cloud chamber through a thin Lucite window.

The disintegrations observed in the cloud chamber are classified according to the number of visible tracks as follows: (1) "Singles," heavily ionizing tracks of short range (<1 cm). (2) "Flags," consisting of two charged members, one of which is short and heavily ionizing. (3) "Stars," with three to six charged members; as the multiplicity of the star increases there is an increasing probability that one member will be too short to be visible. The total number of flags and stars, and their ratios, are given in Table I for peak betatron energies from 20 to 100 Mev.

The relative yield of flags at peak betatron energies of 50 and 100 Mev has been obtained by normalizing some of the data as follows: The 10-minute beta-activity induced in thin copper samples placed in the x-ray beam is taken as a monitor of the beam intensity in the energy range of the betatron spectrum near 25 Mev.[4] Since it is difficult to build up this activity with x-ray pulses coming only once in five seconds, a Victoreen r-thimble is used to measure the relative integrated intensity for each cloud-chamber run. A separate run at the same energy, with the betatron operating at 60 pulses per second, provides excitation for the copper sample, the integrated intensity again being measured with an r-thimble. The Cu^{62} activity corresponding to the integrated x-ray intensity for the cloud-chamber run is derived from these readings. The ratio of flags to copper activity at 50 and 100 Mev gives the relative yield at these peak energies. The results are shown in Table II; the estimated accuracy of each ratio is ten percent.

The ratio of flags to singles has been measured for a portion of the data taken at 100 Mev, for gas pressures of one-half and one

TABLE I. Nuclear disintegrations observed in nitrogen at various peak x-ray energies. These data show the relative abundance of the various types of stars observed at different energies, but are not normalized to yield excitation curves for any one type.

Peak energy	Number of observed tracks per disintegration 2	3	4	5	Stars / Flags
20 Mev	6	0	0	0	0
25	40	0	1	0	0.02
30	125	4	1	0	0.04
40	493	57	20	0	0.16
50	517	79	40	0	0.23
60	147	29	24	0	0.36
70	197	44	22	0	0.34
100	2346	469	296	17	0.33

TABLE II. Yield of flags in nitrogen at peak energies of 50 and 100 Mev relative to the beta-activity (Cu^{62}) induced in Cu samples irradiated by x-rays of the corresponding peak energy and of the same relative intensity.

Peak energy	No. of flags	No. of flags / Copper activity
50 Mev	191	1.00
100	212	0.89

atmosphere. The lower pressure is used to check the possible loss of the shortest singles. The ratio is 4.0, based on a total count of 442 singles and 1623 flags; the same ratio is obtained for both pressures. This result includes a correction for some singles caused by neutron induced reactions,[5] particularly $N^{14}(n, p)C^{14}$.

From the data of Table I and Table II we note the following: (1) The most numerous events are the flags, which according to a preliminary analysis appear to be mostly (γ, pn) disintegrations. The singles, representing (γ, n) disintegrations, comprise only about 16 percent of the events at 100-Mev peak energy. (2) There is no appreciable production of flags by x-rays with energy between 50 and 100 Mev. An approximate normalization of the data taken with a peak x-ray energy of 20 Mev indicates the yield below 20 Mev to be about 5 percent of that with 50-Mev peak energy. (3) There is a significant increase in the ratio of three and four prong stars to flags up to 60 Mev.

We wish to express our appreciation to the betatron operators, Mr. E. L. Martin and Mr. J. McNamara. We are indebted to Dr. G. C. Baldwin and Mr. C. E. Pickert for the use of counting equipment and assistance in the counting of the Cu^{62} activities used to normalize our data at various energies. The cloud-chamber equipment used in this investigation was developed under Contract N7 onr 332 with the ONR.

[1] Some disintegrations caused by radiation from the 100-Mev betatron have been observed in a cloud chamber by G. C. Baldwin and G. S. Klaiber, Phys. Rev. **70**, 259 (1946).
[2] E. R. Gaerttner and M. L. Yeater, Rev. Sci. Inst. **20**, 588 (1949).
[3] Additional discrimination against the electron background is obtained through the use of a short growth time for the tracks.
[4] The $Cu^{63}(\gamma, n)Cu^{62}$ cross section reaches its maximum value at 24 Mev. See G. C. Baldwin and G. S. Klaiber, Phys. Rev. **73**, 1156 (1948).
[5] A correction has been made for these on the basis of their distribution in and out of the beam in the cloud chamber and the intensity of the neutron background as measured in a study of proton recoils observed when the cloud chamber was filled with hydrogen. The number of flags and stars produced by neutrons is negligible.

Erratum: Microwave Spectrum of CH_2CFCl

[Phys. Rev. **77**, 148 (1950)]

J. K. BRAGG, T. C. MADISON, AND A. H. SHARBAUGH
Research Laboratory, General Electric Company, Schenectady, New York

FIGURE 1 of this Letter to the Editor was unfortunately misplaced, and appears on page 152 (January 1, 1950) of this volume.

Erratum: Non-Linear I-V Characteristic of Ge at Very Low Temperatures

[Phys. Rev. **77**, 152 (1950)]

F. K. DU PRÉ
Philips Laboratories, Inc., Irvington-on-Hudson, New York

FIGURE 1 of this Letter to the Editor was unfortunately misplaced, and appears on page 148 (January 1, 1950) of this volume.

Proceedings of the American Physical Society

MINUTES OF THE MEETING OF THE DIVISION OF FLUID DYNAMICS AT THE UNIVERSITY OF VIRGINIA, CHARLOTTESVILLE, VIRGINIA, DECEMBER 28–30, 1949

THE fourth meeting of the Division of Fluid Dynamics was considered a great success by more than a hundred members who attended the three-day session at the University of Virginia. A program, which emphasized the field of "Irreversible Processes in Fluid Dynamics," was arranged by a committee under the chairmanship of J. O. Hirschfelder. Local arrangements and accommodations were provided by a committee under J. W. Beams. Four symposia, two sessions of contributed papers, and two evening lectures comprised the program.

WALKER BLEAKNEY, *Secretary*
Division of Fluid Dynamics
Princeton University
Princeton, New Jersey

Symposium on Fluid Flow

The Thickness of the Transition Region in a Shock Front. DONALD F. HORNIG, *Brown University.*
Relaxation Theories of Viscous and Plastic Flows. HENRY EYRING, *University of Utah.*
Preliminary Study of a Converging Shock Wave. ARTHUR R. KANTROWITZ AND ROBERT W. PERRY, *Cornell University.*

Symposium on Energy and Entropy Changes

Entropy Changes in Fluid Flow. CHARLES F. CURTISS, *University of Wisconsin.*
Maxwell's Demon Cannot Do It—Information and Entropy. L. BRILLOUIN, *Columbia University.*
On the Heat Flux Vector in Moderately Rarefied Gases. C. A. TRUESDELL, *Naval Research Laboratory.*
Interchange of Translational and Vibrational Energy in an Asymmetric Molecular Potential Field. H. M. HULBURT, *Catholic University of America.*

Symposium on Non-Equilibrium Statistical Mechanics

The Relation of the Macroscopic to Molecular Viewpoint in Non-Equilibrium Processes. K. F. HERZFELD, *Catholic University of America.*
Recent Advances in Non-Equilibrium Statistical Mechanics. ELLIOTT W. MONTROLL, *Office of Naval Research.*
The General Theory of Irreversible Processes. JOHN M. RICHARDSON, *Central Experiment Station, Bureau of Mines.*

Symposium on the Theory of Flames

Stability and Transport Characteristics of Flames. BRUCE L. HICKS, *Ballistic Research Laboratories.*
Thermo Reaction Propagation in Flames. HOWARD W. EMMONS, *Harvard University.*
Combustion in Long Closed Tubes at Low Pressure. LELAND B. SNODDY, E. E. HACKMAN, AND J. W. BEAMS, *University of Virginia.*

Evening Lectures

Rockets and Ram Jets. R. E. GIBSON, *Johns Hopkins University.*
Problems in Newer Fields in Fluid Mechanics. JOHN W. BECKER, *Langley Field, Virginia.*

Contributed Papers

1. On the Three-Shock Configuration.* G. RAWLING AND H. POLACHEK, *Naval Ordnance Laboratory, White Oak, Silver Spring 19, Maryland.* (Introduced by F. N. Frenkiel.)—An initial report of investigations of three-shock configuration is presented. The numerical values for isopycnals and isobars are graphed for various strengths of shock wave on the basis of theoretical results of Bargmann.** In particular, the effects of increasing strength of the shock wave on density and on pressure are discussed. Experimental three-shock configurations are illustrated by interferograms and schlieren pictures obtained in the wind tunnel and in the shock tube.

* Under the sponsorship of the ONR.
** V. Bargmann, "On the nearly glancing reflection of shocks," National Defense Research Committee AMP Report 108.2 R (March, 1945).

2. Vibrational Relaxation Times in Polyatomic Gases. R. N. SCHWARTZ, *Naval Ordnance Laboratory, White Oak, Silver Spring, Maryland.*—The method of Zener[1] is extended to treat collisions between molecules with s internal degrees of freedom. Using a one-dimensional model and approximating

the field between two colliding molecules by an exponential, one may write the probability of simultaneously exciting the x-internal coordinate of either molecule from the n_1th to the t_i vibrational state, the x_2-internal coordinate from the n_2th state, etc., while the relative velocity of the molecules change by ΔV, in the form

$$p_{t_1\cdots t_s}^{m_1\cdots m_s} = [V_{t_i}^{n_1}(x_1)\cdots V_{t_s}^{n_s}(x_s)R(\Delta V)]^2.$$

This conceptually simple result is applied (a) to experimentally available data on the effect of foreign gases on relaxation times, and (b) to the question of the possibility of detecting more than one relaxation time in certain polyatomic gases.

[1] C. Zener, Phys. Rev. **37**, 357 (1931).

3. A Modification of the Theory of Kinetics of Condensation and Its Application to Air Condensation in Hypersonic Wind Tunnels. H. GUYFORD STEVER, *Massachusetts Institute of Technology.*—The relationships describing the kinetics of condensation of a vapor involve the liquid phase surface energy as an important property. Generally this surface energy is assumed dependent on temperature but independent of the surface curvature of the liquid phase. In condensation phenomena, the nuclei of condensation often have such small radii of curvature that the surface energy cannot be considered independent of surface curvature. In a project sponsored by the National Advisory Committee for Aeronautics to investigate the possibilities of air condensing in hypersonic wind tunnels, the theory of condensation has been modified to incorporate this surface curvature dependence. The results show that extremely high supersaturation ratios, much higher than predicted by the unmodified theory, can be obtained without getting appreciable condensation rates. The modified theory was applied to nitrogen and oxygen, with results indicating that air condensation should not occur in present hypersonic wind tunnels (stagnation pressures up to 150 atmos., stagnation temperatures down to 240° K) unless higher stagnation pressures or lower stagnation temperatures are used.

4. Dissipation of a Shock Traveling in a Tube.* R. J. EMRICH AND C. W. CURTIS, *Lehigh University.*—The measured strength of a shock produced in a shock tube is always somewhat smaller than predicted by the usual theory which ignores all dissipative effects except those within the shock front itself. Since the measuring station is some distance from the diaphragm, the decrease in strength (and velocity) during travel along the tube has been investigated as a possible explanation of this discrepancy. Using timing techniques similar to those previously described,[1] velocity loss measurements have been carried out in a tube of 3.5-cm diameter for shocks ranging in Mach number from 1.04 to 1.35. The losses in this tube were greater than those in a 15-cm tube by about the inverse ratio of the diameters; the losses in both tubes were considerably larger than predicted by a laminar flow theory attributing dissipation to the effect of wall friction.[2] The measured losses are sufficient to account for a large part of the discrepancy between experimental and predicted shock strengths.

* This work was supported by the ONR under contract N7 onr-39302.
[1] R. J. Emrich and F. B. Harrison, Phys. Rev. **73**, 1255 (1948).
[2] C. duP. Donaldson and R. D. Sullivan, N.A.C.A. Tech. Note 1942 (1949).

5. Some Circular Schlieren Pictures of Shock Wave Reflections.* EDWARD M. LITTLE, *University of Maryland.*—With circular schlieren the change in illumination on the photographic plate is independent of the direction of the gradient of the fluid density. This is valuable here as many shock directions occur in the same picture. A calibrating schlieren lens is in one corner of each picture. This shock tube has a special reflector with its leading edge always exactly in one face of the shock tube, thus eliminating spurious reflections from the underside of the leading edge. The pictures obtained are under conditions varying continuously from diffraction (reflector 13° below sidewall) through "Bargmann?" reflection and Mach reflection to regular reflection (reflector 40° above sidewall). The shock "weakness" varies from 0.77 to 0.86 (weak shocks). The reflected rarefaction from the leading edge is clearly visible in the case of regular reflection. In the cases where it overtakes the shock intersection (some regular reflection and all Mach reflections) there is seen a non-uniform-density region behind the shock intersection as discovered by Bleakney with the interferometer. It also causes a bending backward of the Mach shock at the "triple point" (besides the usual steady-state effect). It also bends back the shock in the diffraction cases.

* This work was performed at the Naval Ordnance Laboratory at White Oak, Silver Spring, Maryland, and is unclassified.

6. Virtual Mass of a Sphere Entering Water Vertically.* ALBERT MAY AND JEAN C. WOODHULL, *Naval Ordnance Laboratory, White Oak, Silver Spring, Maryland.*—The accelerated underwater motion of a body is affected by the "apparent additional" mass of water which shares the acceleration. The adaptability of the concept of virtual mass to water-entry has been discussed frequently and reported in literature under security restrictions, always assuming no variation of drag coefficient with speed or depth of sphere. The authors have determined virtual mass by comparing vertical entry drag forces of half-inch tungsten and steel spheres with others of dural, magnesium and polystyrene, a density range of 16 to 1. Instantaneous C_D values were found at the same speed and depth. Surface-closure of the entry cavities was prevented by using reduced air pressure above the water. This removes the effect of cavity pressure but changes the flow pattern slightly. Compared with previous, roughly estimated added-mass values of about 0.45 that of the displaced water, the authors obtain values less than 0.2; actually, values range from zero to 0.16, near the limit of accuracy. The virtual-mass concept is apparently unimportant for water-entry work over the range investigated.

* Supported by the ONR, Fluid Dynamics Branch (Project NR-062-024).

7. Oscillations of a Cable in a Stream. A. E. SEIGEL, *Naval Ordnance Laboratory, White Oak, Silver Spring, Maryland.* (Introduced by A. May.)—In the flow of a fluid past a straight flexible cylindrical cable an alternating side force perpendicular to the flow velocity is exerted on the cable; this force is a result of the shedding of vortices alternately from side to side of the cylinder. The ratio of the side force to the drag force is a function of Reynolds number only. From experimental results and theoretical considerations the function is completely determined for Reynolds numbers in the range of 20 to 0.5×10^6. The periodic side force tends to vibrate the cable. The partial differential equation of motion which includes the inertia force of the cable, the fluid damping force, and the cable tension force, as well as the side force, is solved. The amplitude of cable vibration is obtained with special attention to resonance conditions.

8. Photographic Observations of Air Flow around Moving Bodies at Mach Numbers up to 9.6. P. A. THURSTON, *Naval Ordnance Laboratory, White Oak, Silver Spring, Maryland.* (Introduced by J. H. McMillen.)—Observations of the flow around projectiles at extremely high Mach numbers have been made by firing bullets at high velocities into gases at reduced temperatures. Both standard and special small bore projectiles moving at speeds up to 7000 ft. per sec. in air and

nitrogen at temperatures down to 120° K were observed by means of spark shadowgraphs. The spark system used coaxial cable energy storage as originally proposed by Beams, and gave an effective light duration of about 10^{-7} sec. From the observed configurations of shock wave and wake, the wave drag and base drag have been calculated, and typical results are presented.

9. Density Measurements in Supersonic Flow by an X-Ray Technique.* EVA WINKLER, *Naval Ordnance Laboratory, White Oak, Silver Spring, Maryland.* (Introduced by R. J. Seeger.)—Air density measurements have been made in the free stream of a supersonic flow by means of the x-ray absorption method. The measurements were made at a Mach number of 2.83 in the NOL 18×18 cm wind tunnel. Excellent agreement has been found with Pitot tube measurements of the same nozzle. The accuracy of the present equipment is limited, for this Mach number, to 5.5 percent. The equipment consists of a Machlett AEG-50 x-ray tube having a beryllium window and two G-M counters one of which measures the initial x-ray intensity for comparison. The results and the general arrangement of the equipment at the wind tunnel will be described.

* Sponsored by the ONR.

10. A Simple Interferometric Test for Conical Flow. J. H. GIESE, F. D. BENNETT, AND V. E. BERGDOLT.—In conical flows the velocity components, pressure, and density do not vary on lines through the vertex of the cone. In this paper it is shown that for interferograms of general conical flows $\delta(y, z)/z = f(y/z)$, where y and z are any set of Cartesian coordinates with origin at the image of the vertex of the cone, and δ is the fringe shift at y, z. Thus, for strictly conical flow, a graph of $\delta(y, z)/z$ *versus* y/z should be a single curve. This suggests a test for approximate conicity that requires very little computation. This test is applied to interferograms obtained from a number of approximately axisymmetric flows at various Mach numbers about cone-cylinders in free flight. Plotted fringe shift data from the region near the nose fall into a narrow band, an indication of approximate conicity. They also closely check the corresponding theoretical fringe shift curve calculated for Taylor-Maccoll flow.

11. On Turbulent Jet Mixing in Two-Dimensional Supersonic Flow. D. BERSHADER AND S. I. PAI, *Institute for Fluid Dynamics and Applied Mathematics, University of Maryland.*—Distributions of mean density in several sections of the mixing region of a rectangular, uniform, fully expanded jet of Mach number 1.7, discharging into the atmosphere, have been calculated from measurements made with the Mach-Zehnder interferometer.* The results thus obtained have been compared with predicted density distributions, calculated by use of a theory somewhat modified from that developed by the second author,[1] which makes use of Reichardt's theory of free turbulence. The theory involves as an unknown parameter the coefficient of eddy kinematic viscosity ϵ, whose value is to be determined from experimental results. Under the present experimental conditions ϵ is assumed constant, corresponding to the assumption of the similarity of the velocity profile over various sections. The value of ϵ which gives best agreement with experiment is $\epsilon = 164$ cm²/sec., over 1000 times the value of the coefficient of laminar kinematic viscosity. The existence of a 1-mm boundary layer[2] at the exit of the nozzle differs from the assumption used in the theory of a zero-thickness mixing region at this point. However, the experimental and theoretical curves fall very close together, except at the ends, if the former curve is plotted using a line 0.16 mm in from the nozzle wall as the axis $y=0$ (y is the coordinate perpendicular to flow). The theoretical density distribution has also been calculated for the laminar case.

* The experimental data used herein was obtained by the first author in research performed with R. Ladenburg at Princeton University.

[1] S. I. Pai, "Two-dimensional jet mixing of a compressible fluid," J. Aero. Sci. 16, 463 (August, 1949).

[2] D. Bershader, "An interferometric study of supersonic channel flow," Rev. Sci. Inst. 20, 260–275 (1949).

12. On the One-Dimensional Theory of Flame Structure. RAYMOND FRIEDMAN AND EDWARD BURKE, *Westinghouse Research Laboratories.* (Introduced by R. C. Mason.)—The variations of temperature and concentration throughout a premixed gas flame are calculated from the fundamental equations in terms of the burning velocity, the reaction zone thickness, the thermal diffusivity, the diffusion coefficient, the heat release pattern, and the rate of formation pattern of a particular species. Four arbitrary patterns are treated. The magnitude of the error introduced by assuming transport coefficients to be independent of temperature is computed. The influence of cylindrical flame curvature is treated. The Mach number is shown to be a pertinent variable in deflagration. Certain experimental data are analyzed in the light of the relations given herein. This is not a new theory of burning velocity, but rather an exposition of the necessary relations which hold between the pertinent variables by virtue of the conservation of matter and energy.

13. Investigation of Turbulent Flames.* BELA KARLOVITZ,** *Bureau of Mines.* (Introduced by Bernard Lewis.)—An extensive study of turbulent flame phenomena was undertaken in order to find a basic understanding of the effect of turbulence, especially of large-scale turbulence, on flame propagation. Bunsen-type turbulent flames were produced under controlled, variable experimental conditions, with flow velocities ranging up to 50 meters per sec., Reynolds numbers up to 100,000, and burner-tube diameters from $\frac{5}{8}$ in. to 2 in. Instantaneous shadow photographs of the flames confirmed the results of previous investigators, according to which the main effect of the large-scale turbulence consists in the random displacement of small portions of the combustion wave. Starting from this observation, a theory of turbulent flame propagation was developed. The theory explains the mechanism of turbulent flame propagation and the peculiar shape of the flame surface and permits calculation of the turbulent burning velocity from known values of turbulence intensity and normal burning velocity. To test this theory, a program for the measurement of the intensity and scale of turbulence was initiated, and a method was developed for accurate measurement of the turbulent burning velocity. The measurements are in progress; data obtained up to date will be presented.

* This research is part of the work being done at the Bureau of Mines on Project No. NA onr 25–47, supported by the ONR and the Army Air Forces.

** Physicist, Physical Chemistry and Physics Section, Explosives Branch, Bureau of Mines, Pittsburgh, Pennsylvania.